17

The Loma Prieta, California, Earthquake of October 17, 1989—Main-Shock Characteristics

PAUL SPUDICH, *Editor*

EARTHQUAKE OCCURRENCE
WILLIAM H. BAKUN and WILLIAM H. PRESCOTT, *Coordinators*

U.S. GEOLOGICAL SURVEY PROFESSIONAL PAPER 1550-A

U.S. DEPARTMENT OF THE INTERIOR
MARCH 3, 1849

UNITED STATES GOVERNMENT PRINTING OFFICE, WASHINGTON : 1996

DEPARTMENT OF THE INTERIOR

BRUCE BABBITT, *Secretary*

U.S. GEOLOGICAL SURVEY

Gordon P. Eaton, *Director*

Manuscript approved for publication, July 13, 1995

Text and illustrations edited by George A. Havach

Library of Congress catalog-card No. 92–32287

For sale by the
U.S. Geological Survey
Information Services
Box 25286
Denver Federal Center
Denver, CO 80225

CONTENTS

THE LOMA PRIETA, CALIFORNIA, EARTHQUAKE OF OCTOBER 17, 1989: EARTHQUAKE OCCURRENCE

MAIN-SHOCK CHARACTERISTICS

SYNOPSIS

By Paul Spudich,
U.S. Geological Survey

CONTENTS

SUMMARY OF SOURCE CHARACTERISTICS

The October 17, 1989, Loma Prieta, Calif., earthquake (0004:15.2 G.m.t. October 18; lat 37.036° N., long 121.883° W.; 19-km depth) had a local magnitude (M_L) of about 6.7, a surface-wave magnitude (M_S) of 7.1, a seismic moment of 2.2×10^{19} N-m to 3.5×10^{19} N-m, a source duration of 6 to 15 s, and an average stress drop of at least 50 bars. Slip occurred on a dipping fault surface about 35 km long and was largely confined to a depth of about 7 to 20 km. The slip vector had a large vertical component, and slip was distributed in two main regions situated northwest and southeast of the hypocenter. This slip distribution caused about half of the earthquake's energy to be focused toward the urbanized San Francisco Bay region, while the other half was focused toward the southeast. Had the rupture initiated at the southeast end of the aftershock zone, shaking in the bay region would have been both longer and stronger. These source parameters suggest that the earthquake was not a typical shallow San Andreas-type event but a deeper event on a different fault with a recurrence interval of many hundreds of years. Therefore, the potential for a damaging shallow event on the San Andreas fault in the Santa Cruz Mountains may still exist.

INTRODUCTION

The source mechanism of the earthquake is one of the best determinations ever obtained, owing to the epicenter's location within a region with good geodetic control and numerous strong-motion accelerometers. In addition, the earthquake was large enough to be well recorded by globally distributed seismometers, though not so large as to clip on many global stations. Thus, we have been afforded an unusual opportunity to study earthquake-source mechanics and to cross-calibrate the source parameters (such as earthquake magnitude, seismic moment, fault location and extent, slip distribution, and associated stress change) determined by inversion of local geodetic data, teleseismic long-period surface waves and body waves, regional surface waves, and local strong-motion accelerations.

The papers in this chapter address and attempt to resolve questions raised in earlier initial analyses of the earthquake. Many of these initial analyses were published in the July, August, and September 1990 issues of *Geophysical Research Letters* and in the October 1991 issue of the *Bulletin of the Seismological Society of America*. Although this introduction does not pretend to be a comprehensive review of the source process of the earthquake, I attempt to summarize the main findings of this chapter and place them in the context of previously unresolved questions.

Several papers in this chapter document original data collection in greater detail than previously presented elsewhere. Lisowski documents and corrects the geodetic data set in the epicentral region previously analyzed by Lisowski and others (1990), which consists of position measurements using the Global Positioning System (GPS), distance measurements using a laser Geodolite, and position changes measured using very long baseline interferometry. Marshall and Stein document the elevation differences observed in the epicentral region and used by Marshall and others (1991). Williams and Segall document an important new geodetic data set; they found that the California Department of Transportation (Caltrans) had conducted a GPS survey in the epicentral region during February and March 1989. Williams and Segall reoccupied eight of the Caltrans stations with GPS receivers in March 1990. Owing to the short timespan between these GPS surveys, they have been able to obtain estimates of coseismic displacements that are less affected by interseismic deformations than the data obtained by Lisowski (this chapter), Marshall and Stein (this chapter), or Snay and others (1991).

Many of the tremendous number of seismic data obtained from the earthquake are not documented in this chapter, except that McNally and others present a unique set of epicentral digital-accelerometer recordings of the main shock and early aftershocks. These recordings show the largest peak accelerations measured during the main shock. Borcherdt (1994) provides references to other local main-shock strong-motion data. The best guide to the global digital-data set is the station list reported by Morelli (1994), and additional pointers and indications of data quality are provided by the first paper of Velasco and others (this chapter).

Parts of some of the papers in this chapter have appeared elsewhere. Beroza expands on the report by Beroza (1991) by including a complete parametrization of his preferred finite-fault rupture model; a comparison of this model with those of Hartzell and others (1991), Steidl and others (1991), and Wald and others (1991); and a calculation of the long-period displacements that his model predicts in the epicentral region. Lisowski documents the data more thoroughly and finds an improved best-fitting fault plane over that of Lisowski and others (1990). Marshall and Stein document their data more completely, reanalyzing their leveling data to account for the covariances of the section elevation differences; they also consider the effect of low-velocity surface layers and low-velocity wedges between the Sargent and San Andreas faults. Wald and others review the rupture model that they previously constructed (Wald and others, 1991), and examine several aspects of the use of such inversions for determining seismic hazards. They demonstrate that the smoothed rupture model derived from inversion of teleseismic body waves can be used to predict local strong ground motions fairly well. They use their preferred rupture model to predict ground motions throughout the epicentral region, and they estimate the regional strong ground motions that would result from a Loma Prieta-type event occurring at shallow depth on a vertical San Andreas fault.

SOURCE PARAMETERS

MAGNITUDE, MOMENT, AND DURATION

From a compilation of global data, the International Seismological Center (1989) determined a surface-wave magnitude (M_S) of 7.1, which agrees with the initial assessment in the monthly "Preliminary Determination of Epicenters" published by the U.S. National Earthquake Information Center. The local magnitude (M_L) was reported by McNally and others (1990) as 6.88±0.44, based on 32 records, including several recordings on Wood-Anderson seismographs in southern California. Uhrhammer and Bolt (1991) reported M_L=6.7±0.09, based on 20 recordings within 105-km epicentral distance. These two estimates agree within their error bounds, and the discrepancy results from the use of different station sets and averaging methods. Both investigations used synthetic Wood-Anderson records derived from strong-motion accelerograms, and so the magnitudes inferred from individual stations are biased by known directivity effects and other amplification factors, such as the likely mantle reflected shear wave that boosted ground motions in San Francisco and Oakland (Somerville and Yoshimura, 1990).

The seismic moments and source durations inferred from local geodetic data, teleseismic body and surface waves, and local strong-motion records largely agree. The seismic moment reported in this chapter ranges from 2.2×10^{19} N-m (1 N-m=10^7 dyne-cm) to 3.5×10^{19} N-m, and the source duration from 6 to 15 s (table 1), with all investigators agreeing that most of the slip occurred within the first 10 s (table 1). The discrepancies appear to result from assumptions of the modeling procedures and variations in data selection. The general agreement of the estimates of seismic moment and source duration is significant because it tends to refute the hypothesis of Wallace and others (1991) that the total source duration was 18 to 30 s and may have involved deep, slow slip. They proposed this hypothesis because several earlier studies of long-period surface waves and free oscillations, including those by Dziewonski and others (1990), Romanowicz and Lyon-Caen (1990), Zhang and Lay (1990), and Jordan (1991), yielded source-duration estimates of 20 to 44 s and centroid depths of about 20 km (see second paper by Velasco and others, this chapter). These depths and durations differ significantly from those inferred from the aftershock distribution and from geodetic and strong-motion models of the earthquake source. Velasco and others show that a shorter duration can be obtained from surface waves if higher resolution Earth velocity and attenuation models are used in the analysis. They believe that the source parameters inferred from surface-wave observations are consistent with those derived from body waves and that there is no evidence for slow, deep slip. Kanamori and Satake

Table 1.—*Determination of seismic moment and duration of the earthquake*

[Data types: btb, broadband teleseismic body waves; g, Geodolite, Global Positioning System; l, leveling; la, local accelerograms; lpb, long-period body waves; lps, long-period surface waves]

Investigators (this chapter)	Data type	Seismic moment (10^{19} N-m)	Duration (s)
Beroza	ls	2.3	[1]6
Choy and Boatwright	btb	2.2	[2]20
Hartzell and others	btb	3.0	[2]13
Horton and others	g, l, la	2.5	9
Kanamori and Satake	lpb, lps	3	6
Lisowski and others	g	2.7±0.3	---
Marshall and Stein	l	2.4±0.2	---
Nabelek	lpb	2.9±0.1	15
Velasco and others	lps	3.0±0.2	11±5
Wald and others	la, lpb	3.0	[1]7
Wu and Rudnicki	g, l	2.5–2.8	---

[1] Starting 1.8 s after the origin time of Dietz and Ellsworth (1990).

[2] 85 percent of seismic moment occurs in the first 7 to 10 s.

(this chapter) also note a similarity of the moments derived from teleseismic body waves and 256-s-period surface waves, which they interpret as indicating no slow slip at the source.

EXTENT AND LOCATION OF FAULTING

LOCATION OF THE FAULT SURFACE

An early controversy over the location of the faulting at depth, caused by a discrepancy between the slip surfaces inferred from geodetic measurements and aftershocks, has largely been resolved. On the basis of line-length changes, GPS data, and leveling data, Lisowski and others (1991) and Marshall and others (1991) obtained preliminary best-fitting fault planes that were displaced by several kilometers from the fault surface defined by aftershocks (Dietz and Ellsworth, 1990). This discrepancy has been extensively studied, and several assumptions of the preliminary geodetic modeling have been identified that would cause the geodetically inferred fault plane to be located systematically too shallow.

The assumption of uniform slip on a rectangular fault plane is tested by Horton and others (this chapter), who invert the leveling data and obtain a smoothly varying slip distribution on a fault plane coincident with the aftershocks. The resulting data misfit is comparable to that of Marshall and others (1991).

The assumption of a laterally homogeneous, elastic Earth is tested by several authors. Steidl and Archuleta (this chapter) point out that slip on a fault plane coincident with the aftershock plane in a laterally homogeneous medium causes almost no motion of the geodetic monument on Loma Prieta. They claim that Lisowski and others (1990) were forced to offset their fault plane from the aftershocks, and that Snay and others (1991) were forced to introduce a bend into their fault surface, in order to match the observed displacement of Loma Prieta peak. This claim is consistent with the observation by Lisowski and others (1990) that the geodetic data most poorly fitted by their preliminary model come from the stations around Loma Prieta peak. Steidl and Archuleta show that if the geodetic observations involving Loma Prieta peak are excluded from the data set, then the surface deformations predicted by the slip model of Steidl and others (1991), in which the fault plane coincides with the aftershock zone, fit the remaining observations as well as do the deformations predicted by the slip model of Lisowski and others (1990). Eberhart-Phillips and Stuart (1992) showed that the low-rigidity material known to be present between the San Andreas and Zayante faults substantially alters the surface deformations caused by buried faults, especially around Loma Prieta, relative to the surface deformations predicted in a layered half-space. They show that to fit the observed displacements (which include the effect of the low-rigidity wedge) by using a half-space model, the fault would have to be shallower and to the southwest of its true position, as Lisowski and others (1990) and Marshall and others (1991) located it.

The effects of the assumption of statistical independence of the geodetic data were estimated by Árnadóttir and others (1992), who tested the effects of the assumed diagonal error-covariance matrices used by Lisowski and others (1990) and Marshall and others (1991). Árnadóttir and others found that if the off-diagonal terms of the error-covariance matrix were included in the misfit statistics for the leveling data, then their inversion method could find a best-fitting fault plane which coincided with the aftershock plane and fitted the leveling data slightly better than did Marshall and others' offset fault plane. Essentially, the difference between their approaches is that Árnadóttir and others used as data the height differences between adjacent bench marks, which is the quantity measured in leveling, whereas Marshall and others used as data the differences between preearthquake and postearthquake bench-mark elevations. Árnadóttir and others' suggestions also apply to the work of Wu and Rudnicki (this chapter), who use Marshall and others' data. Árnadóttir and others found that omission of the off-diagonal elements of the error-covariance matrix does not bias Lisowski and others' (1990) fault location appreciably, although by a more systematic search of model space Árnadóttir and others found a best-fitting fault plane closer to the aftershock plane than that found by Lisowski and others (1990). Williams and others (1993) confirmed that a fault plane coincident with the aftershock zone is consistent with the Caltrans GPS measurements. Marshall and Stein (this chapter), incorporating the suggestions of Árnadóttir and others (1992) and Eberhart-Phillips and Stuart (1992), confirm that the leveling data can be fitted by slip on a fault plane nearly coincident with the aftershock zone. They note, however, that the use of Árnadóttir and others' method achieves this coincidence by seriously downweighting the relatively few bench marks in the areas of greatest elevation change.

EXTENT OF THE FAULT SURFACE

The extent of fault rupture is best defined by modeling strong-motion data. This work assumes that the fault plane coincides with the aftershock zone. Beroza (this chapter) plots his slip distribution along with that of Hartzell and others (1991), Steidl and others (1991), and Wald and others (this chapter) on an identical scale, and all these models, as well as that of Horton and others (this chapter), agree that most of the slip occurred at a depth of 7 to 20 km. In the horizontal direction, rupture was confined to a zone within 20 km of the hypocenter. Beroza (this chapter), Horton and others (this chapter), and Wald and others (this chapter) discuss the differences between the various strong-motion slip models. Long-period body- and surface-wave studies are largely consistent with the extent of faulting observed in strong-motion studies, although the spatial resolution of these long-period studies is poor. Nábělek (this chapter) notes that only the depth distribution of slip can be resolved well from long-period-body-wave studies; the horizontal propagation of rupture in this event is unresolvable if source mechanisms and time functions are unconstrained. He also points out that Hartzell and others could obtain a slip distribution from long-period body waves by assuming a mechanism, rupture velocity, and a slip time function at each point on the fault surface. Judging by the resemblance between Hartzell and others' slip distribution and the strong-motion slip distributions, those assumptions appear to have been appropriate. Kanamori and Satake (this chapter) derive a 35-km upper bound on rupture length from long-period body and surface waves, which they note is anomalously short for an event with a moment magnitude of 6.9.

The fault-length estimates from geodetic studies are probably biased slightly high by an assumption of uniform slip or stress drop over the fault surface. These studies, however, yield fault lengths similar to or slightly larger than those obtained in seismic studies: 32.4 km (Snay and others, 1991), 37 km (Lisowski and others, this chapter), 31 to 37 km (Marshall and Stein, this chapter), and 40 to 44 km (Wu and Rudnicki. this chapter).

If most of the slip in the main shock was confined to a depth greater than 7 km, then the surface cracks observed in the Summit Ridge area and Foothills thrust belt (Ponti and Wells, 1991) may have resulted from folding of surficial sedimentary layers overlying a tectonically offset basement, although other mechanisms, such as landsliding, may be possible. Reches and Zoback (this chapter) examine a model of horizontal elastic layers draped over a faulted basement. They show how termination of the rupture at depth leads to extension southwest of the tip of the buried rupture and compression northeast of the tip; they correlate these zones of extension and compression with the surface cracks observed in the Summit Ridge area and Foothills thrust belt. In their mechanical model, a vertical zone of increased shear stress develops that they correlate with the shallow aftershock zone, although their shear-failure criterion neglects the preexisting stress field. Though not accounting for regions of compression or dilation directly, the mechanical model of Eberhart-Phillips and Stuart (1992) may similarly explain the surface cracks.

SLIP DISTRIBUTION AND MECHANISM

One of the most surprising observations about the slip distribution is as yet unexplained from a mechanical standpoint. The teleseismic observations of Hartzell and others (1991), the strong-motion observations of Steidl and others (1991), Beroza (this chapter), and Wald and others (this volume), and the leveling data of Marshall and Stein (this volume) are all consistent with the conclusion that most slip in the earthquake occurred in two regions, situated northwest and southeast of the hypocenter, and that slip in the southeasterly region was predominantly strike slip, whereas slip in the northwesterly region had a considerable thrust component. Most investigators reported little slip at the hypocenter; there is as yet no satisfactory explanation for the cause of this variation in rake. The slip models of Steidl and others (1991) and Beroza (this chapter) show the largest variations in rake. Beroza's model probably represents an upper bound on the variation in rake because he constructs models with less rake rotation that fit his data nearly as well as does his preferred model. It seems quite well established, however, that slip to the northwest of the hypocenter had a considerably larger thrust component than slip to the southeast. In general, the average slip direction in strong-motion source models agrees well with the mechanism of initial slip at the hypocenter, determined by Oppenheimer (1990) to be oblique slip.

DYNAMIC BEHAVIOR OF THE SOURCE

RUPTURE INITIATION

Wald and others (this chapter) observe that during the first 1.8 s after Dietz and Ellsworth (1990)'s origin time, the earthquake appeared to be a rather small (*M*~5), slowly growing event. After 1.8 s, however, the energy radiated by the source grew enormously, and this later energy was large enough to trigger local strong-motion instruments. Similar behavior was noted in the initiation of the 1979 Imperial Valley, Calif., earthquake (Hartzell and Heaton, 1983) and the 1987 Superstition Hills, Calif., earthquake (Wald and others, 1990). These observations are critical to the question whether large earthquakes start as small earthquakes that grow out of control. A careful analysis of the initiation of these events may provide a critical test of the feasibility of earthquake prediction.

RUPTURE VELOCITY AND RISE TIME

Although most investigators agree on the slip distribution of the earthquake, they differ significantly regarding the temporal evolution of the source. The inversions of Steidl and others (1991), Beroza (this chapter), and Wald and others (this chapter) all assume that slip at any point on the fault can happen only during a relatively brief time window (<2-s duration). The initiation and termination of this time window are controlled by an assumed rupture velocity. Steidl and others obtained an average rupture velocity of 3.0 km/s and a velocity of 3.4 km/s for propagation to the southeast, Beroza obtains a rupture velocity of 2.7 to 3.1 km/s, and Wald and others obtain a rupture velocity of 2.5 km/s. Each model assumes that rupture propagates to the northwest and southeast simultaneously. Horton and others (this chapter) use a frequency-domain inversion technique that allows much greater freedom in the rupture behavior; their rupture model shows rupture to the northwest initiating *after* rupture to the southeast. Moreover, they obtain a higher rupture velocity of 3.5 to 5 km/s. Because of restrictions on the parametrizations in the other studies, it would be impossible for them to obtain this solution. Horton and others' solution must therefore be regarded as preliminary because they use a small data set, and, in particular, the timing of northwest-propagating rupture in their model depends strongly on the assumed timing of the accelerogram at station SAR. The net effect, however, is that the thrust component of the earthquake follows the strike-slip component, consistent with the teleseismic observations of Romanowicz and Lyon-Caen (1990) and Nábělek (this chapter), who observe a predominance of thrust faulting at a late stage of the rupture. These observations, however, do not prove that thrusting occurred late in the rupture process. In fact, they imply a curious scenario of initial oblique slip at the hypocenter (Oppenheimer, 1990), followed by strike-slip faulting to the southeast, then by oblique faulting to the northwest.

The various source models of the earthquake differ radically in the slip duration estimated for each point on the fault. Steidl and others (1991) obtained a slip duration (rise time) of 1.0 s, Beroza (this chapter) 0.3 s, and Wald and others (this chapter) approximately 1.0 s, although Horton and others (this chapter) obtain a rise time of 1.75 s at the point of maximum slip. These varying results have fundamentally different implications for the mechanics of earthquake rupture (Heaton, 1990).

STRESS DROP, FRACTURE ENERGY, AND RECURRENCE INTERVAL

The inferred stress drop and fracture energy of the earthquake generally support a long recurrence interval (much more than 100 yr) for this event, on the basis of the notion that high stress drops and fracture energies correlate with stronger faults having longer recurrence intervals. Kanamori and Satake (this chapter) note that the rupture length of the earthquake is anomalously short relative to those of other earthquakes with similar seismic moments. A short rupture length implies a high stress drop. Kanamori and Satake's calculation of a 50-bar static-stress drop is consistent with Choy and Boatwright's (this chapter) estimate of a dynamic-stress drop of 51 bars. Houston (1990) noted that the earthquake's stress drop is rather high for an interplate event and is more similar to that of intraplate events; she furthermore observed, on the basis of correlation with other events, that a high stress-drop implies a long recurrence interval. From their geodetic model, Wu and Rudnicki (this chapter) calculate a static-stress drop of 20 to 26 bars, which also is probably a lower bound on the stress drop, owing to their high estimates of fault length (table 1). They also estimate a maximum energy-release rate (fracture energy) of more than 5.5×10^6 J/m^2, which they consider to be in the upper range of observed fracture energies, implying a strong fault and a long recurrence interval. All of these stress-drop estimates are averages over a presumed-large fault surface. Taking into account the actual double-peaked slip distribution of the earthquake, Wald and others (this chapter) estimate stress drops of 218 bars for the northwest slip patch and 136 bars for the southeast slip patch. These stress drops further support the notion that the fault segments that slipped in the earthquake were relatively strong. Additional support for this idea comes from Michael and Eberhart-Phillips (1991), who found that the two regions of high slip in the strong-motion models are correlated with regions of high *P*-wave velocity obtained from inversions of earthquake arrival-time data.

STRONG-MOTION GEODESY

Several of the papers in this chapter (for example, Beroza, Horton and others, and Steidl and Archuleta) are notable in showing that the boundary between geodesy and seismology is blurring, with interesting implications for earthquake engineering. These papers predict coseismic static surface deformations from slip models derived from strong-motion accelerograms, using established seismologic methods. It has been recognized that permanent ground offsets can be recovered from digital-accelerometer recordings of ground motions (Anderson and others, 1986). Beroza obtains static displacements of 10 to 20 cm from integration of a digital accelerogram of the earthquake recorded near San Jose, Calif., and he shows that his slip model predicts such displacements. In the future, the behavior of fault slip over periods of 1 s to a few days will probably be observable by a combination of strong-motion accelerometers and GPS instruments. Heaton and Hartzell (1991) noted that from an engineering standpoint, the large static displacements that occur within the first few seconds of an earthquake may have serious consequences for current base-isolated structures because the isolators typically are not designed to accommodate excursions as large as those observed.

IMPLICATIONS FOR SEISMIC HAZARDS

Taken together, these results suggest that the earthquake was not the typical shallow strike-slip San Andreas event anticipated by the Working Group on California Earthquake Probabilities (1988). Beroza (this chapter) points out that the great depth of slip suggests that the earthquake occurred on a fault distinct from the San Andreas fault, and that the San Andreas fault itself may have acted as an obstacle to rupture in this event. He cites the work of Segall and Lisowski (1990), who showed that the movement of Loma Prieta in 1989 was quite different from that in 1906, further distinguishing the 1989 Loma Prieta earthquake from typical San Andreas events. Certainly, the considerable thrust component of slip in 1989 differed considerably from that in 1906. Therefore, Beroza states that the seismic hazard in the Santa Cruz Mountains may still be high, owing to the possibility of a shallow San Andreas event there. Wald and others (this volume), who estimate ground motions for an event on the shallow San Andreas fault, show that such an event might cause stronger shaking in the Santa Cruz Mountains than those caused by the 1989 Loma Prieta earthquake, simply because of its shallower depth.

The earthquake source could have caused considerably more damage, had its rupture behavior not been so mercifully brief and simple, and had it been shallower. Kanamori and Satake (this chapter) show that the duration of the earthquake was considerably shorter than that of the 1988 Armenia earthquake, despite their similar magnitudes. In addition, shaking in the densely urbanized regions of the San Francisco Bay region could have been either significantly stronger or weaker under equally likely rupture scenarios. The bilateral rupture propagation in the earthquake focused a significant fraction of the seismic energy toward the less urbanized southeastward direction; rupture initiation at the southeast end of the causative fault would have increased the intensity of shaking around the bay, whereas rupture initiation at the northwest end of the causative fault would have focused more shaking toward Hollister, Calif., and less toward the bay.

REFERENCES CITED

Anderson, J.G., Bodin, Paul, Brune, J.N., Prince, Jorge, Singh, S.K., Quaas, Roberto, and Onate, Mario, 1986, Strong ground motion from the Michoacan, Mexico, earthquake: Science, v. 233, no. 4768, p. 1043–1049.

Árnadóttir, Thora, Segall, Paul, and Matthews, M.V., 1992, Resolving the discrepancy between geodetic and seismic fault models for the 1989 Loma Prieta, California, earthquake: Seismological Society of America Bulletin, v. 82, no. 5, p. 2248–2255.

Beroza, G.C., 1991, Near-source modeling of the Loma Prieta earthquake: Evidence for heterogeneous slip and implications for earthquake hazards: Seismological Society of America Bulletin, v. 81, no. 5, p. 1603–1621.

Borcherdt, R.D., ed., 1994, The Loma Prieta, California, earthquake of October 17, 1989—strong ground motions: U.S. Geological Survey Professional Paper 1551-A, 272 p.

Choy, G.L., and Boatwright, John, 1990, Source characteristics of the Loma Prieta, California, earthquake of October 18, 1989 from global digital seismic data: Geophysical Research Letters, v. 17, no. 8, p. 1183–1186.

Dietz, L.K., and Ellsworth, W.E., 1990, The October 17, 1989, Loma Prieta, California, earthquake and its aftershocks; geometry of the sequence from high-resolution locations: Geophysical Research Letters, v. 17, no. 9, p. 1417–1420.

Dziewonski, A.M., Ekstrom, Goran, Woodhouse, J.H., and Zwart, Gretchen, 1990, Centroid moment tensor solutions for October–December 1989: Physics of the Earth and Planetary Interiors, v. 62, no. 3–4, p. 194–207.

Eberhart-Phillips, D.M., and Stuart, W.D., 1992, Material heterogeneity simplifies the picture; Loma Prieta: Seismological Society of America Bulletin, v. 82, no. 4, p. 1964–1968.

Hartzell, S.H., and Heaton, T.H., 1983, Inversion of strong ground motion and teleseismic waveform data for the fault rupture history of the 1979 Imperial Valley, California, earthquake: Seismological Society of America Bulletin, v. 73, no. 6, pt. A, p. 1553–1583.

Hartzell, S.H., Stewart, G.S., and Mendoza, Carlos, 1991, Comparison of L_1 and L_2 norms in a teleseismic waveform inversion for the slip history of the Loma Prieta, California, earthquake: Seismological Society of America Bulletin, v. 81, no. 5, p. 1518–1539.

Heaton, T.H., 1990, Evidence for and implications of self-healing pulses of slip in earthquake rupture: Physics of the Earth and Planetary Interiors, v. 64, no. 1, p. 1–20.

Heaton, T.H., and Hartzell, S.H., 1991, Near field ground motions in large earthquakes and base-isolated structures [abs.]: Seismological Research Letters, v. 62, no. 1, p. 49.

Houston, Heidi, 1990, A comparison of broadband source spectra, seismic energies, and stress drops of the 1989 Loma Prieta and 1988 Armenian earthquakes: Geophysical Research Letters, v. 17, no. 9, p. 1413–1416.

International Seismological Centre Bulletin, 1989: v. 26, no. 1, p. 109.

Jordan, T.H., 1991, Far-field detection of slow precursors to fast seismic ruptures: Geophysical Research Letters, v. 18, no. 11, p. 2019–2022.

Kanamori, Hiroo, and Satake, Kenji, 1990, Broadband study of the 1989 Loma Prieta earthquake: Geophysical Research Letters, v. 17, no. 8, p. 1179–1182.

Lisowski, Michael, Prescott, W.H., Savage, J.C., and Johnston, M.J.S., 1990, Geodetic estimate of coseismic slip during the 1989 Loma Prieta, California, earthquake: Geophysical Research Letters, v. 17, no. 9, p. 1437–1440.

Marshall, G.A., Stein, R.S., and Thatcher, Wayne, 1991, Faulting geometry and slip from co-seismic elevation changes; the 18 October 1989, Loma Prieta, California, earthquake: Seismological Society of America Bulletin, v. 81, no. 5, p. 1660–1693.

McNally, K.C., Yellin, Joseph, Protti-Quesada, Marino, Simila, G.W., Malavassi, Eduardo, Schillinger, Walter, Terdiman, Richard, and Zhang, Zhi, 1990, The local magnitude of the 18 October 1989 Santa Cruz Mountains earthquake is M_L=6.9: Geophysical Research Letters, v. 17, no. 10, p. 1781–1784.

Michael, A.J., and Eberhart-Phillips, D.M., 1991, Relations among fault behavior, subsurface geology, and three-dimensional velocity models: Science, v. 253, no. 5020, p. 651–654.

Morelli, Andrea, 1994, 1994 status report of the Federation of Digital Seismographic Networks: Annali di Geofisica, v. 37, no. 5, p. 1037–1112.

Ponti, D.J., and Wells, R.E., 1991, Off-fault ground ruptures in the Santa Cruz Mountains, California; ridge-top spreading versus tectonic extension during the 1989 Loma Prieta earthquake: Seismological Society of America Bulletin, v. 81, no. 5, p. 1480–1510.

Romanowicz, B.A., and Lyon-Caen, Hélène, 1990, The Loma Prieta earthquake of October 18, 1989; results of teleseismic mantle and body-wave inversion: Geophysical Research Letters, v. 17, no. 8, p. 1191–1194.

Oppenheimer, D.H., 1990, Aftershock slip behavior of the 1989 Loma Prieta, California earthquake: Geophysical Research Letters, v. 17, no. 8, p. 1199–1202.

Segall, Paul, and Lisowski, Michael, 1990, Surface displacement in the 1906 San Francisco and 1989 Loma Prieta earthquakes: Science, v. 250, no. 4985, p. 1241–1244.

Snay, R.A., Neugebauer, H.C., and Prescott, W.H., 1991, Horizontal deformation associated with the Loma Prieta earthquake: Seismological Society of America Bulletin, v. 81, no. 5, p. 1647–1659.

Somerville, P.G., and Yoshimura, Joanne, 1990, The influence of critical Moho reflections on strong ground motions recorded in San Francisco and Oakland during the 1989 Loma Prieta earthquake: Geophysical Research Letters, v. 17, no. 8, p. 1203–1206.

Steidl, J.H., Archuleta, R.J., and Hartzell, S.H., 1991, Rupture history of the 1989 Loma Prieta, California, earthquake: Seismological Society of America Bulletin, v. 81, no. 5, p. 1573–1602.

Uhrhammer, R.A., and Bolt, B.A., 1991, The seismic magnitude of the 1989 Loma Prieta main shock determined from strong-motion records: Seismological Society of America Bulletin, v. 81, no. 5, p. 1511–1517.

Wald, D.J., Helmberger, D.V., and Hartzell, S.H., 1990, Rupture process of the 1987 Superstition Hills earthquake from the inversion of strong-motion data: Seismological Society of America Bulletin, v. 80, no. 5, p. 1079–1098.

Wald, D.J., Helmberger, D.V., and Heaton, T.H., 1991, Rupture model of the 1989 Loma Prieta earthquake from the inversion of strong-motion and broadband teleseismic data: Seismological Society of America Bulletin, v. 81, no. 5, p. 1540–1572.

Wallace, T.C., Velasco, A.A., Zhang, Jiajun, and Lay, Thorne, 1991, A broadband seismological investigation of the 1989 Loma Prieta, California, earthquake; evidence for deep slow slip?: Seismological Society of America Bulletin, v. 81, no. 5, p. 1622–1646.

Williams, C.R., Árnadóttir, Thora, and Segall, Paul, 1993, Coseismic deformation and dislocation models of the 1989 Loma Prieta earthquake derived form Global Positioning System measurements: Journal of Geophysical Research, v. 98, no. B3, p. 4567–4578.

Working Group on California Earthquake Probabilities, 1988, Probabilities of large earthquakes occurring in California on the San Andreas Fault: U.S. Geological Survey Open-File Report 88–398, 62 p.

Zhang, Jiajun, and Lay, Thorne, 1990, Source parameters of the 1989 Loma Prieta earthquake determined from long-period Rayleigh waves: Geophysical Research Letters, v. 17, no. 8, p. 1195–1198.

THE LOMA PRIETA, CALIFORNIA, EARTHQUAKE OF OCTOBER 17, 1989: EARTHQUAKE OCCURRENCE

MAIN-SHOCK CHARACTERISTICS

RUPTURE HISTORY OF THE EARTHQUAKE FROM HIGH-FREQUENCY STRONG-MOTION DATA

By Gregory C. Beroza,
Stanford University

CONTENTS

ABSTRACT

I have derived a rupture model for the 1989 Loma Prieta earthquake, using data from 20 strong-motion instruments that recorded the main shock in the near-source region. The earthquake ruptured bilaterally at approximately 80 percent of the local shear-wave velocity over a total distance of slightly more than 30 km, from 13 km northwest to 20 km southeast of the hypocenter. Slip over the rupture surface was highly irregular in both amplitude and direction. Slip amplitude at the hypocenter and immediately updip was only about 1 m. There were two main areas of high slip: one centered 7 km northwest of the hypocenter at a depth of 14 km and the other centered 6 km southeast of the hypocenter at a depth of 12 km. Peak slip amplitudes on both of these high-slip areas exceeded 4.5 m. A surprising aspect of this rupture model is that the rake ranges from predominantly strike slip to the southeast to predominately reverse slip to the northwest. Despite this variation in rake, the equivalent point-source moment tensor matches that found from teleseismic observations. A correlation exists between areas of high slip and areas of low aftershock activity. A simple explanation is that areas of high slip are areas of high strength, which slip only during infrequent large events. Other areas of the fault are weaker and may slip both seismically and aseismically. Most of the slip in the earthquake occurred at 9- to 16-km depth on a structure that dips southwest and runs underneath the surface trace of the San Andreas fault at 8- to 10-km depth. This observation complicates the assessment of seismic hazard on the southern Santa Cruz Mountains section of the San Andreas fault.

INTRODUCTION

In this paper, I present a rupture model of the earthquake, compare this model with other published extended-source models of the main shock, and discuss its implications for earthquake-source mechanics and seismic hazard. The main shock occurred at 00:04:15.2 G.m.t. on October 18, 1989, at lat 37.040° N., long 121.880° W., at 17-km depth (Dietz and Ellsworth, 1990), southwest of the southern Santa Cruz Mountains section of the San Andreas fault. Aftershocks extended bilaterally from the hypocenter for a distance of approximately 50 km, filling a region that had previously shown relatively little microearthquake activity (U.S. Geological Survey staff, 1990). The locations of aftershocks with respect to the hypocenter suggest that the rupture propagated bilaterally along strike and unilaterally updip. Below about 10-km depth, the aftershocks define a plane dipping 65°–70° SW. (Dietz and Ellsworth, 1990) that, if continued to the surface, would crop out near the surface trace of the Sargent fault. Above 10 km depth, however, where the fault is approximately beneath the surface trace of the San Andreas fault, the aftershock distribution is more diffuse and does not define a single plane (Dietz and Ellsworth, 1990). At the south end of the aftershock zone, the fault surface defined by aftershocks grades into a vertical fault plane beneath the surface trace of the San Andreas fault. The local magnitude (M_L) of 6.9 for the earthquake (McNally and others, 1990) is consistent with estimates of the scalar seismic moment of 1.7×10^{19} to 3.4×10^{19} N-m (for example, Kanamori and Satake, 1990), which yield an estimate of M_w=6.9 (Hanks and Kanamori, 1979).

The 1989 Loma Prieta earthquake has been the subject of numerous studies that used teleseismic records to determine the source parameters (Barker and Salzberg, 1990; Choy and Boatwright, 1990; Kanamori and Satake, 1990; Langston and others, 1990; Nábělek, 1990; Romanowicz and Lyon-Caen, 1990; Ruff and Tichelaar, 1990; Zhang and Lay, 1990). All of these studies are quite consistent and indicate oblique slip on a fault dipping approximately 70° and striking approximately 130°. These results, in turn, agree well with the average dip and strike based on well-located aftershocks recorded by the densely spaced, high-gain stations of the U.S. Geological Survey (USGS)'s northern California seismic network (Calnet) (Dietz and Ellsworth, 1990). The teleseismically determined rake is approximately 135° (for example, Zhang and Lay, 1990), consistent with a constant-slip model of the earthquake with 1.6 m of strike slip and 1.2 m of dip slip determined from analysis of geodetic data (Lisowski and others, 1990).

Near-source strong-motion data can greatly increase the resolution of details of the rupture process. In this paper, I analyze strong-motion data from the near-source region of the main shock. I fit the near-source data by modeling the earthquake with spatially varying slip on an extended planar fault. I find that the region of high slip in the earthquake is quite compact, with a rupture length of slightly more than 30 km. There is evidence of complexity in the rupture process, with slip amplitude exceeding 5 m locally and slip direction varying strongly and systematically from northwest to southeast. Finally, because most slip occurred below 10-km depth, the coincidence of long-term forecasts of an earthquake on the San Andreas fault in the southern Santa Cruz Mountains (Working Group on California Earthquake Probabilities, 1988) with the occurrence of the 1989 Loma Prieta earthquake may have been fortuitous. A possible interpretation of my results is that the earthquake began at 18-km depth on a fault distinct from the San Andreas, ruptured updip along that fault, and terminated ~10-km depth when it reached a vertical San Andreas fault, which acted as an obstacle to further rupture propagation.

STRONG-MOTION DATA

The earthquake occurred in a region that is densely instrumented with strong-motion accelerographs. Because strong-motion instruments record data onscale in the near-source region, where the Green's functions for different segments of the fault vary widely, these data can resolve detailed aspects of the rupture process that are unresolvable using data from the teleseismic far field, where most of the variation in the Green's functions for different segments of the fault is simply due to a difference in phase (Aki and Richards, 1980, v. 2, p. 804–805). The abundance of high-quality data in the near-source region of the earthquake provides one of the best opportunities to date to study the rupture process of a large event.

Near-source data were collected on film-recording, analog strong-motion instruments operated by the USGS (Maley and others, 1989) and the California Division of Mines and Geology (CDMG) (Shakal and others, 1989), and on digital instruments deployed in the epicentral region before the main shock by the University of California, Santa Cruz (UCSC) (Simila and others, 1990). Many of these instruments use absolute time from radio station WWVB code. The locations of stations used in the analysis are shown in figure 1 and listed in table 1.

The acceleration data were obtained after instrument correction and resampling at a uniform interval. The data were processed by filtering with a two-pole, zero-phase Butterworth filter with low- and high-cut corner frequencies at 0.33 and 2.0 Hz. The high-frequency corner represents the limit at which the seismograms could be modeled deterministically, and the low-frequency limit was constrained by the requirement in the high-frequency, near-source approximation that the receivers be several wavelengths from the nearest segment of the fault (Spudich and Frazer, 1984). Finally, the horizontal components of motion were rotated into a coordinate system with the x-axis parallel to the strike of the fault (130° clockwise from north), the z-axis pointing downward, and the y-axis forming a right-handed system (220° clockwise from north).

The aftershock zone and the distribution of strong-motion stations deployed by the CDMG, USGS, and UCSC that recorded the main shock are shown in figure 1. Data from the 20 stations (solid triangles, fig. 1) were used; other nearby stations (open triangles) were excluded either because the instruments are not free-field sites (for example, sta. WATS), the source-receiver distances are too large (most stations), or the local site geology makes it difficult to predict waveforms (for example, sta. SCA). The fault-perpendicular (220°) and fault-parallel (130°) components of displacement in the frequency band 0.2–5 Hz for the 20 stations used in the inversion are plotted in figure 2.

Because some of the UCSC stations were not secured to the ground, they may have moved during the earthquake and thus not faithfully recorded true ground acceleration. One UCSC station could be checked because it was deployed very near a CDMG station (SCZ, fig. 1) on the UCSC campus. Except for a difference in the orientation of the sensors, the two seismograms agree quite closely. Another station (LGP) of more concern, located at the Los Gatos Presentation Center, had the highest peak acceleration of any of the stations and may have moved during the earthquake. The closest CDMG station is at the Lexington Dam (LEX). As plotted in figure 2, the 220° component of motion is quite similar at these two stations, whereas the 130°component of motion differs considerably. This is attributable to the fact that the 130° component of motion should be nearly nodal for each station, and so the waveforms are not expected to be similar. The resemblance of the station LGP data to the station LEX data, and the successful prediction of the ground motion at station LGP by the rupture model, indicate that any motion of the instrument with respect to the ground probably did not affect the data greatly. Owing to the important locations of the UCSC stations, I have included them in the analysis. The important features of the rupture model, however, are not determined solely by these data.

By examining the gross features of the displacement data, we can anticipate some aspects of the inversion results. As shown in figure 2, the duration of strong shaking is less than 10 s at all stations, indicating that the strong ground motion is generated by a much smaller source than the ~50-km-long aftershock zone would suggest. The displacements at station COR (fig. 1), which is directly updip from the hypocenter, and at other stations near the center of the aftershock zone (BRN, CAP) are relatively small, indicating that slip in the hypocentral region and directly updip is relatively low. In contrast, displacements at stations to the northwest (LGP, LEX, STG) are much larger. These data are affected primarily by slip on the fault northwest of the hypocenter, indicating that slip in this region is higher than in the hypocentral region. Similarly, the displacements at stations to the southeast (Gilroy array, GHB, HDA) are large, indicating that the south-

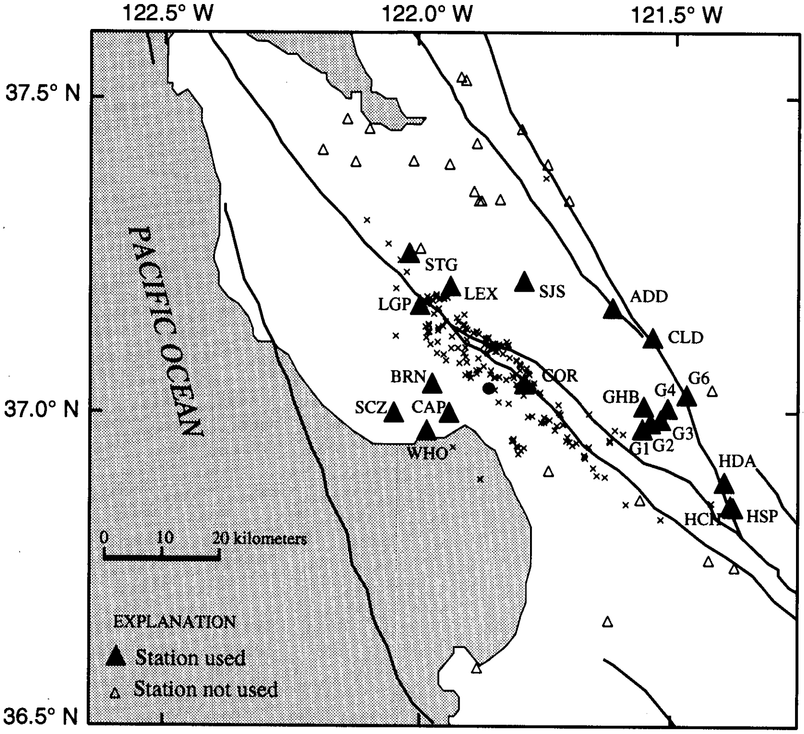

Figure 1.—Epicentral region of the earthquake, showing locations of aftershocks (x's), mapped surface traces of major faults (heavy lines), and strong-motion stations (triangles). Solid triangles, 20 strong-motion stations used in the inversion; open triangles, other stations not used because they were too far from epicenter, had obvious effects due to unmodeled velocity structure, or were not free-field sites.

Table 1.—*Strong-motion stations used in the analysis*

[Organizations: CDMG, California Division of Mines and Geology; UCSC, University of California, Santa Cruz; USGS, U.S. Geological Survey]

Code	Number	Organization	Location
ADD	1652	USGS	Anderson Dam, downstream.
BRN	---	UCSC	5001 Branciforte Ct., Santa Cruz.
CAP	47125	CDMG	Capitola Fire Station.
CLD	57504	CDMG	Coyote Lake Dam.
COR	57007	CDMG	Corralitos.
G1	47379	CDMG	Gilroy array station 1.
G2	47380	CDMG	Gilroy array station 2.
G3	47381	CDMG	Gilroy array station 3.
G4	57382	CDMG	Gilroy array station 4.
G6	57383	CDMG	Gilroy array station 6.
GHB	57476	CDMG	Gilroy historical building.
HCH	1575	USGS	Hollister City Hall.
HDA	1656	USGS	Hollister Airport.
HSP	47524	CDMG	South and Pine Streets, Hollister.
LEX	57180	CDMG	Lexington Dam.
LGP	---	UCSC	Los Gatos Presentation Center.
SCZ	58135	CDMG	UCSC campus.
SJS	57563	CDMG	Santa Theresa Hills, San Jose.
STG	58065	CDMG	Aloha Avenue, Saratoga.
WHO	---	UCSC	738 Cable Court, Santa Cruz.

eastern segment of the rupture zone also had high slip as well. Note that stations HDA and G02 through G04 are all soft-soil sites, and if substantial site amplification occurred, there might be a bias toward higher slip on the southeastern segment of the fault.

Absolute-timing information was available for many of the stations from radio station WWVB code; however, to account for lateral variations in the velocity structure, apparent trigger times at all stations were adjusted so that the initial *S* wave from the hypocenter arrived at the time predicted by the laterally homogeneous model. For stations with absolute-timing information, the average correction to the origin time was about +2 s, too large to be attributable to lateral variations in velocity structure. This discrepancy indicates that the earthquake began with a subevent too small to trigger the strong-motion instruments but large enough to register on the sensitive, high-gain stations that were used to determine the hypocenter. Similar behavior was noted in both the 1979 Imperial Valley, Calif., earthquake (Hartzell and Heaton, 1983) and the 1987 Superstition Hills, Calif., earthquake (Wald and others, 1990). Understanding such earthquake nucleation is a critical problem that is difficult to study with triggered, strong-motion data; however, the advent of continuously recording, broadband, high-dynamic range digital networks will help in this effort.

The data were modeled by varying the rupture time and slip amplitude from a simple assumed starting model, using the tomographic backprojection technique of Olson (1987) adopted to a sparse system with inequality and smoothness constraints (Beroza and Spudich, 1988). The data are linearly related to variations in slip amplitude and nonlinearly related to variations in rupture time, and so a linearization was used, and the inversion process was repeated until the solution converged.

To increase the stability of the solution inequality constraints were applied to both the strike-slip (constrained to be right lateral) and dip-slip (constrained to be reverse) components of motion. These inequality constraints were enforced by a penalty function (Beroza and Spudich, 1988). Smoothness constraints were applied to the slip-amplitude and rupture-time calculations (Hartzell and Heaton, 1983; Beroza and Spudich, 1988).

MODEL PARAMETRIZATION

The fault plane used in the analysis (see section above entitled "Introduction") extends from 20 km northwest to 20 km southeast of the hypocenter. The dipping fault plane intersects the hypocenter at a depth of 18 km, with a strike of 130° and a dip of 70° SW. The modeled extent of the rupture zone in the updip direction from the hypocenter is 14 km, corresponding to depths from 18 km to slightly less than 5 km. A 1-km grid spacing is used in both the updip and along-strike directions, and the model is specified as a triplet of strike-slip amplitude, dip-slip amplitude, and rupture time. In this parametrization, the rake is a derived quantity because the strike-slip and dip-slip components of the slip vector are allowed to vary independently.

The velocity model used to calculate the Green's functions is a piecewise linear-velocity-gradient approximation to the one-dimensional velocity model of Dietz and Ellsworth (1990) based on their analysis of Loma Prieta aftershocks (table 2). Because their model indicates a difference in the velocity of the uppermost layers across the San Andreas fault, a slightly different model was used on the northeast and southwest sides of the fault.

Theoretical seismograms and partial derivatives with respect to model parameters were calculated by using a high-frequency, near-source approximation (Spudich and Frazer, 1984), in which the effects of lateral heterogeneity can be incorporated if the velocity model is sufficiently well known (Cormier and Beroza, 1987), although I have not attempted to do so in this study.

This parametrization of the rupture process allows each segment of the fault to slip once when the rupture front passes with a spatially variable amplitude. The slip velocity is assumed to decay after rupture as the inverse square root of time $t^{-1/2}$, as in crack models of earthquake rupture, and the rise time is assumed to be a uniform 0.3 s everywhere on the fault. A short rise time, which is required by the data, suggests that the duration of slip at any point on the fault is not controlled by the distance to the edge of the fault (Beroza and Spudich, 1988; Heaton, 1990), as is usually assumed (for example, Day, 1982).

The combination of such short rise times and very large displacements indicates that the particle acceleration across the fault plane is quite high. If rise time were allowed to vary, regions of the fault that did not undergo high slip could have much longer rise times; however, the areas of high slip are the most problematic. An alternative expla-

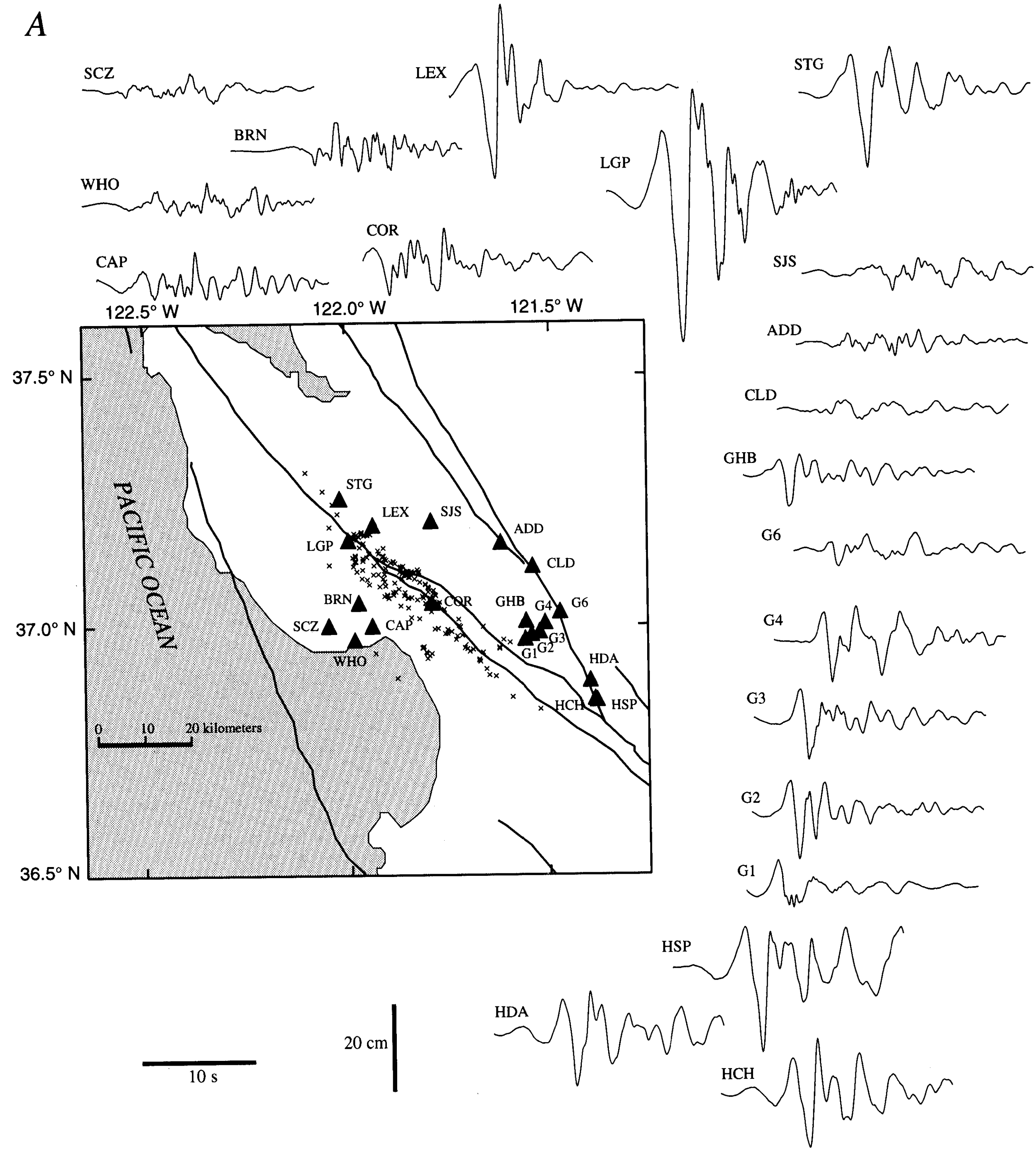

Figure 2.—Fault-perpendicular (220° clockwise from north) (*A*) and fault-parallel (130° clockwise from north) (*B*) components of displacement at 20 strong-motion stations used in inversion, calculated by integrating corrected accelerograms twice to displacement and bandpass filtering between 0.2 and 5 Hz (this passband is used for display only). Note that displacements at stations near hypocenter are smaller than at stations to northwest or southeast. Inset shows locations of stations (see fig. 1 for explanation).

nation is that the true slip-time function decays more quickly than $t^{-1/2}$. Such a slip history could accommodate a longer rise time. Resolution of the observation of short rise times, which imply a high dynamic stress drop, with the low earthquake stress drops inferred by other methods is an important problem in earthquake-source mechanics.

RESULTS

Because this is a linearized inversion, I attempted to converge to a solution from a wide range of starting models. I found no evidence for variations in the rupture velocity large enough to be considered resolvable. Because

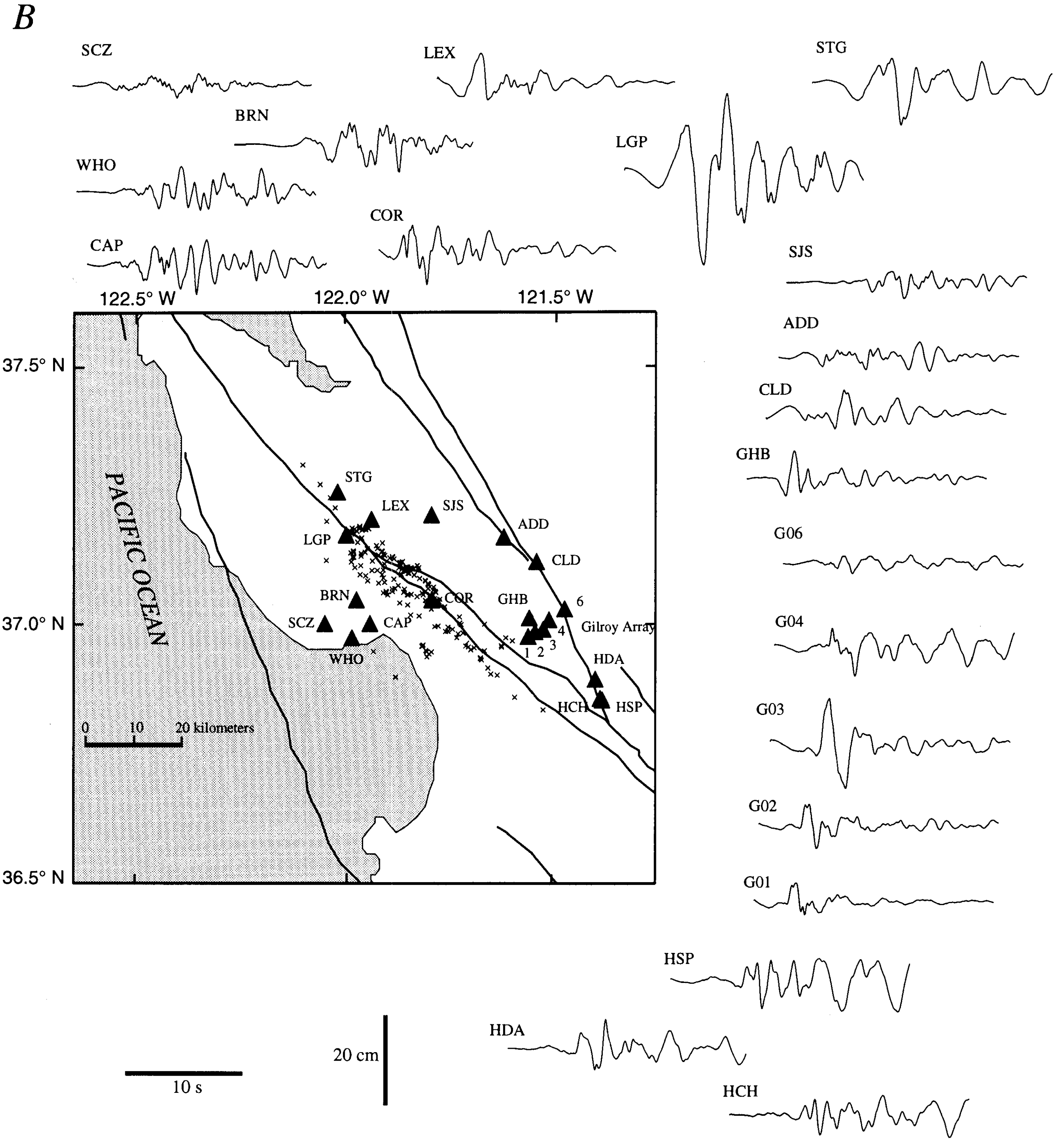

Figure 2.—Continued.

Table 2.—*Parameters used in the velocity model*

[α, *P*-wave velocity; β, *S*-wave velocity; ρ, density]

Depth (km)	α (km/s)	β (km/s)	ρ (kg/m³)
Northeast of fault			
0.0	3.34	1.93	2,500
1.1	5.01	2.89	2,700
9.1	6.26	3.61	2,700
24.5	6.95	4.01	2,800
Southwest of fault			
0.0	3.42	1.97	2,500
1.1	4.58	2.64	2,700
9.1	6.26	3.61	2,700
24.5	6.95	4.01	2,800

the data can be fitted nearly as well without variations in rupture velocity, the rupture velocity was held at a fixed fraction of the local shear-wave velocity, and an inversion was performed for the strike-slip and dip-slip amplitudes. The preferred rupture model has a rupture velocity of 80 percent of the local shear-wave velocity, which amounts to 3.1 km/s at the hypocentral depth and 2.7 km/s at 6-km depth. Much lower or higher rupture velocities substantially degraded the fit to the data.

A rescaled version of the rupture velocity model obtained by the inversion (Beroza, 1991) is shown in figure 3. The hypocenter is located at 18-km depth, 0 km along strike. The top of the assumed fault plane is at 4.8-km depth (14 km updip from the hypocenter). Slip amplitude ranges from 0 to more than 5 m, with a total seismic moment in this rescaled model of 2.3×10^{19} N-m, in agreement with the teleseismically and geodetically determined range 1.7×10^{19}–3.4×10^{19} N-m. The various slip amplitudes and rupture times in the rescaled model are listed in table 3.

The model shown in figure 3 and the fit to the data shown in figure 4 are the results of rescaling the slip amplitudes determined from a least-squares inversion. Before rescaling, the seismic moment was calculated to be 1.3×10^{19} N-m. The slip amplitudes were rescaled to account for a systematic underprediction of amplitudes by the least squares inversion procedure.

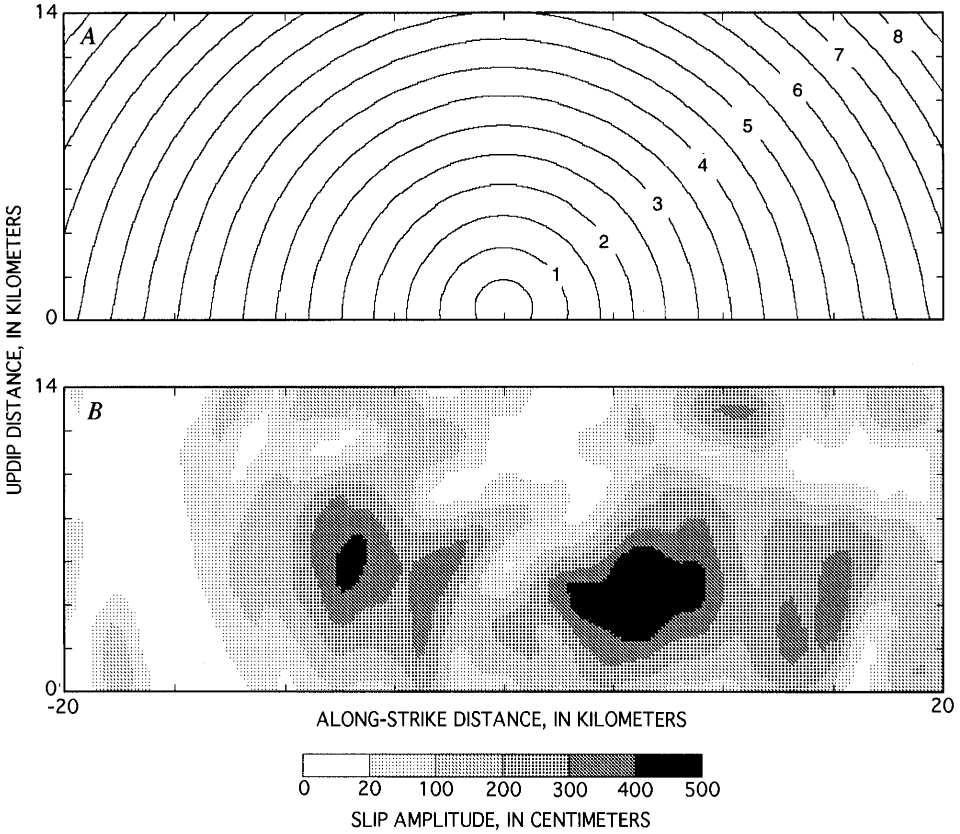

Figure 3.—Rupture model of earthquake. Bottom of fault plane is at 18-km depth, and top at 4.8-km depth. *A*, Rupture time at 0.5-s intervals. Rupture front spreads outward from hypocenter (at 0 km along strike and 0 km updip) at a constant 80 percent of local shear-wave velocity. *B*, Amplitude of slip vector. Slip in hypocentral region and updip from hypocenter is relatively low. Note two high-slip areas at 12- and 14-km depth; most slip occurs at 9- to 16-km depth.

Table 3.—*Rupture model of the earthquake*

[Columns correspond to different distances along dip; step size, 1 km. The first column is the deepest, and the second column corresponds to the depth of the hypocenter. Rows correspond to different distances along strike; step size, 0.5 km. The first row is at the northwest end of the model fault, and the 41st row corresponds to the location of the hypocenter. Positive values are right-lateral and reverse slip]

Rupture time (s)														
6.70	6.78	6.83	6.91	7.00	7.11	7.24	7.38	7.54	7.72	7.92	8.13	8.36	8.60	8.85
6.53	6.61	6.66	6.74	6.83	6.95	7.07	7.22	7.38	7.56	7.76	7.97	8.20	8.45	8.70
6.36	6.44	6.49	6.57	6.67	6.78	6.91	7.05	7.22	7.40	7.60	7.82	8.05	8.29	8.55
6.20	6.27	6.32	6.41	6.50	6.61	6.74	6.89	7.05	7.24	7.44	7.66	7.89	8.14	8.41
6.03	6.10	6.15	6.24	6.33	6.44	6.58	6.72	6.89	7.07	7.28	7.50	7.74	7.99	8.26
5.86	5.93	5.98	6.07	6.16	6.28	6.41	6.56	6.73	6.91	7.12	7.34	7.58	7.84	8.11
5.70	5.76	5.82	5.90	6.00	6.11	6.25	6.40	6.57	6.76	6.97	7.19	7.44	7.69	7.97
5.53	5.59	5.65	5.73	5.83	5.94	6.08	6.23	6.41	6.60	6.81	7.04	7.29	7.55	7.83
5.36	5.43	5.48	5.56	5.66	5.78	5.91	6.07	6.25	6.45	6.66	6.89	7.14	7.41	7.69
5.19	5.26	5.31	5.39	5.49	5.61	5.75	5.91	6.09	6.29	6.51	6.74	7.00	7.27	7.55
5.03	5.09	5.14	5.22	5.32	5.44	5.58	5.75	5.93	6.14	6.36	6.60	6.85	7.13	7.41
4.86	4.92	4.97	5.06	5.16	5.28	5.42	5.59	5.78	5.99	6.21	6.45	6.72	6.99	7.28
4.69	4.75	4.80	4.89	4.99	5.11	5.26	5.43	5.62	5.84	6.06	6.31	6.58	6.86	7.15
4.53	4.58	4.63	4.72	4.82	4.95	5.10	5.27	5.47	5.69	5.92	6.17	6.44	6.72	7.02
4.36	4.41	4.46	4.55	4.65	4.78	4.94	5.12	5.32	5.54	5.77	6.03	6.30	6.59	6.89
4.20	4.24	4.30	4.39	4.49	4.62	4.78	4.96	5.17	5.39	5.63	5.89	6.17	6.46	6.77
4.03	4.07	4.13	4.22	4.32	4.45	4.62	4.81	5.02	5.24	5.49	5.75	6.04	6.33	6.65
3.86	3.90	3.96	4.05	4.16	4.29	4.46	4.65	4.87	5.10	5.35	5.62	5.91	6.21	6.53
3.69	3.74	3.79	3.88	3.99	4.13	4.31	4.50	4.72	4.96	5.22	5.49	5.78	6.09	6.41
3.53	3.57	3.62	3.71	3.83	3.97	4.15	4.35	4.57	4.81	5.08	5.36	5.66	5.97	6.29
3.36	3.40	3.45	3.55	3.67	3.82	4.00	4.20	4.43	4.68	4.95	5.23	5.53	5.85	6.18
3.19	3.23	3.28	3.38	3.51	3.66	3.85	4.06	4.29	4.54	4.82	5.12	5.42	5.74	6.08
3.03	3.06	3.12	3.22	3.35	3.51	3.70	3.92	4.15	4.42	4.70	5.00	5.31	5.64	5.98
2.86	2.89	2.95	3.06	3.19	3.35	3.55	3.78	4.02	4.29	4.58	4.89	5.20	5.53	5.88
2.69	2.72	2.78	2.89	3.03	3.20	3.41	3.63	3.89	4.16	4.46	4.77	5.09	5.43	5.78
2.53	2.55	2.61	2.73	2.87	3.05	3.26	3.50	3.76	4.04	4.35	4.66	4.99	5.33	5.68
2.36	2.38	2.45	2.57	2.72	2.91	3.13	3.37	3.64	3.93	4.24	4.57	4.90	5.24	5.60
2.19	2.22	2.28	2.41	2.57	2.77	3.00	3.25	3.53	3.83	4.15	4.47	4.81	5.16	5.52
2.02	2.05	2.12	2.26	2.42	2.63	2.87	3.13	3.42	3.73	4.05	4.38	4.73	5.08	5.45
1.86	1.88	1.95	2.10	2.28	2.49	2.74	3.01	3.31	3.62	3.95	4.29	4.64	5.00	5.37
1.69	1.71	1.79	1.95	2.13	2.36	2.62	2.90	3.21	3.53	3.86	4.20	4.56	4.93	5.30
1.53	1.54	1.63	1.80	2.00	2.24	2.51	2.80	3.12	3.45	3.78	4.13	4.50	4.87	5.25
1.36	1.38	1.47	1.66	1.88	2.13	2.41	2.72	3.04	3.37	3.72	4.07	4.44	4.81	5.20
1.20	1.21	1.32	1.51	1.75	2.02	2.31	2.63	2.96	3.30	3.65	4.01	4.38	4.76	5.15
1.03	1.05	1.16	1.37	1.63	1.91	2.21	2.54	2.88	3.23	3.58	3.95	4.32	4.71	5.10
.87	.88	1.02	1.24	1.51	1.81	2.13	2.46	2.81	3.17	3.53	3.90	4.27	4.66	5.06
.73	.73	.88	1.13	1.42	1.73	2.06	2.40	2.76	3.12	3.48	3.86	4.24	4.63	5.03
.59	.57	.75	1.03	1.34	1.66	2.01	2.36	2.72	3.08	3.45	3.83	4.21	4.60	5.00
.45	.43	.64	.95	1.27	1.61	1.96	2.32	2.68	3.05	3.42	3.80	4.19	4.58	4.98
.31	.29	.57	.89	1.23	1.58	1.94	2.30	2.66	3.03	3.41	3.79	4.18	4.57	4.97
.22	.00	.55	.87	1.22	1.57	1.93	2.29	2.66	3.03	3.41	3.79	4.17	4.57	4.96
.31	.29	.57	.89	1.23	1.58	1.94	2.30	2.66	3.03	3.41	3.79	4.18	4.57	4.97
.45	.43	.64	.95	1.27	1.61	1.96	2.32	2.68	3.05	3.42	3.80	4.19	4.58	4.98
.59	.57	.75	1.03	1.34	1.66	2.01	2.36	2.72	3.08	3.45	3.83	4.21	4.60	5.00
.73	.73	.88	1.13	1.42	1.73	2.06	2.40	2.76	3.12	3.48	3.86	4.24	4.63	5.03
.87	.88	1.02	1.24	1.51	1.81	2.13	2.46	2.81	3.17	3.53	3.90	4.27	4.66	5.06
1.03	1.05	1.16	1.37	1.63	1.91	2.21	2.54	2.88	3.23	3.58	3.95	4.32	4.71	5.10
1.20	1.21	1.32	1.51	1.75	2.02	2.31	2.63	2.96	3.30	3.65	4.01	4.38	4.76	5.15
1.36	1.38	1.47	1.66	1.88	2.13	2.41	2.72	3.04	3.37	3.72	4.07	4.44	4.81	5.20
1.53	1.54	1.63	1.80	2.00	2.24	2.51	2.80	3.12	3.45	3.78	4.13	4.50	4.87	5.25
1.69	1.71	1.79	1.95	2.13	2.36	2.62	2.90	3.21	3.53	3.86	4.20	4.56	4.93	5.30
1.86	1.88	1.95	2.10	2.28	2.49	2.74	3.01	3.31	3.62	3.95	4.29	4.64	5.00	5.37
2.02	2.05	2.12	2.26	2.42	2.63	2.87	3.13	3.42	3.73	4.05	4.38	4.73	5.08	5.45
2.19	2.22	2.28	2.41	2.57	2.77	3.00	3.25	3.53	3.83	4.15	4.47	4.81	5.16	5.52
2.36	2.38	2.45	2.57	2.72	2.91	3.13	3.37	3.64	3.93	4.24	4.57	4.90	5.24	5.60
2.53	2.55	2.61	2.73	2.87	3.05	3.26	3.50	3.76	4.04	4.35	4.66	4.99	5.33	5.68
2.69	2.72	2.78	2.89	3.03	3.20	3.41	3.63	3.89	4.16	4.46	4.77	5.09	5.43	5.78
2.86	2.89	2.95	3.06	3.19	3.35	3.55	3.78	4.02	4.29	4.58	4.89	5.20	5.53	5.88
3.03	3.06	3.12	3.22	3.35	3.51	3.70	3.92	4.15	4.42	4.70	5.00	5.31	5.64	5.98
3.19	3.23	3.28	3.38	3.51	3.66	3.85	4.06	4.29	4.54	4.82	5.12	5.42	5.74	6.08
3.36	3.40	3.45	3.55	3.67	3.82	4.00	4.20	4.43	4.68	4.95	5.23	5.53	5.85	6.18
3.53	3.57	3.62	3.71	3.83	3.97	4.15	4.35	4.57	4.81	5.08	5.36	5.66	5.97	6.29

Table 3.—*Rupture model of the earthquake*—Continued

Rupture time (s)—Continued

3.69	3.74	3.79	3.88	3.99	4.13	4.31	4.50	4.72	4.96	5.22	5.49	5.78	6.09	6.41
3.86	3.90	3.96	4.05	4.16	4.29	4.46	4.65	4.87	5.10	5.35	5.62	5.91	6.21	6.53
4.03	4.07	4.13	4.22	4.32	4.45	4.62	4.81	5.02	5.24	5.49	5.75	6.04	6.33	6.65
4.20	4.24	4.30	4.39	4.49	4.62	4.78	4.96	5.17	5.39	5.63	5.89	6.17	6.46	6.77
4.36	4.41	4.46	4.55	4.65	4.78	4.94	5.12	5.32	5.54	5.77	6.03	6.30	6.59	6.89
4.53	4.58	4.63	4.72	4.82	4.95	5.10	5.27	5.47	5.69	5.92	6.17	6.44	6.72	7.02
4.69	4.75	4.80	4.89	4.99	5.11	5.26	5.43	5.62	5.84	6.06	6.31	6.58	6.86	7.15
4.86	4.92	4.97	5.06	5.16	5.28	5.42	5.59	5.78	5.99	6.21	6.45	6.72	6.99	7.28
5.03	5.09	5.14	5.22	5.32	5.44	5.58	5.75	5.93	6.14	6.36	6.60	6.85	7.13	7.41
5.19	5.26	5.31	5.39	5.49	5.61	5.75	5.91	6.09	6.29	6.51	6.74	7.00	7.27	7.55
5.36	5.43	5.48	5.56	5.66	5.78	5.91	6.07	6.25	6.45	6.66	6.89	7.14	7.41	7.69
5.53	5.59	5.65	5.73	5.83	5.94	6.08	6.23	6.41	6.60	6.81	7.04	7.29	7.55	7.83
5.70	5.76	5.82	5.90	6.00	6.11	6.25	6.40	6.57	6.76	6.97	7.19	7.44	7.69	7.97
5.86	5.93	5.98	6.07	6.16	6.28	6.41	6.56	6.73	6.91	7.12	7.34	7.58	7.84	8.11
6.03	6.10	6.15	6.24	6.33	6.44	6.58	6.72	6.89	7.07	7.28	7.50	7.74	7.99	8.26
6.20	6.27	6.32	6.41	6.50	6.61	6.74	6.89	7.05	7.24	7.44	7.66	7.89	8.14	8.41
6.36	6.44	6.49	6.57	6.67	6.78	6.91	7.05	7.22	7.40	7.60	7.82	8.05	8.29	8.55
6.53	6.61	6.66	6.74	6.83	6.95	7.07	7.22	7.38	7.56	7.76	7.97	8.20	8.45	8.70
6.70	6.78	6.83	6.91	7.00	7.11	7.24	7.38	7.54	7.72	7.92	8.13	8.36	8.60	8.85

Strike-slip amplitude (m)

0.08	0.08	0.08	0.09	0.20	0.20	0.22	0.24	0.03	0.01	0.01	0.00	0.04	0.13	0.20
.04	.04	.04	.05	.10	.10	.11	.15	.05	.01	.00	.00	.01	.20	.25
.00	.10	.12	.06	.05	.00	.00	.01	.02	.00	.00	.00	.00	.07	.11
.26	.47	.49	.37	.13	.03	.00	.00	.00	.00	.00	.00	.00	.00	.00
.63	.93	.96	.71	.24	.07	.00	.00	.00	.00	.00	.00	.00	.00	.00
.68	1.07	.92	.56	.29	.03	.00	.00	.00	.00	.00	.00	.00	.00	.00
.53	.70	.38	.19	.12	.00	.00	.00	.00	.00	.00	.00	.00	.00	.00
.25	.20	.03	.01	.00	.00	.00	.00	.00	.00	.00	.00	.00	.00	.00
.03	.00	.00	.00	.00	.00	.00	.00	.00	.00	.00	.00	.00	.00	.00
.01	.00	.00	.00	.00	.00	.00	.00	.01	.02	.01	.00	.00	.00	.03
.01	.00	.00	.00	.00	.00	.00	.00	.03	.08	.08	.02	.00	.00	.10
.00	.00	.00	.00	.00	.00	.08	.10	.18	.28	.24	.14	.02	.02	.13
.00	.00	.00	.00	.00	.15	.33	.41	.54	.55	.47	.33	.12	.02	.14
.00	.00	.00	.01	.07	.35	.51	.66	.77	.69	.58	.40	.31	.12	.10
.01	.01	.01	.02	.11	.25	.38	.49	.58	.53	.39	.29	.33	.50	.32
.01	.01	.01	.00	.04	.04	.11	.17	.22	.20	.12	.10	.13	.65	.76
.01	.00	.00	.00	.00	.01	.02	.03	.05	.04	.02	.00	.00	.35	.74
.00	.00	.00	.00	.09	.14	.21	.17	.12	.12	.02	.00	.00	.13	.47
.00	.00	.00	.00	.20	.31	.43	.46	.33	.35	.16	.00	.00	.00	.29
.00	.00	.01	.01	.12	.29	.42	.51	.43	.46	.40	.09	.00	.00	.08
.02	.09	.17	.13	.11	.24	.39	.56	.51	.37	.44	.20	.00	.00	.00
.16	.32	.31	.23	.22	.32	.52	.75	.87	.57	.30	.14	.00	.00	.00
.27	.41	.31	.27	.27	.36	.61	.91	1.19	.98	.38	.06	.00	.22	.24
.29	.40	.38	.37	.42	.51	.66	1.03	1.40	1.28	.53	.04	.19	.64	.71
.35	.51	.57	.60	.69	.77	.82	1.02	1.49	1.65	.73	.01	.37	1.18	1.30
.33	.54	.56	.62	.79	.85	.95	.98	1.23	1.66	1.02	.07	.18	1.35	1.67
.20	.29	.25	.30	.55	.73	.86	.99	1.02	1.30	.95	.15	.00	.98	1.50
.04	.00	.00	.02	.16	.45	.61	.84	.90	1.04	.86	.21	.27	1.06	1.17
.00	.00	.00	.00	.00	.13	.31	.54	.64	.59	.59	.33	.59	1.36	1.06
.00	.00	.00	.00	.00	.00	.08	.32	.45	.21	.14	.27	.84	1.58	1.15
.05	.26	.35	.13	.04	.07	.07	.12	.27	.14	.00	.33	1.21	1.67	1.11
.48	.93	.68	.23	.11	.14	.25	.11	.09	.05	.00	.49	1.39	1.57	.90
.97	1.19	.61	.21	.05	.09	.30	.23	.03	.00	.00	.38	1.29	1.23	.44
.86	.86	.42	.06	.00	.02	.32	.30	.03	.00	.00	.29	.84	.53	.05
.50	.46	.16	.00	.00	.00	.36	.42	.08	.00	.00	.43	.62	.16	.00
.20	.13	.00	.00	.00	.00	.16	.29	.13	.01	.00	.57	.69	.08	.00
.02	.00	.00	.00	.00	.00	.00	.07	.09	.03	.00	.28	.35	.02	.00
.02	.02	.30	.29	.00	.00	.00	.00	.03	.04	.02	.01	.02	.00	.00
.04	.15	.70	.96	.33	.00	.00	.00	.00	.12	.11	.01	.00	.00	.00
.03	.24	.85	1.37	.88	.10	.00	.00	.00	.19	.20	.00	.00	.00	.00
.03	.17	.83	1.55	1.18	.42	.07	.00	.00	.18	.22	.02	.00	.00	.00
.08	.15	.70	1.61	1.67	.91	.22	.00	.00	.18	.21	.02	.00	.00	.00
.13	.22	.66	1.50	1.97	1.71	.68	.00	.00	.09	.12	.03	.00	.00	.00
.14	.25	.63	1.39	2.30	2.54	1.35	.15	.00	.00	.03	.03	.00	.00	.00
.20	.34	.66	1.60	2.95	3.21	1.88	.38	.00	.00	.00	.06	.05	.00	.00

Table 3.—*Rupture model of the earthquake*—Continued

Strike-slip amplitude (m)—Continued														
.58	.75	1.13	2.25	3.53	3.82	2.29	.49	.00	.00	.00	.11	.10	.00	.00
.99	1.54	1.99	2.97	4.18	4.10	2.34	.66	.00	.00	.00	.17	.17	.00	.00
1.24	2.17	2.74	3.61	4.43	3.96	2.50	.91	.07	.00	.01	.27	.23	.01	.00
1.36	2.38	3.09	3.84	4.26	3.92	2.76	1.38	.35	.00	.07	.37	.29	.02	.01
1.18	2.30	3.11	3.74	4.20	4.02	3.19	2.03	.88	.17	.07	.43	.37	.05	.02
1.02	2.13	3.03	3.78	4.27	4.39	3.90	2.66	1.39	.57	.24	.45	.41	.29	.25
1.01	2.09	3.13	4.02	4.69	5.08	4.51	3.19	1.96	1.05	.50	.56	.78	.88	.56
1.06	2.23	3.39	4.39	5.28	5.54	4.87	3.57	2.38	1.51	.76	.72	1.21	1.11	.53
.99	2.23	3.39	4.53	5.36	5.50	4.83	3.53	2.56	1.75	1.01	.87	1.16	.88	.41
.79	1.83	3.01	4.08	4.83	5.02	4.35	3.33	2.56	2.01	1.29	.80	.90	.83	.46
.58	1.42	2.46	3.45	4.20	4.43	3.96	3.19	2.60	2.32	1.34	.50	.83	.97	.71
.52	1.32	2.23	3.23	3.92	4.20	3.94	3.25	2.88	2.44	1.21	.32	.87	1.44	1.28
.62	1.38	2.25	3.27	4.00	4.29	4.04	3.47	3.09	2.54	1.19	.24	1.13	2.13	1.65
.64	1.40	2.23	3.09	3.88	4.16	3.92	3.39	3.01	2.44	.97	.19	1.42	2.60	1.80
.49	1.24	2.01	2.74	3.35	3.61	3.33	2.90	2.62	2.01	.76	.15	1.65	2.99	2.01
.44	1.05	1.75	2.32	2.80	2.94	2.62	2.30	2.17	1.60	.57	.31	2.09	3.31	2.11
.79	1.27	1.72	2.13	2.36	2.38	2.13	1.95	1.90	1.39	.43	.51	2.38	3.45	2.05
1.12	1.77	1.97	2.19	2.19	2.03	1.81	1.77	1.81	1.29	.39	.65	2.60	3.35	1.74
1.22	2.03	2.32	2.34	2.29	1.92	1.76	1.85	1.79	1.26	.42	.86	2.46	2.90	1.48
1.34	2.29	2.66	2.72	2.58	2.29	2.17	2.07	1.91	1.32	.55	.67	1.92	2.29	1.07
1.63	2.72	3.09	3.19	3.01	2.78	2.52	2.25	2.03	1.38	.52	.33	1.15	1.44	.64
1.86	2.90	3.29	3.31	3.09	2.84	2.46	2.32	2.07	1.19	.24	.07	.47	.63	.25
1.74	2.74	3.07	3.01	2.84	2.58	2.42	2.44	1.97	.88	.04	.00	.10	.13	.00
1.40	2.58	2.88	2.97	2.84	2.64	2.74	2.48	1.82	.71	.00	.00	.00	.00	.00
.81	2.17	3.03	3.31	3.33	3.21	3.05	2.58	1.81	.67	.00	.00	.00	.00	.00
.36	1.21	2.66	3.39	3.61	3.62	3.23	2.82	1.97	.73	.00	.00	.00	.00	.00
.14	.47	1.29	2.50	3.09	3.27	3.21	2.86	2.01	.67	.00	.00	.00	.00	.05
.00	.13	.33	1.06	2.05	2.60	2.86	2.60	1.76	.55	.00	.00	.00	.31	.58
.14	.11	.07	.32	1.07	2.01	2.42	2.27	1.41	.34	.00	.00	.22	1.10	1.08
.42	.56	.28	.28	.79	1.49	2.07	1.99	1.12	.17	.00	.00	.61	1.63	1.32
.85	1.15	1.00	.74	.90	1.36	1.79	1.81	1.06	.22	.00	.00	.79	1.95	1.49
1.21	1.68	1.65	1.46	1.26	1.44	1.74	1.66	1.04	.26	.00	.00	.96	2.01	1.40
1.35	1.99	1.95	1.82	1.67	1.58	1.62	1.44	.80	.10	.00	.00	.83	1.77	1.21
1.43	1.99	1.94	1.77	1.65	1.56	1.35	1.02	.37	.00	.00	.00	.66	1.38	.88
1.23	1.74	1.64	1.41	1.28	1.19	1.02	.54	.10	.00	.00	.00	.41	.91	.57
.83	1.08	.94	.82	.68	.63	.51	.27	.05	.00	.00	.00	.19	.44	.27

Dip-slip amplitude (m)														
0.00	0.00	0.03	0.04	0.37	0.37	0.55	0.67	0.11	0.00	0.00	0.00	0.00	0.03	0.06
.00	.00	.00	.00	.15	.15	.23	.48	.23	.00	.00	.00	.00	.06	.10
.00	.12	.13	.00	.00	.00	.00	.01	.07	.00	.00	.00	.00	.04	.09
.41	.73	.72	.39	.00	.00	.00	.00	.00	.00	.00	.00	.00	.00	.04
1.03	1.44	1.41	.98	.18	.00	.00	.00	.00	.00	.00	.00	.00	.00	.01
1.03	1.54	1.28	.76	.34	.04	.02	.00	.00	.00	.00	.00	.00	.00	.00
.71	.91	.44	.17	.14	.00	.00	.00	.00	.00	.00	.00	.00	.00	.00
.35	.25	.00	.00	.00	.00	.00	.00	.00	.00	.00	.00	.00	.00	.00
.08	.03	.00	.00	.00	.00	.00	.00	.00	.00	.00	.00	.00	.00	.00
.02	.00	.00	.00	.00	.00	.00	.00	.00	.01	.05	.00	.00	.00	.00
.00	.00	.00	.00	.00	.00	.00	.00	.00	.01	.11	.19	.04	.00	.00
.00	.00	.00	.00	.00	.00	.00	.00	.05	.05	.09	.30	.25	.01	.00
.00	.00	.00	.00	.00	.00	.00	.00	.08	.22	.19	.34	.40	.09	.00
.00	.00	.04	.08	.19	.18	.16	.12	.03	.31	.45	.54	.88	.52	.01
.01	.04	.15	.28	.49	.60	.57	.50	.21	.13	.43	.54	1.17	1.51	.58
.04	.11	.34	.57	.80	1.03	1.06	.97	.66	.21	.13	.24	.58	1.61	1.37
.09	.31	.67	.88	1.13	1.37	1.47	1.46	1.14	.64	.17	.02	.06	.76	1.21
.22	.59	.77	.96	1.19	1.43	1.60	1.68	1.59	1.06	.50	.08	.00	.35	.67
.34	.55	.54	.78	.98	1.15	1.39	1.47	1.63	1.41	.76	.32	.08	.16	.34
.20	.24	.44	.73	1.05	1.15	1.25	1.34	1.30	1.39	.94	.47	.50	.28	.10
.02	.15	.57	1.01	1.43	1.69	1.66	1.63	1.39	1.12	.86	.45	.74	.97	.41
.03	.25	.77	1.37	1.83	2.25	2.38	2.23	1.91	1.27	.67	.31	.60	1.27	.97
.08	.52	1.16	1.71	2.21	2.60	2.90	2.84	2.44	1.65	.70	.17	.46	1.26	1.23
.40	1.07	1.64	2.15	2.72	3.05	3.19	3.23	2.88	1.95	.77	.08	.18	1.11	1.27
.82	1.46	1.97	2.64	3.25	3.68	3.66	3.41	3.11	2.40	.99	.03	.00	.54	.89
.86	1.46	2.05	2.88	3.57	4.10	4.26	3.70	3.07	2.58	1.42	.20	.00	.19	.42
.70	1.31	1.96	2.66	3.45	4.02	4.37	4.10	3.11	2.38	1.46	.36	.00	.04	.15
.61	1.21	1.88	2.46	3.07	3.70	4.00	4.00	3.25	2.29	1.53	.55	.00	.00	.00

Table 3.—*Rupture model of the earthquake*—Continued

Dip-slip amplitude (m)—Continued														
.58	1.28	1.97	2.52	2.95	3.41	3.66	3.55	3.05	2.17	1.58	.90	.09	.00	.00
.62	1.42	2.07	2.58	2.94	3.21	3.41	3.19	2.66	1.85	1.37	.98	.26	.00	.00
.72	1.63	2.25	2.58	2.84	2.97	3.13	2.80	2.23	1.66	1.27	1.21	.57	.00	.00
1.11	2.13	2.66	2.84	2.94	2.94	2.90	2.44	1.54	1.22	1.28	1.53	.89	.00	.00
1.57	2.58	3.05	3.21	3.15	3.25	3.05	2.36	1.12	.49	.99	1.80	1.16	.00	.00
1.51	2.52	2.86	2.99	3.19	3.41	3.43	2.52	1.02	.08	.47	1.84	1.72	.32	.00
1.15	1.71	1.94	2.36	2.80	3.23	3.47	2.80	1.03	.00	.25	1.38	1.79	.64	.00
.63	.73	1.07	1.76	2.13	2.78	3.39	2.92	1.13	.00	.15	1.04	1.39	.51	.03
.21	.50	.94	1.39	1.67	1.96	2.95	3.13	1.30	.00	.06	.84	1.13	.44	.16
.34	.81	1.17	1.39	1.40	1.31	2.05	2.90	1.67	.12	.00	.66	.83	.33	.33
.57	1.02	1.32	1.57	1.30	.80	1.29	2.34	1.72	.30	.00	.28	.32	.22	.48
.59	1.02	1.51	1.78	1.23	.31	.47	1.74	1.85	.55	.00	.00	.00	.26	.57
.59	1.06	1.72	1.93	1.09	.16	.00	.94	1.77	.81	.00	.00	.00	.27	.63
.82	1.32	1.90	2.03	1.02	.08	.00	.61	1.46	.84	.00	.00	.00	.28	.60
1.04	1.59	2.09	1.84	.65	.01	.00	.33	1.20	.91	.00	.00	.00	.08	.35
1.12	1.74	1.94	1.30	.36	.02	.01	.07	.68	.72	.05	.00	.00	.00	.06
1.04	1.65	1.55	.91	.21	.04	.04	.07	.41	.53	.12	.00	.00	.00	.00
.53	1.13	1.10	.46	.08	.08	.07	.06	.23	.42	.19	.00	.00	.00	.01
.17	.44	.48	.18	.12	.28	.27	.07	.05	.14	.09	.00	.00	.00	.11
.42	.35	.30	.33	.39	.71	.46	.07	.04	.03	.00	.00	.00	.00	.05
.77	1.00	.85	.79	.96	.99	.50	.08	.05	.03	.02	.01	.00	.00	.00
1.09	1.62	1.60	1.44	1.42	1.18	.67	.22	.07	.04	.03	.04	.00	.00	.00
1.17	1.85	1.96	1.88	1.67	1.48	.95	.37	.11	.05	.03	.36	.35	.00	.00
.64	1.48	1.87	1.87	1.85	1.71	1.40	.69	.15	.06	.04	.70	.67	.00	.00
.19	.67	1.33	1.64	1.82	1.94	1.86	1.01	.19	.06	.03	.40	.37	.00	.00
.09	.22	.66	1.28	1.69	2.07	1.96	.99	.20	.03	.03	.10	.06	.00	.00
.06	.29	.50	.91	1.56	1.87	1.73	.88	.14	.02	.03	.08	.01	.00	.00
.16	.49	.85	1.04	1.40	1.64	1.24	.52	.09	.00	.01	.03	.00	.00	.00
.25	.51	1.02	1.35	1.42	1.31	.66	.17	.04	.00	.00	.01	.00	.00	.00
.18	.38	.67	1.13	1.18	.74	.36	.11	.02	.00	.00	.01	.00	.00	.00
.09	.21	.28	.53	.55	.33	.23	.07	.01	.00	.01	.01	.00	.00	.00
.06	.11	.16	.18	.20	.18	.10	.04	.00	.00	.01	.01	.00	.00	.00
.10	.09	.12	.14	.14	.12	.06	.02	.00	.00	.01	.01	.00	.00	.00
.20	.12	.10	.11	.11	.08	.05	.02	.01	.01	.01	.02	.00	.00	.00
.18	.15	.09	.08	.07	.05	.04	.02	.00	.01	.02	.01	.00	.00	.00
.08	.10	.07	.06	.05	.03	.02	.01	.00	.01	.01	.00	.00	.00	.05
.03	.05	.05	.05	.03	.02	.01	.00	.00	.00	.00	.00	.00	.06	.14
.02	.02	.03	.03	.02	.01	.01	.01	.00	.00	.00	.00	.02	.13	.23
.00	.00	.01	.01	.01	.01	.01	.01	.00	.00	.00	.01	.06	.25	.36
.00	.00	.00	.01	.01	.01	.01	.00	.00	.00	.00	.05	.18	.44	.58
.00	.00	.00	.00	.00	.00	.00	.00	.00	.00	.02	.07	.29	.79	.97
.00	.00	.00	.01	.01	.01	.00	.00	.00	.01	.04	.10	.41	1.15	1.13
.00	.00	.00	.01	.01	.01	.01	.01	.01	.02	.06	.10	.51	.99	.76
.00	.00	.00	.01	.01	.01	.01	.00	.01	.02	.06	.08	.28	.49	.40
.00	.00	.00	.00	.00	.00	.00	.00	.00	.02	.05	.06	.05	.15	.18
.00	.00	.00	.00	.00	.00	.00	.00	.01	.03	.06	.06	.03	.01	.02
.00	.00	.00	.00	.00	.00	.00	.00	.02	.06	.08	.05	.00	.00	.00
.00	.00	.00	.00	.00	.00	.01	.02	.05	.09	.09	.03	.00	.00	.00
.01	.00	.00	.00	.00	.00	.01	.04	.08	.10	.07	.01	.00	.00	.00
.03	.01	.00	.00	.00	.00	.01	.05	.09	.10	.05	.00	.00	.00	.11
.09	.04	.00	.00	.00	.00	.00	.03	.08	.15	.09	.07	.07	.11	.28
.25	.17	.03	.00	.00	.00	.00	.01	.16	.30	.29	.31	.19	.22	.29
.32	.28	.03	.01	.00	.00	.00	.00	.24	.31	.35	.36	.12	.13	.10

There are several possible explanations for this amplitude discrepancy, including too short a rise time, a lower average rupture velocity than assumed, and unmodeled slip occurring after the rupture front passed. The discrepancy could not be accounted for by changing the assumed rupture velocity, as discussed above. Similarly, inverting the data using a rise time much longer than the assumed 0.3 s degrades the fit to the data. Finally, allowing the rupture time to be a free parameter results in rupture models that still have the same discrepancy.

I believe that the primary source of the amplitude discrepancy is most likely the inability of the theoretical Green's functions to match the phase of the true Green's functions precisely. In the presence of such errors in phase, the least-squares misfit to the data will be smaller if the amplitudes of the predicted waveforms are smaller than those of the observed waveforms, biasing the solution toward lower slip values and a lower seismic moment. To correct for this bias, I adopt the median ratio of peak amplitudes for the *y* component of motion in the observed versus predicted seismograms to rescale the slip model. The resulting ratio of 1.8 eliminates the waveform-amplitude misfit and scales the seismic moment to 2.3×10^{19} N-m, a result consistent with that determined in other studies. A more satisfactory way to address this problem in future studies would be to use aftershock recordings to calibrate site and path effects.

Deconvolved displacements, obtained by integrating the corrected accelerograms, bandpass filtering between 0.33 and 2 Hz, and deconvolving the assumed slip-velocity function, are compared with the observed data in figure 4. The 220° component of motion at stations near the fault trace, or on the northwest-southeast extension of the fault trace, is predicted quite well by the rupture model; this

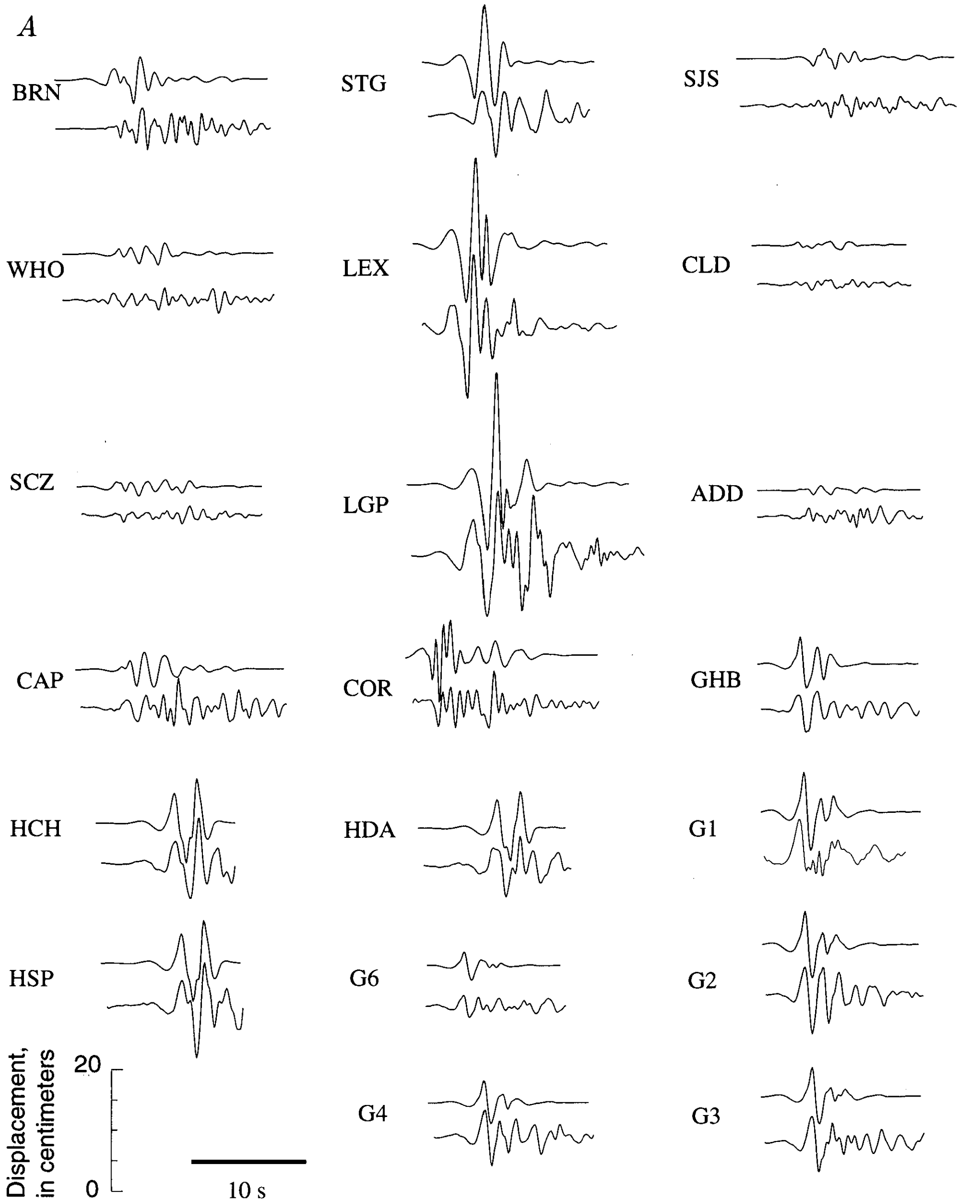

Figure 4.—Fit to fault-perpendicular (220° clockwise from north) (*A*) and fault-parallel (130° clockwise from north) (*B*) components of deconvolved displacement at 20 strong-motion stations used in inversion (see fig. 1 for locations). Upper curve, predicted seismogram; lower curve, observed seismogram. 220° component of displacement was used to scale rupture model so that median peak amplitudes in predicted seismograms fit median peak amplitude in observed seismograms.

component of motion at these stations is dominated by *SH* waves. In contrast, the 130° component of motion at these stations is rather poorly fitted by the rupture model (for example, the 130° component of motion at sta. COR, fig. 1), a result attributable to the fact that this component consists largely of *P–SV* waves and is nearly nodal for an idealized planar fault. Irregularities in fault geometry and lateral heterogeneity in the velocity structure are the probable causes of these discrepancies (Cormier and Beroza, 1987; Beroza and Spudich, 1988). Stations far removed from the fault are not predicted to be nodal, and the model does a much better job of fitting these data.

The slip amplitude in the hypocentral region was found to be approximately 1 m; immediately updip from the hypocenter it is even less. This result is consistent with the observation that the station at Corralitos (COR, fig. 1) recorded relatively small slip amplitudes, despite its location nearly directly updip from the hypocenter. I find two main areas of concentrated slip (fig. 3*B*). One area is centered 7 km northwest of the hypocenter at 14-km depth, with a peak slip of 4.5 m, and is responsible for the large amplitudes observed at stations northwest of the hypocenter. The other area, located 12 km southeast of the hypocenter at 12-km depth, with a peak amplitude of 5.9

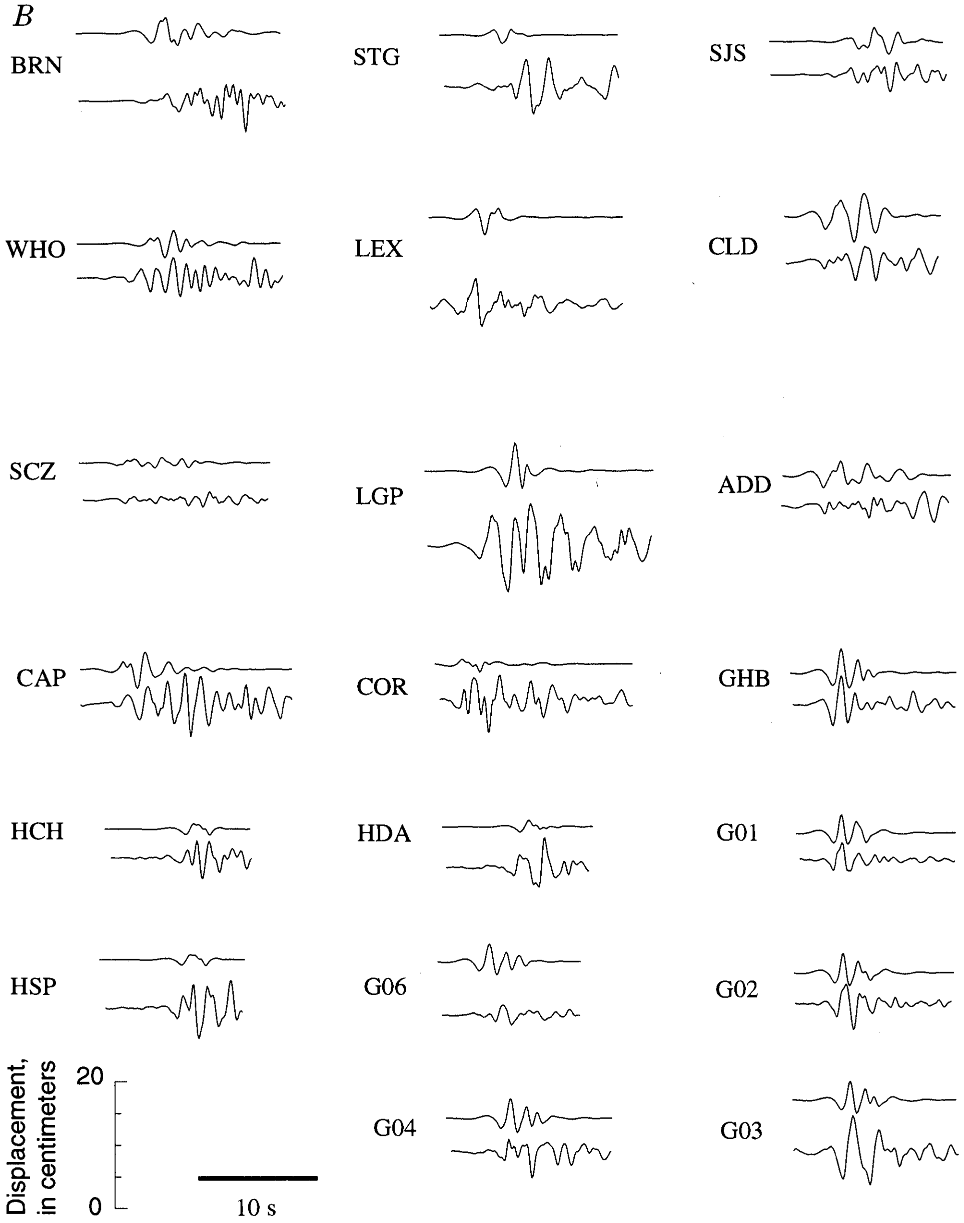

Figure 4.—Continued

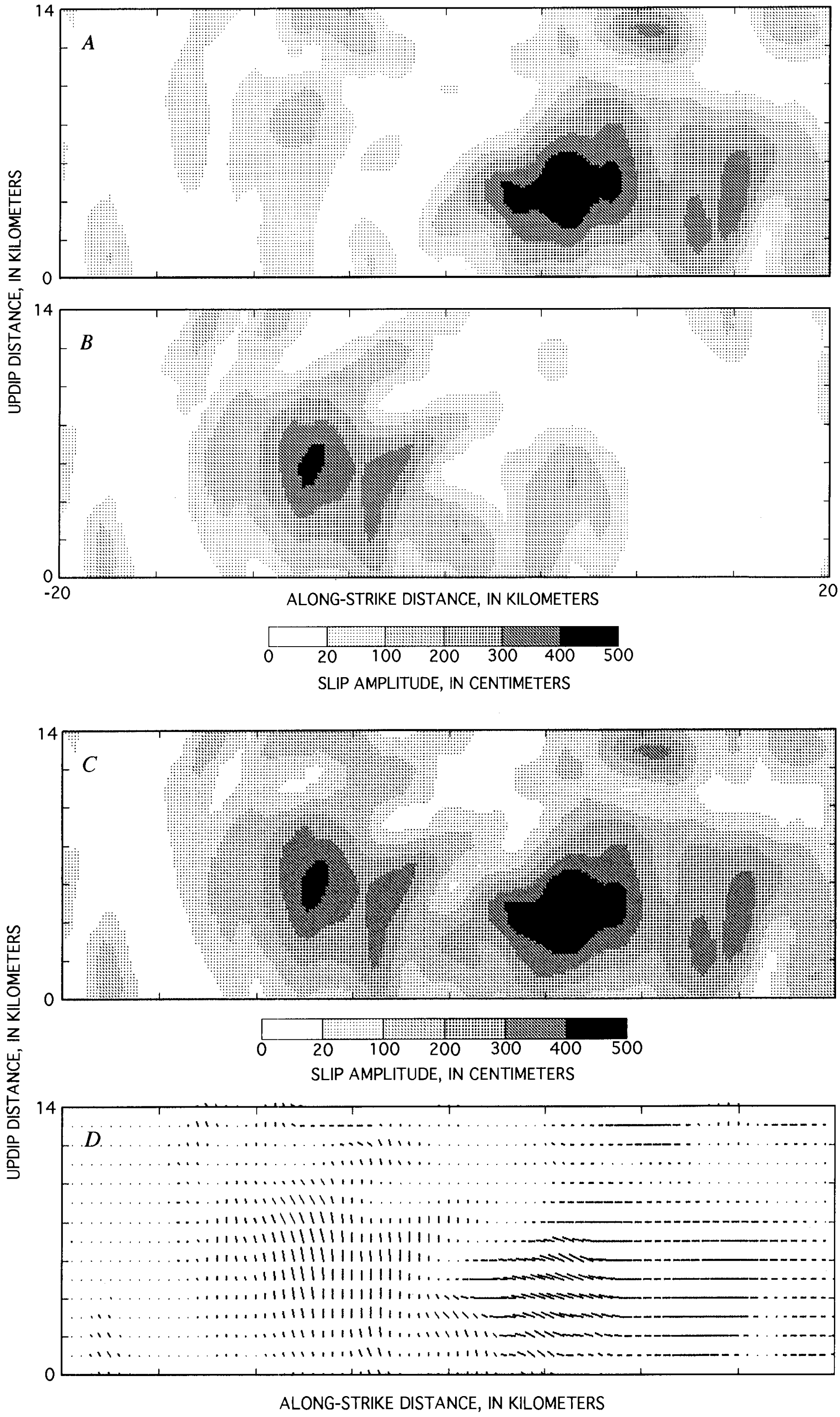

Figure 5.—Slip amplitudes (*A–C*) and rake (*D*) in rupture model of earthquake. *A*, Right-lateral component of slip vector. Note that most slip occurs southeast of hypocenter (at 0 km along strike and 0 km updip). *B*, Reverse dip-slip component of slip vector. Note that most slip occurs northwest of hypocenter. *C*, Total slip. *D*, Local orientation (rake) and relative length of slip vector (motion of hanging wall).

m, is responsible for the large amplitudes observed at stations southeast of the hypocenter. Several other high-slip areas on the southeastern section of the fault are less well constrained, owing to the station distribution.

The overall extent of the high-slip area in this model is from about 13 km northwest of the hypocenter, near the intersection of the surface traces of the Sargent and San Andreas faults, to 20 km southeast of the hypocenter. This area is considerably smaller than the extent of the aftershock zone, which is approximately 50 km. Nearly all the slip occurred at 9- to 16-km depth. Substantial slip is thus confined to an area of about 230 km^2, quite small for an M_L=6.9 event.

With few exceptions (for example, Romanowicz and Lyon-Caen, 1990), slip in the 1989 Loma Prieta earthquake has previously been modeled as oblique, with a constant rake. I allowed the rake to vary in the rupture model by separately estimating variations in the dip-slip and strike-slip amplitudes. The distributions of right-lateral strike slip, reverse slip, and total slip are plotted in figures 5*A*, 5*B*, and 5*C*, respectively, and the local orientation (rake) and relative length of the slip vector in figure 5*D*. Slip near the hypocenter is oblique, but to the northwest it is dominated by the dip-slip component, and to the southeast by the strike-slip component. The peak reverse-slip amplitude is 4.4 m, in the high-slip area northwest of the hypocenter (fig. 3*B*) where the strike-slip amplitude is less than 1 m. The peak strike-slip amplitude is 5.9 m in the high-slip area southeast of the hypocenter (fig. 3*B*), where dip slip is low. Farther to the southeast, slip is purely right lateral. Although I find a strong spatial partitioning of slip, the proportions of the total strike-slip and dip-slip moments are the same in this model as in the teleseismic and geodetic models. This consistency is derived rather than imposed because no teleseismic data and no constraint on the point-source moment tensor are used in the modeling.

The partitioning of total slip into strike-slip and dip-slip components is a surprising result, and it would be useful to determine whether such variations are required by the data. To do so, I devised a simple norm that minimizes the deviation of the slip vector from a constant assumed direction. If s is the estimated slip vector and s_0 is the assumed slip vector, then the norm to be minimized while fitting the data is given by $\alpha(s-s_0)^T(s-s_0)$, where the superscript T denotes the vector transpose and the factor α determines the importance assigned to fitting the assumed rake. By modeling the data with different values of α, the variations in rake required to fit the data can be determined.

In applying this procedure, I assumed the relative proportions of the slip vector to be 1.6 m of strike slip and 1.2 m of dip slip. The data do not strongly constrain the slip on the northwest end of the fault zone to be predominantly dip slip, and oblique slip in the assumed direction will fit the data nearly as well on this segment of the fault. Southeast of the hypocenter, however, oblique slip will seriously degrade the fit to the data because at many stations to the southeast, the contribution of reverse slip to the seismograms is opposite in sign to that for strike slip and opposite to that observed.

COMPARISON WITH OTHER STUDIES

Four extended-source models of the earthquake have previously been published (Beroza, 1991; Hartzell and others, 1991; Steidl and others, 1991; Wald and others, 1991). Although many of the data are common to these four studies, several differences in the analyses can lead to varying results, including different frequency bands, data selection (for example, velocity versus displacement seismograms), station corrections, model parametrizations, matrix-inversion methods, and solution methods for the forward problem. I now briefly review the assumptions used in each study in comparison with those used in this paper.

Beroza (1991) used the horizontal components of displacement in the frequency band 0.33–2 Hz for 20 of the closest strong-motion stations. The parametrization of the rupture history allowed each point of the fault to slip only once, with a constant slip-velocity function ($t^{-1/2}$ singularity) and duration (0.3 s) of slip after rupture. The inversion was performed by using a tomographic backprojection technique that approximates a least-squares inversion with inequality constraints on the slip direction and smoothness constraints on the perturbations to slip amplitude and rupture time. The forward problem was solved by using geometric-ray theory in a time-dependent Kirchoff formulation (Spudich and Frazer, 1984). This method has some advantages over more computationally intensive, complete-seismogram methods in that it eliminates the need for a subfault formulation, but it is applicable only at frequencies high enough that near-field contributions are unimportant.

Steidl and others (1991) modeled strong-motion velocity records from 20 near-source stations filtered over the frequency band 0.05–1 Hz. In their parametrization of the rupture history, they divided the fault plane into subfaults and allowed each subfault to slip once with variable slip amplitude and rupture time, using a constant slip velocity function (isosceles triangle) of 1-s duration. The inversion was performed with inequality and smoothness constraints. The forward problem was solved by using a complete-seismogram method.

Hartzell and others (1991) used teleseismic *P* waves from 24 stations and *SH* body waves from 16 stations in the Global Seismic Network at frequencies above 1 Hz and great-circle distances of 30°–90°. In their parametrization of the rupture history, they divided the fault into subfaults and allowed each subfault to rupture once. The forward problem was solved by using generalized ray theory. The inversion was performed using both L_1 and L_2 norms with inequality and smoothness constraints. Because all the other cited studies used the L_2 norm, I discuss their results for the L_2 norm inversion.

Wald and others (1991) used teleseismic *P*-wave velocity waveforms from 16 stations, teleseismic *SH* velocity waveforms from 8 stations, and velocity records from 16 near-source stations in the frequency band 0.1–1.0 Hz. In their parametrization of the rupture history, they divided the main-shock fault plane into subfaults and allowed each subfault to rupture as many as 3 times at 0.6-s intervals, with a triangular slip-velocity function of 0.7-s duration each time. Seismograms were calculated by using generalized ray theory and the discrete-wavenumber/finite-element (DWFE) method. The inversion was performed by using a least-squares method, with inequality and smoothness constraints imposed on the slip amplitudes.

Although there is substantial overlap in the data sets used, each of the analyses differs substantially. The frequency band used by Hartzell and others (1991), Steidl and others (1991), and Wald and others (1991) includes lower frequencies than that used by Beroza (1991); however, Beroza modeled displacement rather than velocity, a procedure that has the effect of emphasizing lower frequencies. The matrix-inversion methods, though different, should yield similar results because each incorporates smoothing and inequality constraints in a least-squares procedure.

The total slip amplitudes derived for the 1989 Loma Prieta earthquake in these four studies is plotted in figure 6. There are several similarities in the four models. All the studies find low slip in the hypocentral region and a bimodal distribution of slip with respect to the hypocenter. The seismic moments range from 2.3×10^{19} to 3.5×10^{19} N-m, spanning approximately the same range determined teleseismically at longer periods.

The location of the high-slip areas differs among the four models. The spatial distribution of slip amplitude seems to be most similar in the models of Beroza (1991) and Wald and others (1991), although Wald and others show slip extending approximately 5 km farther to the northwest and more slip occurring to the northwest than to the southeast. Peak slip amplitudes in these areas in Steidl and others' (1991) model are approximately 5 km farther from the hypocenter. In Hartzell and others' (1991) model, the location of the high-slip area to the southeast is similar to that in the models of Beroza and of Wald and others, whereas the location of the high-slip area to the northwest is more similar to that in Steidl and others' model. Hartzell and others' model shows an asymmetry of slip not seen in the other models, with nearly all slip occurring to the southeast of the hypocenter. Steidl and others' model has the most symmetrical distribution of slip about the hypocenter. The depth extent of faulting is similar in all the models, except that Hartzell and others' model shows substantially more shallow faulting, possibly because their model does not incorporate any of the near-source data.

Though not shown in figure 6, the rake differs substantially among the four models. Beroza's (1991) model shows a systematic increase in the reverse-slip component from predominantly right-lateral strike slip in the southeast to predominantly reverse dip slip to the northwest. Wald and others' (1991) model shows relatively little variation in rake along strike, whereas the models of Hartzell and others (1991) and Steidl and others (1991) show a similar variation in rake to that in Beroza's model.

In summary, the four extended-source models shown in figure 6 agree surprisingly well, much better than the extended-source models of the 1979 Imperial Valley, Calif., earthquake (Olson and Apsel, 1982; Hartzell and Heaton, 1983; Archuleta, 1984). Nonetheless, substantial differences exist that are important for seismic-hazard assessment—for example, in the depth extent of faulting—and for understanding fault mechanics—for example, in the rapid variation of rake along strike. Further refinements to near-source inversion methods and the use of other data will be required to resolve such ambiguities.

VALIDITY OF THE HIGH-FREQUENCY APPROXIMATION

I have used a high-frequency approximation that is valid, provided that the observer is several wavelengths from the source (Spudich and Frazer, 1984). Thus, it is worth checking whether the approximation is adequate empirically. To do so, I calculated complete synthetic seismograms, using the DWFE method (Olson and others, 1984) as modified by Spudich (1981) for my rescaled extended-source model, for five stations, SJS, LGP, BRN, WHO, and SCZ (fig. 1), located on both sides of the fault over a range of distances.

The complete versus ray-theoretical seismograms for three components of motion in the frequency band (0.33–2.0 Hz) used to generate the rupture model are compared in figure 7. The agreement is generally quite favorable. Even station LGP (fig. 1), which is located directly on the fault, agrees well for two of the three components. Exceptions to a good agreement are a difference in the *y* component at station SJS and an amplitude difference in the *y* component at station LGP. Although the cause of these discrepancies is unclear, they are limited and relatively mild. Thus, the high-frequency approximation appears to be valid over the frequency band used.

By including lower frequencies in the inversion, the point where the high-frequency approximation breaks down can be determined. This point varies from station to station, with a substantially lower frequency of validity for several stations; however, because it is difficult to predict when this breakdown will occur, it is better to be conservative in choosing the lower-frequency limit.

It would be desirable to include lower-frequency data in future inversions. One impediment is that nearly all the stations are analog, and so the low-frequency information is difficult to recover. It is surprising how much of the signal is lost in this way. The same complete seismograms shown in figure 7 are plotted in figure 8, high-pass filtered at 0.25 Hz, which is a typical lower limit for displacement derived from analog strong-motion records. The other seismograms, which are not high-pass filtered, indicate how much signal is lost in the digitization. Potential slow or smooth components of the earthquake rupture that generate no strong high-frequency waves would be much more easily visible at lower frequencies. Accurate digital accelerographs could alleviate this problem.

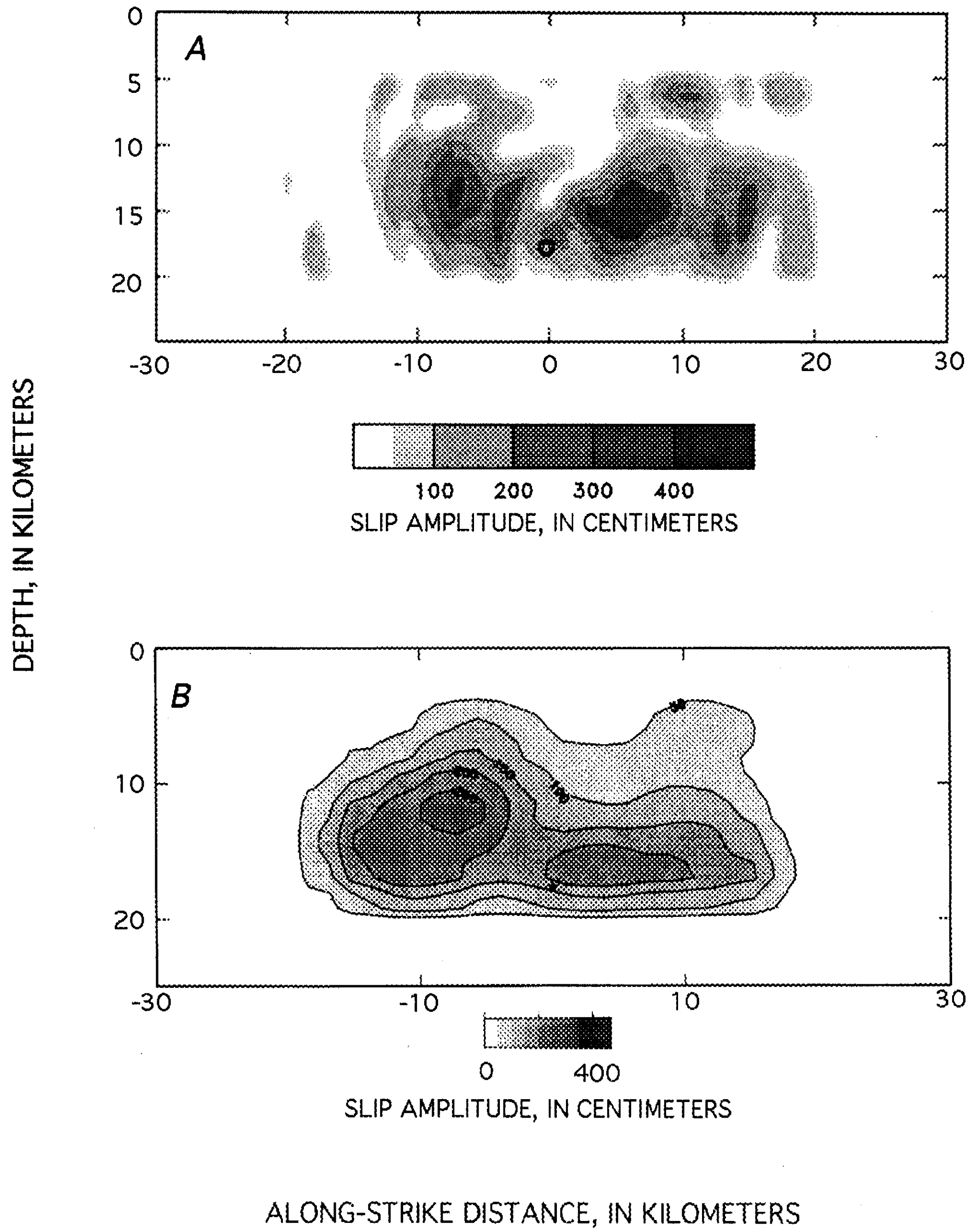

Figure 6.—Amplitude of total slip in extended-source models of earthquake. Star, hypocenter. *A*, Model of Beroza (1991). *B*, Combined strong-motion teleseismic model of Wald and others (1991). *C*, L_2 model of Hartzell and others (1991). *D*, Model of Steidl and others (1991).

COMPARISON WITH LONG-PERIOD NEAR-SOURCE DATA

Although only high-frequency seismograms were used to calculate the rupture model, the availability of digital strong-motion records of the 1989 Loma Prieta earthquake allows a comparison of my rupture model with observations at much longer periods. For this purpose, complete seismograms were calculated, using the DWFE method, for the displacement data from the accelerograph at the station in the Santa Theresa Hills (SJS, fig. 1). These seismograms were then filtered with a zero-phase, low-pass filter at 1 Hz and a high-pass filter at 0.01 Hz. The two seismograms are compared in figure 9.

The agreement is fairly good on all three components, suggesting that the parametrization and assumptions used here are capable of representing most of the slip in the earthquake. The apparent static offset on the 130° and vertical (*z*) components match the observed seismograms quite well, but the 220° component is somewhat overpredicted by the rupture model. The most obvious disagreement between the two seismograms is a tendency for the large displacement pulse to be somewhat broader in the observed waveforms than in the predicted seismo-

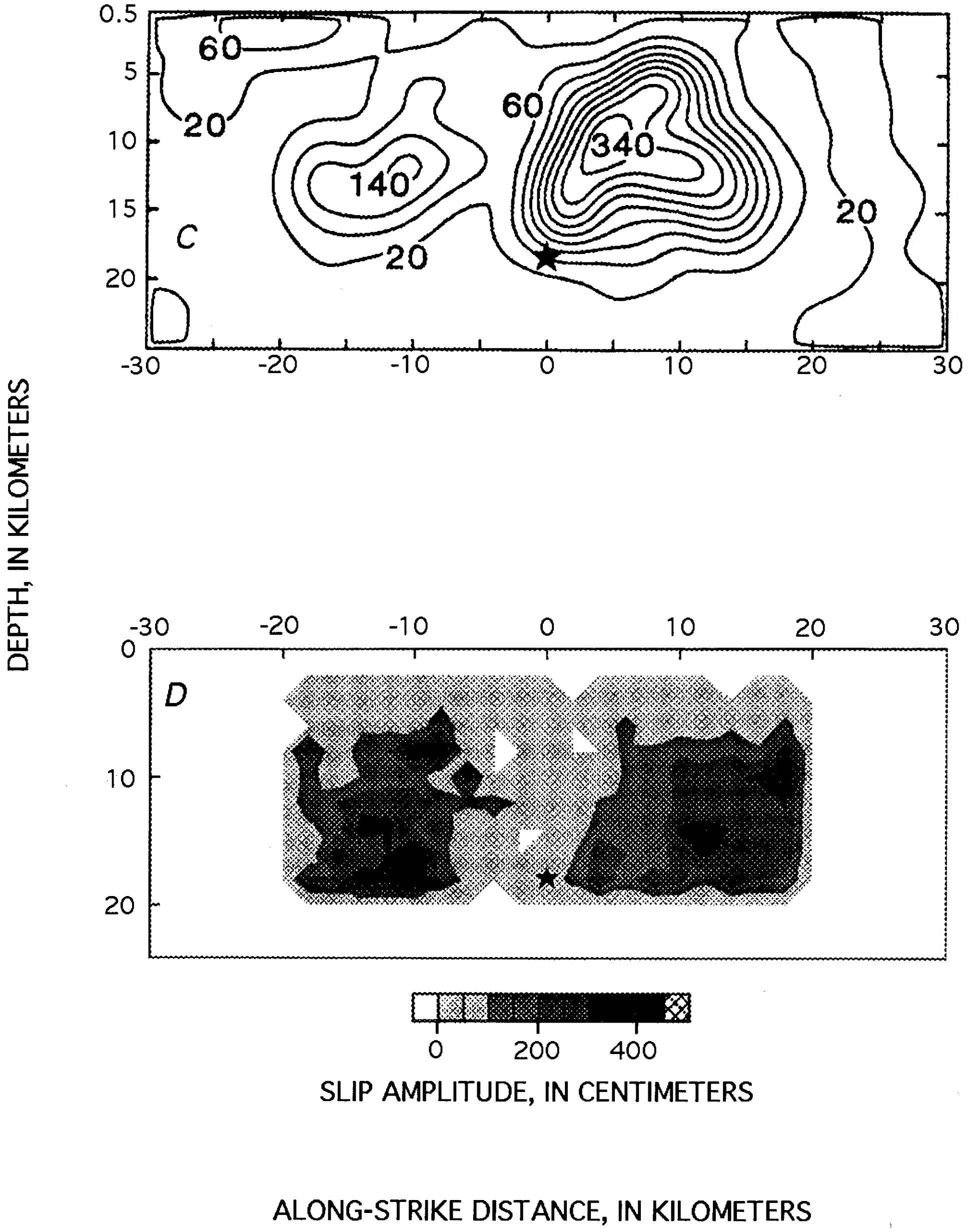

Figure 6.—Continued

grams. This difference could have several causes, including a lower rupture velocity, rupture propagation farther to the northwest, or a longer rise time. The generally good agreement between the predicted and observed seismograms at long periods for this station suggests that the rescaled model correctly recovers the seismic moment of the earthquake and that the parametrization of the rupture process is consistent with the data even at very long periods.

Such long-period near-source data can provide valuable constraints on the rupture history and are not as sensitive to path and site effects as high-frequency data. If the digitization is accurate enough, the strong-motion data can also record the static offset. Measuring static displacements in this way would provide important information and be free of the reference-frame problems that plague most geodetic measurements.

EXTENT OF COSEISMIC RUPTURE AND THE POTENTIAL FOR FUTURE EARTHQUAKES

Coseismic faulting extended over slightly more than half of the 50-km-long aftershock zone, from about 13

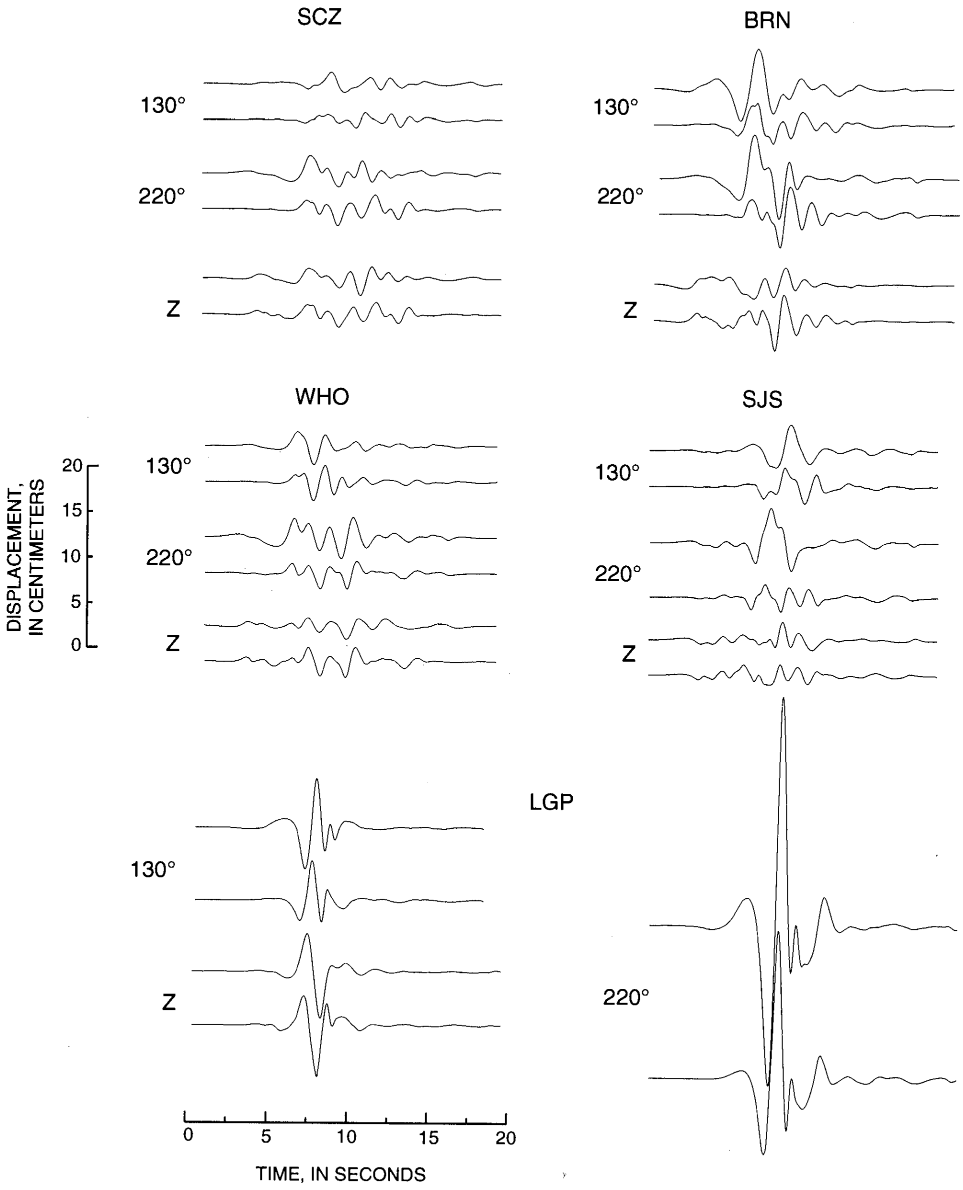

Figure 7.—Theoretical seismograms calculated by using discrete-wavenumber/finite-element method (upper curve) in comparison with ray-theoretical seismograms (lower curve) for 130°, 220°, and vertical (*z*) components of displacement over frequency band 0.33–2 Hz at five strong-motion stations (see fig. 1 for locations).

km northwest to 20 km southeast of the hypocenter. To the northwest, rupture reached the intersection of the San Andreas and Sargent faults. To the southeast, rupture extended into the region where the fault plane delineated by aftershocks warps into a vertical fault (Dietz and Ellsworth, 1990).

The geometry of the Loma Prieta fault plane and the depth of faulting make it difficult definitively to associate the 1989 Loma Prieta earthquake with the San Andreas fault. All we can say is that rupture propagated upward from the hypocenter until it reached a point about 10 km below the surface trace of the San Andreas fault. Slip at shallower depths is much lower in all the extended-source models, and the aftershock distribution becomes diffuse. If the San Andreas fault is vertical in this area, as suggested by the sparse seismicity before the earthquake (Olson, 1990), then the earthquake may have ruptured a fault distinct from the San Andreas and terminated at the lower reaches of the San Andreas fault. The San Andreas fault may even have acted as an obstacle to rupture during the earthquake. The location and geometry of slip in the earthquake cast doubt on long-term forecasts of the 1989

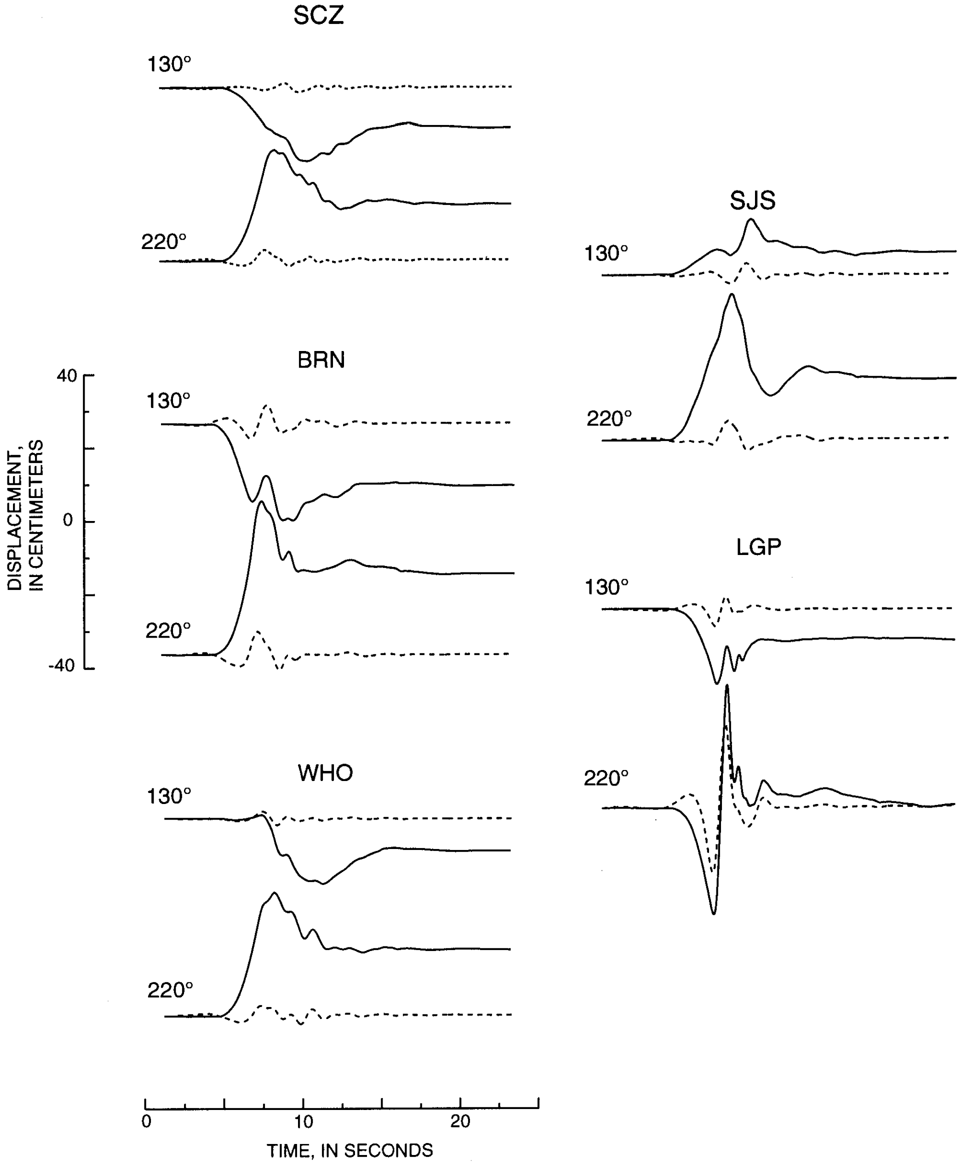

Figure 8.—Theoretical seismograms calculated using discrete-wavenumber/finite-element method for 130° and 220° components of displacement, unfiltered (solid line) and highpass filtered at 0.25 Hz (dashed curve), at five strong-motion stations (see fig. 1 for locations), showing how high-frequency displacement records recovered from analog accelerograms represent only a small fraction of ground motion recorded at longer periods.

Loma Prieta earthquake based on estimates of shallow slip on the San Andreas fault in previous earthquakes.

Additional doubts about any long-term forecast of the earthquake are raised by the work of Segall and Lisowski (1990) who demonstrated that the motion of Loma Prieta (fig. 1) in the 1906 San Francisco earthquake was completely unlike that in 1989. Their analysis indicated that much more strike slip occurred in the southern Santa Cruz Mountains during the 1906 earthquake than during the 1989 earthquake and that much of the slip in 1906 was shallow. Because most slip in the 1989 earthquake occurred below 10-km depth, this earthquake cannot be considered a repeat of the 1906 earthquake in the southern Santa Cruz Mountains, even if both earthquakes occurred on the same fault.

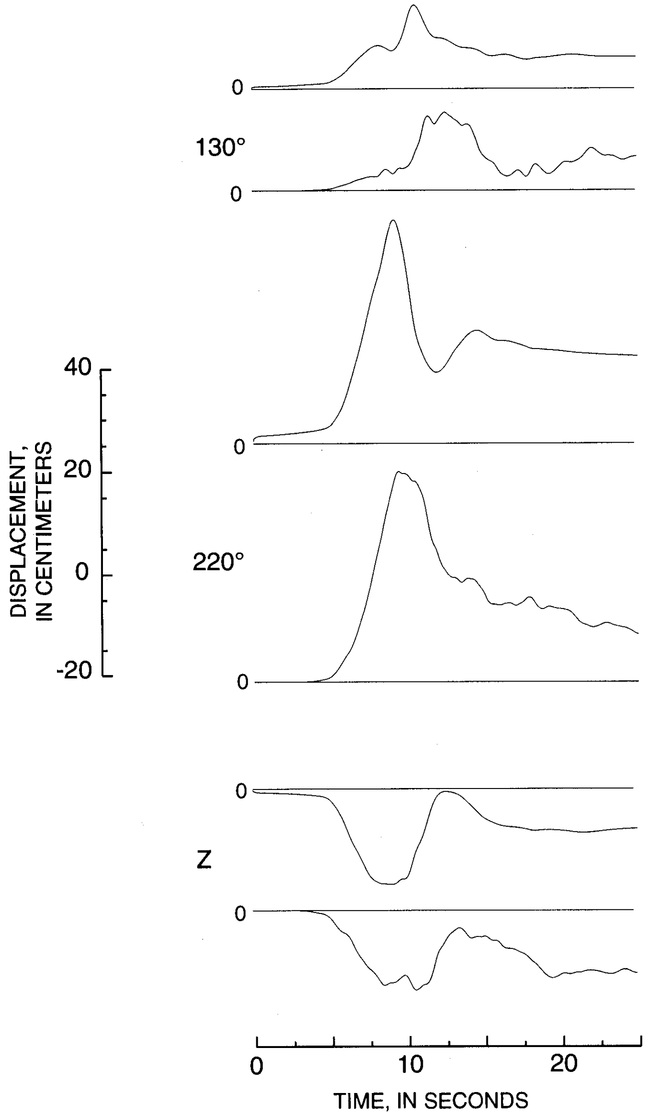

Figure 9.—Theoretical seismograms calculated by using the discrete-wavenumber/finite-element method (upper curve) in comparison with observed seismograms (lower curve) for 130°, 220°, and vertical (*z*) components of displacement over frequency band 0.01–1.0 Hz at station SJS (fig. 1). Vertical component has been inverted so that positive values correspond to upward motion. Horizontal lines, zero displacement level.

The results of this study and of that by Segall and Lisowski (1990) suggest that the coincidence of long-term forecasts of a large earthquake on the southern Santa Cruz Mountains section of the San Andreas fault (Lindh, 1983; Sykes and Nishenko, 1984; Thatcher and Lisowski, 1987; Working Group on California Earthquake Probabilities, 1988) with the occurrence of the 1989 Loma Prieta earthquake may have been only fortuitous. The potential for future earthquakes on this segment of the San Andreas fault is estimated to be extremely low (Working Group on California Earthquake Probabilities, 1990); however, the results presented in this paper suggest that the remaining seismic hazard remains uncertain and may be higher than is widely appreciated.

HETEROGENEOUS FAULTING AND AFTERSHOCKS

Well-located aftershocks from the USGS (Oppenheimer, 1989), as well as large early aftershocks (Simila and others, 1990), are projected onto the assumed fault plane along the fault-normal vector in figure 10. There is a distinct correlation between areas of high slip during the main shock and areas of low aftershock activity. The strongest concentration of aftershocks to the northwest is situated just beyond the end of the high-slip area at the intersection of the San Andreas and Sargent fault traces, about 15 km along strike. Included in this group are the large, early aftershocks located by Simila and others (1990). The area of very low slip directly updip from and southeast of the hypocenter shows a considerable amount of aftershock activity. The two patches of very high slip occurred on parts of the fault that showed very little aftershock activity. Also, very few aftershocks occurred in the hypocentral region.

The tendency for high-slip areas during earthquakes to be deficient in aftershocks relative to adjacent areas of the fault, which has been noted by several investigators (for example, Hartzell and Mendoza, 1988; Beroza and Spudich, 1988; Houston and Engdahl, 1989) is important in understanding the cause of rupture heterogeneity. Two possible explanations for heterogeneous rupture are that the heterogeneity is controlled by fault-zone heterogeneity or by the dynamics of a fault with uniform properties.

In the fault-zone-heterogeneity model, high-slip areas in the main shock are areas of enhanced strength, either because of variations in material properties or because of complexities in the fault-zone geometry (Kanamori, 1981). These areas are too strong to rupture except during large earthquakes, accounting for the observation that high-slip areas show little seismicity during both the aftershock sequence and the interseismic period (for example, Houston and Engdahl, 1989; Schwartz and others, 1989).

In the alternative model, high-slip areas are not due to changes in material properties. Horowitz and Ruina (1989) showed how complex rupture behavior is possible with a spatially homogeneous fault. In their model, a wide range of slip behavior results from a homogeneous fault governed by a state-variable friction law (Dieterich, 1979). In such a model, it is unclear how aftershocks would be related to main-shock slip; however, aftershocks and earthquakes during the interseismic period may be controlled in the same way. If so, then variations in seismicity may result from the same fault-constitutive behavior responsible for the spatial variations in main-shock slip. Thus, it may be impossible to differentiate between the two models by comparing the distribution of main-shock slip with the distribution of seismicity.

The most promising approach to differentiating between these models may be to use independent data to infer variations in fault-zone properties at depth. High-slip areas during the 1989 Loma Prieta earthquake correlate fairly well with areas of high seismic velocities within the fault zone, as determined by Eberhart-Phillips and others (1990) and Lees (1990). If rupture variations during many earthquakes were systematically correlated with such fault-zone heterogeneity, it would argue persuasively for a causal relationship.

VARIATIONS IN SLIP DIRECTION

In the rupture model of the 1989 Loma Prieta earthquake, slip ranges from nearly pure strike slip at the southeast end of the rupture zone to nearly pure reverse slip at the northwest end. Such a strong variation in slip direction over a short distance of about 20 km is a surprising result. As discussed above in the section entitled "Results," slip northwest of the hypocenter could be modeled as oblique without substantially degrading the fit to the data, but it was much more difficult to introduce a substantial reverse-slip component to slip southeast of the hypocenter. Variations in rake during rupture have been observed during other earthquakes, such as the 1979 Imperial Valley, Calif., earthquake (Olson and Apsel, 1982), but not on such a large scale. If this rupture model is correct, there ought to be supporting evidence in other data sets.

Broadband teleseismic studies may provide additional constraints, but apparently the data can be fitted quite well with a point source of oblique slip. Geodetic data could provide an independent check on the rupture model, and other studies (Marshall and others, 1991; see Williams and others, this chapter) support a variation in rake similar to the one found here. Support for this variation might also be found in the focal mechanisms of aftershocks analyzed by Oppenheimer (1990). Although there is a great diversity of mechanisms, he reported that events northwest of the hypocenter tend to have oblique mechanisms, whereas those southeast of the hypocenter tend to have purely strike-slip mechanisms (Oppenheimer, 1990). Beroza and Zoback (1993) tested whether aftershocks relieve the main-shock-induced stress change implied by rupture model and found that they do not. Thus, the use of aftershocks mechanisms may neither confirm nor deny a strong variation in rake.

A source of potential bias in the estimate of rake is the inadequacy of the theoretical Green's functions. If the

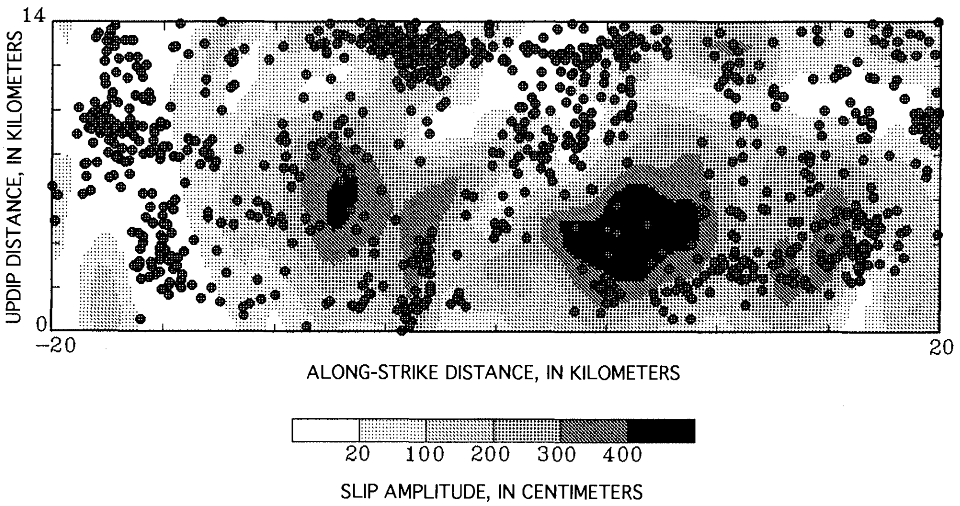

Figure 10.—Distribution of well-located aftershocks of $M \geq 1.0$ that occurred during October 1989 superimposed on assumed fault plane in rupture model (see fig. 3*B*), showing correlation between high-slip areas and areas of low aftershock activity. Note abundant aftershock activity in low-slip areas both updip and northwest of hypocenter (at 0 km along strike and 0 km updip).

polarity of the predicted waves differs substantially from the true polarity, spurious variations in rake might be observed. One approach to addressing this problem is to model the effects of known lateral variations in velocity structure (Eberhart-Phillips and others, 1990; Lees, 1990) on the predicted waveforms by combining dynamic ray tracing with the high-frequency, near-source approximation (Cormier and Beroza, 1987). Another approach is to model the ground motion of aftershocks, for which focal mechanisms are well known (Oppenheimer, 1990). Use of these techniques should allow this issue to be addressed in the future.

CONCLUSIONS

Coseismic faulting extended over slightly more than half of the 50-km-long aftershock zone, from about 13 km northwest to 20 km southeast of the hypocenter. To the northwest, rupture reached the intersection of the San Andreas and Sargent faults. The southeast end of rupture extends to the region where the fault plane delineated by aftershocks warps into a vertical fault. Nearly all of the slip occurs below 10-km depth, and rupture in the updip direction may have been terminated by a vertical San Andreas fault. The depth and location of slip on a dipping fault that terminates ~10 km below the surface trace of the San Andreas fault suggest that forecasts of an M=7 earthquake on the San Andreas fault in the southern Santa Cruz Mountains based on estimates of shallow slip in previous earthquakes may not be relevant for the 1989 Loma Prieta earthquake and that the seismic hazard on this segment of the San Andreas fault remains uncertain.

We find two areas of very high slip: one approximately 7 km northwest of the hypocenter at 12-km depth and another 6 km southeast of the hypocenter at 14-km depth, with peak slip amplitudes of 4.5 and 5.9 m, respectively. These high-slip areas are observed to have a relative paucity of aftershocks, whereas regions of low slip within the rupture zone have a relative abundance of aftershocks. This observation, together with the correlation of areas of high slip with areas of anomalous seismic velocity, suggests that rupture heterogeneity is caused by strength heterogeneity in the fault zone.

There is a surprisingly rapid and strong variation in slip direction from nearly pure strike slip southeast of the hypocenter to nearly pure dip slip to the northwest over a very short distance of ~15 km. This substantial change in rake is corroborated by recently published geodetic models.

ACKNOWLEDGMENTS

This research was supported by U.S. National Science Foundation grant EAR–9011456. Tom Hanks, David Schwartz, Paul Segall, Paul Spudich, and David Wald provided helpful comments and discussions. Steve Hartzell, Jamie Steidl, and Dave Wald kindly provided their rupture models plotted at a common scale for figure 6. Bill Ellsworth provided the carefully processed digital accelerograms from stations SJS used in figure 8 and suggested comparing my model with the data at low frequencies. Marino Protti-Quesada and Walter Schillinger provided data from the UCSC accelerographs. Thanks are also due to the USGS, CDMG, and UCSC for having the foresight to deploy strong-motion instrumentation in the study area.

REFERENCES CITED

Aki, Keiiti, and Richards, P.G. 1980, Quantitative seismology; theory and methods: San Francisco, W.H. Freeman, 2 v.

Archuleta, R.J., 1984, A faulting model for the 1979 Imperial Valley, California, earthquake: Journal of Geophysical Research, v. 89, no. B6, p. 4559–4585.

Barker, J.S., and Salzberg, D.H. 1990, Long-period and broad-band teleseismic body-wave modeling of the October 18, 1989 Loma Prieta earthquake: Geophysical Research Letters, v. 17, no. 9, p. 1409–1412.

Beroza, G.C., 1991, Near-source modeling of the Loma Prieta earthquake; evidence for heterogeneous slip and implications for earthquake hazard: Seismological Society of America Bulletin, v. 81, no. 5, p. 1603–1621.

Beroza, G.C., and Spudich, Paul, 1988, Linearized inversion for fault rupture behavior; application to the 1984 Morgan Hill, California, earthquake: Journal of Geophysical Research, v. 93, no. B6, p. 6275–6296.

Beroza, G.C., and Zoback, M.D., 1993, Mechanism diversity of the Loma Prieta aftershocks and the mechanics of mainshock-aftershock interaction, Science, v. 259, no. 5092, p. 210–213.

Choy, G.L., and Boatwright, John, 1990, Source characteristics of the Loma Prieta, California, earthquake of October 18, 1989 from global digital seismic data: Geophysical Research Letters, v. 17, no. 8, p. 1183–1186.

Cormier, V.F., and Beroza, G.C., 1987, Calculation of strong ground motion due to an extended source in a laterally varying structure: Seismological Society of America Bulletin, v. 77, no. 1, p. 1–13.

Day, S.M., 1982, Three-dimensional finite difference simulation of fault dynamics: rectangular faults with fixed rupture velocity: Seismological Society of America Bulletin, v. 72, no. 3, p. 705–727.

Dieterich, J.H., 1979, Modeling of rock friction; 1, Experimental results and constitutive equations: Journal of Geophysical Research, v. 84, no. B5, p. 2161–2168.

Dietz, L.D., and Ellsworth, W.L., 1990, The October 17, 1989, Loma Prieta, California, earthquake and its aftershocks; geometry of the sequence from high-resolution locations: Geophysical Research Letters, v. 17, no. 9, p. 1417–1420.

Eberhart-Phillips, D.M., Labson, V.F., Stanley, W.D., Michael, A.J., and Rodriguez, B.D., 1990, Preliminary velocity and resistivity models of the Loma Prieta earthquake region: Geophysical Research Letters, v. 17, no. 8, p. 1235–1238.

Hanks, T.C., and Kanamori, Hiroo, 1979, A moment magnitude scale: Journal of Geophysical Research, v. 84, no. B5, p. 2348–2350.

Hartzell, S.H., and Heaton, T.H., 1983, Inversion of strong ground motion and teleseismic waveform data for the fault rupture history of the 1979 Imperial Valley, California, earthquake: Seismological

Society of America Bulletin, v. 73, no. 6, pt. A, p. 1553–1583.

Hartzell, S.H., Stewart, G.S., and Mendoza, Carlos, 1991, Comparison of L_1 and L_2 norms in a teleseismic waveform inversion for the slip history of the Loma Prieta, California, earthquake: Seismological Society of America Bulletin, v. 81, no. 5, p. 1518–1539.

Heaton, T.H., 1990, Evidence for and implications of self-healing pulses of slip in earthquake ruptures: Physics of the Earth and Planetary Interiors, v. 64, no. 1, p. 1–20.

Horowitz, F.G., and Ruina, Andy, 1989, Slip patterns in a spatially homogeneous fault model: Journal of Geophysical Research, v. 94, no. B8, p. 10279–10298.

Houston, Heidi, and Engdahl, E.R., 1989, A comparison of the spatio-temporal distribution of moment release for the 1986 Andreanof Islands earthquake with relocated seismicity: Geophysical Research Letters, v. 16, no. 12, p. 1421–1424.

Kanamori, Hiroo, 1981, The nature of seismicity patterns before large earthquakes, *in* Simpson, D.W., and Richards, P.G., eds., Earthquake prediction; an international review (Maurice Ewing Series, v. 4): Washington, D.C., American Geophysical Union, p. 1–19.

Kanamori, Hiroo, and Satake, Kenji, 1990, Broadband study of the 1989 Loma Prieta earthquake: Geophysical Research Letters, v. 17, no. 8, p. 1179–1182.

Langston, C.A., Furlong, K.P., Vogfjord, K.S., Clouser, R.H., and Ammon, C.J., 1990, Analysis of teleseismic body waves radiated from the Loma Prieta earthquake: Geophysical Research Letters, v. 17, no. 9, p. 1405–1408.

Lees, J.M., 1990, Tomographic *P*-wave velocity images of the Loma Prieta earthquake asperity: Geophysical Research Letters, v. 17, no. 9, p. 1433–1436.

Lindh, A.G., 1983, Preliminary assessment of long-term probabilities for large earthquakes along selected fault segments of the San Andreas fault system in California: U.S. Geological Survey Open-File Report 83-63, 14 p.

Lisowski, Michael, Prescott, W.H., Savage, J.C., and Johnston, M.J.S., 1990, Geodetic estimate of coseismic slip during the 1989 Loma Prieta, California, earthquake: Geophysical Research Letters, v. 17, no. 9, p. 1437–1440.

Maley, R.P., Acosta, A.V., Ellis, F., Etheredge, E.C., Foote, L.J., Johnston, D.A., Porcella, R.L., Salsman, M.J., and Switzer, J.C., 1989, U.S. Geological Survey strong motion records from the northern California (Loma Prieta) earthquake of October 17, 1989: U.S. Geological Survey Open-File Report 89–568, 85 p.

Marshall, G.A., Stein, R.S., and Thatcher, Wayne, 1991, Faulting geometry and slip from co-seismic elevation changes; the 18 October 1989, Loma Prieta, California, earthquake: Seismological Society of America Bulletin, v. 81, no. 5, p. 1660–1693.

McNally, K.C., Yellin, Joseph, Protti-Quesada, Marino, Simila, G.W., Malavassi, Eduardo, Schillinger, Walter, Terdiman, R., and Zhang, Zhi, 1990, The local magnitude of the 18 October 1989 Santa Cruz Mountains earthquake is M_L=6.9: Geophysical Research Letters, v. 17, no. 10, p. 1781–1784.

Mendoza, Carlos, and Hartzell, S.H., 1988, Aftershock patterns and main shock faulting: Seismological Society of America Bulletin, V. 78, no. 4, p. 1438–1449.

Nábělek, J.L., 1990, Rupture process of the October 18, 1989 Loma Prieta earthquake from broadband teleseismic body waves [abs.]: Seismological Research Letters, v. 61, no. 1, p. 46.

Olson, A.H., 1987, A Chebyshev condition for accelerating convergence of iterative tomographic methods—solving large least squares problems: Physics of the Earth and Planetary Interiors, v. 47, p. 333–345.

Olson, A.H., and Apsel, R.J., 1982, Finite faults and inverse theory with application to the 1979 Imperial Valley earthquake: Seismological Society of America Bulletin, v. 72, no. 6, p. 1969–2001.

Olson, A.H., Orcutt, J.A., and Frazer, G.A., 1984, The discrete wave number/finite element method for synthetic seismograms: Royal Astronomical Society Geophysical Journal, v. 77, no. 2, p. 421–460.

Olson, J.A., 1990, Seismicity in the twenty years preceding the Loma Prieta, California earthquake: Geophysical Research Letters, v. 17, no. 9, p. 1429–1432.

Oppenheimer, D.H., 1990, Aftershock slip behavior of the 1989 Loma Prieta, California earthquake: Geophysical Research Letters, v. 17, no. 8, p. 1199–1202.

Romanowicz, B.A., and Lyon-Caen, Hélène, 1990, The Loma Prieta earthquake of October 18, 1989; results of teleseismic mantle and body-wave inversion: Geophysical Research Letters, v. 17, no. 8, p. 1191–1194.

Ruff, L.J., and Tichelaar, B.W., 1990, Moment tensor rate functions for the 1989 Loma Prieta earthquake: Geophysical Research Letters, v. 17, no. 8, p. 1187–1190.

Schwartz, S.Y., Dewey, J.W., and Lay, Thorne, 1989, Influence of fault plane heterogeneity on seismic behavior in the southern Kurile Islands arc: Journal of Geophysical Research, v. 94, no. B5, p. 5637–5649.

Segall, Paul and Lisowski, Michael, 1990, Surface displacement in the 1906 San Francisco and 1989 Loma Prieta earthquakes: Science, v. 250, no. 4985, p. 1241–1244.

Shakal, A.F., Huang, M.J., Reichle, Michael, Ventura, C.E., Cao, T.Q., Sherburne, R.W., Savage, Martha, Darragh, R.B., and Petersen, C., 1989, CSMIP strong-motion records from the Santa Cruz Mountains (Loma Prieta), California earthquake of 17 October 1989: California Division of Mines and Geology, Office of Strong Motion Studies Report 89–06, 196 p.

Simila, G.W., McNally, K.C., Nava, E., Protti-Quesada, Marino, and Yellin, Joseph, 1990, Evidence of very early aftershock activity along the northwest portion of the 18 October 1989 earthquake rupture zone: Geophysical Research Letters, v. 17, no. 10, p. 1785–1788.

Spudich, Paul, and Frazer, L.N., 1984, Use of ray theory to calculate high-frequency radiation from earthquake sources having spatially variable rupture velocity and stress drop: Seismological Society of America Bulletin, v. 74, no. 6, p. 2061–2082.

Steidl, J.H., Archuleta, R.J., and Hartzell, S.H., 1991, Rupture history of the 1989 Loma Prieta, California, earthquake: Seismological Society of America Bulletin, v. 81, no. 5, p. 1573–1602.

Sykes, L.R., and Nishenko, S.P., 1984, Probabilities of occurrence of large plate rupturing earthquakes for the San Andreas, San Jacinto, and Imperial faults, California, 1983–2003: Journal of Geophysical Research, v. 89, no. B7, p. 5905–5927.

Thatcher, Wayne, and Lisowski, Michael, 1987, Long-term seismic potential of the San Andreas fault southeast of San Francisco, California: Journal of Geophysical Research, v. 92, no. B6, p. 4771–4784.

U.S. Geological Survey staff, 1990, The Loma Prieta, California, earthquake; an anticipated event: Science, v. 247, no. 4940, p. 286–293.

Wald, D.J., Helmberger, D.V., and Hartzell, S.H., 1990, Rupture process of the 1987 Superstition Hills earthquake from the inversion of strong-motion data: Seismological Society of America Bulletin, v. 80, no. 5, p. 1079–1098.

Wald, D.J., Helmberger, D.V., and Heaton, T.H., 1991, Rupture model of the 1989 Loma Prieta earthquake from the inversion of strong-motion and broadband teleseismic data: Seismological Society of America Bulletin, v. 81, no. 5, p. 1540–1572.

Working Group on California Earthquake Probabilities, 1988, Probabilities of large earthquakes occurring in California on the San Andreas Fault: U.S. Geological Survey Open-File Report 88–398, 62 p.

———1990, Probabilities of large earthquakes in the San Francisco Bay region, California: U.S. Geological Survey Circular 1053, 51 p.

Zhang, Jiajun, and Lay, Thorne, 1990, Source parameters of the 1989 Loma Prieta earthquake determined from long-period Rayleigh waves: Geophysical Research Letters, v. 17, no. 8, p. 1195–1198.

MAIN-SHOCK CHARACTERISTICS

SOURCE CHARACTERISTICS OF THE EARTHQUAKE FROM GLOBAL DIGITAL SEISMIC DATA

By George L. Choy and John Boatwright,
U.S. Geological Survey

CONTENTS

ABSTRACT

We analyze displacement, velocity, and acceleration records of *P* and *SH* body waves recorded at teleseismic distances to determine the static and dynamic source parameters of the 1989 Loma Prieta earthquake. Three distinct bursts of energy corresponding to three subevents can be recognized in most records. The displacement waveforms indicate that the first subevent contributes a negligible moment, whereas the largest releases of moment and energy are controlled by the second and third subevents, which are located north and south of the initial nucleation. A small fourth subevent needed to model later features of the *P* waveforms suggests that slow slip continued after the major releases of energy occurred. The waveforms are fitted with a fault-plane solution with a strike of 130°, a dip of 65°, and a slip of 140° for all four subevents. The focal depths of the two major subevents are 16 and 12 km, and their asperity radii are 4.0 and 6.0 km, respectively. The seismic moment, M_0, is 2.2×10^{26} dyne-cm. From a spectral analysis of teleseismic velocity, the radiated energy, E_S, is estimated at 1.1×10^{22} dyne-cm, implying an apparent stress of 15 bars. From the level of the high-frequency end of the teleseismic acceleration spectrum and a rupture area of 440 km^2, we derive a dynamic stress drop of 51 bars.

INTRODUCTION

The focal parameters for the 1989 Loma Prieta earthquake, as determined by the U.S. Geological Survey's National Earthquake Information Center (NEIC), are origin time, 0004:15.2 G.m.t. October 18, 1989; location, lat 37.036° N., long 121.883° W.; body-wave magnitude m_b=6.6; and surface-wave magnitude M_S=7.1. This earthquake was well recorded by many digitally recording seismograph networks. The purpose of this paper is to analyze the source characteristics of the earthquake by using high-quality broadband data selected from these stations. By "broadband" we mean that the data are processed so that they are flat to displacement, velocity, or acceleration from frequencies of at least 0.01 to about 5.0 Hz. The advantages of using broadband records to derive details of the rupture process of large earthquakes have been enumerated in recent papers (for example, Choy and Boatwright, 1981, 1988; Choy and Dewey, 1988). Besides the usual parameters of depth, moment, and focal mechanism, these data have sufficient spectral content to provide estimates of radiated energy, associated stresses, and rupture complexity.

DATA PROCESSING

The broadband data analyzed here were obtained from digitally recording stations of the Global Digital Seismograph Network (GDSN), the Chinese Digital Seismograph Network (CDSN), and the Global Seismographic Network (GSN). Only stations at distances greater than 30° from the epicenter are used in our waveform modeling. The global distribution of the stations used is shown in figures 1 and 2. Because raw data from globally recording networks are generally not directly proportional to either displacement or velocity over a wide and continuous range of frequencies, broadband records were obtained by using the method of Harvey and Choy (1982), which uses multichannel instrument deconvolution and, whenever necessary, recombines data recorded on separate channels with overlapping frequency bands. After processing, the body-wave displacements and velocities generally are well determined over the frequency range from at least 0.01 to 5.0 Hz.

ANALYSIS OF THE MAIN SHOCK

From even a preliminary examination of displacement and velocity records, three distinct bursts can be recognized in most of the broadband pulse shapes. A typical short-period record is shown in figure 3*A*. The initial onset represents only a tiny part of the rupture process. As shown in the broadband displacement (fig. 3*B*), this onset is followed by two major releases of moment. Similarly, in the velocity record (fig. 3*C*), this onset is followed by two major episodes of energy release. In our modeling, we associate each arrival of energy release with a subevent.

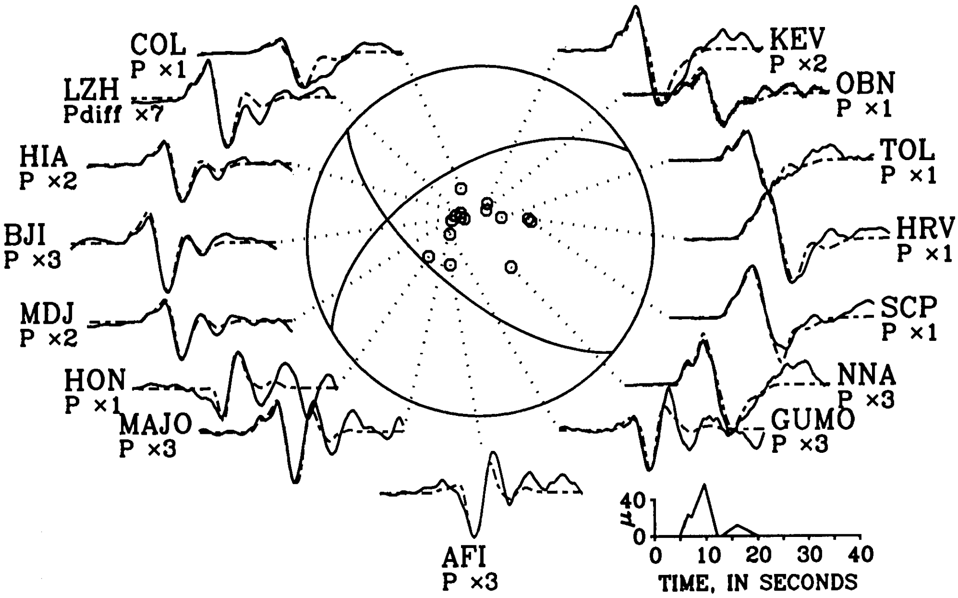

Figure 1.—*P*-wave displacements (solid traces) and synthetic seismograms (dashed traces) at global digital seismic stations (identified by letter codes) of main shock, plotted about focal sphere. Focal mechanism has a strike of 130°, a dip of 65°, and a slip of 140°. Absolute amplitude of data is recoverable by measuring vertical amplitude, comparing it with vertical axis (scaled in microns, μ), and dividing it by magnification factor given next to each displacement trace. Shape of average moment-release rate is plotted on time axis.

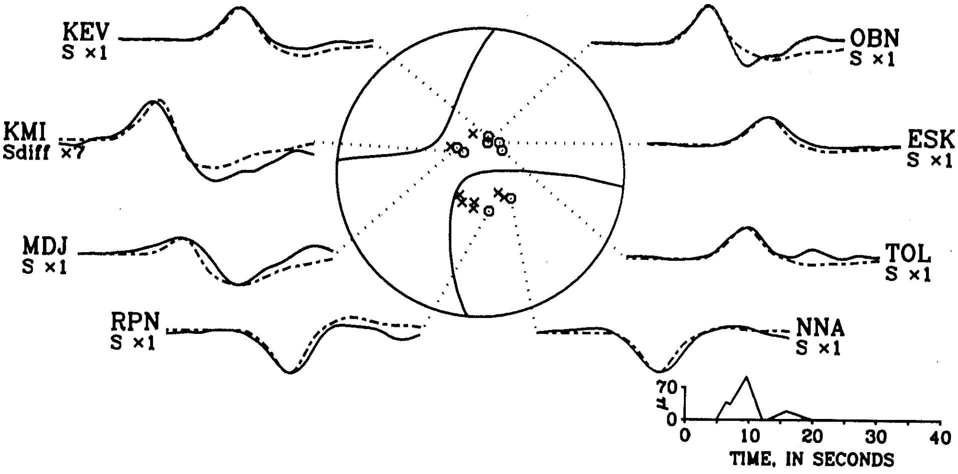

Figure 2.—*SH*-wave displacements (solid traces) and synthetic seismograms (dashed traces) at global digital seismic stations (identified by letter codes) of main shock, plotted about focal sphere with *SH*-nodal lines of fault-plane solution. ×'s indicate *sS* takeoff angles, some of which fall near nodal lines. Absolute amplitude of data is recoverable by measuring vertical amplitude, comparing it with vertical axis (scaled in microns, μ), and dividing it by magnification factor given next to each displacement trace. Shape of average moment-release rate is plotted on time axis.

However, because the arrival of subevent 1 is too small to model, we start our modeling of the rupture process with subevent 2. Finally, because most stations reported only the initial arrival, the hypocenter computed by most reporting agencies refers to the onset of nucleation, which is not necessarily where the major releases of energy occurred.

To exploit the broad-bandwidth data, we used the methods of Choy and Boatwright (1981, 1988) and Choy and Kind (1987) to estimate the focal mechanism, depth, and source duration of the subevents composing the earthquake. For a single shallow source, the far-field *P*-wave displacement, *U*, is given by

$$U(x,t) = G_P * \Omega_P + G_{pP} * \Omega_{pP} + G_{sP} + \Omega_{sP} \qquad (1)$$

where G_i and Ω_i are the propagation and source operators for body waves i=*P*, *pP*, and *sP*. For simple coherent sources, synthetic displacements are computed by using triangular source functions. Displacements for a complex rupture are synthesized by summing the waveforms from a sequence of coherent subevents lagged in time as a function of azimuth. For body waves recorded between distances of approximately $30° < \Delta < 90°$, the propagation operator accounts for geometric spreading, the crustal response at source and receiver, and the effects of propagation in the Earth. To describe attenuation, we use the frequency-dependent dispersive operators of Choy and Cormier (1986), modified, as described by Boatwright and Choy (1986), to account for the regionally strong attenuation along Western United States-shield ray paths (Der and others, 1982). The response of the Earth is calculated by applying the method of Haskell (1962) to an Earth model that uses Jeffreys-Bullen velocities for the structure in the mantle and near the receivers, and the velocity model of Dietz and Ellsworth (1990) for the location of aftershocks in the Loma Prieta region. Displacement data are systematically fitted by trial and error with synthetic seismograms until optimal agreement is obtained between observed and synthetic waveforms. Any remaining discrepancies between the synthetic and observed seismograms are minor and may be due to unknown crustal response near the receivers.

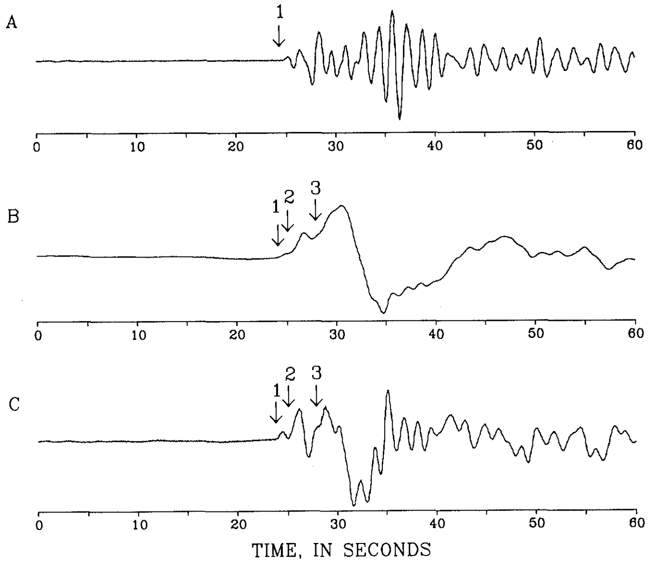

Figure 3.—Three different representations of *P* wave at station TOL. Arrows indicate onsets of subevents 1, 2, and 3. *A*, Raw short-period data. *B*, Broadband displacement. Onset of subevent 1 is clearly subordinate in size to onsets of subevents 2 and 3. *C*, Correponding broadband velocity.

The *P* and *SH* displacement waveforms used in our analysis are plotted about the focal spheres in figures 1 and 2, respectively. The average moment-release rate shows that the rupture process involving subevents 2 and 3 was essentially over within approximately 7 s. A relatively minor fourth subevent is needed to model later features of the *P* waves. The best-fitting solutions for the subevents 2 and 3 have the same focal mechanism (strike, 130°; dip, 65°; slip, 140°). These parameters are exceptionally well constrained to within ±5° because the takeoff angles of the body waves (direct *P*, *pP*, *sP*, *SH*, and *sSH*) straddle both sides of the *P*, *SV*, and *SH* nodal lines. The focal depths are 16 and 12 km, respectively, for subevents 2 and 3. As a small arrival, subevent 4 is poorly constrained; we assume that it has the mechanism and depth of the third and dominant subevent. Subevent 3 releases 50 percent of the moment, while subevents 2 and 4 release 34 percent and 16 percent, respectively. The total moment, M_0, is $\approx 2.0 \times 10^{26}$ dyne-cm. The radiated energy, computed by using the spectral method of Boatwright and Choy (1986), is $1.1 \pm 0.1 \times 10^{22}$ dyne-cm.

From an inversion of the differential arrival times of the subevents, the hypocenters and delay times of subevents 2 and 3 can be found relative to the point of nucleation of subevent 1. Subevent 2 is located 4.5 km from subevent 1, at an azimuth of 028°. The hypocenter of subevent 3 is 8 km away from that of subevent 1 at an azimuth of 168°. The delay times of subevents 2 and 3 relative to subevent 1 are 1.4 and 3.5 s, respectively. The semimajor axes of both 95-percent-confidence ellipses are oriented nearly north-south with lengths of 2.0 km. The azimuths of subevents 2 and 3 relative to subevent 1 differ from the dominant strike delineated by aftershock activity. Because of their spatial proximity and uncertainty, however, the locations of the subevents are not regarded as significantly off the main fault. Furthermore, these locations must be considered preliminary because of the sparsity of data from southern azimuths. The onset of subevent 1 could not be reliably read above the microseism level on records from most island stations.

The average source functions for subevents 2 and 3 have rise times of 1.5 and 2.5 s, with total durations of 7.0 and 5.0 s, respectively. Using the relation of Das and

Kostrov (1986) for the rise time of the source function τ and the asperity radius a, $\tau \approx a/v$, where the rupture velocity v is assumed to be 75 percent of the shear velocity, we obtain asperity radii of 4 and 6 km for subevents 2 and 3, respectively. These geometries are shown as circles on a vertical cross section of aftershocks viewed parallel to the strike of the San Andreas fault (fig. 4). The subevents were located by using the coordinates of the main shock (Dietz and Ellsworth, 1990) as the location of subevent 1.

To extract further information from the teleseismic arrivals, we used the method of Boatwright and Choy (1989) to examine the radiated acceleration in the frequency domain. The first step of this method is shown in figure 5*A*, where the solid curve is the logarithmically averaged acceleration spectrum, corrected for both geometric spreading and anelastic attenuation. This spectrum must still be corrected for the effect of the free surface, that is, the spectral modulations caused by interference of the depth and the direct phases. This free-surface interference (dashed curve, fig. 5*A*) is modeled by accounting for the focal mechanism, the average depth of the rupture, and the depth range of the rupture. Note that the shallow trough at 0.2 Hz in the free-surface spectrum does not fit the shallow trough at 0.4 Hz in the average-acceleration spectrum. This trough at 0.4 Hz is presumed to arise from the complexity of the moment-release rate, not the interference of the free surface.

Dividing the average-acceleration spectrum by the free-surface spectrum yields the corrected acceleration spectrum, which is plotted in figure 5*B*. The ω^2 line that has been fitted to the low-frequency end of the spectrum (0.012–0.06 Hz) corresponds to a seismic moment M_0 of $2.2 \pm 0.5 \times 10^{26}$ dyne-cm, in agreement with the time-domain analysis. Overall, the spectral shape appears to be remarkably similar to Brune's (1970) ω^2 spectral model, notwithstanding the slight modulation from 0.07 to 0.5 Hz. Estimating the corner frequency, f_α, at 0.12 to 0.15 Hz, using the relation

$$r = \frac{2.03\alpha}{2\pi f_\alpha} \tag{2}$$

based on Brune (1970), where α is the *P*-wave velocity, and assuming a corner frequency shift of 1.5, we obtain a source radius r of 13 to 16 km as an estimate of the overall source size. This estimate is larger than the combined asperity radii of the two major subevents derived from the time-domain analysis. Although time-domain analysis helps resolve discrete episodes of stress release, spectral analysis is sensitive to the overall rupture process. The corner frequency of 0.12 to 0.15 Hz is then representative of the overall duration of faulting, about 6 to 8 s. The spectral estimate of source radius should be interpreted as a length characteristic of the overall rupture process.

Our spectral estimate of the source size agrees well with the seismicity pattern that developed during the first few hours after the main shock. The distribution of aftershocks that occurred in the first 3.5 hours after the main shock (fig. 4) suggests that the rupture area can be approximated as an ellipse, with a semimajor axis of 20 km, a semiminor axis of 7 km, and a total rupture area, A, of 440 km^2. This estimate of the overall rupture area can be combined with the high-frequency spectral level, $R\ddot{u}|$, of 1.6×10^7 cm^2/s to estimate the rms dynamic stress drop at

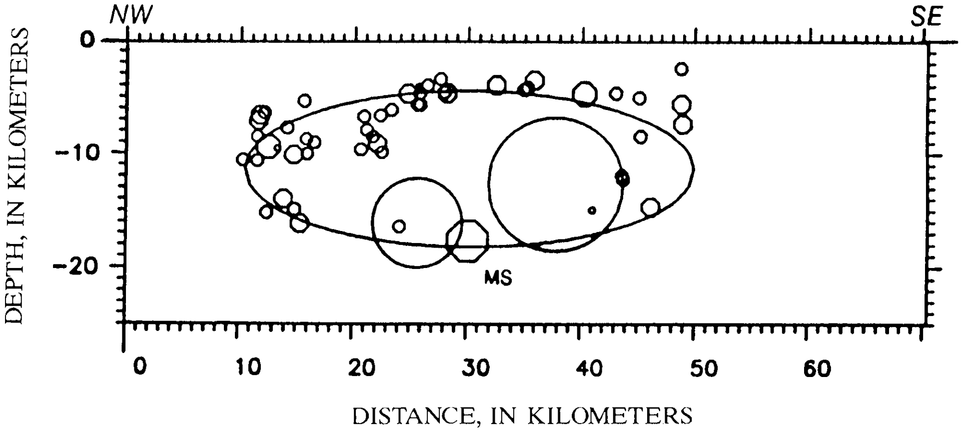

Figure 4.—Aftershocks within first 3.5 hours of main shock (from Eberhart-Phillips and others, 1990). Circular-asperity geometries of subevents 2 and 3 (circles), resolved from time-domain analysis, indicate heterogeneous stress release. Large ellipse outlines rupture zone used in calculating stress drop.

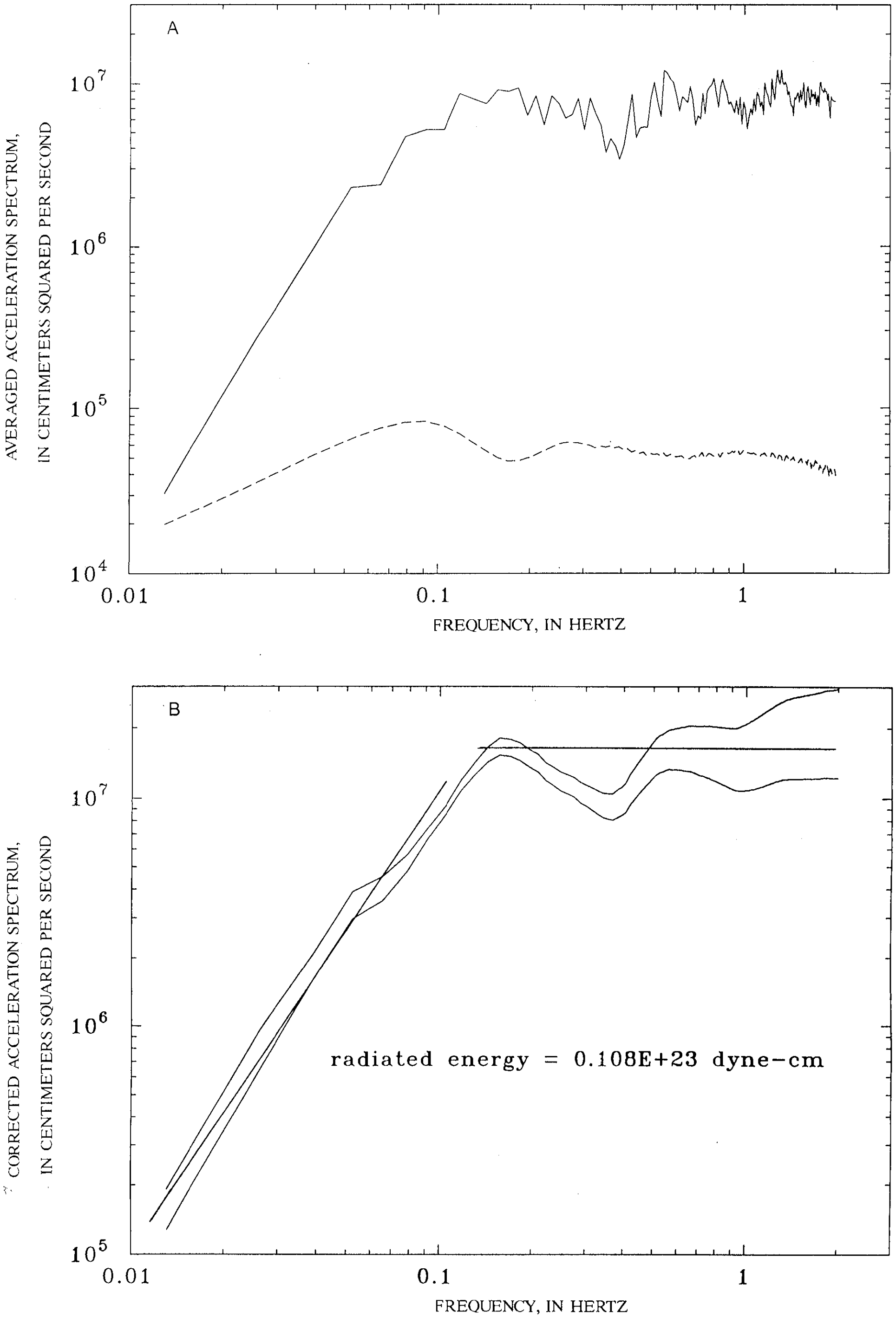

Figure 5.—Acceleration spectra. *A*, Logarithmically averaged acceleration spectrum from 12 stations (solid curve), corrected for geometric spreading and anelastic attenuation. Modulation of free-surface spectrum (dashed curve) fits modulation of averaged acceleration spectrum. Free-surface spectrum is modeled with focal mechanism with a strike of 130°, a dip of 65°, and a slip of 140°; with a centroid depth of 12.0 km; and with a vertical range of rupture of 10.0 km. Units of square centimeters per second result from correction of acceleration spectrum for geometric spreading. *B*, Corrected acceleration spectrum, bounded by 85-percent-confidence limits. Low- and high-frequency parts of spectrum are fitted by ω^2 and flat lines, respectively.

51±12 bars, using equation 4 of Choy and Boatwright (1988) for a rupture direction assumed to be within 60° of updip.

DISCUSSION

From the relative locations of the major subevents and the distribution of aftershocks, the causative fault plane can be identified from the focal mechanism as the nodal plane striking 130°. This fault plane is both colinear with the dominant trend of aftershock activity (Dietz and Ellsworth, 1990) and consistent with the locations of subevents north and south of the initial hypocenter.

The stress release of the main shock is slightly heterogeneous, as indicated by the asperity geometries resolved by the time-domain analysis (fig. 4). Assuming that the coordinates of the main shock obtained by Dietz and Ellsworth (1990) correspond to those of subevent 1, the depth of the initial nucleation is 18 km. The subsequent major releases of stress and energy occur both updip and away from this initial nucleation.

An important characteristic of the aftershock sequence is that almost all the aftershock activity immediately after the main shock is concentrated around and beyond the edges of the asperities derived from seismogram modeling (fig. 4). The absence of activity within these asperities suggests that the areas became inactive after stress was relieved. After the main shock, stress would have been transferred to weaker patches on the fault interface adjacent to the asperities, where failure would continue to occur in the form of small earthquakes.

ACKNOWLEDGMENTS

This research was partly supported by the U.S. Nuclear Regulatory Commission under contract RES82001. We thank C. Mendoza and J.W. Dewey for their reviews, and A. Michael for bringing to our attention the data in figure 4.

REFERENCES CITED

Boatwright, John, and Choy, G.L., 1986, Teleseismic estimates of the energy radiated by shallow earthquakes: Journal of Geophysical Research, v. 91, no. B2, p. 2095–2112.

———1989, Acceleration spectra for subduction zone earthquakes: Journal of Geophysical Research, v. 94, no. B11, p. 15541–15553.

Brune, J.N., 1970, Tectonic stress and the spectra of seismic shear waves from earthquakes: Journal of Geophysical Research, v. 75, no. 26, p. 4997–5009.

Choy, G.L., and Boatwright, John, 1981, The rupture characteristics of two deep earthquakes inferred from broadband GDSN data: Seismological Society of America Bulletin, v. 71, no. 3, p. 691–711.

———1988, Teleseismic and near-field analysis of the Nahanni earthquakes in the Northwest Territories, Canada: Seismological Society of America Bulletin, v. 78, no. 5, p. 1627–1652.

Choy, G.L., and Cormier, V.F., 1986, Direct measurement of the mantle attenuation operator from broadband *P* and S Waveforms: Journal of Geophysical Research, v. 91, no. B7, p. 7326–7342.

Choy, G.L., and Dewey, J.W., 1989, Rupture process of an extended earthquake sequence; teleseismic analysis of the Chilean earthquake of March 3, 1985: Journal of Geophysical Research, v. 93, no. B2, p. 1103–1118.

Choy, G.L., and Kind, Rainer, 1987, Rupture complexity of a moderate-sized (m_b 6.0) earthquake; broadband body-wave analysis of the North Yemen earthquake of 13 December 1982: Seismological Society of America Bulletin, v. 77, no. 1, p. 28–46.

Das, Shamita, and Kostrov, B.V., 1986, Fracture of a single asperity on a finite fault; a model for slow earthquakes?, *in* Das, Shamita, Boatwright, John, and Scholz, C.H., eds., Earthquake source mechanics: American Geophysical Union Geophysical Monogragh 37 (Maurice Ewing series, v. 6), p. 91–96.

Der, Z.A., McElfresh, T.W., and O'Donnell, Anne, 1982, An investigation of the regional variations and frequency dependence of anelastic attenuation in the mantle under the United States in the 0.5–4 Hz band: Royal Astronomical Society Geophysical Journal, v. 69, no. 1, p. 67–99.

Dietz, L.D., and Ellsworth, W.L., 1990, The October 17, 1989 Loma Prieta, California, earthquake and its aftershocks; geometry of the sequence from high-resolution locations: Geophysical Research Letters, v. 17, no. 9, p. 1417–1420.

Eberhart-Phillips, D.M., Michael, A.J., Reasenberg, P.A., Ellsworth, W.L., and Dietz, L.D., 1990, Seismological aspects of the Loma Prieta earthquake, *in* Benuska, Lee, ed., Loma Prieta earthquake reconnaissance report: Earthquake Spectra, v. 6., supp. 90–01.

Harvey, D.J. and Choy, G.L., 1982, Broad-band deconvolution of GDSN data: Royal Astronomical Society Geophysical Journal, v. 69, no. 3, p. 659–668.

Haskell, N.A., 1962, Crustal reflection of plane *P* and *SV* waves: Journal of Geophysical Research, v. 61, no. 12, p. 4751–4767.

MAIN-SHOCK CHARACTERISTICS

COMPARISON OF L_1 AND L_2 NORMS IN A TELESEISMIC-WAVEFORM INVERSION FOR THE RUPTURE HISTORY OF THE EARTHQUAKE

By Stephen H. Hartzell, Gordon S. Stewart,[1] and Carlos Mendoza,
U.S. Geological Survey

CONTENTS

ABSTRACT

We have inverted broadband digital teleseismic body waves (*P* and *SH*) to obtain the slip history of the 1989 Loma Prieta earthquake. Comparison of finite-fault waveform-inversion results, using L_1 and L_2 norms, reveals some basic uncertainties in the rupture history that are not generally appreciated in earthquake-source studies. The more robust features of the source that depend less on the choice of minimization norm are identifiable. From a consideration of first-motion data and forward modeling of body waves, the strike and dip of our model fault plane are set at 126° and 67°, respectively. The waveform-inversion results indicate that most of the moment release occurs over a fault length of 35 to 40 km and a depth range of 2 to 18 km. The hypocenter (at 18-km depth) underwent a relatively small amount of slip. The rupture propagated upward and bilaterally, with a peak slip of about 3 m occurring at 10-km depth. The average velocity of rupture propagation is 2.5 km/s. Although the details of the slip distribution depend on the minimization norm, two main sources are identifiable, with the larger source above and to the southeast of the hypocenter. The rake vector varies considerably over the fault. The southern source is mostly strike slip, whereas the northern source is approximately equally partitioned between dip slip and strike slip. Also, generally more strike slip occurs at shallower depths. Most of the moment release occurs in the first 7.5 s, with an integrated moment of 2.6×10^{26} dyne-cm. Including smaller, peripheral sources that are less well resolved raises the moment estimate to 3.0×10^{26} dyne-cm.

INTRODUCTION

Numerous waveform-inversion studies over the past 10 years have attempted to reconstruct the slip history, both spatially and temporally, of specific earthquakes. The problem has been linearly formulated to solve for slip amplitudes at designated places and times (Trifunac, 1974; Olson and Apsel, 1982; Hartzell and Heaton, 1983, 1986; Frankel and Wennerberg, 1989; Mendoza and Hartzell, 1989; Das and Kostrov, 1990), as well as linearized iterative formulations that solve for both slip amplitudes and rupture times (Jackson and Matsu'ura, 1985; Kikuchi and Fukao, 1985; Fukuyama and Irikura, 1986; Yoshida, 1986; Takeo, 1987; Beroza and Spudich, 1988; Hartzell, 1989; Hartzell and Iida, 1990). Different types of data have been considered, including strong-motion records and teleseismic waveforms. For some earthquakes, a combined data set of strong-motion records and teleseismic waveforms has been used (Hartzell and Heaton, 1983; Mendoza and Hartzell, 1989; Hartzell and Mendoza, 1991). In these studies, wave-propagation codes are generally used to calculate synthetic Green's functions, although empirical Green's functions, such as aftershock records, have also been used (Fukuyama and Irikura, 1986; Hartzell, 1989). In addition, geodetic data have been used to invert for fault-rupture histories (Langbein, 1981; Ward and Barrientos, 1986; Segall and Harris, 1987; Vasco and others, 1988). All of the waveform inversions mentioned above have been done in the time domain; a linear frequency-domain inversion has also been implemented (Olson and Anderson, 1988).

Aside from the consideration of a linear versus iterative formulation, the type of data to invert, the use of synthetic or empirical Green's functions, or time-domain versus frequency-domain inversion, an even more fundamental

---

[1] Current affiliation: Pacific Geophysics, Inc., Pasadena, Calif.

question is the minimization norm to be used in the problem. This aspect of the finite-fault inversion problem is rarely appreciated, and its implications for the resulting source model are poorly understood. The norm of choice has generally been the L_2 or least-squares norm, the popularity of which is based on an extensive literature (Lanczos, 1961; Jackson, 1972; Wiggins, 1972; Aki and Richards, 1980; Menke, 1984). If **b** is the data vector, **A** the matrix of the synthetic seismograms, and **x** the solution vector that relates **A** to **b** in the system of linear equations **Ax=b**, then the L_2 norm minimizes the sum of squares of the differences between predictions and observations, $\|\mathbf{b}-\mathbf{Ax}\|_2$. The model derived from this minimization is one of many possible models that fit the data. Mendez and others (1990) described a wave-equation norm that they applied in the frequency domain which finds a spatially and temporally smooth solution. Another model is obtained by applying an L_1 norm, which minimizes the sum of absolute values of the differences between predictions and observations, $|\mathbf{b}-\mathbf{Ax}|_1$. The L_1 norm was used by Langbein (1981) to invert geodetic data and by Das and Kostrov (1990) to invert long-period teleseismic body waves. However, few inversion studies of fault-rupture history compare the results for different norms (Mendez and others, 1990), and no known study compares L_1 and L_2 models derived from a waveform inversion. Therefore, one objective of this paper is to compare these two models for the 1989 Loma Prieta earthquake. In so doing, we also obtain a better idea of the resolvable features in the slip history of this earthquake.

Another important aspect of this study comes from a comparison of our inversion results, using broadband teleseismic body waves, with those from studies using local strong-motion data. Although few such comparisons are known, those that have been done show encouraging results (Hartzell and Heaton, 1983; Houston and Kanamori, 1986, 1990; Choy and Boatwright, 1988; Hartzell, 1989; Mendoza and Hartzell, 1989). If similar rupture histories can be obtained from only teleseismic data, many more earthquakes for which no strong-motion data are available can be investigated with confidence.

L_1 VERSUS L_2 NORM

The reasons for choosing a particular norm concern the distribution of errors in the data, the distribution of observation points around the source, and the characteristics of the source model considered to be desirable. Least-squares (L_2) analysis assumes that errors in the data have a Gaussian distribution, whereas the model obtained from application of an L_1 norm assumes that the errors have an exponential distribution (Menke, 1984). An exponential distribution with the same mean and variance as a Gaussian distribution has a much longer tail. Thus, the probability of a few outlying points is much higher with an exponential distribution. Therefore, an L_1 minimization can handle a few bad data points better by attaching less weight to them.

An important reason for considering alternative norms was pointed out by Olson and Anderson (1988). An L_2 norm finds the solution that fits the data by minimizing $\|\mathbf{b}-\mathbf{Ax}\|_2$ and the sum of squares of the solution vector, $\|\mathbf{x}\|_2$. Therefore, in an inversion for fault slip, the slip amplitude is generally less than the true amplitude. To compensate, the spatial and temporal distribution of slip may be altered to focus energy toward the observation points. Thus, station-array geometry plays an important role in our ability to resolve the tradeoffs between slip amplitude and its temporal and spatial location on the fault, as demonstrated by Olson and Anderson. An L_1 norm minimizes $|\mathbf{b}-\mathbf{Ax}|_1$ and the sum of absolute values of the solution vector, $|\mathbf{x}|_1$. Therefore, the same tradeoffs exist, but with a different mathematical weighting. These observations motivated Mendez and others (1990) to use a norm that seeks a spatially and temporally smooth solution, and Hartzell and Heaton (1983), Hartzell (1989), and Hartzell and Iida (1990) to use spatial and temporal smoothing constraints with an L_2 norm. Finding the smoothest solution that fits the data not only finds the simplest solution but also resists the focusing of energy toward observation points, although no constraint can make up for a poor station distribution.

In the teleseismic problem that we solve, the tradeoff between slip amplitude and its spatial and temporal location is not as pronounced as it could be in the near-source region, using a sparse strong-motion network. With teleseismic data, the direct phases all leave the source region close to vertically downward. Significant energy, however, cannot be erroneously focused in this direction without disrupting the amplitude of the surface reflected phases.

Our objective in this paper is not to find the optimum norm to be used in finite-fault waveform inversions; neither the L_1 nor L_2 norm is optimal, and many others could be tested. The L_1 and L_2 norms, however, are among the simplest and most widely used. Instead, our objective is to clearly show the differences that exist between L_1 and L_2 solutions for an earthquake with a good data set and to use that comparison to obtain a better idea of the earthquake's true rupture history.

DATA

In this study, we use teleseismic *P* and *SH* body waves recorded by stations in the Global Digital Seismograph Network, the Chinese Digital Seismograph Network, and the Global Seismograph Network (GSN), International Deployment of Accelerometers (IDA), and GEOSCOPE (Institut de Physique du Globe, Paris) networks (table 1). Only stations between distances 30° and 90° are used, to avoid mantle triplications and shadow zones. All the seismograms are low-pass filtered with a corner frequency at 1.0 Hz, using a Butterworth filter (Oppenheim and Schafer, 1975), and resampled at a time step of 0.2 s. With this preprocessing, we lose very little of the waveform information but obtain a more manageable total number of data points (7,910) in the inversion. Of the stations used, 12 have well-recorded long- and short-period *P* waveforms. For these stations, the inversion uses the broadband, deconvolved displacement record (Harvey and Choy, 1982). These deconvolved records recover ground displacement from frequencies of 0.01 to 5.0 Hz. Several of these stations have no intermediate-period broadband channel; to use these stations in the inversion without a broadband deconvolution, we would have to use separate long- and short-period records. For the other waveforms, the inversion uses the broadband recording channel, with the instrument response intact. All 40 of the stations listed in table 1 are included in the inversions, but 6 of them (asterisks) are given near-zero weighting, owing to high levels of noise or nodal characteristics. In this study, "noise" is defined as any component of the waveform not described by the assumed Earth model, including anomalous propagation and receiver effects. Nodal stations are useful in constraining the strike and dip of the fault plane, which are fixed before any inversions are done. These stations, however, are not particularly useful in the inversions, owing to the significant changes in the waveform that can result from small changes in the model. The azimuthal equidistant projection in figure 1 shows all the stations that are given full weight in the inversion. Station coverage is better at azimuths of 0° to 90° and 270° to 360° The effects of the station distribution are discussed in detail below.

P- and *SH*-wave first-motion information for the stations used in this study is plotted in figure 2. The mechanism that we favor from these data and from forward modeling of *P* and *SH* waveforms has a strike, dip, and rake of 126°, 67°, and 138°, respectively. The only station inconsistent with this mechanism is PPT (fig. 2*A*), which has a high-frequency compressional first motion but which plots in a dilatational quadrant. Although the record from station PPT is difficult to read, the long-period energy is most likely dilatational. Our preferred mechanism is essentially the same as that of Romanowicz and Lyon-Caen (1990).

INVERSION METHOD

In our basic formulation of the problem, we follow Hartzell and Heaton (1983). A fault plane striking 126° and dipping 67° is divided into the equal-area subfaults shown in figure 3. The overall dimensions of the fault are chosen to encompass all the aftershocks within the 2-week period after the earthquake, except for a few shallow events to the southeast (U.S. Geological Survey staff, 1990). The fault is 60 km long and extends from 0.5- to 25-km depth, giving a downdip width of 26.6 km. A total of 200 subfaults (20 along strike and 10 downdip) are used, each with dimensions of 3 by 2.66 km. The response of each subfault is calculated for each station in the problem by summing individual point-source responses. Generalized ray theory (Langston and Helmberger, 1975) is used to calculate these point-source responses. The source velocity structure (table 2) is based on the velocity structure used by the U.S. Geological Survey in preliminary locations of aftershocks. All rays with as many as two internal reflections in the layered stack and *P*- to *SV*-wave conversions at the surface and Moho are included in the calculations. Attenuation is introduced by using the frequency dependent t^* operator of Choy and Cormier (1986) for a surface source, where $t^*=1.0$, 0.6, and 0.5 for *P* waves at frequencies of 0.1, 1.0, and 5.0 Hz, respectively. The *S*-wave operator has corresponding values approximately a factor of 4.5 larger. This attenuation operator was derived by simultaneously considering source and propagation path effects. Hartzell (1989) showed the effects of different attenuation models in a similar teleseismic body-waveform inversion. Models with lower attenuation require less slip to match the same observed amplitudes. A secondary effect of lower attenuation is a broadening of slip regions to fit the same pulse widths.

The hypocenter is fixed at 18-km depth (U.S. Geological Survey staff, 1990) at the midpoint of the model fault plane. The rupture velocity is assumed to be constant; however, we try a range of plausible values from 2.1 to 3.1 km/s. The subfault synthetic seismograms for strike-slip (180° rake) and dip-slip (90° rake) mechanisms form the basis of the matrix **A**. The observed waveforms strung end to end compose the data vector **b**. Together, they form an overdetermined system of linear equations **Ax=b**. In forming these matrices, the observed record must be aligned in time with the subfault synthetic seismograms; this operation requires picking the first-arriving energy in the waveforms. Whenever possible, times from short-period records are used. As noted by many investigators, inversion for fault slip is an ill-constrained problem. We follow Hartzell and Heaton (1983), Hartzell (1989), and Hartzell and Iida (1990) by requiring the slip to be positive; this constraint translates into restricting the rake to between 90° and 180°. The problem is also stabilized with smoothing constraints on the slip that require the slip to vary as smoothly as possible and still fit the data. As discussed by Hartzell and Heaton (1983), the gridding of the fault plane into subfaults plays an important role in this smoothing process. If only a few large subfaults are

Table 1.—*Seismic stations used in this study*

[Networks: GEOSCOPE, Institut de Physique du Globe, Paris; GSN, Global Digital Seismograph Network, Chinese Digital Seismograph Network, and Global Seismograph Network; IDA/IRIS, International Deployment of Accelerometers/Incorporated Research Institution for Seismology. Asterisks, records weighted down in inversions]

Record type	Station	Distance (°)	Azimuth (°)	Network
Broadband deconvolved *P* waves.	AFI	69.03	232.67	GSN
	BJI	86.62	319.25	GSN
	COL	31.88	339.34	GSN
	GRFO	84.25	28.45	GSN
	GUMO	84.49	282.75	GSN
	HIA	78.25	323.93	GSN
	HON*	34.95	253.57	GSN
	KEV	71.15	10.95	GSN
	KONO	75.71	23.11	GSN
	MAJO	75.85	305.09	GSN
	SCP	34.21	69.82	GSN
	TOL	84.56	43.11	GSN
Broadband instrumental *P* waves.	ARU	86.96	359.72	GSN
	ESK	74.22	31.40	GSN
	HRV	38.63	65.77	GSN
	MDJ	76.24	315.79	GSN
	NNA	64.54	129.91	IDA/IRIS
	OBN	85.47	11.89	GSN
	RPN	64.87	167.63	IDA/IRIS
	CAY	70.74	98.50	GEOSCOPE
	PPT*	60.26	210.70	GEOSCOPE
	WFM	38.63	65.60	GEOSCOPE
	SSB	84.89	34.80	GEOSCOPE
	KIP*	34.92	253.70	GEOSCOPE
Broadband instrumental *SH* waves.	ARU	86.96	359.72	GSN
	COL*	31.88	339.34	GSN
	ESK	74.22	31.40	GSN
	HIA	78.25	323.93	GSN
	HRV	38.63	65.77	GSN
	MDJ	76.24	315.79	GSN
	NNA	64.54	129.91	IDA/IRIS
	OBN	85.47	11.89	GSN
	RPN	64.87	167.63	IDA/IRIS
	SCP	34.21	69.82	GSN
	TOL	84.56	43.11	GSN
	CAY	70.74	98.50	GEOSCOPE
	PPT*	60.26	210.70	GEOSCOPE
	WFM	38.63	65.60	GEOSCOPE
	SSB	84.89	34.80	GEOSCOPE
	KIP*	34.92	253.70	GEOSCOPE

used, there is insufficient spatial resolution of fault details. If a small subfault size is chosen and no smoothing applied, however, starting and stopping phases from individual subfaults can play an erroneous role in modeling the data. Therefore, our approach is to divide the fault into many relatively small subfaults and then apply smoothing constraints. The program NNLS of Lawson and Hanson (1974), a least-squares routine with constraints, is used to solve the L_2 norm problem, and the linear-programming routine of Bartels and Conn (1980) is used to solve the L_1 norm problem.

RESULTS

Contours of total slip (vector sum of the strike-slip and dip-slip components) for various rupture velocities are shown in figures 4*A* and 4*B* for the L_1 and L_2 solutions, respectively, and the associated moment estimates and residual errors for the two solutions with different rupture velocities are listed in table 3. As the rupture velocity increases, the slip distribution spreads out laterally in both the L_1 and L_2 solutions; the slip distribution is nearly constant with depth. These results indicate that the depth of faulting is well constrained by the data. The depth range over which most slip occurs is from about 2 to 18 km, regardless of the norm. Peak slip occurs at about 10-km depth. From the residual errors listed in table 3, a rupture velocity of 2.5 km/s gives the best fit to the data in both the L_1 and L_2 solutions. An average rupture velocity near 2.5 km/s is also preferred in several other recent source inversions for moderate to large earthquakes (Hartzell and Heaton, 1983; Hartzell and Iida, 1990; Hartzell and Mendoza, 1991).

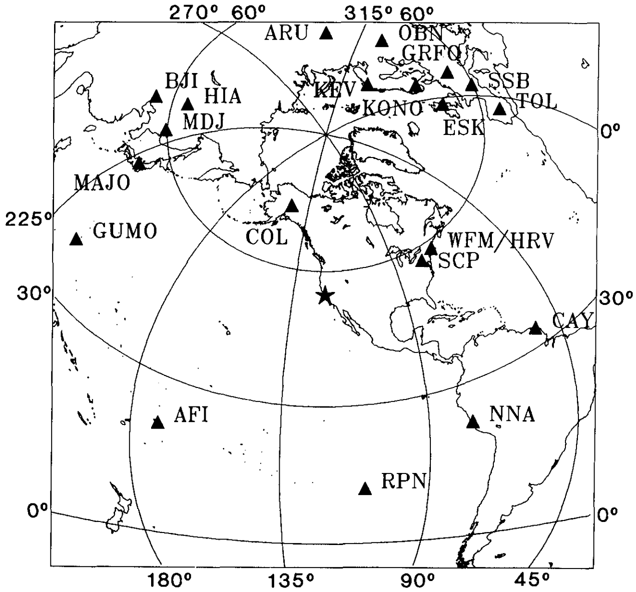

Figure 1.—Azimuthal equidistant plot of stations from which waveform data were given full weight in inversion. Epicenter of earthquake (star) is at center of map, and map radius is 90°.

The L_1 and L_2 solutions with a rupture velocity of 2.5 km/s are compared in figures 5 and 6. No strong argument can be given for one solution over the other; each solution fits the data fairly well, as shown in figure 7. The differences visible in figures 5 and 6 are due solely to the minimization norm. Any evaluation of an earthquake rupture-history model must be tempered with the realization that fundamental uncertainties can exist on the order of the differences visible in figures 5 and 6.

We are now in a position to evaluate those features of the two solutions in figures 5 and 6 that are independent of the choice of an L_1 or L_2 norm. As stated above, both the L_1 and L_2 norms favor an average rupture velocity of 2.5 km/s and have most slip occurring between 2- and 18-km depth. Both the L_1 and L_2 solutions are also characterized by two main sources, a major one to the southeast of the hypocenter and a secondary one to the northwest. However, the L_2 solution is dominated considerably more by the southeastern source. Both solutions have a small amount of slip at the hypocenter and are characterized by upward and bilateral rupture. In both solutions, slip ini-

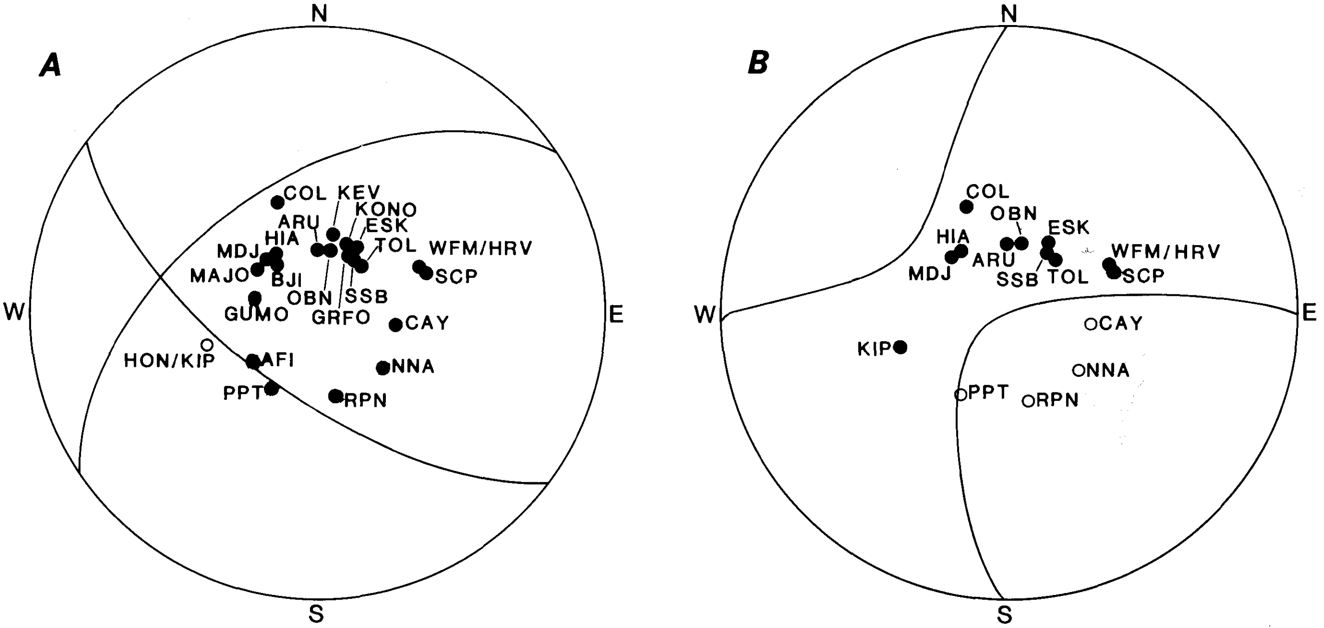

Figure 2.—Equal-area lower-hemisphere projections of *P*-wave (*A*) and *SH*-wave (*B*) focal mechanisms of 1989 Loma Prieta earthquake, based on available teleseismic first-motion data. Strike (126°) and dip (67°) were used in finite-fault waveform inversions; rake (138°) is free to vary spatially from 90° (thrusting) to 180° (strike slip).

tiates in the hypocentral region with a significant thrust component and evolves into almost-pure strike slip at shallower depths, as illustrated in figure 8*C*. The areas of peak slip amplitude have a rake of about 130°, similar to the point-source values obtained by other investigators (Choy and Boatwright, 1990; Kanamori and Satake, 1990; Romanowicz and Lyon-Caen, 1990; Ruff and Tichelaar, 1990; Zhang and Lay, 1990). The rake, however, varies widely with position.

Table 2.—*Source-velocity structure of the earthquake*

[V_P, *P*-wave velocity; V_S, *S*-wave velocity]

V_P (km/s)	V_S (km/s)	Density (g/cm^3)	Thickness (km)
3.50	2.02	1.60	1.0
4.79	2.77	2.05	2.0
5.55	3.20	2.36	4.0
6.24	3.60	2.62	11.0
6.66	3.85	2.77	7.0
8.00	4.62	3.28	---

Although both the L_1 and L_2 solutions have most of their moment release occurring over a fault length of 35 to 40 km, they also have several small sources outside this region. The validity of these small sources is questionable, however, because they are at the limits of our resolution. Comparison between the observed and synthetic seismograms shows little change in the waveforms when these small sources are omitted. As shown in figure 9, the small sources all lie at rupture times greater than about 7.5 s from the hypocenter. In figure 8*A* we integrate the slip distribution for the L_2 solution to obtain a plot of moment release (a comparable distribution is obtained for the L_1 solution). Other investigators have obtained similar moment-release functions from teleseismic data (Choy and Boatwright, 1990; Kanamori and Satake, 1990; Romanowicz and Lyon-Caen, 1990; Ruff and Tichelaar, 1990). The best-resolved and major component of moment release takes place in the first 7.5 s (shaded area, fig. 8*A*). The corresponding distribution of slip on the fault plane is plotted in figure 8*B*. This pattern of faulting is nearly identical to the rupture history obtained by Choy and Boatwright (1990). A source duration of 7.5 s and a rupture length of 35 km also agree closely with the estimates of Kanamori and Satake (1990). The moment estimates listed in table 3 are 3.2×10^{26} dyne-cm for the L_1 solution and 3.0×10^{26} dyne-cm for the L_2 solution. If only the first 7.5 s of each solution is considered, both of these estimates are decreased by 0.4×10^{26} dyne-cm. Our results also agree well with the general fault parameters obtained from geodetic modeling by Lisowski and others (1990), who estimated a fault length of 37 km, a depth range of faulting of 5 to 17.5 km, and a seismic moment of 3.0×10^{26} dyne-cm. No clear surface faulting was associated with the earthquake, and our results are consistent with that observation. The main slip occurring below about 2-km depth is plotted in figure 8*B*. For the L_2 solution, however, a region of dip slip occurs at the northwest end of the fault close to the surface (fig. 5*B*). Although slip on this segment of the fault is not well constrained, as discussed above, it does coincide with a region of surface cracking (Plafker and Galloway, 1989).

One source parameter that we have not yet addressed is the rise time of the source or the duration of faulting at a point on the fault. The source rise time is included in our

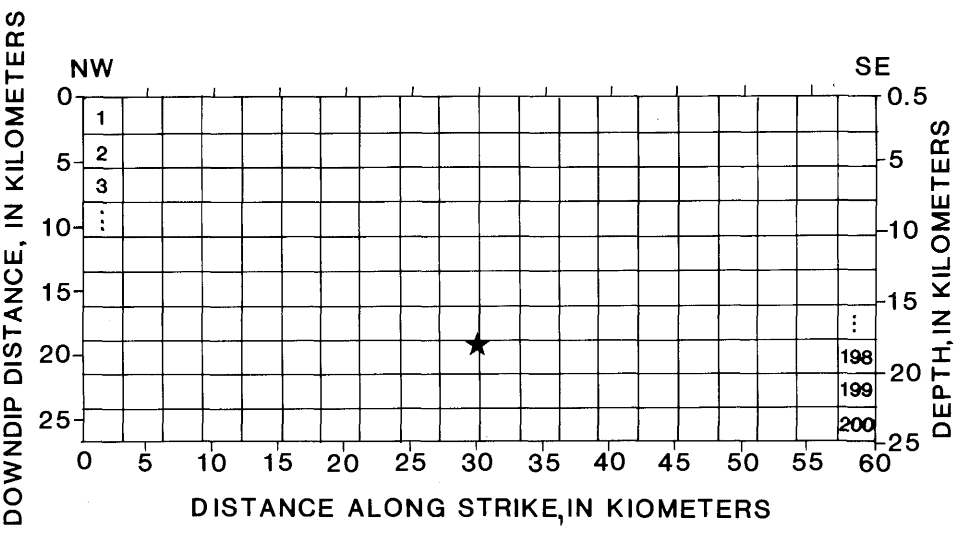

Figure 3.—Parametrization of model fault plane for 1989 Loma Prieta earthquake. Fault is divided into 200 subfaults, each 3.0 by 2.66 km. Teleseismic waveforms are inverted by using two different minimization norms, L_1 and L_2, to obtain optimal slip on each subfault. Hypocenter (star) is at 18-km depth.

modeling by convolving the subfault synthetic seismograms with a source-time function. All the solutions that we have presented so far assume a 1-s-duration, triangular source-time function that is constant over the fault plane. A longer-duration source-time function was tested by using a 3-s-duration triangle. The resulting errors, listed in table 3 for a rupture velocity of 2.5 km/s, are significantly worse than the previous errors.

An important aspect of the finite-fault inversion problem that still needs to be discussed is the effect of station distribution. The number and location of observation records can significantly affect the outcome of an inversion in both teleseismic and strong-motion studies. Olson and Anderson (1988) showed several examples of different strong-motion-station distributions that yield divergent results. For the teleseismic problem, a good station distribution is particularly necessary for a bilateral rupture, such as in the 1989 Loma Prieta earthquake. In a bilateral rupture, the two halves of the fault radiate energy approximately simultaneously. If the fault dimensions are relatively small, the energy from the two halves of the fault will arrive at teleseismic stations with only a small time separation. For the northern and southern sources of the earthquake, the time separation is approximately 1 s for *P* waves and 2 s for *S* waves at stations along the strike of the fault. These time separations are near the limits of resolution of the analysis, and so the slip distribution is sensitive to the phases and stations used in the inversion.

The effects of using three alternative station distributions—(1) a distribution that includes *P*-wave phases only, (2) a distribution that includes nodal phases and omits some nonnodal *SH*-wave phases, and (3) a more nearly uniform station distribution—are shown in figure 10. Only the L_2 solutions are shown; the L_1 solutions yield the same results. The distributions of stations that include the *P*- and *SH*-wave phases used for each inversion are shown in figure 11. The *P*-wave-only solution in figure 10 uses the *P*-wave phases from the preferred station distribution in figure 11*A*. The results in figure 10 should be compared with our preferred solution in figure 5.

The most obvious feature of figure 10 is the instability of the strike-slip component of motion. When only *P*-wave phases are used (fig. 10*A*), the resolution of the strike-slip component is worst; the inversion distributes the slip in a ridge approximately equally north and south of the hypocenter. *SH*-wave phases are important for the earthquake because of the greater separation between arrival times for sources north and south of the hypocenter, and because near-vertical strike-slip faulting is more efficient at producing teleseismic *S* waves than *P* waves. By adding nodal records to the inversion and removing some important nonnodal *SH*-wave phases (fig. 10*B*), the major strike-slip faulting shifts to the north side of the hypocenter. The net result is that the northern source is now larger than the southern source. Because of the less desirable station distribution, we consider this solution to be less likely. Finally, because our preferred distribution has a higher station density in Europe, we considered a more nearly uniform station distribution (fig. 10*C*). Tradeoffs are necessary in choosing such a distribution because the number of stations is limited and station quality is important. The resulting model is nearly identical to our preferred solution in figure 5, in which most strike-slip faulting occurs south of the hypocenter and the larger of the two sources is also south of the hypocenter. These results are consistent with the strong-motion inversion models of Beroza (1991) and Steidl and others (1991). We prefer the solution in figure 5 because it uses all the best-quality records and omits nodal records, which we do not ordinarily use for the above-mentioned reasons.

All three solutions in figure 10 have more shallow dip-slip faulting than our preferred model. This result is most likely erroneous and due to the exclusion of *SH*-wave phases and (or) the inclusion of nodal stations, which contain larger amounts of late-scattered energy. Shallow dip-slip motion is hard to resolve (or omit) in an inversion using only teleseismic *P* waves because the downgoing *P*-wave phase is nearly canceled by the upgoing *pP*-wave phase. The shorter the period of the *P* wave, the better it will be at resolving shallow dip-slip motion. In addition to the three solutions in figure 10, we also tried several inversions including *SV* waves. A judicious selection of these phases added no new information or failed to change the solution significantly from that in figure 5. Owing to the uncertainties in the *SV* waveforms and their likely contamination with converted phases, these inversions are considered less accurate.

The distribution of slip for the L_2 solution and a rupture velocity of 2.5 km/s is compared with the pattern of aftershocks during the 2-week period after the earthquake (Dietz and Ellsworth, 1990; Simila and others, 1990) in figure 12. Most aftershocks plot within the boundaries of the area of major slip. On closer inspection, aftershocks seem to concentrate in the areas of least slip or highest gradient in the main-shock slip. This conclusion is made particularly easy if all the aftershocks are plotted with the same symbol, regardless of magnitude. Several recent studies have found that foreshocks and aftershocks occur in areas that did not slip during the main shock or in areas of stress concentration due to the main-shock slip (Stein and Lisowski, 1983; Mendoza and Hartzell, 1988; Engdahl and others, 1989; Houston and Engdahl, 1989; Schwartz and others, 1989; Hartzell and Iida, 1990).

CONCLUSIONS

The effect of the minimization norm in finite-fault inversions has not been adequately considered. The solutions obtained by using L_1 and L_2 norms for the 1989 Loma Prieta earthquake differ significantly, and we are unable to judge which is better. Neither norm is optimal, and more work is needed to find norms that do not produce undesirable tradeoffs in the earthquake-source model.

By considering L_1 and L_2 solutions, we arrive at the following parameters for the earthquake that are common to both norms. The major faulting has a length of 35 to 40 km and a depth extent from 2 to 18 km. The hypocentral region has only minimal slip. The rupture grows upward from the point of initiation and bilaterally at an average velocity of 2.5 km/s. There are two main areas of slip. The largest is above and southeast of the hypocenter and is centered at 10-km depth; this source dominates the L_2 solution and has more nearly equal weight in the L_1 solution. The second source is northwest of the hypocenter and is also centered at about 10-km depth. The rake varies with position on the fault, ranging from mostly dip slip in the hypocentral region to almost pure strike slip at shallower depths. The southern source also has a larger component of strike-slip motion than the northern source. Most of the moment release occurs in the first 7.5 s, with an integrated moment of 2.6×10^{26} dyne-cm. This part of the rupture is the best resolved. Including peripheral, secondary areas of slip raises the moment to 3.0×10^{26} dyne-cm. The peak slip amplitude is about 3 m, and the preferred average source-time duration is about 1 s.

This study also raises several questions regarding future slip along this section of the San Andreas fault. First, because little slip occurred in the uppermost region of the fault (above 2-km depth), will this section of the fault rupture in another earthquake, or is strain being relieved by another mechanism? Also, both the L_1 and L_2 solutions show slip on the southeastern section of the fault to be considerably larger (fig. 5). Should we expect future slip on the section northwest of the hypocenter, owing to the slip deficit calculated for the earthquake? These questions might be answerable by taking a closer look at the slip history of this section of the San Andreas fault.

ACKNOWLEDGMENTS

The L_1 norm solver was provided by Toshiro Tanimoto. We thank Barbara Romanowicz for supplying the GEOSCOPE data used in this study. The attenuation operators and the broadband, deconvolved P-wave data were

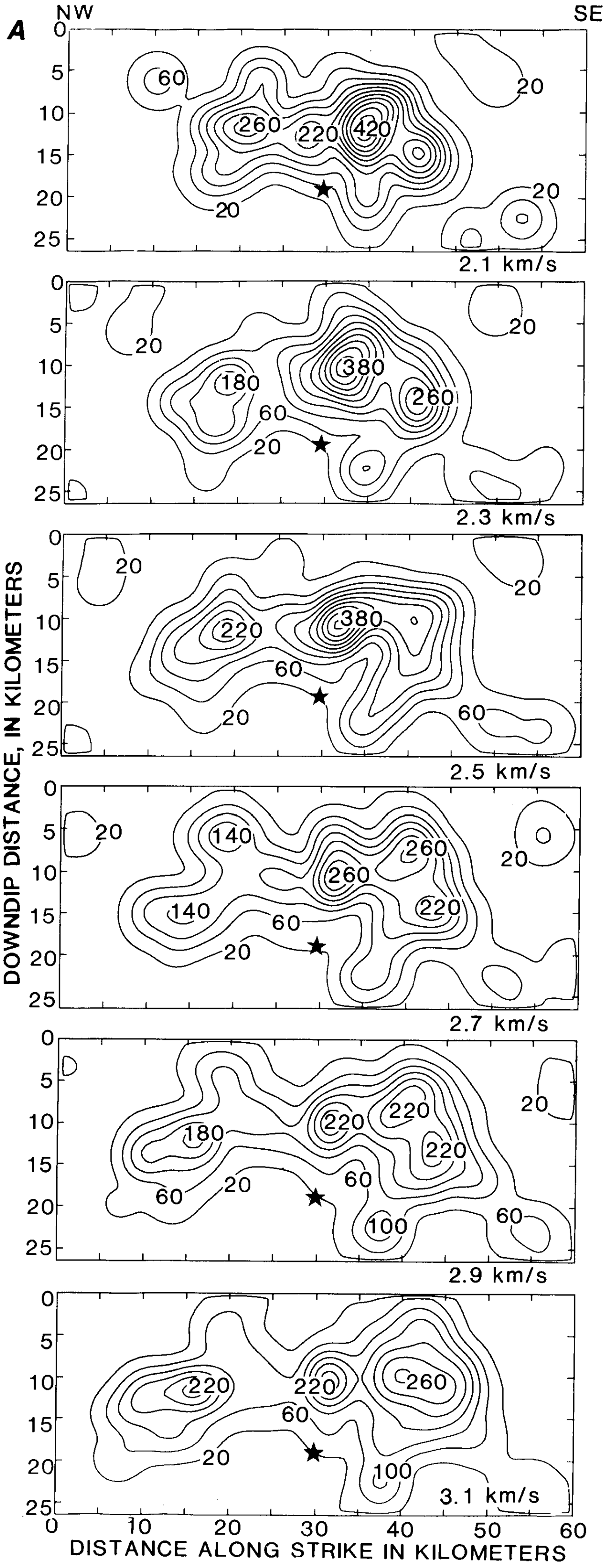

Figure 4.—Contours of total slip (in centimeters) (vector sum of strike-slip and dip-slip motion), using L_1 (*A*) and L_2 (*B*) norms and six different rupture velocities. Rupture velocity of 2.5 km/s gives lowest residual error (table 3). Star, hypocenter.

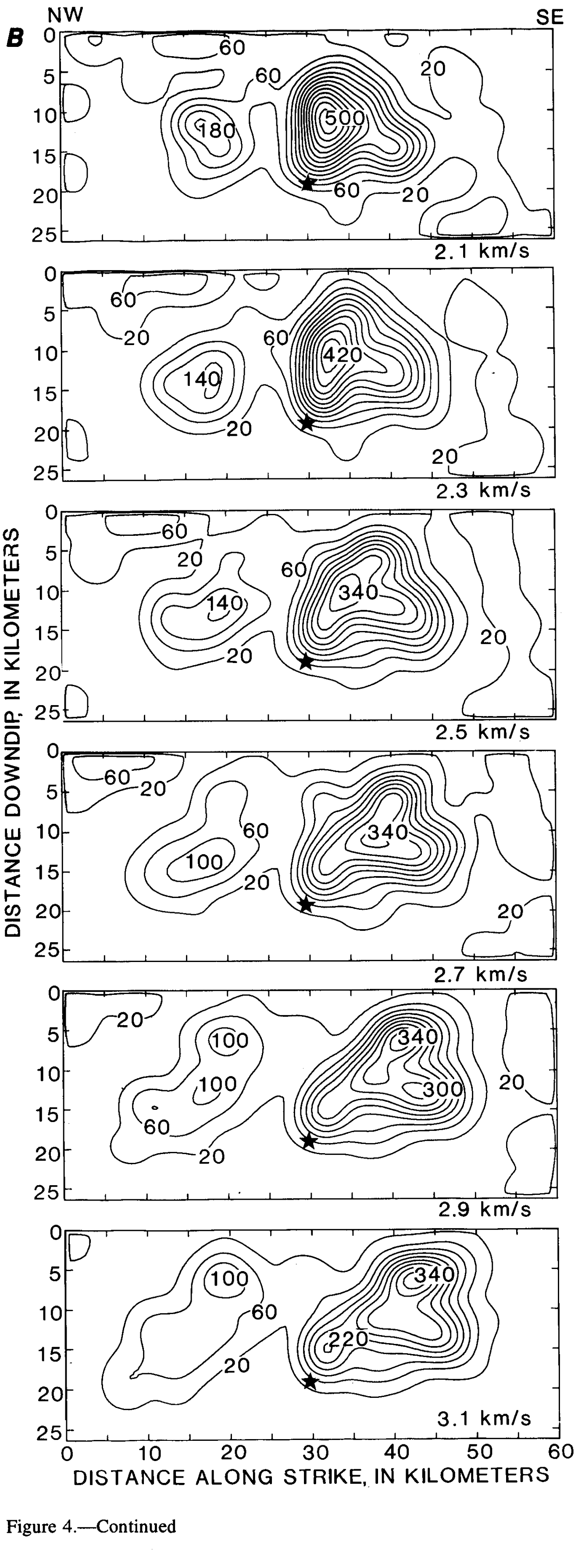

Figure 4.—Continued

Table 3.—*Results of inversion using* L_1 *and* L_2 *norms*

Time-function duration (s)	Norm	Rupture velocity (km/s)	Moment (10^{26} dyne-cm)	Residual error
1.0	L_2	2.1	3.26	17.26
1.0	L_2	2.3	3.14	17.17
1.0	L_2	2.5	2.99	17.10
1.0	L_2	2.7	2.91	17.17
1.0	L_2	2.9	2.86	17.20
1.0	L_2	3.1	2.78	17.27
1.0	L_1	2.1	3.17	1,072.7
1.0	L_1	2.3	3.04	1,067.4
1.0	L_1	2.5	3.19	1,060.1
1.0	L_1	2.7	3.12	1,060.6
1.0	L_1	2.9	2.97	1,061.9
1.0	L_1	3.1	2.98	1,060.3
3.0	L_2	2.5	3.23	17.50
3.0	L_1	2.5	3.37	1,070.8

kindly supplied by George Choy. Aftershock locations were provided by Lynn Dietz. We benefited from discussions with Allen Olson on minimization norms. The manuscript was improved by thoughtful reviews by George Choy, Kaye Shedlock, and Terry Wallace.

REFERENCES CITED

Aki, Keiiti, and Richards, P.G., 1980, Quantitative seismology; theory and methods: San Francisco, W.H. Freeman, 2 v.

Bartels, R.H., and Conn, A.R., 1980, Linearly constrained discrete L_1 problems: Association for Computing Machinery Transactions on Mathematical Software, v. 6, no. 4, p. 594–608.

Beroza, G.C., 1991, Near-source modeling of the Loma Prieta earthquake; evidence for heterogeneous slip and implications for earthquake hazard: Seismological Society of America Bulletin, v. 81, no. 5, p. 1603–1621.

Beroza, G.C., and Spudich, Paul, 1988, Linearized inversion for fault rupture behavior; application to the 1984 Morgan Hill, California earthquake: Journal of Geophysical Research, v. 93, no. B6, p. 6275–6296.

Choy, G.L., and Boatwright, John, 1988, Teleseismic and near-field analysis of the Nahanni earthquakes in the Northwest Territories, Canada: Seismological Society of America Bulletin, v. 78, no. 5, p. 1627–1652.

———1990, Source characteristics of the Loma Prieta, California, earthquake of October 18, 1989 from global digital seismic data: Geophysical Research Letters, v. 17, no. 8, p. 1183–1186.

Choy, G.L., and Cormier, V.F., 1986, Direct measurement of the mantle attenuation operator from broadband *P* and *S* waveforms: Journal of Geophysical Research, v. 91, no. B7, p. 7326–7342.

Das, Shamita, and Kostrov, B.V., 1990, Inversion for seismic slip rate history and distribution with stabilizing constraints; application to the 1986 Andreanof Islands earthquake: Journal of Geophysical Research, v. 95, no. B5, p. 6899–6913.

Dietz, L.D., and Ellsworth, W.L., 1990, The October 17, 1989, Loma Prieta, California, earthquake and its aftershocks; geometry of the sequence from high-resolution locations: Geophysical Research Letters, v. 17, no. 9, p. 1417–1420.

Engdahl, E.R., Billington, Selena, and Kisslinger, Carl, 1989, Teleseismically recorded seismicity before and after the May 7, 1986, Andreanof Islands, Alaska, earthquake: Journal of Geophysical

Research, v. 94, no. B11, p. 15481–15498.

Frankel, Arthur, and Wennerberg, L.G., 1989, Rupture process of the M_s 6.6 Superstition Hills, California, earthquake determined from strong-motion records; application of tomographic source inversion: Seismological Society of America Bulletin, v. 79, no. 2, p. 515–541.

Fukuyama, Eiichi, and Irikura, Kojiro, 1986, Rupture process of the 1983 Japan Sea (Akita-Oki) earthquake using a waveform inversion method: Seismological Society of America Bulletin, v. 76, no. 6, p. 1623–1640.

Hartzell, S.H., 1989, Comparison of seismic waveform inversion results for the rupture history of a finite fault; application to the 1986 North Palm Springs, California, earthquake: Journal of Geophysical Research, v. 94, no. B6, p. 7515–7534.

Hartzell, S.H., and Heaton, T.H., 1983, Inversion of strong ground motion and teleseismic waveform data for the fault rupture history of the 1979 Imperial Valley, California, earthquake: Seismological Society of America Bulletin, v. 73, no. 6, p. 1553–1583.

———1986, Rupture history of the 1984 Morgan Hill, California, earthquake from the inversion of strong motion records: Seismological Society of America Bulletin, v. 76, no. 3, p. 649–674.

Hartzell, S.H., and Iida, Mashiro, 1990, Source complexity of the 1987 Whittier Narrows, California, earthquake from the inversion of strong motion records: Journal of Geophysical Research, v. 95, no. B8, p. 12475–12485.

Hartzell, S.H., and Mendoza, Carlos, 1991, Application of an iterative least squares waveform inversion of strong motion and teleseismic records to the 1978 Tabas, Iran, earthquake: Seismological Society of America Bulletin, v. 81, no. 2, p. 305–331.

Harvey, Danny, and Choy, G.L., 1982, Broad-band deconvolution of GDSN data: Royal Astronomical Society Geophysical Journal, v. 69, no. 2, p. 659–668.

Houston, Heidi, and Engdahl, E.R., 1989, A comparison of the spatio-temporal distribution of moment release for the 1986 Andreanof Islands earthquakes with relocated seismicity: Geophysical Research Letters, v. 16, no. 12, p. 1421–1424.

Houston, Heidi, and Kanamori, Hiroo, 1986, Source spectra of great earthquakes; teleseismic constraints on rupture process and strong motion: Seismological Society of America Bulletin, v. 76, no. 1, p. 19–42.

———1990, Comparison of strong-motion spectra with teleseismic spectra for three magnitude 8 subduction-zone earthquakes: Seismological Society of America Bulletin, v. 80, no. 4, p. 913–934.

Jackson, D.D., 1972, Interpretation of inaccurate, insufficient and inconsistent data: Royal Astronomical Society Geophysical Journal, v. 28, no. 1, p. 97–107.

Jackson, D.D., and Matsu'ura, Mitsuhiro, 1985, A Bayesian approach to nonlinear inversion: Journal of Geophysical Research, v. 90, no. 1, p. 581–591.

Kanamori, Hiroo, and Satake, Kenji, 1990, Broadband study of the 1989

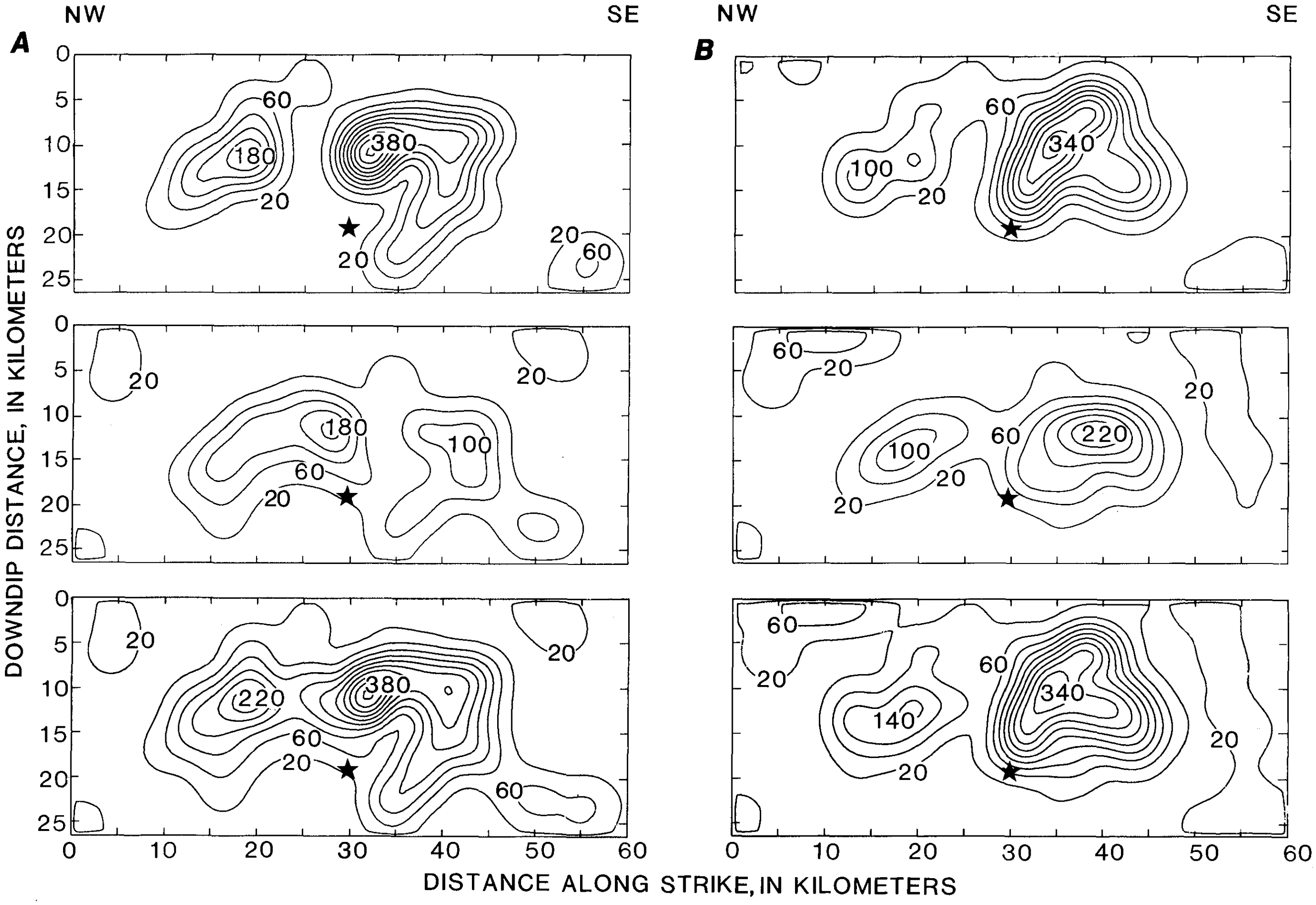

Figure 5.—Contours of slip (in centimeters) in best-fitting L_1 (*A*) and L_2 (*B*) solutions, showing strike slip (180°, top plot), dip slip (90°, middle plot) and vector sum of strike slip and dip slip (bottom plot), using rupture velocity of 2.5 km/s. Star, hypocenter.

Loma Prieta earthquake: Geophysical Research Letters, v. 17, no. 8, 1179–1182.

Kikuchi, Masayuki, and Fukao, Yoshio, 1985, Iterative deconvolution of complex body waves from great earthquakes—the Tokuchi-Oki earthquake of 1968: Physics of the Earth and Planetary Interiors, v. 37, no. 4, p. 235–248.

Lanczos, Cornelius, 1961, Linear differential operators: New York, D. Van Nostrand, 564 p.

Langbein, J.O., 1981, An interpretation of episodic slip on the Calaveras fault near Hollister, California: Journal of Geophysical Research, v. 86, no. B6, p. 4941–4948.

Langston, C.A., and Helmberger, D.V., 1975, A procedure for modelling shallow dislocation sources: Royal Astronomical Society Geophysical Journal, v. 42, no. 1, p. 117–130.

Lawson, C.L., and Hanson, R.J., 1974, Solving least squares problems: Englewood Cliffs, N.J., Prentice-Hall, 340 p.

Lisowski, Michael, Prescott, W.H., Savage, J.C., and Johnston, M.J.S., 1990, Geodetic estimate of coseismic slip during the 1989 Loma Prieta, California, earthquake: Geophysical Research Letters, v. 17, no. 9, p. 1437–1440.

Mendez, A.J., Olson, A.H., and Anderson, J.G., 1990, A norm minimization criterion for the inversion of earthquake ground motion: Geophysical Journal International, v. 102, no. 1, p. 287–298.

Mendoza, Carlos, and Hartzell, S.H., 1988, Aftershock patterns and mainshock faulting: Seismological Society of America Bulletin, v. 78, no. 4, p. 1438–1449.

———1989, Slip distribution of the 19 September 1985 Michoacan, Mexico, earthquake; near-source and teleseismic constraints: Seismological Society of America Bulletin, v..79, no. 3, p. 655–669.

Menke, William, 1984, Geophysical data analysis; discrete inverse theory: Orlando, Fla., Academic Press, 260 p.

Olson, A.H., and Apsel, R.J., 1982, Finite faults and inverse theory with application to the 1979 Imperial Valley earthquake: Seismological Society of America Bulletin, v. 72, no. 6, p. 1969–2001.

Olson, A.H., and Anderson, J.G., 1988, Implications of frequency domain inversion of earthquake ground motions for resolving the space-time dependence of slip on an extended fault: Royal Astronomical Society Geophysical Journal, v. 94, no. 2, p. 443–455.

Oppenheim, A.V., and Schafer, R.W., 1975, Digital signal processing: Englewood Cliffs, N.J., Prentice Hall, 585 p.

Plafker, George, and Galloway, J.P., eds., 1989, Lessons learned from the Loma Prieta, California, earthquake of October 17, 1989: U.S.

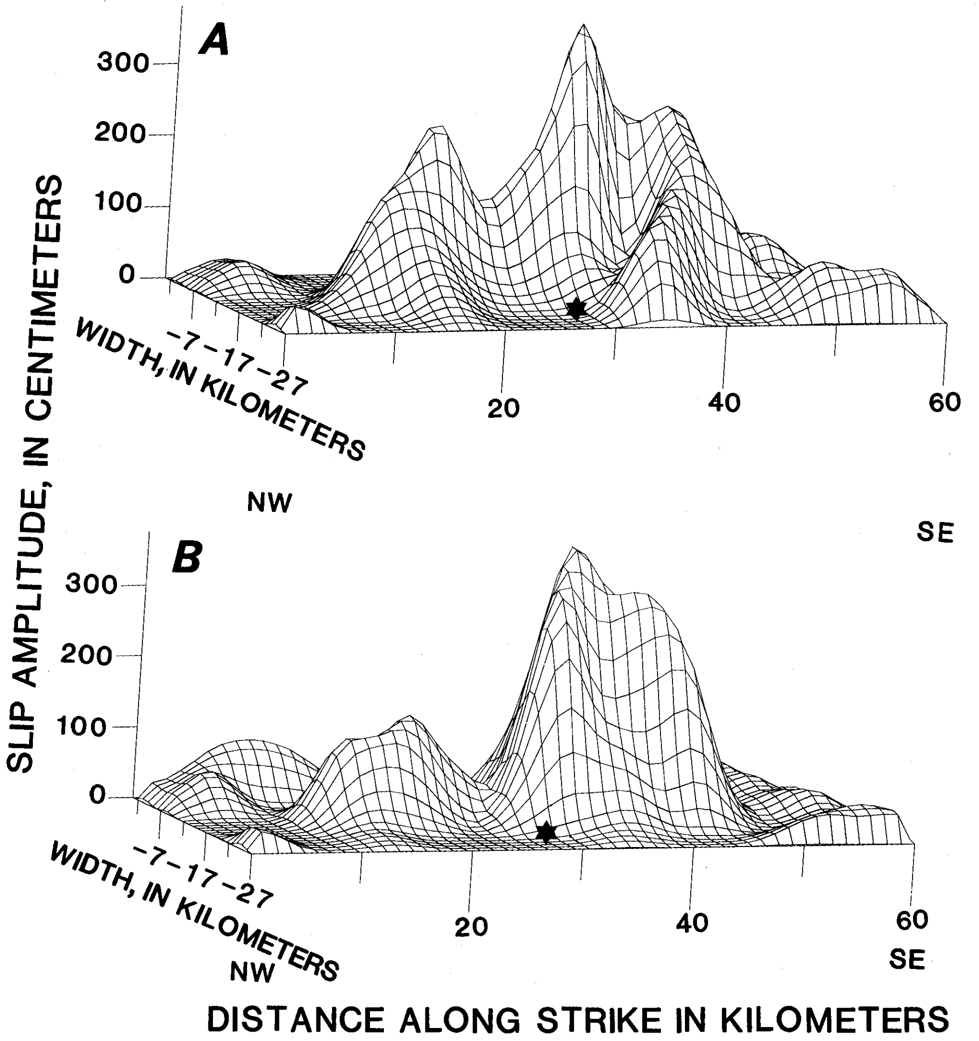

Figure 6.—Three-dimensional plots of total slip (vector sum of strike-slip and dip-slip motion) for best-fitting L_1 (*A*) and L_2 (*B*) solutions. View updip from below hypocenter (star).

Geological Survey Circular 1045, 48 p.

Romanowicz, B.A., and Lyon-Caen, Hélène, 1990, The Loma Prieta earthquake of October 18, 1989; results of teleseismic mantle and body-wave inversion: Geophysical Research Letters, v. 17, no. 8, p. 1191–1194.

Ruff, L.J., and Tichelaar, B.W., 1990, Moment tensor rate functions for the 1989 Loma Prieta earthquake: Geophysical Research Letters, v. 17, no. 8, p. 1187–1190.

Schwartz, S.Y., Dewey, J.W., and Lay, Thorne, 1989, Influence of fault plane heterogeneity on the seismic behavior in the southern Kurile Islands Arc: Journal of Geophysical Research, v. 94, no. B5, p. 5637–5649.

Segall, Paul, and Harris, R.A., 1987, Earthquake deformation cycle on the San Andreas fault near Parkfield, California: Journal of Geophysical Research, v. 92, no. B10, p. 10511–10525.

Simila, G.W., McNally, K.C., Nava, E., Protti-Quesada, Marino, and Yellin, Joseph, 1990, Evidence of very early aftershock activity along the northwest portion of the 18 October 1989 earthquake rupture zone: Geophysical Research Letters, v. 17, no. 10, p. 1785–1788.

Steidl, J.H., Archuleta, R.J., and Hartzell, S.H., 1991, Rupture history of the 1989 Loma Prieta, California, earthquake: Seismological Society of America Bulletin, v. 81, no. 5, p. 1573–1602.

Stein, R.S., and Lisowski, Michael, 1983, The 1979 Homestead Valley earthquake sequence, California; control of aftershocks and postseismic deformation: Journal of Geophysical Research, v. 88, no. B8, p. 6477–6490.

Takeo, Minoru, 1987, An inversion method to analyze the rupture processes of earthquakes using near-field seismograms: Seismological Society of America Bulletin, v. 77, no. 2, p. 490–513.

Trifunac, M.D., 1974, A three-dimensional dislocation model for the San Fernando, California, earthquake of February 9, 1971: Seismo-

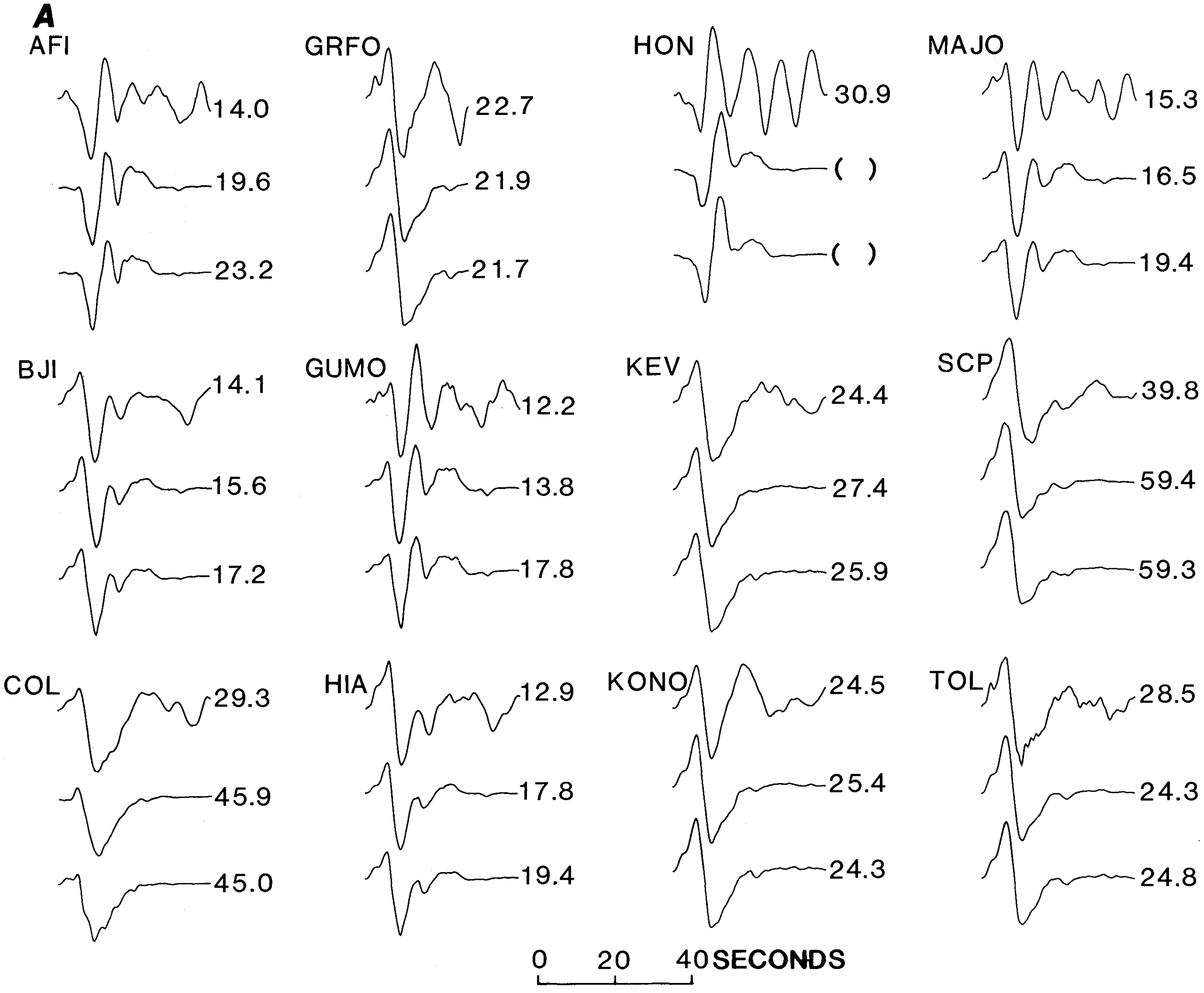

Figure 7.—Comparison of broadband deconvolved (*A*) and instrumental (*B*) *P* waves and broadband instrumental *SH* waves (*C*) (top trace) with predictions of best-fitting solutions for L_2 (middle trace) and L_1 (bottom trace) norms in figures 5 and 6. Broadband deconvolved data records were obtained by performing a simultaneous deconvolution of long- and short-period records. Peak amplitudes in microns (fig. 7*A*) and counts (figs. 7*B*, 7*C*). Synthetic seismograms not assigned an amplitude were downweighted in inversion

logical Society of America Bulletin, v. 64, no. 1, p. 149–172.

U.S. Geological Survey staff, 1990, The Loma Prieta, California, earthquake; an anticipated event: Science, v. 247, no. 4940, p. 286–293.

Vasco, D.W., Johnson, L.R., and Goldstein, N.E., 1988, Using surface displacement and strain observations to determine deformation at depth, with application to Long Valley caldera, California: Journal of Geophysical Research, v. 93, no. B4, p. 3232–3242.

Ward, S.N., and Barrientos, S.E., 1986, An inversion for slip distribution and fault shape from geodetic observations of the 1983 Borah Peak, Idaho, earthquake: Journal of Geophysical Research, v. 91, no. B5, p. 4909–4919.

Wiggins, R.A., 1972, The general linear inverse problem; implication of surface waves and free oscillations for earth structure: Reviews of Geophysics, v. 10, no. 1, p. 251–285.

Yoshida, Shingo, 1986, A method of waveform inversion for earthquake rupture process: Journal of Physics of the Earth, v. 34, no. 3, p. 235–255.

Zhang, Jiajun, and Lay, Thorne, 1990, Source parameters of the 1989 Loma Prieta earthquake determined from long-period Rayleigh waves: Geophysical Research Letters, v. 17, no. 8, p. 1195–1198.

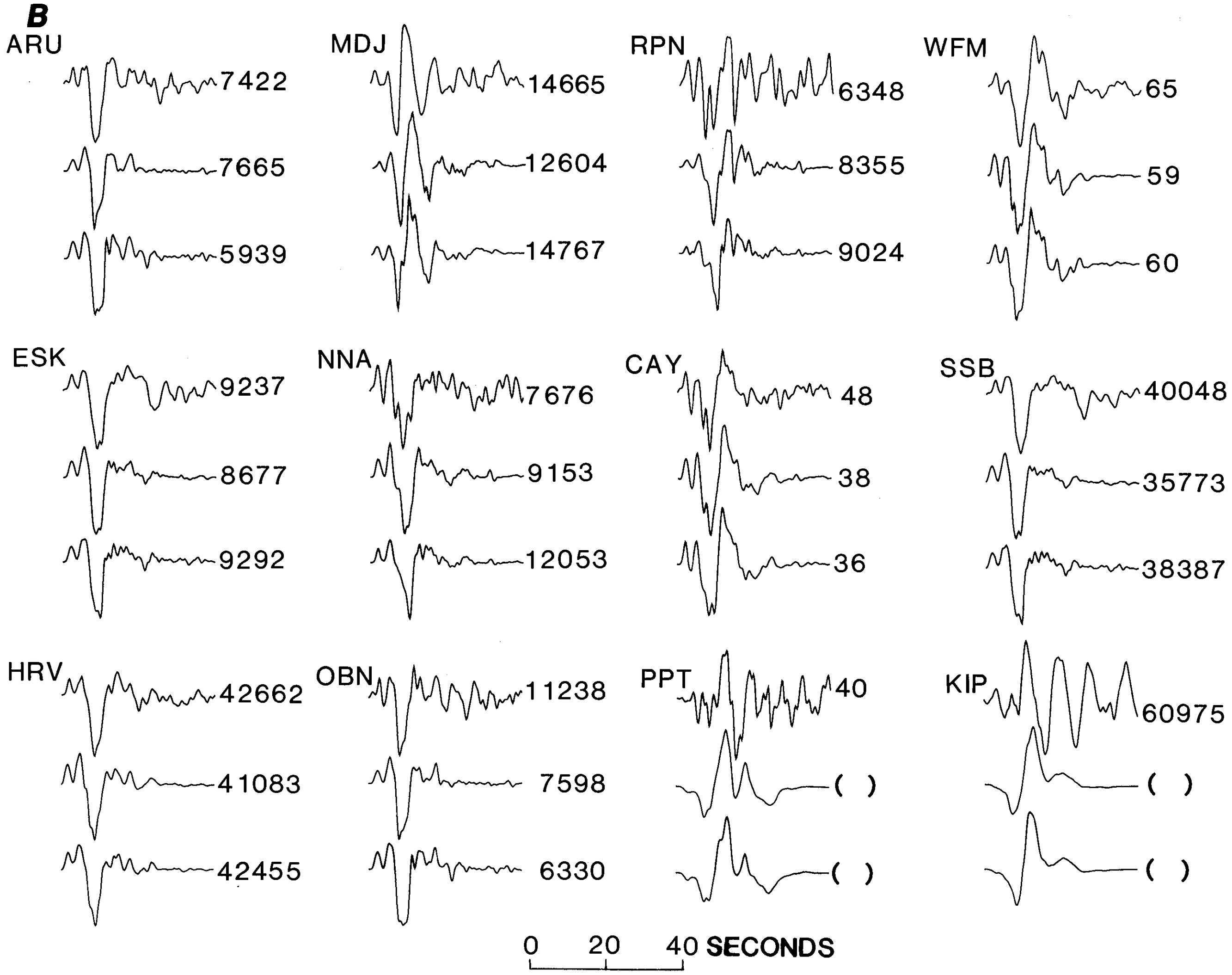

Figure 7.—Continued

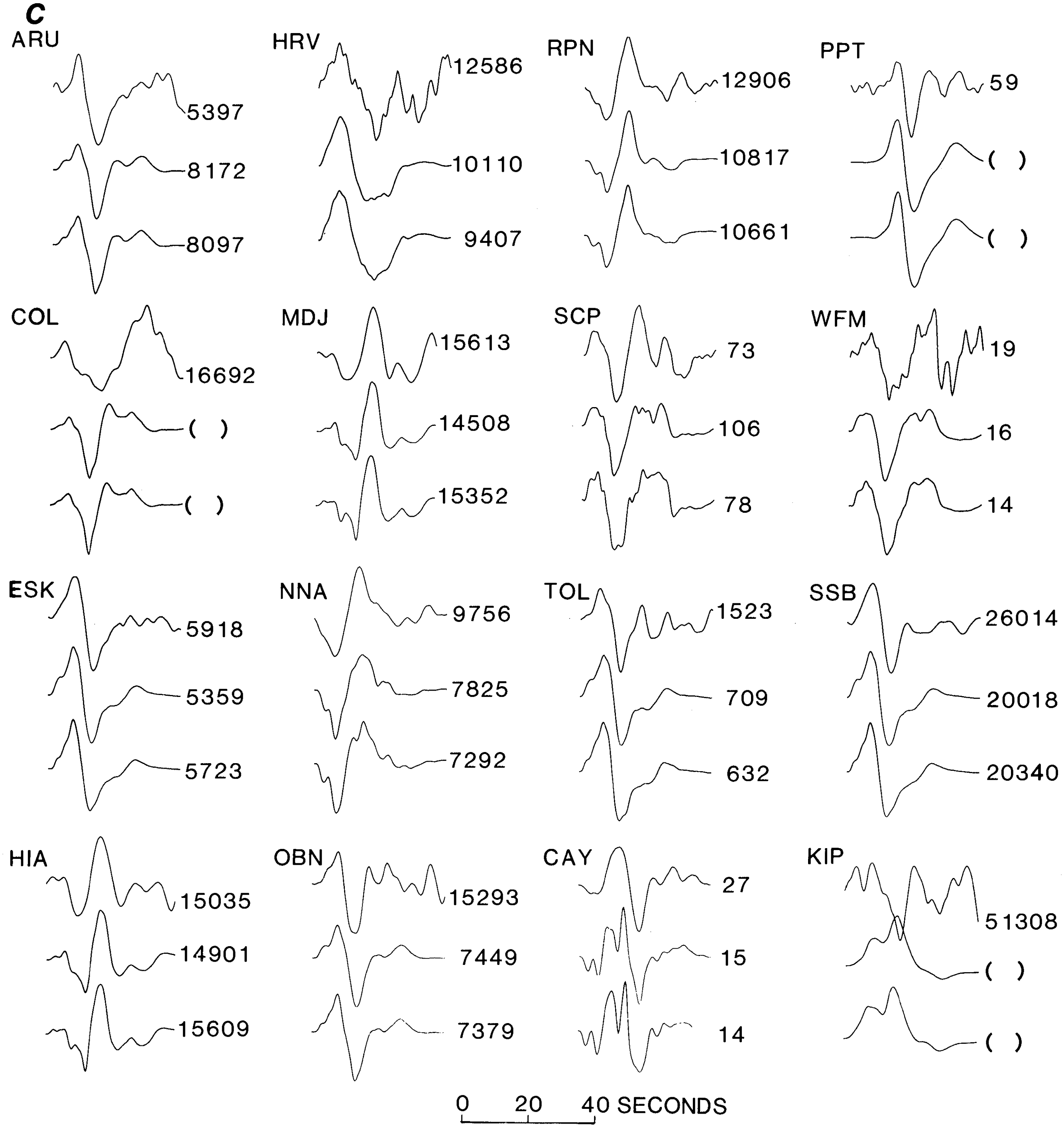

Figure 7.—Continued

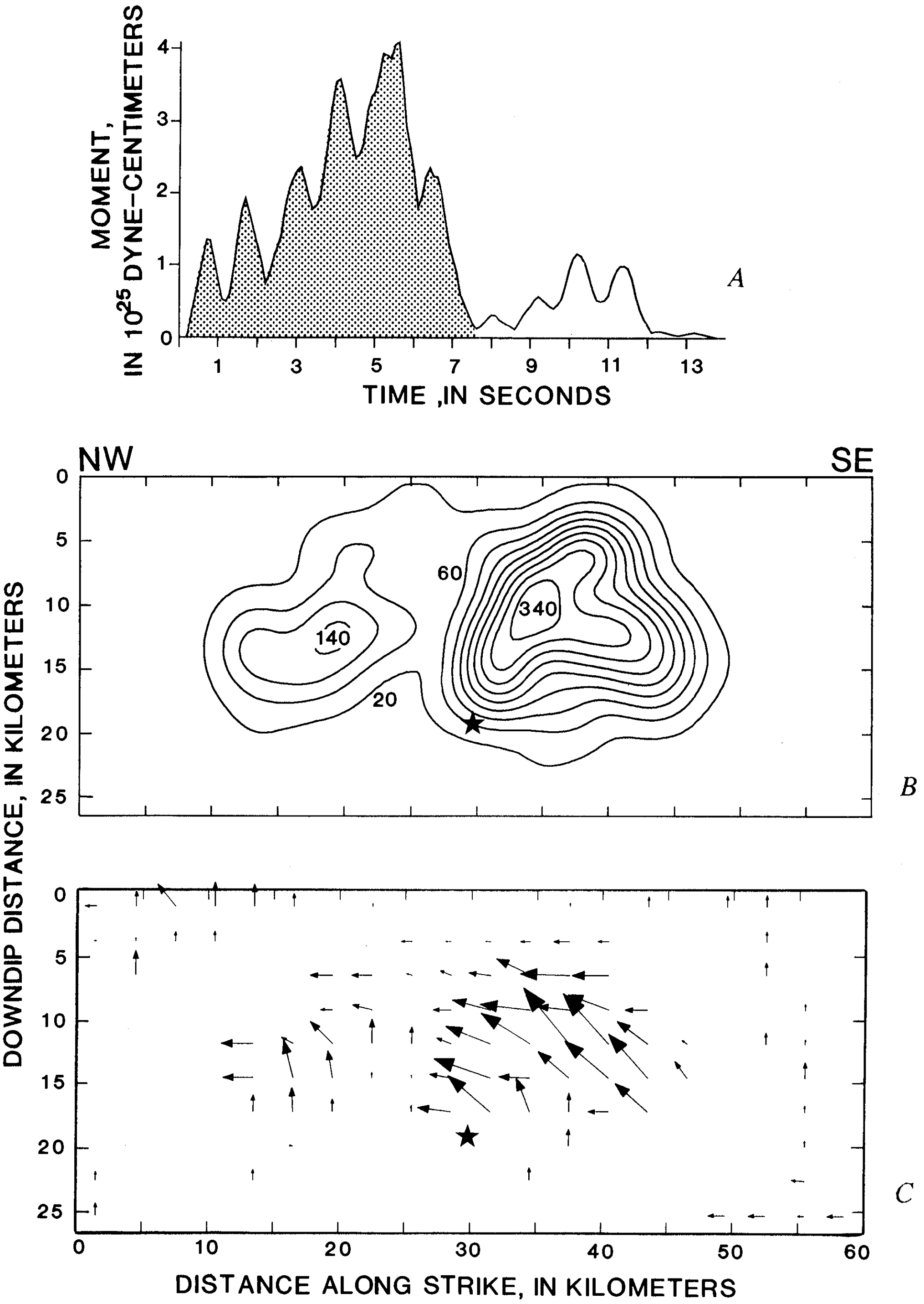

Figure 8.—Best-fitting solution for L_2 norm. *A*, Moment release. Most moment release, which also is best resolved, occurs within the first 7.5 s. *B*, Contours of total slip (in centimeters) as a function of position, corresponding to shaded area of moment-release function in figure 8*A*. *C*, Vector plot of rake as a function of position, including slip vectors on all subfaults. Size of arrows is proportional to amplitude of slip.

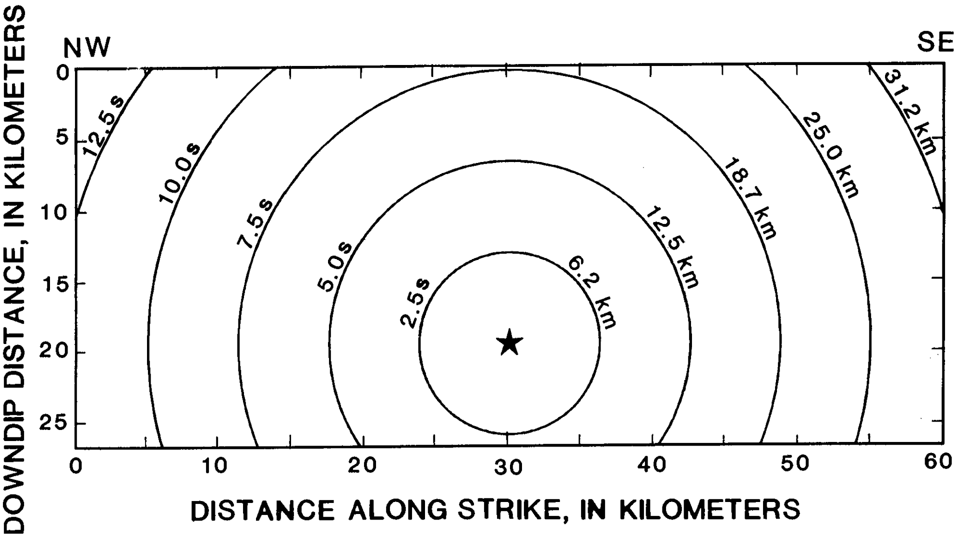

Figure 9.—Contours of rupture front at 2.5-s intervals for a constant rupture velocity of 2.5 km/s, which gave lowest residual error for both L_1 and L_2 norms. Star, hypocenter.

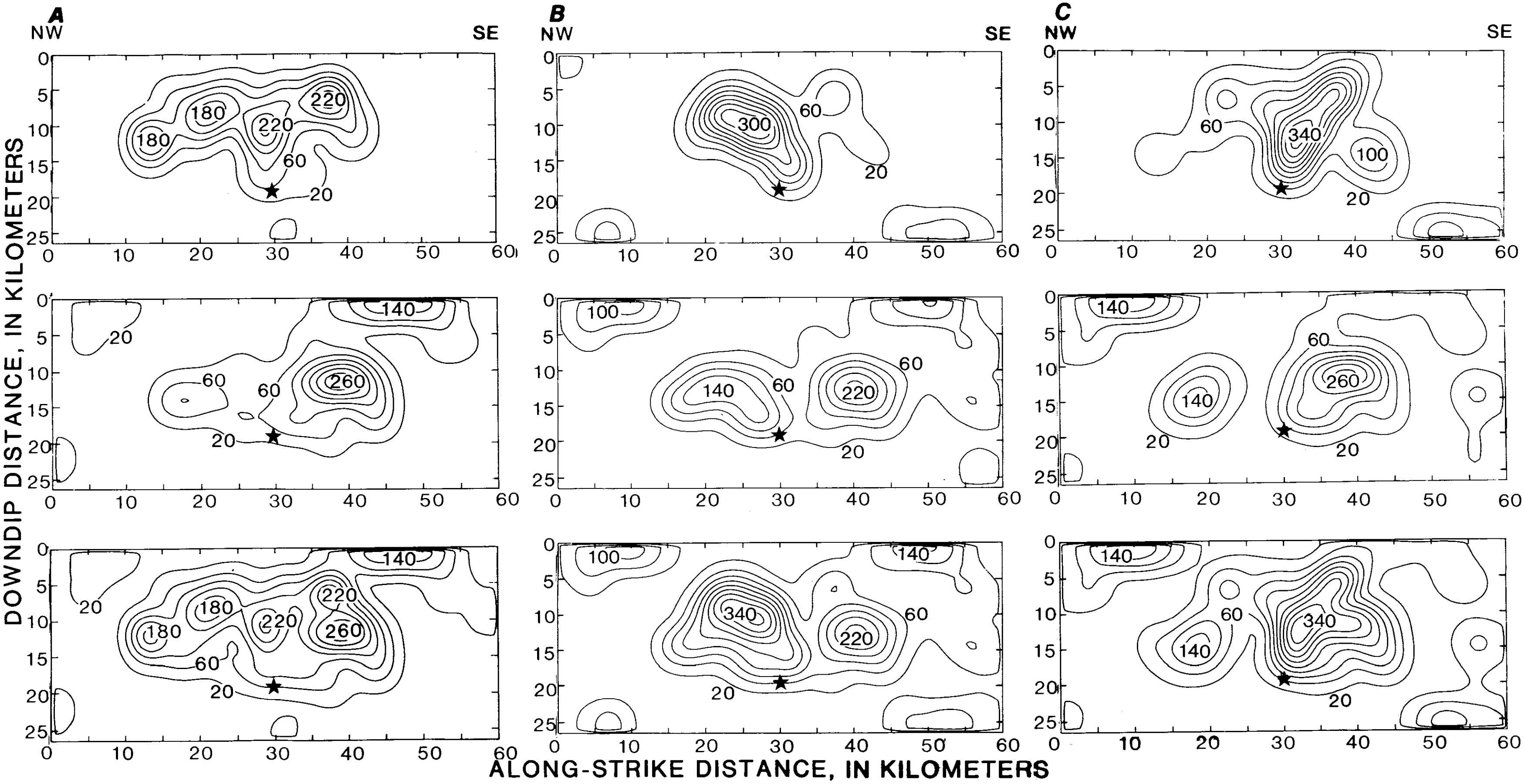

Figure 10.—Contours of slip (in centimeters) in L_2 solution, showing strike slip (180°, top plot), dip slip (90°, middle plot), and vector sum of strike slip and dip slip (bottom plot) for three alternative station distributions: a distribution that includes *P*-wave phases only (*A*), a distribution that includes nodal phases and omits some nonnodal *SH*-wave phases (*B*), and a more nearly uniform distribution (*C*). All inversions use a rupture velocity of 2.5 km/s and a 1-s-duration source-time function. Because rupture is bilateral, with only small time differences between phases arriving from sources on north and south halves of fault, solution is sensitive to phases and stations used in inversion.

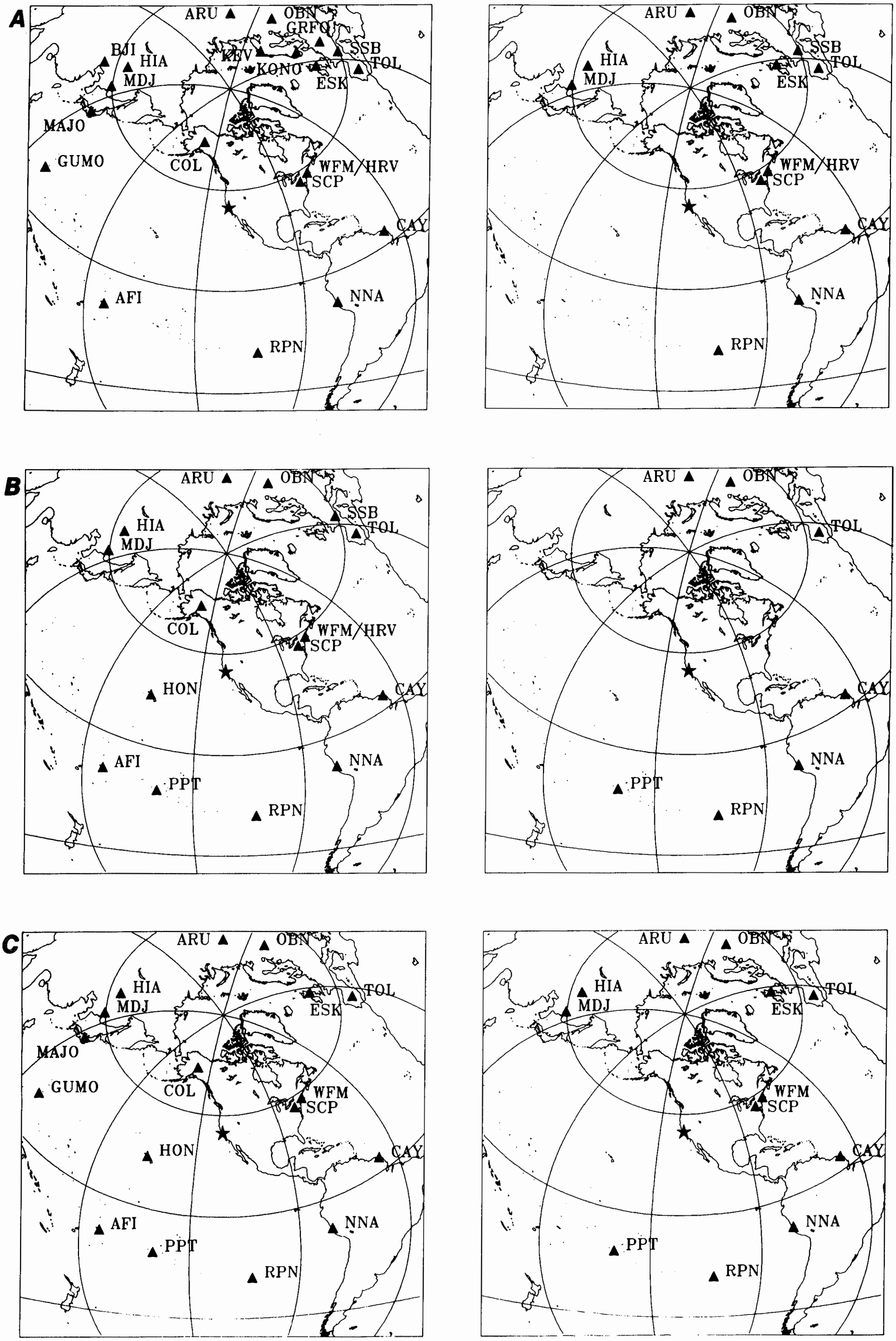
A
ARU
OBN
GRFO
BJI
HIA
MDJ
KEV
KONO
SSB
TOL
ESK
MAJO
GUMO
COL
WFM/HRV
SCP
CAY
AFI
NNA
RPN
ARU
OBN
HIA
MDJ
SSB
TOL
ESK
WFM/HRV
SCP
CAY
NNA
RPN
B
ARU
OBN
HIA
MDJ
SSB
TOL
COL
WFM/HRV
SCP
HON
CAY
AFI
PPT
NNA
RPN
ARU
OBN
TOL
CAY
NNA
PPT
RPN
C
ARU
OBN
HIA
MDJ
ESK
TOL
MAJO
GUMO
COL
WFM
SCP
HON
CAY
AFI
PPT
NNA
RPN
ARU
OBN
HIA
MDJ
ESK
TOL
WFM
SCP
CAY
NNA
PPT
RPN

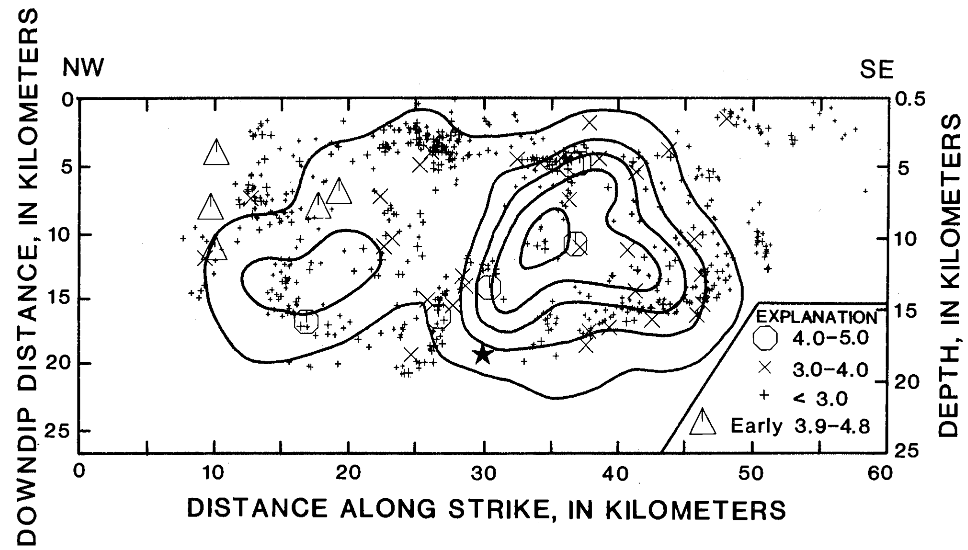

Figure 12.—Comparison of aftershock locations with distribution of slip in best-fitting L_2 solution (fig. 5). Aftershock hypocenters are projected perpendicularly onto dipping plane of model fault. Only aftershocks that occurred during 2-week period after earthquake within a perpendicular distance of 2 km from fault are plotted. Triangles, aftershocks located by Simila and others (1990).

◄ Figure 11.—Azimuthal equidistant plots of stations from which *P* (left plot) and *SH* (right plot) waveform data were used in preferred model (fig. 5) (*A*), and two alternative station distributions: a distribution that includes nodal phases and omits some nonnodal *SH*-wave phases(*B*), and a more nearly uniform distribution (*C*).

FREQUENCY-DOMAIN INVERSION FOR THE RUPTURE CHARACTERISTICS DURING THE EARTHQUAKE, USING STRONG-MOTION DATA AND GEODETIC OBSERVATIONS

By Stephen P. Horton,
Columbia University, Lamont-Doherty Earth Observatory;
John G. Anderson,
University of Nevada, Reno; and
Andres J. Mendez,
GEOENVIRON

CONTENTS

ABSTRACT

We have modeled strong-motion and geodetic data by using a frequency-domain inversion technique to infer the rupture characteristics of the 1989 Loma Prieta earthquake. The inversion determines the static offset from geodetic data and the slip velocity from strong-motion data for individual points on an assumed fault plane. Formulation of the inverse problem in the frequency domain allows inversion of both data sets and eliminates the requirement inherent in time-domain methods to specify the pulse shape, rise time, and rupture dynamics before the inversion. These properties are then derived from the inversion. The assumed fault plane is 16 by 40 km (top edge 4.25 km below the surface), strikes 129°, dips 69° SW., and contains the hypocenter. The total static offset is smoothly distributed, with a maximum slip of 1.4 m and a seismic moment of 2.5×10^{26} dyne-cm; the largest strike-slip displacements are to the southeast, and the largest reverse-slip displacements are to the northwest. The geodetic data are fitted substantially better by our model, which agrees with aftershock locations, than by the models in previous studies, which have the slip surface outside the aftershock zone. Preliminary modeling of the strong-motion data suggests that rupture propagation to the northwest may follow propagation to the southeast, that the rupture velocity of 3.5 km/s (96–100 percent of the local shear-wave velocity) is higher than inferred by other studies, and that the rise time (approx 1.75 s for an area where the highest slip velocities occur) may be longer than previously reported.

INTRODUCTION

The 1989 Loma Prieta earthquake provides an outstanding opportunity to apply the various methods of inferring slip on a finite fault from records of ground motion. More than 25 components of strong ground motion are available from within 40 km of the epicenter, as well as recordings from standard and broadband seismic instruments worldwide. In addition, a dense geodetic network provides data on the permanent ground offsets caused by the earthquake. In this study, both strong-ground-motion records and geodetic data are used to derive slip models for the earthquake.

We use a frequency-domain inversion technique (Olson and Anderson, 1988) with a wave-equation norm (Mendez and others, 1990) to calculate the slip models. Formulation of the inversion within the frequency domain allows both geodetic and seismic data to be modeled by the same procedure, providing an interesting comparison of the resolving power of the two data sets. In addition, the frequency-domain inversion technique eliminates the need to specify source shape, rise time, and rupture dynamics as in most time-domain inversion methods, allowing these parameters in the slip model to be estimated from the solution after the inversion.

We begin by briefly reviewing the results of previous finite-fault-modeling studies of the earthquake. Then, we present the method and data used in this study, along with the inversion results for both the geodetic and strong-motion data. Finally, we compare these results with those of previous studies.

PREVIOUS STUDIES

Three studies have used geodetic data to infer fault geometry and slip for the 1989 Loma Prieta earthquake. Lisowski and others (1990) forward-modeled strain and displacement measurements from before and after the earthquake. Their best-fitting model has 1.6 m of right-lateral strike slip and 1.2 m of reverse slip uniformly distributed on a planar fault surface 37 km long, striking 136°, dipping 70°, and extending from 5- to 17.5-km depth. The fault strike approximately parallels the surface trace of the San Andreas fault and overlaps the area of aftershocks with generally the same length, dip, and depth range. Lisowski and others determined a seismic moment of 3×10^{26} dyne-cm for the main shock.

Snay and others (1991) applied the same technique to an expanded data set and investigated nonplanar geometries. Their preferred fault is "kinked," with two segments: one dipping 90° and extending from 4.8- to 9.0-km depth, and the second dipping 70°, sharing a common edge with the upper surface, and extending from 9.0- to 15.1-km depth. The average slip amplitude predicted for each surface is similar for the strike-slip component, approximately 1.9 m. The dip-slip components, however, differ by a factor of 2: 1.0 m for the upper surface and 2.3 m for the lower. Although the slip amplitudes determined in the "kinked" model are larger than those determined by Lisowski and others (1990), the estimated seismic moment (2.8×10^{26} dyne-cm) is similar because the fault area in Snay and others' study is smaller. This result highlights the tradeoff between fault area and average slip amplitude for models with a constant moment.

Marshall and others (1991) modeled vertical-displacement measurements made in the vicinity of Loma Prieta before and after the earthquake. They searched for the best planar and listric faults, finding that both types of faults produced results consistent with the observed data. Their best-fitting planar model with uniform slip is 34 km long, striking 128°, dipping 60°, and extending from 4- to 15-km depth; the slip is 2.4 m right lateral and 1.7 m reverse. Interestingly, their best-fitting model faults are above and to the southwest of the aftershock zone. They obtained a better fit by dividing the fault into a northwestern segment with larger thrust component and a southeastern segment with larger strike-slip component. This model gives a seismic moment of 2.2×10^{26} dyne-cm for the main shock and an average slip amplitude of 2.1 m.

Four other studies used seismic data to infer the spatial and temporal slip history during the earthquake. These studies all assumed a simple planar fault geometry related to the location of the hypocenter and the distribution of aftershocks. Like the geodetic studies, these studies also systematically investigated the model-parameter space to obtain the best solution; however, the model parameters of concern were rupture velocity and rise time. The studies differed mainly in the data set analyzed and the details of the inferred slip distribution.

The slip model of Steidl and others (1991) was derived from strong-motion data covering a broad range of azimuths and distances. Their best-fitting solution is for a rupture velocity of 3.0 km/s and a rise time of 1.0 s. They found that slip at the southeast end of the fault has a larger strike-slip component and at the northwest end a larger reverse-slip component. They also found larger displacements in these areas than updip from the hypocenter. The seismic moment after scaling by a factor of 1.5 is estimated at 3.5×10^{26} dyne-cm. They found a complex rupture front that propagated faster to the south than to the north but that the areas of high slip at both ends radiated simultaneously.

Beroza (1991) obtained a similar model from a smaller set of strong-motion stations at closer distances. He found that slip varies in amplitude and rake, and that little slip occurs updip from the hypocenter. There are two main areas of concentrated slip: one to the northwest with a larger reverse-slip component, and one to the southeast with a larger strike-slip component. Slip amplitudes in these patches exceed 4.5 m, and the total seismic moment after scaling by a factor of 1.8 is estimated at 2.3×10^{26} dyne-cm. The assumed source pulse used in this study has an extremely short rise time, 0.3 s, and rupture was found to propagate bilaterally from the hypocenter at a velocity of 2.7 to 3.1 km/s, depending on depth.

Wald and others (1991) inverted both teleseismic and strong-motion data. They obtained self-consistent results for separate inversions of the teleseismic or strong-motion data and the combined data set. Their results are generally consistent with the previous seismic studies. They preferred bilateral rupture at a velocity of 2.7 km/s and rise time of 0.7 s. They observed a varying slip amplitude, with slip concentrated in two patches, one to the northwest and another to the southeast, and with little slip updip from the hypocenter. They found similar rakes (145°), however, at both ends of the fault and a larger moment release from the northeastern segment. They showed evidence of a foreshock occurring approximately 2 s before the main energy release; this foreshock had the hypocentral location determined from regional data.

Hartzell and others (1991) reported similar results from inverting teleseismic data. They found the larger moment release from the southeast end to be dominantly strike slip, whereas equal components of strike slip and reverse slip occurred at the north end. Of interest in their study is a comparison of the two norms, L_1 and L_2: they found that the details of the slip distribution are affected by the choice of norm (see Hartzell and others, this chapter).

METHOD

This study utilizes a frequency-domain inversion for slip velocity on a finite fault (Olson and Anderson, 1988) with the wave-equation norm of Mendez and others (1990). The method leads to a wavelike solution that is spatially and temporally smooth. In addition, the method is amenable to different data sets, allowing the use of both geodetic and strong-motion data. We briefly summarize the salient features of the method below (for details, see Olson and Anderson, 1988; Mendez and others, 1990; and Mendez and Anderson, 1991).

At some observation point x, the nth component of velocity can be expressed through the representation theorem as

$$d_n(\mathrm{x},t)=\int_{-\infty}^{\infty} d\tau \int_{\Sigma} \left[\nu_i(\xi,t-\tau)\right]^{\pm} \mathrm{v}_j \sigma_{ij}^{n}(\xi,\mathrm{x};\tau)\, d\xi^2$$

where $d_n(x,t)$ is the nth component of the observed velocity-time series at point x, Σ is the fault surface with normal v, $[v(\xi,t)]$ is a velocity discontinuity across the fault surface at point ξ, and $\sigma_{ij}{}^{n}(\xi,x;\tau)$ is the stress tensor at point ξ due to a point force applied in the nth direction at point x. We define the Fourier transform pair

$$d(f)=\int_{-\infty}^{\infty} d(t)\, e^{i2\pi ft}\, dt \quad \text{and} \quad d(t)=\int_{-\infty}^{\infty} d(f)\, e^{-i2\pi ft}\, df,$$

rewrite the representation theorem in the frequency domain, and discretize the fault surface to give

$$d_n(x,f)= \Delta\Sigma \sum_{k=l}^{K} \left\{ \left[v_s(k,f)\right]^{\pm} T_s^n(k,x;f) + \left[v_d(k,f)\right]^{\pm} T_d^n(k,x;f) \right\} \quad (1)$$

where $d_n(x,f)$ is the Fourier spectral value at frequency f of the observed ground velocity, $[v_s(k,f)]^{\pm}$ is the component of the discontinuity in the direction of strike occurring at the kth segment ($[v_d(k,f)]^{\pm}$ is the dip-slip component), $T_s{}^n(k,x;f)$ is the component of traction resolved in the direction of strike at segment k on the fault surface due to a point force applied in the nth direction at point x ($T_d{}^n(k,x;f)$ is the dip-slip component), K is the total number of fault segments, and $\Delta\Sigma$ is the area of an individual fault segment. Finally, this equation can be written in matrix form as

$$\mathbf{d} = \mathbf{Tv}. \quad (2)$$

Equation 2 is solved independently for each frequency over a finite bandwidth, using the Chebyshev method (Olson, 1987). We used an eigenvalue bandwidth (b/a) of 10.0 in determining the final solution. The time history for each segment on the fault can be obtained by taking the inverse Fourier transform of the spectral values in **v** over this frequency bandwidth.

Equation 2 is generally underdetermined, and its solution is nonunique. A particular solution obtained by singular-value decomposition would have a minimum length as measured with the L_2 norm. The properties of this solution were investigated by Olson and Anderson (1988) and found to be strongly influenced by the station distribution. Recently, Hartzell and others (1991) investigated the difference between time-domain inversions performed by using both the L_1 and L_2 norms and found differences in the characteristics of the inferred slip distributions (see Hartzell and others, this chapter).

This study uses the wave-equation norm of Mendez and others (1990), which minimizes the importance of station distribution. This norm is based on the wave-equation operator

$$\frac{\partial^2}{\partial x^2}+\frac{\partial^2}{\partial y^2}+\frac{f^2}{c^2}$$

A wavelike solution can be found by minimizing the L_2 norm of

$$\mathbf{TD}^{-1}\mathbf{u} = \mathbf{d}$$
$$\mathbf{u} = \mathbf{Dv},$$

where **D** represents the matrix resulting from discretization of the wave-equation operator for a prescribed rupture velocity c over the fault plane. The method produces a wavelike solution with the minimum slip amplitude consistent with the data. We do not perform any rescaling as do Mendez and others (1990) to obtain the most nearly constant slip amplitude.

The model-parameter space is investigated by systematically varying the model parameters to obtain a solution with the minimum data-prediction error. A solution for the static offset is found by varying the strike and dip of the fault surface, and for the velocity discontinuity by varying the rupture velocity c used in constructing the wave-equation norm over the range 2.5–1,000.0 km/s. Varying the model parameters in this way serves to highlight certain features of the solution that are robust, returning with each new parametrization. We believe these robust features of the solutions are significant, and so we stress these characteristics in the discussion below.

DATA

The locations of the geodetic and strong-motion stations used in the inversion are shown in figure 1. The geodetic data are from the Global Positioning Satellite (GPS) measurements (large solid squares) of Lisowski and others (1990) and the leveling measurements (small open squares) of Marshall and others (1991). The strong-motion data were provided by the California Division of Mines and Geology (CDMG); details on the strong-motion stations are listed in table 1.

Geodetic observations form the data set to be inverted for the static offset during faulting. This static offset corresponds to the value of the velocity spectrum at 0.0 Hz and the area under the velocity-time function as shown by evaluating the Fourier transform at 0.0 Hz:

$$v(f=0)=\int_{-\infty}^{\infty} v(t)\,dt = u_{\text{static}}\,.$$

Marshall and others (1991) reported coseismic elevation changes that are used directly in equation 1. The measurements of successive bench marks, however are highly correlated, and so treating the leveling data as independent coseismic station-elevation changes may exaggerate the importance of any measurement error made along the leveling line. We treat the data in this way to compare our results with those of Marshall and others.

GPS measurements provide data on the horizontal and vertical changes in length (as vectors) between station LOMA and the other four GPS stations (fig. 1). These length changes between observations points can be accommodated by modifying equation 1 so that

$$d_n(\boldsymbol{x},f)-d_n(\boldsymbol{y},f)=\Delta\Sigma\sum_{k=1}^{K}\left[v_s(k,f)\right]^{\pm}\left[T_s^n(k,\boldsymbol{x},f)-T_s^n(k,\boldsymbol{y};f)\right]+$$
$$\left[v_a(k,f)\right]^{\pm}\left[T_d^n(k,\boldsymbol{x};f)-T_d^n(k,\boldsymbol{y};f)\right]$$

where $d_n(\boldsymbol{x},f)-d_n(\boldsymbol{y},f)$ is the change in length (the vector component in the *nth* direction) between observation points $\boldsymbol{x}$ and $\boldsymbol{y}$, and $T_s^n(k,\boldsymbol{x};f)-T_s^n(k,\boldsymbol{y};f)$ is the difference in the strike-slip component of traction on the fault plane resulting from point sources applied at $\boldsymbol{x}$ and $\boldsymbol{y}$ $T_d^n(k,\boldsymbol{x};f)-T_d^n(k,\boldsymbol{y};f)$ is the corresponding dip-slip component). Because the velocity discontinuity is linearly related to both the vertical displacement and the length change, both leveling and GPS data may be used simultaneously to solve for the static offset on the fault.

Strong-motion records from SMA–1 accelerometers at seven CDMG stations (fig. 1) were inverted to characterize the dynamic aspects of the rupture process. The data were processed by the CDMG, including digitization, integration (to obtain velocity), and bandpass filtering between 0.1 to 25.0 Hz. We Fourier-transformed the data at intervals of 0.02 Hz for frequencies of 0.1 to 1.0 Hz. The lower limit is directly determined by the high-pass corner frequency of the filter used in processing the data. Reliable information at lower frequencies is not contained in the data.

The upper limit of 1.0 Hz is related to our ability to adequately model the Green's functions. The Green's functions used in this study are produced by the wave-number-integration computer program PROSE (Apsel and Luco, 1983; Luco and Apsel, 1983). This program uses a one-dimensional velocity model but includes near- and far-field terms. The velocity model used in this study is based on the 10-layer model of Deitz and Ellsworth (1990) and is the same as that used by Steidl and others (1991). We believe that a layered velocity model is adequate only at lower frequencies, and so we set the upper frequency limit of the inversion at 1.0 Hz. The need to adequately model the Green's functions led to discarding from the inversion the data from stations where site response appeared to contribute significantly.

RESULTS

Our analysis of geodetic and strong-motion data to determine the rupture characteristics on a finite fault is accomplished in two major steps. The first step involves actual inversion of the data. This inversion results in spectral values (amplitude and phase) for each segment on the fault.

The initial problem to be solved in the first step in the analysis is to define the optimum fault geometry. We prefer that the fault plane contain the hypocenter estimated from regional data (Dietz and Ellsworth, 1990). In addition, the fault plane is chosen to overlap the zone of aftershocks that occurred within 24 hours after the main shock (fig. 2*A*). The aftershocks appear to dip southwest, and the dipping trend is largely confined to depths of 4 to 18 km, although some scattered activity occurs at shallower depth (fig. 2*B*). The fault plane dips 69°. The fault dimensions, 16 by 40 km, were largely determined from figure 2. The fault is divided into 1- by 1-km segments, and the hypocenter (star, fig. 2) is near the center bottom edge of the fault.

The inversion is performed independently for each frequency, and we begin by performing a single inversion at 0.0 Hz. The result can be interpreted directly as the static offset (total slip at points on the fault) and easily evaluated physically. Thus, various fault geometries can easily be tested to obtain a suitable geometry for the inversion at all frequencies. The minimum rms residual (observed minus predicted ground motion) for the inversion was obtained by setting the fault strike at 129° and the dip angle at 69°. The minimum rms residual is found by varying the strike or dip independently in separate inversions of the geodetic data. Fixing the dip at 70∞ and varying the strike from 110° to 150° leads to a minimum rms residual at a strike of 129°, as shown in figure 3*A*; fixing the strike at 129° and varying the dip from 50° to 90° leads to a minimum rms residual at a dip of 69°, as shown in figure 3*B*. This optimum fault geometry is used to invert the geodetic and seismic data.

The static offset during the earthquake, as determined by the inversion of the geodetic data, is plotted in figure 4. The strike-slip component (fig. 4*A*) indicates that motion at the southeast end of the fault was dominantly strike slip. The largest strike-slip displacements, approximately 1.2 m, are centered 7 km southeast of the hypocenter, at 11-km depth; the dip-slip displacement in the same area is only 40 cm. The dip-slip component (fig. 4*B*) indicates that motion at the northwest end of the fault was dominantly dip (reverse) slip. The largest dip-slip motions, approximately 1.2 m, are centered 9 km northwest of the hypocenter at 11-km depth. The total slip (fig. 4*C*) is more nearly uniformly distributed. The area of maximum total slip, about 1.4 m, is centered slightly to the northwest of the hypocenter at about 11-km depth. The seismic moment, based on the total slip amplitude, is 2.5×10^{26} dyne-cm.

The original leveling data are compared with the predicted values from the inversion of the geodetic data in figure 5. The largest values are positive and occur immediately over the northwestern section of the fault. The predicted values generally agree well in both magnitude and sign with the observed data, as shown in figure 5*B*. In areas where the predicted values differ in sign from the observed data—for example, in the east and west—both the actual and predicted ground displacements are small.

Marshall and others (1991) used a misfit-to-noise (*M*/*N*) ratio as a measure of the goodness of fit between predictions and observations. This ratio is given by

$$\frac{M}{N}=\left[\frac{1}{N-N_{\mathrm{f}}}\sum_{i}^{N}\left(\frac{\Delta H_{\mathrm{o}}-\Delta H_{\mathrm{c}}}{\sigma_{\mathrm{o}}}\right)_{i}^{2}\right]^{\frac{1}{2}}$$

where ΔH_0 is the observed elevation change, ΔH_c is the calculated elevation change, N is the number of bench marks, N_f is the number of fixed model parameters (N_f=7),

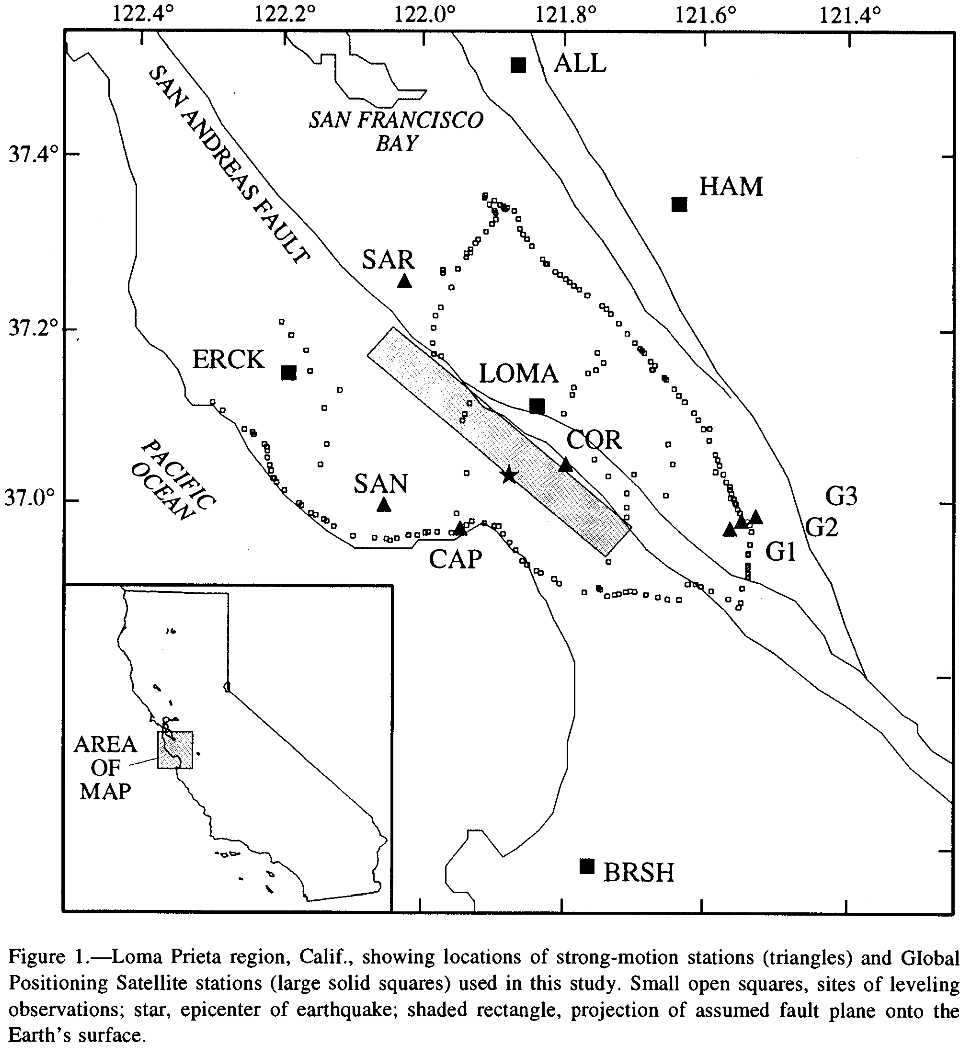

Figure 1.—Loma Prieta region, Calif., showing locations of strong-motion stations (triangles) and Global Positioning Satellite stations (large solid squares) used in this study. Small open squares, sites of leveling observations; star, epicenter of earthquake; shaded rectangle, projection of assumed fault plane onto the Earth's surface.

Table 1.—*California Division of Mines and Geology strong-motion stations used in this study*

Station (fig. 1)	Location	CDMG code	Latitude (°N.)	Longitude (°W.)
CAP	Capitola	125	36.974	121.952
COR	Corralitos	007	37.046	121.803
G1	Gilroy	379	36.973	121.572
G2	Gilroy	380	36.982	121.556
G3	Gilroy	381	36.987	121.536
SAN	Santa Cruz	135	37.001	122.060
SAR	Saratoga	065	37.255	122.031

and σ_0 is the observed error (see Marshall and others, 1991). A prediction fits the observations to within the noise level of the data when $M/N \leq 1.0$ (Marshall and others, 1991). The M/N ratio for the static offset shown in figure 4 is 0.80.

The inversion was also performed for each frequency between 0.1 and 1.0 Hz, using data from the strong-motion stations. For example, contours of the Fourier spectral amplitude determined from the inversion at 0.14 Hz are plotted on the fault plane in figure 6. Because this frequency represents one of the lowest frequencies obtained by inverting the strong-motion data, we expect some correlation between the areas of high slip predicted for the static offset and the areas of high energy release predicted for this frequency. Although both the strike-slip component (fig. 6*A*) and the dip-slip component (fig. 6*B*) are more complex than for the static offset, similarities do exist. In the southeastern area, displacement is dominantly strike slip, and in the northwestern area, dominantly dip slip. The increased complexity may indicate greater spatial resolution at this higher frequency but could also result from some dynamic property of the rupture.

Contouring the Fourier spectral amplitudes on the fault plane (fig. 6) indicates areas of slip or energy release at a particular frequency but gives no information about timing, and so the second step in the analysis is to characterize the dynamic aspects of the rupture process. This step involves taking the inverse Fourier transforms of the spectral values determined in the inversion, resulting in a velocity history for each segment of the fault. The band limitation of the strong-motion data for the earthquake, however, introduces some ambiguity into the interpretation of these time series, as shown in figure 7. A ramp function with an offset of 90 cm that occurs over a period of 1.75 s is plotted in figure 7*A*. The velocity-time series obtained by differentiating this ramp function is plotted in figure 7*B*, and the velocity-time series after bandpass filtering with a Butterworth filter with corner frequencies at 0.1 and 1.0 Hz is plotted in figure 7*C*. The filtering of low frequencies from the velocity-time series results in a band-limited signal characterized by positive and negative swings of approximately equal amplitude. Because the velocity-time series associated with the inversion are also band limited, figure 7*C* indicates that these signals are expected to be double sided. Finally, figure 7*D* shows that integration of the filtered velocity-time series produces no permanent offset.

Figure 8 shows that the inversion velocity-time series and the bandpass-filtered velocity-time series (fig. 7*C*) approximately correspond. From comparison with figure 7, the initial motion of the bandpass-filtered velocity function evidently corresponds to the direction of slip on the fault, and the width of this initial pulse is approximately the same as the duration of slip on the fault. In our model, the initial strong pulses are in the negative direction for both the strike-slip and dip-slip components. Within the coordinate system that we use, this direction corresponds to right-lateral and reverse slip on the fault, as expected.

Time slices of the spatial distribution of the strike-slip and dip-slip distribution of velocity on the fault plane at 1-s intervals are shown in figure 9. T=0 corresponds to the origin time for the hypocentral location reported by Dietz and Ellsworth (1989). Only the negative contours are plotted in figure 9 because we believe that the initial negative pulses are more directly related to the actual velocity pulses on the fault plane and because plotting both the positive and negative contours would be too confusing. The first large energy release (above the noise level of 10 cm/s) occurs after 2 s on the strike-slip component in the area of the hypocenter (star, fig. 9). The rupture propagates largely as strike-slip motion to the southeast until 5 s; the largest energy release occurs at 3 s approximately 7 km southeast of the hypocenter at about 17-km depth. At 5 s, rupture begins in the area just north of the hypocenter on both the strike-slip and dip-slip components and propagates to the northwest until 9 s. The largest energy release during this period occurs on the dip-slip component 20 km northwest of the hypocenter. Contours of slip at the southeast end of the fault between 7 and 9 s are mostly the second negative swing of the bandpass-filtered velocity pulse (see fig. 8). As such, these contours are not interpreted as velocity pulses but are considered noise.

The observed and predicted seismograms at each strong-motion station used in the inversion are compared in figure 10. These predictions match the data extremely well.

DISCUSSION

The model for the static offset (fig. 4) during the 1989 Loma Prieta earthquake derived in this study agrees reasonably well with those of previous studies using geodetic data, given that our model has many more fitting parameters. Our model suggests a smooth distribution of total slip and predicts a seismic moment of 2.5×10^{26} dyne-cm; the seismic moment determined in other studies of the geodetic data ranges from 2.2×10^{26} to 3.0×10^{26} dyne-cm. Our solution is most similar to that of Marshall and others (1991) for a planar fault divided into two segments. By assigning a larger reverse-slip component to the northwestern segment and a larger strike-slip component to the southeastern segment, their data-prediction error was reduced. Our fault is divided into 640 subfaults, providing the opportunity for much spatial variation in slip on the fault plane. A robust feature of our solution is the dominance of dip slip to the northwest (approx 3:1) and of strike slip to the southeast (approx 3:1), although the total slip is more evenly distributed along the fault.

Two substantial differences between our model of the static offset and that of Marshall and others (1991) are that their best-fitting model lies outside the aftershock

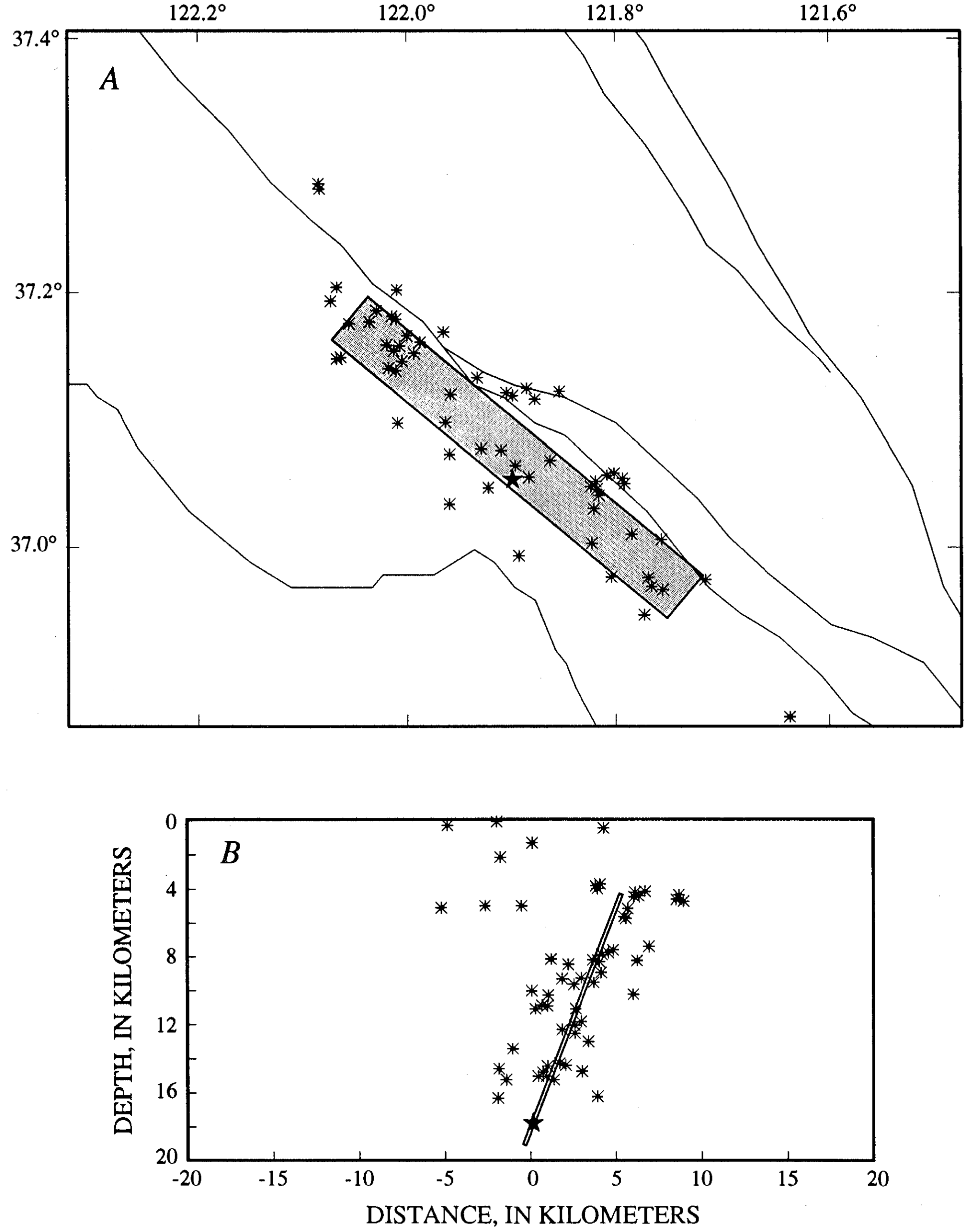

Figure 2.—Postearthquake aftershock activity. *A*, Loma Prieta region, Calif., showing locations of Loma Prieta main shock (star) and epicenters of aftershocks during 24-hour period after earthquake (asterisks). Shaded rectangle, projection of assumed fault plane onto the Earth's surface. Fault is 40 km long and strikes 129°. Note that main shock is located near center of aftershock zone. *B*, Cross section oriented perpendicular to fault. Shaded rectangle, cross section of assumed fault plane. Fault dips 69° SW. and ranges in depth from approximately 4 to 19 km; fault plane contains hypocenter of earthquake (star) and falls within aftershock zone.

zone and their average slip amplitude of 2.1 m is significantly larger than the peak slip amplitude of 1.4 m that we obtain. Because they obtained an M/N ratio of 1.33 for their best (two rake) model, whereas our model has an M/N ratio of 0.8, our model fits the data significantly better. Possible explanations for the better fit include differences in faulting area or elastic constant between the two studies, differences related to modeling ground displacements with a uniform versus a layered half-space, and the ability in our model to concentrate slip where needed to most effectively account for the observations.

The results of our dynamic solution (fig. 9) are consistent with a small foreshock occurring 2 s before the onset of significant energy release and little or no propagation of the rupture front away from the hypocenter during that time, as suggested by Wald and others (1991). These results also indicate a change in rake from nearly strike slip southeast of the hypocenter during the initial stage of faulting, through oblique slip near the hypocenter at the beginning of the second stage of faulting, to nearly reverse slip near the northwest edge of the fault at the end of the second stage. Both Beroza (1991) and Steidl and others (1991) observed a similar rotation in the rake vector from southeast to northwest. This rotation of the rake vector is also consistent with our model of the static offset, as well as that of Marshall and others (1991).

Several features of our model of the dynamic rupture (fig. 9) derived from strong-motion data are robust. The duration of faulting is consistently shorter than 10 s, the rupture velocity is consistently about 3.5 km/s, and radiation of energy typically occurs from the southeast end of the fault before the northwest. The propagation rate of rupture on the fault plane is fairly consistent for different assumed values of c used in constructing the wave-equation norm, leading us to regard this value as a fitting parameter rather than a physical quantity. This result is not completely unexpected because Mendez and others (1990) found that the right rupture velocity (for a synthetic test case) was returned by the inversion, although the wrong c value was used in constructing the norm. Thus, we considered c values as large as 1,000 km/s, which produced a smoothed solution with the general features previously mentioned. The solution in figures 9 through 11 is for c=6 km/s.

Although a duration of faulting shorter than 10 s was found in each finite-fault study using seismic data, rupture velocities in those studies range only from 2.5 to 3.1 km/s. In addition, those studies consistently found that energy radiates from both ends of the fault simultaneously, although Steidl and others (1991) determined that rupture propagated to the southeast faster than to the northwest. Because these results are somewhat inconsistent with ours, we investigated whether they may result from an inaccuracy in the assumed trigger time of station SAR (the trigger time was not recorded).

Station SAR (fig. 1), which lies at the northwest end of the fault and recorded large-amplitude arrivals, is the key to our solution. If this station is omitted from the inversion, the rupture does not propagate to the northwest at all. We estimated a trigger time for this station by assum-

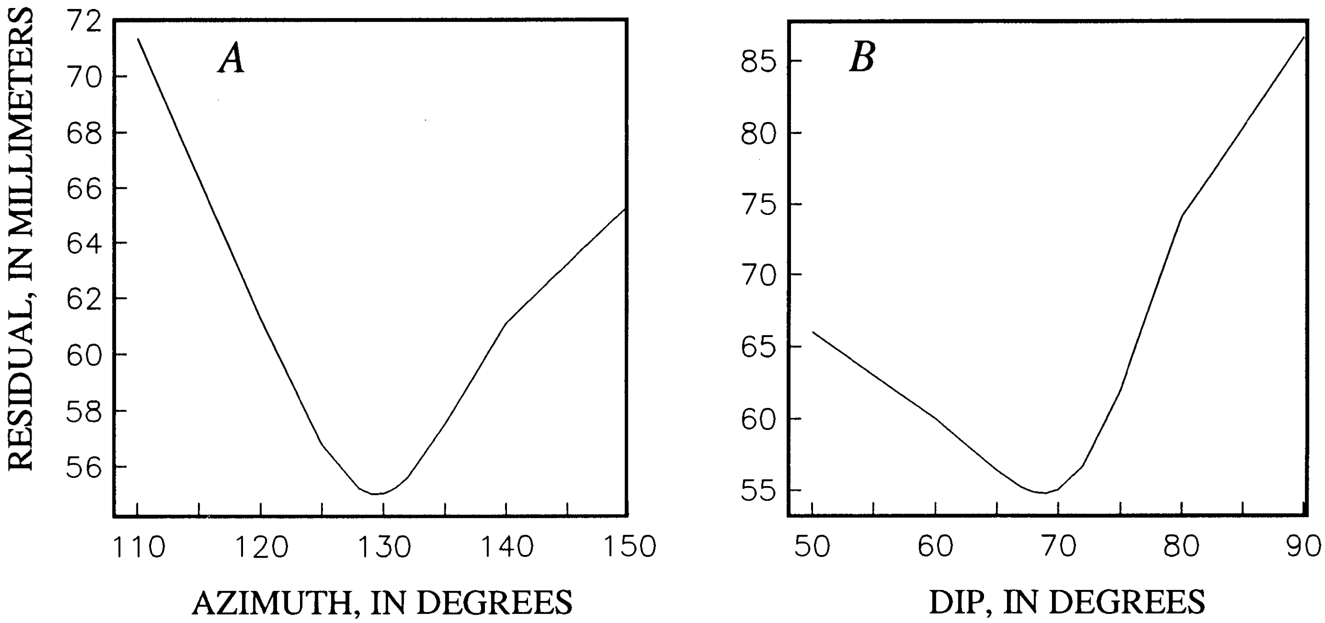

Figure 3.—Rms residual of static offset (observed minus predicted value) determined from inversion as a function of azimuth (*A*) and dip (*B*) of fault. Minimum rms residual occurs at an azimuth of 129° for a constant dip of 70° (fig. 3*A*), and at dip of 69° for a constant azimuth of 129° (fig. 3*B*).

ing that the large pulse of about 2.5 s on the record represents *S*-wave energy arriving from an area southeast of the epicenter. This trigger time is 2.8 s later than would be expected if the *P* wave from the initial energy release at the hypocenter suggested by Deitz and Ellsworth (1990) had triggered the instrument. Wald and others (1991) suggested that the trigger time at this station was delayed by 1.8 s from the *P*-wave-arrival time for energy leaving the hypocenter and shortly before the predicted *S*-wave-arrival time. By varying the assumed trigger time, we determined that a trigger time 1 s earlier (same as that of Wald and others, 1990) scarcely affects the solution, and that a trigger time about 2.8 s earlier is required to make the solution propagate bilaterally. Thus, although we find that

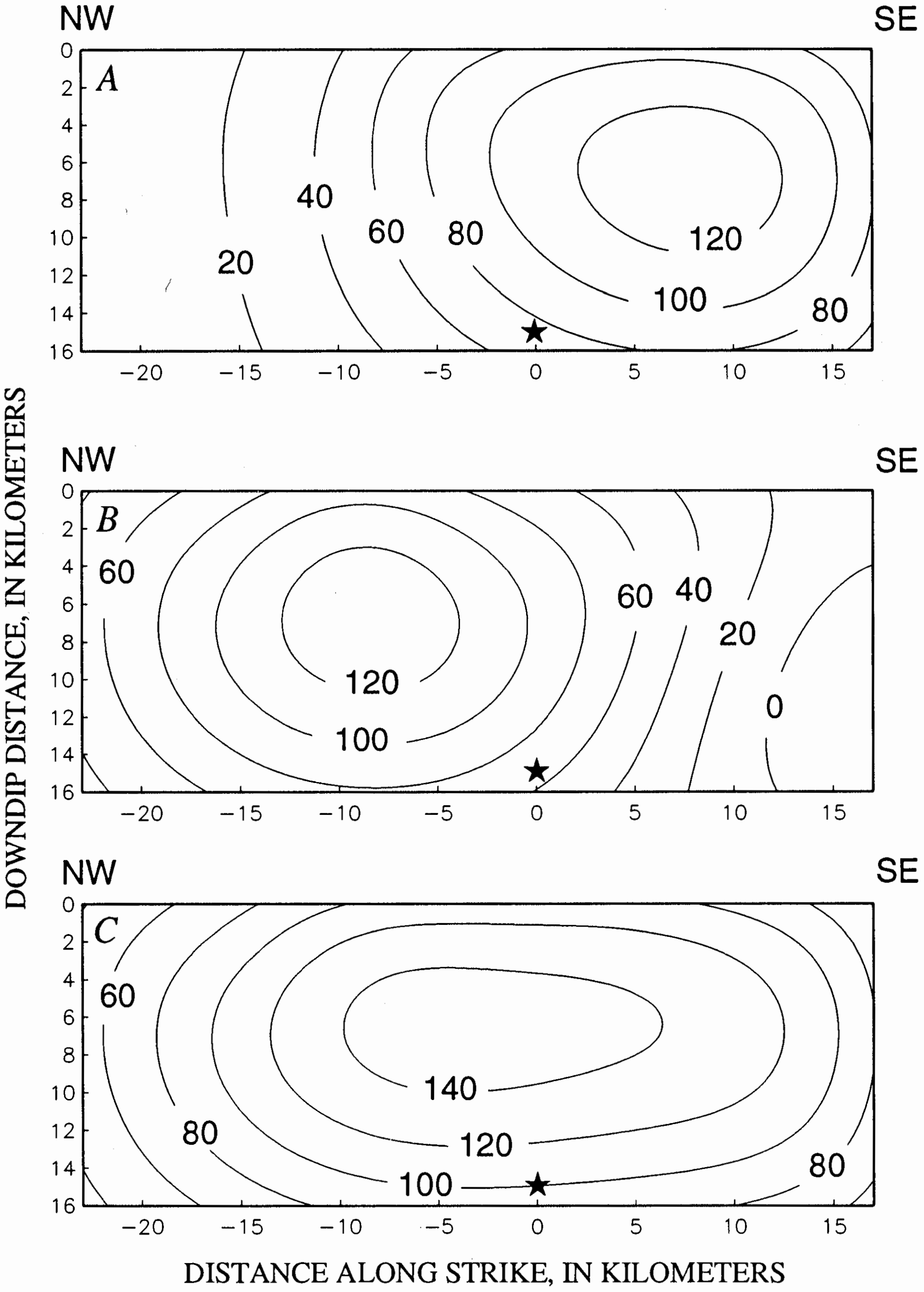

Figure 4.—Contours of static offset (in centimeters) on assumed fault plane, as determined from inversion of geodetic data, showing (*A*) strike-slip (right lateral) component, (*B*) dip-slip (reverse) component, and (*C*) total slip. View downward, normal to fault plane. Top edge of fault is that approximately 4-km depth. Star, hypocenter of earthquake. Contour interval, 20 cm.

rupture propagation to the northwest followed propagation to the southeast, this result depends on the assumed trigger time at station SAR.

The rise time suggested by figures 7 and 8 (approx 1.75 s) is longer than those in other studies, which range from 0.3 to 1.0 s. This rise time is applicable only to the area of

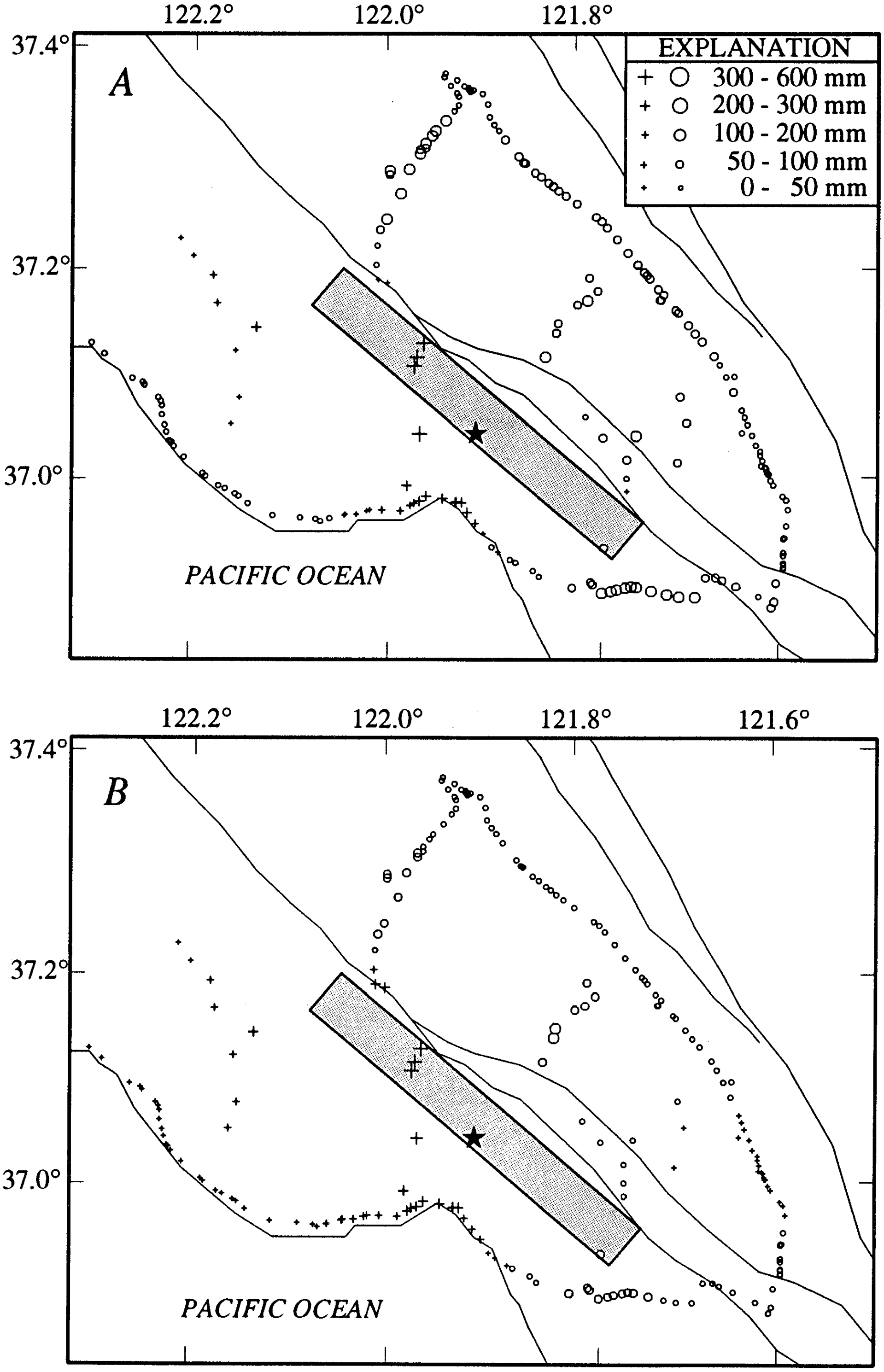

Figure 5.—Loma Prieta region, Calif., showing locations of (*A*) leveling observations of Marshall and others (1991) and (*B*) predicted values from inversion for static offset (see fig. 4). Circles, negative values (relative motion downward); plus signs, positive values (relative motion upward). Largest values are positive and located immediately over northwest side of fault. Star, epicenter of earthquake.

high slip velocity where this segment was located. Shorter rise times are expected for segments of the fault that slipped less. In addition, the rise time measure may be partly related to the shape of the bandpass filter. These qualities of the solution have not been fully explored. Also, because our band-limited velocity functions produce no static offset when integrated, we have no measure of the actual displacement from the strong-motion data.

ACKNOWLEDGMENTS

This research was supported by U.S. National Science Foundation grant EAR–90–11041. Computational time on the Cray Y–MP computer was provided by grants from the San Diego Supercomputer Center and the U.S. National Science Foundation. We thank M. Lisowski and G. Marshall for providing preprints of their papers, and P. Spudich and J. Savage for their thoughtful reviews of the manuscript.

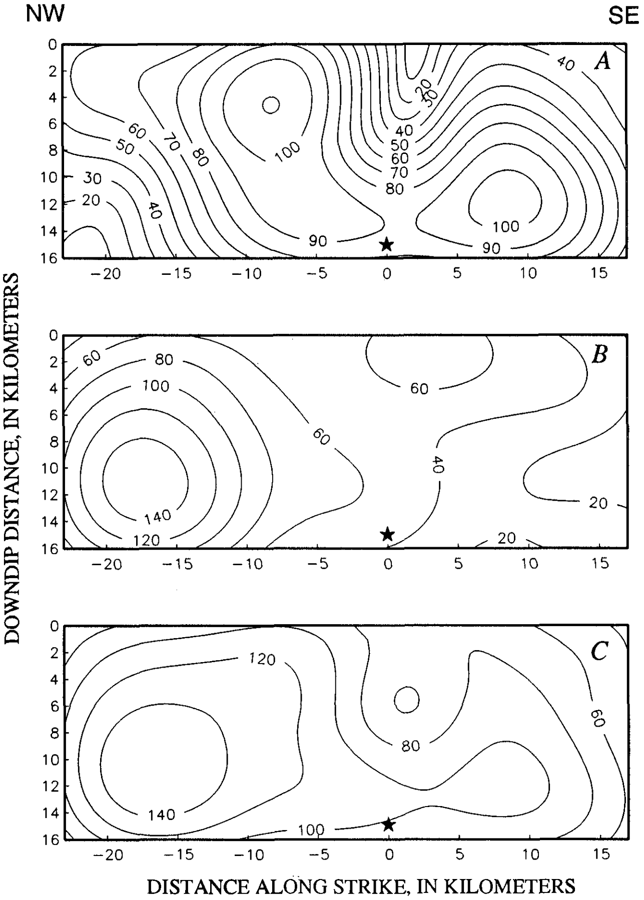

Figure 6.—Contours of Fourier spectral amplitude (in centimeters per second) on assumed fault plane, as determined by inversion at 0.14 Hz, showing (*A*) strike-slip (right lateral) component, (*B*) dip-slip (reverse) component, and (*C*) total velocity. View downward, normal to fault plane. Star, hypocenter of earthquake. Contour intervals: 10 cm/s (fig. 6*A*), 20 cm/s (figs. 6*B*, 6*C*).

REFERENCES CITED

Apsel, R.J., and Luco, J.E., 1983, On the Green's functions for a layered half-space, part II: Seismological Society of America Bulletin, v. 73, no. 4, p. 931–951.

Beroza, G.C., 1991, Near-source modeling of the Loma Prieta earthquake: evidence for heterogeneous slip and implications for the earthquake hazard: Seismological Society of America Bulletin, v. 81, no. 5, p. 1603–1621.

Dietz, L.D., and Ellsworth, W.L., 1990, The October 17, 1989, Loma Prieta, California, earthquake and its aftershocks; geometry of the sequence from high-resolution locations: Geophysical Research Letters, v. 17, no. 9, p. 1417–1420.

Hartzell, S.H., Stewart, G.S., and Mendoza, Carlos, 1991, Comparison of L_1 and L_2 norms in a teleseismic waveform inversion for the slip history of the Loma Prieta, California, earthquake: Seismological Society of America Bulletin, v. 81, no. 5, p. 1518–1539.

Lisowski, Michael, Prescott, W.H., Savage, J.C., and Johnson, M.J.S., 1990, Geodetic estimate of coseismic slip during the 1989 Loma Prieta, California, earthquake: Geophysical Research Letters, v. 17, no. 9, p. 1437–1440.

Luco, J.E. and Apsel, R.J., 1983, On the Green's functions for a layered half-space, part I: Seismological Society of America Bulletin, v. 73, no. 4, p. 909–929.

Marshall, G.A., Stein, R.S., and Thatcher, Wayne, 1991, Faulting geometry and slip from co-seismic elevation changes; the 18 October 1989, Loma Prieta, California, earthquake: Seismological Society of America Bulletin, v. 81, no. 5, p. 1660–1693.

Mendez, A.J., and Anderson, J.G., 1991, The temporal and spatial evolution of the 19 September 1985 Michoacan earthquake as inferred from near-source ground-motion records: Seismological Society of America Bulletin, v. 81, no. 3, p. 844–861.

Mendez, A.J., Olson, A.H., and Anderson, J.G., 1990, A norm minimization criterion for the inversion of earthquake ground motion: Geophysical Journal International, v. 102, no. 2, p. 287–298.

Olson, A.H., 1987, A Chebyshev condition for accelerating convergence of iterative tomographic methods—solving large least squares problems: Physics of the Earth and Planetary Interiors, v. 47, p. 333–345.

Olson, A.H., and Anderson, J.G., 1988, Implications of frequency-domain inversion of earthquake ground motions for resolving the space-time dependence of slip on an extended fault: Royal Astronomical Society Geophysical Journal, v. 94, no. 3, p. 443–455.

Snay, R.A., Neugebauer, H.C., and Prescott, W.H., 1991, Horizontal deformation associated with the Loma Prieta earthquake: Seismological Society of America Bulletin, v. 81, no. 5, p. 1647–1659.

Steidl, J.H., Archuleta, R.J., and Hartzell, S.H., 1991, Rupture history of the 1989 Loma Prieta, California, earthquake: Seismological Society of America Bulletin, v. 81, no. 5, p. 1573–1602.

Wald, D.J., Helmberger, D.V., and Heaton, T.H., 1991, Rupture model of the 1989 Loma Prieta earthquake from the inversion of strong-motion and broadband teleseismic data: Seismological Society of America Bulletin, v. 81, no. 5, p. 1540–1572.

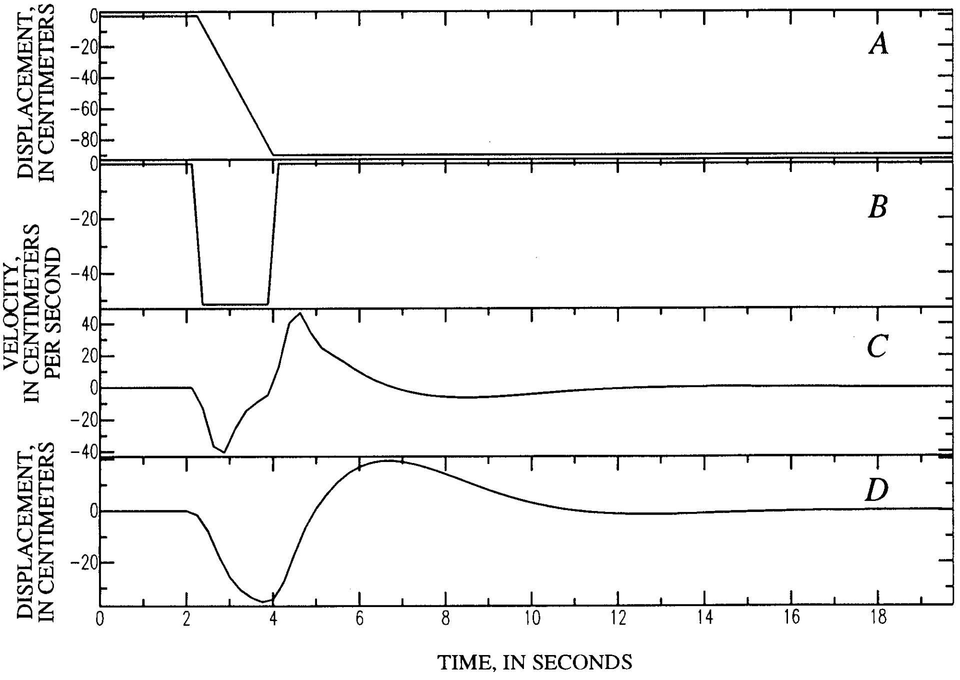

Figure 7.—Effect of band limitation on strong-motion data. *A*, Ramp function with 90 cm of offset occurring over a period of 1.75 s. *B*, Velocity-time series obtained by differentiating ramp function in figure 7*A*. *C*, Velocity-time series after bandpass filtering between 0.1 and 1.0 Hz. *D*, Displacement-time series obtained by integrating filtered velocity-time series in figure 7*C*.

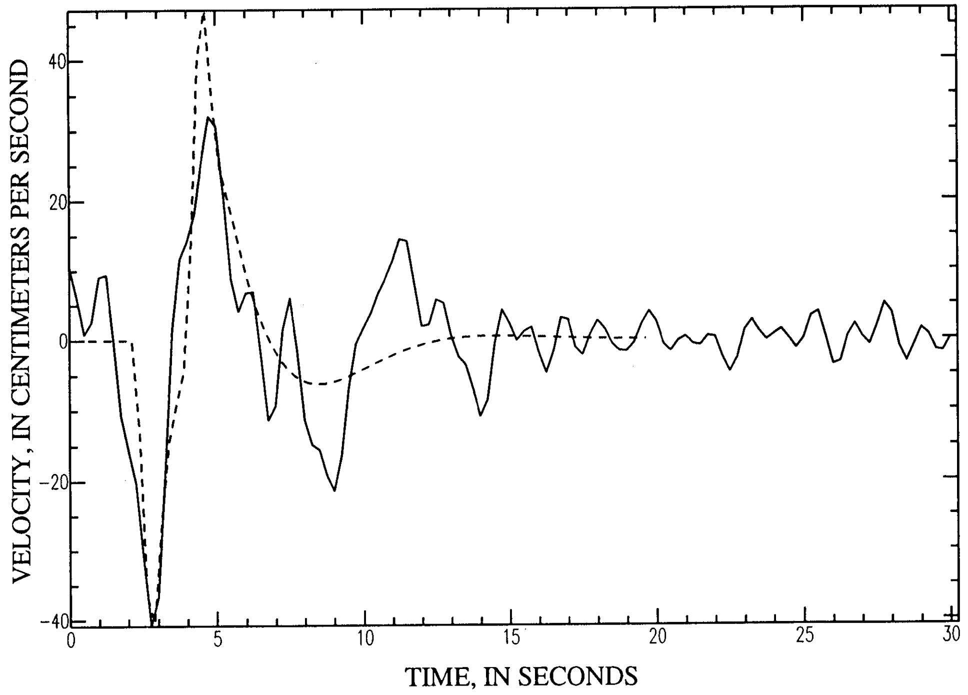

Figure 8.—Velocity-time series from inversion for static offset (solid curve) and bandpass-filtered velocity history from figure 7*C* (dashed curve). Inversion velocity-time series is for strike-slip component of Fourier spectral amplitude on a segment at southeast end of fault, where slip velocities are highest at 3 s (see fig. 9).

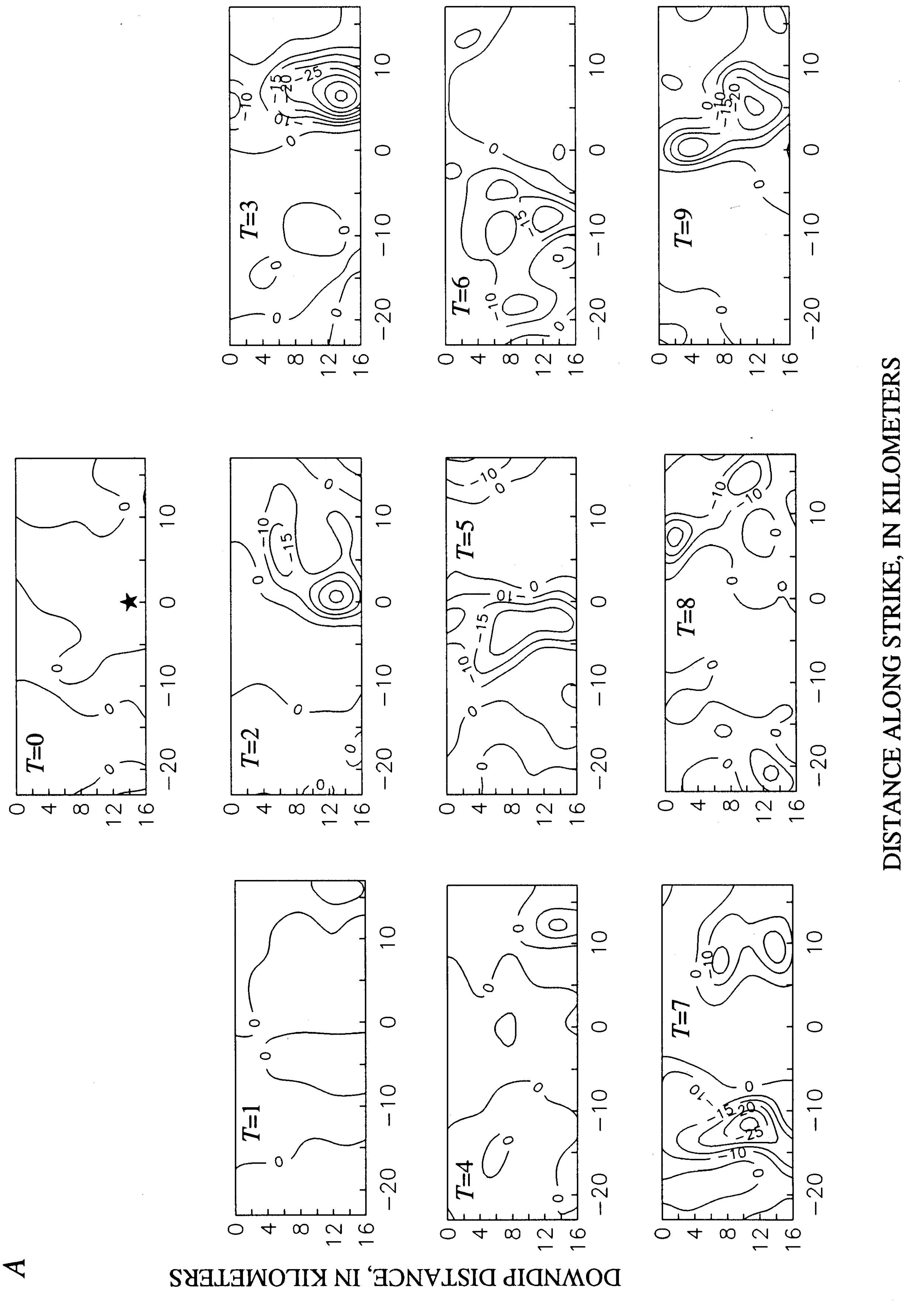

Figure 9.—Contours of strike-slip (*A*) and dip slip (*B*) components of velocity on fault plane at 1-s intervals. *T*=0 corresponds to initial earthquake rupture. Star, hypocenter of earthquake.

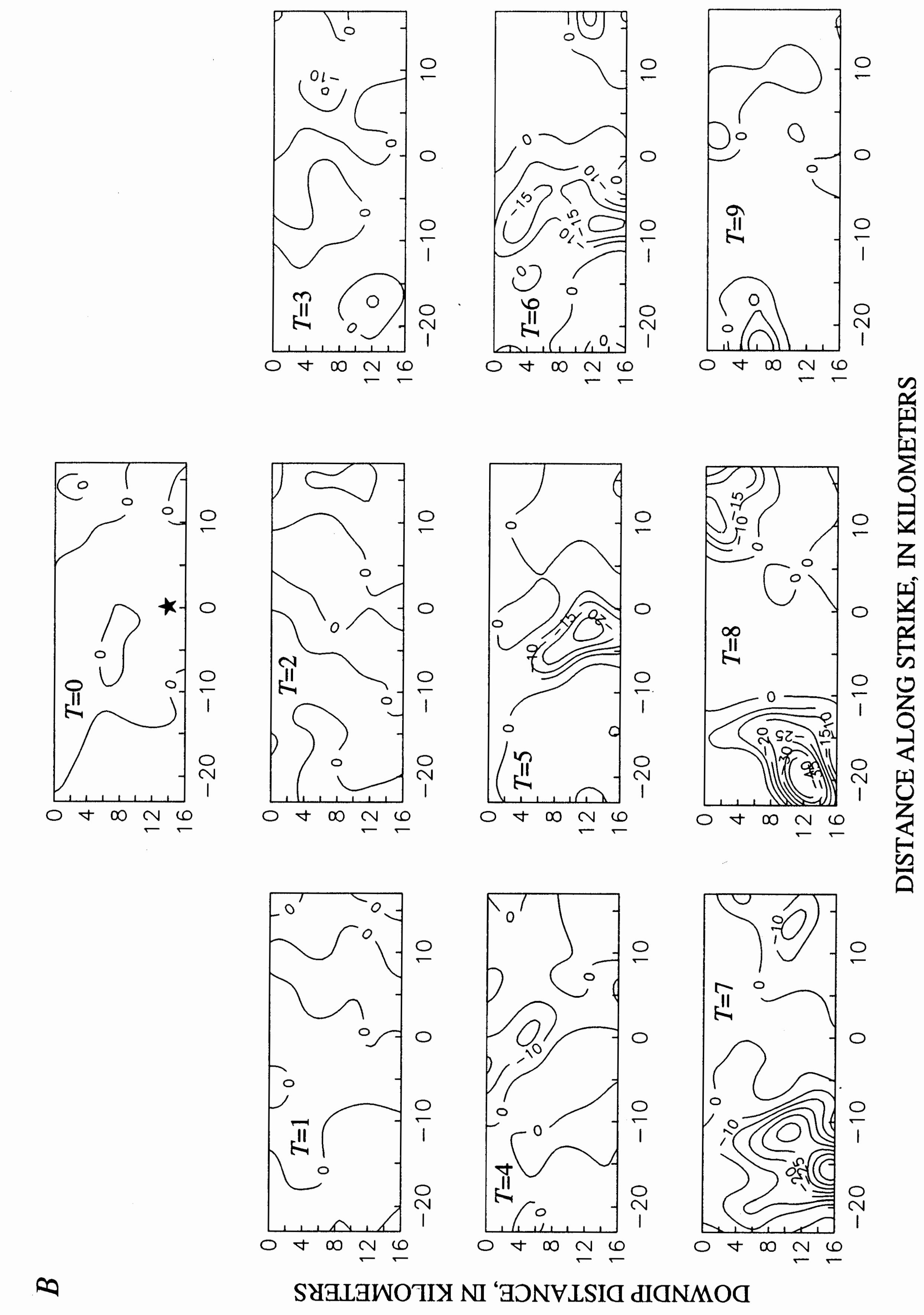

Figure 9.—Continued

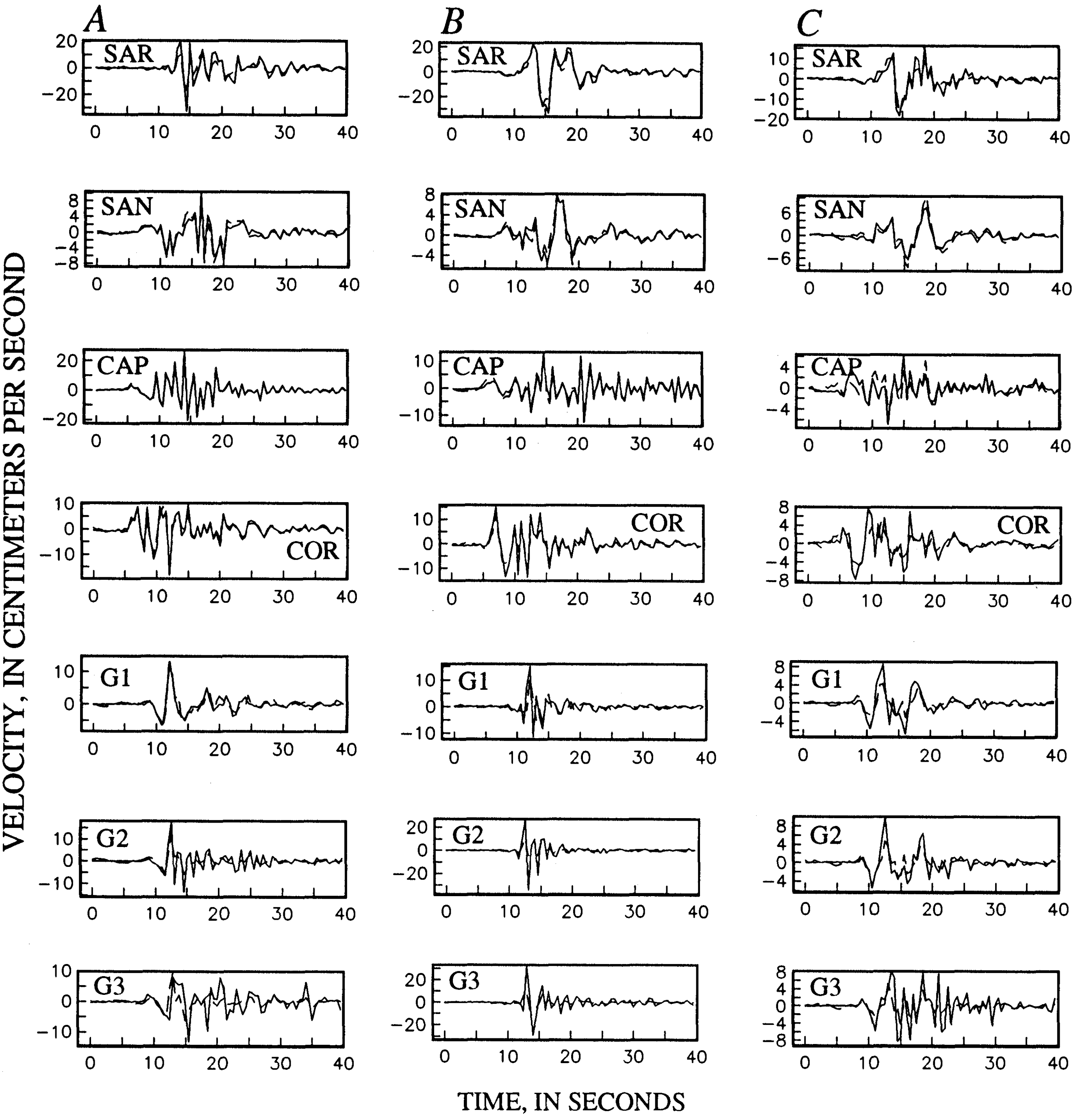

Figure 10.—Observed (solid curve) and predicted (dashed curve) seismograms for vertical (*A*), east-west (*B*), and north-south (*C*) components of motion at strong-motion stations used in inversion.

THE LOMA PRIETA, CALIFORNIA, EARTHQUAKE OF OCTOBER 17, 1989: EARTHQUAKE OCCURRENCE

MAIN-SHOCK CHARACTERISTICS

BROADBAND STUDY OF THE SOURCE CHARACTERISTICS OF THE EARTHQUAKE

By Hiroo Kanamori,[1]
California Institute of Technology;
and
Kenji Satake,
University of Michigan

CONTENTS

ABSTRACT

We have determined the source characteristics of the 1989 Loma Prieta earthquake, using teleseismic data. The solution from body waves gives a mechanism with a strike of 128°, a dip of 70°, a rake of 138°, and a seismic moment of 3×10^{26} dyne-cm (M_w=6.9). This solution is similar to those obtained from long-period Rayleigh and Love waves, P_{nL} waves, and first-motion data. The body-wave solution suggests a depth of about 15 km. The effective duration of the source is 6 s, suggesting lengths of 30 and 15 km for bilateral and unilateral faulting, respectively. Considering the extent of the aftershock zones, we estimate a total rupture length of 35 km. The strike-slip and thrust components of coseismic slip are 177 and 159 cm, respectively. The large thrust component raises an important question regarding the recurrence pattern. If the 1989 Loma Prieta earthquake is a characteristic earthquake with a recurrence interval of about 100 yr, the 159-cm displacement implies a long-term uplift rate of about 1 cm/yr, which appears too high for this region. Three hypotheses for reconciling this apparent conflict are that (1) the geometry of plate motion along the Santa Cruz Mountains section of the San Andreas fault changes on a time scale of several thousand years, and so the coseismic displacement has not accumulated enough to produce high topographic relief; (2) the coseismic-slip direction varies from event to event; and (3) the slip plane of the 1989 Loma Prieta earthquake is distinct from the Pacific-North America plate boundary—if so, then this earthquake is a rather rare, noncharacteristic event. The surface slip of about 1 m for the 1906 San Francisco earthquake is one of the key data in long-term forecasting. No surface slip was observed in the 1989 Loma Prieta earthquake, even if the horizontal slip at depth was as large as 1.8 m. This discrepancy points to a risk of relying too heavily on surface observations for long-term seismic-risk analysis.

INTRODUCTION

The 1989 Loma Prieta earthquake occurred within a seismic gap that had been identified as having a higher than 30 percent (in 30 yr) probability of producing an earthquake of M=6.5–7 (Lindh, 1983; Sykes and Nishenko, 1984; Scholz, 1985; Working Group on California Earthquake Probabilities, 1988). This forecast was based on the historical seismicity and low background seismicity in this gap, and on the amount of surface break (approx 1 m) in the 1906 San Francisco earthquake. Thatcher and Lisowski (1987) argued, however, on the basis of geodetic data, that the coseismic slip for the 1906 earthquake was about 2.6 m, and so it will take more than 150 yr to accumulate this amount of slip (a long-term slip rate of 1.5 cm/yr is assumed for the San Andreas fault in this region), implying that a large earthquake is unlikely in the next few decades.

Now that the 1989 Loma Prieta earthquake has occurred, it is important to assess how it compares with the published forecast. To this end, we have analyzed seismic data, primarily broadband seismograms, to determine the source characteristics of the earthquake. The data are summarized in table 1.

---

[1] Contribution No. 4846, Division of Geological and Planetary Sciences, California Institute of Technology, Pasadena, CA 91125.

Table 1.—*Stations and data sets used to determine the source characteristics of the 1989 Loma Prieta earthquake*

Station	Δ (°)	ϕ (°)	ϕ_B (°)	Phases
ARU	86.9	360	0	P, SH, R_1, G_1
OBN	85.4	12	343	P, SH, R_1, G_1
SSB	84.9	35	320	P
HRV	38.6	66	279	P, SH, R_1, G_1
WFM	38.6	66	279	P, SH
ANMO	12.6	95	284	R_1, G_1
CAY	70.7	99	307	P, SH
RPN	64.9	168	349	P, SH, R_1, G_1
PPT	60.3	211	25	P, SH
KIP	35.0	254	56	SH

MECHANISM

Because the most complete data we could obtain are broadband data from International Deployment of Accelerometers/Incorporated Research Institution for Seismology (IDA/IRIS) and GEOSCOPE stations, we first describe the source mechanism calculated from these data. In our analysis, all the seismograms are deconvolved to ground-motion displacements; the data are plotted in figure 1. We used the method of Kikuchi and Kanamori (1989) to invert the records and determine the mechanism. The observed seismograms are matched by synthetic seismograms computed for a sequence of subevents distributed on a fault plane. The Green's functions for five independent moment-tensor elements are computed, and the subevents are represented by a linear combination of these elements.

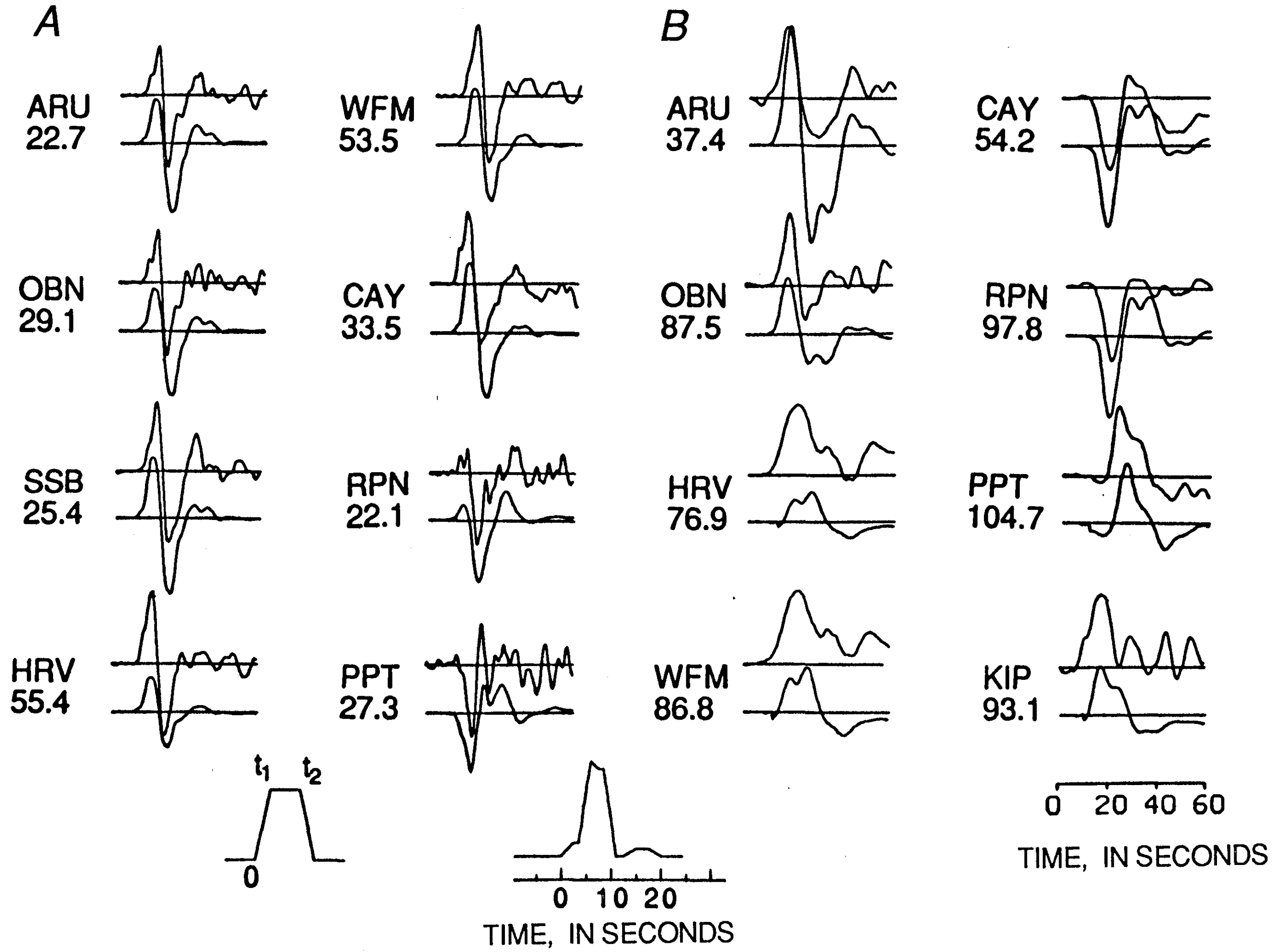

Figure 1.—Observed (top plot) and synthetic (bottom plot) seismograms of *P*-wave (*A*) and *SH*-wave (*B*) ground-motion displacement in 1989 Loma Prieta earthquake. Numbers below three-letter station codes are absolute displacement amplitude (distance from baseline to either peak or trough of observed displacement, whichever is larger) (in microns). Trapezoidal source and time function for three-event source are shown at bottom. Stations are arranged in order of increasing azimuth clockwise from north.

By minimizing the difference between the observed and synthetic seismograms, we determine the moment tensor or mechanism of all subevents, as well as their spatial location and timing.

Because many free parameters are involved in this type of inversion, tradeoffs between different source parameters could occur. First, we use a simplification to obtain the overall model. We assume a single source with a trapezoidal time function (t_1, t_2), as shown in figure 1; we vary t_1 and t_2 to obtain the best solution. We use the parameters listed in table 2 for both the source and receiver structures (common to all the stations). We use an attenuation time constant $t^*=1$ and 4 s and weights of 3 and 1 for *P* and *S* waves, respectively. We tried three discrete depths, 10, 15, and 20 km, and obtained a best fit at 15 km. The inversion results in $t_1=2.5$ s, $t_2=5$ s, a seismic moment (M_0) of 2.4×10^{26} dyne-cm, and a focal mechanism with a strike of 128°, a dip of 70°, and a rake of 138°. Though simple, this source explains the overall features of the observed waveform, and the residual (observed minus synthetic) waveforms are very small.

In the method of Kikuchi and Kanamori (1989), the inversion obtains successive point sources to fit the residual waveforms. In our model, the first point source explains most of the data, and so the other point sources are relatively small.

Table 2.—*Parameters used for source and receiver structures*

α (km/s)	β (km/s)	ρ (g/cm³)	*H* (km)
5.5	3.18	2.6	4
6.3	3.64	2.67	23.4
6.8	3.93	2.8	5.0
8.0	4.64	3.2	---

We assume that the mechanism of all subevents is the same as that of the first subevent, and invert the data. Because later subevents are small and their significance is questionable, we consider the first two or three subevents with a total seismic moment of 2.9×10^{26} or 3.1×10^{26} dyne-cm, respectively. The synthetic waveforms in the three-event model are compared with the observed seismograms in figure 1. Because of noise in the data, especially the significant site response at some stations (for example, KIP), the decision on where to terminate the sequence (iteration in the inversion) is arbitrary. If we include all subevents, the total seismic moment increases considerably. Considering the total seismic moment calculated from long-period waves (as described below), we judge a seismic moment significantly larger than 3×10^{26} dyne-cm to be unrealistic. In the section below entitled "Coseismic Slip," we use a rounded value of 3×10^{26} dyne-cm for the seismic moment of this subevent; from body-wave data alone, any value between 2.5×10^{26} and 3.5×10^{26} dyne-cm is acceptable. The results are summarized in figure 2 and listed in table 3.

Although the effective duration of the principal subevent is 5 s (fig. 1), we estimate an effective duration of 6 s, allowing for the contributions from smaller subevents.

We use the method of Kawakatsu (1989) and invert long-period surface waves to determine the centroid moment tensor (CMT) of the source. In this inversion, we use both the fundamental-mode and overtone Love and Rayleigh waves. The pass band of the filter is from 3.5 to 7 MHz. The results are shown in figures 2*A* and 2*B* and listed in table 3.

To examine the possible increase in seismic moment at long periods, we invert surface waves at a period of 256 s separately, using the method of Kanamori and Given (1981). In this inversion, the dip angle of one of the nodal planes (70°) is fixed to avoid instability in the inversion;

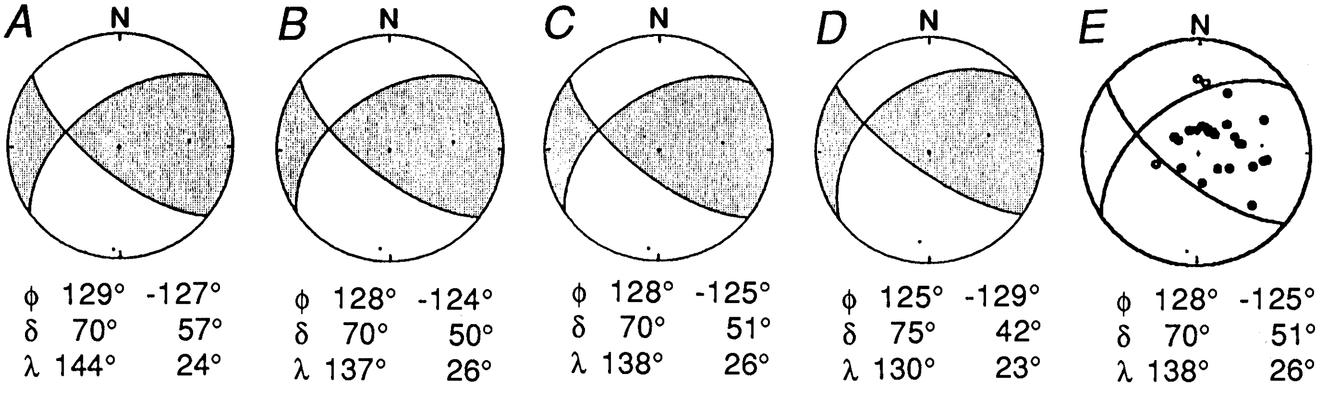

Figure 2.—Equal-area lower-hemisphere projections of focal mechanisms for 1989 Loma Prieta earthquake, arranged in order by decreasing period, obtained from different data sets: (*A*) long-period surface waves, (*B*) centroid moment tensor, (*C*) *P-SH* waves, (*D*) P_{nL} waves, and (*E*) first motions. Nodel-plane parameters: φ, strike; δ, dip; λ, rake. Nodal planes for first-motion data (fig. 2*E*) are from solution obtained from *P-SH* waves.

Table 3.—*Source characteristics of the 1989 Loma Prieta earthquake*

Data	M_0 (10^{26} dyne-cm)	ϕ_1 (°)	δ_1 (°)	λ_1 (°)	ϕ_2 (°)	δ_2 (°)	λ_2 (°)
P and SH waves-------	3	128	70	138	−125	51	26
Surface waves ---------	2.5	128	70	137	−124	50	26
R_1 and G_1 waves------	2.8	129	[1]70	144	−127	57	24
P_{nL} waves--------------	2.9	125	75	130	−129	42	23

[1] Fixed.

the mechanism is illustrated in figure 2*C*. The estimated seismic moment is 2.8×10^{26} dyne-cm, essentially the same as in the body-wave and CMT solutions. No evidence was found for an increase in seismic moment with period. The first-motion data plotted in figure 2*E* are also consistent with the body-wave and CMT solutions.

Woods and others (in press) used P_{nL} waves recorded at Pasadena, Calif., to determine the source mechanism by matching the waveforms with synthetic seismograms. Their preferred solution is plotted in figure 2*D* and listed in table 3.

The mechanisms obtained from data sets with different periods are essentially the same (fig. 2; table 3), and the seismic moment determined from body waves (period, approx 10 s) is about the same as that determined from surface waves with a period of 256 s, suggesting a simple source for the earthquake. The estimated seismic moment is 3×10^{26} dyne-cm, which gives M_w=6.9.

SOURCE DURATION AND RUPTURE LENGTH

Figure 1 shows that the effective duration of the source is about 6 s, a value that can be used to infer the rupture length. If the rupture is unilateral, then the effective duration τ is given by $\tau=(L/V)-(L\cos\Theta/c)$, where L is the rupture length, V is the rupture velocity, Θ is the azimuth of the station measured from the rupture direction, and c is the body-wave phase velocity along the free surface. Because the P-wave phase velocity is much higher than the rupture velocity, the second term is much smaller than the first. Thus, the rupture length L is approximately $L=V\tau$=15 km if τ=6 s and V=2.5 km/s. If the rupture is bilateral, then the rupture length is about twice that for a unilateral rupture—that is, 30 km.

The main shock is located near the center of the aftershock zone (U.S. Geological Survey staff, 1990), suggesting bilateral faulting. If the fault rupture is bilateral, our estimate of the effective duration, (6 s), suggests that L=30 km. The total length of the aftershock zone is about 40 km (U.S. Geological Survey staff, 1990). Although teleseismic data cannot resolve details of the slip distribution on the fault, the rupture length almost certainly does not exceed the length of the aftershock zone. In the following calculations, we use L=35 km, although a shorter rupture length is not precluded.

COMPLEXITY

As shown in figure 1, the source process of the earthquake is simple. The displacement waveform of the earthquake is compared with that of the 1988 Armenia earthquake (M_w=6.7), as recorded at station HRV, in figure 3. Comparison at other stations exhibits essentially a similar difference. The seismograms in figure 3 suggest that the duration of the 1988 Armenia earthquake was 40 s or even longer, in striking contrast to that of the 1989 Loma Prieta earthquake (approx 6 s). Pacheco and others (1989) suggested a substantial variation in focal mechanisms during the first 10 s of the 1988 Armenia earthquake.

This comparison clearly demonstrates the simplicity of the source process of the 1989 Loma Prieta earthquake, which involved a relatively short fault segment. This difference in source complexity may have profoundly influenced the damage potential of this earthquake. Although it is generally agreed that the heavy damage caused by the 1988 Armenia earthquake was primarily due to poor building construction, the source complexity and long duration almost certainly contributed as well. Because source complexity is closely related to local tectonic structure, earthquakes of the same magnitude as the 1989 Loma Prieta earthquake in different tectonic environments can be even more damaging than that earthquake.

COSEISMIC SLIP

If we assume a fault length of 35 km, a fault width 12 km, a rigidity of 3×10^{11} dyne/cm^2, we calculate a coseismic slip of 238 cm from the estimated seismic moment of 3×10^{26} dyne-cm. The strike-slip and thrust components of displacement are 177 and 159 cm, respectively. The average stress drop is estimated at 50 bars.

DISCUSSION AND CONCLUSION

Two aspects of the 1989 Loma Prieta earthquake are noteworthy: the thrust component, as large as 159 cm, and the short rupture length, only 35 km, for an M_w=6.9 earthquake. The large thrust component (1.6 m) raises an important question regarding the recurrence interval of earthquakes along the Santa Cruz Mountains section of the San Andreas fault.

The long-term forecast of this earthquake is based on a combination of the historical seismicity, the estimated slip rate along the Santa Cruz Mountains section of the San Andreas fault, and the surface slip (approx 1 m) in the 1906 San Francisco earthquake (Lindh, 1983; Sykes and Nishenko, 1984; Scholz, 1985). Implicit in this forecast is a relatively short recurrence interval, about 80 to 100 yr. If the 1989 Loma Prieta earthquake is a characteristic event to be expected along this section of the San Andreas fault, with a recurrence interval of about 100 yr, the thrust component of 1.6 m during the earthquake implies a long-term uplift rate of about 1 cm/yr, comparable to the highest rate observed in the world (for example, Yonekura, 1983). An uplift rate this large is generally associated with spectacular topographic relief. Although the long-term uplift rate in the epicentral area is unknown, the regional geomorphology does not seem to reflect such a high rate. We present three hypotheses to reconcile this apparent conflict.

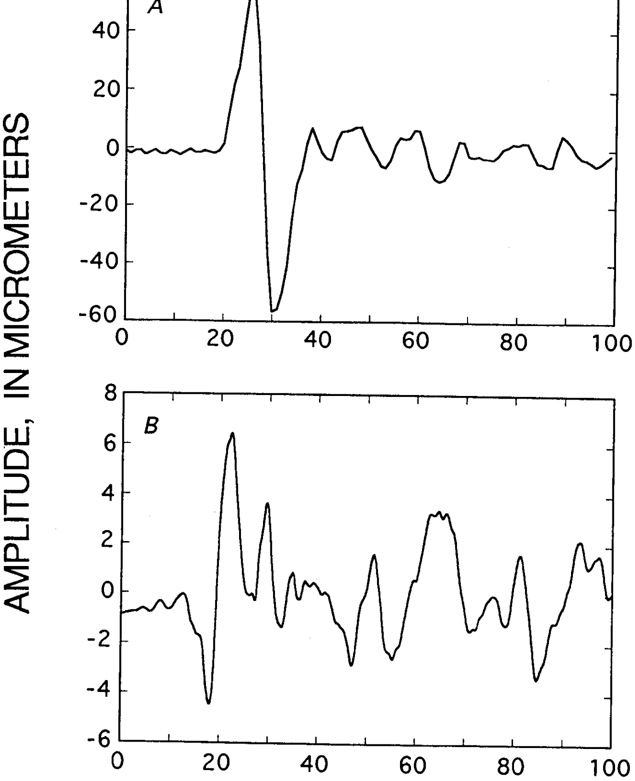

Figure 3.—Displacement records of 1989 Loma Prieta earthquake (*A*) and 1988 Armenia earthquake (*B*) from station HRV.

The first hypothesis is that the geometry of plate motion along the Santa Cruz Mountains section of the San Andreas fault changes on a time scale of several thousand years, and so not enough coseismic vertical displacement has accumulated to produce high topographic relief. If so, then the 1989 Loma Prieta earthquake can be considered a characteristic event along this section of the fault on this time scale.

The second hypothesis is that the coseismic-slip direction varies from event to event. For example, in the 1906 San Francisco earthquake, the motion along this section of the San Andreas fault was essentially strike slip, driven by much larger strike-slip displacements along the adjacent section. Even in the earlier events, which involved the Santa Cruz Mountains section only, the motion could have been primarily strike slip if sufficient stress had not accumulated there to cause vertical displacement.

The third hypothesis is that the slip plane of the 1989 Loma Prieta earthquake is distinct from the Pacific-North America plate boundary. If so, then this earthquake is a rather rare event and not a characteristic event along the San Andreas fault. Although no obvious geologic evidence exists, this conclusion cannot be ruled out.

The short rupture length, about 35 km, of the 1989 Loma Prieta earthquake is highly anomalous, in light of the empirical data available for shallow crustal earthquakes, as shown in figure 4. In fact, the estimated magnitude of the forecasted event is based on the empirical relation plotted in figure 4. For example, Scholz (1985) identified a 75-km-long slip-deficit segment along the Santa Cruz Mountains section of the San Andreas fault and forecast an M=6.9 earthquake. Lindh (1983) identified a 35-km gap and associated it with an M=6.5 earthquake. Both of these estimates are consistent with the empirical relation plotted in figure 4. The anomalous fault-length/moment relation for the 1989 Loma Prieta earthquake is the cause of the discrepancy between the predicted and observed events.

The surface slip of about 1 m during the 1906 San Francisco earthquake is one of the key data in a long-term forecast. Thatcher and Lisowski (1987) argued, however, that the slip of 2.4 m at depth determined from geodetic data should be used for estimating long-term probability. No surface slip was observed in the 1989 Loma Prieta earthquake, even if the horizontal slip at depth was as large as 1.8 m. This discrepancy points to a risk of relying too heavily on surface observations for long-term seismic-risk analysis.

The case for a long-term forecast of the 1989 Loma Prieta earthquake testifies to the importance of synthesizing seismologic, geologic, geodetic, and historical data to obtain probabilistic parameters for long-term hazard assessment and planning. The quantitative analysis of modern seismologic data has revealed many important details, such as source complexity, fault geometry, and rupture length, which, in conjunction with the probabilistic parameters, provide key information for implementing effective seismic-hazard-reduction measures.

ACKNOWLEDGMENTS

This research was partly supported by U.S. Geological Survey grants 14-08-0001-G1773 and 14-08-0001-G1832; the second author was supported by the Fellowship for Research Abroad of the Japanese Society for the Promotion of Science. We benefited from discussions with Don Helmberger throughout our study. We thank Holly Given and Barbara Romanowicz for providing us with key data from IDA/IRIS and GEOSCOPE stations. Some of the first-motion data were supplied by Laura Jones.

REFERENCES CITED

Kanamori, Hiroo, and Allen, C.R., 1986, Earthquake repeat time and average stress drop, *in* Pas, Shamita, Boatwright, John, and Scholz, C. H., eds., Earthquake source mechanics (Maurice Ewing Series, v. 6): Washington, D.C., American Geophysical Union, p. 227–235.

Kanamori, Hiroo, and Given, J.W., 1981, Mechanism of Mt. St. Helens eruption determined from long-period surface waves [abs.]: Eos (American Geophysical Union Transactions), v. 62, no. 45, p. 966.

Kanamori, Hiroo, and Magistrale, H.W., 1989, State of stress in seismic gaps along the San Jacinto fault, *in* Litehiser, J.J., ed., Observatory seismology; an anniversary symposium on the occasion of the centennial of the University of California at Berkeley seismographic stations: Berkeley, University of California Press, p. 179–186.

Kawakatsu, Hitoshi, 1989, Centroid single force inversion of seismic waves generated by landslides: Journal of Geophysical Research, v. 94, no. B9, p. 12363–12374.

Kikuchi, Masayuki, and Kanamori, Hiroo, 1989, [Analysis of multiple events with mechanism changes] [abs.]: Seismological Society of Japan Program and Abstracts, no. 1, p. 3 [in Japanese].

Lindh, A.G., 1983, Preliminary assessment of long-term probabilities for large earthquakes along selected fault segments of the San Andreas fault system in California: U.S. Geological Survey Open-File Report 83-63, 14 p.

Pacheco, J.F., Estabrook, C.H., Simpson, D.W., and Nábělek, J.L., 1989, Teleseismic body wave analysis of the 1988 Armenian earthquake: Geophysical Research Letters, v. 16, no. 12, p. 1425–1428.

Scholz, C.H., 1985, The Black Mountain asperity; seismic hazard of the southern San Francisco Peninsula, California: Geophysical Research Letters, v. 12, no. 10, p. 717–719.

Sykes, L.R., and Nishenko, S.P., 1984, Probabilities of occurrence of large plate rupturing earthquakes for the San Andreas, San Jacinto, and Imperial faults, California, 1983–2003: Journal of Geophysical Research, v. 89, no. B7, p. 5905–5927.

Thatcher, Wayne, and Lisowski, Michael, 1987, Long-term seismic potential of the San Andreas Fault southeast of San Francisco, California: Journal of Geophysical Research, v. 92, no. B6, p. 4771–4784.

U.S. Geological Survey Staff, 1990, The Loma Prieta, California, earthquake; an anticipated event: Science, v. 247, no. 4940, p. 286–293.

Woods, B.B., Zhao, L.-S., Helmberger, D.V., Thio, H.-K., and Kanamori, Hiroo, in press, The Loma Prieta earthquake sequences as observed at Pasadena: Geophysical Research Letters.

Working Group on California Earthquake Probabilities, 1988, Probabilities of large earthquakes occurring in California on the San Andreas Fault: U.S. Geological Survey Open-File Report 88-398, 62 p.

Yonekura, Nobuyuki, 1983, Late Quaternary vertical crustal movements in and around the Pacific as deduced from former shoreline data, *in* Hilde, T.W.C., and Uyeda, Seiya, eds., Geodynamics of the western Pacific-Indonesian region (Geodynamics Series, v. 11): Washington, D.C., American Geophysical Union, p. 41–50.

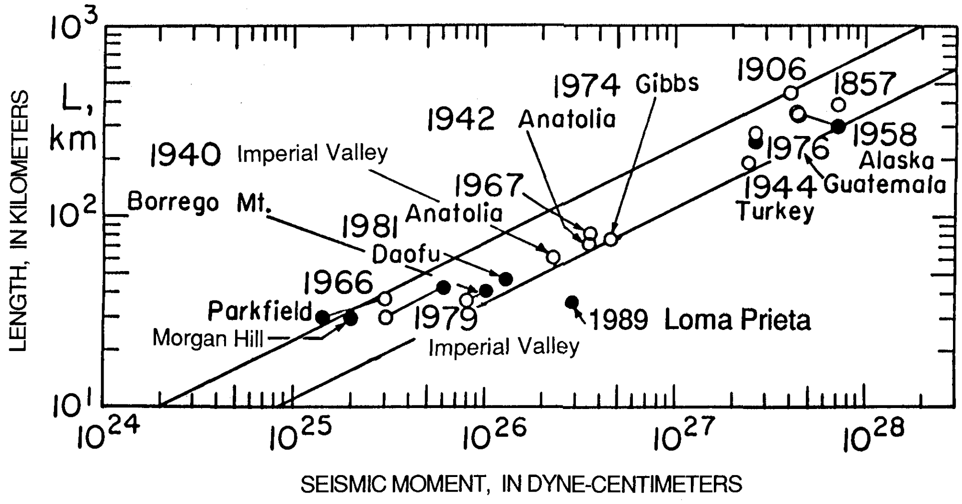

Figure 4.—Fault length as a function of seismic moment for shallow crustal earthquakes along active plate boundaries (from Kanamori and Magistrale, 1989). Solid lines indicate range of data points. Data from Kanamori and Allen (1986) (dots) and Scholz and others (1986) (circles).

THE LOMA PRIETA, CALIFORNIA, EARTHQUAKE OF OCTOBER 17, 1989: EARTHQUAKE OCCURRENCE

MAIN-SHOCK CHARACTERISTICS

GEODETIC MEASUREMENTS OF COSEISMIC HORIZONTAL DEFORMATION

By Michael Lisowski, Mark H. Murray, and Jerry L. Svarc,
U.S. Geological Survey

CONTENTS

ABSTRACT

Geodolite, Global Positioning System (GPS), and very long baseline interferometry surveys of the Loma Prieta region record the rate of secular deformation during the decades before the earthquake and the coseismic deformation associated with the earthquake. We estimate the coseismic offsets along 85 Geodolite lines and at 4 GPS stations by projecting the average rates of line-length change or displacement up to the time of the 1989 Loma Prieta earthquake. The rupture zones of the 1979 Coyote Lake, 1984 Morgan Hill, and 1987 Mount Lewis, Calif., earthquakes extend along the east edge of the regional geodetic network, and so we use the same method to calculate coseismic offsets at the times of these earthquakes along nearby Geodolite lines. Many measurements are from two stations 160 m apart on Loma Prieta, which is 11 km northeast of the epicenter, near the center of the rupture zone. Local surveys indicate that the northern station was coseismically displaced about 40 mm northward and 70 mm downward relative to the southern station, assuming that the southern station was stable. We use a Monte Carlo fault-parameter estimation to find a uniform-slip dislocation model of the fault rupture that best reproduces the observed coseismic deformation, and to assess the data sensitivity. Our best-fitting rupture model strikes 138°±4° N., dips 79°±8° SW., is 34±6 km long, extends from a depth of 7±3 to 13±5 km, and has a slip amplitude of 5±4 m and a rake of 153°±6°. The width of the rupture zone and the slip amplitude correlate closely but individually are poorly resolved. The location of this best-fitting model has an uncertainty of about 3 km; the geodetic moment is $2.7\pm0.3\times10^{19}$ N-m. The geodetic data clearly preclude rupture extending to the near surface. Coseismic deformation between the San Andreas and Calaveras faults to the east and south of the rupture zone is poorly fitted by our model.

INTRODUCTION

The 1989 Loma Prieta earthquake ruptured a section of the San Andreas fault where the U.S. Geological Survey (USGS) has monitored crustal deformation since the early 1970's with an extensive and frequently measured geodetic network (Lisowski and others, 1991). The subset of this regional geodetic network measured before and after the earthquake is mapped in figure 1. The geodetic data consist primarily of precise electronic distance measurements (EDM's) and coseismic displacements at a few Global Positioning System (GPS) stations and two very long baseline interferometry (VLBI) sites. The VLBI measurements were made by the U.S. National Aeronautics and Space Administration (NASA) and the U.S. National Geodetic Survey (NGS). Clark and others (1985) described precision geodesy with VLBI; general descriptions of GPS surveying and data reduction may be found in the reviews by Dixon (1991) and Hagar and others (1991). Although widespread secondary surface cracking accompanied the earthquake, no tectonic surface rupture was observed (U.S. Geological Survey staff, 1990). In this paper, we discuss these geodetic observations in detail, determine the coseismic offsets, and use these offsets to estimate the location, geometry, and slip of the buried earthquake rupture.

We limit our discussion and analysis to the data collected and reduced by the USGS' Crustal Strain Project, and to the two VLBI displacements. The data set is similar to that used in our initial study of the earthquake (Lisowski and others, 1990a). Other workers have collected and analyzed complementary geodetic data sets (Marshall and others, 1991; Snay and others, 1991; Williams and others, 1993). Our fault-rupture models are derived from the data presented in this paper, and we model the fault rupture as a single, planar dislocation with uniform slip. The reader interested in more complex fault-rupture models derived from different or more comprehensive geodetic data sets is referred to the reports by Marshall and others (1991), Snay and others (1991), Árnadóttir and others (1992), Williams and others (1993), Árnadóttir and Segall (1994), and Marshall and Stein (this chapter). Árnadóttir and Segall (1994) used the most comprehensive data set and discuss uniform- and variable-slip fault-rupture models. Postseismic deformation following the 1989 Loma Prieta earthquake was discussed by Savage and others (1994) and Bürgmann and others (1994).

We measure the distance between permanent geodetic stations with a Geodolite, an electro-optical laser distancemeter. Aircraft measurements of temperature and humidity and ground measurements of atmospheric pressure are used to correct for variations in the refractive index of air. The precision σ obtained with a Geodolite by using these techniques is given by

$$\sigma = \left[a^2 + b^2 L^2\right]^{1/2} \qquad (1)$$

where a=3 mm, b=0.2 ppm (dimensionless), and L is the distance measured (Savage and Prescott, 1973; Savage and others, 1986, p. 7459–7460). A precision of 5 mm is typical for a 20-km-long line. We occasionally use endpoint meteorology along some short-range (<5 km long) lines, increasing the uncertainty in the scale error b to 2 ppm.

Geodolite surveys of the Loma Prieta region were typically conducted every 1 to 5 yr, except for a subset of lines (dotted, fig. 1) from station Loma USE on Loma Prieta to stations Eagle Rk, Allison, and Hamilton that have been measured monthly since 1981 (Lisowski and others, 1990b, 1993). Beginning in 1987, these Geodolite measurements were supplemented by monthly GPS observations between station LP1 (approx 160 m south of sta. Loma USE) and stations Allison and Eagle Un (approx 30 m south of sta. Eagle Rk). In 1988 and 1989, the displacement vectors between station LP1 and stations Hamilton and Brush 2 were measured several times. The precision of the GPS-measured relative positions at the 30- to 60-km separations of these stations is also about 0.2 ppm, although it depends on the orientation of each line and the techniques used to process the data (Davis and others, 1989; Prescott and others, 1989; Larson and Agnew, 1991; Murray, 1991). We processed the GPS results with the computer program GAMIT (Schaffrin and Bock, 1988; Dong and Bock, 1989) for preearthquake measurements and with the Bernese software (Beutler and others, 1987; Davis and others, 1989) for postearthquake observations. We also processed the data from preearthquake surveys with the Bernese software, and obtained results similar to those obtained with GAMIT. As discussed by Lisowski and others (1993), we used the GAMIT preearthquake solutions because we were able to process a few more surveys; the postearthquake surveys were processed only with the Bernese software.

METHOD USED TO ESTIMATE COSEISMIC OFFSET OR DISPLACEMENT

Ideally, we would like to obtain geodetic observations immediately before and after an earthquake: then, the coseismic offset would simply be the difference between any two observations. The Geodolite and GPS observations from Loma Prieta come closest to that ideal, with surveys a few weeks before and few days after the earthquake. Measurements at other sites were less timely; several lines had not been measured for more than 5 yr before the earthquake. About 35 mm/yr of secular deformation is distributed across the San Andreas fault system in the San Francisco Bay region (Lisowski and others, 1991). Although the rate of line-length change along an individual line may be only a small fraction of this secular deformation, the total change over several years can be substantial. We need a method to separate this secular change from the coseismic change to best estimate the coseismic deformation.

Our experience indicates that secular line-length changes are generally a linear function of time. Therefore, we fit a model that includes a slope and intercept (that is, a straight line) and one or more coseismic offsets. In addition to an offset at the time of the 1989 Loma Prieta earthquake, for affected lines we include the offset at the time of the 1979 Coyote Lake M_L=5.9 earthquake (King and others, 1981), the 1984 Morgan Hill M_L=6.2 earthquake (Bakun and others, 1984; Prescott and others, 1984), or the 1986 Mount Lewis M_L=5.9 earthquake. The locations of the epicenters and rupture zones of these earthquakes are shown in figure 1. The slope, intercept, and coseismic offsets were determined by a weighted least-squares fit to the observations of each line or vector component. We assume that the line length, L, can be described by

$$L = L_0 + (t - t_0)\frac{dL}{dt} \qquad (t < t_{\mathrm{eq1}}) \qquad (2)$$

and

$$L = L_0 + (t - t_0)\frac{dL}{dt} + \sum_{k=1}^{n} \Delta L_{\mathrm{eq}_k} \qquad (t < t_{\mathrm{eq}k}) \qquad (3)$$

where L_0 is the line length at time t_0; dL/dt is the average rate of line-length change; and $\Delta L_{\mathrm{eq}k}$ is the coseismic offset at $t_{\mathrm{eq}k}$, the time of the kth earthquake. Many lines are offset by more than one earthquake. Thus, we estimate the average rates of line-length change and the coseismic offsets along 86 Geodolite and 3 GPS lines (table 1). Clark and others (1990) used the same method to determine the coseismic displacements of the VLBI sites at Fort Ord (near sta. Brush 2), the Presidio, and Point Reyes (fig. 1).

We test the assumption of a constant dL/dt by computing the probability that a sequence of random numbers (normal distribution, with σ the same as the standard error in an observation for that line) would furnish a better fit to the straight line than do the actual observations. A linear rate of change with one or more coseismic offsets does not provide an appropriate fit to the line-length observations when the χ^2 probability in table 1 is greater than 95 percent. In most of these observations, either our previous error estimates are too low, or there are one or more measurement blunders. We delete any obvious blunders and recompute the slope and offsets. The normalized rms residual, σ_0, is given by

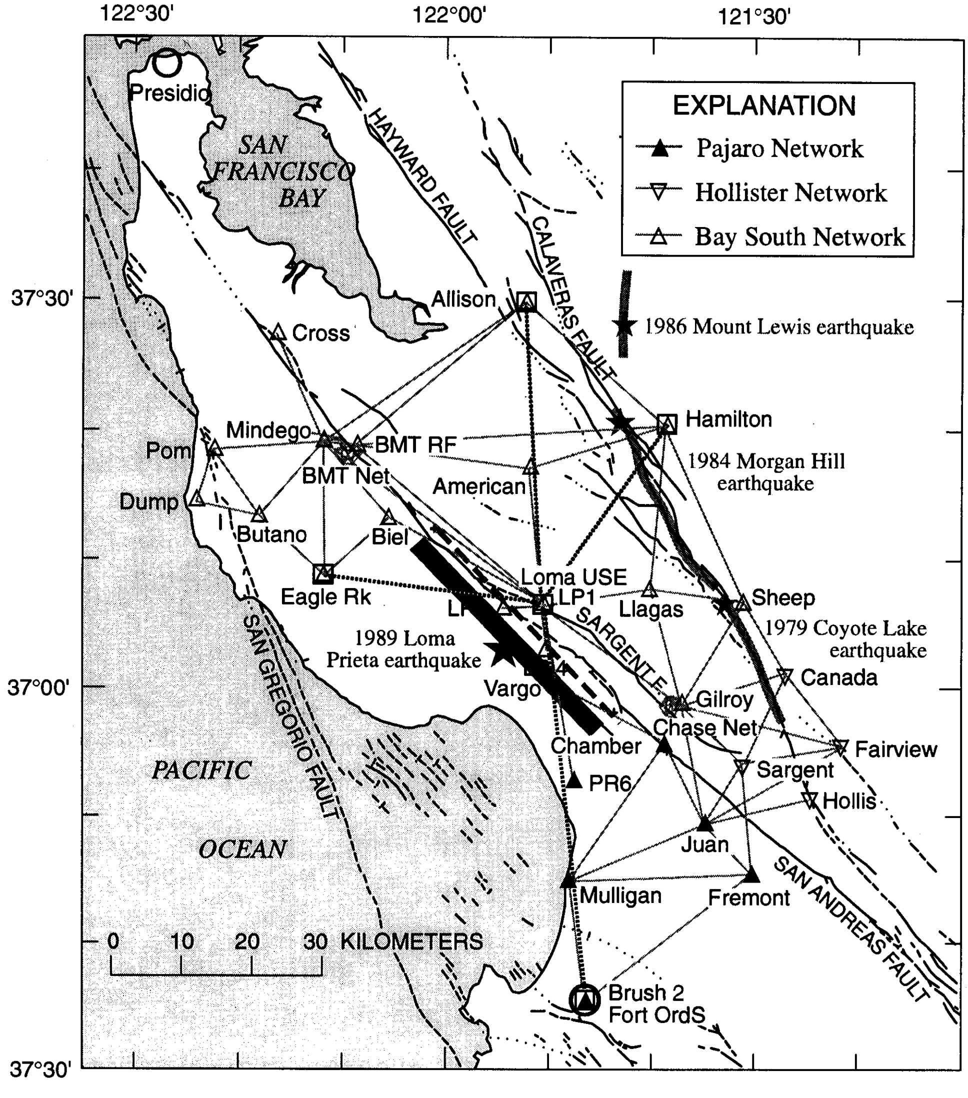

Figure 1.—San Francisco Bay region, showing locations of major faults (irregular lines, dashed where inferred; from Jennings, 1975), epicenters (stars) and rupture zones (shaded bands) of recent earthquakes, and stations in regional geodetic network. Triangles, Geodolite stations; squares, Global Positioning System stations; circles, very long baseline interferometry sites. Heavy-shaded rectangle, surface projection of best-fitting, uniform-slip dislocation model for 1989 Loma Prieta earthquake; heavy-dashed line, intersection of rupture plane with surface of the Earth. Stations Loma USE and LP1 are separate monuments on Loma Prieta.

$$\sigma_0 = \left[\frac{1}{n-m} \sum_{\mathrm{i}} \frac{(O_{\mathrm{i}} - C_{\mathrm{i}})^2}{\mathrm{s}_{\mathrm{i}}^2} \right]^{-½} = \left(\frac{1}{\mathrm{n-m}} \chi^2 \right)^{½}, \qquad (4)$$

where n is the number of data, m is the number of unknowns, O_i is the observed value, C_i is the calculated value, and s_i is the assigned standard error for the ith observation. $\sigma_0=1$ if the normalized rms residual from our linear fit with offsets equals the previous error estimate. We scale the uncertainties in the computed values by the normalized rms residual (σ_0) if $\sigma_0>1$; that is, the standard deviations listed in table 1 are the larger of either the experimental uncertainty based on previous error estimates or the theoretical uncertainty derived from the weighted-least-squares fit.

At several sites, the measurement history is complicated by the use of different, but nearby, monuments. When possible, we use local surveys or directly measured length differences to correct the line lengths observed from these eccentric monuments to those that would have been measured from the primary monuments. This technique gives us a longer time series that better determines the rate of line-length change. The precision of these eccentric corrections is generally better than that of the measured distance. Here, we assume that the standard deviation of a reduced line length is given by equation 1, and ignore any uncertainty in the eccentric correction.

We assume a constant deformation rate before and after an earthquake. Postseismic slip, viscoelastic relaxation, or other transient deformation may occur after an earthquake (Thatcher, 1983). After the 1979 Coyote Lake and 1984 Morgan Hill earthquakes, for example, the rates of line-length change on several lines increased and then appeared to decay to the normal rate within about 1 yr. We exclude the anomalous data obtained just after these earthquakes from our analysis. The coseismic offsets listed in table 1 for these earthquakes are then the offsets accumulated until the rate of line-length change returns to its preearthquake rate. We cannot do the same for the 1989 Loma Prieta earthquake, however, because we measured most of the Geodolite lines only once after the earthquake. Some Geodolite lines and GPS-measured relative positions from Loma Prieta were measured many times after the earthquake, and there is a subtle, but significant change, in the deformation rate (Savage and Lisowski, 1995). In our analysis of the GPS-measured coseismic displacements, we allow for different rates of change before and after the earthquake. We describe the north, east, and up vector components by

$$C = C_0 + (t - t_0)\frac{dC_1}{dt} \qquad (t < t_{\mathrm{eq}}) \qquad (5)$$

and

$$C = C_0 + (t_{\mathrm{eq}} - t_0)\frac{dC_1}{dt} + (t - t_{\mathrm{eq}})\frac{dC_2}{dt} + \Delta C_{\mathrm{eq}} \qquad (t_{\mathrm{eq}} < t) \qquad (6)$$

where C_0 is the initial value of the vector component at time t_0; dC_1/dt is the average rate of line-length change before the earthquake; dC_2/dt is the average rate of line-length change after the earthquake; and ΔC_{eq} is the coseismic offset at t_{eq}, the time of the earthquake.

GEODOLITE, GPS, AND VLBI MEASUREMENTS

The Geodolite lines and GPS vectors measured before and after the 1989 Loma Prieta earthquake are parts of several networks (fig. 1). A network is an arbitrary regional grouping of lines with a similar measurement history. We have determined the coseismic deformation in the Pajaro, Hollister, Bay South, and Loma Prieta Monitor regional networks and in the Black Mountain and Chase small-aperture, fault-crossing networks. We discuss the data from each network separately, concluding with a short summary of Clark and others' (1990) VLBI results from the Fort Ord and Presidio sites.

PAJARO NETWORK

The Pajaro network extends along Monterey Bay; most stations are located near or west of the San Andreas fault. Lines from station Juan to stations Gilroy, Sargent, Fairview, and Hollis cross the Sargent or Calaveras fault and tie stations in the Pajaro network into stations in the Bay South and Hollister networks (fig. 1). We surveyed the Pajaro network nine times between 1973 and 1983, and again 3 months after the 1989 Loma Prieta earthquake (figs. 2*A*, 2*B*). Several lines in the network showed significant rates of line-length change. The 6- to 8-yr gap between the last survey and the earthquake makes the correction for secular change especially important in accurately estimating the coseismic offset. We directly estimate coseismic offsets at the time of the 1979 Coyote Lake and 1989 Loma Prieta earthquakes. Only the lines Brush 2 to Mulligan and Brush 2 to Fremont (fig. 1) were measured after the 1979 Coyote Lake earthquake and before the 1984 Morgan Hill earthquake. We use a dislocation model, with the geometry and location of the earthquake rupture reported by Prescott and others (1984) and the coseismic offsets at the time of the 1984 Morgan Hill earthquake listed in table 1, to estimate the coseismic offset in the Pajaro network at the time of the 1984 Morgan Hill earthquake; these modeled offsets are listed in parentheses in table 1.

The linear rate of line-length change as a function of time with two coseismic offsets provides a good fit to most of the data from the Pajaro network (table 1). The lines LP1 to Vargo and Juan to Sargent (fig. 1) are exceptions, with a χ^2 probability greater than 95 percent. No individual data points stand out as blunders in the plots, although many of the frequent measurements of the line Juan to Sargent after the 1974 Hollister earthquake are anomalous. Other measurements from station Sargent made at the same time also show a larger than expected scatter; Savage and others (1976, 1979) speculated that those measurements are contaminated by systematic error. The normalized rms residual for the line LP1 to Vargo is twice the expected value. This line is steep (800-m elevation change in 11 km), and trees around Vargo block or partly

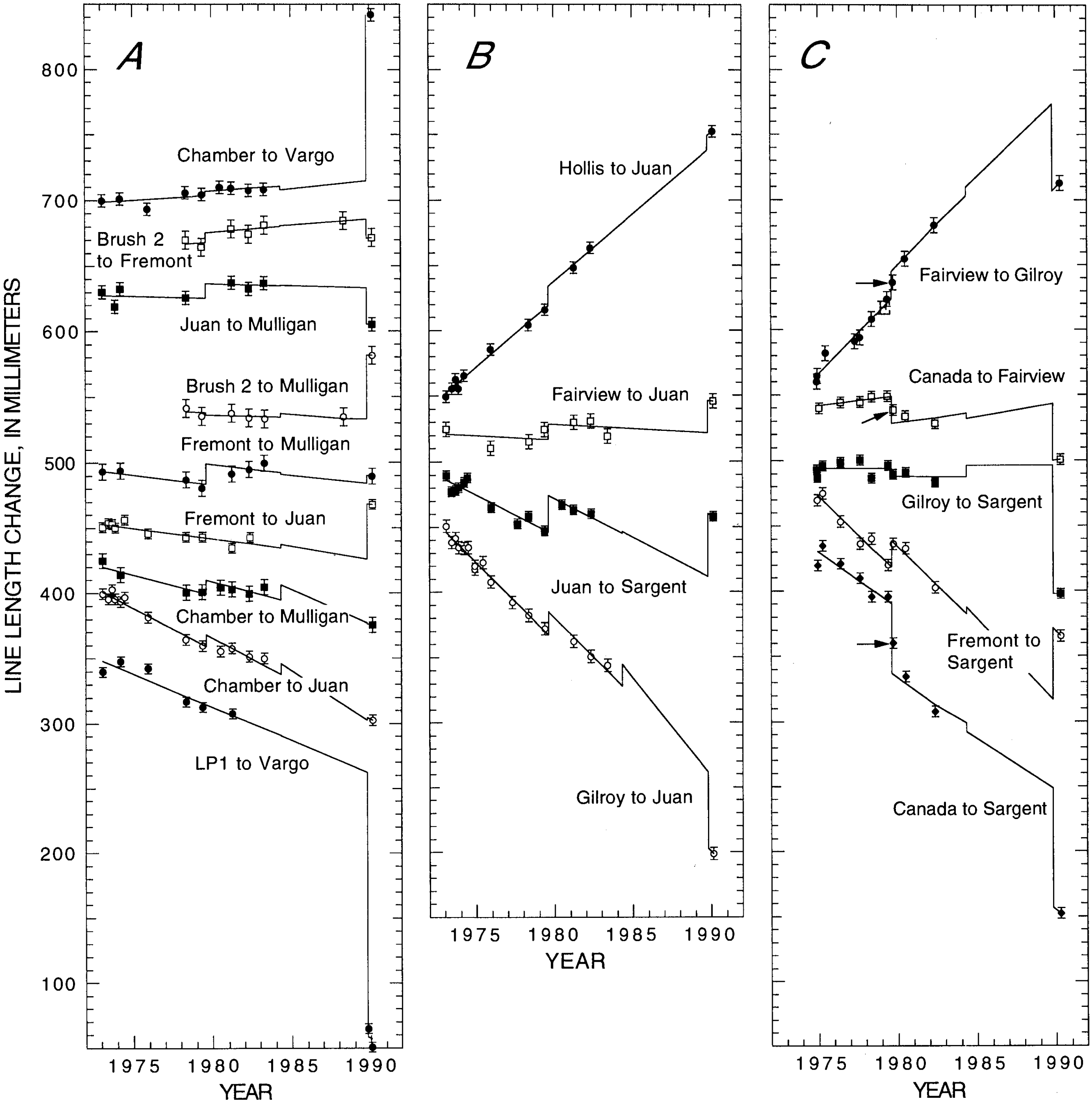

Figure 2.—Line-length change (observed line length L less a constant nominal length L_0) as a function of time for lines between stations in Pajaro and Hollister networks. Curves show best-fitting linear rate of line-length change from data points, with offsets at times of 1979 Coyote Lake and 1989 Loma Prieta earthquakes; error bars, 1σ. *A*, Lines in Pajaro network west of the Sargent fault. *B*, Lines in Pajaro network crossing the Sargent or Calaveras fault. *C*, Lines in Hollister network. Arrows designate data points that were excluded from analysis.

Table 1.—*Rates of secular line-length change and coseismic offsets on networks in the San Francisco Bay region*

[Values in parentheses were calculated with a dislocation model; values marked with an asterisk are corrected for local motion between stations LP1 and Loma USE (fig. 1), assuming that station LP1 is stable]

Station 1	Station 2	L (km)	No. of surveys	Interval	dL/dt (mm/yr)	χ^2 probability (pct)	σ_0	Coseismic offset (mm)			
								Coyote Lake 1979.597	Morgan Hill 1984.313	Mount Lewis 1986.25	Loma Prieta 1989.794
				Pajaro network							
Brush 2	Fremont	30.4	7	78.3–90.1	1.0±1.2	17	0.55	7.4±8.5	(0.6)	---	−14.4±10.9
Brush 2	Mulligan	17.8	7	78.4–90.1	−.3±0.8	26	.65	−2.0±5.8	(2.7)	---	48.4±7.5
Chamber	Juan	13.4	14	73.1–90.1	−6.4±0.6	51	.97	8.8±4.7	(8.1)	---	1.9±6.7
Chamber	Mulligan	24.5	9	73.1–90.1	−3.2±1.0	28	.76	10.7±6.9	(11.4)	---	−.9±10.5
Chamber	Vargo	18.0	10	73.1–90.1	.7±0.8	27	.78	3.6±5.6	(−2.5)	---	126.9±8.6
Fremont	Juan	9.9	11	73.1–90.1	−1.6±0.6	64	1.05	−.1±4.9	(2.5)	---	42.5±6.8
Fremont	Mulligan	26.4	8	73.1–90.1	−1.5±1.1	29	.74	15.7±8.1	(−1.2)	---	5.8±11.1
Juan	Mulligan	21.2	8	73.1–90.1	−.3±1.3	65	1.05	11.2±10.2	(0.3)	---	−28.0±11.7
LP1	Vargo	11.4	8	73.1–90.1	−5.4±1.6	99	2.24	2.9±12.3	(−0.4)	---	−203.3±17.3
Fairview	Juan	23.0	8	73.1–90.1	−.7±1.4	87	1.34	11.7±9.9	(−1.7)	---	24.2±14.1
Gilroy	Juan	17.8	17	73.1–90.1	−12.1±0.7	27	.86	17.9±5.6	(16.6)	---	−59.0±7.5
Hollis	Juan	15.9	11	73.1–90.1	10.2±0.7	24	.77	14.7±5.6	(−0.8)	---	10.9±7.8
Juan	Sargent	10.7	14	73.1–90.1	−6.1±0.8	97	1.42	27.9±5.6	(1.2)	---	48.5±8.9
				Hollister network							
Canada	Fairview	13.3	8	75.0–90.3	1.5±1.1	39	0.83	−20.3±5.6	(−4.0)	---	−43.1±11.0
Canada	Sargent	14.3	9	75.0–90.3	−8.7±1.8	99	1.82	−53.3±10.1	(−6.7)	---	−91.8±18.6
Fairview	Gilroy	23.9	10	74.9–90.3	12.6±1.2	56	.99	21.6±7.2	(6.9)	---	−66.7±13.0
Fremont	Sargent	16.6	10	74.9–90.3	−11.9±1.2	78	1.18	20.5±6.0	(5.1)	---	54.2±12.9
Gilroy	Sargent	11.7	11	74.9–90.3	.0±1.2	96	1.45	−6.0±6.1	(8.9)	---	−89.9±12.6
				Bay South network							
Canada	Gilroy	15.6	12	74.9–85.8	3.7±1.1	29	0.82	1.3±4.7	−6.7±6.3	---	−51.9±7.5
Canada	Sheep RM2	12.2	7	78.4–85.9	4.0±3.8	91	1.57	11.3±10.8	−52.3±18.9	---	−30.3±18.6
Gilroy	Llagas	17.6	11	77.3–85.8	−2.3±1.2	32	.82	9.4±5.1	11.0±6.0	---	−48.5±7.9
Gilroy	LP1	24.9	10	78.5–85.8	3.0±2.3	83	1.25	12.5±8.4	−11.3±11.2	---	−19.0±14.1
Gilroy	Sheep RM1	17.4	11	75.4–85.8	−13.1±1.3	46	.94	−2.7±7.1	−27.9±5.2	---	−57.8±8.4
Hamil ec	Llagas	23.2	16	74.3–86.3	−12.2±1.0	90	1.25	2.4±5.7	−113.5±6.8	---	33.3±9.1
Hamilton	Sheep RM2	27.5	13	73.3–86.3	.6±1.0	24	.80	29.3±7.3	−6.0±6.2	---	−13.9±8.6
Llagas	LP1	15.9	17	72.5–86.3	.5±0.8	95	1.33	−6.5±5.7	20.6±5.1	---	−54.0±6.0
Llagas	Sheep RM2	13.5	13	72.5–86.3	7.1±0.6	56	1.00	36.3±4.0	51.7±4.2	---	92.1±5.5
Allison	BMT RF	31.7	9	78.0–90.1	−.8±1.2	50	.94	---	2.9±9.2	---	−39.2±11.8
Allison	Hamilton	26.7	28	72.1–89.8	7.1±0.7	99	1.44	---	17.5±6.6	25.7±5.9	.6±6.9
Allison	Mindego	35.2	7	78.5–90.1	3.1±2.0	36	.75	---	−25.1±12.2	---	−32.1±15.1
American	BMT RF	25.2	6	78.0–90.1	5.7±3.9	97	1.88	---	−15.6±25.0	---	−27.5±25.4
Amer RM3	Hamilton	20.7	14	74.4–90.1	4.9±0.8	93	1.33	---	11.2±6.4	---	77.3±8.2
Biel	Eagle Rk	12.3	7	78.4–90.1	−.9±0.7	32	.76	---	---	---	101.5±7.2
Biel	Mindego	14.3	8	77.3–90.1	1.0±0.6	17	.66	---	---	---	−117.3±7.2
Butano	Dump	8.9	9	76.9–90.1	.6±0.5	2	.45	---	---	---	−39.7±5.7
Butano	Eagle Rk	12.8	11	76.9–90.1	.6±0.4	51	.97	---	---	---	−95.2±5.5
Butano	Mindego	13.8	9	76.9–90.1	−.2±0.6	60	1.02	---	---	---	6.5±6.8
Butano	Pom	11.5	8	76.9–90.1	.7±0.9	98	1.66	---	---	---	−46.2±11.1
Cross RM1	Mindego	16.5	8	78.5–90.1	−2.3±0.7	9	.55	---	---	---	−15.9±7.1
Dump	Pom	7.6	7	78.4–90.1	.3±0.9	92	1.44	---	---	---	−6.3±9.6
Eagle Rk	Mindego	19.1	11	71.7–90.1	−3.6±0.4	47	.94	---	---	---	−20.4±6.8
Mindego	Pom	15.8	8	76.9–90.1	2.3±0.6	59	1.01	---	---	---	−1.8±7.5
				Loma short-range network							
LP1	LP2	5.7	10	70.5–89.9	−1.5±0.8	99	2.59	---	---	---	−38.3±13.1
LP1	LP4	6.6	9	70.5–89.9	−4.0±0.8	99	2.23	---	---	---	−194.8±12.9
				Loma Geodolite monitor network							
Allison	Loma USE	43.1	31	87.1–90.1	−11.8±2.3	3	.76	---	---	---	65.4±6.0, 107.4±6.0*
Eagle Rk	Loma USE	31.5	34	87.1–90.1	5.0±1.7	19	.88	---	---	---	256.4±4.5, 255.4±4.5*

Table 1.—*Rates of secular line-length change and coseismic offsets on networks in the San Francisco Bay region*—Continued

Station 1	Station 2	*L* (km)	No. of surveys	Interval	*dL/dt* (mm/yr)	χ^2 probability (pct)	σ_0	Coseismic offset (mm)			
								Coyote Lake 1979.597	Morgan Hill 1984.313	Mount Lewis 1986.25	Loma Prieta 1989.794
Loma Geodolite monitor network—Continued											
Hamilton	Loma USE	31.2	32	87.1–90.1	−8.5±1.7	1	0.70	---	---	---	11.9±4.6, 52.9±4.6*
Loma DWR	PR 6	26.0	9	83.9–89.8	−4.7±1.5	39	.87	---	---	---	−273.9±10.1
Loma GPS monitor network											
LP1	Allison	43.3	29	87.2–90.2	−12.1±1.6	95	1.24	---	---	---	112.6±3.2
LP1	Eagle Un	31.4	21	87.7–90.2	8.3±2.9	66	1.05	---	---	---	246.8±5.0
LP1	Hamil Un	31.4	12	88.1–90.2	−5.7±4.3	97	1.45	---	---	---	59.5±5.5
Bay South lines from station Loma USE											
American	Loma USE	19.7	17	73.9–90.1	−3.5±0.8	99	1.74	---	1.4±7.3	---	−94.4±7.9, −50.4±7.9*
Biel	Loma USE	25.4	14	72.5–90.1	2.4±0.5	70	1.09	---	9.9±7.5	---	216.8±7.9, 227.8±7.9*
BMT RF	Loma USE	35.4	9	78.5–90.1	.6±1.6	39	.85	---	−22.2±10.0	---	139.9±13.8, 158.9±13.8*
Loma USE	Mindego	39.2	10	72.5–90.1	1.3±0.9	30	.80	---	−17.3±10.8	---	158.0±12.8
Chase network											
Ch1	Ch2	1.1	8	70.9–90.8	−0.4±0.4	52	.95	---	---	---	11.6±7.7
Ch1	Ch3	1.0	8	70.9–90.8	−.6±0.4	57	.99	---	---	---	12.7±7.6
Ch1	Ch4	1.3	8	70.9–90.8	−.8±0.6	94	1.47	---	---	---	16.5±11.3
Ch1	Ch5	0.9	8	70.9–90.8	.2±0.4	37	.83	---	---	---	−3.7±7.6
Ch1	Ch6	1.8	9	70.9–90.8	−2.5±0.4	75	1.15	---	---	---	32.4±8.9
Ch1	Ch7	1.7	10	70.9–90.8	−.2±0.6	98	1.61	---	---	---	.1±11.9
Ch1	Ch8	1.7	10	70.9–90.8	2.4±0.6	98	1.59	---	---	---	−9.8±11.7
Ch2	Ch3	.9	8	70.9–90.8	−.3±0.4	9	.55	---	---	---	12.8±7.6
Ch2	Ch4	2.0	5	73.9–90.8	.6±0.6	34	.65	---	---	---	−1.1±10.1
Ch2	Ch5	2.1	8	70.9–90.8	.2±0.5	87	1.32	---	---	---	3.5±10.4
Ch2	Ch7	2.3	9	70.9–90.8	−1.8±0.4	41	.88	---	---	---	−8.9±7.9
Ch2	Ch8	1.6	9	70.9–90.8	−.1±0.4	73	1.13	---	---	---	−17.0±8.7
Ch3	Ch4	1.2	8	70.9–90.8	.3±0.4	17	.66	---	---	---	−5.0±7.7
Ch3	Ch8	2.2	3	71.9–90.8	1.0±0.5	0	.00	---	---	---	−15.9±9.0
Ch4	Ch5	1.0	8	70.9–90.8	−.8±0.4	16	.64	---	---	---	27.4±7.6
Ch5	Ch6	1.4	9	70.9–90.8	−2.7±0.5	91	1.36	---	---	---	54.6±10.4
Ch5	Ch7	1.9	9	70.9–90.8	.6±0.6	94	1.44	---	---	---	10.7±11.2
Ch5	Ch8	2.4	9	70.9–90.8	2.4±0.4	72	1.12	---	---	---	−1.2±8.9
Ch6	Ch7	1.0	9	70.9–90.8	−.5±0.4	40	.87	---	---	---	14.9±7.6
Ch7	Ch8	1.3	9	70.9–90.8	−.3±0.7	99	1.93	---	---	---	4.8±14.7
Black Mountain network											
BMT10	BMT11	1.3	10	70.4–91.8	0.3±0.2	65	1.06	---	---	---	1.9±3.6
BMT10	BMT9	2.5	9	70.4–91.8	−.5±0.2	40	.88	---	---	---	7.8±3.4
BMT10	PAWT	4.0	10	70.4–91.8	−.5±0.2	78	1.17	---	---	---	−17.0±4.2
BMT11	BMT RF	3.0	10	70.4–91.8	−.3±0.2	47	.93	---	---	---	5.2±3.3
BMT11	BMT9	3.2	10	70.4–91.8	.5±0.2	92	1.37	---	---	---	17.0±4.6
BMT11	PAWT	3.3	9	70.4–91.8	−.4±0.3	97	1.54	---	---	---	−15.3±5.5
BMT11	Sky1	2.1	5	82.2–91.8	.8±0.6	9	.31	---	---	---	−6.1±4.3
BMT RF	BMT9	1.8	10	70.4–91.8	.1±0.2	8	.61	---	---	---	2.2±3.3
BMT RF	Mindego	4.6	12	78.0–91.8	1.8±0.3	13	.72	---	---	---	8.9±3.5
BMT RF	RF5 Reset	4.7	5	82.1–91.8	1.7±0.6	58	.94	---	---	---	15.1±4.2
BMT RF	Sky1	3.2	4	82.1–90.6	.1±1.5	98	2.53	---	---	---	37.0±10.7
BMT9	Sky1	4.4	5	82.2–91.8	1.8±0.6	40	.73	---	---	---	13.6±4.2
PAWT	RF1	4.2	12	70.3–91.8	1.4±0.2	48	.96	---	---	---	10.8±3.4
PAWT	Sky1	2.1	9	71.5–91.8	.2±0.3	94	1.44	---	---	---	1.9±4.8

block the line-of-sight. The line-of-sight was totally blocked after 1981, and we had to clear it to measure this line after the 1989 Loma Prieta earthquake. We have found larger than expected scatter in some other steep lines (Savage and others, 1992). The combination of a steep line and partly blocked line-of-sight could explain the low precision. Measurements of the line Vargo to Chamber were shifted to station Vargo RM 1 in 1979 because trees blocked the line-of-sight. The difference in the distances measured in 1979 is used to correct all subsequent measurements of the lines from Vargo RM1 to those stations that would have been observable from the primary station Vargo.

We added the most southern station, Brush 2, to the Pajaro network in 1978. This station is critical to our analysis of the coseismic displacements because it is on the same hill as the VLBI site FortOrdS. Unlike the Geodolite and GPS measurements, the VLBI-measured coseismic displacements are relative to distant reference points (see subsection below entitled "Observations at Fort Ord and the Presidio"). By assigning the same coseismic horizontal displacement at station FortOrdS to station Brush 2 we fix the coseismic rigid-body translation of the geodetic network as a whole.

HOLLISTER NETWORK

Five lines from the Hollister network provide a tie between stations in the Hollister, Pajaro, and Bay South networks. The coseismic offsets along these lines allow us to compute the coseismic displacements of the stations Canada, Fairview, and Sargent (fig. 1). These lines were last surveyed in 1982. Our linear fits include coseismic offsets at the times of the 1979 Coyote Lake and 1989 Loma Prieta earthquakes (fig. 2*C*). We use the dislocation model discussed in the preceding subsection to estimate the coseismic offset at the time of the 1984 Morgan Hill earthquake; the modeled values are listed in parentheses in table 1. The lines Fairview to Gilroy, Fremont to Sargent, and Canada to Sargent cross creeping sections of the San Andreas and Calaveras faults at low angles and thus have high rates of secular line-length change. All the lines crossing the Calaveras fault have accelerated rates of line-length change after the 1979 Coyote Lake earthquake that appear to return to normal about 1 yr after the earthquake. We exclude the anomalous 1979.9 data (arrows, fig. 2*C*) from our analysis. The coseismic offsets listed in table 1, therefore, include this postseismic transient.

BAY SOUTH NETWORK

The Bay South network extends to the northwest from stations LP1, Gilroy, and Sheep; the subset of lines measured before and after the 1989 Loma Prieta earthquake is shown in figure 1. The rupture zones of the 1979 Coyote Lake, 1984 Morgan Hill, and 1986 Mount Lewis earthquakes are along the east edge of this network. We first discuss complexities in the measurement history, then the sites with multiple main stations, and, finally, the measurements.

Several different survey monuments were used at stations American and Sheep (fig. 1) because tree growth blocked the lines-of-sight. We use local surveys to obtain a continuous time series for the line lengths into stations Sheep and American. As discussed earlier, we ignore possible error introduced by eccentric corrections. At station Sheep, some lines are corrected to station SheepRM1, and others to station SheepRM2, depending on which station has the most observations. We use different stations at Mount Hamilton and Loma Prieta, depending on the direction of the line. At Mount Hamilton, we use station Hamilton for most lines, and station Hamil Ec for the lines to stations Sheep and Llagas. At Loma Prieta, we use the station Loma USE for the lines to the north, and station LP1 for the lines to the south. The lines from station Loma USE are discussed in the next section.

The nine lines between stations Canada, Gilroy, Sheep, Llagas, LP1, and Hamilton (fig. 1) are near the rupture zones of the 1979 Coyote Lake, 1984 Morgan Hill, and 1989 Loma Prieta earthquakes, and we calculate the coseismic offsets for these earthquakes. The line-length change as a function of time for these lines is plotted in figure 3*A*. We measured the lines Llagas to SheepRM2, Hamilton to Sheep, and Hamil Ec to Llagas frequently after the 1979 Coyote Lake and 1984 Morgan Hill earthquakes and observed accelerated line-length changes for about 1 yr after these earthquakes. The time decay of this transient deformation is clearest along the line Hamil Ec to Llagas. We excluded the anomalous observations (data points marked with horizontal arrows and between vertical arrows, fig. 3*A*) from our analysis.

We calculated the coseismic offsets at the times of the 1984 Morgan Hill and 1989 Loma Prieta earthquakes along

Figure 3.—Line-length change (observed line length L less a constant nominal length L_0) as a function of time between stations in Bay South network. Curves show best-fitting linear rate of line-length change from data points; error bars, 1σ. *A*, Lines east of the San Andreas fault and near rupture zones of 1979 Coyote Lake and 1984 Morgan Hill earthquakes. Offsets occur at times of 1979 Coyote Lake, 1984 Morgan Hill, and 1989 Loma Prieta earthquakes. Data points designated by horizontal arrows and between vertical arrows were excluded from anlaysis. *B*, Lines east of the San Andreas fault and near or north of rupture zone of 1984 Morgan Hill earthquake. Offsets occur at times of 1984 Morgan Hill and 1989 Loma Prieta earthquakes; curves for lines Allison to Hamilton and Amer RM3 to Hamilton (dashed section of curve) include offset for 1986 Mount Lewis earthquake. *C*, Lines crossing or west of the San Andreas fault. Offset occurs at time of 1989 Loma Prieta earthquake.

the lines between stations Hamilton, Allison, American, BMT RF, and Mindego (figs. 1, 3*B*). The lines Allison to Hamilton, Amer RM3 to Hamilton, and American to BMT RF are poorly fitted by a linear rate of line-length change (table 1). The lines into station American are steep, difficult to measure because of poor visibility (smog) in the

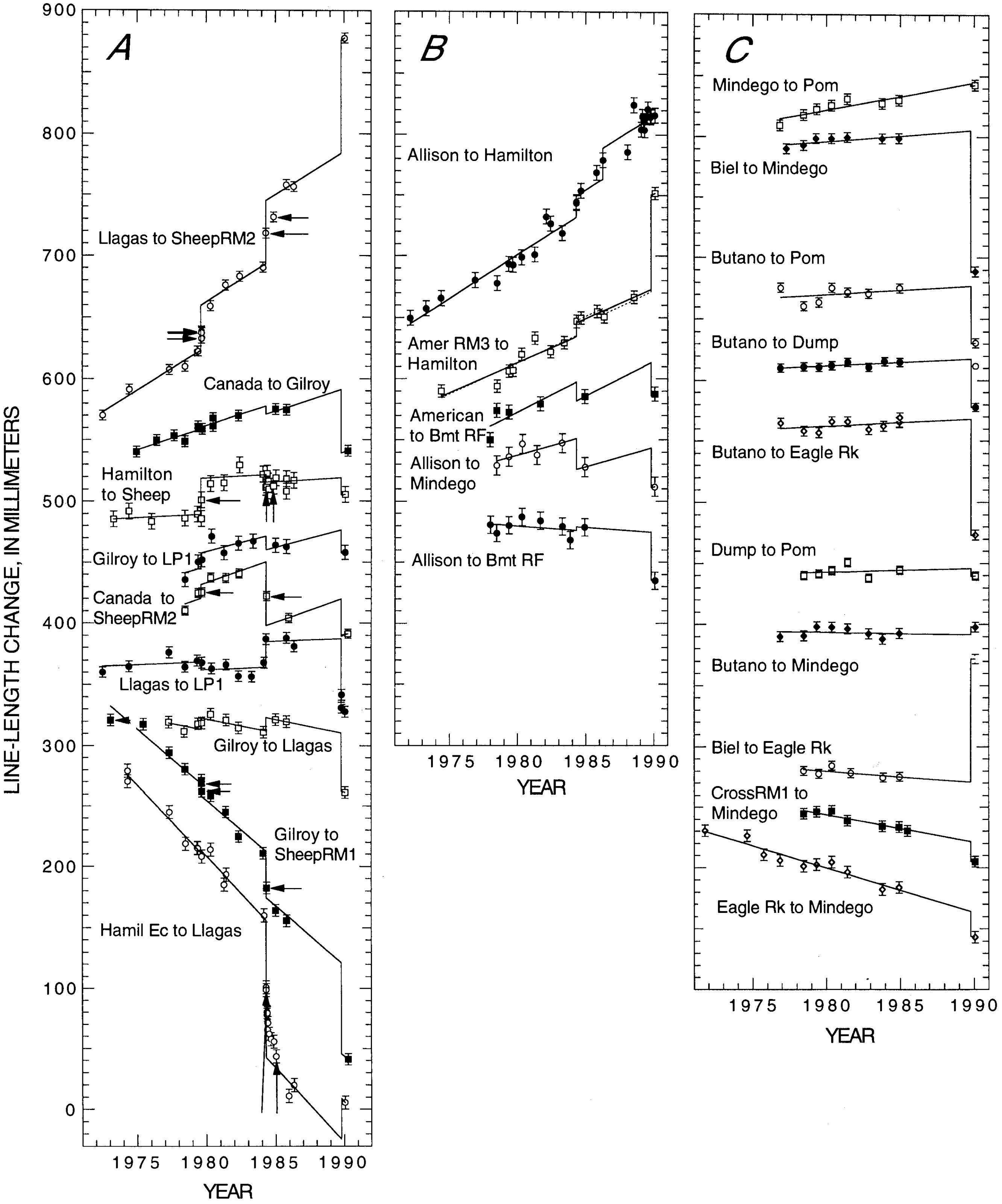

Santa Clara Valley; and Federal Aviation Administration regulations prohibit line-of-sight meteorologic flights. Because of these factors, our standard formula (eq. 1) probably underestimates the uncertainty in the measurements to station American. The line Allison to Hamilton has several unexplained, anomalous measurements. We included an additional coseismic offset at the time of the 1986 Mount Lewis earthquake along the lines Allison to Hamilton and Amer RM3 to Hamilton. The frequent measurements of the line Allison to Hamilton just before the 1989 Loma Prieta earthquake are from GPS surveys made as part of the Loma Prieta Monitor network. The GPS data, which allow a good determination of the coseismic offset at the time of the 1986 Mount Lewis earthquake, show no significant coseismic offset along this line from the 1989 Loma Prieta earthquake. The coseismic offset at the time of the 1986 Mount Lewis along the line Amer RM3 to Hamilton (dashed line, fig. 3*B*) is insignificant and is omitted from table 1.

The subset of the Bay South network west of the San Andreas fault is a group of relatively short lines for which we determined a coseismic offset only at the time of the 1989 Loma Prieta earthquake (fig. 3*C*). A linear rate of line-length change fits all the lines except Butano to Pom. We offer no explanation for the misfit of this line, but as shown in figure 3*C*, the scatter in the data is relatively small.

MEASUREMENTS FROM LOMA PRIETA

Loma Prieta, the summit of the Santa Cruz Mountains, is a primary point in the trilateration and GPS networks. The peak is covered with communication buildings and antennas, which limit lines-of-sight. We use two geodetic monuments located 160 m apart on opposite ends of the peak (fig. 4). Station Loma USE is a standard U.S. Army Corps of Engineers tablet set in a drill hole in bedrock at the north end of the peak, and station LP1 is a standard USGS National Center for Earthquake Research (NCER) tablet attached to galvanized pipe driven into well-consolidated sedimentary deposits at the south end of the peak. We use station Loma USE for most Geodolite lines directed to the north, station LP1 for lines directed to the south, and station LP1 for all GPS surveys. In 1983, vandals removed the tablet from station Loma USE; we set a new tablet, LomaNCER, in the drill hole and stamped it "Loma NCER 1983." For all practical purposes, stations Loma USE and LomaNCER represent the same physical point, and so we refer to all measurements from either tablet as being from station Loma USE. Of greater concern is the stability of the geodetic monuments on Loma Prieta. We determine the coseismic displacements of several monuments on Loma Prieta; description of these monuments is given in table 2. We start with a discussion of the coseismic offsets observed on the summit and then discuss the coseismic offsets between the summit and distant points.

Angle, distance, and GPS measurements on Loma Prieta allow us to determine the coseismic displacements between station LP1 and stations Loma USE, Loma CGS, Sue, and Loma DWR, and between station LP1 and stations Loma Azi and Loma No. 3 (fig. 4; table 3). We find that the group of stations at the north end of the peak moved 30 to 60 mm northeastward and 70 to 80 mm downward relative to station LP1. No significant change was noted in the interstation distance or relative elevation of station LP1, Loma Azi, or Loma No. 3. The coseismic displacements between stations on the north and south end of the peak are much greater than the uncertainty in the coseismic offset to distant stations. The important questions are whether the relative motion on Loma Prieta is from surficial fracturing of incompetent material and which, if any, of the monuments are stable. Robert McLaughlin (oral commun., 1989) observed no fractures on the peak except for a crack above a roadcut; he noted that the bedrock at the north end of the peak is not as competent as that along the ridge and at the south end of the peak. If the observed movements are the result of surficial fracturing induced by strong ground motions, then the sense of motion (downward relative to sta. LP1) and the geology suggest that the stations at the north end of

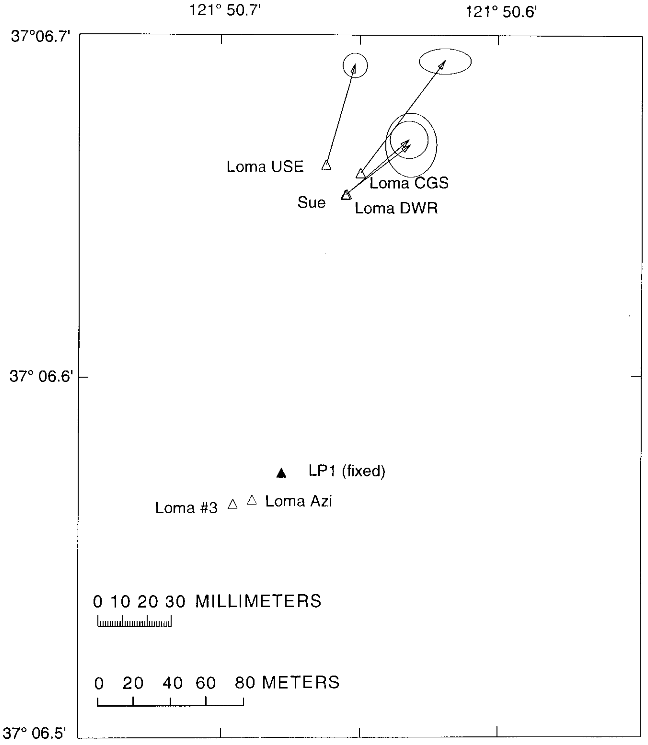

Figure 4.—Schematic map of Loma Prieta area, showing locations of some monuments on peak and coseismic offsets relative to station LP1.

Table 2.—*Description of monuments on Loma Prieta*

[NCER, National Center for Earthquake Research; USGS, U.S. Geological Survey]

Station	Stamping	Agency	Year established
LP1	LOMA PRIETA NET 1	USGS NCER	1970
Loma USE	LOMA PRIETA 2 1957	U.S. Army Corps of Engineers.	1957 (removed in 1983)
Loma NCER	LOMA 1983	USGS NCER	1983 (set in drill hole of sta. Loma USE)
Loma CGS	LOMA PRIETA 1851 1958	U.S. Coast and Geodetic Survey.	1958
Loma DWR	Unstamped	California Department of Water Resources.	1960
Loma Azi	LOMA PRIETA 1954	U.S. Coast and Geodetic Survey.	1954 (azimuth mark)
Loma No. 3	LOMA PRIETA #3 1960	California Department of Water Resources.	1960
Sue	Sue 79 SC Cnty Survey	Santa Clara County	1979

Table 3.—*Coseismic displacements between monuments on Loma Prieta relative to station LP1 (fig. 1)*

Station	North (mm)	East (mm)	Up (mm)	Length (mm)
Loma USE/Loma NCER	42±2	12±2	−71±6	42±2
Loma CGS	47±2	35±4	−78±6	54±2
Loma DWR	23±3	26±3	−82±6	27±3
Sue	21±5	27±4	−73±6	25±4
Loma Azi	---	---	−1±6	3±2
Loma No. 3	---	---	−1±6	1±2

the peak are more likely to have been affected. We assume that station LP1 is stable, and correct the observations from station Loma USE for the local coseismic offset. We return to this question in the section below entitled "Simple Dislocation Model of the Earthquake Rupture." We now discuss the coseismic offsets or displacements measured between Loma Prieta and distant points.

The 6-km-long lines LP1 to LP2 and LP1 to LP4 cross the San Andreas and Sargent faults near the epicenter of the 1989 Loma Prieta earthquake (fig. 1). The orientation of these lines and the close proximity of these stations to the faults make them sensitive to shallow lateral slip across the faults; that is, line-length change will be a large fraction of the amount of shallow lateral slip on the faults. We measured the lines every few years beginning in 1970 and last in 1981. The long gap (fig. 5) between the last measurement and the earthquake is not so important because of the relatively low rates of secular line-length change (table 1). These rates are consistent with little or no shallow lateral slip (creep) on the San Andreas or Sargent fault in the years before the 1989 Loma Prieta earthquake. Right-lateral shear from loading of the San Andreas fault would slowly shorten the north-south-trending line LP1 to LP4 and extend the east-west-trending line LP1 to LP2. Our linear fits show that the line LP1 to LP4 contracted at a significant rate (-4.0±0.8 mm/yr) but that the line LP1 to LP2 also contracted (-1.5±0.8 mm/yr). The scatter in these linear rates of line-length change are 2 to 3 times larger than the 3 mm expected for a 6-km-long line. The lines are steep, and at different times the laser was partly blocked by trees or bushes at stations LP2 and LP4. This combination of circumstances can result in partial illumination of the bank of retroreflectors, making the perceived height of the reflector incorrect and any misalignment of the reflectors critical. Although the scatter about the linear fits is larger than expected, we identified only one clear outlier, the first (Oct. 19, 1989) postearthquake survey of the distance from station LP1 to station LP4 (arrow, fig. 5). This distance is more than 20 mm shorter than other Geodolite and GPS measurements made 3 days to 2 months later. Both lines shortened during the earthquake, but the coseismic offsets are only a small fraction of the coseismic slip across the rupture zone and are consistent with the observation of no tectonic surface rupture. The secular and coseismic shortening of the line LP1 to LP2 suggests a component of reverse slip on one or both of the faults. Station LP2 is located on Skyland Ridge but is well beyond the south limit of a zone of conspicuous extensional cracks mapped by Ponti and Wells (1991).

Loma Prieta is the central of four sites frequently monitored with Geodolite and GPS measurements. Monthly Geodolite measurements of the lines from station Loma USE to stations Eagle Rk, Allison, and Hamilton (fig. 1) began in 1981 (Lisowski and others, 1990b, 1993), and these lines were measured 2 weeks before and 2 days after the earthquake. The line from station Loma DWR to station PR 6 was monitored for about 1 yr, beginning in 1983. Monthly GPS measurements of the lines between stations LP1, Eagle Un, and Allison began in 1987. Station Eagle Un is the alternative site used for GPS measurements because the station used in Geodolite surveys, Eagle Rk, is located next to a large, metal-covered lookout tower. Station Hamilton was occupied once in 1988 and regularly, beginning in 1989. GPS measurements of the lines between stations LP1, Eagle Un, Allison, and Hamilton were made 2 weeks before and a few days after the earthquake. Station Brush 2 was occupied once in 1988, once in 1989, and regularly after the earthquake. A VLBI station, Fort Ord, located 7 km to the north was occupied in 1987 and simultaneously with station Brush 2 in 1988. No direct measurements were made from station Brush 2 in 1987. We use the 1988 eccentric tie to reduce the 1987 observations at station FortOrd to those at station Brush 2. We assume no relative motion between stations Brush 2 and FortOrd, and we include the random error of the eccentric tie in the uncertainty of the reduced 1987 measurements.

We computed the secular rate of line-length change and the coseismic offset for the 1987–90 subset of the frequent Geodolite and GPS measurements (fig. 6). Note that the Geodolite measurements are from station Loma USE, whereas the GPS measurements are from station LP1. The secular rates of line-length change measured with Geodolite and GPS are similar, but the coseismic offsets differ. We obtain similar coseismic offsets if we correct for the coseismic motion between the stations (table 1). Savage and Lisowski (in press) discuss possible changes in the extension rates of these lines and vectors after the 1984 Morgan Hill and 1989 Loma Prieta earthquakes.

The GPS measurements provide all three components of the coseismic displacement between stations Allison,

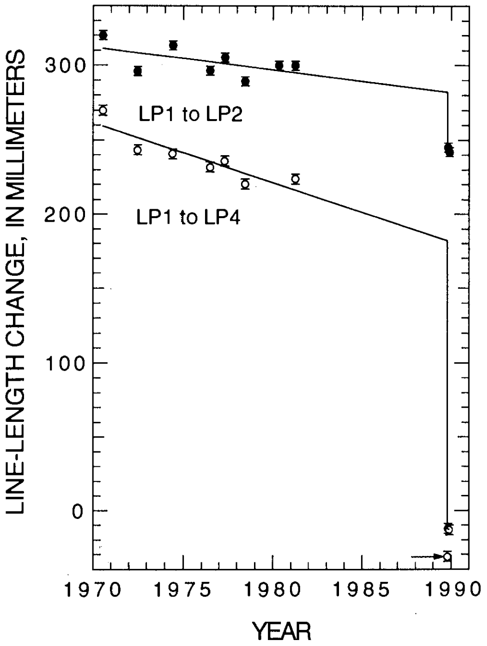

Figure 5.—Line-length change (observed line length L less a constant nominal length L_0) as a function of time along two 6-km-long lines measured from station LP1. Curves show best-fitting linear rate of line-length change from data points; error bars, 1σ. Offset occurs at time of 1989 Loma Prieta earthquake. Arrow designates data point that was excluded from analysis.

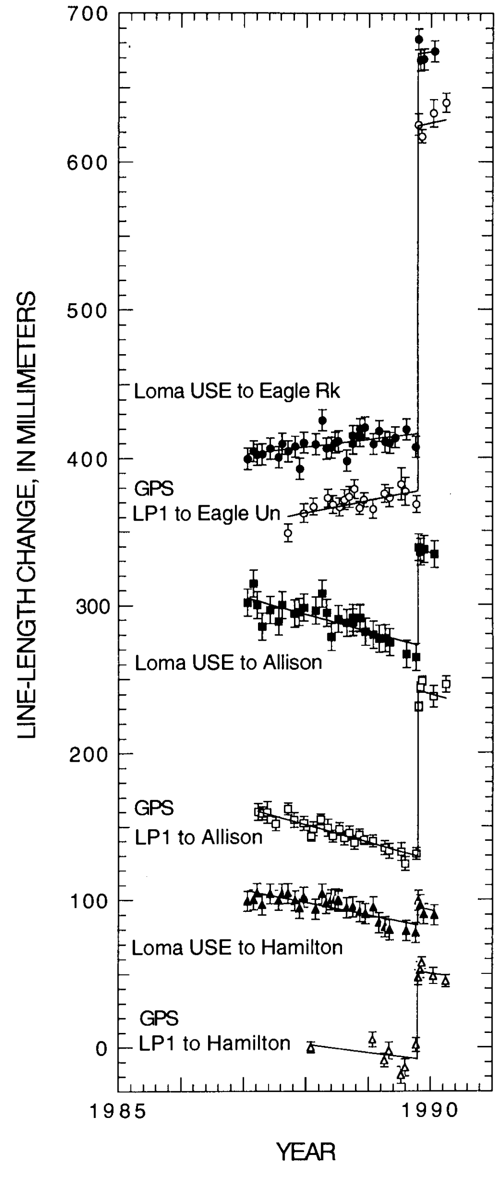

Figure 6.—Line-length change (observed line length L less a constant nominal length L_0) as a function of time along a subset of three frequently measured lines between Geodolite and Global Positioning System stations. Curves show best-fitting linear rate of line-length change from data points; error bars, 1σ. Offset occurs at time of 1989 Loma Prieta earthquake. Note large difference between offsets along lines Loma USE to Allison and LP1 to Allison, and along lines Loma USE to Hamilton and LP1 to Hamilton.

Eagle Un, Hamilton, LP1, and Brush 2. The changes in the north, east, and up vector components relative to station LP1 in a local coordinate system are plotted in figure 7. For example, the coseismic motion of station Allison relative to station LP1 is north, west, and up. We find that the rates of change in some of these components before and after the earthquake differ significantly (table 4). The rate of change in the vertical component between stations LP1 and Brush 2 is not well determined, and so we also compute the offset by differencing the weighted-mean value before and after the earthquake (table 4). The only direct measure of elevation change reported here comes

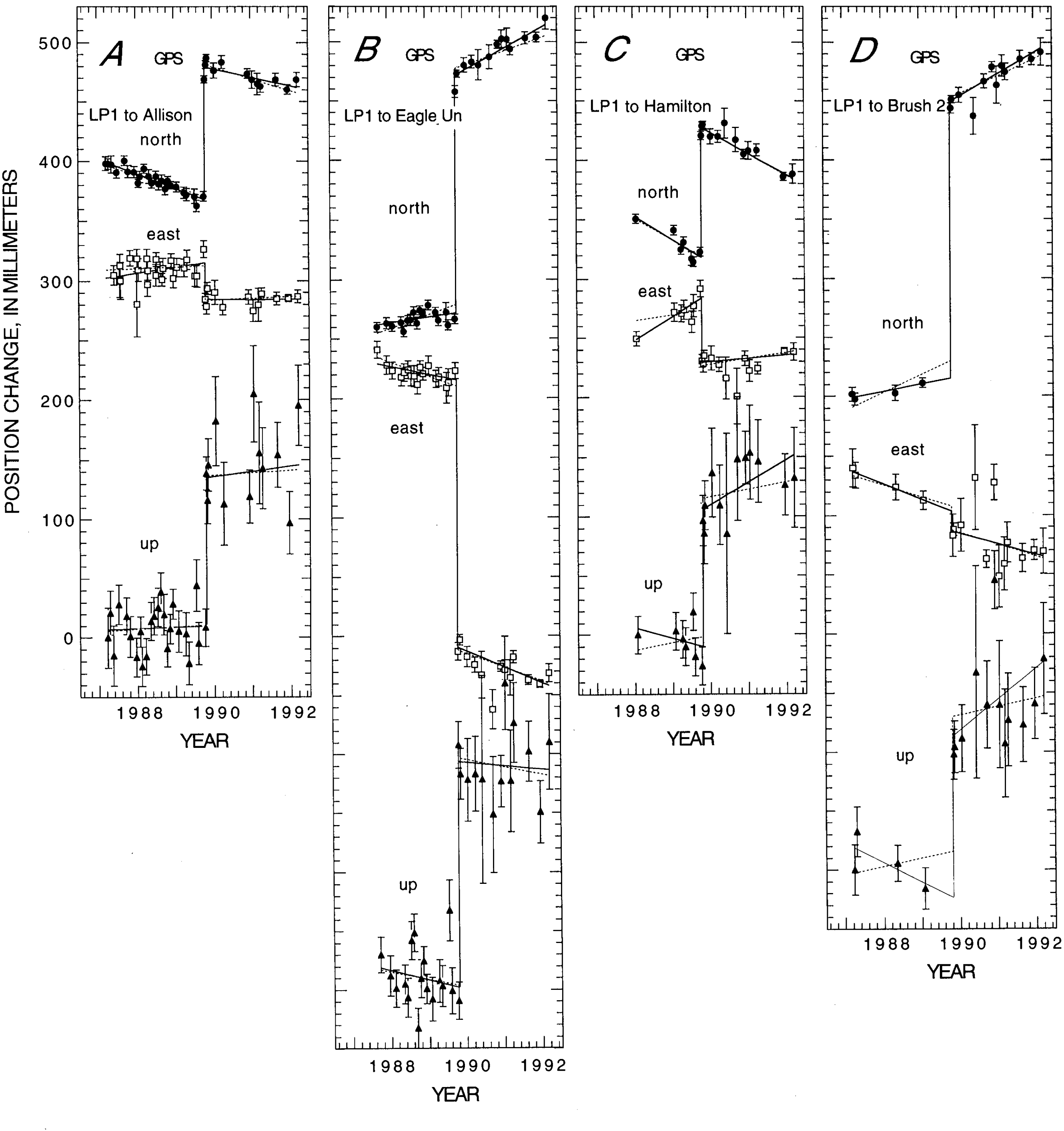

Figure 7.—Position change (north, east, and up vector components C less a constant nominal component C_0) as a function of time between stations LP1 and (*A*) station Allison, (*B*) station Eagle Un, (*C*) station Hamilton, and (*D*) station Brush 2. Curves show best-fitting linear rate of line-length change from data points; error bars, 1σ. Offset occurs at time of 1989 Loma Prieta earthquake.

Table 4.—*Changes in the vector components of coseismic displacement and coseismic offsets along lines in the Loma Prieta Monitor network*

[All values are Global Positioning System measurements relative to station LP1 (fig. 1) within a local coordinate system at the second station]

	Rate before earthquake (mm/yr)	Rate after earthquake (mm/yr)	Rate change (mm/yr)	Coseismic offset (mm)
		LP1 to Allison		
North	−12.2±1.2	−6.5±1.7	5.7±2.1	111.1±2.3
East	4.3±2.4	.1±1.4	−4.2±2.8	−31±3.6
Up	1.2±5.7	8.4±6.7	7.2±8.8	123.5±9.8
Length	−12.4±1.2	−6.5±1.7	−6.5±1.7	112±2.2
		LP1 to Eagle Un		
North	4.7±2.5	14.5±1.7	9.8±3.0	201.7±3.3
East	−6.7±2.7	−9.9±2.4	−3.2±3.6	−228.2±4.8
Up	−8.1±9.9	4.2±7.2	12.3±12.2	186.9±13.8
Length	7.4±2.6	11.7±2.3	4.3±3.5	250.6±4.6
		LP1 to Hamilton		
North	−19.7±4.2	−16.6±1.2	3.1±4.4	109.4±2.8
East	20.4±6.1	4.1±1.4	−16.3±6.3	−53.4±4.5
Up	−9.5±10.4	17.7±4.6	27.2±11.4	120.0±8.4
Length	−4.8±5.2	−11.1±1.1	−6.3±5.3	60.4±4.1
		LP1 to Brush		
North	6.4±1.7	13.4±1.7	7.0±2.4	235.2±3.3
East	−13.1±2.9	−4.3±2.3	8.8±3.7	−21.8±5.4
Up	−16.5±13.6	12.9±3.9	29.4±14.1	128.6±21.8
Up[1]				118.3±27.6
Length	−7.8±1.8	−14±1.9	−6.2±2.6	−237.8±3.5

[1] Difference of mean values before and after the earthquake.

from the GPS vectors. We note that Loma Prieta subsided about 0.12 m relative to stations Allison and Hamilton and about 0.25 m relative to station Eagle Rk.

Four Geodolite lines to stations in the Bay South network were measured from station Loma USE (fig. 8). We corrected these measurement after the earthquake for the coseismic offset of station Loma USE relative to station LP1. We calculated the coseismic offsets at the times of the 1984 Morgan Hill and 1989 Loma Prieta earthquakes along the lines from station Loma USE to stations Mindego, Biel, BMT RF, and American (fig. 1). The line Loma USE to American is poorly fitted by a linear rate of line-length change (table 1). As mentioned above, the lines into station American are difficult to measure, and the previous error estimate is probably too small.

CHASE NETWORK

The 2-km-aperture Chase network (fig. 9) extends across the Sargent fault and has station Gilroy (Ch4) in common with the South Bay and Hollister networks (fig. 1). Three of its stations are southwest of the Sargent fault, and the other five are northeast of the fault. We surveyed the Chase network annually with a Geodolite between 1970 and 1976, and once more in 1980. The network was surveyed again in 1990, 1 yr after the 1989 Loma Prieta

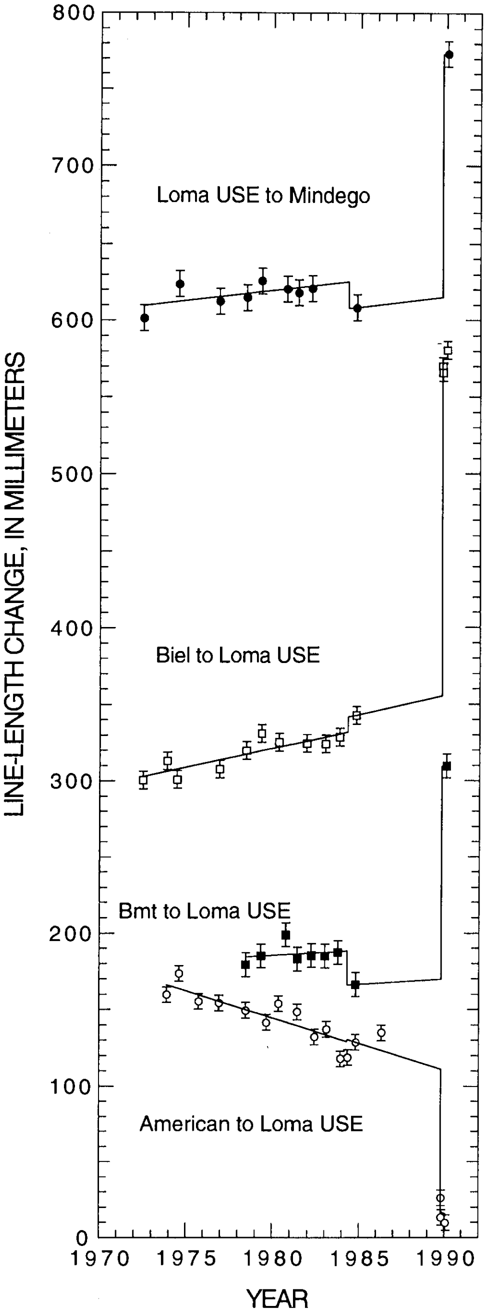

Figure 8.—Line-length change (observed line length L less a constant nominal length L_0) as a function of time between station Loma USE and stations in Bay South network. Curves show best-fitting linear rate of line-length change from data points; error bars, 1σ. Offsets occur at times of 1984 Morgan Hill and 1989 Loma Prieta earthquakes.

earthquake. We used end-point meteorology in the 1990 survey only. The relatively low rates of line-length change in the northeastern part of the network (fig. 10*A*) and the significant rates of extension and contraction in the low-angle fault-crossing lines (fig. 10*B*) are consistent with 2±1 mm/yr of shallow creep on the Sargent fault and an accumulation of right-lateral shear strain at the rate of 1 ppm/yr in the network. The estimated coseismic offsets are substantial but poorly determined because of the long interval between the last survey and the earthquake. A few centimeters of sympathetic slip on the Sargent fault during the 1984 Morgan Hill and 1989 Loma Prieta earthquakes is possible and not constrained by our observations. Such slip would shorten the north-south and extend the east-west fault-crossing lines by a large fraction of the lateral-slip amplitude. We see no such systematic pattern in the individual lines, possibly owing to the strain imposed by the 1989 Loma Prieta earthquake. The largest coseismic offsets are along in north-south-trending lines along the east edge of the network (lines Ch5 to Ch6, Ch1 to Ch6, Ch4 to Ch5), which show extensions of 30 to 60 mm.

BLACK MOUNTAIN NETWORK

The 3-km-aperture Black Mountain network (figs. 11, 12), which straddles the San Andreas fault on the southern part of the San Francisco peninsula, includes stations Mindego and BMT RF (also called BMT8) in common with the South Bay network (fig. 1). We surveyed the Black Mountain network with a Geodolite nearly annually from 1970 to 1981 and less frequently thereafter; the last survey was just 2 months before the 1989 Loma Prieta earthquake. We also surveyed the network 2 months, 1 yr, and 2 yr after the earthquake. Aircraft-flown metrology was used in all but the second survey after the earthquake; therefore, the uncertainty of a typical observation is that given by equation 1.

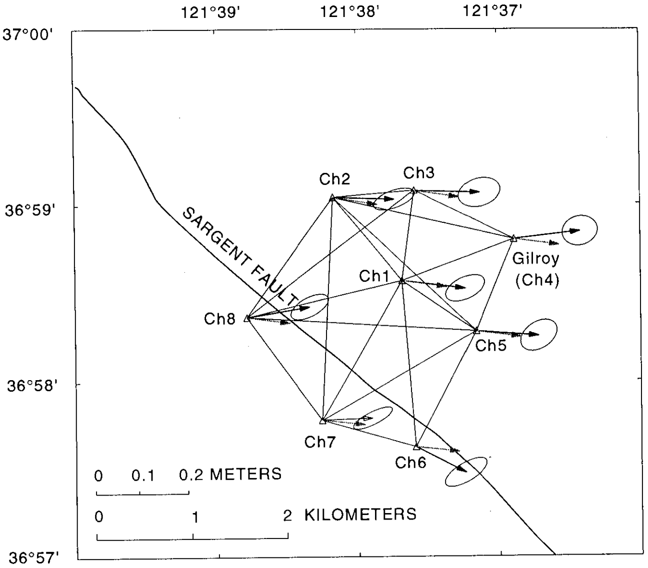

Figure 9.—Chase small-aperture network, showing observed (black vectors, with 95-percent-confidence ellipses) and calculated (gray vectors) coseismic displacements at Geodolite stations. Station Gilroy (CH4) is in common with Bay South network.

The average rate of line-length change between stations in the Black Mountain network is less than 1.7 mm/yr (table 1), consistent with the strain rates expected across a locked San Andreas fault. Fault creep (continuous shallow slip) at rate of 1.5 mm/yr could also explain the rates of line-length change, but no other evidence for creep across this section of the San Andreas fault is available. Coseismic offsets are as large as 17 mm. These changes are about that expected from the strain released by earthquake rupture. Shallow slip on the San Andreas fault does not appear to have occurred in the network before or after the 1989 Loma Prieta earthquake. Langbein (1990) reported a few millimeters of postseismic slip along the San Andreas fault in a network located near the northwest end of the Loma Prieta rupture zone.

VLBI OBSERVATIONS AT FORT ORD AND THE PRESIDIO

NASA's Crustal Dynamics Project and the NGS deployed mobile VLBI systems at Fort Ord, the Presidio, and Point Reyes before and after the 1989 Loma Prieta earthquake. The locations of these sites were determined with respect to a North American reference frame through the fixed VLBI observatories at Mojave, Hat Creek, and Vandenberg, Calif., and Fairbanks, Alaska. Clark and others (1990) estimated the coseismic displacement by projecting the average displacement rate from 1983 to the time of the earthquake. They reported that the Fort Ord site was displaced 49±4 mm toward N. 11°±4° E., and the Presidio site 12±5 mm toward S. 32°±4° E. No significant vertical displacement was observed at any site, and no significant horizontal displacement was observed at Point Reyes.

Two different sites were used at Fort Ord. From 1983 to February 1988, all observations were made from the main VLBI site at Fort Ord. Subsequently, this survey monument was destroyed by construction, and VLBI observations were transferred to a site 8.9 km to the south called FortOrdS. At the time of Clark and others' (1990) report, there was some uncertainty about the tie between the sites, and so Clark and others determined offsets both at the time of the monument change and at the time of the 1989 Loma Prieta earthquake. The VLBI station FortOrdS is on the same hill as the Geodolite and GPS station Brush 2.

SIMPLE DISLOCATION MODEL OF THE EARTHQUAKE RUPTURE

We use the coseismic offsets and displacements to estimate the geometry, location, and slip of the Loma Prieta rupture zone. We represent the Earth as an elastic half-space, and the rupture zone as a dipping rectangular cut (dislocation loop) buried in the half-space (Mansinha and Smylie, 1971). The slip across the cut (Burgers vector) is uniform and is allowed to have both dip-slip and strike-slip components. Our model has nine unknowns: four that describe the geometry of the dislocation (strike, dip, width, length), three its location (latitude, longitude, depth), and two the slip (slip, rake). We prescribe the geometry and location of the dislocation, and use a least-squares inversion to determine the slip and rake that best reproduce the observed coseismic surface deformation. There is no unique solution; our best-fitting model provides the minimum normalized rms residual of the data to the model (eq. 5). Despite coseismic offsets that average 15 times larger than the instrument noise, we find that a surprisingly wide range of model faults adequately fit the data.

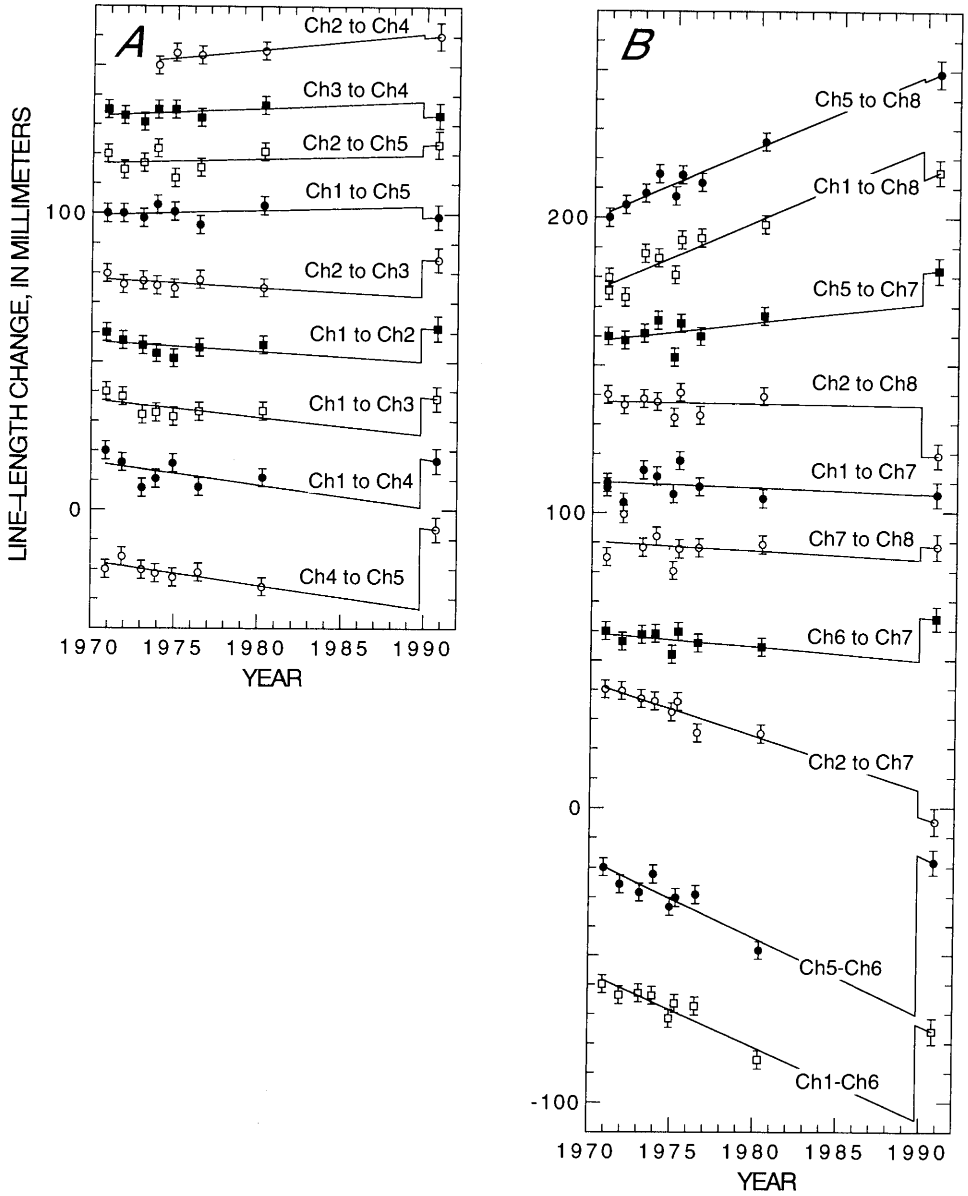

Figure 10.—Line-length change (observed line length L less a constant nominal length L_0) as a function of time between stations in Chase network along lines that (*A*) do not cross or are east of and (*B*) cross or are west of the Sargent fault. Curves show best-fitting linear rate of line-length change from data points; error bars, 1σ. Offset occurs at time of 1989 Loma Prieta earthquake.

The geometry of the initial model fault is based on the locations of the main shock and aftershocks (Dietz and Ellsworth, 1990). The main shock has a focal depth of 17.6 km. The aftershocks define a 45-km-long zone trending N. 50° W., extending from a depth of 4 to 18 km, and dipping 65° SW. Aftershocks in the southeastern 10 km of the rupture zone are on a near-vertical plane aligned with the San Andreas fault and extending to a depth of only 10 km.

How we treat the data from Loma Prieta is critical to our modeling of the fault rupture. Loma Prieta, which is close to the center of the rupture zone, has the largest and best determined coseismic offsets and displacements. The coseismic displacement between the monuments on Loma Prieta is several times larger than the uncertainty in the coseismic offsets to distant sites. We can use the data as is, correct them by assuming that one of the monuments is stable, downweight them, or disregard them. We assume that station LP1 is stable and correct the data from station Loma USE for its coseismic offset relative to station LP1. Even with this assumption, which might be considered optimistic, some crucial rupture parameters are not well constrained by our geodetic data.

The geometry, location, and slip of our best-fitting rupture model are listed in table 5. Most of the observed coseismic deformation can be reproduced by 5±4 m of slip at a rake of 153°±6° on a 34±6-km-long buried rupture plane dipping 79°±8° SW. and extending from a depth of 7±3 to 13±5 km. The geodetic moment ($M_0=\mu Ab$, where μ is the rigidity [3×10^{10} Pa], A is the area of the slip zone, and b is the slip amplitude) is $2.7\pm0.3\times10^{19}$ N-m. The normalized rms residual is 2.71; that is, the average residual is about 3 times larger than our previous error estimate.

We used the coseismic offsets and the GPS- and VLBI-measured displacements to determine the coseismic station displacements, which are compared with those calculated from the best-fitting uniform-slip dislocation model in figures 9, 11, and 13. The displacements calculated from the coseismic offsets alone are uncertain by a rigid-body motion of the network as a whole. The VLBI-measured displacement of station FortOrdS determines

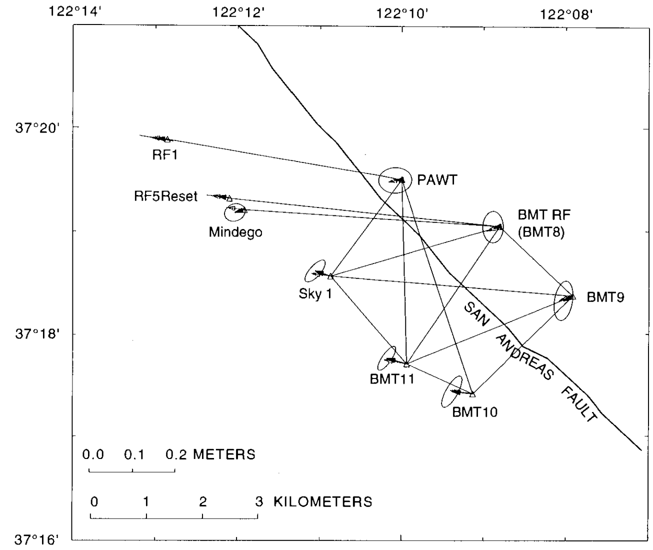

Figure 11.—Black Mountain small-aperture network, showing observed (black vectors, with 95-percent-confidence ellipses) and calculated (gray vectors) coseismic displacements at Geodolite stations. Station Mindego and BMT RF (BMT8) are in common with Bay South network.

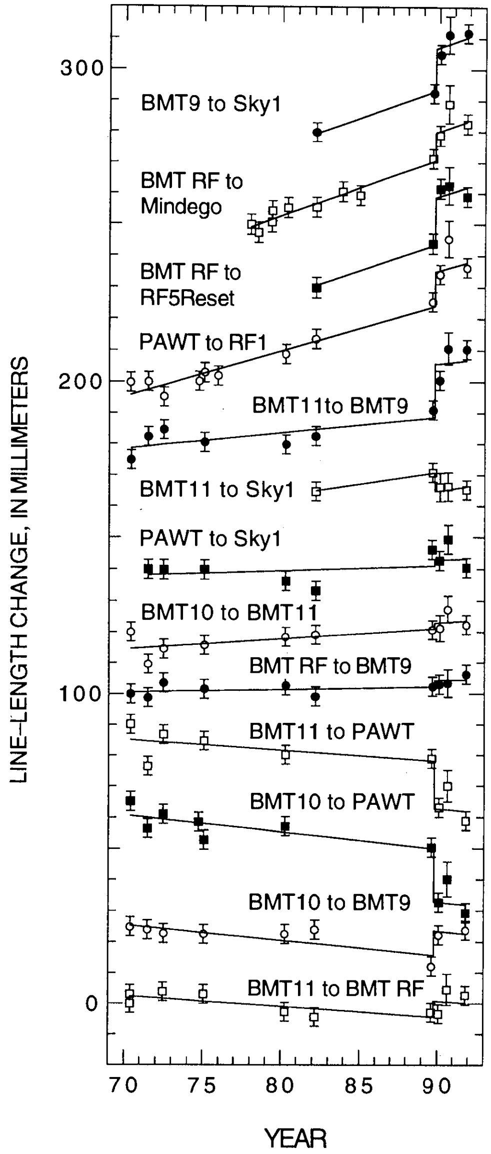

Figure 12.—Line-length change (observed line length L less a constant nominal length L_0) as a function of time between stations in Black Mountain network. Curves show best-fitting linear rate of line-length change from data points; error bars, 1σ. Offset occurs at time of 1989 Loma Prieta earthquake.

Table 5.—*Parameters of best-fitting, uniform-slip dislocation model*

[Data from station Loma USE (fig. 1), corrected for coseismic offset relative to station LP1. Depth is to top of fault plane; width is downdip; latitude and longitude locations are surface projection of northwest corner of fault plane. Uncertainties are ranges of values with 68-percent-confidence limit of model]

Strike (from north)	Dip	Length (km)	Width (km)	Depth (km)	Lat N.	Long W.	Slip (m)	Rake	Moment (10^{19} N-m)
138°±4°	79°±8°	34±6	6±5	7±3	37.19°±0.02°	121.99°±0.03°	6±4	153°±6°	2.7±0.3

the rigid-body translation of the network, and the GPS-measured displacement of stations Allison, Hamilton, and EagleUn relative to station LP1 determines the rigid-body rotation of the network. The combination of VLBI, GPS, and EDM data thus provides a unique solution for the observed displacement of the stations within the geometri-

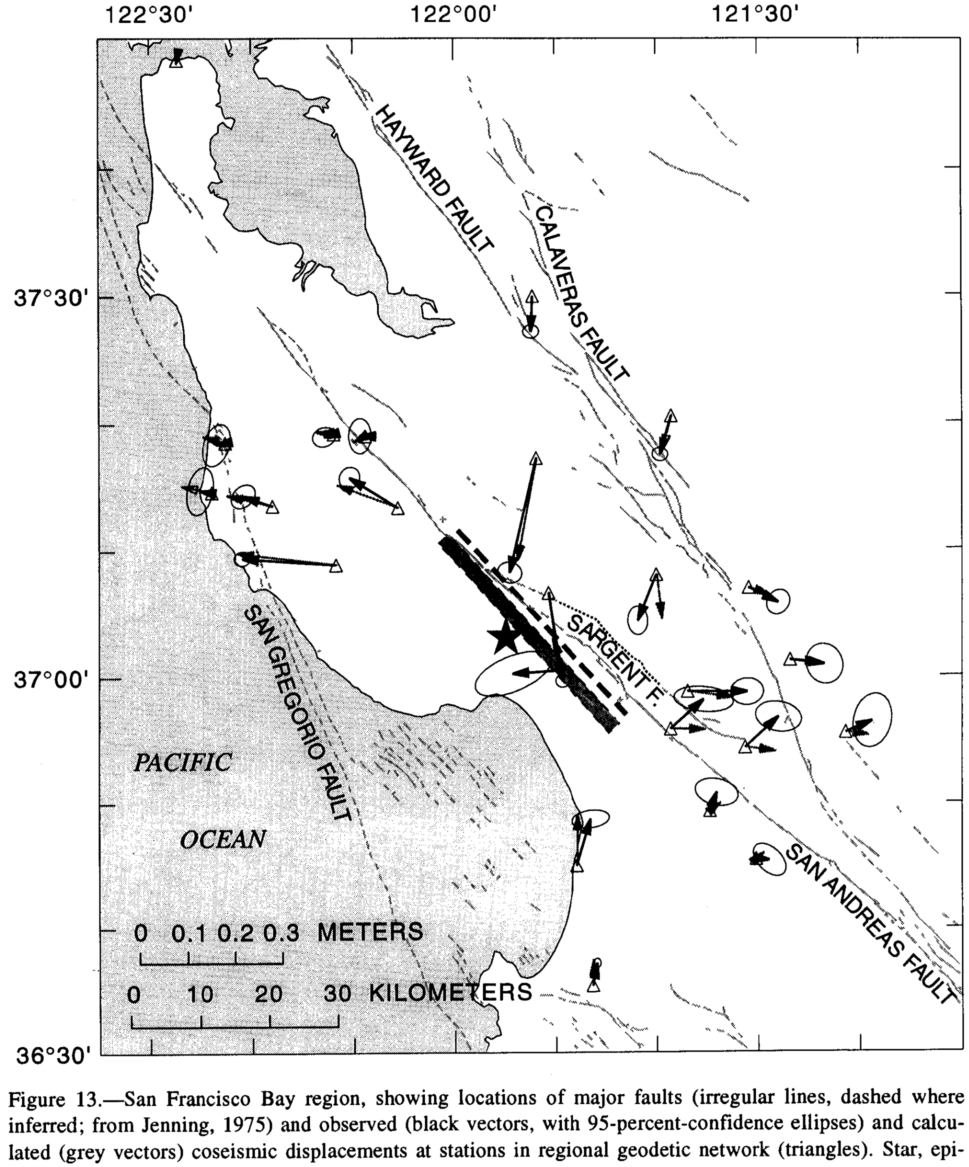

Figure 13.—San Francisco Bay region, showing locations of major faults (irregular lines, dashed where inferred; from Jenning, 1975) and observed (black vectors, with 95-percent-confidence ellipses) and calculated (grey vectors) coseismic displacements at stations in regional geodetic network (triangles). Star, epicenter of 1989 Loma Prieta earthquake; dashed rectangle, surface projection of best-fitting, uniform-slip dislocation model for earthquake; heavy-dashed line, intersection of rupture plane with surface of the Earth.

cally rigid part of the network. Stations Cross, LP2, LP4, Hollis, and PR6 are measured from only one other station, and so we exclude these stations from our displacement solution. The displacements of many stations are overdetermined (there are 22 degrees of freedom), and the normalized rms residual from the least-squares adjustment for the coseismic displacements is only 1.1 times larger than expected, indicating that the observed changes are self-consistent and that our previous error estimate is reasonable.

The Black Mountain and Chase networks each include one station (Gilroy in the Chase network, BMT RF in the Black Mountain network) for which the displacement is uniquely determined. The displacement of station Mindego in the Black Mountain network also is uniquely determined, but this station is not rigidly tied to the other stations in the network. Stations Gilroy and BMT RF fix the rigid-body translation of these networks as a whole, but the displacements of the other sites in the networks are uncertain by a rigid-body rotation about this station. To test our model, we add the rigid-body rotation that best reproduces the predicted displacements (so-called model coordinate solution of Segall and Matthews, 1988).

The station displacements most poorly fitted by the model are in the epicentral area (sta. Vargo, fig. 1), and between the Calaveras and San Andreas faults (stas. Llagas, Gilroy, Chamber, Sargent). The measurements of lines between the Calaveras and San Andreas faults show coseismic effects and aftereffects from the 1979 Coyote Lake, 1984 Morgan Hill, and 1989 Loma Prieta earthquakes. We excluded anomalous data from as long as 1 yr after these earthquakes from our analysis. Along these lines, our assumption of a linear rate of line-length change over time, even with these anomalous data excluded, may be incorrect. Other known sources of deformation, such as triggered right-lateral slip on the Calaveras and San Andreas faults southeast of the rupture zone (Behr and others, 1990; Galehouse, 1990; McClellan and Hay, 1990) are small and most likely surficial phenomena. No obvious sources are known that could account for the difference between predicted and observed coseismic displacements in the area between the San Andreas and Calaveras faults. Careful modeling of the 1979 Coyote Lake and 1984 Morgan Hill earthquakes might eliminate some uncertainties about the rate of deformation during the decade before the 1989 Loma Prieta earthquake.

The fit of our model to the data could also be improved with a more complex model of the Earth (Eberhart-Phillips and Stuart, 1992), the rupture geometry (Snay and others, 1991), or the slip distribution (Marshall and others, 1991; Árnadóttir and Segall, 1994; Marshal and Stein, this chapter), or by including other sources of deformation. Our best-fitting rupture model is the simplest that can explain most of the coseismic deformation reported here. We show in the next section that the geometry, location, and slip of even this simple model are poorly resolved by the data.

DISCUSSION

How well do our geodetic data define the Loma Prieta rupture zone? To assess the range of model faults consistent with our data, we randomly vary the seven parameters describing the fault geometry and location, and solve for the slip and rake with a least-squares inversion. We limit our search to faults that strike 125°–145° from north, dip 60°–90° SW., with a length of 25 to 45 km, a downdip width of 1 to 19 km, a latitude and longitude position ±5 km from that in the starting model, and a depth to the top of the rupture plane of 2 to 10 km. We use an *F*-ratio test to approximate confidence regions. Model faults within a particular confidence region result in a normalized rms residual, σ_0 (eq. 4), that is less than a particular value σ_{0a}. Given σ_{0opt} for the optimal model, all models with $\sigma_0<\sigma_{0a}$ are consistent at the 100α-percent-confidence level, where:

$$\sigma_{0\alpha} = \sigma_{0_{opt}}\left[1+\frac{m}{n-m}\mathrm{F}(m, n-m, 1-\alpha)\right]^{1/2}, \qquad (7)$$

and n is the number of model parameters, m is the number of data, and F is the F distribution with m unknowns and n–m degrees of freedom (Draper and Smith, 1981). That is, the confidence region for each parameter is approximated from the range of values given by all the models consistent with the optimal model at a specified confidence level. Remember that models with a normalized rms residual near 1, on average, reproduce the observed coseismic changes within their uncertainty. Árnadóttir and Segall (1994) found that the *F*-ratio test tends to slightly underestimate confidence regions relative to those predicted by bootstrapping techniques which rely on random resampling of the original data.

We attempt to reproduce n=99 data, 85 line-length changes, and 4 GPS (three vector components each)- and 2 VLBI (two vector components each)-measured displacements. The model fault is described by m=9 parameters. Our best-fitting rupture model has a normalized rms residual of 2.73, a misfit about 3 times the estimated error in the data. Using the *F*-ratio test (eq. 7), we find that rupture models with a normalized rms residual less than 2.97 are within the 95-percent-confidence limit of our best-fitting model, and those models with a normalized rms less than 2.87 are within the 68-percent-confidence limit of our best-fitting model. The normalized rms residual is plotted as a function of the fault geometry and location in figures 14*A* through 14*H*. The shape and edge of the cloud of data points are important to our discussion. The nor-

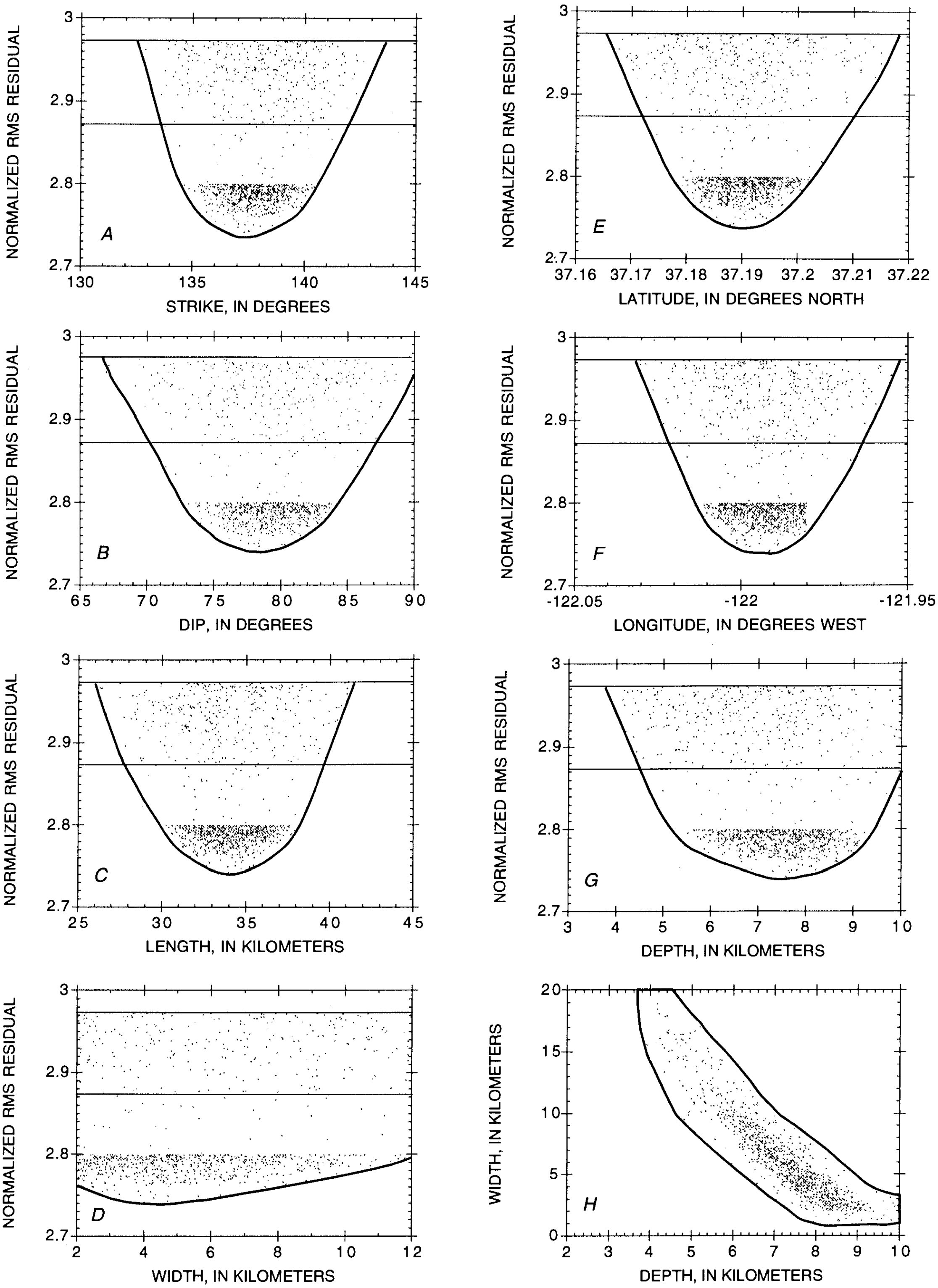

Figure 14.—Ranges of fault geometries and locations allowed at 95-percent-confidence limit in best-fitting, uniform-slip dislocation model for 1989 Loma Prieta earthquake. *A*, Fault strike. *B*, Fault dip. *C*, Fault length. *D*, Fault width. *E*, Latitude of source. *F*, Longitude of source. *G*, Depth of source. *H*, Width versus depth of source. *I*, Fault slip. *J*, Fault rake. *K*, Seismic moment.

malized rms residual has a well-defined minimum for all the fault geometry and location parameters except fault width, which is poorly resolved and correlates closely with fault depth. The normalized rms residual is plotted as a function of the inverted parameters of slip and rake, and the calculated geodetic moment, in figures 14*I* through 14*K*. The slip correlates closely with fault width, and because the width is poorly determined, the slip also is poorly determined. The rake and moment exhibit well-defined minimums. The uncertainties listed in table 5 are those that are within the 68-percent-confidence limit of our best-fitting model. We are, quite frankly, surprised at the range of model parameters that provide an adequate fit to the data, indicating that our surface geodetic data are rather insensitive to a buried source of deformation.

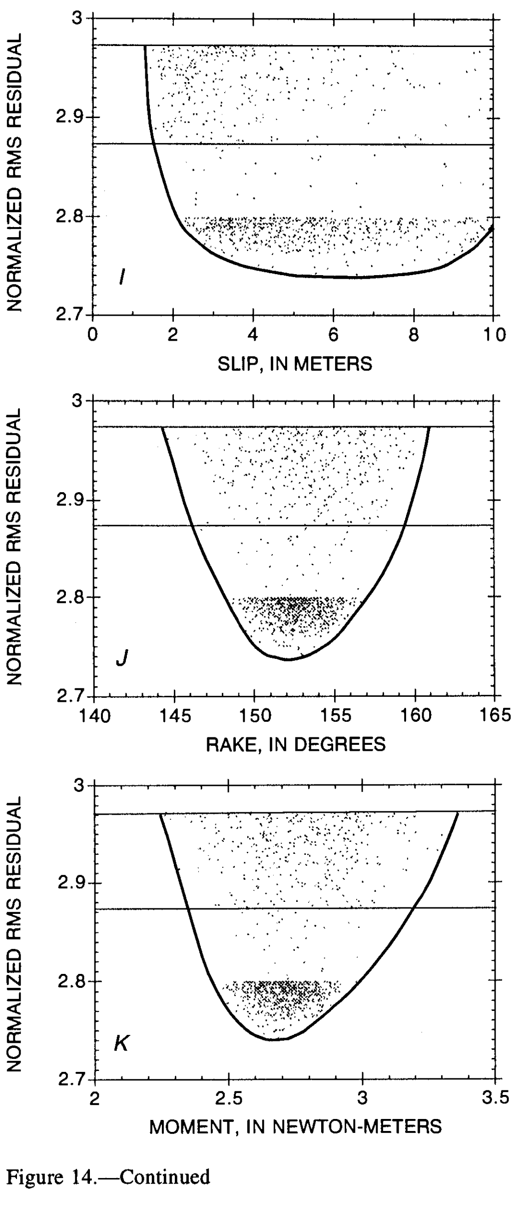

Figure 14.—Continued

ABSENCE OF SURFACE RUPTURE

The data plotted in figure 14 and listed in table 5 indicate that the geodetic observations are best fitted by a rupture that terminates well short of the Earth's surface. The lengths of the lines LP1 to LP2 and LP1 to LP4, which cross the San Andreas fault near the epicenter, changed by only a fraction of a meter (table 1), even though the total slip was more than 2 m. These results are quite consistent with the absence of any surface expression of primary rupture. There has been some discussion in the literature on the question of how much slip occurred along this section of the fault in the 1906 San Francisco earthquake. Thatcher and Lisowski (1987) inferred from triangulation observations that the average slip amplitude from the surface to 10-km depth was 2.6±0.2 m. Primarily on the basis of an observation of an apparent fault offset in the summit railway tunnel south of Wrights station (Lawson, 1908), Scholz (1985) argued that the slip amplitude along this section of the fault in 1906 was 1.5 m, significantly less than farther north along the peninsula, and that this section of the fault must rupture more frequently to make up the slip deficit that was "observed" in 1906. The occurrence of the 1989 Loma Prieta earthquake seems to support to this argument, although no surface slip was observed in 1989. Therefore, surface slip does not seem to be a valid criterion for earthquake prediction along this section of the San Andreas fault.

CONCLUSIONS

We use Geodolite and GPS surveys both before and after the 1989 Loma Prieta earthquake to estimate the coseismic offsets along 85 lines and at 4 sites. The coseismic displacment of two VLBI sites was previously determined by Clark and others (1990). To correct for secular offsets or displacements, we project the average rate of change to the time of the earthquake. The offsets and displacements are mostly consistent with a linear rate of change as a function of time, with offsets at the time of earthquakes. Along many lines, we allowed for additional offsets at the times of the 1979 Coyote Lake, 1984 Morgan Hill, and 1986 Mount Lewis earthquakes. Lines near the ruptures zones of the 1979 Coyote Lake and 1984 Morgan Hill earthquakes show accelerated rates of line-length change that appear to decay to the previously observed rates within about 1 yr. We excluded anomalous measurements after these earthquakes from the analysis.

Local surveys on Loma Prieta, a peak 3 km from the San Andreas fault and 11 km from the epicenter of the 1989 earthquake, show that monuments at the north end of the peak were displaced 30 to 60 mm to the northeast and subsided 70 to 80 mm relative to monuments about

160 m away on the south end of the peak. The sense of motion is consistent with shaking-induced instability of the north end of the peak, although no local ground fracturing was observed after the earthquake. In our analysis of the data from Loma Prieta to distant points, we assume that the southern stations are stable, and correct observations from the northern stations for local coseismic movements, although none of the stations on the peak may be stable. In any case, the occurrence of relative motion between the stations on Loma Prieta, with no obvious local ground fracturing, questions whether the observed changes to distant points truly represent tectonic deformation.

We use a Monte Carlo fault-parameter estimation to find a best-fitting, uniform-slip dislocation model and to assess the data sensitivity. Well-defined minimums in the normalized rms residual exist for all parameters describing the fault geometry and location, except fault width, which correlates closely with fault depth. The inverted parameter of slip correlates closely with fault width and exhibits no well-defined minimum in normalized rms residual. The inverted parameter of rake and the calculated geodetic moment, however, are well defined. Although the minimums in the normalized rms residual are well defined for most fault-rupture parameters, the uncertainty is quite large (table 5). The geodetic data, however, are consistent with the observation of no tectonic surface rupture.

The combination of Geodolite, GPS, and VLBI measurements provides a unique solution for the coseismic displacements. The normalized rms residual from the displacement adjustment indicates that our previous estimates of the average error in the coseismic offsets are only slightly low. The coseismic offsets of the geodetic stations located between the San Andreas and Calaveras faults to the east and south of the Loma Prieta rupture zone are poorly fitted by our dislocation model. Many of the lines in this area had not been measured since 1986, some since 1982, and all were affected by the 1979 Coyote Lake and 1984 Morgan Hill earthquakes. The deformation history of this region is complex, and our method may underestimate the error in the linear rates of line-length change and, correspondingly, in the coseismic offsets at the time of the 1989 Loma Prieta earthquake. There may be other unmodeled sources for the deformation, but the obvious choices of sympathetic slip on the San Andreas or Calaveras fault do not account for the observed changes.

ACKNOWLEDGMENTS

Immediately after the earthquake, we received valuable field assistance from K. Hudnut, F. Webb, and S. Larsen of the California Institute of Technology and M. Jackson of the University of Colorado. We appreciate the efforts of the current USGS field crew, W.K. Gross, G.D. Hamilton, J.M. Sutton, C. Stiffler, and K. Clark, and other individuals who served on past field parties. K. Wendt aided with the data reduction. We used a computer program provided by Paul Segall to calculate the coseismic displacements.

REFERENCES CITED

Árnadóttir, Thora, and Segall, Paul, 1994, The 1989 Loma Prieta earthquake imaged from inversion of geodetic data: Journal of Geophysical Research, v. 99, no. B11, p. 21835–21855.

Árnadóttir, Thora, Segall, Paul, and Matthews, M.V., 1992, Resolving the discrepancy between geodetic and seismic fault models for the 1989 Loma Prieta, California, earthquake: Seismological Society of America Bulletin, v. 82, no. 5, p. 2248–2255.

Bakun, W.H., Clark, M.M., Cockerham, R.S., Ellsworth, W.L., Lindh, A.G., Prescott, W.H., Shakal, A.F., and Spudich, Paul, 1984, The 1984 Morgan Hill, California, earthquake: Science, v. 255, no. 4659, p. 288–291.

Behr, Jeffrey, Bilham, Roger, Bodin, Paul, Burford, R.O., and Bürgmann, Roland., 1990, Aseismic slip on the San Andreas fault south of Loma Prieta: Geophysical Research Letters, v. 17, no. 9, p. 1445–1448.

Beutler, Gerhart, Abell, M.D., Bauersima, I., Gurtner, W., Mader, G.L., Rothacher, M., Schildknecht, 1987, Evaluation of the 1984 Alaska Global Positioning System campaign with the Bernese GPS software: Journal of Geophysical Research, v. 92, no. B2, p. 1295–1304.

Bürgmann, Roland, Arrowsmith, Ramón, and Dumitru, Trevor, 1994, Rise and fall of the southern Santa Cruz Mountains, California, from fission tracks, geomorphology, and geodesy: Journal of Geophysical Research, v. 99, no. B10, p. 20181–20202.

Clark, T.A., Corey, B.E., Davis, J.L., Elgered, G., Herring, T.A., Hinteregger, H.F., Knight, C.A., Levine, J.I., Lundquist, G., Ma, Choppo, Nesman, E.F., Phillips, R.B., Rogers, A.E.E., Rönnäng, B.O., Ryan, J.W., Schupler, B.R., Shaffer, D.B., Shapiro, I.I., Vandenberg, N.R., Webber, J.C., and Whitney, A.R., 1985, Precision geodesy using the Mark III very-long-baseline interferometer system: Institute of Electrical and Electronics Engineers Transactions on Geoscience and Remote Sensing, v. GE–23, no. 4, p. 438–449.

Clark, T.A., Ma, Choppo, Sauber, J.M., Ryan, J.W., Gordon, David, Shaffer, D.B., Caprette, D.S., and Vandenberg, N.R., 1990, Geodetic measurement of deformation in the Loma Prieta, California, earthquake with very long baseline interferometry: Geophysical Research Letters, v. 17, no. 8, p. 1215–1218.

Davis, J.L., Prescott, W.H., Svarc, J.L., and Wendt, K.J., 1989, Assessment of Global Positioning System measurements for studies of crustal deformation: Journal of Geophysical Research, v. 94, no. B10, p. 13635–13650.

Dietz, L.D., and Ellsworth, W.L., 1990, The October 17, 1989, Loma Prieta,California, earthquake and its aftershocks; geometry of the sequence from high-resolution locations: Geophysical Research Letters, v. 17, no. 9, p. 1417–1420.

Dixon, T.H., 1991, An introduction to the Global Positioning System and some tectonic applications: Reviews of Geophysics, v. 29, p. 249–276.

Dong, Danan, and Bock, Yehuda, 1989, Global Positioning System network analysis with phase ambiguity resolution applied to crustal deformation studies in California: Journal of Geophysical Research, v. 94, no. B4, p. 3949–3966.

Draper, N.R., and Smith, Harry, 1981, Applied regression analysis (2d ed.): New York, Wiley, 709 p.

Eberhart-Phillips, D.M., Stuart, W.D., 1992, Material heterogeneity simplifies the picture; Loma Prieta: Seismological Society of America Bulletin, v. 82, no. 4, p. 1964–1968.

Galehouse, J.S., 1990, Effect of the Loma Prieta earthquake on surface slip along the Calaveras fault in the Hollister Calif. area: Geophysical Research Letters, v. 17, no. 8, p. 1219–1222.

Hagar, B.H., King, R.W., and Murray, M.H., 1991, Measurement of crustal deformation using the Global Positioning System: Annual Reviews of Earth and Planetary Sciences, v. 19, p. 351–382.

Jennings, C.W., compiler, 1975, Fault map of California, with locations of volcanoes, thermal springs, and thermal wells: California Division of Mines and Geology Geologic Data Map 1, scale 1:750,000.

King, N.E., Savage, J.C., Lisowski, Michael, and Prescott, W.H., 1981, Preseismic and coseismic deformation associated with the Coyote Lake, California, earthquake: Journal of Geophysical Research, v. 86, no. B2, p. 892–898.

Langbein, J.O., 1990, Postseismic slip on the San Andreas Fault at the northwestern end of the 1989 Loma Prieta earthquake rupture zone: Geophysical Research Letters, v. 17, no. 8, p. 1223–1226.

Larson, K.M., and Agnew, D.C., 1991, Application of the Global Positioning System to crustal deformation measurement 1. Precision and accuracy: Journal of Geophysical Research, v. 96, no. B10, p. 16547–16565.

Lawson, A.C., chairman, 1908, The California earthquake of April 18, 1906; report of the State Earthquake Investigation Commission: Carnegie Institution of Washington Publication 87, 2 v.

Lisowski, Michael, Prescott, W.H., Savage, J.C., and Johnston, M.J., 1990a, Geodetic estimate of coseismic slip during the 1989 Loma Prieta,California, earthquake: Geophysical Research Letters, v. 17, no. 9, p. 1437–1440.

Lisowski, Michael, Prescott, W.H., Savage, J.C., and Svarc, J.L., 1990b, A possible geodetic anomaly observed prior to the Loma Prieta, California, earthquake: Geophysical Research Letters, v. 17, no. 8, p. 1211–1214.

Lisowski, Michael, Savage, J.C., and Prescott, W.H., 1991, The velocity field along the San Andreas fault in central and southern California: Journal of Geophysical Research, v. 96, no. B5, p. 8369–8389.

Lisowski, Michael, Savage, J.C., Prescott, W.H., Svarc, J.L., and Murray, M.H., 1993, No convincing precursory geodetic anomaly observed, The Loma Prieta, California, Earthquake of October 17, 1989—preseismic observations: U.S. Geological Survey Professional Paper 1550–C, p. C67–C72.

Mansinha, Lalatendu, and Smylie, D.E., 1971, The displacement fields of inclined faults: Seismological Society of America Bulletin, v. 61, no. 5, p. 1433–1440.

Marshall, G.A., Stein, R.S., and Thatcher, Wayne, 1991, Faulting geometry and slip from co-seismic elevation changes; the 18 October 1989, Loma Prieta, California, earthquake: Seismological Society of America Bulliten, v. 81, no. 5, p. 1660–1693.

McClellan, P.H., and Hay, E.A., 1990, Triggered slip on the Calaveras fault during the magnitude 7.1 Loma Prieta, California, earthquake: Geophysical Research Letters, v. 17, no. 8, p. 1227–1230.

Murray, M.H., 1991, Global Positioning System measurement of crustal deformation in central California: Cambridge, Massachusetts Institute of Technology, Ph.D. thesis, 310 p.

Ponti, D.J., and Wells, R.E., 1991, Off-fault ground ruptures in the Santa Cruz Mountains, California; ridge-top spreading versus tectonic extension during the 1989 Loma Prieta earthquake: Seismological Society of America Bulletin, v. 81, no. 5, p. 1480–1510.

Prescott, W.H., King, N.E., and Gu Guohua, 1984, Preseismic, coseismic and postseismic deformation associated with the 1984 Morgan Hill, California, earthquake, in Bennett, J.H., and Sherburne, R.W., eds., The 1984 Morgan Hill California earthquake: California Division of Mines and Geology Special Publication 68, p. 137–148.

Prescott, W.H., Davis, J.L., and Svarc, J.L., 1989, Global Positioning System measurements for crustal deformation; precision and accuracy: Science, v. 244, no. 4910, p. 1337–1340.

Savage, J.C., and Lisowski, Michael, 1995, Changes in long-term extension rates associated with the Morgan Hill and Loma Prieta earthquakes in California: Geophysical Research Letters, v. 22, no. 7, p 759-762.

Savage, J.C., Lisowski, Michael, and Prescott, W.H., 1992, Strain accumulation across the Wasatch fault near Ogden, Utah: Journal of Geophysical Research, v. 97, no. B2, p. 2071–2083.

Savage, J.C., Lisowski, Michael, and Svarc, J.L., 1994, Postseismic deformation following the 1989 (M=7.1) Loma Prieta, California, earthquake: Journal of Geophysical Research, v. 99, no. B7, p. 13757–13765.

Savage, J.C., and Prescott, W.H., 1973, Precision of Geodolite distance measurements for determining fault movements: Journal of Geophysical Research, v. 78, no. 26, p. 6001–6007.

Savage, J.C., Prescott, W.H., and Gu Guohua, 1986, Strain accumulation in southern California, 1973–1984: Journal of Geophysical Research, v. 91, no. B7, p. 7455–7473.

Savage, J.C., Prescott, W.H., Lisowski, Michael, and King, N.E., 1979, Geodolite measurements of deformation near Hollister, 1971–1978: Journal of Geophysical Research, v. 84, no. B13, p. 7599–7615.

Savage, J.C., Spieth, M.A., and Prescott, W.H., 1976, Preseismic and coseismic deformation associated with the Hollister, California, earthquake of November 28, 1974: Journal of Geophysical Research, v. 81, no. 20, p. 3567–3574.

Schaffrin, Burkhard, and Bock, Yehuda, 1988, A unified scheme for processing GPS dual-band phase observations: Bulletin Géodésique, v. 62, no. 2, p. 142–160.

Scholz, C.H., 1985, The Black Mountain asperity; seismic hazard of the southern San Francisco Peninsula, California: Geophysical Research Letters, v. 12, no. 10, p. 717–719.

Segall, Paul, and Matthews, M.V., 1988, Displacement calculations form geodetic data and the testing of geophysical deformation models: Journal of Geophysical Research, v. 93, no. B12, p. 14954–14966.

Snay, R.A., Neugebauer, H.C., and Prescott, W.H., 1991, Horizontal deformation associated with the Loma Prieta earthquake: Seismological Society of America Bulletin, v. 81, no. 5, p. 1647–1659.

Thatcher, Wayne, 1983, Nonlinear strain buildup and the earthquake cycle on the San Andreas fault: Journal of Geophysical Research, v. 88, no. B7, p. 5893–5902.

Thatcher, Wayne, and Lisowski, Michael, 1987, Long-term potential of the San Andreas fault southeast of San Francisco, California: Journal of Geophysical Research, v. 92, no. B1, p. 4771–4784.

U.S. Geological Survey staff, 1990, The Loma Prieta, California, earthquake; an anticipated event: Science, v. 247, no. 4940, p. 286–293.

Williams, C.R, Árnadóttir, Thora, and Segall, Paul, 1993, Coseismic deformation and dislocation models of the 1989 Loma Prieta earthquake derived from Global Positioning System measurements: Journal of Geophysical Research, v. 98, no. B3, p. 4567–4578.

THE LOMA PRIETA, CALIFORNIA, EARTHQUAKE OF OCTOBER 17, 1989: EARTHQUAKE OCCURRENCE

MAIN-SHOCK CHARACTERISTICS

ELEVATION CHANGES ASSOCIATED WITH THE EARTHQUAKE AND THEIR USE TO INFER FAULT-SLIP GEOMETRY

By Grant A. Marshall and Ross S. Stein,
U.S. Geological Survey

CONTENTS

ABSTRACT

Leveling surveys conducted before and after the 1989 Loma Prieta earthquake provide observations of the coseismic elevation changes. We use these data to define the spatial pattern of elevation change and to deduce the faulting geometry and distribution of slip. Both planar and curved (listric and negatively listric) faults produce elevation changes consistent with observations. Using an elastic half-space, we treat the data as correlated observations and find that 60 percent of the observed signal can be modeled by a planar rupture surface that extends from 6- to 12-km depth, is 32 km long and 7 km wide, and dips 64° SW. With a slip amplitude of 3.6 m, this model fault produces a geodetic moment of 2.6×10^{19} N-m. A larger dip-slip component is found northwest of the epicenter (rake, 144°) and a larger strike-slip component southeast of the epicenter (rake, 157°). Models with larger rake variations (>40°) marginally reduce the fit to the data but require a seismic moment of only 1.8×10^{19} N-m. The rupture plane lies 2 km southwest of the aftershock zone. When a low-modulus layer or wedge is added to the model for consistency with the seismic *P*-wave-velocity structure, the fault deepens and locates adjacent to the aftershock zone, coming within 1.5 km of the hypocenter.

INTRODUCTION

Precise geodetic leveling surveys conducted both before and after the 1989 Loma Prieta earthquake provide observations of the coseismic elevation changes. Although no active program of vertical-deformation monitoring using leveling has been pursued along this section of the San Andreas fault zone, previous leveling surveys for topographic-control and land-subsidence studies have been used together with postearthquake releveling to construct the coseismic elevation changes. Station separation for more than half of this extensive network of vertical-control bench marks is about 1 km.

In this study, we focus on the broad-scale pattern of vertical deformation and its interpretation in terms of fault geometry and slip. We use simple uniform-slip elastic-dislocation models to approximate the rupture surface at depth. In two different approaches, we treat the leveling observations as either independent or correlated elevation changes. We compare our models incorporating a heterogeneous elastic structure with the half-space models for consistency with the seismic-velocity models of Eberhart-Phillips and others (1990). We then compare the model rupture surface with seismologic, geologic, and other geodetic observations.

DATA

LEVELING NETWORK

The leveling network circumscribes the southern Santa Cruz Mountains and encloses most of the aftershock zone (fig. 1). The network spans 15 to 20 km (one hypocentral depth) on each side of the San Andreas fault and 67 km along strike. Postearthquake surveys were chosen to give maximum coverage of the aftershock zone and the area of expected vertical deformation. The leveling routes cross the San Andreas and Sargent faults in four places. The network is divided into seven routes (inset, fig. 1), each approximately parallel or perpendicular to the San Andreas fault.

Preearthquake leveling surveys were performed by both the U.S. National Geodetic Survey (NGS) and the U.S. Geological Survey (USGS) between 1948 and 1989. Postearthquake surveys were conducted from February through June 1990. We treat all of the vertical deformation occurring between the preearthquake and postearthquake surveys as "coseismic," noting that little postearthquake slip was observed between October 1989 and June 1990 (Behr and others, 1990; Langbein, 1990).

LEVELING ERRORS

Leveling can be contaminated by both systematic and random errors. Systematic errors generally produce a correlation between observed geodetic tilt and topographic slope, as is true for miscalibrated leveling rods (Jackson and others, 1981; Stein, 1981) and is sometimes true for atmospheric-refraction errors (Stein and others, 1986). Random errors have several causes: inaccurate readings of the leveling instrument caused by atmospheric scintillation and ground vibrations, incorrectly entered numerical values (blunders), random variations in the degree to which the instrument and rods are out of plumb, and so on. The NGS corrects all data for level collimation, rod

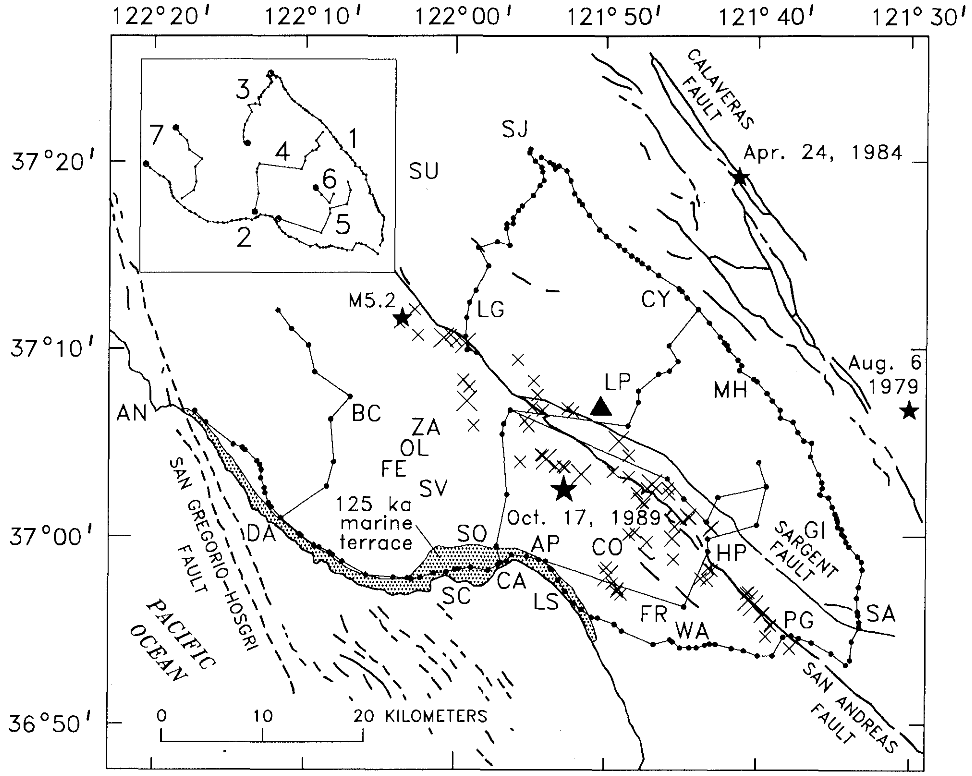

Figure 1.—Schematic map of Loma Prieta region, Calif., showing location of leveling network of 211 bench marks. Inset shows locations of leveling routes 1 through 7; bench marks (dots) indicate zero-distance points in profiles shown in figure 7. Stars, epicenters of Loma Prieta (Oct. 17, 1989; M_s=7.1), Coyote Lake (Aug. 6, 1979; M_s=5.9), and Morgan Hill (Apr. 24, 1984; M_L=6.1) earthquakes; crosses, epicenters of Loma Prieta aftershocks of M>2. Quaternary faults (dashed where inferred) from Jennings (1975). AN, Point Año Nuevo; AP, Aptos; BC, Boulder Creek; CA, Capitola; CO, Corralitos; CY, Coyote; DA, Davenport; FE, Felton; FR, Freedom; GI, Gilroy; HP, Hecker Pass; LG, Los Gatos; LP, Loma Prieta (triangle); LS, La Selva Beach; MH, Morgan Hill; OL, Olympia; PG, Pajaro Gap; SA, Sargent; SC, Santa Cruz; SJ, San Jose; SO, Soquel; SU, Sunnyvale; SV, Scotts Valley; WA, Watsonville; ZA, Zayante.

calibration, thermal expansion of the rod tapes, earth tides and associated gravitational effects, and atmospheric refraction. For the 1990 surveys, the thermal and refraction corrections were computed from the observed temperature gradient at the leveling instrument.

In contrast, the third-order USGS leveling data are not corrected for refraction, earth tides, or thermal-expansion effects. Refraction, collimation, and rod-calibration errors, which can lead to systematic errors detectable in third-order work, are evaluated by searching for height-dependent correlations. Profiles of elevation change and topography are shown in figure 2 for leveling routes 4 (fig. 2*A*) and 7 (fig. 2*B*), both of which cross substantial topography and show no correlation (positive or negative) between the tilt of elevation change and topographic slope. No such correlations are recognizable in the other coseismic data, although errors of ≤100 mm would be difficult to detect in the presence of large tectonic deformation.

Random error can be gaged from the height difference between adjacent bench marks when they are double-run (leveling in both directions), and from circuit misclosures. Random error accumulates with the square root of distance, expressed as $\alpha\sqrt{L}$, where α (in millimeters per kilometer$^{1/2}$) is computed from the double-run sections and L is the length of each section (in kilometers). The observed α values listed in table 1 are derived from the statistics of all double-run sections and have been normalized to a distance of 1 km. The maximum allowable discrepancy between the forward and backward runs of each double-run section is the field tolerance, β. If this field tolerance is not met, the section must be rerun until the forward and backward runs agree to within the tolerance. In practice, arithmetic means of several runs are used for final elevation differences when the field tolerance cannot be met after several attempts. If random errors are normally distributed, then $\alpha = \frac{1}{3}\beta$. Generally, $\alpha < \frac{1}{3}\beta$ because the errors are not normally distributed or because the number of double-run sections used to compute α is small.

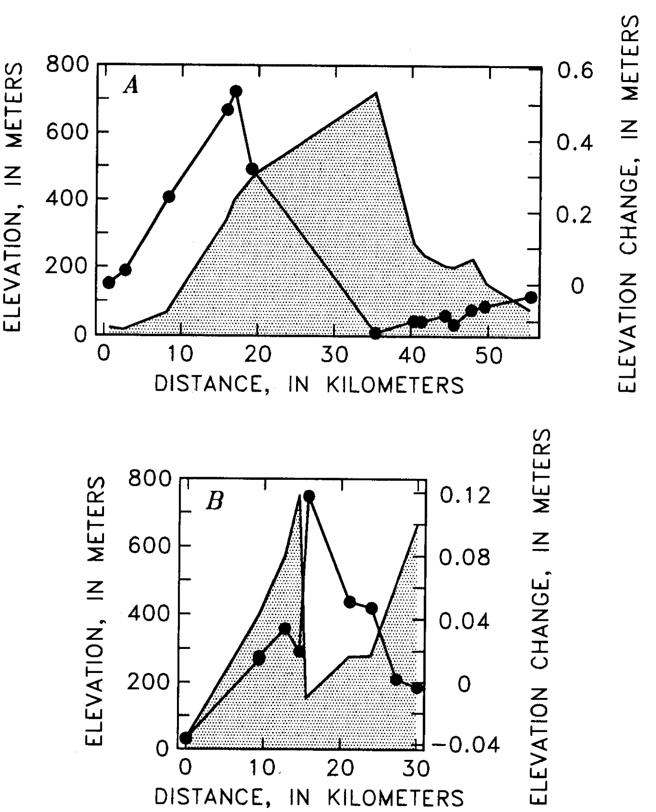

Figure 2.—Profiles of topography (shaded curve) and coseismic elevation change (dots) along leveling routes 4 (*A*) and 7 (*B*) (see inset, fig. 1). No consistent positive or negative correlation between topography and elevation change is observed.

We have assigned α values to each survey on the basis of observed circuit misclosures. In the absence of large blunders or length-dependent systematic errors, observed circuit misclosures give an estimate of the random survey error. The accuracy of the 1990 surveys can be determined by examining five closed circuits. All the circuits are mapped in figure 3, and the observed misclosure, length, and allowable misclosure for each circuit are listed in table 2.

The assigned α values (table 1) are computed from the misclosures of circuits by the formula

$$\alpha^2 = \frac{1}{n}\sum \frac{e_i^2}{L_i}, \qquad (1)$$

where e_i is the misclosure (in millimeters), L_i is the length (in kilometers) of the *ith* circuit, and n is the number of circuits (Bomford, 1971, p. 816). Generally, this calculation leads to more conservative assignments of error than does the observed α value. Where circuit-closure data are unavailable, the α value is assigned by setting the ratio β/α equal for all first-order surveys. All third-order surveys have been assigned an α value on the basis of the single preearthquake circuit 5 misclosure, which yields a 7-mm/$\sqrt{\text{km}}$ mean error, whereas the expected error for third-order levels is 12 mm/$\sqrt{\text{km}}$. Because circuit 5 was closed with several rod pairs, this small misclosure is consistent with an absence of rod-calibration error. Pure errors represented by circuit misclosures have been used to scale the relative precision of each survey.

The error assigned to each coseismic elevation change is based on survey precision and on the uncertainty and magnitude of the subsidence corrections (see app. 1). Relative uncertainties, δ_i, for each coseismic data point are computed as

$$\delta_i^2 = \alpha_{\text{post}}^2 + \alpha_{\text{pre}}^2 + (\gamma S_i)^2, \qquad (2)$$

Table 1.—*Specifications for leveling surveys*

[Agencies: NGS, U.S. National Geodetic Survey; USGS, U.S. Geological Survey. Assigned α values are derived from circuit misclosures. n.a., not available]

Leveling route (inset, fig. 1)	Survey agency and designation		Survey date	Order of leveling (run)	Field tolerance, β (mm)	Observed α value (mm)	Assigned α value (mm)
1	NGS	L25239.1	Jan.–Feb. 1990	1st (single)	4.0	0.77	2.5
	NGS	L25172, L25174	Feb.–Mar. 1989	1st (single)	4.0	.84	2.5
	NGS	L22841	July–Sept. 1972	1st (double)	3.0	.98	1.9
	NGS	L21038, L21016.1, L21026.2	Mar.–May 1967	1st (double)	4.0	1.67	2.5
2	NGS	L25239.1, L25239.2	Feb. 1990	1st (single)	4.0	.11	2.5
	NGS	L25251.8	June 1990	1st (single)	4.0	1.32	2.5
	NGS	L25174	Mar. 1989	1st (single)	4.0	.84	2.5
	NGS	L24298	1978	1st (double)	3.0	.89	1.9
	NGS	L22841, L22869	July–Oct. 1972	1st (double)	3.0	.89	1.9
3	NGS	L25239.3	Feb.–Mar. 1990	1st (single)	4.0	1.30	2.5
	NGS	L21016.9	Jan.–Mar. 1967	1st (double)	4.0	1.67	2.5
	NGS	L18119.9	Dec. 1960	1st (double)	4.0	2.25	2.5
4	NGS	L25239.4	Mar.–Apr. 1990	1st (single)	4.0	.80	2.5
	USGS	PV 80, PV 208, PV 220	1948/53	3d single)	n.a.	n.a.	6.8
5	NGS	L25239.6	Apr. 1990	1st (single)	4.0	.75	2.5
	USGS	PV 220, PV 208	1953	3d (single)	n.a.	n.a.	6.8
6	NGS	L25239.5	Apr. 1990	1st (single)	4.0	1.50	2.5
	USGS	PV 220	1953	3d (single)	n.a.	n.a.	6.8
7	NGS	L25251.7, L25251.8	May–June 1990	1st (single)	4.0	1.72	2.5
	USGS	PV 218	1953/54	3d (single)	n.a.	n.a.	6.8

where α_{post} is the α value for the postearthquake survey, α_{pre} is the α value for the preearthquake survey, S_i is the subsidence correction for the *ith* data point, and γ is a parameter that depends on our confidence in the estimated subsidence rate. For points with a subsidence correction based on extensometer data, γ=0.15; for all other points, we assign γ=0.33.

The relative uncertainty indicates the relative importance of the elevation change at a point i with respect to any other point j. The uncertainty between two adjacent points i and i+1 is given by

$$\sigma_{(i,i+1)} = \left[(\delta_i^2 + \delta_{i-1}^2)L\right]^{1/2} \tag{3}$$

where L is the survey distance between the two points (in kilometers). The coseismic elevation changes and their relative uncertainties are listed in table 3. Each bench mark is identified by its NGS archival reference number (ACRN).

The coseismic signal available for modeling is best described by a signal-to-noise (*S*/*N*) ratio. The observed elevation-change signal is based on section-elevation changes (each section consists of two adjacent bench marks). The signal for the *ith* section, ΔH_i, is given by the difference between the coseismic elevation changes of the two bench marks at each end, $\Delta H_i = dH_{i+1} - dH_i$. The total error, σ_i, for each ΔH_i is calculated from equation 3 and is proportional to the square root of the survey length of the section and to the square root of the sum of squares of the uncertainties of the two observations. The *S*/*N* ratio is given by

$$\frac{S}{N} = \left[\frac{1}{n}\sum_{i}^{n}\left(\frac{\Delta H_i}{\sigma_i}\right)^2\right]^{1/2}, \tag{4}$$

where n is the total number of sections used in the calculation (table 4). The *S*/*N* ratio is ≤3 for 81 percent of all the sections in the network (leveling routes 1, 2, 5, 7). The area of large signal near the epicenter has a moderate *S*/*N* ratio of 4 to 6, because the coseismic elevation changes are derived from less precise preearthquake surveys that have poor spatial resolution and larger uncertainty (leveling routes 3, 4, 6). The *S*/*N* ratio of the entire Loma Prieta leveling-data set is 3.3, despite the high quality and resolution of the 1990 surveys. In effect, the leveling routes around the periphery of the network receive a higher weight by virtue of their high precision and bench-mark density, whereas those in the interior of the network receive a relatively lower weight. If all the data were of equal precision and density, the interior routes of the network would have had much larger *S*/*N* ratios.

OBSERVED COSEISMIC ELEVATION CHANGE

The observed coseismic elevation changes are mapped in figure 4*A*. Maximum uplift of 550 mm occurs just to the northwest of the epicenter, on the west side of the San Andreas fault (fig. 1). Maximum subsidence of 100 mm occurs at both the northeast and southwest ends of the network. Maximum coastal uplift occurs where the bench marks are closest to the San Andreas fault. Along the northwest section of the coastline, between Santa Cruz (SC, fig. 1) and Point Año Nuevo (AN, fig. 1), the observations show little or no uplift. To the east of the San Andreas fault, a broad 50-mm downwarp extends along the fault zone.

Repeated coseismic vertical deformation may give rise to the observed height of the coastal marine terraces. Noting the similarity between terrace-uplift profiles and the vertical deformation predicted by Lisowski and others' (1990) coseismic model of the earthquake, Anderson (1990), Valensise and Ward (1991), and Valensise (1992) suggested that Loma Prieta-type events, if repeated every 300 to 600 yr, could produce the observed terrace deformation. The observed coseismic elevation changes from the earthquake are plotted along with the observed long-term vertical deformation of the youngest (125 ka) marine terrace in figure 5*A*. At distances greater than 25 km south of Point Año Nuevo, the two profiles are similar, although the terrace deformation is broader, partly because the leveling route does not everywhere coincide with the terrace's inner edge. Within 25 km of Point Año Nuevo, the uplift recorded by the terrace is not observed coseismically.

An alternative interpretation of the long-term uplift is uniform coastward tilting normal to the San Andreas fault. If this interpretation is correct, then the terrace heights would be inversely proportional to their distance from the fault, unrelated to parameters of the earthquake. Terrace height as a function of distance normal to the San Andreas fault is plotted in figure 5*B*. Uniform tilting is seen to be a plausible explanation for the terrace height, except near the San Gregorio-Hosgri fault at Point Año Nuevo. Thus, although the similarity of the coseismic deformation to the 125-ka deformation suggests that permanent uplift associated with dip slip on the San Andreas fault is recorded by the terraces, uniform regional tilting may also account for the terrace uplift. In both cases, discrepancies near the San Gregorio-Hosgri fault may be due to dip-slip motion on the San Gregorio-Hosgri fault or to obliquity

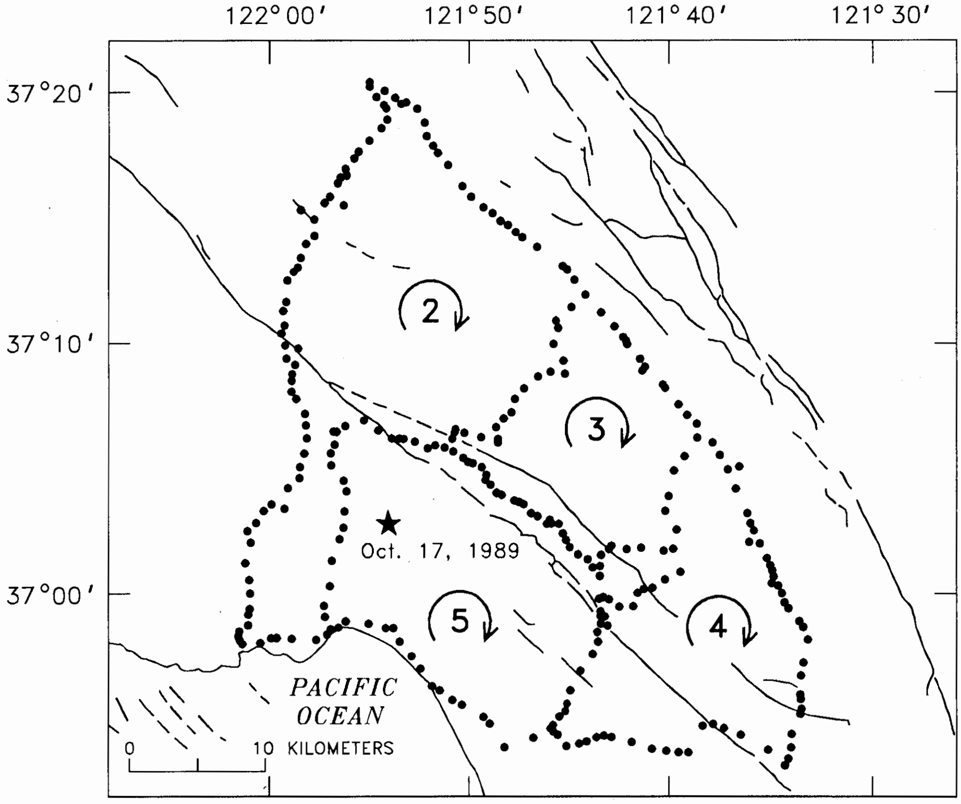

Figure 3.—Schematic map of Loma Prieta region, Calif., showing locations of leveling circuits (numbered loops) formed by 1990 releveling survey. Circuit misclosures computed in clockwise direction as indicated are listed in table 1. Leveling circuit 5 is closed by both preearthquake and postearthquake leveling. Circuit 1 is the outer perimeter loop.

of the long-term San Andreas fault slip, as proposed by Valensise and Ward (1991).

Table 2.—*Leveling circuits and misclosures*

[Observed misclosure is computed in clockwise direction. Allowable misclosure is based on normal random error, $\alpha = \frac{1}{3}\beta$. NGS, U.S. National Geodetic Survey]

Circuit (fig. 3)	Date	Circuit length (km)	Observed misclosure (mm)	Allowable misclosure (mm)
1	1990	79.9	−51.34	±17.9
2	1990	146.0	−38.82	±16.1
3	1990	81.3	+15.86	±12.0
4	1990	90.5	−9.82	±12.7
5	1990	105.0	−18.56	±13.7
5	[1]1953/72	105.0	−70.00	[2]±123.0

[1] 5 km of the preseismic loop is closed with an NGS 1972 height difference.

[2] Based on $\alpha = 12\ \mathrm{mm}/\sqrt{\mathrm{km}}$.

MODELING ELEVATION CHANGES

To model the observed coseismic elevation changes, we constructed a series of three-dimensional models, each of which utilizes an elastic-half-space Earth structure and model faults with uniform slip. We first construct planar rectangular model faults and search for the model that best fits the observations; the data are considered to be independent point elevation changes. Next, we allow the model fault to take on listric and negatively listric shapes. In an additional experiment, we consider the observed elevation changes to be correlated and model the section-elevation changes between adjacent bench marks. In our final series of models, we examine faults with alongstrike variations in rake.

To assess the influence of nonhomogeneous elastic Earth structure, we then tested several two-dimensional boundary-element models. In these tests, we compute the vertical displacement for a set of points aligned perpendicular to the strike of a model thrust fault embedded in a nonhomogeneous elastic medium. These displacements are then modeled with a two-dimensional elastic half-space, to deduce the correction that should be applied to our three-dimensional-half-space results to account for nonhomogeneous Earth structure. These nonhomogeneous-elastic-media calculations are designed to test the effects of a realistic Earth structure on the basis of calculated seismic-velocity models of the Loma Prieta region. We consider both a layered elastic structure and a wedge-shaped low-modulus region.

ELASTIC-HALF-SPACE MODELS

PLANAR ONE-RAKE MODEL

The earthquake rupture can be described as a superposition of moment-tensor point sources buried within a uniform elastic half-space (Ward and Barrientos, 1986; Barrientos and others, 1987). The model-fault geometry and source parameters are fixed; the uniform slip is defined by a least-squares inversion. When the data are considered to be independent point elevation changes, a constant elevation-change offset is also determined by inversion. Because the coseismic elevation changes are independent of a datum (zero-level elevation change is unknown), the model must include an elevation-change offset that, together with the slip amplitude, best fits the observations (in a second approach, the need for an elevation-change offset is eliminated by constructing elevation-change differences between adjacent bench marks). The data are weighted by the square of the observed errors, σ_0, which are proportional to the relative uncertainties, $\sigma_0 = \sqrt{L_c}\delta_i$, where L_c is a characteristic length scale for the network ($L_c \approx 10$ km). Note that we model the elevation change of each bench mark, which is treated as independent, and there are no correlations between bench marks. The characteristic length scale is chosen so that the *S/N* ratio calculated both by section and by bench mark is the same; without the characteristic length scale, the magnitude of the signal is unbounded, owing to the arbitrary datum.

To account for correlations in the leveling observations, we also model the section-elevation changes. In these models, differencing the coseismic elevation changes of adjacent bench marks eliminates the elevation-change offset, and so we invert only for the slip amplitude, with the section-elevation changes weighted by the square of the uncertainties given by equation 3. Each section has a length scale (the leveled distance between adjacent bench marks), and the characteristic network length scale L_c is not required. Before inverting the section-elevation changes, we remove bench marks that create spikes, and sections with excessive tilt. Spikes, defined by adjacent sections that have large tilts of opposite sign, indicate a disturbed bench mark or leveling-observation blunder. Steps in the leveling data indicate blunders in the leveling observations and are characterized by individual sections that have excessively large tilt. For spikes, the causative bench mark is removed, and a new section is formed by differencing the bench marks on either side. The magnitude of tilt that is used to define spikes and steps is chosen to maximize the percentage of signal modeled, while at the same time removing as few of the data as possible (fig. 6).

Each model fault is described by eight fixed model parameters. The location of the model fault is designated by the coordinates of its upper northwest corner; the latitude, longitude, and vertical depth of this corner locate the fault in space. The fault area is described by an alongstrike length and a downdip width. The strike is defined as the angle measured clockwise from north, and the rake is measured on the fault surface counterclockwise from the strike azimuth. The dip is the acute angle between horizontal and the fault surface.

Our systematic forward search of parameter space begins by finding the best-fitting planar model fault. In this initial phase of modeling, we make no assumptions about fault geometry or location, as might be derived from aftershock locations, focal mechanisms, or previous studies. Instead, we adopt strikes and rakes that reflect the general strike of the San Andreas fault in the Loma Prieta region and a reverse-oblique style of faulting. These and all other model parameters, however, are assigned large ranges in the initial parameter-space search. During successive parameter-space searches, these ranges are narrowed, guided by the values that produce the best fit to the data.

NONPLANAR ONE-RAKE MODEL

For curved fault shapes, one additional parameter is required. The downdip fault shape in cross section can be described by the relation $x=b_1z+b_2z^2$, where x is the horizontal distance perpendicular to the fault strike in the direction of dip (Ward and Barrientos, 1986), z is the depth, and b_1 and b_2 describe the cross-sectional shape of the fault surface: b_1 is the cotangent of the dip at the upper edge of the fault, and b_2 is the fault curvature. When $b_2=0$, the model fault is planar (fig. 7*A*); when $b_2>0$, the model fault is listric (fig. 7*B*); and when $b_2<0$, the model fault is negatively listric, a "shoulder thrust" in geologic parlance (fig. 7*C*). We examine fault curvature over a narrower range of initial parameters, using our acquired knowledge of the best-fitting planar-fault geometry. The ranges of parameters tested are listed in table 5.

TWO-RAKE MODEL

In an additional but limited modeling run, two new parameters are added to the model. By introducing an alongstrike segmentation, we create northwestern and southeastern fault segments with independent rakes. Slip is constrained to be uniform for both segments and is determined by inversion. Because Beroza (1991), Steidl and others (1991), and Wald and others (1991) modeled variations in rake in their analyses of strong-motion seismic data, we test whether the leveling observations also constrain variations in rake. This new parametrization is used to determine the best rakes and relative segment lengths for our best-fitting planar-model geometry and for perturbations to it.

ELASTIC-HALF-SPACE RESULTS

All models are ranked according to their misfit to the observations. Model misfits are characterized by a reduced χ^2 term here called the misfit-to-noise (*M*/*N*) ratio, computed as

$$\frac{M}{N}=\left[\frac{1}{n-N_f}\sum_{i}^{n}\left(\frac{\Delta H_o-\Delta H_c}{\sigma_o}\right)^2\right]^{1/2}, \qquad (5)$$

where ΔH_0 is the observed elevation change, ΔH_c is the calculated elevation change, σ_0 is the observed error, n is the number of bench marks, and N_f is the number of free model parameters computed from the data (N_f=10, planar; N_f=11, curved; N_f=12, two-rake, because we have used the data to find the best values of all the parameters). For the section-elevation-change models, the values of ΔH_0 and ΔH_c refer to section-elevation changes, the observed error is calculated by using equation 3, and n is the number of sections modeled. If a model fits the observations to within the noise level of the data, then $M/N\leq 1.0$. Our best-fitting one-rake model has an *M*/*N* ratio of 1.62 for independent data and 1.57 for correlated data, and the segmented two-rake model has an *M*/*N* ratio of 1.33 for independent data. Because all of these models have *M*/*N* ratios >1.0, we have not modeled all the observed signal. The fit is improved by 4 percent when the data are treated as correlated observations, as indicated by the percentage of signal modeled. Árnadóttir and others (1992) also found solutions for both correlated and independent data similar to our models, but the misfits they reported are larger. We calculate an *M*/*N* ratio of 1.61 for Árnadóttir and others' best model. Our use of the characteristic length scale, when modeling the data as independent observations, properly scales that problem, and so we obtain *M*/*N* ratios comparable to those in the models with correlated data. Because we have removed spikes and steps from the data before modeling the section-elevation changes, the data set that we invert may differ slightly from that of Árnadóttir and others. We have also removed the adjustment (see app. 1) to the third-order USGS data for the section-elevation-change models.

Parameter values and inversion results for the best-fitting planar, listric, and negatively listric model faults, the two-rake model fault, and the section-elevation-change models are listed in table 6. The uncertainties shown for the slip and moment are derived from the inversion and depend on the weighted rms residuals. Each one-rake fault fits the data equally well ($1.57\leq M/N\leq 1.67$) and produces a similar moment release. With independent data, the two-rake model fault significantly improves the fit and greatly reduces the magnitudes of slip and moment. With correlated data, the two-rake model fault does not improve the

Table 3.—*Coseismic elevation changes along leveling routes*

[See inset, figure 1, for locations of leveling routes. ACRN, U.S. National Geodetic Survey archival reference number. A constant can be freely added to all elevation-change observations. Note that duplicate bench marks are listed at overlapping end points of leveling routes]

ACRN	Survey distance (km)	Latitude °N.	Longitude °W.	Coseismic elevation change (mm)	Relative uncertainty, δ_i (mm)
Leveling route 1					
HS5161	0.000	37.3519	121.9169	18.2	4.3
HS5160	.598	37.3489	121.9175	15.1	4.3
HS2891	1.745	37.3414	121.9111	8.7	4.4
HS2886	2.598	37.3461	121.9036	12.4	4.5
HS5162	4.166	37.3411	121.8958	5.4	4.6
HS2828	4.787	37.3394	121.8914	1.8	4.6
HS2826	4.968	37.3381	121.8906	1.0	4.6
HS2825	5.086	37.3378	121.8894	1.1	4.6
HS2822	5.383	37.3361	121.8894	.3	4.5
HS5163	5.709	37.3378	121.8864	.1	4.6
HS2813	6.972	37.3344	121.8764	−7.6	5.1
HS2814	8.568	37.3253	121.8697	−9.8	4.9
HS2811	10.085	37.3142	121.8678	−10.2	4.6
HS2810	10.957	37.3075	121.8625	−17.9	4.3
HS2809	11.753	37.3022	121.8581	−16.6	4.6
HS2806	13.031	37.2944	121.8506	−24.9	4.0
HS2796	15.012	37.2797	121.8364	−33.6	4.0
HS2795	15.846	37.2744	121.8308	−34.9	4.0
HS2792	15.982	37.2736	121.8294	−35.0	4.0
HS2789	17.378	37.2653	121.8183	−30.7	4.0
HS2788	18.111	37.2617	121.8114	−31.3	4.0
HS2787	19.036	37.2564	121.8033	−33.5	4.0
HS4926	19.609	37.2533	121.7981	−36.0	4.0
HS5164	19.615	37.2536	121.7981	−41.1	4.0
HS2785	20.301	37.2494	121.7917	−27.6	4.1
HS2784	21.212	37.2450	121.7842	−29.5	4.0
HS5165	22.505	37.2381	121.7719	−31.5	4.0
HS4141	24.649	37.2261	121.7506	−32.6	4.0
HS2778	25.464	37.2225	121.7450	−31.9	4.0
HS2776	26.325	37.2167	121.7392	−31.5	4.0
HS2775	27.865	37.2061	121.7281	−28.6	4.0
HS2773	29.592	37.1942	121.7156	−31.7	4.0
HS2769	31.084	37.1836	121.7047	−32.3	4.0
HS2771	31.091	37.1839	121.7047	−32.9	4.0
HS5166	32.057	37.1769	121.6978	−31.9	4.0
HS2768	32.432	37.1744	121.6947	−31.5	4.0
HS5167	32.881	37.1714	121.6919	−31.9	4.0
HS2762	34.168	37.1619	121.6831	−32.0	4.0
HS2757	34.957	37.1569	121.6775	−37.5	4.0
HS2758	35.919	37.1525	121.6808	−42.5	4.0
HS2759	35.930	37.1525	121.6805	−42.4	4.0
HS2761	36.014	37.1525	121.6805	−41.5	4.0
HS2754	37.913	37.1433	121.6639	−37.2	4.0
HS2753	38.236	37.1411	121.6614	−36.3	4.0
HS2751	39.739	37.1303	121.6500	−34.6	4.0
HS5168	40.908	37.1228	121.6428	−32.7	4.0
HS5169	41.933	37.1156	121.6353	−31.3	4.0
HS2745	43.419	37.1031	121.6222	−27.5	4.0
HS2743	44.781	37.0956	121.6156	−16.7	4.0
HS2742	44.826	37.0953	121.6156	−17.1	4.0
HS5170	46.147	37.0850	121.6086	−18.7	4.0
HS5171	47.156	37.0853	121.5997	−17.6	4.0
HS2738	47.740	37.0719	121.6011	−26.0	4.0
HS2737	49.664	37.0561	121.5922	−18.8	4.0
HS2736	50.366	37.0500	121.5892	−15.1	4.0
HS2733	51.125	37.0439	121.5864	−13.3	4.0
HS2727	52.380	37.0367	121.5917	−8.2	4.0
HS2725	53.422	37.0344	121.5811	−11.8	4.0
HS5172	54.449	37.0258	121.5769	−11.2	4.0
HS2724	55.119	37.0203	121.5736	−13.6	4.0
HS2723	55.512	37.0172	121.5719	−7.9	4.0
HS5143	56.083	37.0125	121.5700	−7.6	4.0
HS2720	56.822	37.0078	121.5706	−6.4	4.0
HS2721	57.287	37.0069	121.5669	−6.7	4.0
HS2722	57.320	37.0069	121.5672	−6.3	4.0
HS2719	57.607	37.0058	121.5658	−7.1	4.0
HS2718	57.664	37.0025	121.5653	−7.2	4.0
HS5144	58.146	37.0006	121.5631	−8.9	4.0
HS3323	58.200	37.0006	121.5636	−10.1	4.0
GU2195	58.785	36.9950	121.5611	−8.7	4.0
GU2192	59.329	36.9908	121.5583	−8.5	4.0
GU2190	60.917	36.9811	121.5483	−10.5	4.0
GU2189	61.564	36.9775	121.5444	−14.8	4.0
GU2188	62.363	36.9692	121.5417	−18.0	4.1
GU2180	63.974	36.9544	121.5442	−16.3	4.1
GU2178	65.207	36.9442	121.5464	−15.3	4.1
GU4096	65.308	36.9433	121.5467	−12.0	4.0
GU2177	66.625	36.9311	121.5469	−14.5	4.0
GU2176	66.879	36.9286	121.5469	.2	4.0
GU2174	67.554	36.9219	121.5467	17.0	4.0
GU2175	67.791	36.9208	121.5472	23.0	4.0
GU2173	68.173	36.9178	121.5467	.0	4.0
Leveling route 1—Continued					
GU2172	68.187	36.9172	121.5467	5.5	4.0
GU2171	68.274	36.9172	121.5467	−6.3	4.0
GU2167	69.904	36.9042	121.5553	−27.7	4.0
GU2154	71.743	36.8878	121.5567	−39.2	4.0
GU2151	72.394	36.8825	121.5600	−42.3	4.0
GU4097	74.431	36.8922	121.5742	−21.4	4.0
Leveling route 2					
GU4097	0.000	36.8922	121.5742	−21.4	4.0
GU2161	2.766	36.9014	121.5975	−31.6	4.0
GU2162	4.252	36.9067	121.6128	−37.5	4.1
GU2163	5.070	36.9094	121.6203	−51.3	4.0
GU2226	6.117	36.9092	121.6308	−50.3	4.0
GU2229	8.532	36.8917	121.6425	−78.2	4.0
GU2231	10.120	36.8922	121.6600	−88.8	4.0
GU2232	11.305	36.8944	121.6728	−104.5	4.0
GU2233	12.923	36.8975	121.6900	−103.7	4.0
GU2235	14.374	36.9008	121.7056	−104.8	4.0
GU4098	14.966	36.9014	121.7117	−90.2	4.0
GU2237	15.546	36.9003	121.7181	−94.9	4.0
GU2239	16.468	36.8986	121.7275	−88.0	4.0
GU2240	17.132	36.8972	121.7344	−82.5	4.0
GU2242	17.952	36.8956	121.7444	−83.1	4.0
GU2245	19.356	36.9033	121.7536	−70.7	3.6
GU2246	19.720	36.9053	121.7564	−68.0	5.8
GU2248	21.899	36.9003	121.7764	−44.6	3.0
GU2260	26.209	36.9103	121.8117	−7.8	3.4
GU2262	27.316	36.9156	121.8194	−5.8	3.3
GU2264	29.151	36.9225	121.8375	15.7	5.2
GU2265	29.794	36.9250	121.8444	20.2	3.2
GU2266	31.156	36.9317	121.8569	32.1	4.6
GU2269	32.092	36.9361	121.8639	16.5	3.8
GU2268	32.100	36.9361	121.8639	24.3	3.6
GU2273	33.700	36.9483	121.8733	53.9	9.0
GU2276	34.877	36.9572	121.8817	108.9	3.5
GU2277	36.273	36.9669	121.8914	137.8	6.1
GU2279	37.317	36.9756	121.8972	166.7	5.0
GU2278	37.457	36.9758	121.8975	165.0	4.3
GU2281	37.958	36.9764	121.9031	170.4	6.5
GU2282	38.207	36.9758	121.9044	159.0	5.0
GU2283	39.528	36.9792	121.9181	151.6	7.0
GU2285	41.374	36.9814	121.9364	150.6	7.7
GU2286	42.225	36.9769	121.9431	132.0	7.4
GU2287	42.767	36.9753	121.9494	118.2	7.0
GU2290	43.234	36.9731	121.9528	112.0	5.3
GU2289	44.452	36.9683	121.9636	86.8	5.5
GU2291	46.234	36.9692	121.9842	80.8	7.3
GU2294	47.406	36.9692	121.9967	73.9	6.0
GU1941	47.786	36.9683	122.0014	65.0	7.6
GU1944	48.822	36.9656	122.0117	35.4	3.5
GU3223	50.089	36.9656	122.0244	37.3	3.9
GU1945	50.331	36.9647	122.0250	45.9	4.0
GU1954	52.171	36.9614	122.0411	25.8	3.1
GU1959	53.149	36.9589	122.0511	19.4	3.0
GU1960	53.944	36.9611	122.0556	15.8	3.0
GU1964	55.451	36.9622	122.0728	10.5	3.0
GU1970	58.303	36.9644	122.1033	1.6	3.0
GU1972	60.897	36.9747	122.1300	.5	3.0
GU1974	61.947	36.9811	122.1397	10.2	3.0
GU1975	62.447	36.9833	122.1436	6.9	3.0
GU1976	63.587	36.9878	122.1550	−.5	3.0
GU1978	64.232	36.9903	122.1617	3.0	3.0
GU1979	66.032	36.9986	122.1764	5.3	3.0
HT1572	66.418	37.0011	122.1792	6.1	3.0
HT1568	69.463	37.0153	122.2000	−3.7	3.0
HT1567	70.723	37.0247	122.2108	−4.1	3.0
HT1566	71.272	37.0286	122.2144	−1.6	3.0
HT1565	71.391	37.0292	122.2156	−5.9	3.0
HT1564	72.456	37.0372	122.2194	−1.5	3.0
HT1563	73.464	37.0431	122.2208	−2.7	3.0
HT1562	74.448	37.0517	122.2244	−2.8	3.0
HT1559	75.468	37.0597	122.2242	−1.9	3.0
HT1558	75.930	37.0636	122.2253	4.5	3.0
HT1557	76.345	37.0669	122.2281	1.0	3.0
HT1556	78.305	37.0778	122.2428	4.7	3.0
HT1555	78.635	37.0800	122.2453	−3.7	3.0
HT1552	80.343	37.0833	122.2558	−4.4	3.0
HT1547	82.141	37.1044	122.2872	−.5	3.0
HT1545	83.794	37.1142	122.3006	−5.4	3.0

Table 3.—*Coseismic elevation changes along leveling routes*—Continued

ACRN	Survey distance (km)	Latitude °N.	Longitude °W.	Coseismic elevation change (mm)	Relative uncertainty, δ_i (mm)
Leveling route 3					
HS3165	0.000	37.1706	121.9889	37.1	4.0
HS3174	2.091	37.1678	121.9786	71.6	4.0
HS3160	1.793	37.1833	121.9908	−1.9	4.0
HS3154	4.014	37.2008	121.9900	−17.9	4.0
HS3150	5.706	37.2147	121.9869	−56.1	4.0
HS3145	6.958	37.2242	121.9800	−108.0	4.0
HS3140	10.143	37.2469	121.9653	−144.9	4.1
HS3141	10.232	37.2469	121.9653	−136.5	4.1
HS3188	12.161	37.2636	121.9769	−59.7	4.2
HS3132	12.845	37.2681	121.9561	−95.5	4.1
HS3271	14.161	37.2669	121.9408	−126.4	4.4
HS3131	14.676	37.2819	121.9444	−81.9	4.5
HS3130	15.162	37.2856	121.9436	−57.0	7.1
HS3127	15.868	37.2869	121.9375	−66.0	7.4
HS3125	16.486	37.2908	121.9383	−75.8	9.4
HS3124	17.504	37.2978	121.9308	−76.9	14.6
HS3122	18.045	37.3019	121.9267	−95.3	17.4
HS3120	19.473	37.3108	121.9164	−111.3	25.0
HS3118	20.888	37.3194	121.9072	9.9	32.5
HS3117	21.617	37.3244	121.9017	20.8	33.3
HS3109	22.509	37.3319	121.9025	−6.4	39.9
HS3108	22.814	37.3347	121.9036	.2	41.5
HS2891	23.822	37.3414	121.9111	8.7	40.7
Leveling route 4					
GU2287	0.000	36.9753	121.9494	118.2	7.0
GU4169	1.933	36.9906	121.9567	150.3	7.0
HS5196	7.398	37.0358	121.9431	342.3	7.0
HS5202	15.016	37.0947	121.9492	570.4	7.0
HS5203	15.934	37.1022	121.9464	620.4	7.0
HS5205	18.230	37.1144	121.9389	395.2	7.0
HS5224	34.410	37.1025	121.8056	−86.3	7.0
HS5229	39.352	37.1236	121.7942	−65.2	7.0
HS5231	40.445	37.1322	121.7917	−69.9	7.0
HS5233	43.345	37.1483	121.7708	−56.3	7.0
HS5235	44.533	37.1519	121.7597	−83.2	7.0
HS5238	46.850	37.1603	121.7489	−47.3	7.0
HS5239	48.527	37.1722	121.7583	−41.0	7.0
HS2775	54.309	37.2061	121.7281	−28.6	7.0
Leveling route 5					
HS5281	0.000	37.0681	121.6589	−62.2	7.0
HS5283	2.786	37.0453	121.6519	−48.2	7.0
HS5285	7.981	37.0108	121.6619	−35.8	7.0
GU4175	15.066	36.9972	121.7167	−5.4	7.0
GU4177	16.759	36.9861	121.7169	39.3	7.0
GU4185	25.263	36.9353	121.7422	−60.3	7.0
GU2278	48.142	36.9758	121.8975	165.0	7.0
Leveling route 6					
HS5283	0.000	37.0453	121.6519	−48.2	7.0
HS5247	7.309	37.0344	121.7072	−82.0	7.0
HS5252	11.399	37.0133	121.7172	−58.9	7.0
HS5256	14.701	37.0325	121.7428	−40.6	7.0
HS5262	18.295	37.0508	121.7619	−16.8	7.0
HS5205	39.535	37.1144	121.9389	395.2	7.0
Leveling route 7					
HT1568	0.000	37.0153	122.2000	−3.7	7.0
HT3637	9.170	37.0444	122.1494	47.8	7.0
HT3636	9.189	37.0444	122.1489	49.4	7.0
HT3633	12.315	37.0672	122.1400	66.1	7.0
HT3631	14.278	37.1083	122.1442	52.3	7.0
HT3595	17.254	37.1286	122.1217	150.1	7.0
HT3600	22.709	37.1500	122.1636	83.7	7.0
HT3603	25.685	37.1739	122.1694	80.1	7.0
HT3607	28.969	37.1914	122.1908	34.7	7.0
HT3612	31.738	37.2069	122.2053	30.0	7.0

Table 4.—*Signal-to-noise ratios along leveling routes*

Leveling route (inset, fig. 1)	Number of sections	Signal-to-noise ratio
1	86	2.1
2	71	2.8
3	22	5.5
4	13	6.5
5	6	2.9
6	5	4.1
7	9	2.4
1–7	212	3.3

fit to the observations but can provide an equally good fit with 13 percent less moment. Each model fault is about 34 km long, stretching over just half the length of the aftershock zone of October 1989. The fault strikes 127°–129°, similar to the aftershock zone (Dietz and Ellsworth, 1990), and approximately parallels the Santa Cruz Mountains section of the San Andreas fault. The depth of burial of the upper edge of each fault surface is 4 to 5 km; deeper faults are preferred when modeling with correlated data. The planar model fault dips 60°, approximately the average dip of each of the nonplanar model faults; with correlated data, the faults dip slightly steeper. With independent data, the model faults lie above and to the west of the main-shock hypocenter and aftershocks, whereas with correlated data they lie at the west edge of the aftershock zone but still do not intersect the hypocenter. The closest distance between any typical good-fitting model fault and the main-shock hypocenter is 6 km. Contours of observed, predicted, and residual (observed minus predicted) elevation changes are mapped in figure 4 for the best-fitting planar one-rake model fault with independent data. Profiles of the elevation changes for the one- and two-rake model faults are plotted along with the observations in figures 8*A* and 8*B*, respectively. In five places, notable misfits are visible in the one-rake model: (1) at the Sargent fault crossing on leveling route 1 (inset, fig. 1), (2) near the San Andreas fault crossing on leveling route 2, (3) in the center of leveling route 3, (4) near the Sargent fault on leveling route 6, and (5) near the Sargent fault on leveling route 4. These misfits may occur where nontectonic or secondary deformation has disturbed the bench marks. If, for example, we remove a small fraction (13 percent) of the bench marks in the network at sites where notable misfits to our best model fault occur, then the *M*/*N* ratio is reduced to 1.13 for the one-rake planar model fault. The two-rake model fault, however, explains the misfits on leveling routes 2 and 6.

To examine the variation in our best parameter values and the inversion results with independent data, we select an acceptable range of *M*/*N* ratios above the minimums for the one-rake planar, listric, and negatively listric model faults. The acceptable ranges in the fixed parameters and the corresponding inversion results for each model fault at an *M/N* ratio of the best value plus 5 percent are listed in table 7. Depth of burial is well constrained between 4- and 6-km depth. Strike is constrained to a 5° range that at its upper bound includes the strike of the observed aftershock locations. For planar model faults, acceptable dips vary only slightly, whereas for nonplanar model faults, the dip of the upper edge of the rupture surface is not well constrained. Our results do not indicate a preference between planar and nonplanar model faults within the range of curvatures tested. The inversion results indicate a consistent determination of the moment release, whereas slip amplitude varies by a factor of as much as 2. Because the geodetic moment is proportional to the product of the fault area and the slip amplitude ($M_0=\mu As$, where μ is the elastic rigidity, A is the fault area, and s is the average slip amplitude), models with similar moment release and fault length exhibit a tradeoff between slip amplitude and fault width. The distance between the fault surface and the hypocenter is consistently greater than 4 km. The best-fitting faults do not pass through the main-shock hypocenter. The best-fitting model fault that passes within 1 km of the main shock is listric and has an *M/N* ratio of 2.54, whereas the best-fitting one-rake model fault has an *M/N* ratio of 1.61. Results of the section-elevation-change models, though within 5 percent of the *M/N* ratio for models with independent data, are omitted from table 5 and indicate somewhat different parameter values. We note that model discrimination is weaker, and the acceptable range of parameters values is larger, with correlated data.

Use of a two-rake model fault significantly improves the fit by reducing the *M/N* ratio from 1.61 to 1.33 with independent data. Although we have added two new degrees of freedom to the model, the improvement in fit is significant above the 99-percent-confidence level. We follow the method of Barrientos and others (1987, 1989) to analyze the significance of this improvement in fit. The geometry of the two-rake model fault changes only slightly from that of the one-rake model fault: The dip is slightly greater at 62°, the depth of burial is 4.5 km, and the

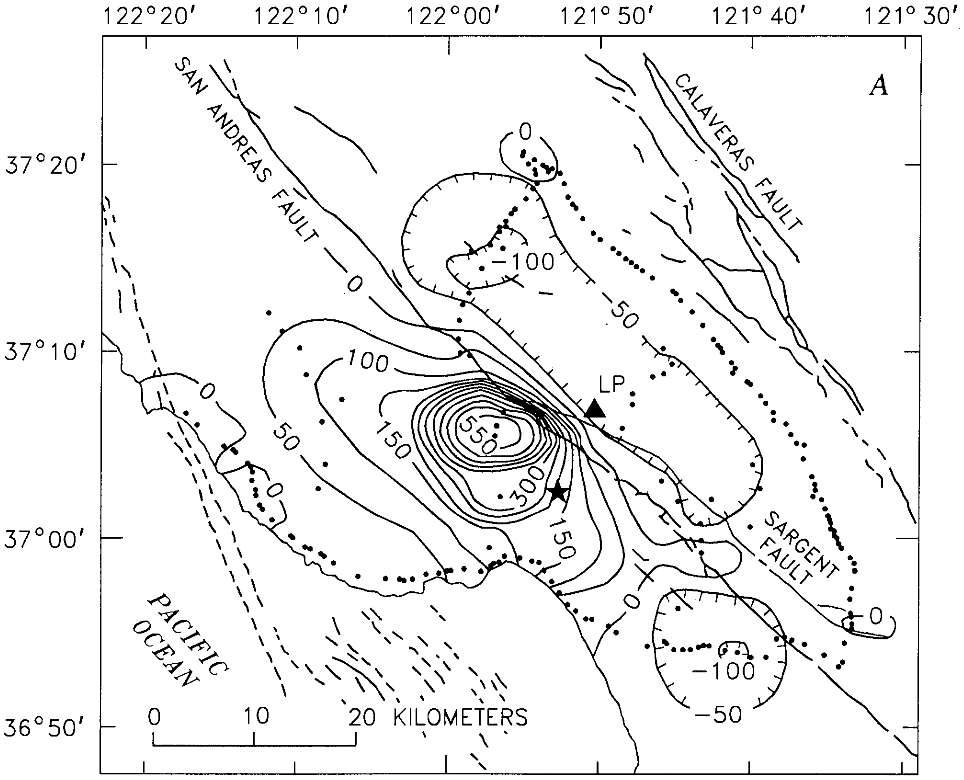

Figure 4.—Schematic map of Loma Prieta region, Calif., showing contours of observed (*A*), predicted (*B*), and residual (*C*) (observed minus predicted) coseismic elevation change. Predicted and residual elevation changes for one-rake planar model fault are listed in table 4. Star, epicenter of Loma Prieta earthquake of October 17, 1989 (M_s=7.1); triangle, Loma Prieta; dots, bench marks. Map in figure 4*C* was constructed by contouring residual elevation changes, not by subtracting predicted from observed contours. Residual and observed contours are valid only where they are adjacent to bench marks. Contour intervals: 50 mm (figs. 4*A*, 4*B*), 20 mm (fig. 4*C*; shaded where positive).

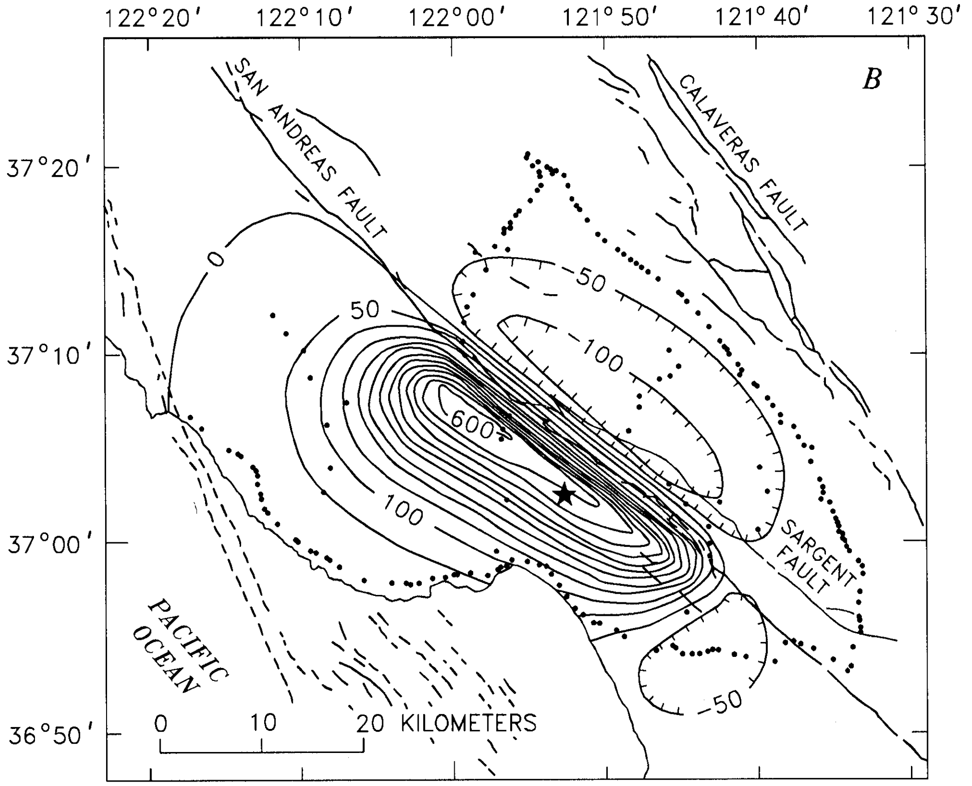

Figure 4.—Continued

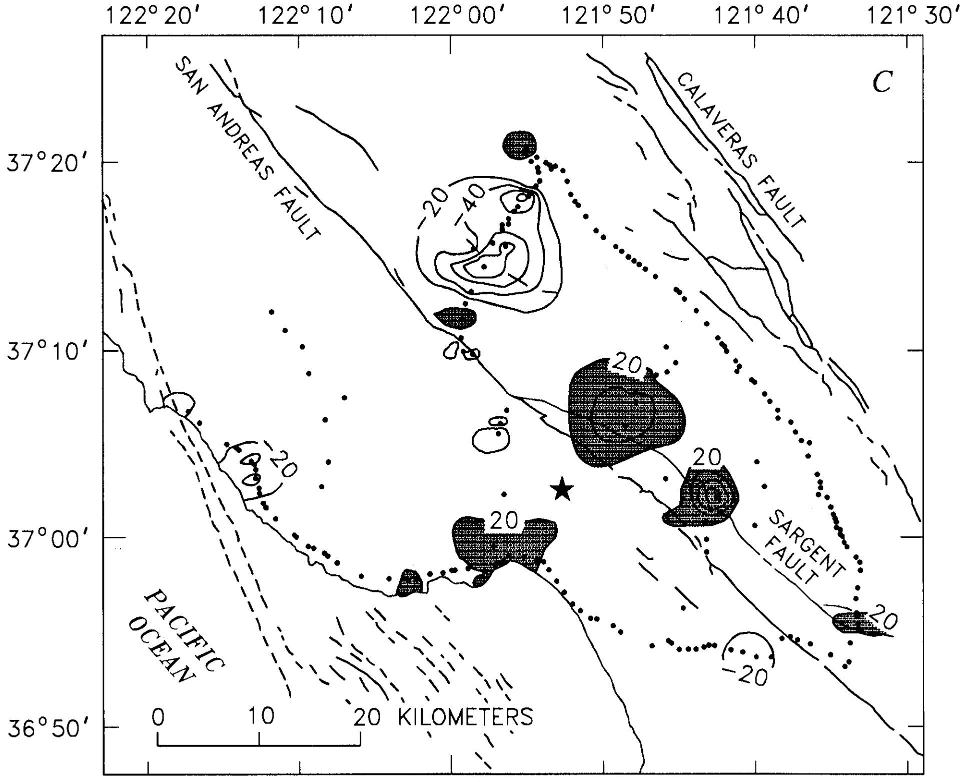

Figure 4.—Continued

length is 37 km. The segment lengths are equal (18.5 km each) and have rakes of 116° in the northwest and 163° in the southeast, similar to the average rake values determined from modeling of strong-motion data (115° NW., 156° SE.; Steidl and others, 1991). The two-rake model fault is illustrated in figure 9. With correlated data, the best two-rake model fits the data no better than the one-rake model. We prefer the two-rake model because it produces the same data misfit with a lower moment—it is a more efficient source. Furthermore, the greater width of the two-rake model fault is more consistent with the spatial extent of the aftershock zone. In comparison with the two-rake model with independent data, the variation in rake is subtle (13°) for the section-elevation-change model. A still more efficient source is obtained if we use the two-rake model with independent data to model the section-elevation changes; then, the M/N ratio is 1.64, and the seismic moment is 1.8×10^{19} N-m.

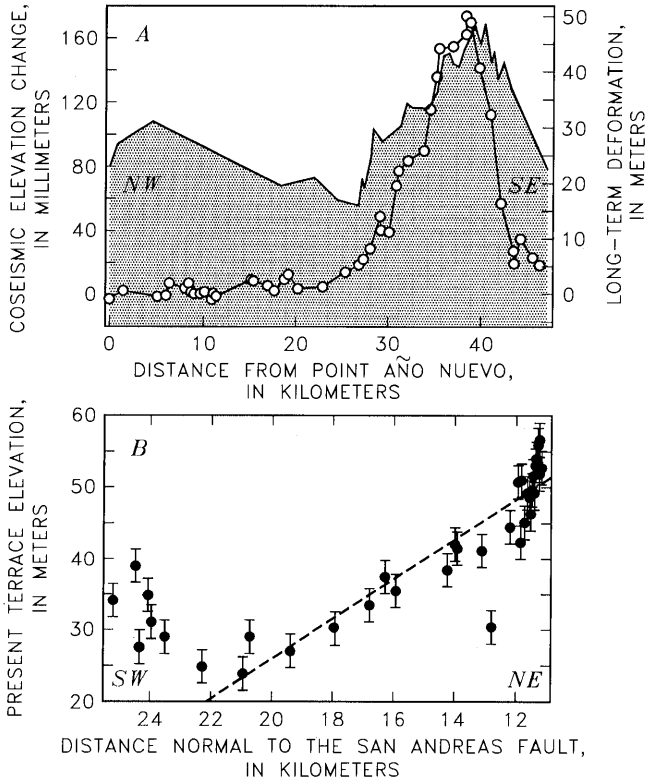

Figure 5.—Marine-terrace deformation. *A*, Profiles of coseismic (circles) and long-term (shaded curve) coastal deformation; long-term deformation is derived from 125-ka marine terrace. Profile is projected along lat N. 115° E. from Point Año Nuevo. Note that leveling route does not everywhere coincide with inner edge of terrace (see fig. 1) *B*, Terrace elevation as a function of perpendicular distance from the San Andreas fault. Dashed line shows linear fit to data, excluding first seven data points.

SENSITIVITY OF RESULTS TO DATA DISTRIBUTION

Because peak-elevation changes are measured on few bench marks and are derived from third-order preearthquake levelings (route 4, inset, fig. 1), we examine how these data influence the goodness of fit of one-rake models with independent data. When we remove leveling route 4, our best-fitting planar-fault geometry

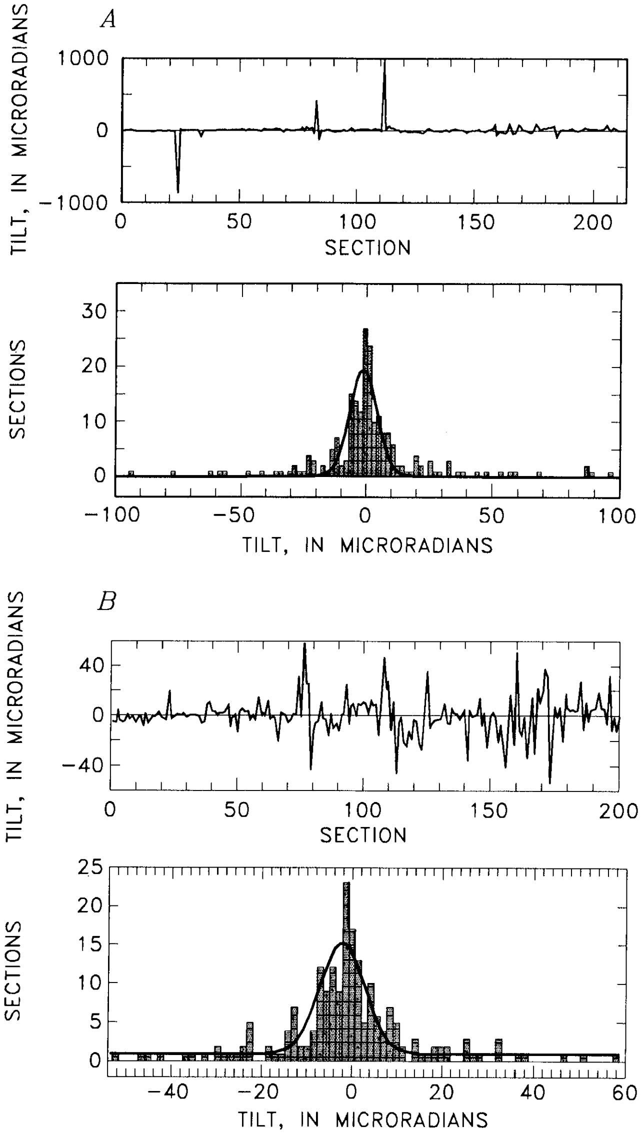

Figure 6.—Coseismic section-elevation changes, showing tilt by section (upper plot) and histogram of tilt populations (lower plot). *A*, Entire data set. Tilt population: standard deviation, 8 microradians; mean, -1 microradian. *B*, Data set with four bench marks with spikes greater than 40 microradians and eight sections with steps greater than 70 microradians omitted. Tilt population: standard deviation, 7 microradians; mean, -2 microradians. Tilt limits: spikes, 40 microradians; steps, 70 microradians. Note that tilt limits are 5 and 9 times the original standard deviation, respectively, and that only 5 percent of data are omitted.

(table 6) gives the same *M*/*N* ratio as with all the data, indicating that the best-model selection is insensitive to these data.

If all third-order leveling and data with large subsidence corrections are removed (leveling routes 3–7, inset, fig. 1), the precise first-order surveys (leveling routes 1, 2) that circumscribe the aftershock zone remain. Using only these observations increases the acceptable range of fault parameters. The best-fitting planar one-rake model obtained using all the data (table 6), however, remains among the best-fitting models. Marginally better fits can be obtained by changing the fault geometry as follows: length, <34 km; width, <9 km; strike, <128°; dip, >50°, and rake, >145°; however, these faults are displaced still farther to the southwest of the aftershock zone. Faults with a width >10 km, a strike >130°, a dip <50°, a rake <140°, and a depth <5 km are precluded when only leveling routes 1 and 2 are used. Thus, the less precise data from the interior of the network do not dictate the modeling results, although including them limits the range of acceptable models.

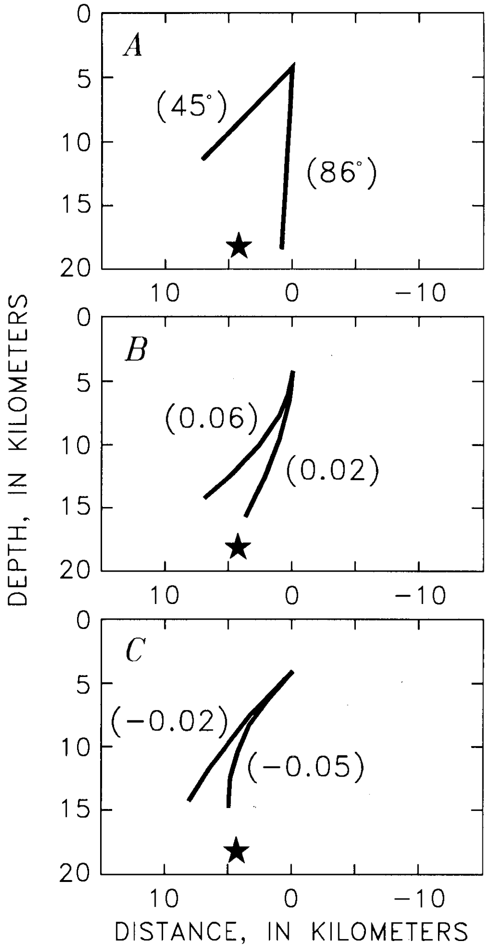

Figure 7.—Profiles of model faults: (*A*) planar, (*B*) listric, and (*C*) negatively listric. In figure 7*A*, maximum and minimum dips are shown; in figures 7*B* and 7*C*, maximum and minimum curvatures are shown. Dip of upper edge of fault is 85° in figure 7*B* and 45° in figure 7*C*. Downdip fault widths are arbitrary. Star, location of hypocenter relative to strikeline.

If the model fault is restricted to lie within the aftershock zone, a substantial misfit results. Translating the best-fitting fault perpendicular to strike 2 km to the northeast, and increasing the dip to 65° and the downdip width to 13 km, so that the fault approximately coincides with the aftershock zone and the main-shock hypocenter, the minimum *M*/*N* ratio we obtain is 3.01, representing an 86-percent increase in the average misfit relative to our best-fitting fault. Increasing the fault dip from 60° through 65°–70° produces large misfits adjacent to the east side of the San Andreas fault, resulting from excessively large subsidence (leveling routes 3–6, inset, fig. 1). Increasing the downdip width of the fault produces too much deformation in the far field at any of the three dips tested, too much uplift along the coast (leveling route 2), and too much subsidence inland (leveling route 1); in addition, the peak uplift along leveling route 4 cannot be modeled with a wider fault.

The section-elevation-change models place nearly all weight on the leveling routes at the periphery of the network, owing to the high bench-mark density; the interior leveling routes receive less weight because the section lengths are longer than those of the exterior leveling routes (see eq. 3). For section-elevation changes, the exterior data have 50 times the weight of the interior data, whereas with independent elevation changes, the exterior data have 17 times the weight of the interior data. The fact that wider variation in parameter values is acceptable for the section-elevation-change models stems from the absence of constraints furnished by the large signal of the interior data, consistent with results of the data-sensitivity tests.

NONHOMOGENEOUS ELASTIC MODELS

Next, we examine the systematic bias inherent in the use of an elastic half-space in place of more realistic Earth structure. Eberhart-Phillips and others (1990) demonstrated a marked velocity gradient with depth in the southern Santa Cruz Mountains: Seismic *P*-wave velocities range from 3.2 to 5.6 km/s in the uppermost 3 to 5 km, increasing to 6.5 to 6.8 km/s below 10- to 15-km depth. Reches and Zoback (1990) argued that strain is concentrated in the low-modulus (low velocity) layer. To test whether the modulus contrast caused by the velocity and associated rock-density gradient influences the deduced fault geometry and slip, we carry out a suite of simple boundary-element tests.

Table 5.—*Ranges of parameters of one-rake model faults*

[Dip on nonplanar faults is for upper edge of fault surface. Latitude and longitude are for vertical projection onto the Earth's surface of northwest corner of upper edge of fault surface. Strike is measured clockwise from north. Rake is measured on fault surface counterclockwise from strike azimuth. Downdip fault shape is described by the relation $x=b_1z+b_2z^2$, where x is the horizontal distance perpendicular to strike in the direction of dip and z is the depth]

Parameter	Planar fault	Listric fault	Negatively listric fault
Length (km)	20→40	30→35	30→35
Width (km)	3→24	7→16	6→12
Dip (°)	45→86	66→85	45→59
Latitude (°N.)	37.127→37.265	37.149→37.184	37.147→37.177
Longitude (°W.)	122.099→121.939	122.027→121.983	122.031→121.990
Depth (km)	0→9	1→6	3→5
Strike (°)	120→140	125→130	126→130
Rake (°)	120→160	140→150	140→150
b_2 (km^{-1})	0	.02→0.06	−.05→ −0.02
Number of models computed.	64,000	32,000	32,000

Table 6.—*Best-fitting uniform-elastic-half-space models*

[Length is measured along strike. Width is measured downdip. Latitude and longitude are for vertical projection onto the Earth's surface of northwest corner of upper edge of fault surface. Depth is to upper edge of fault surface. Strike is measured clockwise from north. Rake is measured on fault surface counterclockwise from strike azimuth. Downdip fault shape is described by the relation $x=b_1z+b_2z^2$, where x is the horizontal distance perpendicular to strike in the direction of dip and z is the depth. Distance to hypocenter is closest approach between fault surface and hypocentral location of Dietz and Ellsworth (1990). Geodetic moment is based on shear modulus $\mu=3.23\times10^{10}$ Pa]

	Fixed parameters										Inversion results			
Fault style	Length (km)	Width (km)	Dip, upper edge (°)	Dip, lower edge (°)	Latitude (°N.)	Longitude (°W.)	Depth (km)	Strike (°)	Rake (°)	b_2 (km^{-1})	Distance to hypocenter (km)	Slip (m)	Geodetic moment (10^{19} N-m)	M/N ratio
							Independent data							
Planar	34	9	60	60	37.161	122.013	4	128	145	0.000	6	2.9±0.1	2.9±0.1	1.62
Listric	34	11	75	45	37.159	122.014	4	127	143	.040	5	2.4±0.1	2.9±0.1	1.67
Negatively listric.	34	6	51	72	37.159	122.021	5	127	142	−.045	8	4.3±0.1	2.8±0.1	1.61
Two-rake planar.	[1]37	9	62	62	37.164	122.014	4.5	128	[2]116/163	.000	6	2.1±0.1	2.2±0.1	1.33
							Correlated data							
Planar	31	4	66	66	37.136	121.971	7	129	155	0.000	7	7.4±0.4	3.0±0.2	1.57
Two-rake planar.	32	7	64	64	37.140	121.972	6	129	[2]144/157	.000	6	3.6±0.2	2.6±0.2	1.57

[1] Two-rake fault is segmented halfway along strike; each segment is 18.5 km long.

[2] First rake value applies to northwest segment, and second to southeast segment.

LAYERED MODEL

We conducted three experiments to assess the effects of the modulus contrast at Loma Prieta. In the first experiment, we considered a dip-slip fault of infinite length along strike embedded in a layer over a half-space, using the boundary-element program of King and Ellis (1990). Shear and normal stresses were prescribed to be continuous across the layer interface. Taking a 5-km-thick layer velocity of 4 km/s and a density of 2,700 kg/m^3, with an underlying-half-space velocity of 6.7 km/s and a density of 3,000 kg/m^3, yields a contrast in Young's modulus, E, between the half-space and the layer of 3 (3.6×10^{10} Pa above and 11.2×10^{10} Pa below). Poisson's ratio is 0.25 in both the layer and the underlying half-space. In our test, we used a contrast in Young's modulus of 5 to examine the maximum possible effects of the weak layer. Uniform slip was imposed on a 65°-dipping fault extending from 6- to 18-km depth. The vertical deformation calculated for this model was then inverted, assuming a uniform half-space.

WEDGE MODEL

In the second experiment, we replaced the low-modulus layer with a wedge extending from the San Andreas fault 10 km to the west and extending vertically from the surface to a depth of 7 km, (see Eberhart-Phillips and Stuart, 1992). The wedge exaggerates the observed across-fault modulus contrast, particularly near the surface, and thus furnishes an upper-bound case to assess how nonhomogeneous Earth models affect the fault parameters. Both the layer and wedge models are approximations to features observed in Eberhart-Phillips and others' (1990) seismic-velocity model. Young's modulus in the wedge is 3.5×10^{10} Pa, and in the surrounding medium 8.8×10^{10} Pa, for a contrast of 2.5. Note that the fault contacts the wedge at a depth of 5 to 7 km (fig. 10*E*). Poisson's ratio within the wedge is 0.333, and in the surrounding medium 0.258.

In the third experiment, we retained the wedge geometry but imposed a uniform shear-stress drop on the fault, rather than uniform fault slip. This condition, also used by Eberhart-Phillips and Stuart (1992), results in tapered slip. For an elastic half-space, the condition produces maximum slip at the center of the fault; in the wedge model,

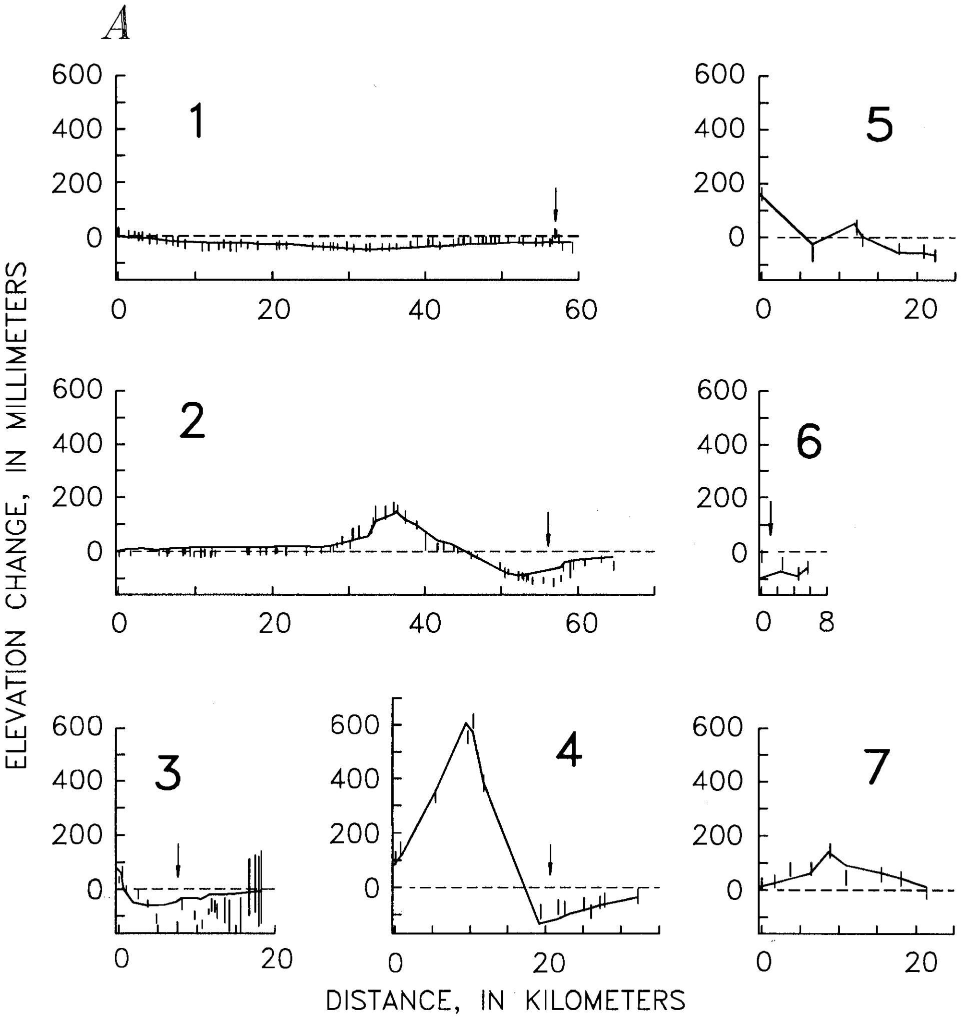

Figure 8.—Profiles of best one-rake (*A*) and two-rake (*B*) planar model faults and observed coseismic elevation changes along leveling routes 1 through 7 (see inset, fig. 1). Vertical bars indicate relative uncertainty of determinations; note that relative uncertainties are large where substantial subsidence corrections have been made (for example, profile 3). Arrows indicate locations where notable misfits occur; note that misfits are substantially reduced for two-rake model fault (fig. 8*B*).

slip is concentrated near the top of the fault because the wedge is more compliant than its surroundings.

MODIFICATIONS TO HALF-SPACE MODELS

Models with a nonhomogeneous elastic structure reduce the misfit of the geodetic fault plane to the aftershock zone and main-shock hypocenter. In the layered model, the location of the upper edge of the fault, its dip, and the slip amplitude are nearly unaffected by the low-modulus layer. The upper edge of the fault, however, locates 1 km too shallow, and the lower depth is as much as 2.3 km too shallow. Thus, if a contrast in Young's modulus of as much as 5 is appropriate for Loma Prieta, then faults would extend 2 to 3 km deeper and be slightly steeper than those deduced by half-space models. Inclusion of the low-modulus layer therefore moves faults several kilometers closer to the main-shock hypocenter than do half-space models (compare figs. 10*B*, 10*D*).

Similarly, imposing uniform slip on the fault in the wedge model results in the fault locating 1 km to the east of its former position, and the fault width increases by several kilometers. With the uniform-shear-stress wedge model, the fault again is found to locate 1 km farther east than for a half-space; in addition, the fault width is found to increase by 4 to 5 km, the slip is reduced by 25 to 30 percent, and the dip may increase slightly (<5°). The effect of these changes is shown in figure 10*E*. The fault lies closer to the aftershock zone and main-shock hypocenter, although the locations of the fault and aftershocks do not coincide. The improvements in fit to the aftershock zone gained by considering a nonhomogeneous structure are illustrated in figure 11, which also shows the dependence of the fit on hypocentral distance for elastic-half-space planar model faults.

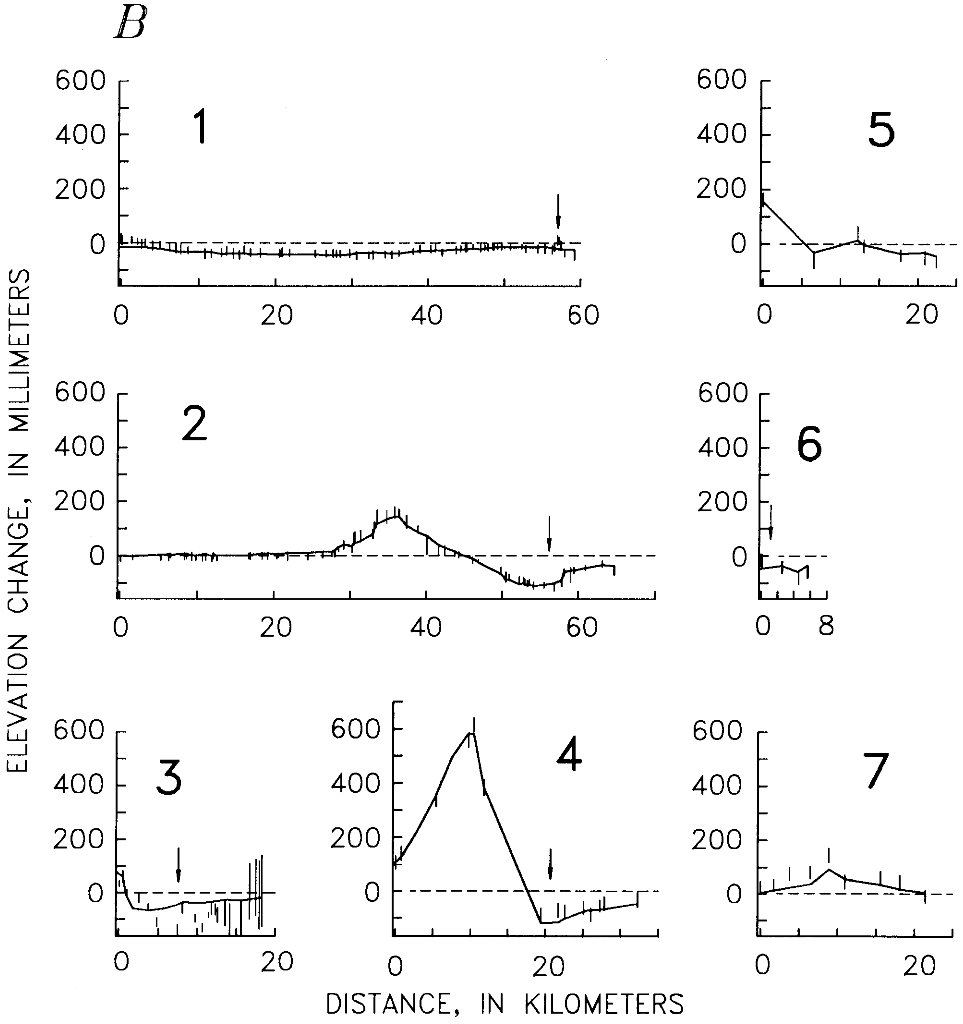

Figure 8.—Continued

Table 7.—*Ranges of parameters for uniform-elastic-half-space models*

[Dip on nonplanar faults is for upper edge of fault surface. Latitude and longitude are for vertical projection onto the Earth's surface of northwest corner of upper edge of fault surface. Strike is measured clockwise from north. Rake is measured on fault surface counterclockwise from strike azimuth. Downdip fault shape is described by the relation $x=b_1z+b_2z^2$, where x is the horizontal distance perpendicular to strike in the direction of dip and z is the depth. Geodetic moment is based on shear modulus $\mu=3.23\times10^{10}$ Pa]

Fixed parameter	Planar fault	Listric fault	Negatively listric fault
Length (km)	32→35	30→35	31→35
Width (km)	9→11	7→12	6→10
Dip (°)	57→60	66→85	48→55
Latitude (°N.)	37.153→37.167	37.147→37.172	37.148→37.169
Longitude (°W.)	122.023→122.003	122.031→121.997	122.027→121.998
Depth (km)	4→5	4→6	4→5
Strike (°)	126→129	125→130	126→129
Rake (°)	139→147	140→150	140→150
b_2 (km^{-1})	0	.020→0.060	-.045→ -0.020
Number of models	641	200	90
		Inversion results	
Distance to hypocenter (km).	5→7	4→7	6→8
Slip (m)	2.3→3.0	2.1→4.2	2.5→4.6
Geodetic moment (10^{19} N-m).	2.6→3.0	2.6→3.4	2.6→3.1
M/*N* ratio	1.62→1.70	1.67→1.75	1.61→1.69

Although all non-half-space models move the fault closer to the aftershock zone, none moves it far enough, and so we have made the modulus contrast as large as permitted by the velocity data of Eberhart-Phillips and others (1990). We note that the uniform-shear-stress-drop model produces about the same geodetic moment as the uniform-slip model because the increased fault width is compensated by the decreased slip. The top of the fault surface undergoes increased slip in the presence of the more compliant wedge under the uniform-shear-stress-drop assumption, a plausible result for an individual earthquake. Over many earthquake cycles, however, uniform slip from

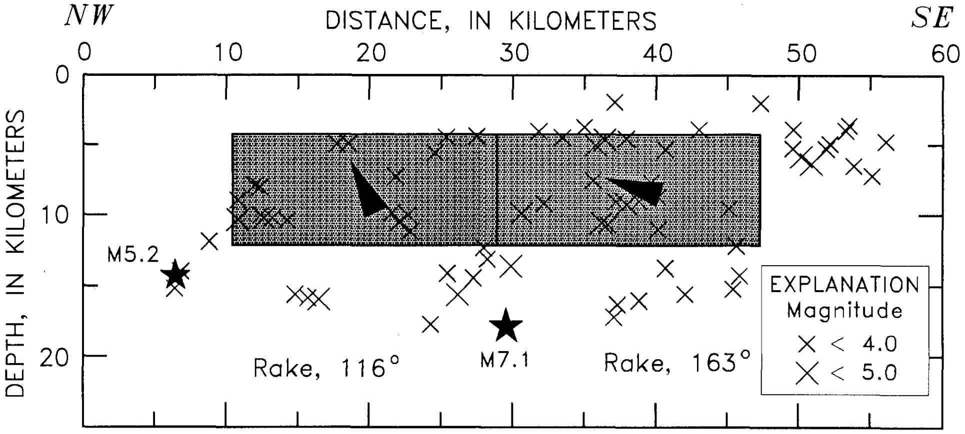

Figure 9.—Alongstrike cross section of two-rake model fault from southwest side. Arrowheads indicate slip direction of hanging-wall block. Stars, main shock and largest aftershock. Fault motion is primarily dip slip to northwest of hypocenter and primarily strike slip to southeast of hypocenter.

the Earth's surface to the base of the seismogenic layer must prevail, and so it is unclear which assumption best represents the Loma Prieta rupture.

DISCUSSION

COMPARISON OF GEODETIC RESULTS WITH STUDIES OF SEISMICITY AND GEOLOGY

The seismic-source mechanism and waveforms of the 1989 Loma Prieta earthquake appear to have simple characteristics, in comparison with those of other earthquakes of similar magnitude, such as the 1988 M=6.7 Armenia earthquake (Kanamori and Satake, 1990). Nevertheless, seismologic studies of the Loma Prieta mechanism suggest a range of source parameters, some of which are compatible with our geodetic results. The source mechanisms found in 10 such studies are compared with the results of our elastic-half-space modeling with independent data in table 8. Four of these studies provide estimates of the strike, dip, and rake that fall within our acceptable model range: the first-motion mechanisms of Plafker and Galloway (1989) and Oppenheimer (1990), and the body-wave inversions of Choy and Boatwright (1990) and Langston and others (1990). Of the 10 studies, 5 report a fault dip and seismic moment consistent with our acceptable model range, and most of the studies agree with our values of strike and rake. The seismologic determination of the source dip, however, is least consistent with our results. The 10 studies report dips ranging from 53° to 85°, and several studies have solutions with dips ≥70°, a value that produces significant misfits to the leveling observations. Seismic values of the fault rake, which range from 110° to 155°, also exceed our acceptable model range. Seismic moments derived from surface-wave analy-

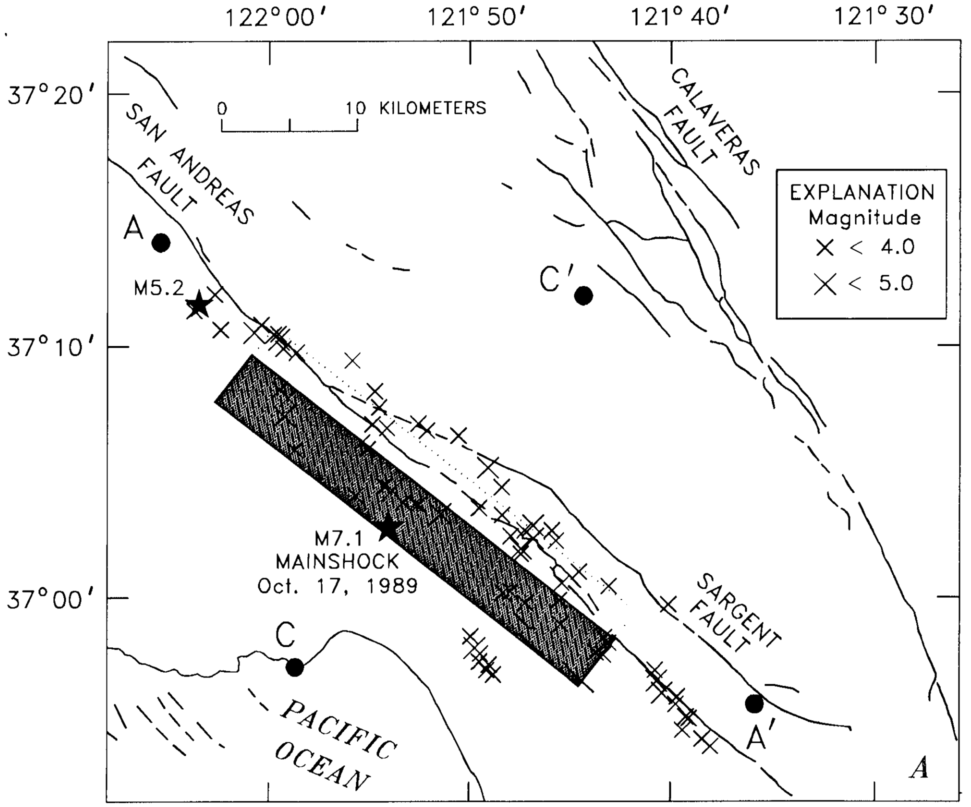

Figure 10.—Schematic map (*A*) and cross sections (*B–F*) of Loma Prieta region, Calif., showing locations of aftershocks of $M \geq 3$ (Dietz and Ellsworth, 1990) and vertical projection of best-fitting planar model fault (shaded rectangle). Dotted line, updip projection. Quaternary faults (dashed where inferred) from Jennings (1975). Cross sections *C–C′* (figs. 10*B*–10*E*) show updip projection of fault surface (dotted line) and locations of the San Andreas (SA) and Sargent (S) faults. *B*, Results for elastic-half-space two-rake model fault with independent data. *C*, Results for elastic-half-space two-rake model fault with correlated data: *D*, Corrections for low-modulus layer (shaded area) over half-space. E_1, E_2, Young's modulus. *E*, Corrections for low-modulus wedge (shaded area) in half-space. E_1, E_2, Young's modulus. *F*, Alongstrike projection of fault surface. Bold rectangle, elastic half-space; dotted rectangle, layer over half-space; long-dashed rectangle, wedge in half-space; short-short-long-dashed rectangle, model fault with correlated data.

ses (Romanowicz and Lyon-Caen, 1990; Zhang and Lay, 1990) and from the body-wave solutions of Barker and Salzberg (1990), Nábělek (1990), and Kanamori and Satake (1990), however, agree with the calculated geodetic moment. Seismic moments derived from data at different frequencies and from different studies vary by a factor of as much as 2.

The consistency between the seismic and geodetic results can be addressed further by examining the spatial relation between the geodetically determined fault surface and the main shock and its aftershocks. Dietz and Ellsworth (1990) found that the aftershock distribution is approximately planar, extending upward from the main-shock hypocenter along a 65°-dipping zone that is 4 to 5 km wide perpendicular to strike. Along strike, Loma Prieta aftershocks tend to cluster around the periphery of a central zone that is depleted of aftershocks. The observed vertical-deformation field is best modeled by a rupture surface approximately parallel to and southwest of the aftershock zone, with a homogeneous elastic Earth structure and independent data. Correlated data reduce this discrepancy and place the fault closer to the aftershock zone. Models that lie within the aftershock zone increase the misfit to the correlated observations by 3 percent. Our models of nonhomogeneous elastic structure also suggest a significant reduction of the misfit of the geodetic fault plane to the aftershock zone and main-shock hypocenter. Our best-fitting planar model faults are mapped in figure 10, with aftershocks of $M \geq 3$ from Dietz and Ellsworth (1990). In map view, the epicenter nearly bisects the fault plane along strike, consistent with bilateral rupture as modeled by Beroza (1991), Steidl and others (1991), and Wald and others (1991). The updip projection of the model fault surface at its northwest terminus coincides with the trace of the San Andreas fault; at its southeast end, the updip projection is equidistant between the Sargent and San Andreas faults. Most aftershock activity is clustered approximately 4 to 5 km northeast and below our elastic-half-space model fault (fig. 10*B*). Including correlations in the leveling data or nonhomogeneous elastic structure improves the fit to the aftershocks, as shown in figures 10*C* through 10*F*. Our acceptable range of latitudes and longitudes allows the elastic model fault to move less than 2 km perpendicular to strike, and the results of our nonhomogeneous tests indicate that the half-space solutions may shift the fault plane 1 km perpendicular to strike.

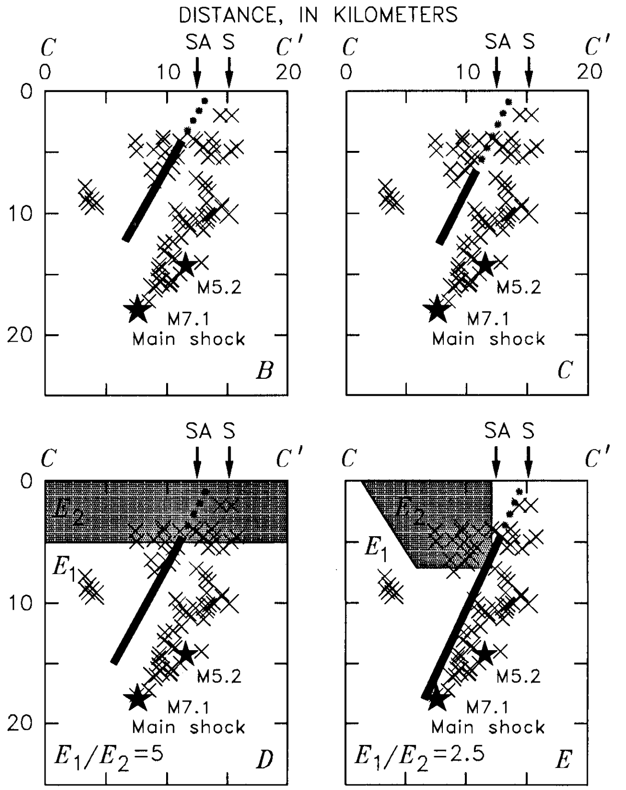

Figure 10.—Continued

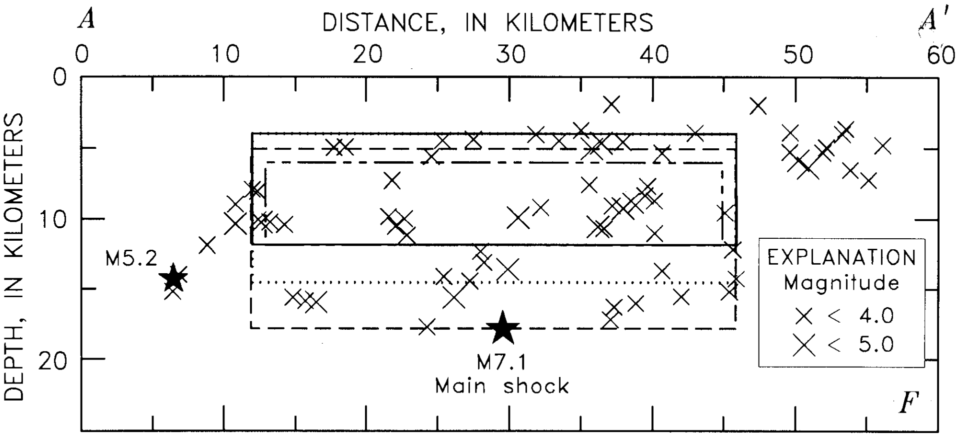

Figure 10.—Continued

Thus, if our two-dimensional nonhomogeneous models are appropriate for the Loma Prieta region, then the combined results indicate that the discrepancy between the position of the geodetic fault plane and the aftershock zone is small (~1 km). In modeling with correlated data, this discrepancy becomes insignificant.

Studies of teleseismic body waves place centroidal depths between 8 and 16 km, shallower than the main-shock hypocenter, which is presumably the depth of rupture initiation (table 8). These teleseismic studies generally only weakly constrain the spatial extent of significant slip on the fault plane. Modeling of local strong-motion seismic data provides better resolution, and these studies suggest that moment release is concentrated in two zones lying between about 9- and 16-km depth (Beroza, 1991; Steidl and others, 1991; Wald and others, 1991). The location of the rupture surface, as constrained by vertical geodetic data and corrections for nonhomogeneous elastic structures, suggests that significant moment release occurred from 6- to 18-km depth, moderately consistent with these interpretations of the strong-motion data.

Focal mechanisms of aftershocks are diverse over short spatial scales. Oppenheimer (1990) presented focal mechanisms for a representative sample of aftershocks; the variations in and distinctness of the aftershock mechanisms, in comparison with the main-shock mechanism, could mean that the aftershocks occurred on structures adjacent to the main-shock rupture surface. The misfit of our model faults to the aftershock zone, however, could also be due to unmodeled three-dimensional variations in elastic modulus or to greater variations in fault geometry or slip distribution. Inaccurate velocity models used to locate the aftershocks might also explain part of this misfit.

The oblique slip inferred from geodetic observations is consistent with the abundance of young (Pliocene-Quaternary) fold structures and reverse faults identified throughout the Santa Cruz Mountains. The Loma Prieta rupture occurred within a structural domain, bounded by the San Gregorio-Hosgri fault in the west, the Ben Lomond, Zayante, and Vergeles faults in the southwest, and a discontinuous series of faults east of the San Andreas fault (Aydin and Page, 1984) that is characterized by southwest-dipping faults and northwest-trending folds. At the surface, the fault features indicate both strike-slip and reverse displacements. The surface projection of model faults compatible with the vertical geodetic data could match either the Sargent or the San Andreas fault.

RELATION TO OTHER GEODETIC STUDIES

A geodetic model (Lisowski and others, 1990) derived from precise electronic distance measurement (EDM), Global Positioning System (GPS) vectors, and very long baseline interferometry (VLBI) observations is not fully consistent with our best-fitting model fault (table 8). Lisowski and others modeled the offsets in the relative positions of geodetic stations, using an elastic dislocation, and determined the source mechanism: strike, 136°; dip, 70°; rake, 144°; geodetic moment, 3.0×10^{19} N-m. The rake and moment of their solution are consistent with our results, whereas the strike and dip do not fall within our acceptable model range. Their model has a strike slightly different from that of the aftershock zone, producing a close fit to the aftershocks in the northwest but a misfit of about 2 km in the southeast. Although their model agrees better with the locations of aftershocks, it has an *M/N* ratio of 2.4 (twice as large as that of our best fitting model) when used to model the coseismic elevation changes. Likewise, our model doubles the average misfit of their obser-

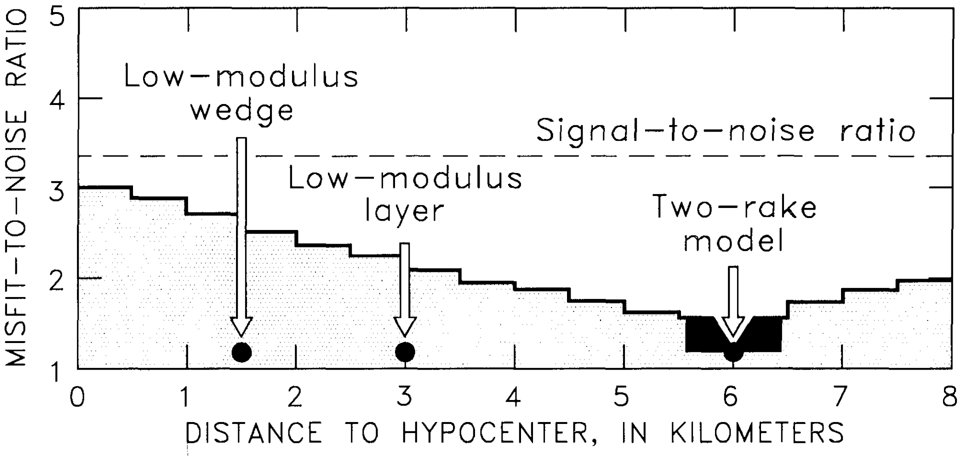

Figure 11.—Misfit-to-noise ratio for one-rake (shaded area) and two-rake (black area) planar model faults versus distance to hypocenter. Best-fitting faults are those with smallest misfit-to-noise ratio and a corresponding hypocentral distance of 6 km. Two-rake model substantially reduces misfit of elevation change. Low-modulus layer and wedge reduce misfit of model fault surface to aftershock zone.

Table 8.—*Comparison of fault parameters from seismologic studies with the results of our elastic-half-space modeling*

[Boldface values are consistent with our ranges of model parameters listed at bottom. Strike is measured clockwise from north. Rake is measured on fault surface counterclockwise from strike azimuth. Depth from *P*-wave first-motion data is depth to rupture initiation; depth from body-wave data is average depth; and depth from body- and surface-wave data is centroidal depth, using a 4-km radius. Do., ditto]

Strike (°)	Dip (°)	Rake (°)	Seismic moment (10^{19} N-m)	Depth (km)	Type of data	Reference
120–140	**55–85**	**125–155**	- -	18	*P*-wave first motions	Oppenheimer (1990).
122–138	**60–80**	**115–145**	- -	19	do	Plafker and Galloway (1989).
130	73	**146**	**2.8**	18	Body waves	Barker and Salzberg (1990).
125–135	**60–70**	**135–145**	2.0–2.2	**12–16**	do	Choy and Boatwright (1990).
117–127	**53–63**	**139–149**	2.1–2.4	**8**	do	Langston and others (1990).
126–130	61–65	127–131	**3.0–3.1**	**11–12**	do	Nábělek (1990).
126	66	138	1.7	**10**	do	Romanowicz and Lyon-Caen (1990).
132–144	71–81	110–130	1.5–2.5	**10–12**	do	Ruff and Tichelaar (1990).
125–129	70–75	**130–144**	**2.5–3.0**	**15**	Body and surface waves	Kanamori and Satake (1990).
122–132	61–71	127–137	**2.8–3.8**	20	Surface waves	Romanowicz and Lyon-Caen (1990).
125–135	65–75	**130–140**	**2.9–3.9**	**12–22**	do	Zhang and Lay (1990).
136	70	**142–147**	**2.6–3.4**	**11**	Horizontal deformation	Lisowski and others (1990).
126–129	57–60	139–147	2.6–3.0	8	Vertical deformation (elastic half-space).	This study.

vations. Future studies that combine both geodetic data sets are needed to find the fault geometry and source mechanism that are most consistent with all the observations.

CONCLUSION

Observations of coseismic elevation changes associated with the 1989 Loma Prieta earthquake favor a rupture surface extending from 6- to 12-km depth, dipping 64°. With a geodetic moment of 2.6×10^{19} N-m, slip direction on this rupture surface ranges in rake from 144° northwest of the epicenter to 157° southeast of the epicenter, with a slip amplitude of 3.6 m. A two-rake model fault produces the same fit to the observations as a one-rake model fault, with 13 percent less moment. Thus, the two-rake model fault is a more efficient source of surface deformation and, in our judgment, more probable. With independent data, two-rake models with a rake variation greater than 40° can be found that offer smaller model misfit and less moment.

The rupture surface determined by our half-space modeling lies 1 to 2 km southwest of most aftershocks and is 6 km from the main-shock hypocenter. With independent data, preferred model faults lie still farther away from the aftershock zone, whereas with correlated data, faults can be found within the aftershock zone that produce only a few-percent increase in model misfit.

The strength of the section-elevation-change modeling is that the correlation of the leveling observations is incorporated into the analysis. Although the section-elevation-change modeling is more sensitive to outliers (such as spikes and steps), we have found that these features can be objectively purged. The weakness of the section-elevation-change modeling stems from the uniquely inhomogeneous distribution of the Loma Prieta data set, in which most of the signal is contained in a few long sections in the interior of the network. Although the influence of these sections is modest with independent data, it is almost nonexistent in the section-elevation-change modeling. Thus, most of the signal we seek to explain with the section-elevation-change modeling has no influence on model selection, and our ability to discriminate among candidate model faults is greatly diminished.

Two-dimensional models with nonhomogeneous elastic structure reduce the misfit between the geodetic fault plane and the aftershock zone, suggesting that more complex (three dimensional) models of the modulus structure of the crust might bring the geodetic and seismic observations into even-better accord. Using a low-modulus layer or wedge model instead of a uniform half-space also deepens and steepens the fault.

The connection between the Loma Prieta rupture surface at depth and the known faults mapped at the Earth's surface remains unclear. Because both listric and negatively listric faults are permitted by the vertical geodetic data, a connection can be inferred to either the San Andreas or the Sargent fault. Further study of the localized anomalous elevation changes seen in some of the leveling data, along with observations of surface displacements northeast of the San Andreas fault (Haugerud and Ellen, 1990), may provide the necessary evidence to infer a connection to shallow surface faults.

ACKNOWLEDGMENTS

All of the postearthquake leveling was funded by the USGS, NGS, and Santa Cruz County Public Works Department. We thank the NGS leveling crew, including Richard Hattesohl, Leonard Bergman, Don Breidenbach, Jim Palo, Scott Hanford, Chris Jacobs, and Verland Pierson, for their expertise in performing a careful and timely leveling job and in releveling after the earthquake. Emery Balazs helped to define and organize the leveling project at the NGS. Gary Perasso provided field-summary books and helpful discussions on the USGS leveling data. Kim Vester provided access to and information about Santa Cruz County leveling data. Accurate subsidence corrections could not have been made without the depth-to-water and extensometer data provided by the Santa Clara Valley Water Conservation District, with the assistance of Adele Sheperd and Lauren Mall. Robert Johnson of the Monterey County Flood Control and Water Conservation District supplied additional depth-to-water data for Monterey County. We greatly appreciate the guidance and encouragement of Wayne Thatcher and the contributions of Geoffrey C.P. King and Jian Lin in creating and testing, respectively, the boundary-element program, and the generosity of Donna Eberhart-Phillips for sharing her finite-element results with us. Thoughtful reviews of the manuscript were provided by Mike Lisowski, David Oppenheimer, and Richard Snay.

REFERENCES CITED

Anderson, R.S., 1990, Evolution of the northern Santa Cruz Mountains by advection of crust past a San Andreas Fault bend: Science, v. 249, no. 4967, p. 397–401.

Árnadóttir, Thora, Segall, Paul, and Matthews, M.V., 1992, Resolving the discrepancy between geodetic and seismic fault models for the 1989 Loma Prieta, California, earthquake: Seismological Society of America Bulletin, v. 82, no. 5, p. 2248–2255.

Aydin, Atilla, and Page, B.M., 1984, Diverse Pliocene-Quaternary tectonics in a transform environment, San Francisco Bay region, California: Geological Society of America Bulletin, v. 95, no. 11, p. 1303–1317.

Bakun, W.H., Clark, M.M., Cockerham, R.S., Ellsworth, W.L., Lindh, A.G., Prescott, W.H., Shakal, A.F., and Spudich, Paul, 1984, The 1984 Morgan Hill, California, earthquake: Science, v. 225, no. 4659, p. 288–291.

Barker, J.S., and Salzberg, D.H., 1990, Long-period and broad-band teleseismic body-wave modeling of the October 18, 1989 Loma Prieta earthquake: Geophysical Review Letters, v. 17, no. 9, 1409–1412.

Barrientos, S.E., Stein, R.S., and Ward, S.N., 1987, Comparison of the 1959 Hebgen Lake, Montana, and the 1983 Borah Peak, Idaho, earthquakes from geodetic observations: Seismological Society of America Bulletin, v. 77, no. 3, p. 784–808.

———1989, Errata; comparison of the Hebgen Lake, Montana and the 1983 Borah Peak, Idaho, earthquakes from geodetic observations: Seismological Society of America Bulletin, v. 79, no. 6, p. 2018.

Behr, Jeffrey, Bilham, Roger, Bodin, Paul, Burford, R.O., and Bürgmann, Roland, 1990, Aseismic slip on the San Andreas fault south of Loma Prieta: Geophysical Research Letters, v. 17, no. 9, p. 1445–1448.

Beroza, G.C., 1991, Near-source modeling of the Loma Prieta earthquake; evidence for heterogeneous slip and implications for earthquake hazard: Seismological Society of America Bulletin, v. 81, no. 5, p. 1603–1621.

Bomford, Guy, 1971, Geodesy: Oxford, U.K., Oxford University Press, 855 p.

Choy, G.L., and Boatwright, John, 1990, Source characteristics of the Loma Prieta, California, earthquake of October 18, 1989 from global digital seismic data: Geophysical Research Letters, v. 17, no. 8, p. 1183–1186.

Dietz, L.D., and Ellsworth, W.L., 1990, The October 17, 1989, Loma Prieta, California, earthquake and its aftershocks; geometry of the sequence from high-resolution locations: Geophysical Research Letters, v. 17, no. 9, p. 1417–1420.

Eberhart-Phillips, D.M., Labson, V.F., Stanley, W.D., Michael, A.J., and Rodriguez, B.D., 1990, Preliminary velocity and resistivity models of the Loma Prieta earthquake region: Geophysical Research Letters, v. 17, no. 8, p. 1235–1238.

Eberhart-Phillips, D.M., and Stuart, W.D., 1992, Material heterogeneity simplifies the picture; Loma Prieta: Seismological Society of America Bulletin, v. 82, no. 4, p. 1964–1968.

Haugerud, R.A., and Ellen, S.D., 1990, Coseismic ground deformation along the northeast margin of the Santa Cruz Mountains, stop 7 *of* Schwartz, D.P., and Ponti, D.J., eds., Field guide to neotectonics of the San Andreas fault system, Santa Cruz Mountains, in light of the 1989 Loma Prieta earthquake: U.S. Geological Survey Open-File Report 90–274, p. 32–36.

Jackson, D.D., Lee, W.B., and Liu, C.-C., 1981, Height dependent errors in southern California leveling, *in* Simpson, D.W., and Richards, P.G., eds., Earthquake prediction; an international review: Washington, D.C., American Geophysical Union, p. 457–472.

Jennings, C.W., compiler, 1975, Fault map of California: Sacramento, California Division of Mines and Geology, scale 1:750,000.

Kanamori, Hiroo, and Satake, Kenji, 1990, Broadband study of the 1989 Loma Prieta earthquake: Geophysical Research Letters, v. 17, no. 8, p. 1179–1182.

King, G.C.P., and Ellis, Michael, 1990, The origin of large local uplift in extensional regions: Nature, v. 348, no. 6303, p. 689–693.

King, N.E., Savage, J.C., Lisowski, Michael, and Prescott, W.H., 1981, Preseismic and coseismic deformation associated with the Coyote Lake, California, earthquake: Journal of Geophysical Research, v. 86, no. B2, p. 892–898.

Langbein, J.O., 1990, Post-seismic slip on the San Andreas fault at the northwestern end of the 1989 Loma Prieta earthquake rupture zone: Geophysical Research Letters, v. 17, no. 8, p. 1223–1226.

Langston, C.A., Furlong, K.P., Vogfjord, K.S., Clouser, R.H., and Ammon, C.J., 1990, Analysis of teleseismic body waves radiated from the Loma Prieta earthquake: Geophysical Research Letters, v. 17, no. 9, p. 1405–1408.

Lisowski, Michael, Prescott, W.H., Savage, J.C., and Johnston, M.J.S., 1990, Geodetic estimate of coseismic slip during the 1989 Loma Prieta, California, earthquake: Geophysical Research Letters, v. 17, no. 9, p. 1437–1440.

Nábělek, J.L., 1990, Rupture process of the October 18, 1989 Loma

Prieta earthquake from broadband teleseismic body waves [abs.]: Seismological Research Letters, v. 61, no. 1, p. 46.

Oppenheimer, D.H., 1990, Aftershock slip behavior of the 1989 Loma Prieta, California earthquake: Geophysical Research Letters, v. 17, no. 8, p. 1199–1202.

Plafker, George, and Galloway, J.P., eds., 1989, Lessons learned from the Loma Prieta, California, earthquake of October 17, 1989: U.S. Geological Survey Circular 1045, 48 p.

Poland, J.F., and Ireland, R.L., 1988, Land subsidence in the Santa Clara Valley, California, as of 1982: Washington, D.C., U.S. Government Printing Office, 61 p.

Prescott, W.H., King, N.E., and Gu Guohua, 1984, Preseismic, coseismic, and postseismic deformation associated with the 1984 Morgan Hill, California, earthquake, *in* Bennett, J.H., and Sherburne, R.W., eds., The 1984 Morgan Hill, California earthquake: California Division of Mines and Geology Special Publication 68, p. 137–148.

Reasenberg, P.A., and Ellsworth, W.L., 1982, Aftershocks of the Coyote Lake, California, earthquake of August 6, 1979; a detailed study, Journal of Geophysical Research, v. 87, no. B13, p. 10637–10655.

Reches, Ze'ev, and Zoback, M.D., 1990, Theoretical analysis of the deformation of a layered sequence above a fault—preliminary application to the Loma Prieta earthquake, chap. 10 *of* Nur, Amos, Mavko, Gary, and Zoback, Mark, eds., Stanford rock physics and borehole geophysics, v. 40, p.X1–X22.

Romanowicz, B.A., and Lyon-Caen, Hélène, 1990, The Loma Prieta earthquake of October 18, 1989; results of teleseismic mantle and body wave inversion: Geophysical Research Letters, v. 77, no. 8, p. 1191–1194.

Ruff, L.J., and Tichelaar, B.W., 1990, Moment tensor rate functions for the 1989 Loma Prieta earthquake: Geophysical Research Letters, v. 17, no. 8, p. 1187–1190.

Steidl, J.H., Archuleta, R.J., and Hartzell, S.H., 1991, Rupture history of the 1989 Loma Prieta, California, earthquake: Seismological Society of America Bulletin, v. 81, no. 5, 1573–1602.

Stein, R.S., 1981, Discrimination of tectonic displacement from slope-dependent errors in geodetic leveling from southern California, 1953–1979, *in* Simpson, D.W., and Richards, P.G., eds., Earthquake prediction; an international review: Washington, D.C., American Geophysical Union, p. 441–456.

Stein, R.S., Whalen, C.T., Holdahl, S.R., Strange, W.E., and Thatcher, Wayne, 1986, Saugus-Palmdale, California, field test for refraction error in historical leveling surveys: Journal of Geophysical Research, v. 91, no. B9, p. 9031–9044.

Valensise, Gianluca, 1994, Geologic assessment of the relative contribution of strike-slip faulting, reverse-slip faulting, and bulk squeezing in the creation of the central Santa Cruz Mountains, California, *in* Simpson, R.W., ed., The Loma Prieta, California, earthquake of October 17, 1989—tectonic processes and models: U.S. Geological Survey Professional Paper 1550–F, p. 17–34.

Valensise, Gianluca, and Ward, S.N., 1991, Long-term uplift of the Santa Cruz coastline in response to repeated earthquakes along the San Andreas fault: Seismological Society of America Bulletin, v. 81, no. 5, p. 1694–1704.

Wald, D.J., Helmberger, D.V., and Heaton, T.H., 1991, Rupture model of the 1989 Loma Prieta earthquake from the inversion of strong motion and broadband teleseismic data: Seismological Society of America Bulletin, v. 81, no. 5, p. 1540–1572.

Ward, S.N., and Barrientos, S.E., 1986, An inversion for slip distribution and fault shape from geodetic observations of the 1983 Borah Peak, Idaho, earthquake: Journal of Geophysical Research, v. 91, no. B5, p. 4909–4919.

Zhang, Jiajun, and Lay, Thorne, 1990, Source parameters of the 1989 Loma Prieta earthquake determined from long-period Rayleigh waves: Geophysical Research Letters, v. 17, no. 8, p. 1195–1198.

APPENDIX 1: CORRECTIONS AND ADJUSTMENTS TO LEVELING DATA

To isolate the elevation change associated with the earthquake ("coseismic"), each survey route must be corrected to eliminate other sources of elevation change, on the basis of knowledge of subsidence caused by ground-water withdrawal during the coseismic time interval, and on the preearthquake rate of subsidence. In some places, the preearthquake subsidence pattern can easily be attributed to tectonic or nontectonic sources (for example, water withdrawal); in other places, disturbed bench marks can lead to unpredictable patterns. Leveling routes 1 through 3 (inset, fig. 1) have preearthquake leveling histories; whereas leveling routes 4 through 7 do not. Leveling routes 4 through 7 are primarily located in mountainous regions and are unlikely to be influenced by ground-water-withdrawal-induced subsidence.

Land subsidence due to ground-water withdrawal in San Jose is documented by leveling surveys and compaction monitoring. Multiple releveling projects during 1934–67 have documented approximately 2.5 m of land subsidence in San Jose. In 1960, the USGS installed several extensometers (corehole compaction-measuring devices; Poland and Ireland, 1988) in San Jose and Sunnyvale, five of which remain in operation today and are maintained by the Santa Clara Valley Water Conservation District. These extensometers provide an excellent record of the compacting aquifer system and, in comparison with leveling data, confirm that land subsidence is compensated by compaction at depths of 61 to 305 m. The land subsidence, which is correlated with ground-water withdrawal and an associated water-table decline, has slowed drastically since the introduction of substantial surface-water imports during the late 1960's (Poland and Ireland, 1988). An example extensometer record for well 7S/1E–16C11 in San Jose is shown in figure 12, along with depth-to-water data for the period 1982–90. Note that during the coseismic interval 1989–90 along leveling route 1, the aquifer system shows a net expansion or land-surface rebound.

To correct leveling routes 1 through 3 (inset, fig. 1) for nontectonic subsidence effects, we use both preearthquake leveling and extensometer data. Subsidence-rate functions are determined from preearthquake leveling surveys, and subsidence corrections are computed by multiplying the subsidence-rate functions by the coseismic time intervals. In this correction, subsidence rates are implicitly assumed to remain constant over time. Near the extensometer sites where subsidence is greatest, however, the observed rates vary over time; for bench marks near the extensometer sites, the subsidence-rate functions have been modified by the observed rate changes. Preearthquake leveling data for routes 1 through 3 are plotted in figure 13. The preearthquake interval for leveling route 1 (1967–89) spans both the August 6, 1979, M_L=5.9 Coyote Lake, Calif., earthquake and the April 24, 1984, M_L=6.1 Morgan Hill, Calif., earthquake (King and others, 1981; Reasenberg and Ellsworth, 1982; Bakun and others, 1984; Prescott and others, 1984). Although the vertical deformation along leveling route 1 from these two events is small (+8 to -10 mm), we remove their contributions to elevation change. Bench marks seated in bedrock presumably are least affected by nontectonic subsidence and so are used to establish the zero-elevation-change datum for the preearthquake surveys. The San Jose subsidence basin is evident in the profiles for leveling routes 1 (1967–89) and 3 (1960–67), and subsidence rates apparently decline after 1967. Subsidence-rate modifications are made for all bench marks that lie within this subsidence basin. To correct for subsidence-rate changes, the subsidence-rate functions are multiplied by a rate-correction factor, which is the ratio of the subsidence rate during the coseismic interval to that during the preearthquake interval. Average subsidence rates and rate-correction factors along leveling routes 1 and 3 are listed in table 9; these average rates are derived from readings of the two extensometers at the San Jose site. Extensometer-tape readings for the period 1982–90 are listed in table 10; increasing values indicate compaction during the period between readings, whereas decreasing values indicate expansion. Poland and Ireland (1988) discussed extensometers and presented compaction data for the period 1960–81.

Depth-to-water records for wells along leveling routes 1 and 2 (inset, fig. 1) were examined to assess the validity of our assumption of constant subsidence rates in areas outside the San Jose subsidence basin. The locations of the 16 wells whose histories we examined are shown in figure 13. The coupling of land subsidence to water-table fluctuations is not spatially uniform; except in one well, no large water-table fluctuations were noted that would require a modification of the subsidence rates represented by the leveling data outside the San Jose area. Well 12S/2E–15E01 (fig. 13*B*) near Watsonville (WA, fig. 1) has a larger ratio of subsidence to water-table decline than that observed in San Jose, possibly indicating that subsidence is particularly sensitive to the water table there. The ratio of subsidence to water-table decline, and the total water-table decline during the period 1978–89, are used to predict subsidence of the junction-point bench mark between these two preearthquake surveys and thus to adjust the datum level for the preearthquake leveling survey along route 2.

Corrected coseismic profiles along leveling routes 1 through 3 were computed by subtracting the subsidence-correction functions from the observed-elevation-change profiles. The correction functions may not contain all the bench marks of the coseismic survey, and so they are interpolated for missing points. Because subsidence basins and the subsidence patterns determined from preearthquake leveling have primarily short spatial wavelengths, elevation-change profiles generally are smoother after correction. Reduction of the short-wavelength com-

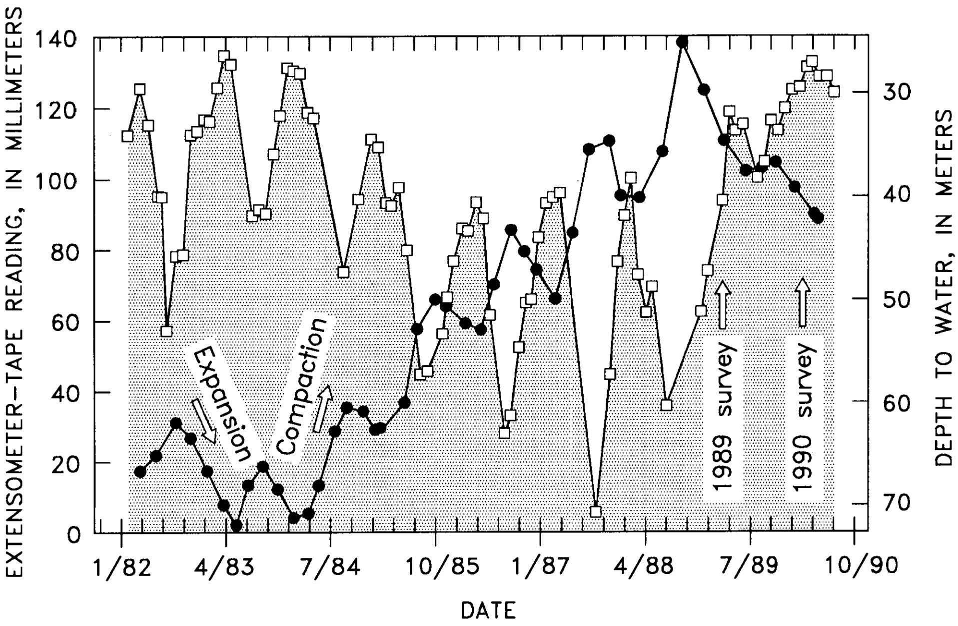

Figure 12.—Extensometer readings (circles) and depth-to-water records (squares) for 305-m-deep well 7S/1E–16C11 in San Jose. Increasing readings indicate compaction, whereas decreasing readings indicate expansion of aquifer system in depth range 0–305 m.

ponents serves as a test of the efficacy of the correction. The corrections for leveling routes 1 through 3 are all well behaved, except at the north end of leveling route 2 between 55 and 84 km. We believe that this problem originates in the north half of the 1972 survey, where a height-dependent error may have occurred; thus, we neglected the subsidence correction for this area. The observed and corrected elevation changes and the correction functions along leveling routes 1 through 3 are plotted in figure 14.

For the network to be self-consistent, overlapping end points of each survey route must have the same coseismic elevation change. To accomplish this agreement, we adjust the third-order USGS data. The test for the efficacy of these adjustments is that the circuit misclosure of the adjusted data must be smaller than that of the observed data. We use the original field data from the USGS surveys and thus remove all previous USGS adjustments.

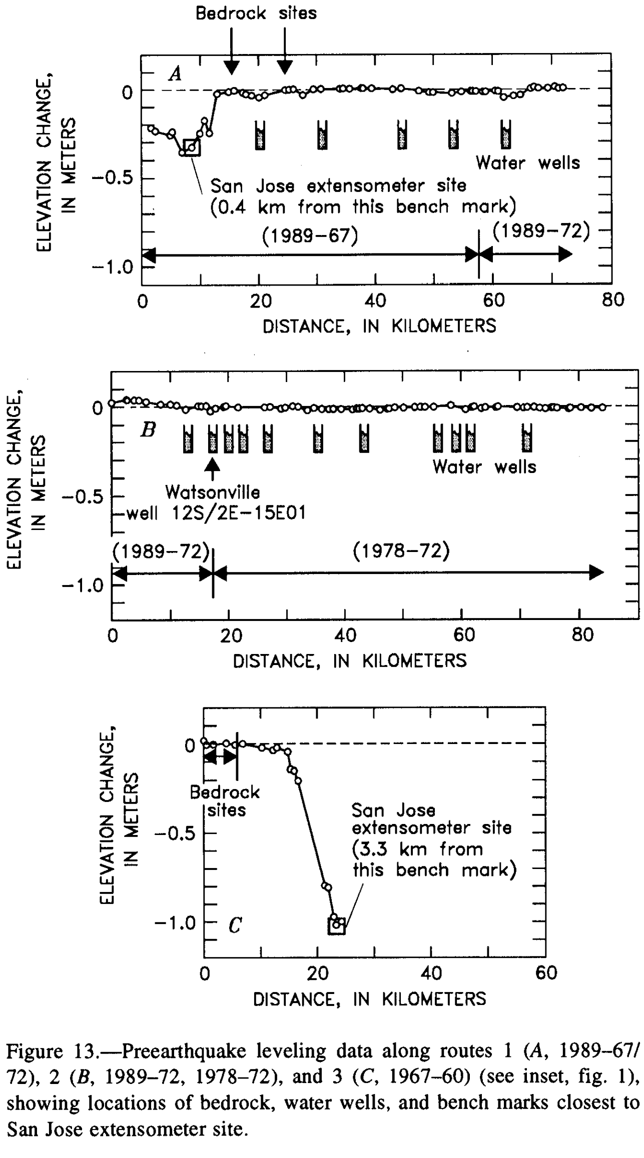

Figure 13.—Preearthquake leveling data along routes 1 (*A*, 1989-67/72), 2 (*B*, 1989-72, 1978-72), and 3 (*C*, 1967-60) (see inset, fig. 1), showing locations of bedrock, water wells, and bench marks closest to San Jose extensometer site.

The end point of leveling route 4 has an unadjusted coseismic mismatch with leveling routes 1 and 2 of 115 mm, which, using the assigned α value (see table 1), is about twice as great as the expected random error for the length of this leveling route. We apply an adjustment of 2 mm/km to the 1953 elevations along leveling route 4, so that the adjusted coseismic elevation changes match at both ends. At the junction of leveling routes 5 and 6, the mismatch is 46 mm, which is about the expected random error at this point for both leveling routes. The misfit is divided equally, and so leveling route 6 is adjusted by 0.5 mm/km and leveling route 5 by 0.6 mm/km. After these adjustments, the computed circuit misclosure for the preearthquake circuit is reduced from -70 to +15 mm. These adjustments reduce the 1953 circuit misclosure to that of the precise 1990 survey (-19 mm; see table 2). The adjusted and subsidence-corrected coseismic elevation changes used in our modeling, and their relative uncertainties, are listed in table 3; each bench mark is identified by its ACRN. The elevation changes listed in table 3 are relative to an arbitrary datum, and so a constant can be added to all the bench marks. Specifications for all the data listed in table 3 are listed in table 1.

APPENDIX 2: DATA TABLES

All the postearthquake elevation-change observations made by the NGS are listed in tables 11 through 24, along with the corresponding historical leveling data, our corrections, and some additional data that were analyzed for use in the subsidence corrections. The title of each table corresponds to the survey titles as named during the 1990 survey.

Tables 11 through 13 contain only NGS orthometric heights for which all standard NGS corrections have been applied. These heights, however, may differ from current NGS data-base values because some heights were obtained from unadjusted ("print file") elevations. Also included in these tables are our earthquake and subsidence corrections to the coseismic elevation changes; these corrections are omitted from the orthometric heights listed in these tables. The coseismic correction was computed by assuming right-lateral slip on a vertical fault for both the 1979 Coyote Lake and 1984 Morgan Hill earthquakes. For the 1979 Coyote Lake earthquake, we used 0.33 m of slip on a 20-km-long fault plane extending from 4- to 12-km depth. For the 1984 Morgan Hill earthquake, we used 0.76 m of slip on a 25-km-long fault plane extending from 4- to 10-km depth (King and others, 1981; Reasenberg and Ellsworth, 1982; Bakun and others, 1984; Prescott and others, 1984). Tables 14 through 24 contain NGS, USGS, and Santa Cruz County leveling data.

The USGS data are all from surveys dated 1953, although a few are actually from 1948. In some places, both

Table 9.—*Average subsidence rates along leveling routes 1 and 3*

[First, the average of the first and second readings of the cable extensometer after manual oscillation was computed; then, this average was combined with the reading of the pipe extensometer to compute the average subsidence rate]

Leveling route (inset, fig. 1)	Survey interval	Average subsidence rate (mm/yr)	Rate-correction factor (Coseismic rate/ preearthquake rate)
1	1989–90	−18.67	−1.28
	1967–89	14.57	---
3	1967–90	13.31	.07
	1960–67	181.93	---

1953 observed and adjusted heights are listed. The adjusted heights are the observed heights adjusted by us as described here; the observed heights are the original field observations with the original USGS adjustments removed. The USGS heights were measured with a three-wire leveling instrument and one 3-yd (3 m)-long, single-piece leveling rod; some rod-calibration tables are available. Leveling was conducted between NGS bench marks and adjusted to closure with previous NGS heights for those bench marks.

The Santa Cruz County data are all surveys dated "1970." Although the precise dates for these surveys are unknown, we were told by Santa Cruz County officials that they were conducted during the late 1960's and early 1970's. The heights were measured with a three-wire leveling instrument and a folding leveling rod ("Philadelphia rod") ruled in hundredths of feet; we do not know whether the rods had been calibrated. Leveling was conducted between USGS bench marks and adjusted to closure with previous USGS heights for those bench marks. Original unadjusted heights may be obtained from the Santa Cruz County Public Works Department, Office of the Surveyor, where the original leveling books are kept. The designations listed for the Santa Cruz bench marks are in the form of a height (in feet), an equal sign, and a integer designation (for example, "271.52=301"); the actual stampings on the marks are simply the height (in feet). The integer following the equal sign is the index number given to that bench mark by Santa Cruz County. The index numbers are used to find the adjusted heights listed in an index-card file and to locate the bench marks on a map in the Office of the Surveyor.

We did not use coseismic elevation changes constructed from the Santa Cruz County data for several reasons. Extensive research on the original field books is required, and the quality of the data is uncertain. Three leveling rods were used during the surveys, only one of which is still available for calibration, and the correspondence between rod serial numbers and particular surveys is uncertain. Tilt of elevation change and slope of topography appear to be correlated along several of the leveling routes that we examined, indicating a rod-calibration problem.

The locations of all the bench marks at which coseismic elevation changes were measured (both those used in this study and those not used) are shown in figure 15.

Table 10.—*Extensometer-tape readings in two wells in San Jose for the period 1982–90*

[F.O., first reading of tape, before manual oscillation; M.O., second reading of tape, after counterweight was manually oscillated]

Date	Well 7S/1E–16C11 pipe (305 m) (mm)	Well 7S/1E–16C5 cable (277 m)	
		F.O. (mm)	M.O. (mm)
1/22/82	- -	0.00	0.31
3/26/82	.00	−7.01	−10.97
6/4/82	4.27	−12.80	−8.84
8/27/82	14.02	−8.84	3.66
10/18/82	- -	2.74	.31
10/28/82	9.45	2.74	.31
1/10/83	−.30	- -	- -
3/25/83	−9.75	- -	−15.54
5/18/83	−15.54	−23.47	−21.34
7/15/83	−3.96	−21.95	−8.23
9/15/83	1.53	−8.53	−.30
11/17/83	−5.18	−10.06	−9.45
1/30/84	−13.41	−13.72	−13.41
4/6/84	−12.19	−16.15	−12.50
5/29/84	−4.27	−17.07	−3.35
7/26/84	11.28	−3.05	7.01
9/17/84	18.29	8.23	17.07
11/27/84	16.77	12.80	16.15
1/16/85	11.58	9.75	12.80
2/27/85	12.50	- -	- -
3/27/85	- -	10.36	10.97
5/20/85	19.51	10.67	20.42
7/19/85	40.24	20.12	36.88
9/30/85	48.77	37.49	44.50
11/22/85	46.64	43.28	43.89
2/13/86	41.76	40.23	40.54
4/24/86	39.93	30.78	37.19
6/17/86	53.04	35.97	46.94
8/29/86	68.58	47.55	58.52
10/27/86	62.18	55.17	55.17
12/19/86	57.00	53.95	54.56
3/9/87	48.77	49.99	49.99
5/21/87	67.97	48.77	63.70
8/5/87	91.44	- -	- -
8/10/87	- -	61.57	81.99
9/17/87	- -	81.38	85.95
10/27/87	93.88	80.77	- -
12/15/87	78.34	67.06	68.89
3/7/88	77.73	- -	- -
3/8/88	- -	66.75	70.41
6/9/88	90.83	70.10	78.64
9/8/88	121.62	79.25	97.23
9/12/88	- -	97.23	- -
9/15/88	- -	97.23	98.76
12/7/88	108.21	86.87	91.44
3/6/89	93.88	88.09	70.10
6/8/89	85.35	61.26	69.49
9/5/89	86.57	68.88	76.20
10/20/89	88.09	66.14	61.27
1/9/90	80.77	60.66	49.07
4/4/90	73.15	48.16	- -
4/16/90	- -	48.46	44.50
4/23/90	71.63	- -	- -

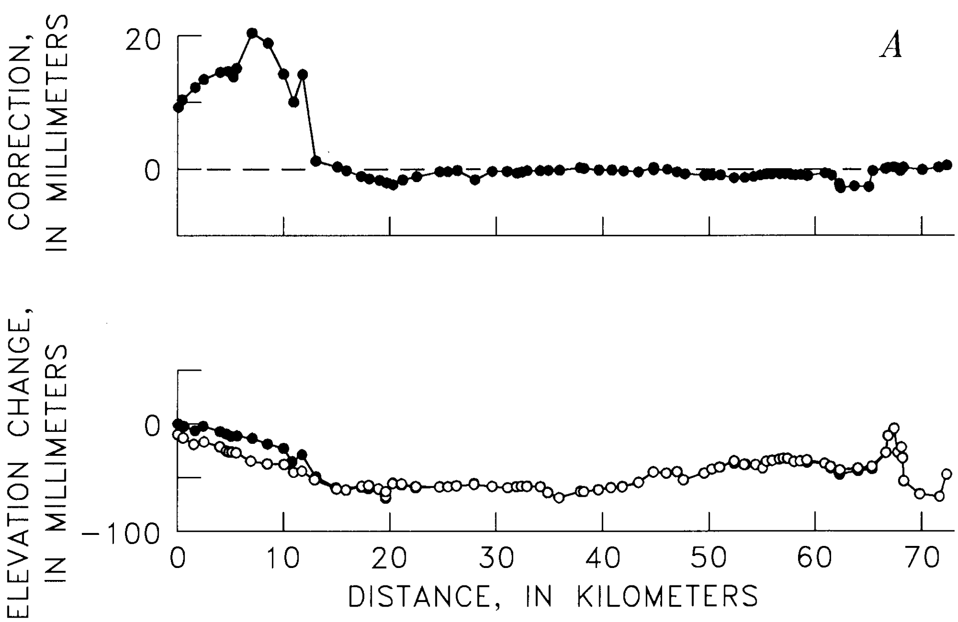

Figure 14.—Observed (dots) and corrected (circles) coseismic elevation changes and correction functions along leveling routes 1 (*A*), 2 (*B*), and 3 (*C*) (see inset, fig. 1, for locations). Note change of scale between correction function and elevation changes in figures 14*A* and 14*B* but not in figure 14*C*.

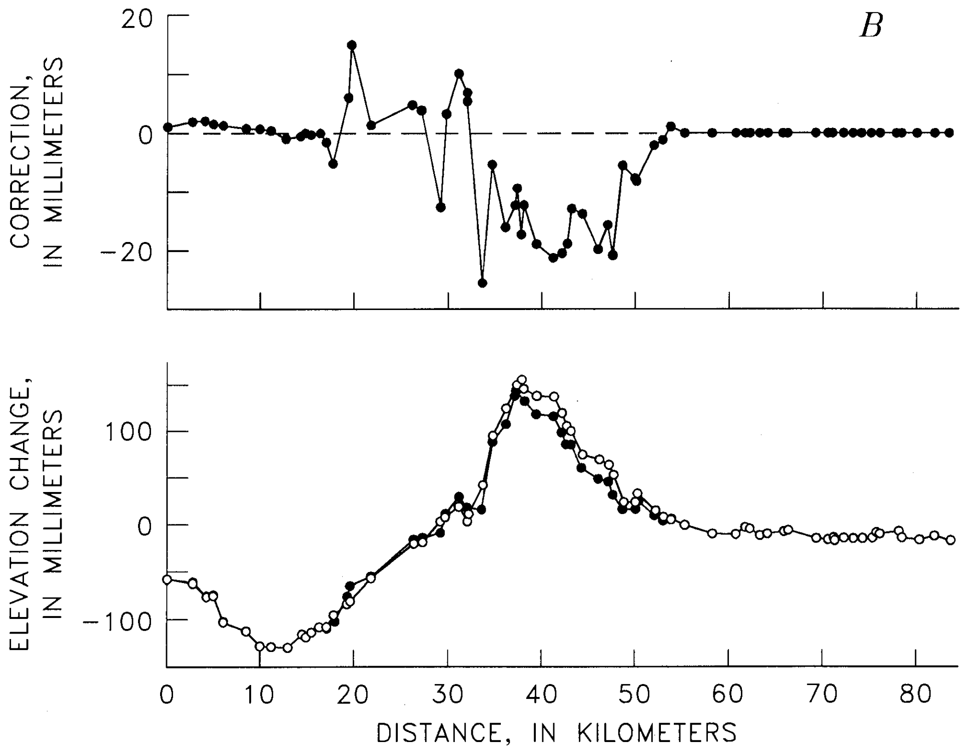

Figure 14.—Continued

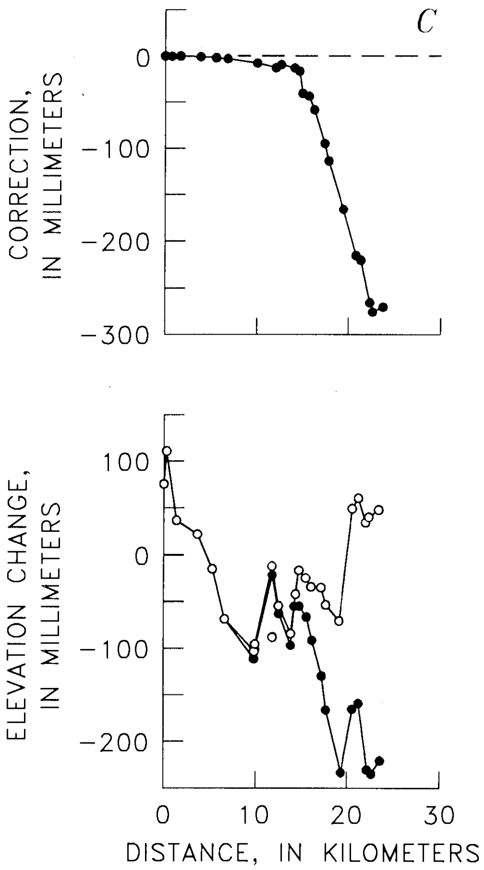

Figure 14.—Continued

Table 11.—*Leveling observations along a line from San Jose through Gilroy and Sargent to Watsonville*

					Orthometric height (m)							
ACRN	Designation	Latitude N.	Longitude W.	Leveled distance (km)	1967 (3–5) L21038, L21016.1, L21016.2	1968 (10–11) L21602	1969 (3–10) L219691, L21746	1972 (7–9) L22841	1989 (2–7) L2517.2, L2517.4	1990 (1–2) L25239.1	Subsidence correction (mm)	Earthquake correction (mm)
HT0651	V 1197	37°47′33″	122°16′07″	−69.693	- - -	- - -	2.62559	- - -	2.56716	- - -	- - -	- - -
HT0648	U 469	37°47′26″	122°15′32″	−68.804	- - -	- - -	3.77282	- - -	3.72073	- - -	- - -	- - -
HT0649	Oakland 6	37°47′15″	122°15′15″	−67.980	- - -	- - -	- - -	- - -	3.21844	- - -	- - -	- - -
HT0020	Oakland 8 reset	37°47′20″	122°14′24″	−66.407	- - -	- - -	- - -	- - -	16.86315	- - -	- - -	- - -
HT3546	K 1444	37°46′53″	122°14′01″	−65.067	- - -	- - -	- - -	- - -	10.13692	- - -	- - -	- - -
HT3547	L 1444	37°46′35″	122°13′31″	−64.108	- - -	- - -	- - -	- - -	12.70819	- - -	- - -	- - -
HT0012	Oakland 7	37°46′09″	122°13′43″	−63.295	- - -	- - -	4.63102	- - -	4.60421	- - -	- - -	- - -
HT0010	Q 148 reset	37°46′19″	122°13′21″	−62.224	- - -	- - -	5.88354	- - -	5.85996	- - -	- - -	- - -
HT0008	20 G	37°46′09″	122°13′06″	−61.648	- - -	- - -	6.06521	- - -	6.04251	- - -	- - -	- - -
HT0003	San Leandro NW base	37°45′48″	122°12′34″	−60.679	- - -	- - -	2.70758	- - -	2.67620	- - -	- - -	- - -
HT0002	N 554	37°45′18″	122°12′02″	−59.486	- - -	- - -	1.91654	- - -	1.89311	- - -	- - -	- - -
HT3555	M 1444	37°45′02″	122°11′42″	−58.777	- - -	- - -	- - -	- - -	3.56099	- - -	- - -	- - -
HT0281	M 554	37°44′39″	122°11′17″	−57.872	- - -	- - -	3.52047	- - -	3.49978	- - -	- - -	- - -
HT0252	K 738 reset	37°44′16″	122°10′50″	−56.828	- - -	- - -	7.56252	- - -	7.53342	- - -	- - -	- - -
HT0253	941 4711 tidal 6	37°44′25″	122°10′47″	−56.424	- - -	- - -	7.08717	- - -	7.06291	- - -	- - -	- - -
HT0245	L 554	37°44′06″	122°10′27″	−55.636	- - -	- - -	12.27936	- - -	12.25369	- - -	- - -	- - -
HT3556	U 1435	37°43′53″	122°10′09″	−55.022	- - -	- - -	- - -	- - -	12.95211	- - -	- - -	- - -
HT3557	X 1435	37°43′25″	122°09′39″	−53.865	- - -	- - -	- - -	- - -	15.80825	- - -	- - -	- - -
HT0241	K 554	37°43′06″	122°09′28″	−53.171	- - -	- - -	15.93973	- - -	15.90496	- - -	- - -	- - -
HT0239	T 1197	37°42′40″	122°08′58″	−52.027	- - -	- - -	12.63164	- - -	12.59509	- - -	- - -	- - -
HT0240	M 148	37°42′28″	122°08′46″	−51.549	- - -	- - -	- - -	- - -	11.50655	- - -	- - -	- - -
HT0238	J 554	37°42′08″	122°08′18″	−50.574	- - -	- - -	12.24255	- - -	12.21673	- - -	- - -	- - -
HT0237	H 554	37°41′27″	122°07′36″	−48.888	- - -	- - -	11.13984	- - -	11.11455	- - -	- - -	- - -
HT1876	Q 1256	37°41′13″	122°07′15″	−48.178	- - -	- - -	- - -	- - -	13.97392	- - -	- - -	- - -
HT0236	L 148	37°41′09″	122°07′17″	−47.988	- - -	- - -	14.61744	- - -	14.58750	- - -	- - -	- - -
HT1866	R 1256	37°40′56″	122°06′59″	−47.387	- - -	- - -	- - -	- - -	11.92283	- - -	- - -	- - -
HT0223	S 1197	37°40′35″	122°06′33″	−46.417	- - -	- - -	16.35982	- - -	16.33930	- - -	- - -	- - -
HT0226	K 148	37°39′58″	122°05′55″	−44.946	- - -	- - -	22.49624	- - -	22.46721	- - -	- - -	- - -
HT3558	V 1435	37°39′36″	122°05′29″	−43.970	- - -	- - -	- - -	- - -	25.59443	- - -	- - -	- - -
HT0208	N 1197	37°39′22″	122°05′12″	−43.337	- - -	- - -	21.92241	- - -	21.90318	- - -	- - -	- - -
HT0207	V 591	37°39′16″	122°05′06″	−43.117	- - -	- - -	20.49403	- - -	20.47668	- - -	- - -	- - -
HT0201	P 1197	37°38′46″	122°04′31″	−41.858	- - -	- - -	13.29236	- - -	13.27336	- - -	- - -	- - -
HT0200	Q 1197	37°38′31″	122°04′14″	−41.252	- - -	- - -	12.84962	- - -	12.82873	- - -	- - -	- - -
HT3559	C 1447	37°38′03″	122°03′42″	−40.036	- - -	- - -	- - -	- - -	7.15201	- - -	- - -	- - -
HT0197	R 1197 reset	37°37′30″	122°03′05″	−38.626	- - -	- - -	- - -	- - -	4.53620	- - -	- - -	- - -
HT2434	X 1446	37°37′33″	122°03′02″	−38.575	- - -	- - -	- - -	- - -	6.19229	- - -	- - -	- - -
HT3562	F 1447	37°36′39″	122°02′06″	−36.356	- - -	- - -	- - -	- - -	16.70963	- - -	- - -	- - -
HT0187	253	37°36′21″	122°01′34″	−35.336	- - -	- - -	25.63398	- - -	25.61522	- - -	- - -	- - -
HT0185	M 1197	37°36′04″	122°01′28″	−34.320	- - -	- - -	20.44525	- - -	20.42730	- - -	- - -	- - -
HT2446	Y 1446	37°35′34″	122°01′07″	−33.109	- - -	- - -	- - -	- - -	17.96061	- - -	- - -	- - -
HT0184	B 46 reset	37°35′40″	122°00′59″	−32.687	18.02171	- - -	18.08764	- - -	18.07497	- - -	- - -	- - -
HT0182	50.5	37°35′08″	122°00′13″	−31.187	15.32380	- - -	15.38993	- - -	15.37849	- - -	- - -	- - -
HS3384	L 177	37°34′56″	121°59′43″	−30.387	16.02651	- - -	16.08962	- - -	16.07170	- - -	- - -	- - -
HS3383	K 177	37°34′46″	121°59′04″	−29.352	19.91230	- - -	19.96777	- - -	19.89738	- - -	- - -	- - -
HS3382	Niles AZ MK	37°34′42″	121°58′54″	−29.121	19.47716	- - -	19.53420	- - -	19.48375	- - -	- - -	- - -
HS3381	F 148	37°34′43″	121°58′53″	−29.063	22.58309	- - -	22.64050	- - -	22.59410	- - -	- - -	- - -
HS3549	R 874	37°34′41″	121°58′19″	−28.230	29.28733	- - -	29.34630	- - -	29.31619	- - -	- - -	- - -
HS3379	Q 874	37°34′30″	121°58′20″	−27.840	27.25989	- - -	27.31696	- - -	27.28474	- - -	- - -	- - -
HS3565	Switch	37°34′21″	121°58′11″	−27.448	25.61108	- - -	25.66508	- - -	25.62402	- - -	- - -	- - -
HS3375	T 591	37°34′09″	121°57′55″	−26.871	24.82369	- - -	24.87956	- - -	24.83114	- - -	- - -	- - -
HS3374	B 148 reset	37°33′47″	121°57′32″	−26.054	- - -	- - -	- - -	- - -	22.58554	- - -	- - -	- - -
HS3370	M 886	37°32′30″	121°57′18″	−23.616	17.87337	- - -	17.93522	- - -	17.91673	- - -	- - -	- - -
HS5153	K 1447	37°32′05″	121°57′14″	−22.805	- - -	- - -	- - -	- - -	22.11553	- - -	- - -	- - -
HS3337	D 175	37°31′26″	121°56′59″	−21.450	15.26510	- - -	15.32480	- - -	15.32068	- - -	- - -	- - -
HS3335	F 1076	37°31′00″	121°56′45″	−20.514	8.85408	- - -	8.91096	- - -	8.90941	- - -	- - -	- - -
HS5154	D 1447	37°30′48″	121°56′41″	−20.068	- - -	- - -	- - -	- - -	10.13647	- - -	- - -	- - -
HS5155	J 1447	37°30′23″	121°56′25″	−19.280	- - -	- - -	- - -	- - -	10.67165	- - -	- - -	- - -
HS2880	N 874	37°29′15″	121°55′53″	−17.047	13.86164	- - -	13.90928	- - -	13.90672	- - -	- - -	- - -
HS2877	Q 591 reset	37°28′39″	121°55′33″	−16.023	- - -	- - -	13.14489	- - -	13.14609	- - -	- - -	- - -
HS4395	C 1371	37°27′34″	121°55′10″	−13.702	- - -	- - -	- - -	- - -	4.08388	- - -	- - -	- - -
HS2856	D 1076	37°27′07″	121°54′46″	−12.603	3.71923	- - -	3.75836	- - -	3.75451	- - -	- - -	- - -
HS2852	Jacklin RM 1	37°26′21″	121°54′23″	−11.066	3.32197	- - -	3.36280	- - -	3.34855	- - -	- - -	- - -
HS2851	M 874	37°26′10″	121°54′20″	−10.752	3.94223	- - -	3.98305	- - -	3.97993	- - -	- - -	- - -
HS5156	G 1447	37°25′55″	121°54′17″	−10.246	- - -	- - -	- - -	- - -	5.60388	- - -	- - -	- - -
HS5157	D 176 reset	37°25′40″	121°54′30″	−9.547	- - -	- - -	- - -	- - -	4.52166	- - -	- - -	- - -
HS2849	Z 174	37°25′33″	121°54′12″	−8.940	5.24552	- - -	5.29129	- - -	5.27474	- - -	- - -	- - -
HS2969	Milpitas	37°25′31″	121°54′12″	−8.866	5.30201	- - -	5.34227	- - -	5.33907	- - -	- - -	- - -
HS2968	Milpitas RM 1	37°25′31″	121°54′11″	−8.851	5.62744	- - -	5.66884	- - -	5.66102	- - -	- - -	- - -
HS2848	L 874	37°24′58″	121°54′03″	−7.777	8.19467	- - -	8.27074	- - -	8.24521	- - -	- - -	- - -
HS2847	G 554	37°24′50″	121°54′01″	−7.524	10.09069	- - -	10.13329	- - -	10.11783	- - -	- - -	- - -
HS3086	K 179 reset	37°24′30″	121°53′20″	−6.091	- - -	- - -	- - -	- - -	14.99672	- - -	- - -	- - -
HS5158	M 1447	37°24′15″	121°53′59″	−4.898	- - -	- - -	- - -	- - -	11.20016	- - -	- - -	- - -
HS5159	N 1447	37°23′17″	121°53′54″	−3.135	- - -	- - -	- - -	- - -	15.13748	- - -	- - -	- - -
HS2840	X 147	37°22′44″	121°53′50″	−2.118	19.14230	- - -	19.15978	- - -	19.06579	- - -	- - -	- - -
HS2838	B 1076	37°22′06″	121°53′47″	−0.963	16.98160	- - -	16.96284	- - -	16.84116	- - -	- - -	- - -
HS5161	G 1448	37°21′07″	121°55′01″	0.000	- - -	- - -	- - -	- - -	17.22686	17.22686	9.81	- - -
HS2835	C 1121 reset	37°21′41″	121°53′42″	0.088	18.22893	- - -	18.18108	- - -	18.00880	- - -	- - -	- - -
HS5160	L 1447	37°20′56″	121°55′03″	0.598	- - -	- - -	- - -	- - -	22.74936	22.74729	10.78	- - -
HS2833	U 174	37°21′06″	121°53′28″	1.173	19.41924	- - -	19.37769	- - -	19.22744	- - -	- - -	- - -
HS2891	Z 111 reset 1962	37°20′29″	121°54′40″	1.745	23.22841	- - -	- - -	- - -	23.05946	23.05275	12.64	3.10
HS2885	Z 876 reset	37°20′58″	121°53′59″	2.060	- - -	- - -	19.75525	- - -	19.59935	- - -	- - -	- - -
HS2886	B 112	37°20′46″	121°54′13″	2.598	22.14169	- - -	- - -	- - -	21.94914	21.94754	14.02	3.21
HS5162	E 1447	37°20′28″	121°53′45″	4.166	- - -	- - -	- - -	- - -	23.47840	23.47067	14.82	- - -
HS2828	P 7 reset 1965	37°20′22″	121°53′29″	4.787	26.51995	- - -	26.46974	- - -	26.30861	26.29759	15.14	3.66

Table 11.—*Leveling observations along a line from San Jose through Gilroy and Sargent to Watsonville*—Continued

					Orthometric height (m)							
ACRN	Designation	Latitude N.	Longitude W.	Leveled distance (km)	1967 (3–5) L21038, L21016.1, L21016.2	1968 (10–11) L21602	1969 (3–10) L219691, L21746	1972 (7–9) L22841	1989 (2–7) L2517.2, L2517.4	1990 (1–2) L25239.1	Subsidence correction (mm)	Earthquake correction (mm)
HS2826	D 886	37°20′17″	121°53′26″	4.968	26.45147	- - -	26.40250	- - -	26.23949	26.22769	15.17	3.63
HS2825	A 326 reset 1970	37°20′16″	121°53′22″	5.086	- - -	- - -	- - -	- - -	25.69628	25.68429	14.90	- - -
HS2822	M 177	37°20′10″	121°53′22″	5.383	27.34161	- - -	27.29548	- - -	27.14673	27.13324	14.23	4.59
HS5163	I 19=96 reset 1976	37°20′16″	121°53′11″	5.709	- - -	- - -	- - -	- - -	23.70753	23.69523	15.60	- - -
HS2813	A 1122	37°20′04″	121°52′35″	6.972	27.00560	- - -	26.92388	- - -	26.69688	26.68216	20.90	5.17
HS2814	San Jose AZ MK	37°19′31″	121°52′11″	8.568	29.61819	- - -	29.54719	- - -	29.34023	29.32154	19.12	5.45
HS2811	B 149	37°18′51″	121°52′04″	10.085	30.56198	- - -	30.50680	- - -	30.36366	30.34000	14.52	6.13
HS2810	L 591	37°18′27″	121°51′45″	10.957	32.42800	- - -	32.38979	- - -	32.30360	32.26790	10.23	6.41
HS2809	2=J 19	37°18′08″	121°51′29″	11.753	36.57012	- - -	36.51550	- - -	36.37031	36.34033	14.63	6.54
HS2806	C 886 reset 1962	37°17′40″	121°51′02″	13.031	44.16217	- - -	44.17860	- - -	44.18479	44.13360	1.69	6.81
HS2796	A 1076	37°16′47″	121°50′11″	15.012	50.19516	- - -	50.21369	- - -	50.23496	50.17403	.70	6.83
HS2795	Q 877 reset 1964	37°16′28″	121°49′51″	15.846	64.08164	- - -	64.10134	- - -	64.13296	64.07007	–.03	7.04
HS2792	B 1121	37°16′25″	121°49′46″	15.982	53.18187	- - -	53.20085	- - -	53.23023	53.16702	–.17	7.14
HS2789	P 453	37°15′55″	121°49′06″	17.378	55.37796	- - -	55.40304	- - -	55.41240	55.35291	–.81	7.37
HS2788	R 174	37°15′42″	121°48′41″	18.111	54.71156	- - -	54.73644	- - -	54.73319	54.67250	–1.39	7.41
HS2787	QQ 453	37°15′23″	121°48′12″	19.036	57.36310	- - -	57.38652	- - -	57.38041	57.31731	–1.60	7.59
HS4926	JCT	37°15′12″	121°47′53″	19.609	- - -	- - -	- - -	- - -	58.85663	58.79086	–1.82	- - -
HS5164	JCT RM3	37°15′13″	121°47′53″	19.615	- - -	- - -	- - -	- - -	59.13915	59.06825	–1.82	- - -
HS2785	P 174	37°14′58″	121°47′30″	20.301	59.23695	- - -	59.25801	- - -	59.24368	59.18601	–2.08	7.58
HS2784	N 453	37°14′42″	121°47′03″	21.212	60.02265	- - -	60.03420	- - -	60.04362	59.98473	–1.42	7.39
HS5165	H 1447	37°14′17″	121°46′19″	22.505	- - -	- - -	- - -	- - -	65.40824	65.34790	–.88	- - -
HS4141	L 453	37°13′34″	121°45′02″	24.649	79.23240	- - -	79.23369	- - -	79.28453	79.22396	.03	6.59
HS2778	M 174	37°13′21″	121°44′42″	25.464	74.60063	- - -	74.60037	- - -	74.65133	74.59144	–.01	6.09
HS2776	P 19	37°13′00″	121°44′21″	26.325	77.65145	- - -	77.65462	- - -	77.70273	77.64330	.04	5.56
HS2775	L 174	37°12′22″	121°43′41″	27.865	79.83738	- - -	79.84146	- - -	79.85548	79.79742	–1.46	5.30
HS2773	Y 176	37°11′39″	121°42′56″	29.592	88.56798	- - -	88.56946	- - -	88.61912	88.55947	.07	4.79
HS2769	Perrys	37°11′01″	121°42′17″	31.084	91.36767	- - -	91.36921	- - -	91.41696	91.35666	.01	4.23
HS2771	Perrys RM 4	37°11′02″	121°42′17″	31.091	- - -	- - -	91.56066	- - -	91.60079	91.53994	.01	- - -
HS5166	A 1448	37°10′37″	121°41′52″	32.057	- - -	- - -	- - -	- - -	94.02074	93.96089	.07	- - -
HS2768	K 453 reset 1974	37°10′28″	121°41′41″	32.432	- - -	- - -	- - -	- - -	96.86834	96.80890	.09	- - -
HS5167	B 1448	37°10′17″	121°41′31″	32.881	- - -	- - -	- - -	- - -	98.37293	98.31317	.12	- - -
HS2762	J 453	37°09′43″	121°40′59″	34.168	101.44952	- - -	101.45073	- - -	101.50033	101.44053	.20	1.45
HS2757	A 177	37°09′25″	121°40′39″	34.957	102.87953	- - -	102.87917	- - -	102.93175	102.86655	.29	.90
HS2758	A 1077 X	37°09′09″	121°40′51″	35.919	105.35747	105.45392	105.35041	- - -	105.40869	105.33849	.29	–.16
HS2759	B 1077 X	37°09′09″	121°40′50″	35.930	105.58296	105.67947	105.57601	- - -	105.63412	105.56405	.33	–1.07
HS2761	C 1077 X	37°09′09″	121°40′50″	36.014	102.74605	102.84134	102.73934	- - -	102.79502	102.72574	.25	–1.46
HS2754	R 19	37°08′36″	121°39′50″	37.913	106.83633	106.93251	106.83503	- - -	106.88920	106.82443	.45	–1.93
HS2753	RV 2501	37°08′28″	121°39′41″	38.236	107.53127	107.62476	107.53570	- - -	107.57909	107.51500	.24	–2.32
HS2751	D 1080	37°07′49″	121°39′00″	39.739	106.96565	107.06415	106.96679	- - -	107.01052	106.94802	.13	–3.00
HS5168	N 1448	37°07′22″	121°38′34″	40.908	- - -	- - -	- - -	- - -	103.46770	103.40712	.10	- - -
HS5169	P 1448	37°06′56″	121°38′07″	41.933	- - -	- - -	- - -	- - -	99.96772	99.90848	.08	- - -
HS2745	E 1080	37°06′11″	121°37′20″	43.419	95.79480	95.88446	95.79689	- - -	95.83563	95.78015	.04	–4.89
HS2743	A 812	37°05′44″	121°36′56″	44.781	95.41833	95.51439	95.41404	- - -	95.46137	95.41688	.19	–6.02
HS2742	T 19 reset 1938	37°05′43″	121°36′56″	44.826	93.66576	93.76229	93.66226	- - -	93.71473	93.67007	.47	–6.24
HS5170	D 1448	37°05′06″	121°36′31″	46.147	- - -	- - -	- - -	- - -	87.24420	87.19758	.05	- - -
HS5171	C 1448	37°05′07″	121°35′59″	47.156	- - -	- - -	- - -	- - -	85.93072	85.88483	–.26	- - -
HS2738	G 1080	37°04′19″	121°36′04″	47.740	80.47289	80.54364	80.45440	- - -	80.49911	80.44464	–.45	–8.86
HS2737	C 812	37°03′22″	121°35′32″	49.664	74.75169	74.83194	74.74230	- - -	74.77397	74.72653	–.62	–9.08
HS2736	M 149	37°03′00″	121°35′21″	50.366	71.19232	71.26762	71.17744	- - -	71.21151	71.16765	–.76	–8.96
HS2733	Rucker reset 1957	37°02′38″	121°35′11″	51.125	- - -	69.28362	- - -	- - -	69.22693	69.18477	–.84	- - -
HS2727	E 812 reset 1973	37°02′12″	121°35′30″	52.380	- - -	- - -	- - -	- - -	67.49486	67.45765	–.96	- - -
HS2725	D 812	37°02′04″	121°34′52″	53.422	67.11539	67.19149	67.09881	- - -	67.12845	67.08759	–1.07	–8.35
HS5172	Q 1448	37°01′33″	121°34′37″	54.449	- - -	- - -	- - -	- - -	62.83462	62.79470	–.76	- - -
HS2724	N 149	37°01′13″	121°34′25″	55.119	61.93561	62.00800	61.91427	- - -	61.96063	61.91852	–.56	–7.66
HS2723	L 1193	37°01′02″	121°34′19″	55.512	- - -	61.11025	61.01426	- - -	61.05964	61.02322	–.54	- - -
HS5143	E 1448	37°00′45″	121°34′12″	56.083	- - -	- - -	- - -	- - -	60.67193	60.63577	–.51	- - -
HS2720	Z 19	37°00′28″	121°34′14″	56.822	62.80408	62.88158	- - -	- - -	62.83183	62.79699	–.47	–6.86
HS2721	Y 19	37°00′25″	121°34′01″	57.287	61.20904	61.28681	- - -	- - -	61.23684	61.20166	–.49	–6.42
HS2722	11	37°00′25″	121°34′02″	57.320	60.84984	60.92697	60.83076	- - -	60.87549	60.84059	–.60	-6.13
HS2719	P 149	37°00′21″	121°33′57″	57.607	- - -	- - -	- - -	- - -	59.86798	59.83225	–.59	- - -
HS2718	RV 22	37°00′09″	121°33′55″	57.664	60.49429	60.57143	- - -	- - -	60.52009	60.48431	–.58	–6.27
HS5144	F 1448	37°00′02″	121°33′47″	58.146	- - -	- - -	- - -	- - -	59.78645	59.74900	–.55	- - -
HS3323	D 1236	37°00′02″	121°33′49″	58.200	- - -	- - -	- - -	60.53572	60.55068	60.51207	–.55	–7.12
GU2195	C 1193	36°59′42″	121°33′40″	58.785	57.35129	57.42843	- - -	57.35129	57.37748	57.34027	–.51	–7.56
GU2192	Q 149 reset 1967	36°59′27″	121°33′30″	59.329	- - -	59.02364	- - -	58.94728	58.97008	58.93271	–.83	–7.99
GU2190	D 1193	36°58′52″	121°32′54″	60.917	- - -	53.80850	- - -	53.73351	53.76051	53.72144	–.56	–8.40
GU2189	RV 24	36°58′39″	121°32′40″	61.564	- - -	52.14657	- - -	52.06820	52.08874	52.04508	–.91	–8.87
GU2188	R 149	36°58′09″	121°32′30″	62.363	- - -	54.07306	- - -	53.98806	53.97888	53.93024	–2.65	–9.12
GU2180	E 1193	36°57′16″	121°32′39″	63.974	- - -	46.44321	- - -	46.35519	46.35174	46.30512	–2.29	–9.43
GU2178	F 1193	36°56′39″	121°32′47″	65.207	- - -	43.28335	- - -	43.19479	43.18976	43.14411	–2.37	–9.61
GU4096	M 1448	36°56′36″	121°32′48″	65.308	- - -	- - -	- - -	- - -	42.92262	42.88038	–2.21	- - -
GU2177	S 149	36°55′52″	121°32′49″	66.625	- - -	44.02923	- - -	43.95420	44.01788	43.97529	–.11	–8.99
GU2176	G 1193	36°55′43″	121°32′49″	66.879	- - -	46.00386	- - -	45.93814	45.97923	45.95170	.30	–8.93
GU2174	E 1236	36°55′19″	121°32′48″	67.554	- - -	- - -	- - -	44.81370	44.85771	44.84713	.45	–8.54
GU2175	SF 138	36°55′15″	121°32′50″	67.791	- - -	42.10530	- - -	- - -	42.09616	42.09158	.42	- - -
GU2173	K 1193	36°55′04″	121°32′48″	68.173	- - -	46.09696	- - -	46.04545	46.08843	46.06083	.37	–8.16
GU2172	12 41	36°55′02″	121°32′48″	68.187	- - -	46.38910	- - -	46.33795	46.37990	46.35768	.28	–7.65
GU2171	Sargent AZ MK	36°55′02″	121°32′48″	68.274	- - -	46.35530	- - -	46.29594	46.33384	46.29952	.02	–7.32
GU2167	G 1236	36°54′15″	121°33′19″	69.904	- - -	- - -	- - -	48.62907	48.67581	48.62064	.52	–6.97
GU2155	F 1236	36°53′42″	121°33′20″	70.975	- - -	- - -	- - -	43.90135	43.94900	43.93368	.55	–6.66
GU2154	B 1193	36°53′16″	121°33′24″	71.743	- - -	44.97181	- - -	44.90292	44.93956	44.87223	–.12	–6.24
GU2151	A 1193	36°52′57″	121°33′36″	72.394	- - -	45.68985	- - -	45.62485	45.67091	45.60102	.39	–5.56
GU4097	U 1448	36°53′32″	121°34′27″	74.431	- - -	- - -	- - -	- - -	54.58518	54.53649	.73	- - -
GU2161	K 812	36°54′05″	121°35′51″	77.197	- - -	- - -	- - -	40.90965	40.96978	40.91139	1.19	–4.96
GU2162	E 20	36°54′24″	121°36′46″	78.683	- - -	- - -	- - -	37.94356	38.01785	37.95440	2.01	–4.74
GU2163	L 1236	36°54′34″	121°37′13″	79.501	- - -	- - -	- - -	38.35744	38.43214	38.35483	2.02	–4.57
GU2226	M 1236	36°54′33″	121°37′51″	80.548	- - -	- - -	- - -	37.43106	37.50049	37.42382	1.67	–3.87
GU2229	N 1236	36°53′30″	121°38′33″	82.963	- - -	- - -	- - -	28.96355	29.02759	28.92277	1.33	–3.45
GU2230	W 149	36°53′28″	121°38′58″	83.574	- - -	- - -	- - -	29.28700	29.34896	29.21428	1.19	–3.11
GU2231	P 1236	36°53′32″	121°39′36″	84.551	- - -	- - -	- - -	24.90692	24.96232	24.84626	.76	–2.42
GU2232	Q 1236	36°53′40″	121°40′22″	85.736	- - -	- - -	- - -	19.23247	19.28686	19.15505	.68	–2.17

Table 11.—*Leveling observations along a line from San Jose through Gilroy and Sargent to Watsonville*—Continued

ACRN	Designation	Latitude N.	Longitude W.	Leveled distance (km)	Orthometric height (m)						Subsidence correction (mm)	Earthquake correction (mm)
					1967 (3–5) L21038, L21016.1, L21016.2	1968 (10–11) L21602	1969 (3–10) L219691, L21746	1972 (7–9) L22841	1989 (2–7) L2517.2, L2517.4	1990 (1–2) L25239.1		
GU2233	R 1236	36°53′51″	121°41′24″	87.354	- - -	- - -	- - -	18.88477	18.93404	18.80269	.35	−1.58
GU2235	Y 149	36°54′03″	121°42′20″	88.805	- - -	- - -	- - -	12.21096	12.24087	12.10724	−.82	−1.01
GU4098	V 1448	36°54′05″	121°42′42″	89.397	- - -	- - -	- - -	- - -	14.11705	13.99848	−.38	- - -
GU2237	S 1236	36°54′01″	121°43′05″	89.977	- - -	- - -	- - -	11.89650	11.94221	11.81938	.05	.00
GU2239	T 1236	36°53′55″	121°43′39″	90.899	- - -	- - -	- - -	10.35522	10.39775	10.28159	−.14	.00
GU2240	U 1236	36°53′50″	121°44′04″	91.563	- - -	- - -	- - -	8.63629	8.68082	8.57030	−.02	.00
GU2242	M 20 reset 1964	36°53′44″	121°44′40″	92.383	- - -	- - -	- - -	8.66899	8.68768	8.57506	−1.54	.00

Table 12.—*Leveling observations along a line from Watsonville to Santa Cruz*

[See figure 1 for locations. Number(s) in parentheses below year of survey indicate month(s) when survey was conducted. L-number is U.S. National Geodetic Survey designation. Subsidence correction applies to 1978–90 height difference]

ACRN	Designation	Latitude N.	Longitude W.	Leveled distance (km)	Orthometric height (m)			Subsidence correction (mm)
					1972 (7–9) L22841	1978 (5) L24298	1990 (2) L25239.2	
GU2242	M 20 reset 1964	36°53′44″	121°44′40″	0.000	8.69274	8.67814	8.57506	−1.54
GU2245	V 1236	36°54′12″	121°45′13″	1.404	10.18733	10.17828	10.09895	−5.23
GU2246	W 1236	36°54′19″	121°45′23″	1.768	7.46515	7.46053	7.39289	6.11
GU4162	H 249 reset 1979	36°54′28″	121°45′37″	2.204	- - -	- - -	8.12852	- - -
GU2248	X 1236	36°54′01″	121°46′35″	3.947	5.46739	5.45611	5.39828	15.16
GU4161	A 1455	36°53′39″	121°47′56″	6.166	- - -	- - -	7.10690	- - -
GU2260	Z 1236	36°54′37″	121°48′42″	8.257	22.37276	22.36318	22.34565	1.55
GU2262	A 1237	36°54′56″	121°49′10″	9.364	37.47246	37.46232	37.44568	5.03
GU2264	E 249	36°55′21″	121°50′15″	11.199	47.88581	47.86756	4.85577	3.88
GU2265	C 1237	36°55′30″	121°50′40″	11.842	36.09285	36.08243	36.09116	−12.69
GU2266	D 1237	36°55′54″	121°51′25″	13.204	15.87628	15.86939	15.89721	3.31
GU2269	RV 6	36°56′10″	121°51′50″	14.140	23.43842	23.42989	23.43879	10.52
GU2268	E 1237	36°56′10″	121°51′50″	14.148	23.37247	23.36326	23.37856	7.17
GU2272	C 249	36°56′52″	121°52′20″	15.636	- - -	- - -	35.90532	- - -
GU2273	F 1237	36°56′54″	121°52′24″	15.748	33.08911	33.06446	33.07778	5.78
GU2276	G 1237	36°57′26″	121°52′54″	16.925	37.22072	37.20603	37.29474	−25.77
GU2277	H 1237	36°58′01″	121°53′29″	18.321	31.53158	31.51163	31.61853	−5.42
GU2279	J 1237	36°58′32″	121°53′50″	19.365	30.37252	30.35453	30.49432	−16.16
GU2278	RV 5	36°58′33″	121°53′51″	19.505	29.78264	29.76600	29.90682	−12.16
GU2281	RV 4	36°58′35″	121°54′11″	20.006	32.16769	32.14712	32.28531	−9.40
GU2282	K 1237	36°58′33″	121°54′16″	20.255	34.82839	34.81040	34.94245	−17.43
GU2283	L 1237	36°58′45″	121°55′05″	21.576	40.88461	40.86311	40.98057	−12.16
GU2285	M 1237	36°58′53″	121°56′11″	23.422	22.61641	22.59380	22.70805	−19.33
GU2286	N 1237	36°58′37″	121°56′35″	24.273	24.54349	24.52137	24.61802	−21.60
GU2287	Z 212	36°58′31″	121°56′58″	24.815	19.40660	19.38520	19.46904	−20.60
GU2290	P 1237	36°58′23″	121°57′10″	25.282	16.45093	16.43249	16.51665	−19.13
GU2289	61.94	36°58′06″	121°57′49″	26.500	18.84766	18.82875	18.88675	−13.08
GU2291	55.79	36°58′09″	121°59′03″	28.282	16.97265	16.95073	16.99658	−14.04
GU2294	51.93	36°58′09″	121°59′48″	29.454	15.79953	15.77982	15.82329	−20.19
GU1941	R 1237	36°58′06″	122°00′05″	29.834	8.63581	8.61349	8.64272	−15.67
GU1944	S 1237	36°57′56″	122°00′42″	30.870	7.31218	7.29741	7.31251	−21.01
GU3223	941 3745 tidal 4	36°57′56″	122°01′28″	32.137	- - -	13.21725	13.23207	−5.58
GU1945	14	36°57′53″	122°01′30″	32.379	4.20406	4.18806	4.21113	−7.69

Table 13.—Leveling observations along a line from Santa Cruz through Los Gatos to San Jose

[See figure 1 for locations. Numbers in parentheses below year of survey indicate months when survey was conducted. L-numbers are U.S. National Geodetic Survey designations. Subsidence correction applies to 1967–90 height difference]

					Orthometric height (m)				
ACRN	Designation	Latitude N.	Longitude W.	Leveled distance (km)	1954 (4–7) L15275.9, L15275.10	1960 (9–12) L18119.9, L18119.10	1967 (1–3) L21016.9, L21016.10, L21016.13	1990 (2–3) L25239.3	Subsidence correction (mm)
GU3223	941 3745 tidal 4	36°57′56″	122°01′28″	0.000	---	---	---	13.23207	---
GU1945	14	36°57′53″	122°01′30″	.147	---	---	---	4.21146	---
GU1952	T 1237	36°58′05″	122°01′42″	.601	---	---	---	4.55344	---
GU4167	B 1455	36°58′15″	122°01′50″	1.042	---	---	---	4.41596	---
GU1953	W 212	36°58′26″	122°01′50″	1.472	---	---	---	6.58358	---
GU4163	C 1455	36°58′42″	122°01′24″	2.329	---	---	---	8.12574	---
GU4164	D 1455	36°59′10″	122°01′22″	3.365	---	---	---	12.63562	---
GU4165	E 1455	36°59′24″	122°01′15″	3.796	---	---	---	26.60844	---
GU4166	F 1455	36°59′58″	122°01′12″	4.970	---	---	---	78.09381	---
HT3563	G 1455	37°00′31″	122°01′13″	6.103	---	---	---	103.22221	---
HT3564	H 1455	37°01′14″	122°01′34″	7.519	---	---	---	135.67828	---
HT3565	J 1455	37°02′08″	122°01′13″	9.482	---	---	---	169.60427	---
HT3566	K 1455	37°02′34″	122°01′24″	10.349	---	---	---	156.57370	---
HT3567	M 1455	37°03′12″	122°02′19″	10.506	---	---	---	135.65247	---
HT3568	L 1455	37°03′18″	122°03′04″	10.662	---	---	---	156.30220	---
HT3569	N 1455	37°03′20″	122°03′31″	10.819	---	---	---	109.07614	---
HT3570	P 1455	37°03′19″	122°03′36″	10.975	---	---	---	106.74056	---
HT1429	L 249	37°03′05″	122°03′43″	11.132	---	---	---	91.08537	---
HT1430	RV 12	37°02′55″	122°03′48″	11.288	---	---	---	89.43701	---
HT3571	Q 1455	37°02′51″	122°00′53″	11.445	---	---	---	166.37080	---
HT3572	R 1455	37°03′19″	122°00′35″	12.525	---	---	---	174.13167	---
HT3573	S 1455	37°03′39″	122°00′11″	13.729	---	---	---	192.78908	---
HS4900	TRAILL	37°03′31″	121°59′35″	15.070	---	---	---	281.51432	---
HS5175	T 1455	37°04′19″	121°59′24″	15.560	---	---	---	248.10103	---
HS5176	U 1455	37°04′42″	121°58′43″	16.947	---	---	---	306.37117	---
HS5177	V 1455	37°05′10″	121°58′40″	17.909	---	---	---	346.31595	---
HS5178	W 1455	37°05′43″	121°58′30″	19.063	---	---	---	387.01594	---
HS5179	X 1455	37°06′20″	121°58′24″	20.378	---	---	---	370.64274	---
HS5180	Y 1455	37°06′48″	121°58′24″	21.425	---	---	---	423.19583	---
HS5181	Z 1455	37°07′20″	121°58′21″	22.477	---	---	---	469.51265	---
HS5182	A 1456	37°07′59″	121°58′48″	23.891	---	---	---	553.06745	---
HS5183	B 1456	37°08′16″	121°59′02″	24.628	---	---	---	543.58833	---
HS3171	R 1077 reset 1970	37°08′44″	121°59′03″	25.590	---	---	---	558.60804	---
HS5184	C 1456	37°09′06″	121°59′01″	26.676	---	---	---	485.80749	---
HS5185	D 1456	37°09′26″	121°58′52″	27.590	---	---	---	423.41982	---
HS5186	E 1456	37°09′42″	121°59′21″	28.580	---	---	---	365.70972	---
HS3165	P 878	37°10′14″	121°59′20″	29.779	322.14184	322.06118	322.07113	322.14841	.00
HS3174	R 878	37°10′04″	121°58′43″	30.300	205.79353	205.74637	205.73157	205.84335	.00
HS5187	F 1456	37°10′41″	121°59′39″	30.821	---	---	---	263.53229	---
HS3160	M 878	37°11′00″	121°59′27″	31.572	228.18700	228.13815	228.12361	228.16190	.00
HS5188	G 1456	37°11′41″	121°59′32″	32.974	---	---	---	203.69486	---
HS3154	K 878	37°12′03″	121°59′24″	33.793	203.28128	203.23991	203.23140	203.25366	.00
HS3150	D 177	37°12′53″	121°59′13″	35.485	135.17397	135.12746	135.11170	135.09580	.00
HS5189	H 1456	37°13′19″	121°58′57″	36.454	---	---	---	124.60494	---
HS3145	C 177	37°13′27″	121°58′48″	36.737	121.88043	121.83275	121.82025	121.75144	−1.01
HS5190	J 1456	37°13′55″	121°58′36″	37.904	---	---	---	112.04248	---
HS5191	K 1456	37°14′24″	121°58′20″	38.896	---	---	---	104.06291	---
HS3140	G 386	37°14′49″	121°57′55″	39.922	93.57815	93.53010	93.50326	93.39370	−4.86
HS4911	VASO-	37°14′50″	121°57′54″	39.975	---	---	---	92.90174	---
HS3141	G 875	37°14′49″	121°57′55″	40.011	93.31040	93.27220	93.24122	93.13894	−5.97
HS5192	L 1456	37°15′24″	121°57′51″	41.256	---	---	---	85.22922	---
HS3188	F 180	37°15′49″	121°58′37″	41.940	77.42417	77.38116	77.34461	77.31581	−9.29
HS3132	T 1122	37°16′05″	121°57′22″	42.624	---	71.64922	71.61770	71.55630	−6.11
HS5193	M 1456	37°16′26″	121°57′04″	43.424	---	---	---	67.62296	---
HS3271	A 887 reset 1962	37°16′01″	121°56′27″	43.940	---	---	71.65135	71.55339	−11.71
HS3131	S 1122	37°16′55″	121°56′40″	44.455	---	63.34012	63.27957	63.22391	−13.90
HS3130	E 875	37°17′08″	121°56′37″	44.941	61.54129	61.45800	61.30408	61.24838	−38.94
HS3127	U 176 reset 1940	37°17′13″	121°56′15″	45.647	58.95799	58.87831	58.71350	58.64586	−41.86
HS3125	D 875	37°17′27″	121°56′18″	46.265	59.19844	59.09533	58.87475	58.78229	−56.81
HS3124	T 176 reset 1962	37°17′52″	121°55′51″	47.283	---	---	52.26381	52.13361	−93.45
HS3122	S 176 reset 1962	37°18′07″	121°55′36″	47.824	---	---	50.23288	50.06486	−112.92
HS3120	R 176 reset 1962	37°18′39″	121°54′59″	49.252	---	---	42.33935	42.10389	−164.32
HS3118	P 176	37°19′10″	121°54′26″	50.667	34.32425	33.93393	33.12257	32.95738	−215.25
HS3117	D 877	37°19′28″	121°54′06″	51.396	31.00216	30.60606	29.77560	29.61618	−220.37
HS3109	C 112	37°19′55″	121°54′09″	52.288	30.60766	30.13155	29.13692	28.90626	−264.40
HS3108	B 875	37°20′05″	121°54′13″	52.593	28.52997	28.02726	26.99132	26.75623	−275.48
HS2891	Z 111 reset 1962	37°20′29″	121°54′40″	53.601	---	24.23590	23.22121	23.00027	−269.78
HS5160	L 1447	37°20′56″	121°55′03″	54.722	---	---	---	22.69595	---
HS5161	G 1448	37°21′07″	121°55′01″	55.311	---	---	---	17.17585	---

Table 14.—*Leveling observations along a line from Capitola through Loma Prieta to Coyote*

[See figure 1 for locations. Numbers in parentheses below year of survey indicate months when survey was conducted; month of 1953 survey is unknown. L-number is U.S. National Geodetic Survey designation; PV numbers are U.S. Geological Survey (USGS) field-summary-book designations. Obs., original field observations, with previous USGS adjustments removed; adj., observations adjusted for consistent coseismic network (see text)]

ACRN	Designation	Latitude N.	Longitude W.	Leveled distance (km)	Orthometric height (m)		
					1953 (obs.)	1953 (adj.)	1990 (3–4) L25239.4
					PV 80, PV208, PV220		
GU2286	N 1237	36°58′37″	121°56′35″	0.000	---	---	24.61802
GU2287	Z 212	36°58′31″	121°56′58″	.540	19.47200	19.35700	19.46874
GU4168	N 1456	36°58′59″	121°57′22″	1.631	---	---	10.90370
GU4169	32 WLS	36°59′26″	121°57′24″	2.473	12.55000	12.44000	12.58387
HS5194	P 1456	37°00′19″	121°57′08″	4.081	---	---	32.43278
HS5195	Q 1456	37°01′18″	121°57′01″	6.098	---	---	63.00953
HS5196	Chiseled square A	37°02′09″	121°56′35″	7.938	69.45100	69.35200	69.68787
HS5197	R 1456	37°02′44″	121°56′18″	9.183	---	---	70.75253
HS5198	S 1456	37°03′19″	121°56′21″	10.388	---	---	80.92999
HS5199	T 1456	37°04′09″	121°56′15″	12.079	---	---	141.75804
HS5200	U 1456	37°04′36″	121°56′21″	12.914	---	---	176.51875
HS5201	1940	37°05′10″	121°57′02″	14.197	---	---	253.93246
HS5202	28 WLS	37°05′41″	121°56′57″	15.556	338.66800	338.58500	339.14897
HS5203	Chiseled square B	37°06′08″	121°56′47″	16.474	393.53200	393.45100	394.06493
HS5210	Z 1456	37°06′39″	121°56′52″	17.769	---	---	437.11351
HS5204	Burdett	37°06′37″	121°56′43″	18.074	---	---	458.02049
HS5205	27 WLS	37°06′52″	121°56′20″	18.770	471.42400	471.34800	471.73675
HS5206	V 1456	37°07′06″	121°55′26″	20.234	---	---	477.26362
HS5207	W 1456	37°06′40″	121°54′40″	21.624	---	---	548.68660
HS5208	X 1456	37°06′22″	121°53′56″	22.910	---	---	572.60387
HS5209	Y 1456	37°06′19″	121°53′36″	23.577	---	---	609.21796
HS5211	A 1457	37°06′19″	121°53′20″	24.432	---	---	687.67126
HS5212	B 1457	37°06′17″	121°52′45″	25.372	---	---	762.65041
HS5213	C 1457	37°05′56″	121°52′02″	26.767	---	---	768.58749
HS5214	D 1457	37°06′01″	121°51′42″	27.478	---	---	844.04796
HS5215	E 1457	37°05′56″	121°51′13″	28.106	---	---	906.54151
HS5216	F 1457	37°05′49″	121°50′41″	29.151	---	---	939.09174
HS5217	G 1457	37°06′22″	121°50′49″	30.546	---	---	1,024.92195
HS5218	Loma Prieta reset 1958	37°06′40″	121°50′35″	30.796	---	---	1,154.12757
HS5219	LOMA	37°06′41″	121°50′35″	31.045	---	---	1,154.70909
HS5220	Loma Prieta 1	37°06′35″	121°50′37″	31.295	---	---	1,152.23547
HS5221	H 1457	37°06′25″	121°50′14″	31.544	---	---	906.77804
HS5222	J 1457	37°06′35″	121°50′06″	31.997	---	---	870.71964
HS5223	K 1457	37°06′18″	121°49′14″	33.535	---	---	788.32005
HS5224	HJH 55	37°06′09″	121°48′20″	34.950	728.26800	728.22600	728.13323
HS5225	L 1457	37°06′19″	121°48′18″	35.769	---	---	600.76979
HS5226	M 1457	37°06′41″	121°48′19″	36.585	---	---	480.67933
HS5227	N 1457	37°06′47″	121°48′25″	37.650	---	---	364.02224
HS5228	P 1457	37°07′11″	121°48′06″	38.787	---	---	300.72020
HS5230	Q 1457	37°07′25″	121°47′40″	39.885	---	---	279.08001
HS5229	TBM angle iron	37°07′25″	121°47′39″	39.892	276.80400	276.77200	276.70031
HS5231	HJH 53	37°07′56″	121°47′30″	40.985	246.37300	246.34400	246.26767
HS5232	R 1457	37°08′26″	121°46′58″	42.420	---	---	227.65294
HS5233	Chiseled square C	37°08′54″	121°46′15″	43.885	207.11700	207.09400	207.03122
HS5234	S 1457	37°09′07″	121°45′35″	45.050	---	---	203.26228
HS5235	TBM spike	37°09′07″	121°45′35″	45.073	201.97200	201.95100	201.86131
HS5236	T 1457	37°09′05″	121°44′49″	46.341	---	---	191.44521
HS5237	U 1457	37°09′37″	121°44′56″	47.370	---	---	230.54392
HS5238	TBM manhole	37°09′37″	121°44′56″	47.390	230.22200	230.20600	230.15221
HS5239	HJH 51	37°10′20″	121°45′30″	49.067	156.36400	156.35200	156.30456
HS5240	V 1457	37°11′03″	121°45′12″	50.963	---	---	145.71067
HS5241	W 1457	37°11′16″	121°45′19″	51.695	---	---	94.49410
HS5242	X 1457	37°11′47″	121°44′31″	53.190	---	---	76.86677
HS2775	L 174	37°12′22″	121°43′41″	54.849	79.81900	79.81900	79.78395
HS2776	P 19	37°13′00″	121°44′21″	56.388	---	---	77.63078

Table 15.—*Leveling observations along a line from 9.6 km south of Morgan Hill to Loma Prieta*

[See figure 1 for locations. Number in parentheses below year of survey indicates month when survey was conducted; month of 1953 survey is unknown. L-number is U.S. National Geodetic Survey designation; PV-number is U.S. Geological Survey (USGS) field-summary-book designation. Obs., original field observations, with previous USGS adjustments removed; adj., observations adjusted for consistent coseismic network (see text)]

ACRN	Designation	Latitude N.	Longitude W.	Leveled distance (km)	Orthometric height (m)		
					1953 (obs.)	1953 (adj.)	1990 (4) L25239.5
					PV220		
HS5243	Q 1458	37°01′50″	121°39′20″	0.000	---	---	103.30476
HS5244	P 1458	37°01′49″	121°39′49″	1.359	---	---	108.51847
HS5245	N 1458	37°01′58″	121°40′57″	3.171	---	---	134.40205
HS5246	M 1458	37°01′50″	121°41′39″	4.277	---	---	130.16365
HS5247	Chiseled square 1	37°02′04″	121°42′26″	5.612	148.60100	148.62000	148.45545
HS5248	L 1458	37°01′50″	121°42′34″	6.357	---	---	230.89985
HS5249	K 1458	37°01′36″	121°42′56″	7.649	---	---	350.51604
HS5250	J 1458	37°01′11″	121°43′05″	8.844	---	---	456.09991
HS5251	H 1458	37°00′48″	121°43′01″	9.694	---	---	520.93831
HS5252	114 JD	37°00′48″	121°43′02″	9.702	521.12900	521.14500	521.00357
HS5253	Y 1459	37°01′03″	121°43′24″	10.518	---	---	559.60387
HS5254	G 1458	37°01′22″	121°43′37″	11.149	---	---	571.23601
HS5255	X 1459	37°01′37″	121°44′15″	12.154	---	---	595.91950
HS5256	115 JD	37°01′57″	121°44′34″	13.004	634.32700	634.34200	634.21884
HS5257	W 1459	37°02′17″	121°44′49″	13.810	---	---	632.27002
HS5258	F 1458	37°02′32″	121°44′59″	14.328	---	---	639.93276
HS5259	P 1459	37°02′55″	121°45′14″	15.180	---	---	649.37932
HS5260	E 1458	37°02′52″	121°45′34″	15.880	---	---	701.83374
HS5261	Q 1459	37°02′55″	121°45′46″	16.254	---	---	732.00264
HS5262	116 JD	37°03′03″	121°45′43″	16.598	756.42800	756.44000	756.34069
HS5263	V 1459	37°03′10″	121°46′15″	17.554	---	---	738.38598
HS5264	D 1458	37°03′22″	121°46′39″	18.393	---	---	771.94006
HS5265	R 1459	37°03′38″	121°47′02″	19.198	---	---	763.99801
HS5266	C 1458	37°03′46″	121°47′16″	19.659	---	---	792.56946
HS5267	B 1458	37°03′50″	121°47′36″	20.393	---	---	834.10806
HS5268	N 1459	37°04′04″	121°48′08″	21.320	---	---	855.10936
HS5269	END	37°04′25″	121°48′46″	22.565	---	---	848.20998
HS5271	A 1458	37°04′40″	121°48′59″	23.245	---	---	908.00462
HS5272	S 1459	37°04′49″	121°48′57″	23.527	---	---	914.07271
HS5273	Z 1457	37°05′07″	121°49′16″	24.254	---	---	874.75632
HS5274	T 1459	37°05′18″	121°49′43″	25.190	---	---	894.27193
HS5275	Y 1457	37°05′24″	121°49′54″	25.613	---	---	905.70397
HS5276	M 1459	37°05′31″	121°50′15″	26.288	---	---	914.85099
HS5216	F 1457	37°05′49″	121°50′41″	27.443	---	---	939.12012
HS5215	E 1457	37°05′56″	121°51′13″	28.502	---	---	906.57015

Table 16.—*Leveling observations along a line from Morgan Hill to Watsonville*

[See figure 1 for locations. Number in parentheses below year of survey indicates month when survey was conducted; month of 1953 survey is unknown. L-number is U.S. National Geodetic Survey designation; PV-numbers are U.S. Geological Survey (USGS) field-summary-book designations. Obs., original field observations, with previous USGS adjustments removed; adj., observations adjusted for consistent coseismic network (see text)]

ACRN	Designation	Latitude N.	Longitude W.	Leveled distance (km)	Orthometric height (m)		
					1953 (obs.)	1953 (adj.)	1990 (4) L25239.6
					PV208, PV220		
HS5168	N 1448	37°07′22″	121°38′34″	0.000	---	---	103.40712
HS5169	P 1448	37°06′56″	121°38′07″	1.020	---	---	99.90679
HS5277	Chiseled square 3	37°06′26″	121°38′05″	2.569	96.51000	96.48300	96.48369
HS5278	R 1458	37°05′39″	121°38′42″	4.297	---	---	102.69264
HS5279	S 1458	37°05′06″	121°39′10″	5.579	---	---	111.92432
HS5280	Chiseled square B	37°05′05″	121°39′12″	5.647	112.89600	112.87000	110.35487
HS5279	S 1458	37°05′06″	121°39′10″	5.579	---	---	111.92432
HS5281	109 JD	37°04′05″	121°39′32″	7.545	130.46300	130.43800	130.33963
HS5282	T 1458	37°03′25″	121°39′40″	8.857	---	---	116.77682
HS5283	110 JD	37°02′43″	121°39′07″	10.331	102.58700	102.56400	102.47966
HS5243	Q 1458	37°01′50″	121°39′20″	12.028	---	---	103.30476
HS5284	U 1458	37°00′57″	121°38′57″	14.040	---	---	98.28815
HS5285	38 WLS	37°00′39″	121°39′43″	15.526	109.07800	109.05800	108.98607
HS5288	L 1459	37°00′13″	121°40′16″	16.882	---	---	143.68643
HS5286	V 1458	37°00′16″	121°40′49″	17.563	---	---	149.51767
HS5287	W 1458	37°00′02″	121°41′06″	18.286	---	---	184.20379
GU4170	X 1458	36°59′32″	121°41′14″	19.203	---	---	220.40284
GU4171	Y 1458	36°59′25″	121°41′58″	20.326	---	---	278.43834
GU4172	Z 1458	36°59′40″	121°42′20″	21.175	---	---	327.78833
GU4173	Chiseled triangle A	36°59′50″	121°42′47″	22.214	---	---	389.73900
GU4175	36 WLS	36°59′50″	121°43′00″	22.611	406.73500	406.71800	406.67640
GU4176	B 1459	36°59′24″	121°42′54″	23.275	---	---	371.84734
GU4177	Chiseled square 2	36°59′10″	121°43′01″	24.304	315.72500	315.70900	315.71218
GU4178	C 1459	36°59′06″	121°42′47″	24.847	---	---	288.18594
GU4179	D 1459	36°58′49″	121°43′00″	25.650	---	---	249.36555
GU4180	E 1459	36°58′45″	121°42′36″	26.278	---	---	214.85295
GU4181	F 1459	36°58′30″	121°43′07″	27.546	---	---	159.18544
GU4182	G 1459	36°58′06″	121°43′06″	28.427	---	---	109.08097
GU4183	H 1459	36°57′34″	121°43′20″	29.569	---	---	59.13198
GU4184	J 1459	36°56′54″	121°44′01″	31.158	---	---	35.16116
GU4185	33 WLS reset 1965	36°56′07″	121°44′32″	32.808	21.07700	21.06500	20.96856
GU4186	W 17	36°55′31″	121°44′42″	33.953	---	---	17.04438
GU4187	W 16	36°55′10″	121°44′49″	34.600	---	---	12.49995
GU4188	K 1459	36°55′01″	121°45′09″	35.319	---	---	12.50816
GU4189	W 9	36°54′37″	121°45′32″	36.326	---	---	8.56993
GU4162	H 249 reset 1979	36°54′28″	121°45′37″	36.778	---	---	8.14009
GU2246	W 1236	36°54′19″	121°45′23″	37.215	---	---	7.40400
GU2245	V 1236	36°54′12″	121°45′13″	37.586	---	---	10.10877

Table 17.—*Leveling observations along a line from Watsonville, through Freedom, Browns Valley Road, and Casserly Road, to 6.1 km northwest of Watsonville*

[See figure 1 for locations. Numbers in parentheses below year of survey indicate months when survey was conducted; month of 1970 survey is unknown. L-number is U.S. National Geodetic Survey designation]

ACRN	Designation	Latitude N.	Longitude W.	Leveled distance (km)	Orthometric height (m)	
					1970	1990 (4–5) L25251.1
GU4183	H 1459	36°57′34″	121°43′20″	0.000	- - -	59.13198
GU4203	157.24=118	36°57′23″	121°43′35″	.506	47.92800	47.91718
GU4204	150.42=119	36°57′38″	121°43′47″	1.127	45.84800	45.87621
GU4205	A 1460	36°57′54″	121°44′14″	2.032	- - -	39.47554
GU4206	133.06=121	36°58′14″	121°44′15″	3.150	40.56000	40.62783
GU4207	138.62=122	36°58′34″	121°44′29″	3.900	42.25000	42.37796
GU4208	271.10=319	36°59′21″	121°44′19″	5.492	82.63000	82.76526
GU4209	423.34=318	36°59′35″	121°44′03″	6.165	129.03300	129.12294
HS5289	412.23=317	37°00′06″	121°44′20″	7.231	125.64600	125.96969
HS5290	B 1460	37°00′23″	121°44′45″	8.069	- - -	174.79177
HS5291	737.58=316	37°00′48″	121°45′04″	8.970	224.81500	225.12059
HS5292	C 1460	37°01′09″	121°45′46″	9.896	- - -	244.48891
HS5293	739.34=315	37°01′16″	121°45′27″	10.449	225.35000	225.36587
HS5294	D 1460	37°01′24″	121°46′07″	11.229	- - -	192.87509
HS5295	529.07=314	37°01′34″	121°46′43″	12.050	161.26000	161.39395
HS5296	411.31=313	37°00′59″	121°47′15″	13.544	125.36700	125.60414
HS5297	361.00=312	37°00′29″	121°47′36″	14.729	110.03400	110.29602
HS5298	323.74=311	37°00′03″	121°47′47″	15.558	98.67500	98.93378
GU4210	270.33=310	36°59′19″	121°47′59″	16.985	82.39500	82.63666
GU4211	236.78=309	36°58′50″	121°48′00″	17.875	72.17200	72.38569
GU4212	295.16=308	36°58′17″	121°47′39″	19.074	89.96600	90.12004
GU4213	257.94=307	36°57′54″	121°47′32″	19.783	78.62000	78.75199
GU4214	223.07=306	36°57′36″	121°47′11″	20.511	67.99000	68.09088
GU4215	149.99=304	36°56′59″	121°46′17″	22.303	45.71700	45.71554
GU4216	Gaging station	36°56′21″	121°46′10″	23.739	- - -	32.74371
GU4217	Z 1459	36°56′04″	121°46′18″	24.324	- - -	35.32309
GU2250	T 738 reset 1963	36°55′32″	121°45′44″	25.605	27.50600	27.47638
GU4188	K 1459	36°55′01″	121°45′09″	27.021	- - -	12.49315

Table 18.—*Leveling observations along a line from 0.5 km west of Corralitos through Freedom Boulevard to Aptos*

[See figure 1 for locations. Number in parentheses below year of survey indicates month when survey was conducted; month of 1970 survey is unknown. L-number is U.S. National Geodetic Survey designation]

ACRN	Designation	Latitude N.	Longitude W.	Leveled distance (km)	Orthometric height (m)	
					1970	1990 (4) L25251.2
GU4210	270.33=310	36°59′19″	121°47′59″	0.000	82.39500	82.63666
GU4218	E 1460	36°59′20″	121°48′05″	.168	- - -	77.26547
GU4219	271.52=301	36°59′18″	121°48′20″	.553	82.75900	82.99344
GU4220	469.60=300	36°59′40″	121°48′54″	1.722	143.13500	143.41648
GU4221	K 1460	36°59′29″	121°49′17″	2.441	- - -	126.06179
GU4222	48	36°59′25″	121°49′38″	2.985	113.76000	113.52423
GU4223	J 1460	36°59′15″	121°50′09″	4.013	- - -	110.88108
GU4224	H 1460	36°59′12″	121°50′46″	4.966	- - -	111.28063
GU4225	G 1460	36°59′04″	121°51′43″	6.422	- - -	69.80046
GU4226	R 125	36°58′12″	121°52′21″	8.241	- - -	54.80430
GU4227	F 1460	36°58′31″	121°53′07″	9.992	- - -	46.45767
GU2278	RV 5	36°58′33″	121°53′51″	11.336	29.80000	29.91452

Table 19.—*Leveling observations along a line from 0.8 km northwest of Freedom, through Valley Road and Buena Vista Drive, to 0.6 km south of La Selva Beach*

[See figure 1 for locations. Numbers in parentheses below year of survey indicate months when survey was conducted; month of 1970 survey is unknown. L-number is U.S. National Geodetic Survey designation]

ACRN	Designation	Latitude N.	Longitude W.	Leveled distance (km)	Orthometric height (m)	
					1970	1990 (4–5) L25251.3
GU4217	Z 1459	36°56′04″	121°46′18″	0.000	- - -	35.32309
GU4228	1	36°56′26″	121°46′51″	1.086	43.29800	43.30354
GU4229	158.34=96	36°56′22″	121°47′17″	1.827	48.26000	48.29119
GU4230	97	36°56′25″	121°47′49″	2.666	51.08000	51.11660
GU4231	35.89=98	36°56′16″	121°48′21″	3.689	10.94000	10.96152
GU4232	67.40=219	36°56′36″	121°48′52″	4.672	20.54300	20.60159
GU4233	93.74=220	36°56′49″	121°49′19″	5.473	28.57300	28.62398
GU4234	130.54=221	36°57′03″	121°49′45″	6.290	39.78800	39.86020
GU4235	277.62=223	36°57′13″	121°50′45″	7.945	84.61700	84.71139
GU4236	R 121	36°56′56″	121°51′00″	8.594	- - -	86.33585
GU4237	227 reset	36°56′32″	121°51′23″	9.798	51.56600	51.60000
GU2269	RV 6=4	36°56′10″	121°51′50″	10.955	23.46000	23.43919

Table 20.—*Leveling observations along a line from 5.3 km north of Soquel, through Laurel Glen Road and Granite Creek Road, to 2.7 km north of Scotts Valley*

[See figure 1 for locations. Number in parentheses below year of survey indicates month when survey was conducted; month of 1970 survey is unknown. L-number is U.S. National Geodetic Survey designation]

ACRN	Designation	Latitude N.	Longitude W.	Leveled distance (km)	Orthometric height (m)	
					1970	1990 (5) L25251.4
HS5195	Q 1456	37°01′18″	121°57′01″	0.000	- - -	63.00953
HS5300	225.29=273	37°02′06″	121°56′47″	1.601	68.66800	68.91768
HS5301	L 1460	37°02′43″	121°57′05″	2.868	- - -	83.43431
HS5302	326.21=275	37°03′12″	121°57′16″	3.891	99.42700	99.75107
HS5303	M 1490	37°03′24″	121°57′30″	4.463	- - -	140.12288
HS5304	616.48=276	37°03′20″	121°57′43″	5.024	187.90200	188.58406
HS5305	N 1460	37°03′22″	121°58′12″	5.870	- - -	114.50819
HS5306	329.11=277	37°03′15″	121°58′36″	6.445	100.31200	100.60661
HS5307	P 1460	37°02′55″	121°58′51″	7.177	- - -	95.08478
HS5308	273.96=278	37°02′27″	121°59′01″	8.106	83.50400	83.73823
HS5309	Q 1460	37°02′02″	121°59′08″	9.005	- - -	80.62321
HS5310	179.72=279	37°01′40″	121°59′11″	9.674	54.77900	54.96567
HS5311	164.37=280	37°01′25″	121°59′19″	10.271	50.10100	50.26312
HS5312	145.36=281	37°01′05″	121°59′46″	11.320	44.30600	44.41088
HS5313	224.23=282	37°01′37″	121°59′42″	12.181	68.34400	68.50599
HS5314	R 1460	37°02′21″	121°59′45″	13.702	- - -	135.22959
HS5315	490.32=284	37°02′49″	121°59′51″	14.666	149.44900	149.67292
HS5316	S 1460	37°03′04″	121°59′48″	15.215	- - -	177.79975
HS5317	723.10=285	37°03′21″	121°59′47″	15.748	220.40200	220.66285
HS5299	S 1455	37°03′38″	121°59′47″	16.609	- - -	192.80965

Table 21.—*Leveling observations along a line from the junction of Mount Hermon Road and Zayante Road 1 km east of Felton through Olympia to 4.3 km northeast of Zayante*

[See figure 1 for locations. Number in parentheses below year of survey indicates month when survey was conducted; month of 1970 survey is unknown. L-number is U.S. National Geodetic Survey designation]

ACRN	Designation	Latitude N.	Longitude W.	Leveled distance (km)	Orthometric height (m)	
					1970	1990 (5) L25251.5
HT3570	P 1455	37°03′19″	122°03′36″	0.000	- - -	106.74056
HT3569	N 1455	37°03′20″	122°03′31″	.140	- - -	109.07589
HT3574	312.55=65	37°03′36″	122°03′26″	.525	95.26700	95.35649
HT3575	T 1460	37°04′18″	122°03′19″	1.898	- - -	106.51974
HT3576	373.95=399	37°04′55″	122°02′58″	3.211	113.98000	114.15402
HT3577	379	37°05′00″	122°02′59″	3.374	122.92900	123.09959
HT3578	Gaging station	37°05′09″	122°02′45″	3.908	115.67000	116.47835
HT3579	415.66=381	37°05′22″	122°02′37″	4.541	126.69400	127.52141
HT3580	V 1460	37°05′37″	122°02′27″	5.108	- - -	163.04166
HT3581	U 1460	37°06′01″	122°02′00″	6.331	- - -	147.60536
HT3582	495.98=383	37°06′18″	122°01′33″	7.148	151.17500	152.13281
HT3583	539.94=384	37°06′35″	122°01′11″	8.353	164.57300	165.56408

Table 22.—*Leveling observations along a line from Felton, through Boulder Creek and China Grade Road, to the Santa Cruz-San Mateo County line*

[See figure 1 for locations. Numbers in parentheses below year of survey indicate months when survey was conducted; months of 1953 and 1970 surveys are unknown. PV-numbers are U.S. Geological Survey (USGS) field-summary-book designations. Obs., original field observations, with previous USGS adjustments removed]

ACRN	Designation	Latitude N.	Longitude W.	Leveled distance (km)	Orthometric height (m)		
					1953 (obs.) PV218	1970	1990 (5–6) L25251.6
HT3570	P 1455	37°03′19″	122°03′36″	0.000	- - -	- - -	106.74056
HT3584	W 1460	37°03′11″	122°04′07″	.960	- - -	- - -	85.42397
HT3585	X 1460	37°03′33″	122°04′40″	2.181	- - -	- - -	91.51486
HT3586	296.80=74	37°04′06″	122°04′54″	3.344	- - -	90.46500	90.54245
HT3587	324.23=72	37°04′27″	122°04′53″	4.214	- - -	98.82400	98.90366
HT3588	Y 1460	37°04′59″	122°04′40″	5.506	- - -	- - -	94.53565
HT3589	177 reset	37°05′20″	122°05′14″	6.743	- - -	96.42000	96.47190
HT3590	390.58=179	37°05′43″	122°05′45″	7.980	- - -	119.05000	119.13706
HT3591	446.86=181	37°06′22″	122°06′19″	9.617	- - -	136.20000	136.27642
HT3592	457.31=182	37°06′28″	122°06′44″	10.395	- - -	139.39000	139.46544
HT3593	Z 1460	37°06′46″	122°06′52″	11.017	- - -	- - -	141.07272
HT3594	501.74=184	37°07′09″	122°07′11″	12.026	- - -	152.93000	153.00554
HT3595	BEN 8	37°07′43″	122°07′18″	13.053	150.20200	150.20000	150.31979
HT3596	A 1461	37°07′40″	122°07′53″	14.339	- - -	- - -	166.63621
HT3597	566.17=187	37°07′55″	122°08′11″	15.064	- - -	172.57000	172.68552
HT3598	640.87=188	37°08′18″	122°08′33″	15.997	- - -	195.34000	195.39077
HT3599	799.37=190	37°08′41″	122°09′21″	17.578	- - -	243.65000	243.70177
HT3600	46 WLS	37°09′00″	122°09′49″	18.508	276.42500	276.43000	276.47643
HT3601	B 1461	37°09′22″	122°09′39″	19.019	- - -	- - -	247.76378
HT3602	C 1461	37°09′55″	122°09′43″	20.095	- - -	- - -	259.91990
HT3603	916 SF	37°10′26″	122°10′10″	21.484	279.17300	279.18100	279.22082
HT3604	D 1461	37°11′04″	122°10′46″	23.116	- - -	- - -	305.98060
HT3605	E 1461	37°11′06″	122°11′00″	23.487	- - -	- - -	346.52185
HT3606	F 1461	37°11′10″	122°11′14″	23.917	- - -	- - -	394.54974
HT3607	48 WLS	37°11′29″	122°11′27″	24.768	484.99500	485.00400	484.99741
HT3608	G 1461	37°11′36″	122°11′36″	25.321	- - -	- - -	540.41797
HT3609	H 1461	37°11′49″	122°11′40″	25.810	- - -	- - -	572.08818
HT3610	J 1461	37°11′56″	122°11′58″	26.278	- - -	- - -	606.54402
HT3611	K 1461	37°12′09″	122°12′08″	26.874	- - -	- - -	651.69761
HT3612	49 WLS	37°12′25″	122°12′19″	27.537	671.43100	671.44100	671.42870
HT3613	L 1461	37°12′33″	122°12′03″	27.947	- - -	- - -	686.34978
HT3614	M 1461	37°12′48″	122°12′20″	28.719	- - -	- - -	706.35417

Table 23.—*Leveling observations along a line from 1 km east of Felton, through Felton Empire Road and Bonny Doon Road, to 1.4 km southeast of Davenport*

[See figure 1 for locations. Number in parentheses below year of survey indicates month when survey was conducted; months of 1953 and 1970 surveys are unknown. L-number is U.S. National Geodetic Survey designation; PV-number is U.S. Geological Survey (USGS) field-summary-book designation. Obs., original field observations, with previous USGS adjustments removed]

ACRN	Designation	Latitude N.	Longitude W.	Leveled distance (km)	Orthometric height (m)		
					1953 (obs.) PV218	1970	1990 (6) L25251.7
HT3570	P 1455	37°03′19″	122°03′36″	0.000	- - -	- - -	106.74056
HT3584	W 1460	37°03′11″	122°04′07″	.961	- - -	- - -	85.42219
HT3615	N 1461	37°03′04″	122°04′40″	1.897	- - -	- - -	132.66295
HT3616	P 1461	37°02′56″	122°04′58″	2.402	- - -	- - -	160.46799
HT3617	Q 1461	37°02′59″	122°05′27″	3.192	- - -	- - -	225.17783
HT3618	R 1461	37°03′07″	122°05′40″	3.673	- - -	- - -	270.27996
HT3619	S 1461	37°03′14″	122°05′44″	4.225	- - -	- - -	304.49007
HT3620	170	37°03′21″	122°06′02″	4.896	- - -	363.45000	363.46421
HT3621	T 1461	37°03′28″	122°06′20″	5.341	- - -	- - -	404.93420
HT3622	168	37°03′36″	122°06′28″	5.838	- - -	443.64000	443.64950
HT3623	167	37°03′41″	122°06′45″	6.285	- - -	476.87000	476.86497
HT3624	U 1461	37°03′32″	122°06′54″	6.844	- - -	- - -	512.70295
HT3625	1822.20=360	37°03′29″	122°07′21″	7.540	- - -	555.41000	555.42330
HT3626	V 1461	37°04′00″	122°07′17″	8.748	- - -	- - -	601.72882
HT3627	163	37°04′20″	122°07′40″	9.672	- - -	614.27000	614.30540
HT3628	W 1461	37°04′40″	122°07′57″	10.534	- - -	- - -	663.20385
HT3629	X 1461	37°05′26″	122°08′18″	10.994	- - -	- - -	759.81158
HT3631	43 WLS	37°06′30″	122°08′39″	11.223	754.26300	754.27400	754.28303
HT3632	Z 1461	37°04′52″	122°08′21″	11.453	- - -	- - -	638.85854
HT3633	41 WLS	37°04′02″	122°08′24″	13.186	576.08000	576.09500	576.11380
HT3634	1707.48=202	37°03′45″	122°08′49″	14.018	- - -	520.44100	520.45432
HT3635	A 1462	37°03′11″	122°09′11″	15.164	- - -	- - -	450.14035
HT3636	40 WLS	37°02′40″	122°08′56″	16.312	404.66300	404.67900	404.68017
HT3637	REF WLS	37°02′40″	122°08′58″	16.331	404.01000	404.03000	404.02556
HT3638	122°0.26=366	37°02′12″	122°09′04″	17.243	- - -	371.93700	371.92109
HT3639	B 1462	37°01′51″	122°09′17″	18.108	- - -	- - -	301.01995
HT3640	C 1462	37°01′39″	122°09′27″	18.732	- - -	- - -	237.56842
HT3641	D 1462	37°01′22″	122°09′55″	19.645	- - -	- - -	173.17029
HT3642	E 1462	37°01′02″	122°10′02″	20.135	- - -	- - -	123.63265
HT3643	86.24=199	37°00′42″	122°10′32″	21.331	- - -	26.28600	26.23643
HT1572	H 1238	37°00′04″	122°10′45″	22.456	- - -	- - -	17.38950

Table 24.—*Leveling observations along a line from Santa Cruz through Davenport to 1 km northwest of the Santa Cruz-San Mateo County line*

[See figure 1 for locations. Number(s) in parentheses below year of survey indicates month(s) when survey was conducted; months of 1953 and 1970 surveys are unknown. L-number is U.S. National Geodetic Survey designation; PV-number is U.S. Geological Survey (USGS) field-summary-book designation. Obs., original field observations, with previous USGS adjustments removed. Subsidence correction applies to 1978–90 height difference]

ACRN	Designation	Latitude N.	Longitude W.	Leveled distance (km)	Orthometric height (m)					Subsidence correction (mm)
					1953 (obs.) PV218	1970	1972 (9–10) L22869	1978 (5) L24298	1990 (2) L25251.8	
GU4167	B 1455	36°58′15″	122°01′50″	0.000	---	---	---	---	4.41596	---
GU4240	M 1462	36°57′49″	122°02′04″	1.248	---	---	---	---	16.43267	---
GU1954	V 1237	36°57′41″	122°02′28″	1.935	---	---	16.66813	16.65667	16.66569	−8.09
GU1959	W 1237	36°57′32″	122°03′04″	2.913	---	---	20.90586	20.89493	20.89860	−2.00
GU1960	X 1237	36°57′40″	122°03′20″	3.708	---	---	27.23047	27.22063	27.22301	−.92
GU1964	Y 1237	36°57′44″	122°04′22″	5.215	---	---	28.97503	28.96455	28.96023	1.31
GU4239	L 1462	36°57′42″	122°05′15″	6.559	---	---	---	---	17.55808	---
GU1970	A 1238	36°57′52″	122°06′12″	8.067	---	---	37.42997	37.42533	37.41212	.00
GU1971	B 1238	36°58′10″	122°06′58″	9.253	---	---	22.21088	22.19706	22.15864	.00
GU4238	83.13=196	36°58′21″	122°07′37″	10.329	---	25.33800	---	---	25.29608	---
GU1972	C 1238	36°58′29″	122°07′48″	10.661	---	---	30.61819	30.59394	30.57968	.00
GU1974	W 1241	36°58′52″	122°08′23″	11.711	---	---	25.86363	25.85264	25.84810	.00
GU1975	D 1238	36°59′00″	122°08′37″	12.211	---	---	39.76853	39.75735	39.74951	.00
GU1976	E 1238	36°59′16″	122°09′18″	13.351	---	---	22.43417	22.41807	22.40278	.00
GU1978	F 1238	36°59′25″	122°09′42″	13.996	---	---	31.25946	31.24745	31.23566	.00
GU1979	G 1238	36°59′55″	122°10′35″	15.796	---	---	21.60505	21.59166	21.58221	.00
HT1572	H 1238	37°00′04″	122°10′45″	16.182	---	---	17.42189	17.40993	17.40127	.00
HT3654	K 1462	37°00′24″	122°11′09″	16.985	---	---	---	---	33.64295	---
HT1568	N 212	37°00′55″	122°12′00″	19.227	30.35400	30.35400	30.35193	30.33650	30.31804	.00
HT1567	62.66=255	37°01′29″	122°12′39″	20.487	---	19.09800	19.08944	19.07194	19.05309	.00
HT1566	L 1238	37°01′43″	122°12′52″	21.036	---	---	25.62267	25.60467	25.58826	.00
HT1565	X 1241	37°01′45″	122°12′56″	21.155	---	---	31.58854	31.57324	31.55260	.00
HT3653	93.17=270	37°01′48″	122°13′02″	21.351	---	28.56300	---	---	28.51359	---
HT1564	76.85=256	37°02′14″	122°13′10″	22.220	---	23.42200	23.41831	23.40107	23.38483	.00
HT3652	24.85=269	37°02′25″	122°13′40″	22.860	---	7.57300	---	---	7.47924	---
HT1563	43.94=257	37°02′35″	122°13′15″	23.228	---	13.39300	13.37642	13.35670	13.33919	.00
HT1562	M 1238	37°03′06″	122°13′28″	24.212	---	---	7.12583	7.10686	7.08926	.00
HT3651	188.54=267	37°03′12″	122°14′30″	24.722	---	57.46000	---	---	57.40858	---
HT1559	L 212	37°03′35″	122°13′27″	25.232	---	33.94700	33.93433	33.91710	33.90047	.00
HT1558	N 1238	37°03′49″	122°13′31″	25.694	---	---	21.80674	21.78391	21.77368	.00
HT3650	187.39=266	37°03′44″	122°15′04″	26.107	---	57.11600	---	---	57.07146	---
HT1557	60.71=259	37°04′01″	122°13′41″	26.109	---	18.50000	18.48609	18.46317	18.44942	.00
HT3649	J 1462	37°04′21″	122°15′29″	27.371	---	---	---	---	63.89437	---
HT1556	P 1238	37°04′40″	122°14′34″	28.069	---	---	28.43204	28.40855	28.39844	.00
HT3648	116.40=264	37°04′48″	122°15′50″	28.384	---	50.71900	---	---	50.65059	---
HT1555	K 212	37°04′48″	122°14′43″	28.399	---	30.84800	30.81644	30.79572	30.77721	.00
HT1554	321.22=261	37°05′07″	122°15′00″	29.343	---	97.90900	97.90094	97.89572	97.90777	.00
HT1552	Y 1241	37°05′00″	122°15′21″	30.107	---	---	148.16900	148.15189	148.13270	.00
HT1549	R 1238	37°05′48″	122°16′36″	30.615	---	---	5.73782	5.71298	5.66232	.00
HT3644	19.13=272	37°05′48″	122°16′38″	30.676	---	5.83000	---	---	5.73119	---
HT3647	H 1462	37°05′03″	122°15′43″	30.770	---	---	---	---	116.02240	---
HT3646	G 1462	37°04′54″	122°15′43″	31.184	---	---	---	---	103.58959	---
HT1547	S 1238	37°06′16″	122°17′14″	31.905	---	---	9.91889	9.89843	9.88313	.00
HT3645	F 1462	37°05′04″	122°16′03″	32.092	---	---	---	---	45.96247	---
HT1545	Z 1241	37°06′51″	122°18′02″	33.558	---	---	30.12716	30.10597	30.08577	.00

Figure 15.—Schematic map of Loma Prieta region, Calif., showing locations of leveling network of bench marks used in this study (dots) and additional bench marks for which coseismic elevation changes were measured (triangles). Unused bench marks were surveyed by Santa Cruz County at low precision; unassessed elevation-dependent error evident in Santa Cruz County observations limits their utility for geodetic modeling. Quaternary faults (dashed where inferred) from Jennings (1975). LP, Loma Prieta (solid triangle).

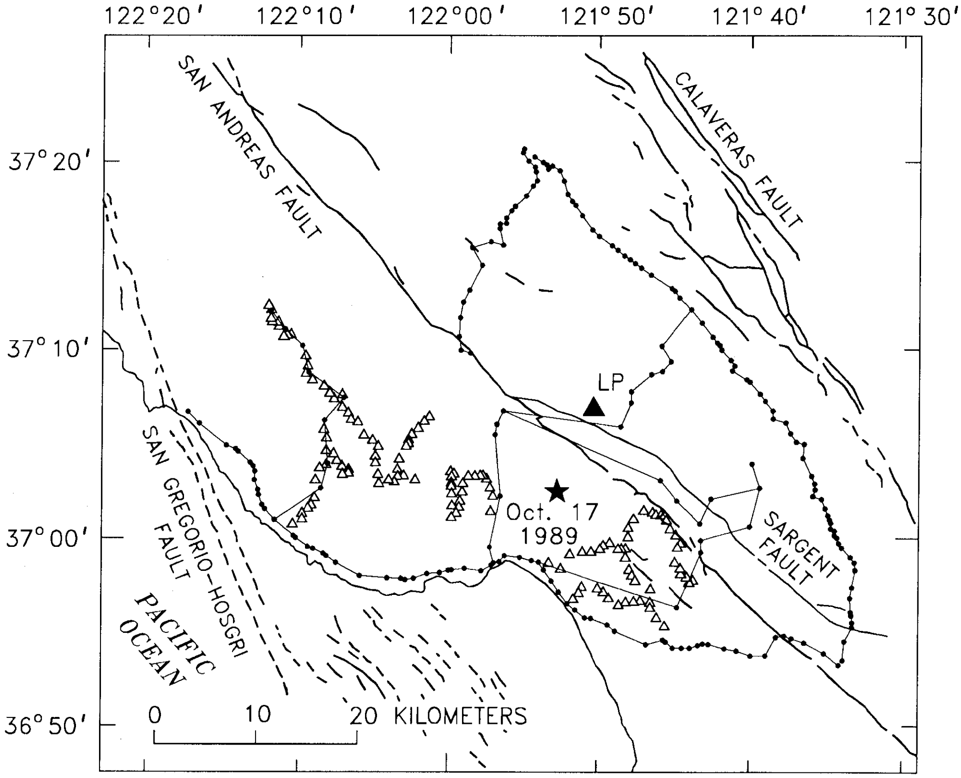

THE LOMA PRIETA, CALIFORNIA, EARTHQUAKE OF OCTOBER 17, 1989:
EARTHQUAKE OCCURRENCE

MAIN-SHOCK CHARACTERISTICS

MAIN-SHOCK AND VERY EARLY AFTERSHOCK ACTIVITY[1]

By Karen C. McNally,
University of California, Santa Cruz;
Gerald W. Simila,
California State University, Northridge;
and
Judy G. Brown,
University of California, Santa Cruz

CONTENTS

ABSTRACT

A data set consisting of main-shock and very early aftershock records was acquired from four digital accelerometers deployed before the 1989 Loma Prieta earthquake. We find that 34 aftershocks of $M \geq 3.8$ occurred within the first 3 ¼ hours after the main shock. We outline our procedures for event location, relocation, and magnitude determination.

INTRODUCTION

After the August 8, 1989 (M=5.3), Lexington Reservoir, Calif. (fig. 1), earthquake, four three-component digital accelerometers (Teledyne Geotech model A–700) were temporarily deployed by the University of California, Santa Cruz (UCSC), to monitor for an anticipated large earthquake in the Santa Cruz Mountains. Main-shock records from these four stations are shown in figure 2; the locations of the stations (triangles, fig. 1) are listed in table 1. The instruments were placed in homes and laboratories for electrical power, security, and ease of access, where they could be monitored readily by checking a light on the instrument to see whether it had been triggered by an earthquake. All the instruments were oriented to true north, with an estimated compass measurement error of ±5°, and were set above ground; none was bolted down, owing to the temporariness of the deployment and the heavy 44-lb (20 kg) weight of the instrument in its cast-aluminum case.

The instrument at station BRAN (fig. 1) was located at the residence of Richard Terdiman at 5001 Branciforte Drive in Santa Cruz, Calif. The site is a flat area near the top of a steep hill on the west side of Branciforte Creek (fig. 1). The instrument was placed on the concrete floor of a detached wood-frame garage (three sided, open in the front) that was located on bedrock at the cut-in side of the hillside. After the main shock, the house, which was on the outer hillslope side, was red tagged (deemed unsuitable for habitation) but still standing. The instrument was found with some empty cardboard boxes and an empty wooden chest leaning on top of it; the records obtained are shown in figure 2.

The instrument at station LGPC (fig. 1) was located in the house of Richard Holley, caretaker of the Los Gatos Presentation Center, at 19600 Bear Creek Road, a mountainous area of Los Gatos within the Loma Prieta rupture zone. The center used to be a private school called Montezuma School, as shown on the U.S. Geological Survey (USGS) map of the Castle Rock Ridge 7.5-minute quadrangle, and is now a convent. The instrument was placed on a detached concrete pad in the basement/storage area. The wood-frame house is built on a steep hill, where the single-story building is essentially a two-story structure on the downhill side and the lower story is used only for storage. The house lost its chimney, and the entire foundation had to be replaced, after the main shock; a retaining wall behind, and the walkway leading to, the house were both cracked. After the main shock, the con-

---

[1] Contribution No. 189, Charles F. Richter Seismological Laboratory and Institute of Tectonics, University of California, Santa Cruz, CA 95064.

crete pad beneath the instrument was found to be separated from an adjacent concrete step by a few centimeters; whether or not this was so before the earthquake is unknown. Fred Followell observed some evidence indicating "chatter" between the step and the pad, but no other evidence suggesting scraping or upending of the instrument. Also, Mr. Holley stated, "when they pulled out the old concrete pad, I was surprised to see that it was sitting on bricks." A baseline shift is visible on the vertical and north-south components of the records from station LGPC (figs. 3, 4; Yi-Ben Tsai, written commun., 1991), and so these records should be used with caution. However, the high frequencies appear valid, especially in the first part of the record. The baseline shifts could have been caused by a sudden tilt of the instrument with the pad itself.

The instrument at station UCSC (fig. 1) was located in the Charles F. Richter Seismological Laboratory in the Applied Sciences Building at UCSC. The building is a three-story cast-in-place concrete structure with a basement. The instrument was placed unbolted on the first floor in room 195, the seismology shop. The Applied Sciences Building sustained some damage during the main shock, mostly due to differential settling. A free-field strong-motion accelerograph operated by the California Division of Mines and Geology (CDMG) is located near the parking lot adjacent to the building. The main shock registered peak accelerations of 0.47 *g* (horizontal), and 0.40 *g* (vertical) on this instrument, in comparison with our lower values registered inside the building (fig. 5), as would be expected.

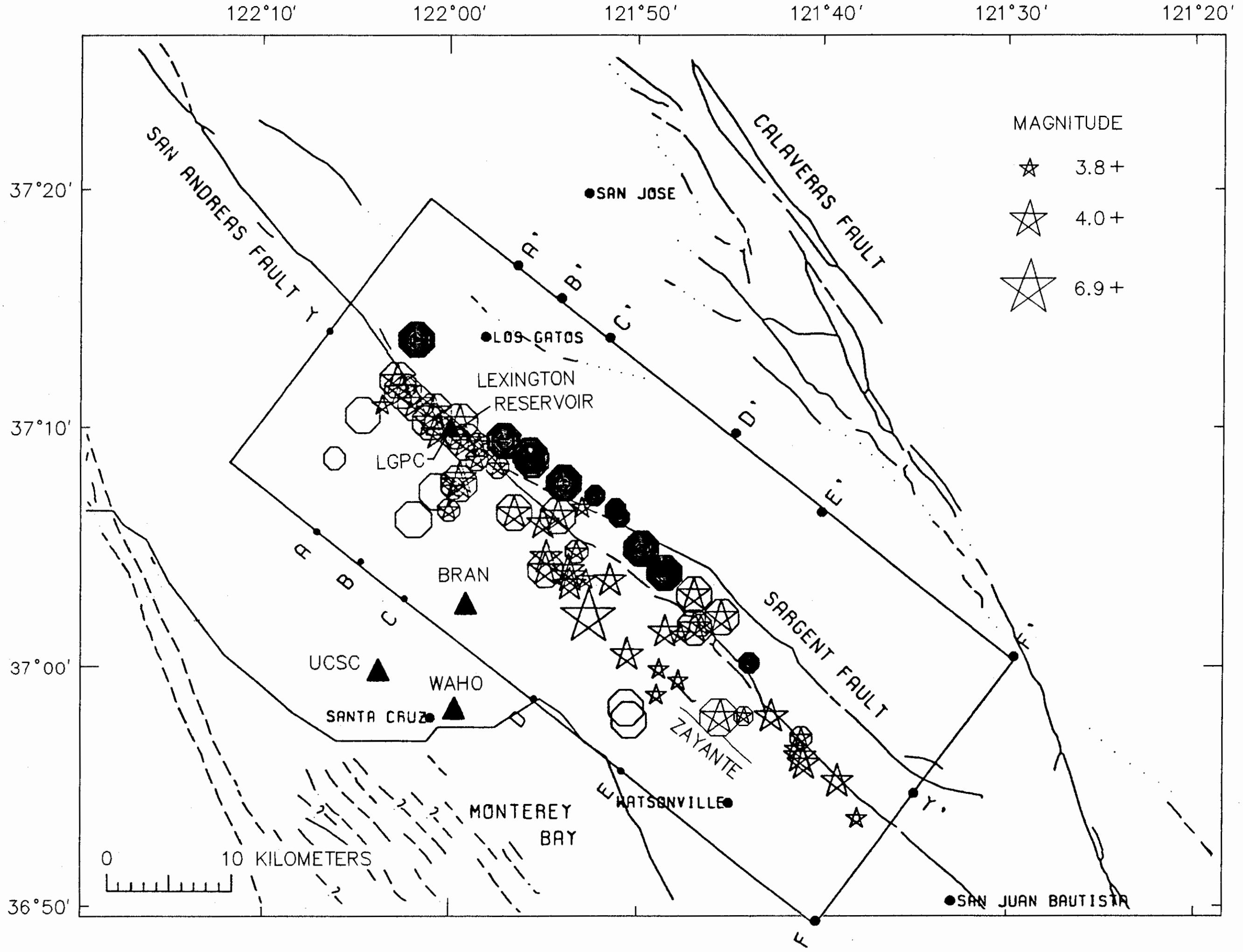

Figure 1.—Schematic map of Loma Prieta region, Calif., showing locations of rupture zone (rectangle), orthogonal cross sections *A–A'* (see fig. 7) and longitudinal cross section *Y–Y'* (see fig. 8), main shock (large star), aftershocks that occurred during first 2 hours and 22 minutes after main shock (circled stars) and until November 7, 1989 (stars), and other events interpreted to lie east (large dots) and west (circles) of main aftershock zone, including four foreshocks (small dots) of 1988 and 1989 (see table 2). Irregular lines, major faults (dashed where inferred, queried where uncertain); triangles, four temporary stations installed by the University of California, Santa Cruz.

The instrument at station WAHO (fig. 1) was located in the house of Walter Schillinger at 738 Cable Court, near the Yacht Harbor in downtown Santa Cruz. The instrument was placed on the concrete garage floor of a two-story wood-frame house or condominium. The attached garage protrudes from the house, half inside and half outside the main structure. The building did not sustain any structural damage. The records obtained are shown in figure 6.

These four instruments recorded the main shock and aftershocks, but their memories were filled within 10 hours of the main shock. Within 2 days of the main shock, the four original stations were serviced, and five additional stations, AHCR, BGST, CTES, LGPS, and LPVF (table 1), also equipped with Teledyne Geotech model A–700 digital accelerometers were installed. In addition, analog velocity recorders (Sprengnether model MEQ–800) were colocated at all nine stations. The station locations and all the aftershocks recorded at all nine stations are shown in figure 1 of Simila and others (1990) and listed in tables 1 through 4.

Owing to the large size of the main shock (M_L=6.9±0.44, McNally and others, 1990; M_L=6.7±0.09, Uhrhammer and Bolt, 1991), nearby high-gain seismographs operated by the USGS and the University of California, Berkeley (UCB), were driven offscale, and so the seismograms for the main shock and very early aftershocks from these nearby stations were nearly useless. Because the digital accelerometers have a wide dynamic range, however, they collected data for events spanning two orders of magnitude in acceleration. Three of the original four stations (LGPC, UCSC, WAHO, fig. 1) had trigger thresholds of 0.0088 *g* and peak settings of 1.0 *g*, and one station (BRAN) had a trigger threshold of 0.0044 *g* and a peak setting of 0.5 *g*. Total pretrigger and posttrigger recording time on the instrument is 35 s, unless it is retriggered; the sampling rate is 200 samples per second. All the instruments triggered on the main shock and produced a 35-s

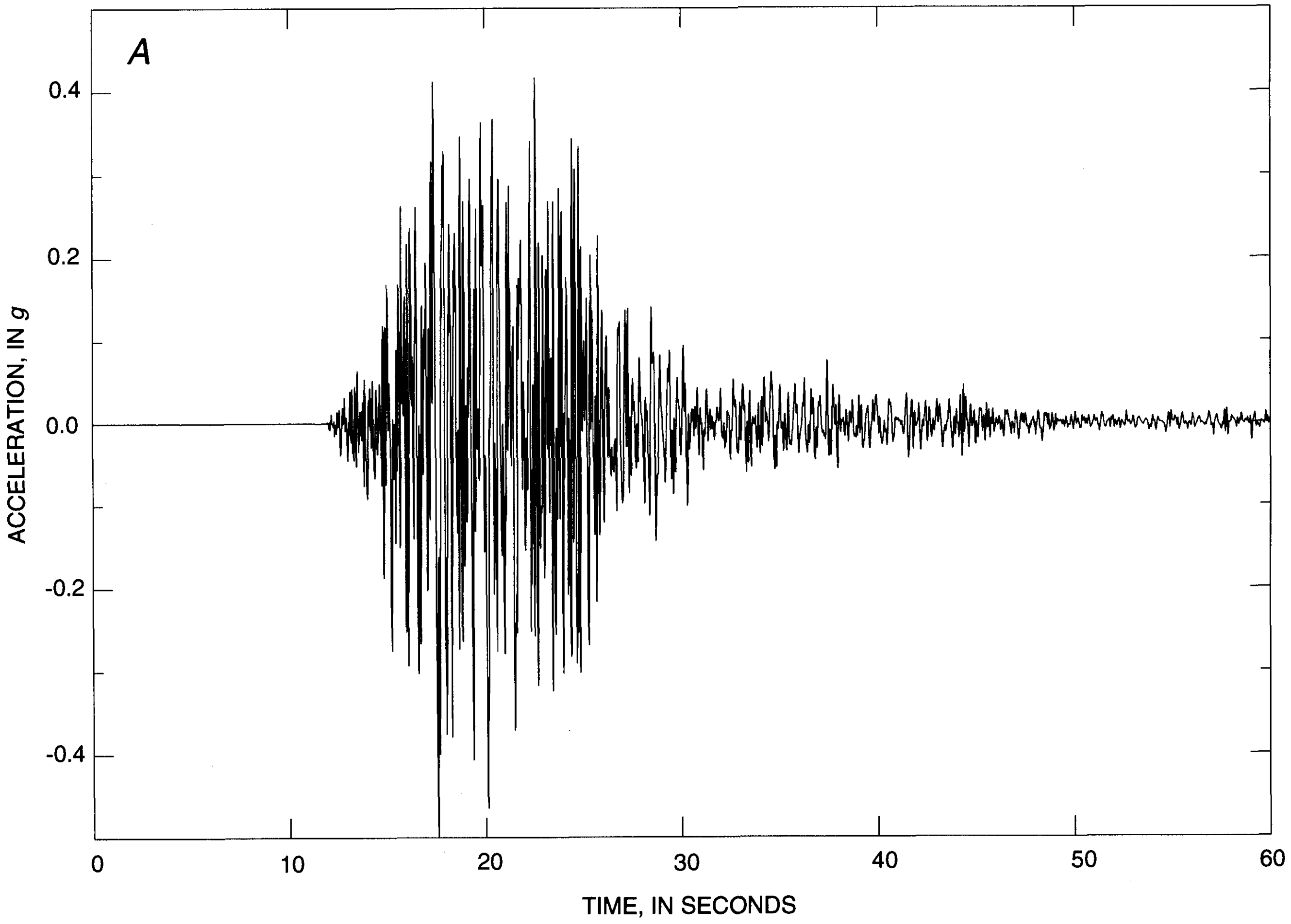

Figure 2.—Digital accelerograms of Loma Prieta main shock recorded at station BRAN (fig. 1), showing east-west (*A*), north-south (*B*), and vertical (*C*) components. East, north, and up directions are all positive. Sampling rate, 200 samples per second; trigger threshold, 0.0044 *g*; full scale, 0.50 *g*; peak amplitude, 0.46 *g* (fig. 2*B*; note that records in figs. 2*A* and 2*C* are probably clipped at 0.50 *g*).

record, including 17 s of pretrigger data in memory (the 17-s setting was customized for us by the manufacturer to retain *P*-wave arrivals in special studies of large earthquakes using temporary deployments). Our aftershock records for the first 34 minutes after the main shock provide nearly continuous detection; subsequently, the instruments continued to retrigger and record main-shock and very early aftershock activity for about 41 minutes. This data set provides a unique opportunity to analyze the early fault-rupture history of the earthquake.

DATA ANALYSIS

To accurately locate these very early aftershocks requires a joint relocation procedure involving several steps. The first step is to select calibration events (Simila and others, 1990). We used a set of 31 well-recorded aftershocks from the period October 20 through November 7, 1989 (see tables 2, 4). Arrival times of *P* and *S* waves recorded by the colocated analog and digital accelerometers, and *P*-wave-phase data from USGS stations within 30 km of the main shock (see tables 1, 3), were analyzed with the earthquake-location computer program HYPOINVERSE (Klein, 1989), along with Dietz and Ellsworth's (1990) two-sided velocity model. From the combined data sets, we obtained traveltime adjustments for the four UCSC stations (see table 3) and an average local Poisson's ratio (ratio of *P*- to *S*-wave velocities) of $\sigma=1.71$. These traveltime adjustments and σ values were carefully calculated through an iterative procedure of locating the events, modifying the adjustments and σ values, and then relocating the events until the *P*- and *S*-wave residuals at individual stations and the rms residuals for the solutions were minimized.

The next step was to relocate the main shock, using *P*- and *S*-wave traveltimes from the four UCSC stations with the new traveltime adjustments and σ values and, as in the first step, using the *P*-wave traveltimes of the USGS stations and the model and delay times of Dietz and Ellsworth (1990). Both location and depth were particularly well constrained by the excellent horizontal-component *S*-wave arrivals at the four original stations (BRAN, LGPC, UCSC, WAHO, fig. 1). Although these four sta-

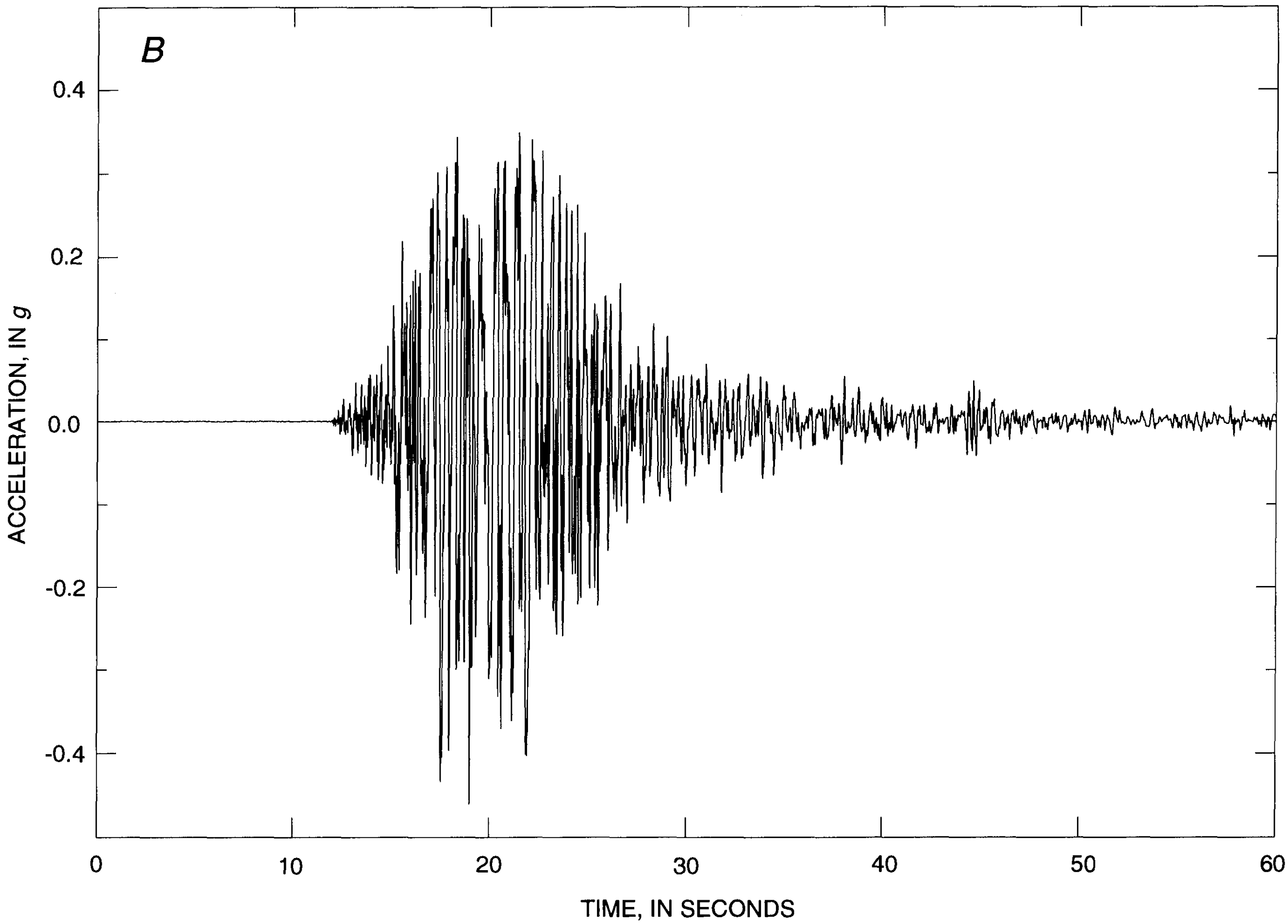

Figure 2.—Continued

tions within 7 to 16 km of the main shock are all west (southwest to northwest) of the epicenter, the overall azimuthal coverage for the main shock is complete when the data from the UCSC and USGS stations are combined. The traveltime residuals for the USGS stations that recorded the main shock were found to be similar to the average rms residuals (at the same stations) for the calibration events. These average residuals were then added to the standard traveltime adjustments for the USGS stations. (To maintain a nearly homogeneous station-array configuration for all events, *P*-wave-phase data from the USGS stations that recorded sporadically were not used.) The calibration aftershocks were then relocated (see table 2).

The final step was to relocate all aftershocks of $M \geq 3.8$ by using data from the UCSC stations with the new traveltime adjustments (see table 3) and $\sigma=1.71$. The first *P*-wave arrivals for the main-shock hypocenter were set for stations BRAN, WAHO, UCSC and LGPC, using the calculated traveltimes for their distances of 9.8, 12.9, 17.1, and 19.1 km, together with the new adjustments, as 00 h 04 min and 18.52, 18.47, 19.10, and 19.83 s, respectively. Time was thus established for the remaining digital records. (The main-shock *S*-wave arrival times were 00 h 04 min and 21.82, 21.17, 21.90, and 22.83 s, respectively.) The main shock contained multiple ruptures that are evident in figures 2 through 6; here, we refer to the first break as the main-shock hypocenter. For six early aftershocks, we have data from only the four original UCSC stations. At these stations, uncertainties are larger, but the traveltime adjustments help compensate for this difficulty somewhat. These initial locations were obtained by using the main-shock hypocenter as the starting location. Locations were then recalculated with the new epicenters as the starting locations but with several starting depths, to estimate location stability. Also, the main shock was relocated by using data from the same four stations, for another measure of location uncertainty. When the starting location was that of the known main-shock hypocenter, the solution moved 1.9 km northwest and +0.6 km in depth. The statistical precision of this solution is rms=0.16, horizontal error (ERH)=2.2 km, and vertical error (ERZ)=31.6 km. However, when the coordinates of the closest station and a 12-km depth (the default) were used as the starting

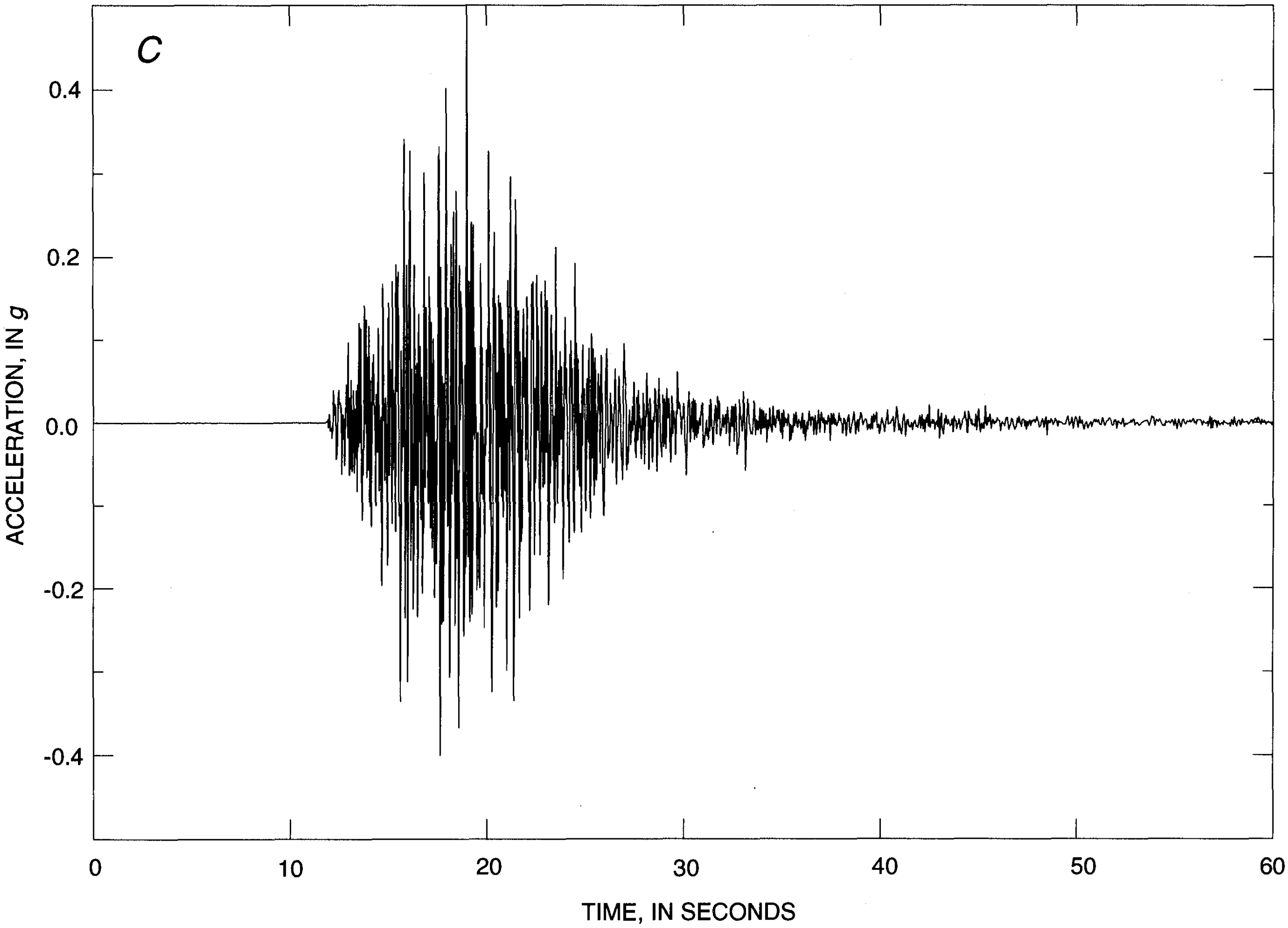

Figure 2.—Continued

location, the solution moved 5.2 km due west and +3.8 km in depth. We believe that these values of ~5 km may be a more realistic estimate of the uncertainty in location for early aftershocks located with only the four original UCSC stations than the statistical precision of rms=0.08, ERH=2.15 km, and ERZ=1.15 km calculated for the test solution. The locations of all events of $M_L \geq 3.8$ are summarized in table 2 and detailed in table 4.

The event magnitudes listed in tables 2 and 4 were calculated from the measured Wood-Anderson amplitudes reported by UCB (University of California, Berkeley, 1989), using the method of Richter (1935, 1958). These amplitudes were incorporated into the program HYPOINVERSE in conjunction with the phase data, so that both the location and magnitude (M_L) could be determined. UCB standard magnitude corrections were used for stations BRK (+0.2), MHC (+0.1), MIN (-0.1), and BKS (0.0). Some of our final magnitudes differ from those of UCB because of both roundoff and differences in earthquake locations. Also, our magnitudes should be compared with the magnitude called M_L(c) by UCB in their 1989 catalog, which indicates that the data are from recalibrated instruments. In addition, the local magnitude (M_L') was estimated from measurements of Wood-Anderson records synthesized (Uhrhammer and Collins, 1990) from the digital-accelerometer records, using the method of McNally and others (1990) with the distance corrections of Bakun and Joyner (1984) and Hutton and Boore (1987). A regression between M_L and M_L' yielded the relation $M_L{}^+ = (0.94 \pm 0.25) M_L' - 0.30$. This magnitude, $M_L{}^+$, was used for aftershocks with no UCB Wood-Anderson amplitudes available (7 events; pluses, table 2).

Of the 43 events ($M \geq 3.8$) that we recorded within the first 24 hours after the main shock, 24 were of $M \geq 4.0$ (table 2). Because the magnitudes and distances from the recording station place fundamental constraints on the

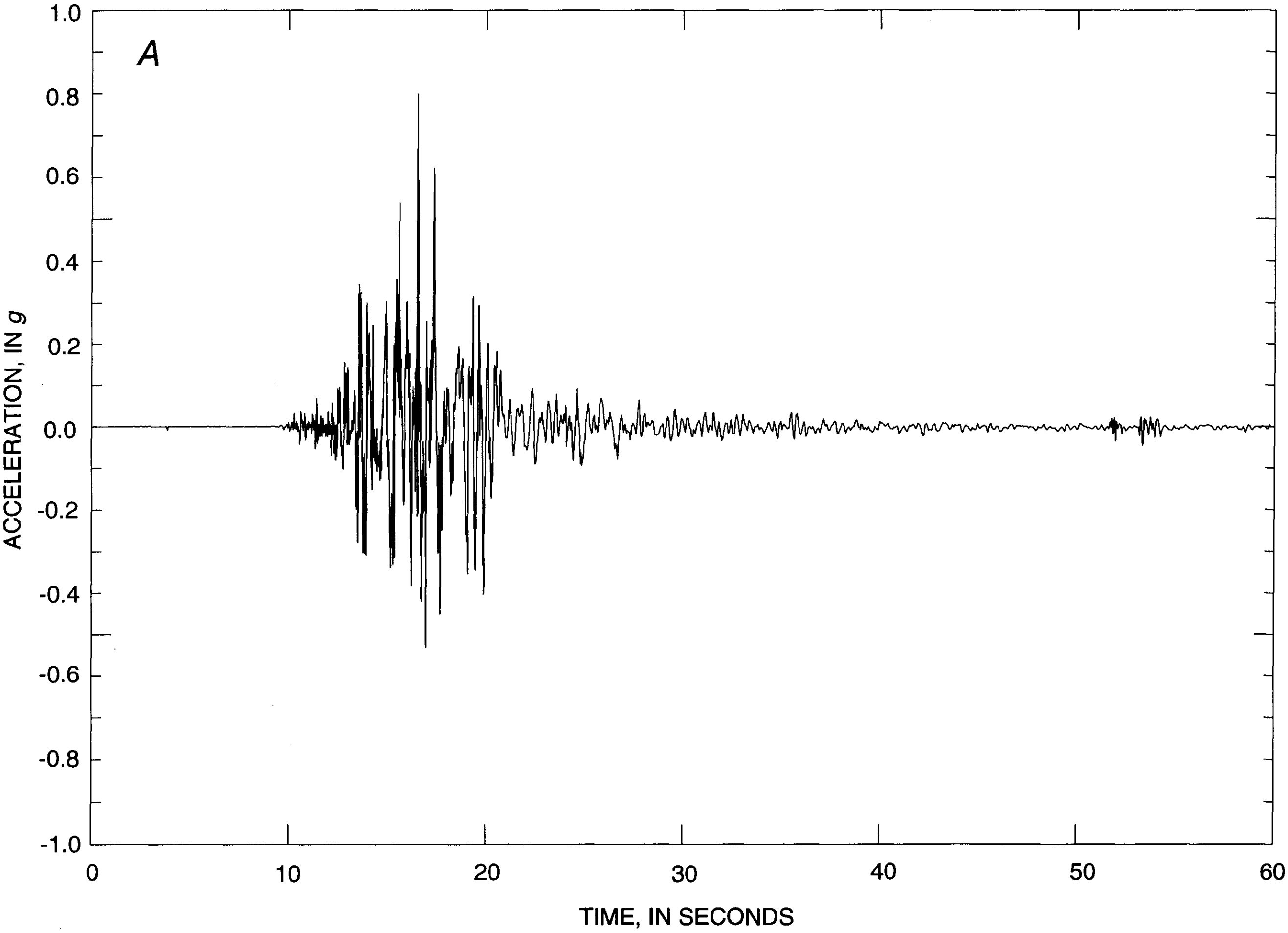

Figure 3.—Digital accelerograms of Loma Prieta main shock recorded at station LGPC (fig. 1), showing east-west (*A*), north-south (*B*), and vertical (*C*) components. East, north, and up directions are all positive. Sampling rate, 200 samples per second; trigger threshold, 0.0088 *g*; full scale, 1.0 *g*; peak amplitude 0.80 *g* (fig. 3*A*; note that records in figs. 3*B* and 3*C* are probably clipped at 1.0 *g*). Baseline offset may reflect sudden tilting of instrument (see fig. 4).

minimum threshold for detection and location determination, we analyzed several later aftershocks of $M>4.0$ to evaluate the event detectability southeastward along the fault zone as a function of distance. Specific aftershocks included in our tests are the secondary sequence at 1014 G.m.t. October 19 near the Zayante fault at lat 36°58′ N., long 121°50′ W. ($M=4.6$), and the event at 0127 G.m.t. October 25 ($M=4.6$) northeast of the main shock at lat 37°05′ N., long 121°50′ W. (Oppenheimer, 1990). These tests indicate that any events of $M\geq4.5$ at distances ≤25 km from station BRAN along the San Andreas fault would have been recorded at the four original stations during the first 34 minutes after the main shock.

RESULTS

The locations of aftershocks of $M_L\geq3.8$ are shown in figure 1. Within several minutes of the main shock, most aftershocks occurred near the northwestern part of the Loma Prieta rupture zone, in the vicinity of the San Andreas-Sargent fault intersection and northwestward. The first, second, and fourth aftershocks were located west of the San Andreas fault. Because of timing uncertainties and station limitations in number and azimuth, these locations may be suspect. However, the later occurrence of several very well recorded aftershocks ($M<3.8$) in the same area—for example, the event at 1402 G.m.t. October 23 (table 4)—suggests that the locations of these very early events may reflect a second, westerly zone of faulting activity. Alternatively, if errors in depth are greater than we estimate, these events may lie on the main-shock rupture surface, at greater depth.

Cross sections orthogonal to the San Andreas fault (*A–A′* through *F–F′*, fig. 1) for all events (tables 2, 4) are shown in figure 7, and the distribution of hypocenters ($M\geq3.8$) in a longitudinal cross section (*Y–Y′*) in figure 8. Our early aftershock pattern for the first 2 hours and 22 minutes after the main shock is consistent with the observation that aftershocks are generally absent in main slip zones of large earthquakes (Mendoza and Hartzell, 1988). Regarding the absence of early aftershock activity to the

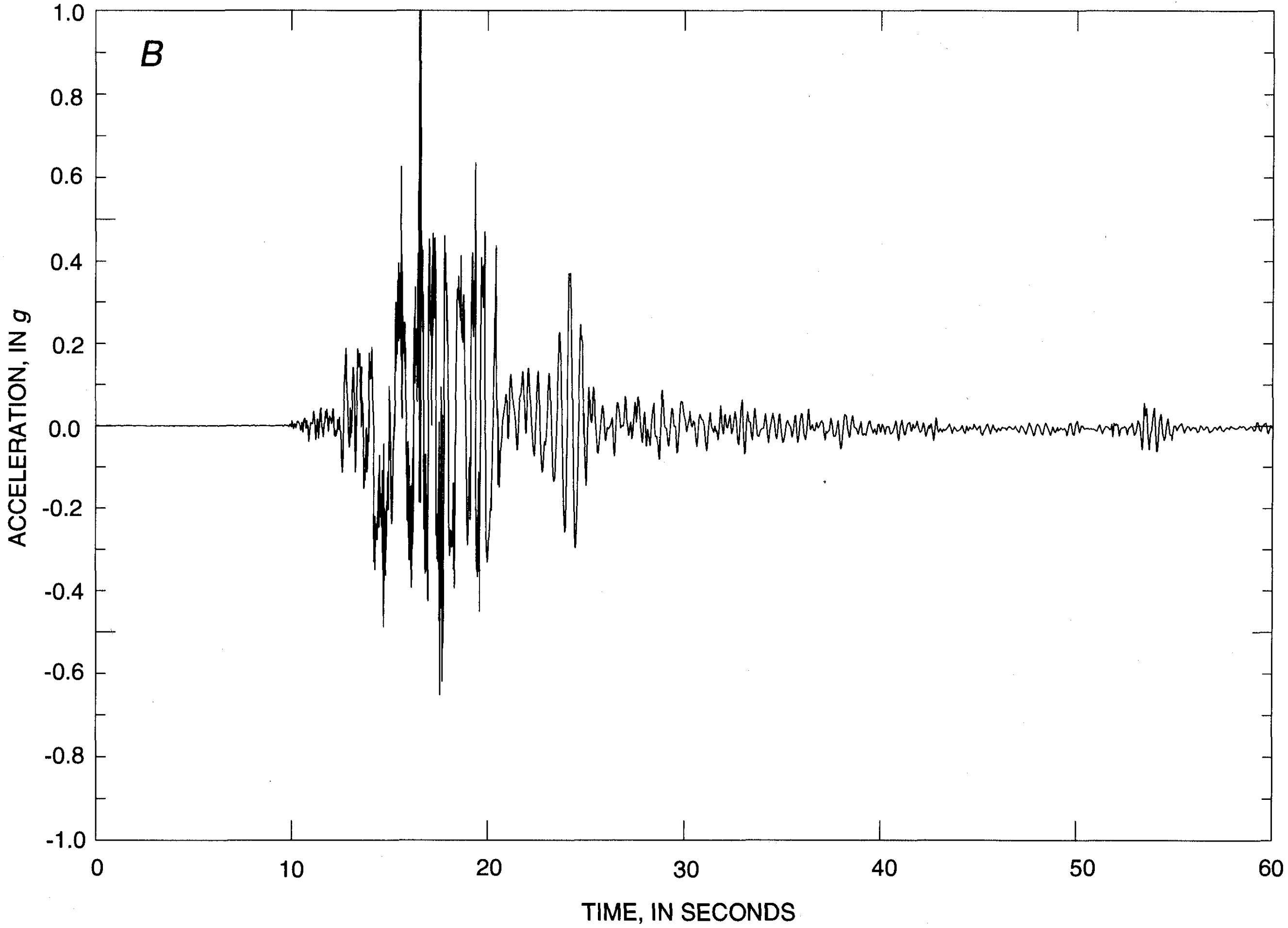

Figure 3.—Continued

southeast, however, we cannot eliminate the possibility of magnitude detection-threshold limitations in our data set.

CONCLUSIONS

We find that 34 significant aftershocks of $M_L \geq 3.8$ occurred within 3 ¼ hours of the main shock. Most of these events are located northwest of the main-shock hypocenter, largely concentrated near the intersection of the San Andreas and Sargent faults.

ACKNOWLEDGMENTS

This research was partly supported by the William M. Keck Foundation, the U.S. National Science Foundation (grant EAR–9002704), the USGS (grant 14–08–0001–G1839), and the UCSC Division of Graduate Studies and Research and the Division of Natural Sciences. The second author was supported by the Minority Access to Energy Related Careers (MAERC) program of the Associated Western Universities/U.S. Department of Energy. We thank the researchers, visiting researchers, staff, and graduate students of the Charles F. Richter Seismological Laboratory at UCSC, who made an extraordinary effort to maintain field instruments and analyze data after the earthquake, particularly Walter Schillinger, Instrument Specialist for UCSC's Department of Earth Sciences, who was primarily responsible for maintaining the four digital accelerometers. We also thank the following for providing data and information relevant to this study: David Oppenheimer of the USGS; Robert Uhrhammer and Rick McKenzie of the UCB Seismographic Observatory; and L. Katherine Hutton of the California Institute of Technology. We are grateful to Paul Spudich and Lynn Dietz for their reviews of the manuscript. Yi-Ben Tsai of the Pacific Gas & Electric Co. generously provided an independent assessment of the accelerograms recorded at station LGPC.

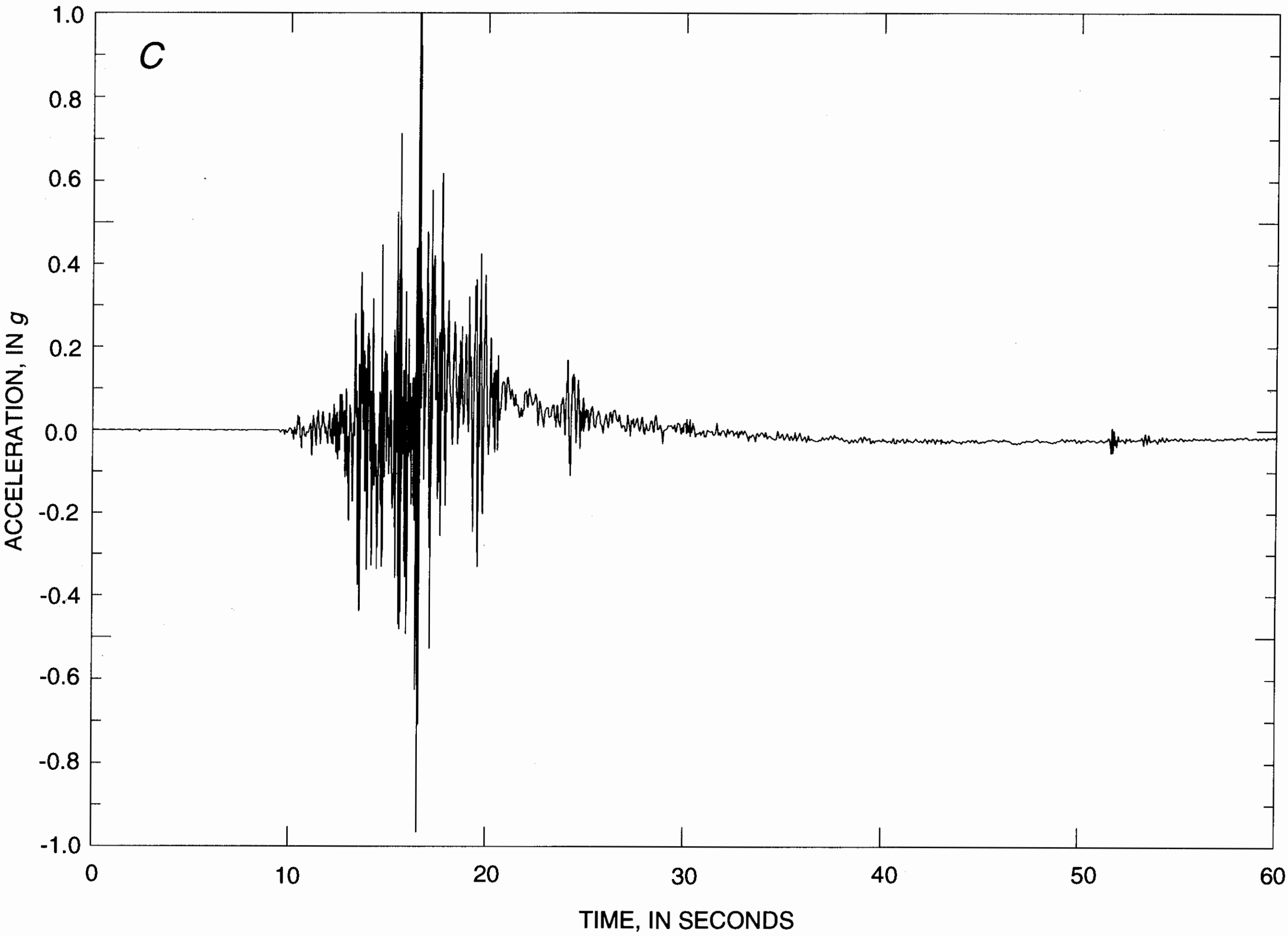

Figure 3.—Continued

REFERENCES CITED

Bakun, W.H., and Joyner, W.B., 1984, The M_L scale in central California: Seismological Society of America Bulletin, v. 74, no. 5, p. 1827–1843.

Dietz, L.D., and Ellsworth, W.L., 1990, The October 17, 1989 Loma Prieta earthquake and its aftershocks; geometry of the sequence from high-resolution locations: Geophysical Research Letters, v. 17, no. 9. p. 1417–1420.

Hutton, L.K., and Boore, D.V., 1987, The M_L scale in southern California: Seismological Society of America Bulletin, v. 77, no. 6, p. 2074–2094.

Klein, F.W., 1989, User's guide to HYPOINVERSE, a program for VAX computer to solve for earthquake locations and magnitudes: U.S. Geological Survey Open-File Report 89–314, 58 p.

McNally, K.C., Yellin, Joseph, Protti-Quesada, Marino, Simila, G.W., Malavassi, Eduardo, Schillinger, Walter, Terdiman, Richard, and Zhang, Zhi, 1990, The local magnitude of the 18 October 1989 Santa Cruz Mountains earthquake is M_L=6.9: Geophysical Research Letters, v. 17, no. 10, p. 1781–1784.

Mendoza, Carlos, and Hartzell, S.H., 1988, Aftershock patterns and main shock faulting: Seismological Society of America Bulletin, v. 78, no. 4, p. 1438–1449.

Oppenheimer, D.H., 1990, Aftershock slip behavior of the 1989 Loma Prieta, California earthquake: Geophysical Research Letters, v. 17, no. 8, p. 1199–1202.

Richter, C.F., 1935, An instrumental earthquake-magnitude scale: Seismological Society of America Bulletin, v. 25, no. 1, p. 1–32.

———1958, Elementary seismology: San Francisco, W.H. Freeman and Co., 578 p.

Simila, G.W., McNally, K.C., Nava, E.M., Protti-Quesada, Marino, and Yellin, Joseph, 1990, Evidence of very early aftershock activity along the northwest portion of the 18 October 1989 earthquake rupture zone: Geophysical Research Letters, v. 17, no. 10, p. 1785–1788.

Uhrhammer, R.A., and Bolt, B.A., 1991, The seismic magnitude of the 1989 Loma Prieta main- shock determined from strong-motion records: Seismological Society of America Bulletin, v. 81, no. 5, p. 1511–1517.

Uhrhammer, R.A., and Collins, E.R., 1990, Synthesis of Wood Anderson seismograms from broadband digital records: Seismological Society of America Bulletin, v. 80, no. 3, p. 702–716.

University of California, Berkeley, 1989, Seismographic Stations Bulletin: v. 59, no. 1–2, 117 p.

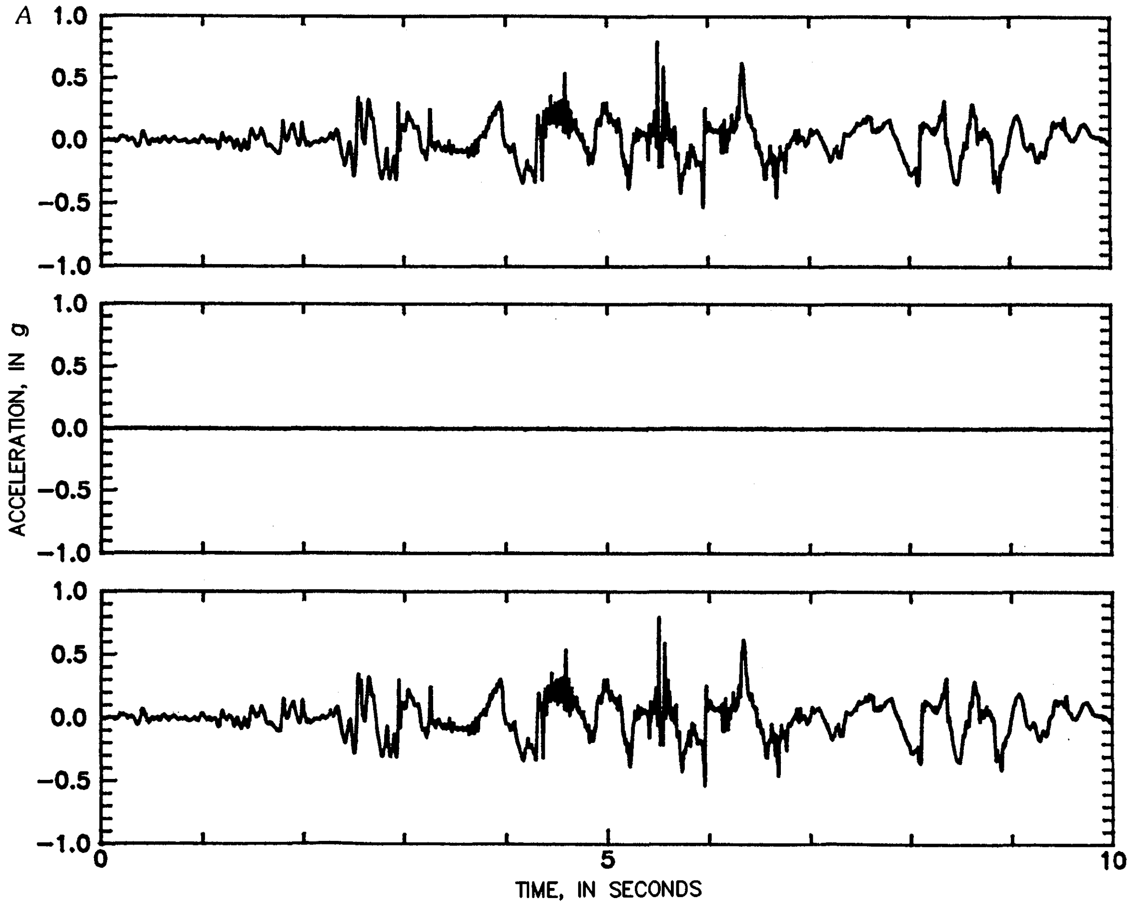

Figure 4.—Baseline-corrected digital accelograms of Loma Prieta main shock recorded at station LGPC (fig. 1), showing east-west (*A*), north-south (*B*), and vertical (*C*) components. East, north, and up directions are all positive. Top plot, original record; middle plot, baseline correction; bottom plot, baseline-corrected record (Yi-Ben Tsai, written commun., 1991).

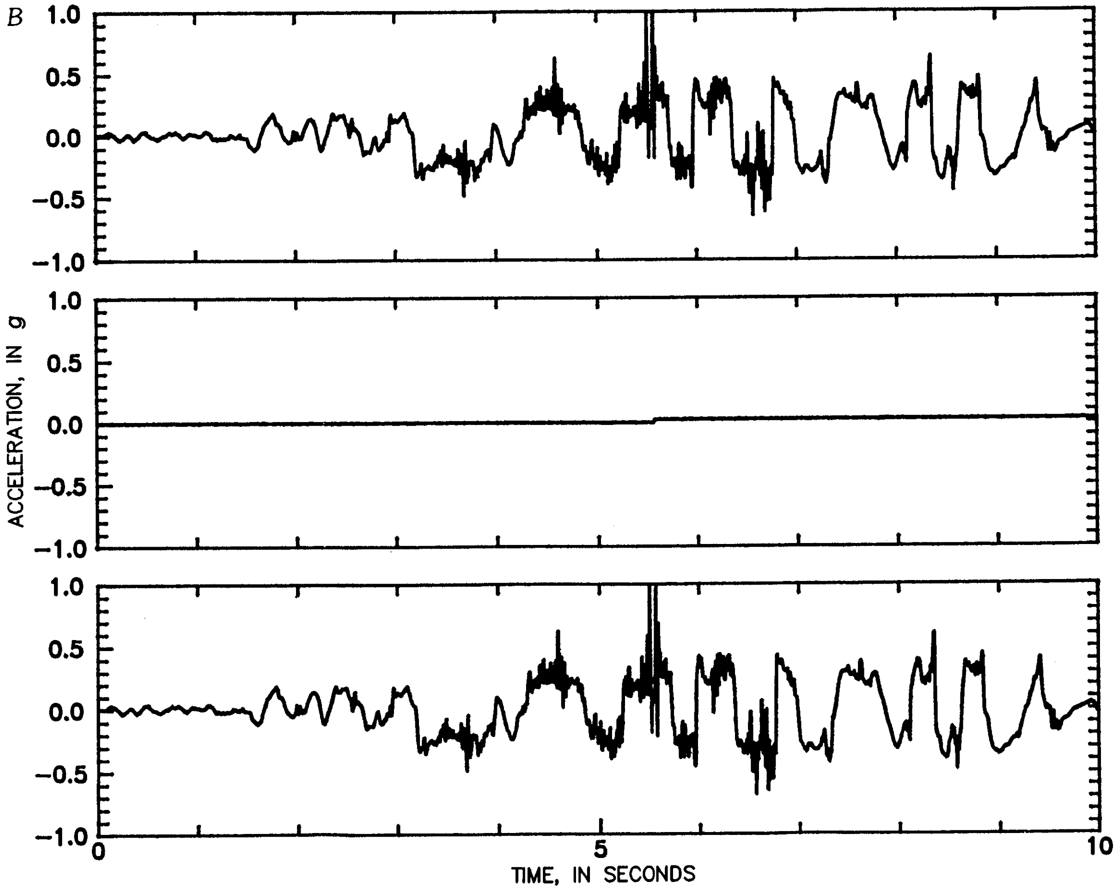

Figure 4.—Continued

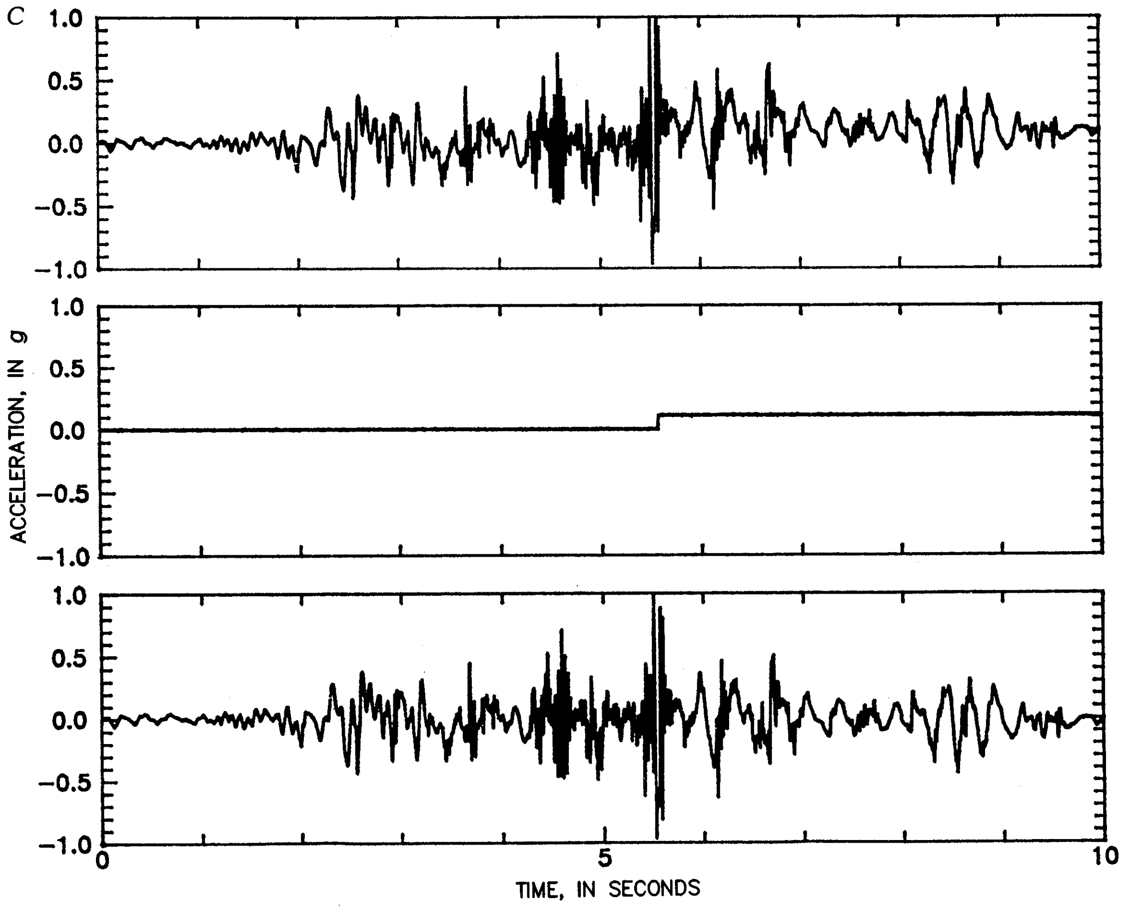

Figure 4.—Continued

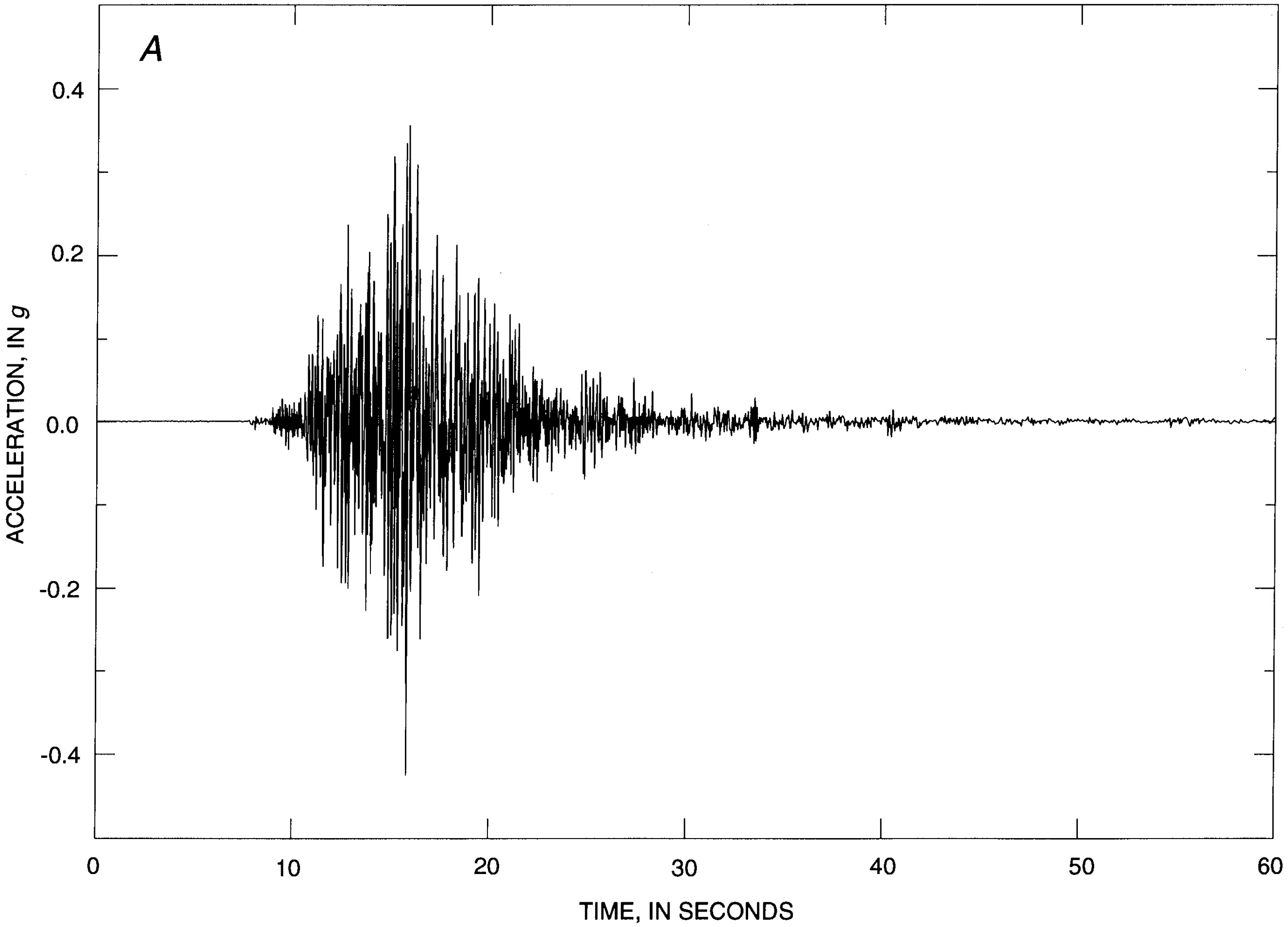

Figure 5. Digital accelerograms of Loma Prieta main shock recorded at station UCSC (fig. 1), showing east-west (*A*), north-south (*B*), and vertical (*C*) components. East, north, and up directions are all positive. Sampling rate, 200 samples per second; trigger threshold, 0.0088 *g*; full scale, 1.0 *g*; peak amplitudes: 0.42 *g* (fig. 5*A*), 0.31 *g* (fig. 5*B*), 0.22 *g* (fig. 5*C*).

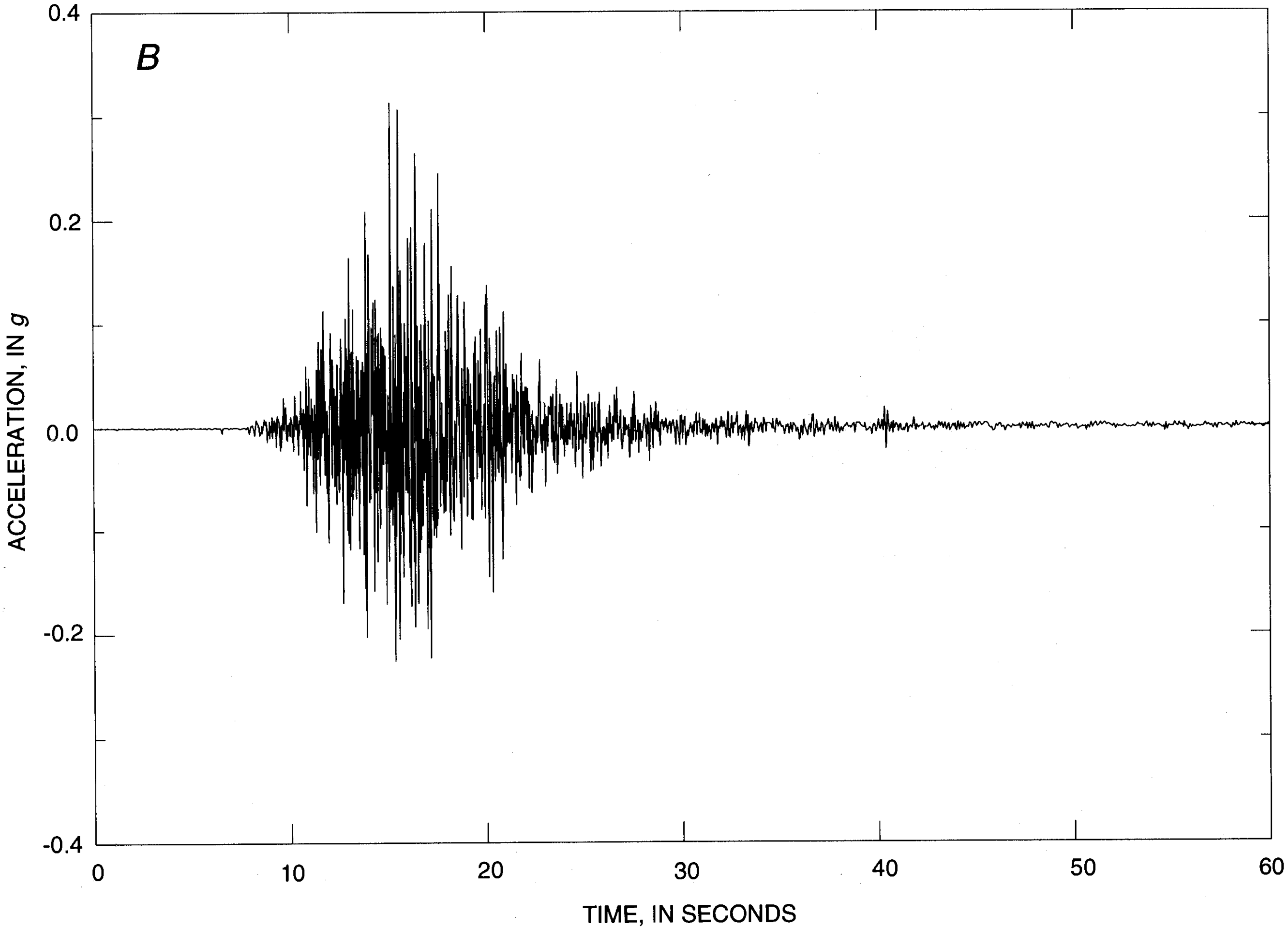

Figure 5. Continued

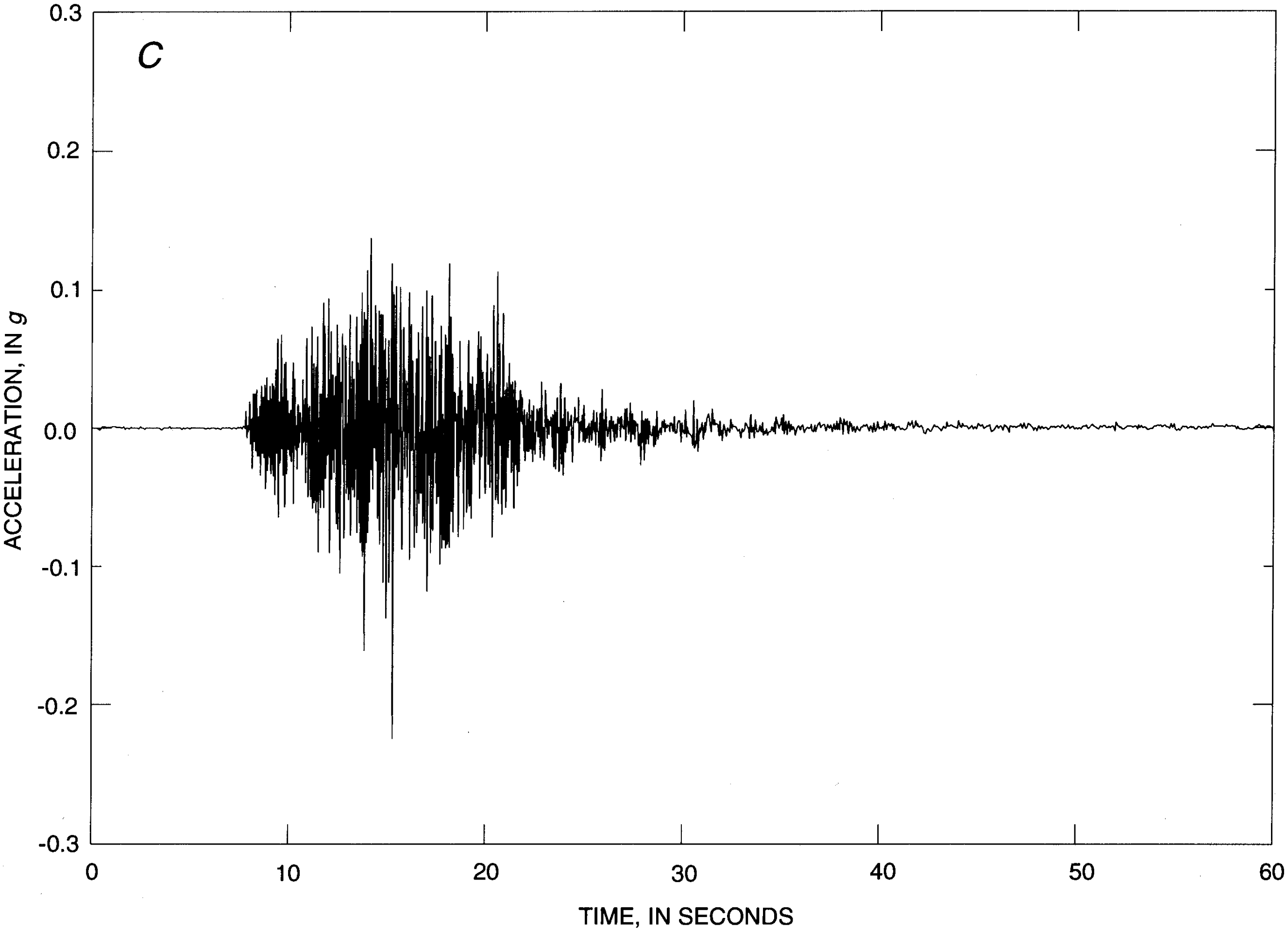

Figure 5. Continued

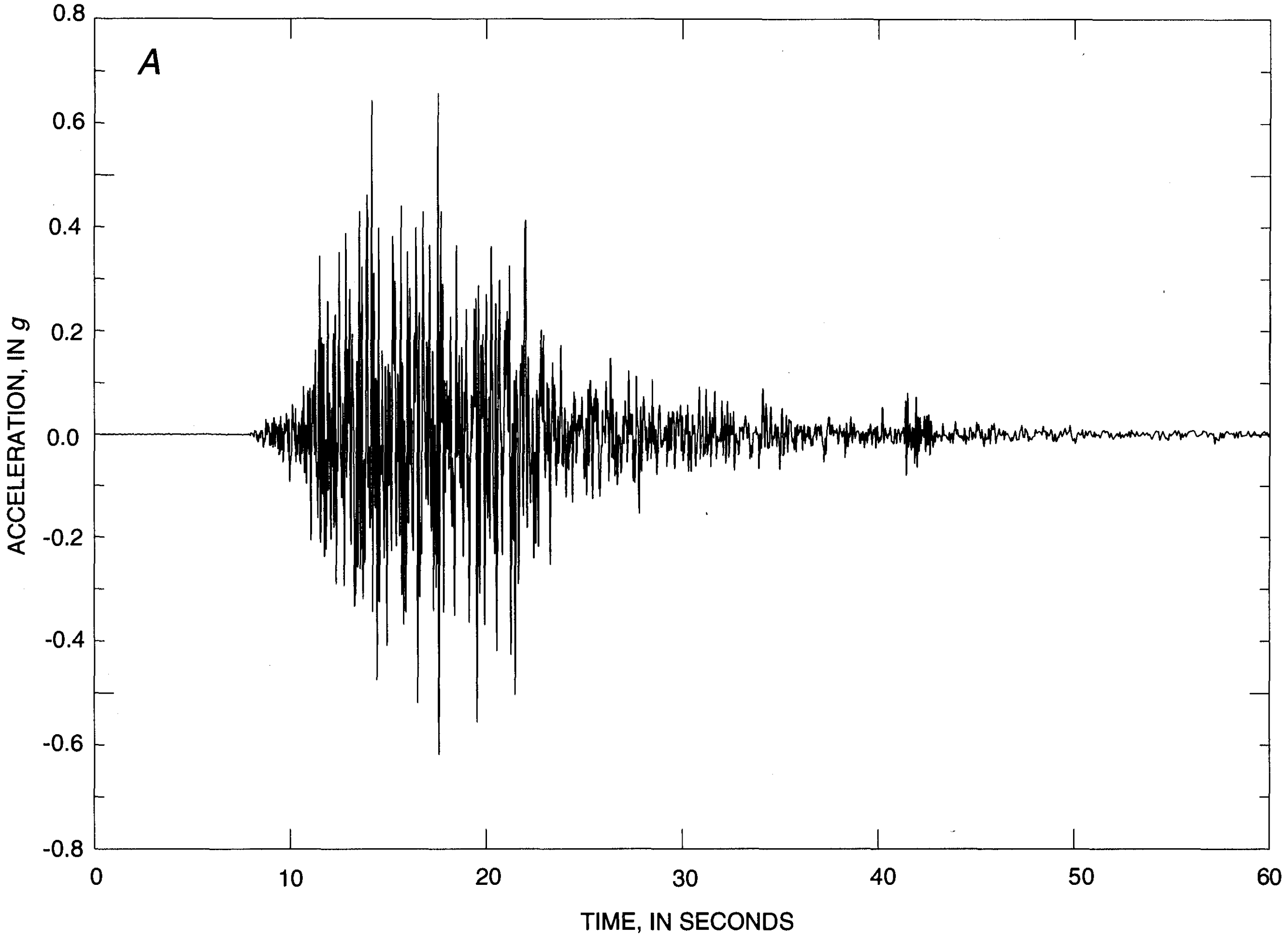

Figure 6.—Digital accelerograms of Loma Prieta main shock recorded at station WAHO (fig. 1), showing east-west (*A*), north-south (*B*), and vertical (*C*) components. East, north, and up directions are all positive. Sampling rate, 200 samples per second; trigger threshold, 0.0088 *g*; full scale 1.0 *g*; peak amplitudes: 0.66 *g* (fig. 6*A*), 0.38 *g* (fig. 6*B*), 0.27 *g* (fig. 6*C*).

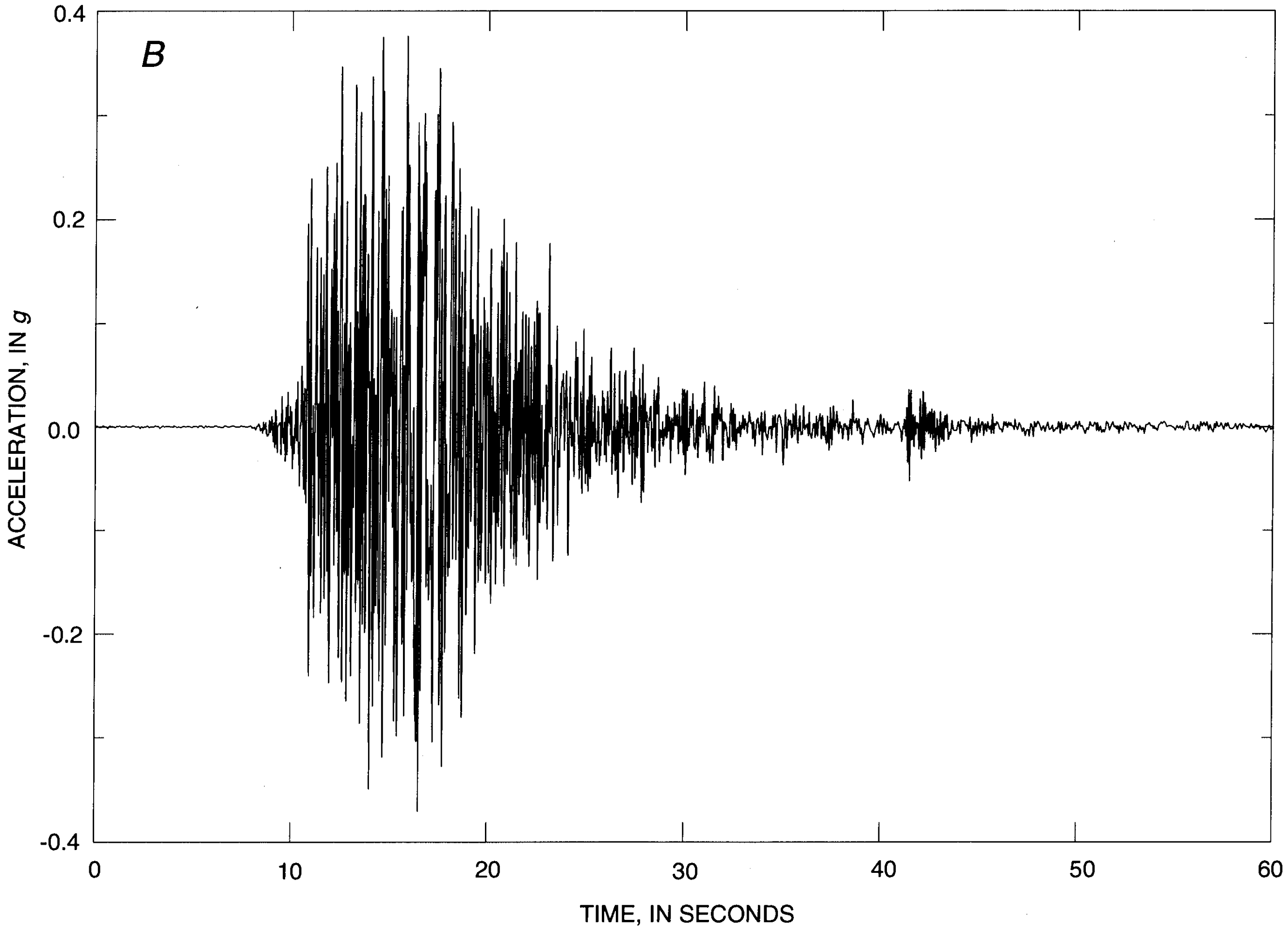

Figure 6.—Continued

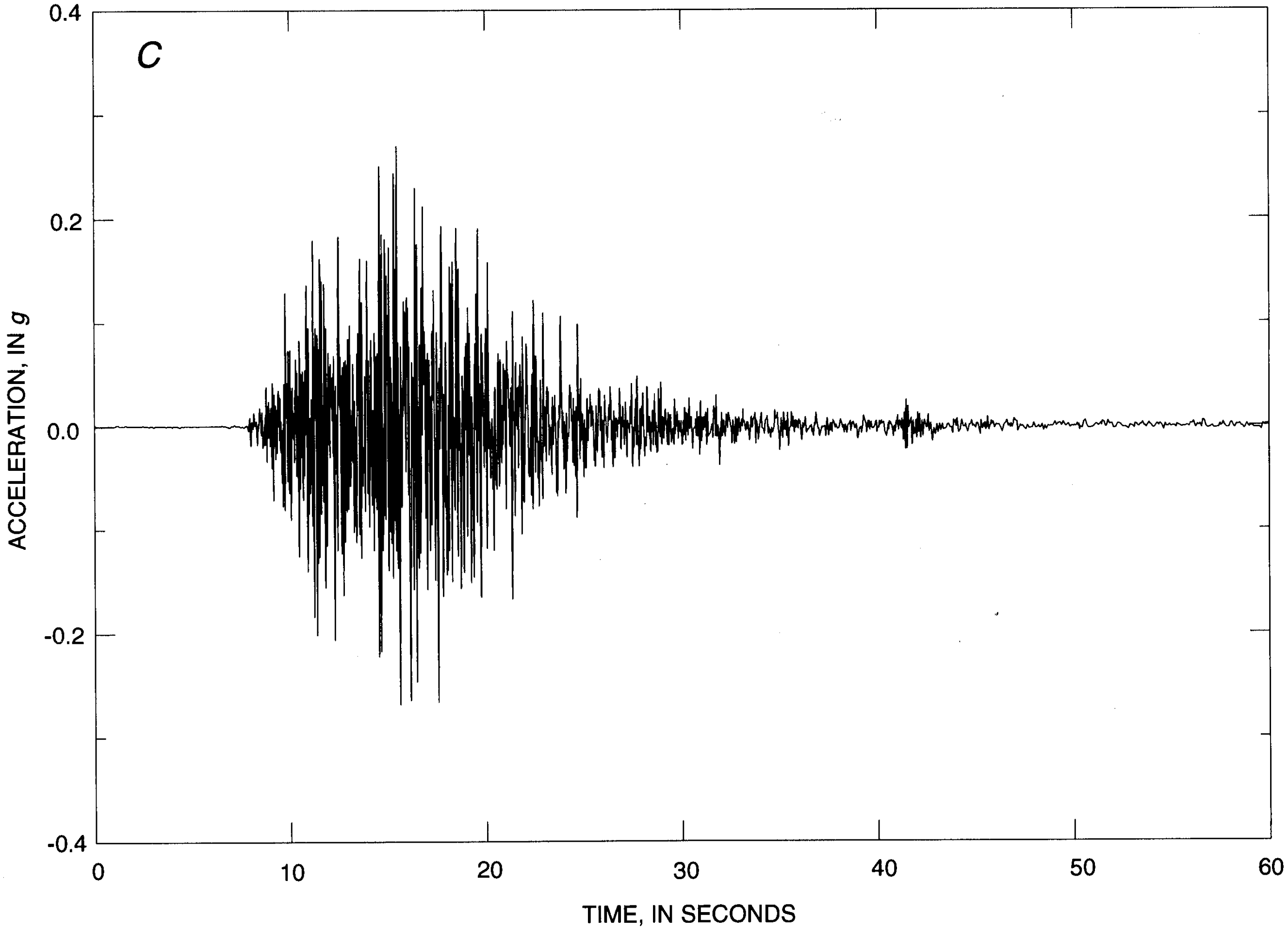

Figure 6.—Continued

Table 1.—*Temporary stations deployed by the University of California, Santa Cruz, in the Loma Prieta area*

Station	Location		Elevation (m)	Address	Description and dates of operation
	Lat N.	Long W.			
BRAN	37°02.82′	121°59.10′	103	5001 Branciforte Drive	On concrete floor in wood-frame garage detached from house. Santa Cruz, CA. Aug. 15–Nov. 16, 1989.
LGPC	37°10.32′	122°00.60′	481	19600 Bear Creek Road Los Gatos, CA	On detached concrete pad in basement/storage area (downhill side) of a wood-frame single-story house built on a moderately steep hillside. Aug. 15, 1989–Mar. 5, 1990.
UCSC	37°00.00′	122°03.72′	243	Applied Sciences Building McLaughlin Drive University of California Santa Cruz, CA	On floor of first-story seismology laboratory (room 195) in a large four-story cast-in-place reinforced-concrete office building. Aug. 9, 1989–Jan. 16, 1990.
WAHO	36°58.40′	121°59.73′	21	738 Cable Court Santa Cruz, CA	On concrete in attached garage that protrudes from a two-story wood-frame condominium. Aug. 9–Nov. 17, 1989.
AHCR	37°10.20′	122°03.84′	--	---	Oct. 28, 1989–Jan. 11, 1990.
BGST	37°06.48′	121°54.30′	--	---	Oct. 22, 1989–Mar. 5, 1990.
CTES	37°07.56′	121°56.58′	--	---	Oct. 20–Nov. 7, 1989.
LGPS	37°13.20′	121°56.58′	--	---	Oct. 20–Nov. 7, 1989.
LPVF	37°08.52′	121°58.38′	--	---	Oct. 22, 1989–Mar. 7, 1990.

Table 2.—*Seismicity* ($M_L \geq 3.8$) *in the Loma Prieta area*

[Magnitude (M_L) of the October 18 (G.m.t.) main shock from McNally and others (1990); magnitudes of aftershocks with a listing of "+" were calculated from the local magnitude M_L', that is, Wood-Anderson records synthesized from digital strong-motion records at stations BRAN, LGPC, UCSC and WAHO (see figs. 1 and 8 for locations) and calibrated to M_L by the relation $M_L{}^{+}=0.94(\pm 0.25)M_L{}'-0.30$. Otherwise, M_L is calculated from the University of California, Berkeley, Wood-Anderson amplitude relative to a specific location. Event with an "R" has a restricted depth; events with a listing of "O" are not in the U.S. Geological Survey aftershock list; events with a listing of "c" were used to calibrate joint relocation and redetermination of Poisson's ratio and station delay. SAF, San Andreas fault; events not located east (E) or west (W) of the fault occurred on the fault. ERH, horizontal-location error; ERZ, vertical-depth error; UCSC, University of California, Santa Cruz]

Year	Date	Time (G.m.t.)	M_L	Listing	Latitude N.	Longitude W.	Depth (km)	Location on SAF	No. of *P*/*S* phases	No. of *P*/*S* phases at UCSC stations	Residual (s)	ERH (km)	ERZ (km)
1988	June 27	1843:22.41	5.3	- -	37°07.88′	121°53.83′	12.14	E	38	0	0.08	0.35	0.77
1989	Aug. 8	0813:27.45	5.3	- -	37°09.03′	121°55.65′	13.36	E	37	0	.07	.39	.76
		0844:09.77	4.5	- -	37°08.82′	121°55.55′	12.38	E	38	0	.07	.36	.75
		1553:28.16	4.7	- -	37°09.63′	121°57.04′	14.35	E	35	0	.08	.41	.84
	Oct. 18	0004:14.94	6.9	+	37°02.26′	121°52.52′	19.96	- -	28	8	.12	.53	1.04
		0004:47.17	4.7	+, O	37°06.31′	122°01.84′	9.97	W	6	6	.08	1.68	1.65
		0005:01.11	4.0	+, O	37°07.49′	122°00.61′	2.35	W	6	6	.11	8.67	7.17
		0005:14.91	4.2	+, O	37°11.21′	122°01.72′	8.38	- -	6	6	.06	1.55	.88
		0005:34.39	4.1	+, O	37°10.66′	122°04.52′	4.27	W	8	6	.10	2.68	2.80
		0006:04.32	3.9	+, O	37°05.01′	121°53.17′	3.95	- -	7	6	.06	1.27	3.58
		0006:10.95	3.8	+, O	37°08.54′	121°57.39′	8.11	- -	6	6	.05	1.25	1.03
		0007:13.67	4.7	- -	37°12.15′	122°02.65′	4.62	- -	9	6	.55	3.86	1.02
		0007:43.34	5.0	- -	36°57.99′	121°45.48′	R16.00	- -	6	6	.20	2.19	- - -
		0008:21.11	4.7	- -	37°04.26′	121°54.85′	19.99	- -	15	6	.36	1.12	2.37
		0008:46.32	3.9	- -	37°09.75′	121°59.60′	12.41	- -	7	4	.22	1.61	1.82
		0008:58.05	4.3	O	37°06.50′	121°54.17′	1.09	- -	6	6	.29	2.50	1.83
		0009:55.83	3.9	- -	37°00.35′	121°43.82′	14.98	E	5	1	.03	4.37	10.70
		0011:49.40	3.9	- -	37°08.85′	122°06.07′	13.66	W	5	5	.09	8.30	6.91
		0012:42.34	4.5	- -	37°09.57′	121°59.07′	2.45	- -	17	8	.29	.71	.87
		0013:08.92	4.1	- -	37°10.84′	122°00.78′	8.56	- -	19	6	.38	.76	3.14
		0016:54.63	4.0	- -	37°06.63′	121°56.51′	4.90	- -	24	8	.28	.35	.43
		0017:13.58	3.9	+	37°07.63′	121°59.76′	11.42	- -	13	2	.12	.89	.45
		0017:33.01	4.0	- -	37°10.41′	122°00.95′	9.48	- -	13	1	.17	1.11	.49
		0019:17.26	3.9	- -	37°08.83′	121°58.50′	7.72	- -	23	4	.14	.28	.48
		0023:37.22	3.9	- -	37°01.93′	121°46.48′	1.68	- -	30	3	.25	.34	.76
		0025:04.61	4.9	- -	37°03.23′	121°46.85′	5.85	- -	30	6	.17	.33	.75
		0030:41.63	4.2	- -	37°07.83′	121°59.46′	10.96	- -	19	5	.08	.36	.60
		0035:25.89	3.9	- -	37°11.85′	122°02.29′	9.64	- -	19	2	.11	.83	.43
		0038:28.20	4.2	- -	37°10.41′	121°59.41′	8.44	- -	33	5	.11	.32	.44
		0041 24.10	5.0	- -	37°11.70′	122°02.40′	11.99	- -	32	6	.19	.46	.66
		0045:38.72	3.9	- -	36°57.21′	121°41.09′	5.30	- -	30	0	.15	.41	.90
		0058:01.18	3.8	- -	37°09.48′	121°58.39′	3.98	- -	11	2	.15	.67	.98
		0058:55.79	3.9	- -	37°06.73′	122°00.00′	17.68	- -	24	4	.12	.56	1.26
		0103:59.09	3.8	- -	37°06.80′	121°51.07′	3.27	E	24	2	.18	.35	.91
		0121:18.69	3.9	- -	36°58.03′	121°44.27′	13.02	- -	30	0	.14	.46	1.28
		0215:49.81	4.4	- -	37°02.28′	121°45.33′	1.26	- -	25	4	.16	.38	.53
		0226:05.73	4.2	- -	37°01.84′	121°46.82′	1.59	- -	29	3	.26	.63	1.26
		0302:43.09	3.9	- -	37°06.83′	121°52.87′	3.81	- -	25	2	.15	.44	.76
		0321:47.72	3.9	- -	37°06.47′	121°50.87′	4.52	E	29	0	.13	.42	.57
		0323:56.23	4.0	- -	37°08.07′	121°59.38′	14.44	- -	32	2	.09	.34	.80
		0335:45.45	3.9	- -	37°07.36′	121°52.18′	8.24	E	5	0	.04	3.36	9.25
		0346:29.32	3.8	- -	37°01.53′	121°47.59′	11.41	- -	9	0	.18	1.01	2.69
		0416:32.44	4.1	- -	37°03.62′	121°53.55′	13.61	- -	33	2	.09	.36	.77
		0450:26.91	4.3	- -	37°09.91′	122°00.55′	9.81	- -	31	2	.14	.31	.70
		0518:33.87	4.2	- -	37°00.67′	121°50.47′	17.34	- -	25	2	.12	1.36	.66
		0639:10.17	4.4	- -	36°58.10′	121°42.68′	14.70	- -	16	0	.07	1.59	1.60
		1022:04.61	4.4	- -	37°01.65′	121°48.42′	10.71	- -	32	3	.16	.41	.98
		1801:03.49	3.8	- -	36°56.73′	121°41.42′	6.06	- -	26	0	.13	.53	.69
	Oct. 19	0355:00.19	3.9	c	36°59.59′	121°47.73′	17.18	- -	34	0	.07	.46	.91
		0845:49.67	4.0	c	36°58.44′	121°50.54′	9.14	W	31	0	.13	.59	.81
		0953:50.02	4.5	c	36°56.43′	121°41.15′	8.97	- -	32	0	.17	.61	.90
		1014:34.90	4.6	c	36°57.93′	121°50.38′	8.90	W	27	0	.12	.56	.56
		1225:33.29	4.0	c	36°56.13′	121°40.95′	8.37	- -	30	0	.11	.49	.78
		1715:05.52	4.0	c	36°55.39′	121°39.13′	4.57	- -	34	0	.12	.41	.45
	Oct. 20	0018:20.51	4.2	c	37°06.19′	121°54.98′	9.16	- -	28	3	.10	.32	1.01
		0812:53.91	3.9	c	37°11.08′	122°03.47′	14.72	- -	37	0	.10	.43	.92
	Oct. 21	0049:43.02	4.4	c	37°03.80′	121°51.38′	14.67	- -	35	6	.19	.50	1.08
		2214:56.42	4.6	c	37°04.22′	121°53.62′	15.61	- -	44	6	.14	.32	.60
	Oct. 22	1424:36.59	3.9	c	36°58.98′	121°48.90′	19.07	- -	38	6	.19	.57	1.09
	Oct. 25	0127:26.24	4.6	c	37°05.15′	121°49.69′	8.74	E	46	8	.16	.29	.69
		1300:41.85	3.8	c	36°53.86′	121°38.07′	5.54	- -	19	0	.09	.56	.69
		2201:49.37	3.9	c	37°00.07′	121°48.77′	15.86	- -	31	2	.14	.53	.90
	Oct. 26	0901:29.03	3.8	c	37°03.84′	121°52.68′	10.95	- -	34	4	.17	.37	.90
	Oct. 30	1117:13.45	3.9	c	37°04.41′	121°48.69′	8.85	E	38	0	.07	.28	.51
	Nov. 2	0550:10.64	4.6	c	37°04.14′	121°48.43′	9.53	E	44	6	.22	.40	1.02
	Nov. 5	0130:42.05	4.1	c	37°04.77′	121°54.80′	11.77	- -	43	6	.16	.32	.65
		1337:33.88	4.2	c	37°03.98′	121°53.52′	13.49	- -	37	2	.04	.32	.57
	Nov. 7	2342:37.39	4.2	c	37°13.86′	122°01.64′	8.77	E	29	1	.09	.35	.52

Table 3.—*P-wave station delays determined in this study and used for event relocation*

[Asterisks, delays calculated by using alternate Pacific side of crustal-velocity model of Dietz and Ellsworth (1990); pluses, UCSC stations. The *S*-wave delay is equal to 1.71 (Poisson's ratio, determined in this study) times the *P*-wave delay, according to allowance of the computer program HYPOINVERSE (Klein, 1989)]

Station	Delay	Station	Delay
+BRAN	−0.08	HSPM	0.35*
+LGPC	.17	JALM	−.11*
+UCSC	−.56	JBCM	.01
+WAHO	−.48	JBLM	−.33
BSLM	.97*	JBMM	.11*
BVYM	−.42	JBZM	.30
CADM	.26*	JCBM	.16*
CALM	.66*	JECM	−.01
CAOM	.53*	JHLM	−.04*
CCOM	.90*	JLXM	.02*
CMHM	.81*	JPLM	.12
CMJM	.64*	JPPM	.02
CSCM	.56*	JRGM	−.18
HAZM	−.45	JRRM	−.05*
HCAM	.28*	JSCM	−.25
HCBM	−.18	JSGM	.29*
HCRM	.05*	JSMM	−.09
HDLM	−.27	JSSM	−.01*
HFEM	.21*	JSTM	.19*
HFHM	.51*	JTGM	.07
HFPM	−.68	JUCM	−.34
HGSM	.32*	+CTES	.07
HGWM	−.29	+LPVF	.05
HJSM	.45*	HJGM	−.53
HKRM	.62*	JBGM	.05
HMOM	−.37	JHPM	−.19
HPRM	.06*	JPSM	−.24

Table 4.—Details of seismicity in the Loma Prieta rupture zone

[Event with an "R" has a restricted depth. DMIN, distance to nearest stations (in kilometers); GAP, largest azimuthal gap between stations; ERH, horizontal-location error; ERZ, vertical-depth error]

Date (yymmdd)	Time (G.m.t.)	Latitude N.	Longitude W.	Depth (km)	M_L	No. of *P*/*S* phases	GAP (°)	DMIN (km)	Rms residual (s)	ERH (km)	ERZ (km)
Earthquakes on the San Andreas fault											
891018	0004:14.94	37°02.26′	121°52.52′	19.96	6.9	28	52	1	0.12	0.53	1.04
891018	0005:14.91	37°11.21′	122°01.72′	8.38	4.2	6	305	2	.06	1.55	.88
891018	0006:04.32	37°05.01′	121°52.17′	3.95	3.9	7	267	10	.06	1.27	3.58
891018	0006:10.95	37°08.54′	121°57.39′	8.11	3.8	6	249	6	.05	1.25	1.03
891018	0007:13.67	37°12.15′	122°02.65′	4.62	4.7	9	244	5	.55	3.86	1.02
891018	0007:43.34	37°57.99′	121°45.45′	16.00R	5.0	6	317	21	.20	2.19	- -
891018	0008:21.11	37°04.26′	121°54.85′	19.99	4.7	15	69	8	.36	1.12	2.37
891018	0008:46.32	37°09.75′	121°59.60′	12.41	3.9	7	118	2	.22	1.61	1.82
891018	0008:58.05	37°06.50′	121°54.17′	1.09	4.3	6	262	12	.29	2.50	1.83
891018	0012:42.34	37°09.57′	121°59.07′	2.45	4.5	17	69	3	.29	.71	8.7
891018	0013:08.92	37°10.84′	122°00.78′	8.56	4.1	19	84	3	.38	.76	3.14
891018	0015:10.79	37°00.09′	121°48.18′	16.53	3.7	21	152	6	.10	.47	1.19
891018	0016:54.63	37°06.63′	121°56.51′	4.90	4.0	24	108	7	.28	.35	.43
891018	0017:13.58	37°07.63′	121°59.76′	11.42	3.9	13	108	5	.12	.89	.45
891018	0017:33.01	37°10.41′	122°00.95′	9.48	4.0	13	78	1	.17	1.11	.49
891018	0019:17.26	37°08.83′	121°58.50′	7.72	3.9	23	78	4	.14	.28	.48
891018	0023:37.22	37°01.93′	121°46.48′	1.68	3.9	30	68	4	.25	.34	.76
891018	0024:35.61	37°10.12′	121°59.46′	6.68	3.4	31	58	2	.13	.43	.22
891018	0025:04.61	37°03.23′	121°46.85′	5.85	4.9	30	92	13	.17	.33	.75
891018	0027:10.31	37°07.93′	122°00.10′	17.80	3.4	16	131	4	.48	2.38	1.60
891018	0029:53.93	37°07.36′	121°57.76′	3.66	3.4	18	125	7	.25	.57	1.07
891018	0030:41.63	37°07.83′	121°59.46′	10.96	4.2	19	108	5	.08	.36	.60
891018	0035:25.89	37°11.85′	122°02.29′	9.64	3.9	19	84	4	.11	.83	.43
891018	0037:13.43	37°04.25′	121°54.66′	14.14	3.2	13	78	6	.20	1.43	3.09
891018	0038:28.20	37°10.41′	121°59.41′	8.44	4.2	33	47	2	.11	.32	.44
891018	0040:57.13	37°09.08′	121°57.57′	9.06	3.1	29	59	3	.17	.40	.72
891018	0041:24.10	37°11.70′	122°02.40′	11.99	5.0	32	58	4	.19	.46	.66
891018	0045:38.72	36°57.21′	121°41.09′	5.30	3.9	30	104	1	.15	.41	.90
891018	0058:01.18	37°09.48′	121°58.39′	3.98	3.8	11	88	4	.15	.67	.98
891018	0058:55.79	37°06.73′	122°00.00′	17.68	3.9	24	73	6	.12	.56	1.26
891018	0108:09.18	37°11.92′	122°02.77′	11.27	3.7	25	57	4	.15	.49	.64
891018	0116:19.46	37°11.10′	121°59.91′	6.05	3.6	17	185	2	.17	1.33	.75
891018	0121:18.69	36°58.03′	121°44.27′	13.02	3.9	30	128	4	.14	.46	1.28
891018	0122:44.49	37°07.76′	121°58.62′	17.79	3.4	13	105	6	.20	1.59	1.67
891018	0130:50.82	37°06.47′	121°55.39′	8.20	3.2	26	73	7	.15	.42	1.14
891018	0145:57.48	37°01.76′	121°47.63′	10.45	3.6	31	63	3	.07	.30	.75
891018	0215:49.81	37°02.28′	121°45.33′	1.26	4.4	25	102	5	.16	.38	.53
891018	0226:05.73	37°01.84′	121°46.82′	1.59	4.2	29	102	10	.26	.63	1.26
891018	0230:29.59	37°10.81′	122°00.26′	6.86	3.3	30	52	1	.13	.37	.28
891018	0236:01.99	37°09.69′	121°58.61′	8.36	3.3	33	58	3	.12	.37	.51
891018	0248:51.92	37°11.01′	121°59.66′	5.88	2.9	23	60	2	.13	.45	.36
891018	0249:49.07	37°08.57′	121°58.55′	9.69	- -	23	62	4	.09	.49	.40
891018	0302:43.09	37°06.83′	121°52.87′	3.81	3.9	25	84	8	.15	.44	.76
891018	0323:56.23	37°08.07′	121°59.38′	14.44	4.0	32	68	4	.09	.34	.80
891018	0346:29.32	37°01.53′	121°47.59′	11.14	3.8	9	162	27	.18	1.01	2.69
891018	0414:47.99	37°07.66′	121°59.10′	14.71	3.5	33	69	5	.09	.35	.81
891018	0416:32.44	37°03.62′	121°53.55′	13.61	4.1	33	75	7	.09	.36	.77
891018	0428:14.79	36°58.66′	121°46.41′	14.47	3.5	34	126	5	.12	.36	.96
891018	0450:26.91	37°09.91′	122°00.55′	9.81	4.3	31	60	2	.14	.31	.70
891018	0518:33.87	37°00.67′	121°50.47′	17.34	4.2	25	217	11	.12	1.36	.66
891018	0538:02.15	37°08.65′	122°02.78′	16.47	3.2	42	113	3	.08	.46	.71
891018	0639:10.17	36°58.10′	121°42.68′	14.70	4.4	16	257	19	.07	1.59	1.60
891018	0644:56.29	37°10.45′	121°59.39′	7.63	3.6	18	54	3	.07	.44	.84
891018	1022:04.61	37°01.65′	121°48.42′	10.71	4.4	32	57	2	.16	.41	.98
891018	1801:03.49	36°56.73′	121°41.42′	6.06	3.8	26	121	1	.13	.53	.69
891019	0355:00.19	36°59.59′	121°47.73′	17.18	3.9	34	100	3	.07	.46	.91
891019	0953:50.02	36°56.43′	121°41.15′	8.97	4.5	32	120	2	.17	.61	.90
891019	1225:33.29	36°56.13′	121°40.95′	8.37	4.0	30	121	2	.11	.49	.78
891019	1715:05.52	36°55.39′	121°39.13′	4.57	4.0	34	109	1	.12	.41	.45
891020	0018:20.51	37°06.19′	121°54.98′	9.16	4.2	28	50	7	.10	.32	1.01
891020	0812:53.91	37°11.08′	122°03.47′	14.72	3.9	37	60	4	.10	.43	.92
891021	0049:43.02	37°03.80′	121°51.38′	14.67	4.4	35	43	4	.19	.50	1.08
891021	0102:45.66	37°03.54′	121°51.27′	10.53	- -	34	43	4	.15	.40	.89
891021	1057:04.33	37°10.26′	121°58.75′	8.29	- -	35	52	3	.18	.38	.52
891021	1452:24.08	37°06.43′	121°52.90′	2.93	- -	44	56	2	.13	.24	.21
891021	2214:56.42	37°04.22′	121°53.62′	15.61	4.6	44	59	4	.14	.32	.60
891022	0944:57.89	36°55.73′	121°40.34′	5.24	3.5	47	117	1	.24	.54	.78
891022	1424:36.59	36°58.98′	121°48.90′	19.07	3.9	38	110	2	.19	.57	1.09

Table 4.—Details of seismicity in the Loma Prieta rupture zone—Continued

Date (yymmdd)	Time (G.m.t.)	Latitude N.	Longitude W.	Depth (km)	M_L	No. of *P*/*S* phases	GAP (°)	DMIN (km)	Rms residual (s)	ERH (km)	ERZ (km)
Earthquakes on the San Andreas fault—Continued											
891025	0027:32.88	37°09.09′	122°03.70′	12.78	- -	28	106	3	0.07	0.43	0.84
891025	1300:41.85	36°53.86′	121°38.07′	5.54	3.8	19	143	4	.09	.56	.69
891025	2201:49.37	37°00.07′	121°48.77′	15.86	3.9	31	90	2	.14	.53	.90
891026	0901:29.03	37°03.84′	121°52.68′	10.95	3.8	34	49	4	.17	.37	.90
891028	1116:04.10	37°03.60′	121°49.26′	4.94	- -	15	90	1	.04	.39	.48
891028	1120:27.75	37°09.23′	122°03.39′	11.28	- -	39	72	3	.10	.35	.64
891028	2127:48.81	36°53.40′	121°37.32′	12.23	3.4	21	186	3	.15	1.14	2.01
891029	1310:57.32	37°04.21′	121°54.70′	14.06	3.2	32	70	6	.13	.42	.87
891030	1541:54.12	37°03.68′	121°54.03′	1.65	- -	34	50	4	.23	.37	.62
891031	0834:51.18	37°03.68′	121°48.99′	8.38	3.6	35	105	6	.25	.52	1.64
891104	0716:04.18	37°49.03′	122°08.61′	7.88	3.6	35	295	44	.14	3.52	1.21
901105	0130:42.05	37°04.77′	121°54.80′	11.77	4.1	43	63	3	.16	.32	.65
891105	1337:33.88	37°03.98′	121°53.52′	13.49	4.2	37	82	4	.04	.32	.57
Earthquakes east of the San Andreas fault											
880627	1843:22.41	37°07.88′	121°53.83′	12.14	5.3	38	61	5	0.08	0.35	0.77
890808	0813:27.45	37°09.03′	121°55.65′	13.36	5.3	37	51	2	.07	.39	.76
890808	0844:09.77	37°08.82′	121°55.55′	12.38	4.5	38	51	3	.07	.36	.75
890808	1553:28.16	37°09.63′	121°57.04′	14.35	4.7	35	69	2	.08	.41	.84
891018	0009:55.83	37°00.35′	121°43.82′	14.98	3.9	5	266	31	.03	4.37	10.70
891018	0103:59.09	37°06.80′	121°51.07′	3.27	3.8	24	71	5	.18	.35	.91
891018	0131:51.45	37°12.79′	122°02.17′	13.22	3.2	5	280	5	.07	4.10	5.28
891018	0321:47.72	37°06.47′	121°50.87′	4.52	3.9	29	59	1	.13	.42	.57
891018	0335:45.45	37°07.36′	121°52.18′	8.24	3.9	- -	- -	- -	- -	- -	- -
891021	1254:39.23	37°09.43′	121°56.13′	2.30	3.3	- -	- -	- -	- -	- -	- -
891023	2127:40.64	37°08.31′	121°55.15′	8.10	3.1	- -	- -	- -	- -	- -	- -
891025	0127:26.24	37°05.15′	121°49.69′	8.74	4.6	46	37	3	.16	.29	.69
891030	1117:13.45	37°04.41′	121°48.69′	8.85	3.9	38	39	3	.07	.28	.51
891101	0803:17.25	37°06.26′	121°50.45′	4.25	3.7	38	35	1	.11	.25	.45
891102	0550:10.64	37°04.14′	121°48.43′	9.53	4.6	44	41	2	.22	.40	1.02
891107	2342:37.39	37°13.86′	122°01.64′	8.77	4.2	29	78	5	.09	.35	.52
Earthquakes west of the San Andreas fault											
891018	0004:47.17	37°06.31′	122°01.84′	9.97	4.7	63	13	8	0.08	1.68	1.65
891018	0005:01.11	37°07.49′	122°00.61′	2.35	4.0	61	65	5	.11	8.67	7.17
891018	0005:34.39	37°10.66′	122°04.52′	4.27	4.1	82	80	6	.10	2.68	2.80
891018	0011:49.40	37°08.85′	122°06.07′	13.66	3.9	52	77	9	.09	8.30	6.91
891019	0845:49.67	36°58.44′	121°50.54′	9.14	4.0	311	49	1	.13	.59	.81
891019	1014:34.90	36°57.93′	121°50.38′	8.90	4.6	271	54	1	.12	.56	.56
891019	1059:57.73	36°57.44′	121°49.68′	8.92	3.6	271	55	2	.14	.60	.71
891019	1115:22.60	36°57.42′	121°49.61′	8.58	3.6	211	55	2	.14	.64	.89
891023	1402:20.10	37°07.39′	122°03.00′	6.09	- -	40	88	5	.18	.37	.58
891025	0027:02.15	36°55.40′	121°50.23′	3.84	- -	82	25	6	.12	2.26	2.80

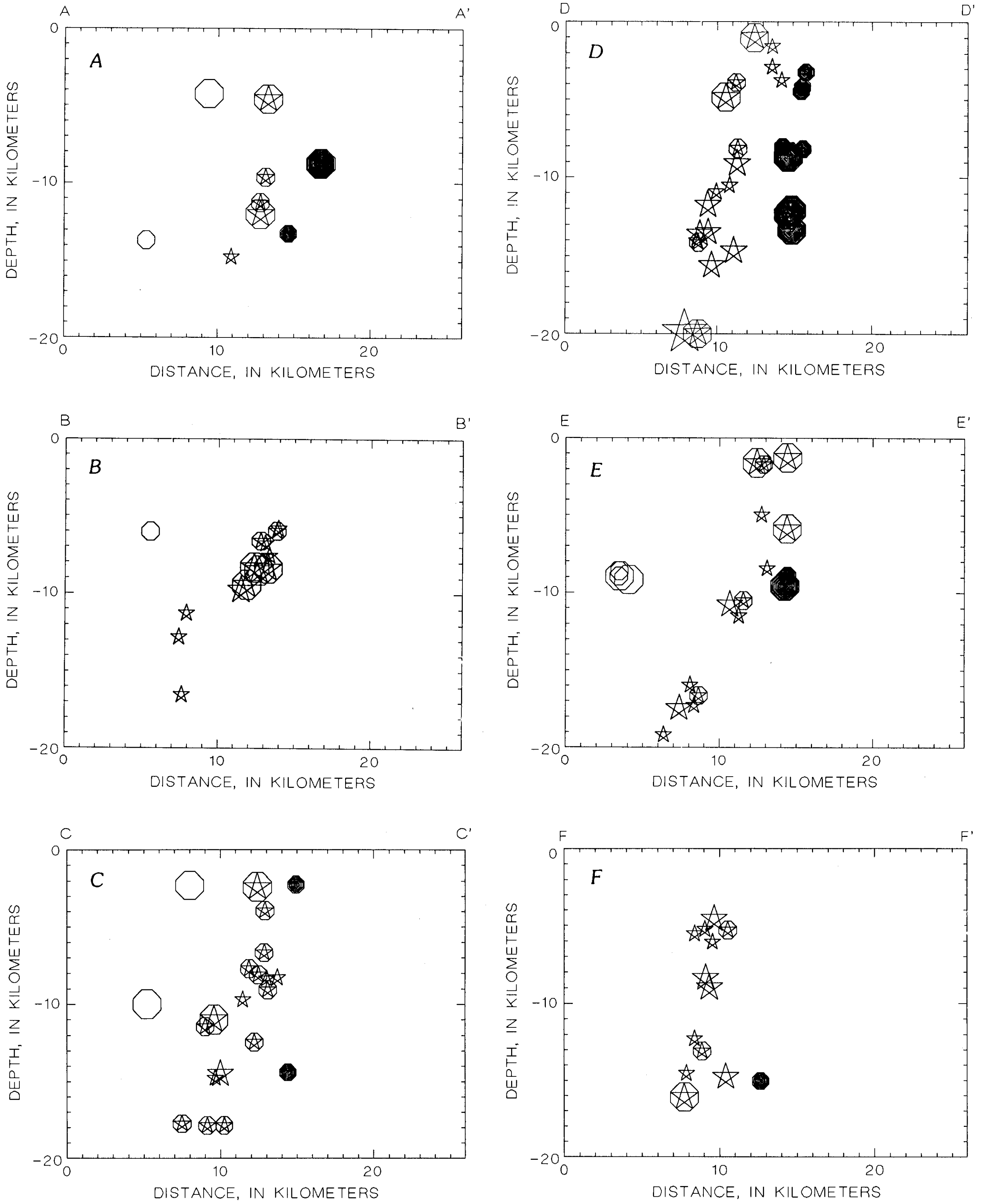

Figure 7.—Seismicity in the Loma Prieta rupture zone (see fig. 1) along orthogonal cross sections *A–A′* (*A*), *B–B′* (*B*), *C–C′* (*C*), *D–D′* (*D*), *E–E′* (*E*), and *F–F′* (*F*). Same symbols as in figure 1. See tables 2 and 4 for details on events. Note that all relocated events of all magnitudes are shown in these cross sections.

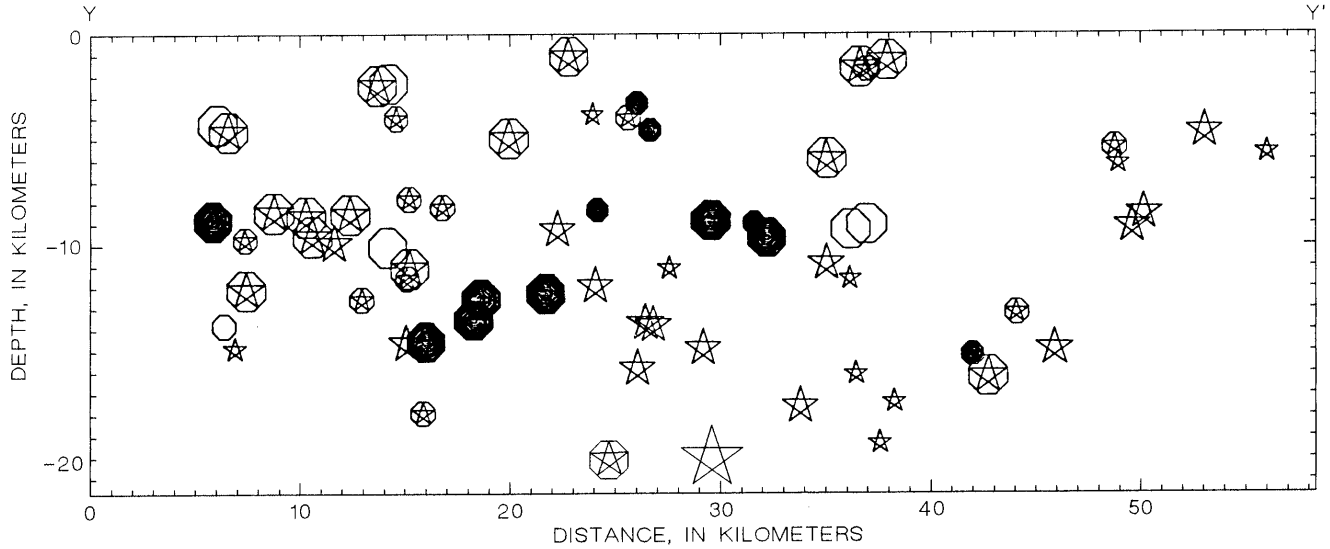

Figure 8.—Seismicity (M_L≥3.8) in the Loma Prieta rupture zone (see fig. 1) along longitudinal cross section *Y–Y'*. Same symbols as in figure 1. Note that main part of aftershock zone is devoid of events until 3 hours and 19 minutes after main shock.

THE LOMA PRIETA, CALIFORNIA, EARTHQUAKE OF OCTOBER 17, 1989:
EARTHQUAKE OCCURRENCE

MAIN-SHOCK CHARACTERISTICS

DOWNDIP GEOMETRY OF THE LOMA PRIETA RUPTURE FROM TELESEISMIC WAVEFORM INVERSION

By John L. Nábělek,
Oregon State University

CONTENTS

ABSTRACT

The 1989 Loma Prieta earthquake was well recorded by global digital seismic networks. The azimuthal coverage provided by stations is excellent, and the recorded body waves can be deconvolved to yield broadband displacements, with excellent consistency of waveform and amplitude among stations. I use broadband teleseismic *P* and *SH* waves from 27 stations to investigate the rupture process of the earthquake. An inversion using a point-source model gives the following estimates of the average (centroidal) parameters: strike, 127°±2°; dip, 63°±1°; rake, 129°±2°; depth, 10.5±1 km; and seismic moment, $2.9 \pm 0.1 \times 10^{19}$ N-m (M_w=6.9). The estimated source-time function indicates that the source duration was about 15 s and that about 85 percent of the moment was released during the first 10 s. Very little azimuthal variation in pulse duration is observed, indicating a bilateral rupture. Setting up a line grid along the indicated dip, I investigate the seismic-moment release and the evolution of the rupture as a function of depth. I find that the Loma Prieta rupture extended updip from a nucleation depth of about 17.5 km, that 70 percent of the moment was released within the depth range 8–13 km, and that no significant moment was released at depths above 5 km. Inversions indicate that in the lower two-thirds of the fault surface, the slip had, on average, a larger strike-slip component than in the upper third. Two-dimensional source parametrizations produce unstable results, and so lateral variations in the moment release cannot be determined from this data set.

INTRODUCTION

In this paper, I present the results of an analysis of teleseismic body waves to examine the rupture process of the 1989 Loma Prieta earthquake. The goal of this study was, first, to derive basic centroidal source parameters and, second, to focus on the downdip geometry of the fault surface, to determine the seismic-moment release as a function of depth, and to investigate whether any downdip variation in fault orientation and slip direction is discernible. I first present the results of my analysis and then discuss how they compare with those of other body-wave studies using related data sets.

DATA SET

In this investigation, I used *P* waves in the epicentral-distance range 30°–95° and *SH* waves in the epicentral-distance range 30°–75° recorded by stations in the Incorporated Research Institutions for Seismology/Global Seismic Network (IRIS/GSN), GEOSCOPE (Institut National des Sciences de l'Univers, France), and the Global Digital Seismograph Network (GDSN), and by one unaffiliated station in Japan; altogether, 41 waveforms were utilized. In general, the data quality is very high, with good coherency both in amplitude and wave shape between stations along similar wave paths. Only a few waveforms were rejected because of anomalous behavior due either to instrument malfunction or to unusual propagation paths; the rejected waveforms are of *P* waves from stations HON and KIP in Hawaii and of *SH* waves from station COL in Alaska.

Table 1.—*Crustal model and attenuation parameters used in this study*

[t^*=1 s for *P* waves; t^*=4 s for *SH* waves]

Layer	Thickness (km)	v_p (km/s)	v_s (km/s)	Density (g/cm^3)
		Source		
1	0.5	3.38	1.95	1.97
2	.5	4.29	2.48	2.22
3	2.0	4.80	2.77	2.36
4	2.0	5.37	3.10	2.52
5	2.0	5.74	3.32	2.63
6	2.0	6.15	3.55	2.74
7	4.0	6.25	3.61	2.77
8	5.0	6.27	3.62	2.78
9	7.0	6.67	3.86	2.89
Half-space	--	8.00	4.62	3.26
		Receiver		
Half-space		6.00	3.47	2.70

I used very broad band data streams for stations with broadband sensors (which are proportional to ground velocity), intermediate-band streams for digital World Wide Seismic Station Network (WWSSN) stations, and a combination of short- and long-period streams for Seismic Research Observatory/Automatic Seismic Research Observatory (SRO/ASRO) stations; I used long-period streams (1 sample per second) for a few stations where higher resolution streams were unavailable. All the raw seismograms were converted to broadband ground displacement by removing the instrument response. The resulting data were resampled at a rate of 5 samples per second and high-pass filtered with a cutoff frequency of 0.01 Hz to remove long-period instabilities.

The modeling and inversion techniques applied to the data are simple extensions of those described earlier (Nábělek, 1984, 1985). Teleseismic body waves in the above-mentioned distance ranges avoid the complexities due to upper-mantle triplications and core interactions. The waveforms contain direct phases, reflections from the free surface, as well as converted phases due the crustal structure, that are accounted for in the modeling procedure. The observed seismograms were simultaneously inverted for the desired source parameters by minimizing the L_2 norm. The waveform-inversion window always included the first 40 s after the onset of the direct *P*- or *S*-wave phase, as applicable. The assumed source crustal structure (table 1) used to locate aftershocks is based on that of Dietz and Ellsworth (1990), thus allowing a direct comparison between my results and theirs. Most other investigators have used similar structural parameters.

POINT-SOURCE MODEL

The simplest parametric source model used here is a point source. Inversion using this model gives centroidal averages of the source parameters: The source mechanism (strike, dip, rake), depth, seismic moment, and source-time function. The estimated parameters for this inversion are listed in table 2, the derived source-time function is plotted in figure 1, and the match between the observed and synthetic seismograms is shown in figure 2. This simple model fits the general features of the observed seismograms remarkably well, although some consistent discrepancies immediately after the onset of *P* waveforms (during the first quarter-cycle of waveforms from stations to the east—for example, CAY—the amplitudes are slightly underestimated, whereas for the northwestern stations—for example, MDJ—they are slightly overestimated) indicating that the source mechanism may have had a larger-than-average strike-slip component during the early stages of the rupture process. Later parts of the *P*-wave seismograms from western stations also show a consistent phase mismatch that may indicate a change in source mechanism toward the end of the rupture process (fig. 2*A*). The source-time function (fig. 1) is rather simple: After an initial slow rise lasting about 4 s, 70 percent of the moment is released in a simple 5-s-long pulse, followed by some additional moment release over the next 6 s. The total rupture time of the earthquake is 15 s. No consistent significant misfits in pulse widths occur between the model waveforms and those from stations on azimuths along the fault strike, indicating a bilateral rupture. The derived source orientation is similar to that found in many other studies. The estimate of the source mechanism is highly stable and does not depend strongly on the assumed crustal structure or other model parameters. The strongest tradeoff occurs between the estimated source depth and the seismic moment. To show this interplay, the seismic-moment estimate as a function of depth is plotted in figure 3, where the estimated moment decreases from about 3.5×10^{19} N-m at 7-km depth to about 2.5×10^{19} N-m at 15-km depth. The variance of the misfit plotted in figure 3 shows a well-defined minimum at about 10-km depth, with an uncertainty of about ±1 km. Within this range, the seismic moment ranges from 2.8×10^{19} to 3.0×10^{19} N-m.

The centroidal parameters for the Loma Prieta rupture obtained here generally agree with many other estimates from various studies, as discussed below. Here, I comment on some significant discrepancies in the seismic-moment estimates between some body-wave investigations. The moment of 2.9×10^{19} N-m obtained here is at the higher end of the estimated values, some of which are as low as 1.9×10^{19} N-m. This discrepancy cannot be accounted for simply by variations in the data; figure 2 shows that the data are fitted in amplitude quite well. In my opinion, most of the lower estimates are due to a combination of the following factors: (1) deeper source depth for which the seismic moment was estimated; (2) use of a shorter

Table 2.—*Point-source parameters of the earthquake as determined in this study*

Strike	Dip	Rake	M_0 (N-m)	M_w
127°±2°	63°±1°	129°±2°	$2.9 \pm 0.1 \times 10^{19}$	6.9

source-time function, that is, assuming that the contributions after the first 10 s are insignificant; and (3) use of ground-velocity seismograms, which are poorer in low-frequency components than the ground-displacement seismograms used here.

I believe that the seismic moment estimated here is appropriate for the following reasons. (1) It agrees with estimates in several other body-wave studies that also found a similar source depth (for example, Hartzell and others, 1991; Wald and others, 1991). (2) It agrees with estimates based on geodetic observations, as well as those based on surface waves (although for such estimates the depth remains problematic). (3) In inversions using only subsets of stations over narrow ranges of distances and azimuths to investigate whether the moment release indicated by the last 6 s of the source-time function depends somewhat on a particular set of stations or waveforms, I have found that this later moment release is a consistent feature required by both *P* and *SH* waves. (4) Because the moment determination from broadband-displacement body-wave pulses depends on accurate integration of the estimated moment-rate-time function (source-time function), which may be difficult if the waveforms are rich in high frequencies, I have also inverted waveforms that were low-pass filtered with a cutoff frequency at 0.03 Hz. The amplitudes of low-frequency waves are directly proportional to the seismic moment, and so this procedure provides a more direct estimate; the resulting seismic moment remained the same as in the broadband inversion.

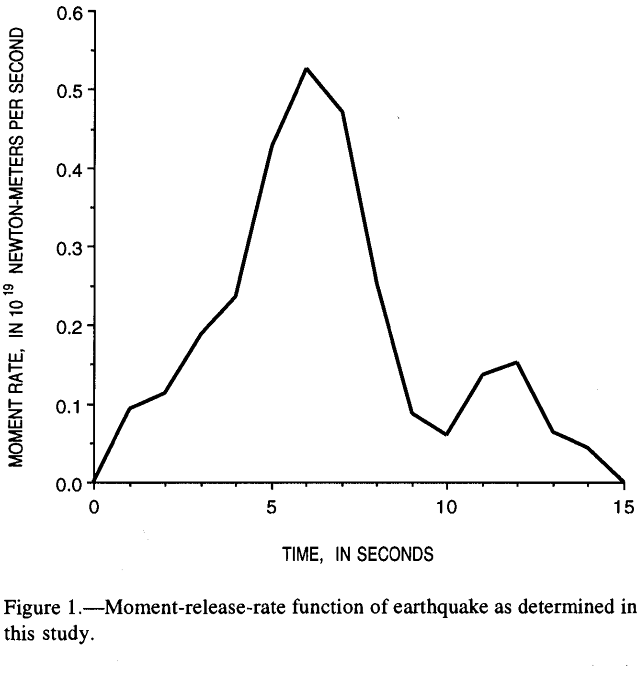

Figure 1.—Moment-release-rate function of earthquake as determined in this study.

FINITE ONE-DIMENSIONAL MODEL

We now attempt to determine how the moment release was distributed along the fault width (along-dip direction), considering that the rupture did not reach the surface, and so it is of interest to determine at what depth it stopped. Also, it has been suggested (Wallace and others, 1991) on the basis of surface-wave observations, which give a substantially deeper seismic-moment centroid (~20 km; Romanowicz and Lyon-Caen, 1990; Zhang and Lay, 1990; Wallace and others, 1991) than body waves, that some significant moment release occurred below the nucleation point of the rupture, which, according to U.S. Geological Survey (USGS) estimates, was situated at about 17-km depth.

For this analysis, the model is parametrized as follows (fig. 4). Using the same source orientation as that determined in the point-source inversion, we assume that it remains unchanged for the whole duration of the rupture. We distribute nine point sources along the width at 2.8-km grid spacing (2.5-km depth interval): One source is located at the nucleation depth (17.5 km), six are located above it, and two are located below it. We assume a rupture-front-propagation velocity of 3 km/s between the gridpoints and the nucleation point. The only parameters that we invert for are the moment-rate functions at each gridpoint. The assumed rupture-front-propagation velocity is not a rupture velocity in the true sense because it defines only a time after which the gridpoint is allowed to be active. Setting the rupture velocity precisely is not critical as long as it is not too low, because once a gridpoint becomes active, it is allowed to be active for the entire source-process time. This detail distinguishes the rupture parametrization used here from that adopted in other studies. If the data demand that the rupture velocity be lower than that assumed, the moment-rate function will remain zero for some time after the source is allowed to turn on. We assign a rupture velocity to minimize the effect of inversion instabilities, which could result in noncausal moment release. To further stabilize the inversion, the moment-rate functions are discretized at a relatively low rate of 0.5 sample per second and are required to be non-negative at all times.

The reason why a complete two-dimensional fault model is not introduced at this stage is that teleseismic body waves, owing to their steep takeoff angles and the presence of strongly reflected phases from the free surface, are primarily sensitive to depth-dependent source

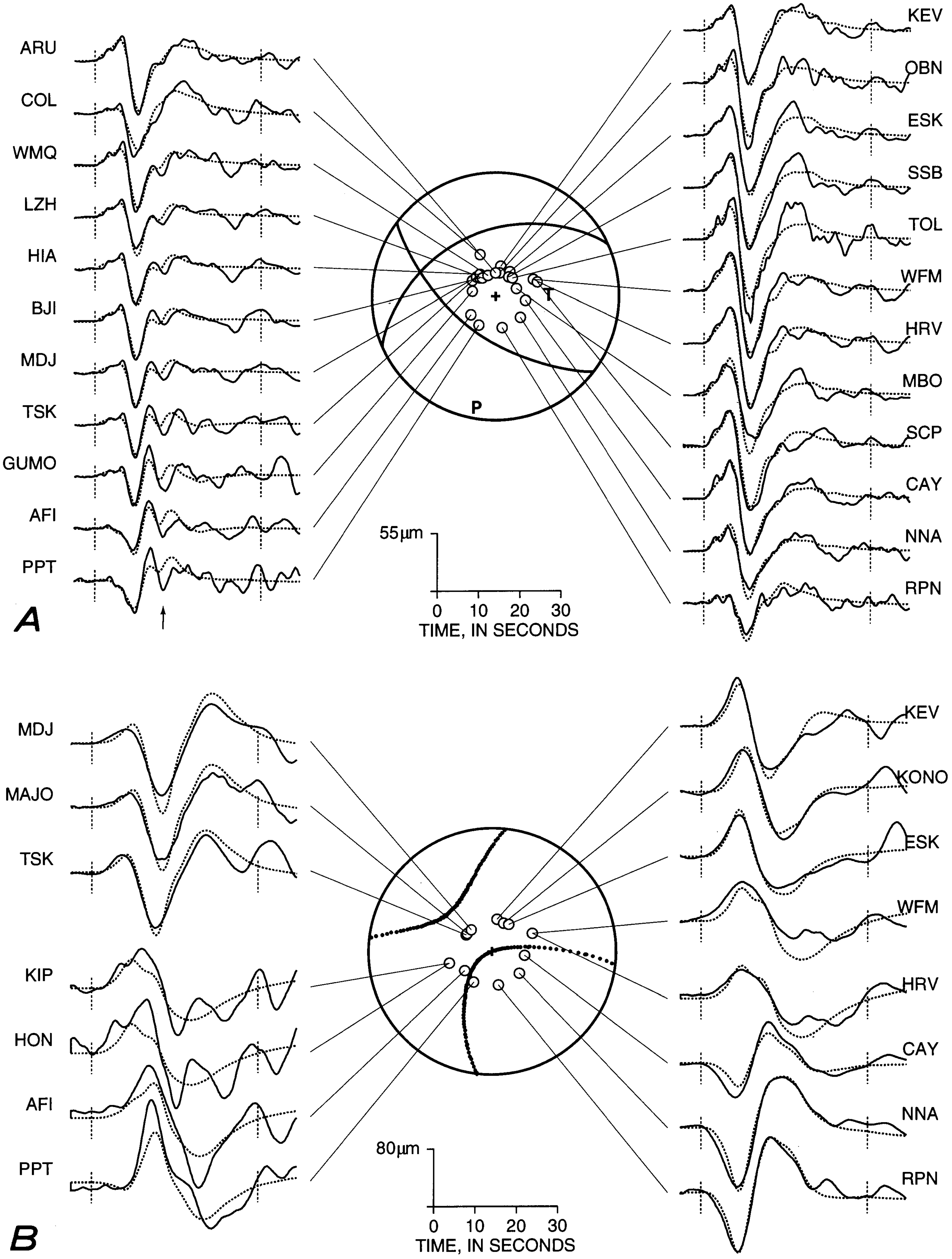
ARU
COL
WMQ
LZH
HIA
BJI
MDJ
TSK
GUMO
AFI
PPT
A
KEV
OBN
ESK
SSB
TOL
WFM
HRV
MBO
SCP
CAY
NNA
RPN
T
P
55µm
0 10 20 30
TIME, IN SECONDS
MDJ
MAJO
TSK
KIP
HON
AFI
PPT
B
KEV
KONO
ESK
WFM
HRV
CAY
NNA
RPN
80µm
0 10 20 30
TIME, IN SECONDS

variations; any effects related to the finite lateral extent of the source affect the waveforms much less and are much harder to resolve.

The results of this inversion are shown in figures 5 and 6. The moment-rate functions for each gridpoint are shown in figure 5. Note that the rupture, after starting at 17.5-km depth, propagates essentially updip. The moment release is rather slow at the deepest sections of the fault but intensifies at about 12.5-km depth. At 7.5-km depth, the rupture is arrested for a moment and then restarts again, releasing some additional moment. Note that this model integrates the lateral rupture propagation at a given depth to the moment-release rate at the corresponding gridpoint; however, because the moment-release-rate functions at each depth are relatively short, the lateral extent of the rupture cannot be large.

The corresponding depth distribution of the seismic moment is plotted in figure 6. Note that at the bottom of the fault plane, around the nucleation depth, only a small amount of moment is released, and no significant release occurs below 20-km depth. The moment release and, thus, the slip are concentrated between 12.5- and 7.5-km depth. Again, no significant moment release occurs above 5 km. The total seismic moment for this model is 2.95×10^{19} N-m. Note that at 5- to 7.5-km depth, where the rupture appears to have been interrupted, the San Andreas fault apparently intersects the fault on which the earthquake occurred. This fault interaction appears to have affected the rupture, first stopping it and then allowing only a small additional slip in the vicinity of the intersection (fig. 5).

The finite-width model generally improves the fit to the data over the point-source model. The improvement is particularly noticeable for *P* waves from the western stations (fig. 7), where the fit of the phase between the later parts of the observed and synthetic waveforms is considerably better.

VARIABLE-MECHANISM MODEL

In the above models, we assumed that the source orientation is constant over time. The data misfits with respect to the centroidal model indicate that slip in the rupture-nucleation area might have had a larger-than-average strike-slip component and that, although the finite one-dimensional model decreases the misfit in the later parts of the waveforms, some consistent discrepancies still remain. In the next model, we investigate whether the remaining significant inconsistencies can be removed by allowing the source orientation to change with depth. In this set of inversions, the model consists of three point sources distributed updip from the nucleation point (the previous models indicate no significant moment release below the nucleation depth). As before, we assume a rupture-front-propagation velocity of 3 km/s and fix the strike to that found earlier. We invert for the dip, rake, and moment-release rate of each point source. The results, as shown in figures 8 and 9, indicate a steeper dip and a larger strike-slip component in the lower part of the fault surface, in agreement with the source mechanism derived from regional first-motion polarities. In its lower two-thirds, the fault surface is remarkably planar, and the mechanism remains constant. In the uppermost part, however, the slip appears to have a large thrust component. To investigate the stability of these results, I used many different starting models, including those with fault strike as one of the free parameters, but obtained essentially the same results.

◄ Figure 2.—Match between observed (solid curve) and synthetic (dotted curve) seismograms for *P* (*A*) and *SH* (*B*) waves in point-source inversion. Amplitudes are normalized to 40° epicentral distance. Vertical dotted lines delimit inversion window. Circles in focal-mechanism solution indicate nodal planes and takeoff directions of direct waves. P and T, inferred axes of maximum and minimum compressional stress (pressure and tension axes), respectively. Arrow in figure 2*A* denotes part of waveforms where consistent phase mismatch occurs.

ATTEMPTS AT MORE DETAILED SOURCE MODELS

The quality of the data is high, especially for *P* waves, for which the waveforms vary coherently from station to

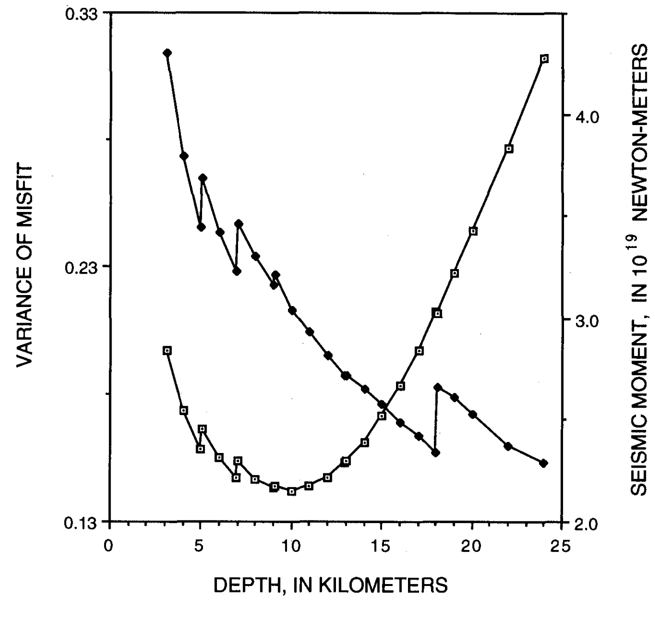

Figure 3.—Estimated seismic moment (M_0) (dots) and variance of misfit (squares) as functions of assumed point-source depth. Discontinuities in curves are artifacts of layer boundaries in crustal model.

station. It is therefore tempting to see whether the fit can be improved further by introducing more sophisticated source models. The obvious next step is to introduce two-dimensionality into the fault surface. Two-dimensional rupture models were, in fact, derived by several investigators, using teleseismic and strong-motion data, but they disagree in some important details. Although Beroza (1991), Hartzell and others (1991), Steidl and others (1991), and Wald and others (1991) broadly agreed that there were two primary loci of moment release, both at about 10- to 15-km depth and separated laterally by about 10 km, they disagreed on the sense of slip in those regions. The models of Beroza (1991) and Steidl and others (1991) suggest that slip to the southeast of the hypocenter was essentially strike slip, whereas slip to the northwest of the hypocenter was almost pure dip slip; the models of Hartzell and others (1991) and Wald and others (1991) exhibit no such large lateral change in slip direction, although various scattered regions of the fault plane show some significant thrust components. My motivation in testing two-dimensional fault models was to see whether I could resolve these outstanding questions concerning partitioning of the strike-slip and dip-slip motion.

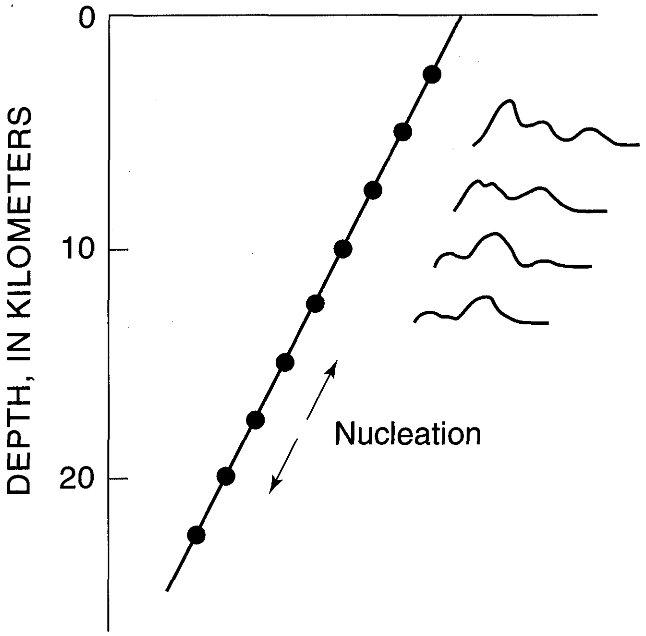

Figure 4.—Parametrization of one-dimensional finite-source model. At each gridpoint, only moment-release-rate function (irregular curves) was determined, assuming that rupture nucleated at 17.5-km depth and rupture front propagated at a velocity of 3 km/s. After passage of rupture front, elements of moment-release-rate function were allowed to assume arbitrary nonnegative values.

The models that I considered were direct two-dimensional extensions of the one-dimensional models discussed in the preceding sections. They differed from those used in previous studies in having fewer restrictions on the time function at each gridpoint. Previous investigators assumed a uniform rupture velocity and fixed source-time function (rise time) at each gridpoint. Thus, each gridpoint was prescribed to slip at a particular time and only for a fixed duration; optimum rupture velocity and rise time were found by trial and error. In the models considered here, the gridpoints were not constrained to act only in a restricted time frame but were allowed to slip arbitrarily once the rupture front has passed, and the slip direction

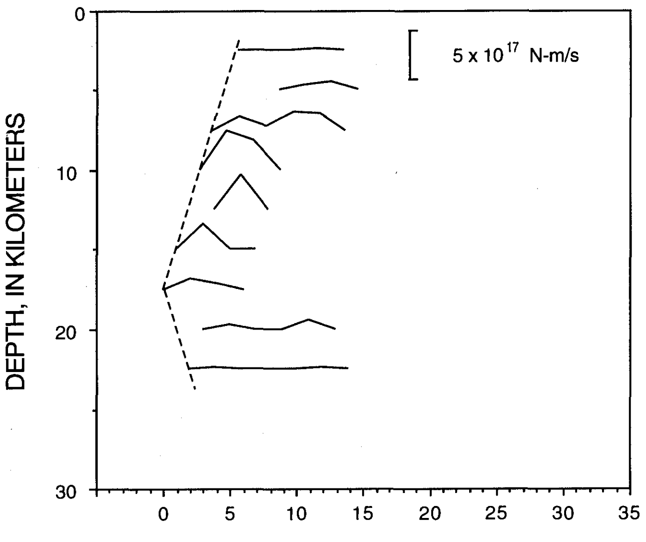

Figure 5.—Moment-release-rate function at various depths, determined by using model shown in figure 4. Only nonzero elements are plotted. Dashed line, 3-km/s isochron.

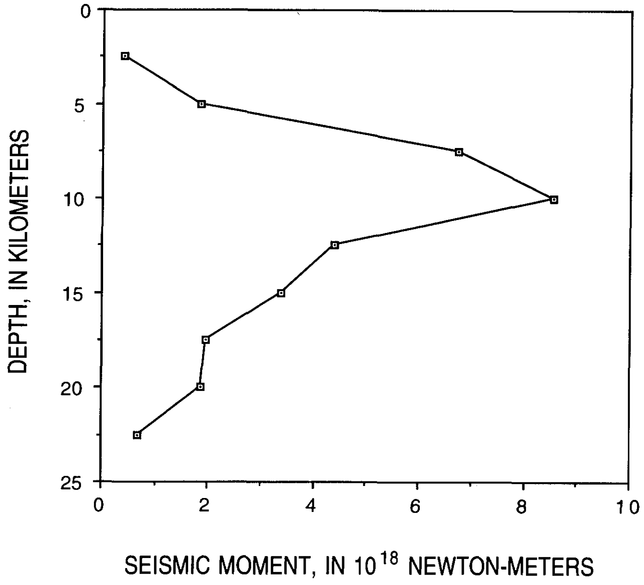

Figure 6.—Distribution of seismic-moment (M_0) release as a function of depth for earthquake, determined by using model shown in figure 4.

was allowed to vary. Even simple two-dimensional models (grids of 7 or 9 points) improved the fit to the data considerably; however, the addition of new degrees of freedom to the model introduced tremendous instability and a tradeoff between the grid parameters, and no conclusive answers were obtainable. In comparison with other studies (Hartzell and others, 1991; Wald and others, 1991), relaxing the restrictions on the grid time functions appears to make the inversion unstable. The reason for this instability is the difficulty in resolving lateral source dimensions: If the rupture is tightly constrained from the start, seemingly stable results are obtainable; but if the constraint is removed, the stability disappears. The results, therefore, depend strongly on the appropriateness of the constraint. For the 1989 Loma Prieta earthquake, the resolution of lateral source dimensions is made difficult by the emergent features of the body waveforms, in turn making it difficult to pinpoint the arrivals from the nucleation point that provide the reference from which the rupture's lateral extent is measurable.

One way in which the resolution of the areas of accelerated moment release could be improved is by emphasizing higher frequencies in the data. This improvement would be possible, however, only at the expense of decreased resolution of the smaller component of moment release and the average parameters. One straightforward way is to use ground-velocity waveforms instead of the ground-displacement waveforms used here. Wald and others (1991) used ground-velocity records, and Hartzell and others (1991) used a combination of ground-displacement and ground-velocity records, as data for their inversions; their lateral resolution of the areas of accelerated moment release should therefore in principle be better. Hartzell and others showed, however, that also for their data set the lateral distribution of moment release is quite unstable. Nevertheless, neither the teleseismic models of Wald and others (1991) and Hartzell and others (1991) nor the two-dimensional models examined here indicate large lateral variations in slip direction.

EFFECTS OF ASSUMED CRUSTAL STRUCTURE

One additional question is whether our results could be significantly biased by the assumed crustal structure for the source region. I tested a range of structures within the realm of possibility, from simple half-space models to layered models of various complexity, and found that the centroidal source mechanism is highly stable with respect

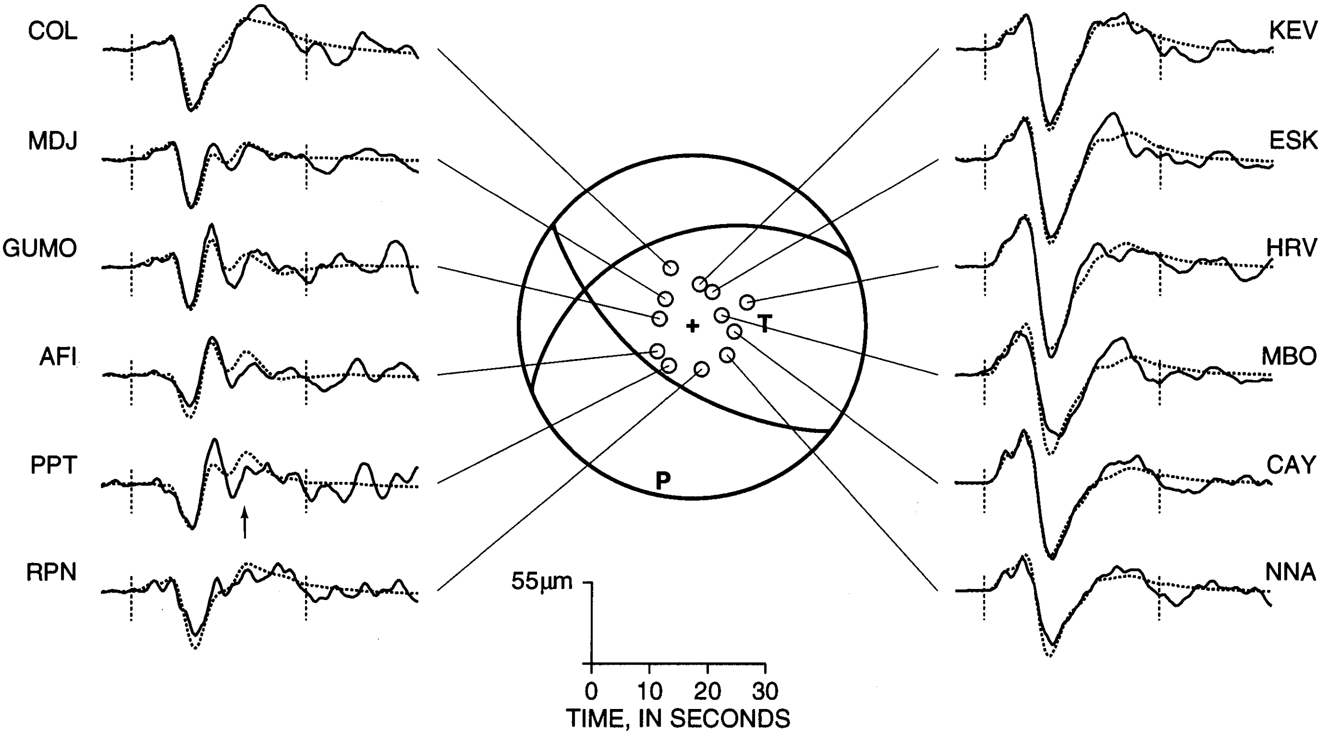

Figure 7.—Match between observed (solid curve) and synthetic (dotted curve) *P*-wave seismograms at representative stations in one-dimensional model. Amplitudes are normalized to 40° epicentral distance. Vertical dotted lines delimit inversion window. Circles in focal-mechanism solution indicate nodal planes and takeoff directions of direct waves. P and T, inferred axes of maximum and minimum compressional stress (pressure and tension axes), respectively. Phase mismatch in part of waveforms denoted by arrow is improved in comparison with point-source model (fig. 2*A*). Match for *SH* waves is qualitatively similar to that shown in figure 2*B*.

to all structures. The seismic moment and centroidal depth behave predictably: As the average velocity of the medium increases, the estimated values of both the centroidal depth and seismic moment increase slightly. Most types of crustal layering do not significantly affect the results presented here. All estimated parameters were found to be stable for purely homogeneous crustal models (half-space) and for those involving a steady increase in the medium velocity with depth; in particular, the assigned Moho depth does not play an important role. One class of structures, however, that could potentially influence the inference about the later parts of the rupture process involves a low-velocity zone in the lower crust. Such structures, which have been suggested for several areas around the San Andreas fault zone (Blümling and Prodehl, 1983; Blümling and others, 1985), produce strong late-arriving reflections similar to the late-arriving energy observed in *P* waves in the west half of the focal sphere.

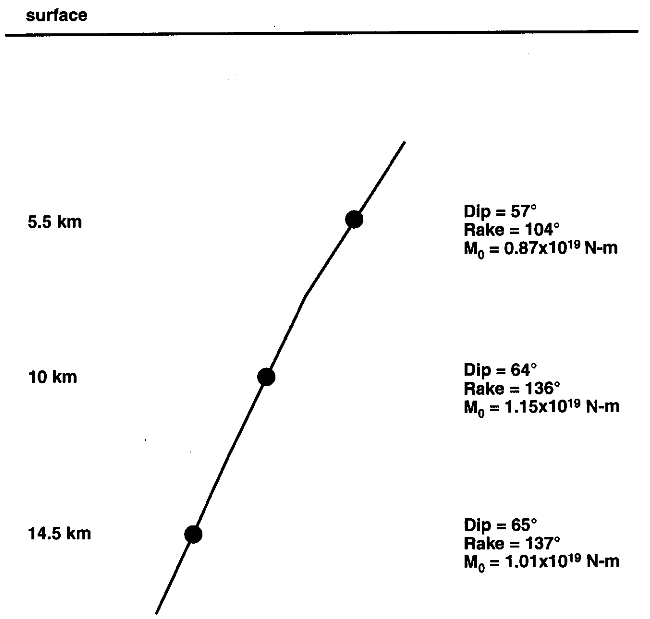

Figure 8.—Results of inversion using a variable-mechanism model parametrization.

P-wave synthetic seismograms for the model listed in table 1 are shown in figure 10*A*. To emphasize the effect of crustal reflections, only the first 10 s of the source-time function (fig. 1) was used. A large mismatch is evident in the later parts of the waveforms, indicating the need for additional moment release. The seismograms in figure 10*B*, which were calculated for a crustal model with a low-velocity layer at a depth of 20 km, show large reflections similar to the later phases from the western stations. When inverting the whole data set, however, this model consistently produced a poorer fit to the data than

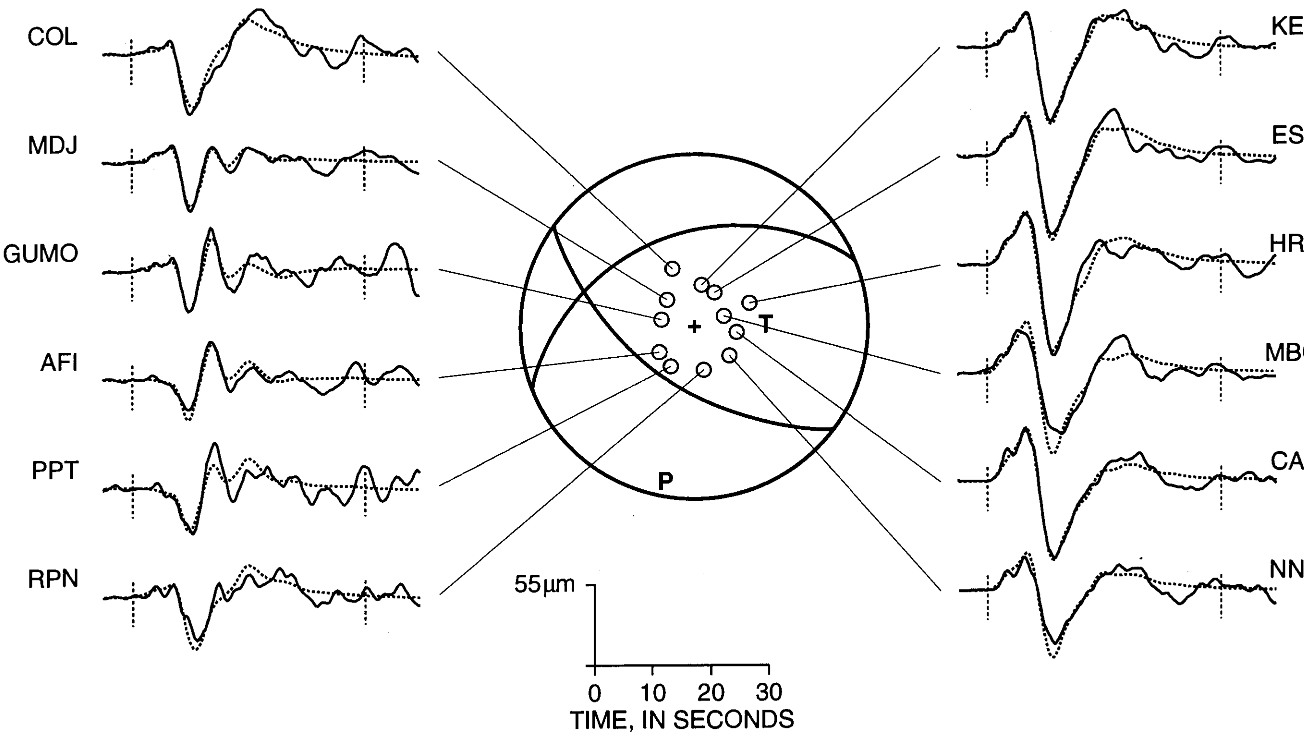

Figure 9.—Match between the observed (solid curve) and synthetic (dotted curve) *P*-wave seismograms at representative stations in variable-mechanism model. Amplitudes are normalized to 40° epicentral distance. Vertical dotted lines delimit inversion window. Circles in focal-mechanism solution indicate nodal planes and takeoff directions of direct waves. P and T, inferred axes of maximum and minimum compressional stress (pressure and tension axes), respectively. Match for *SH* waves is qualitatively similar to that shown in figure 2*B*.

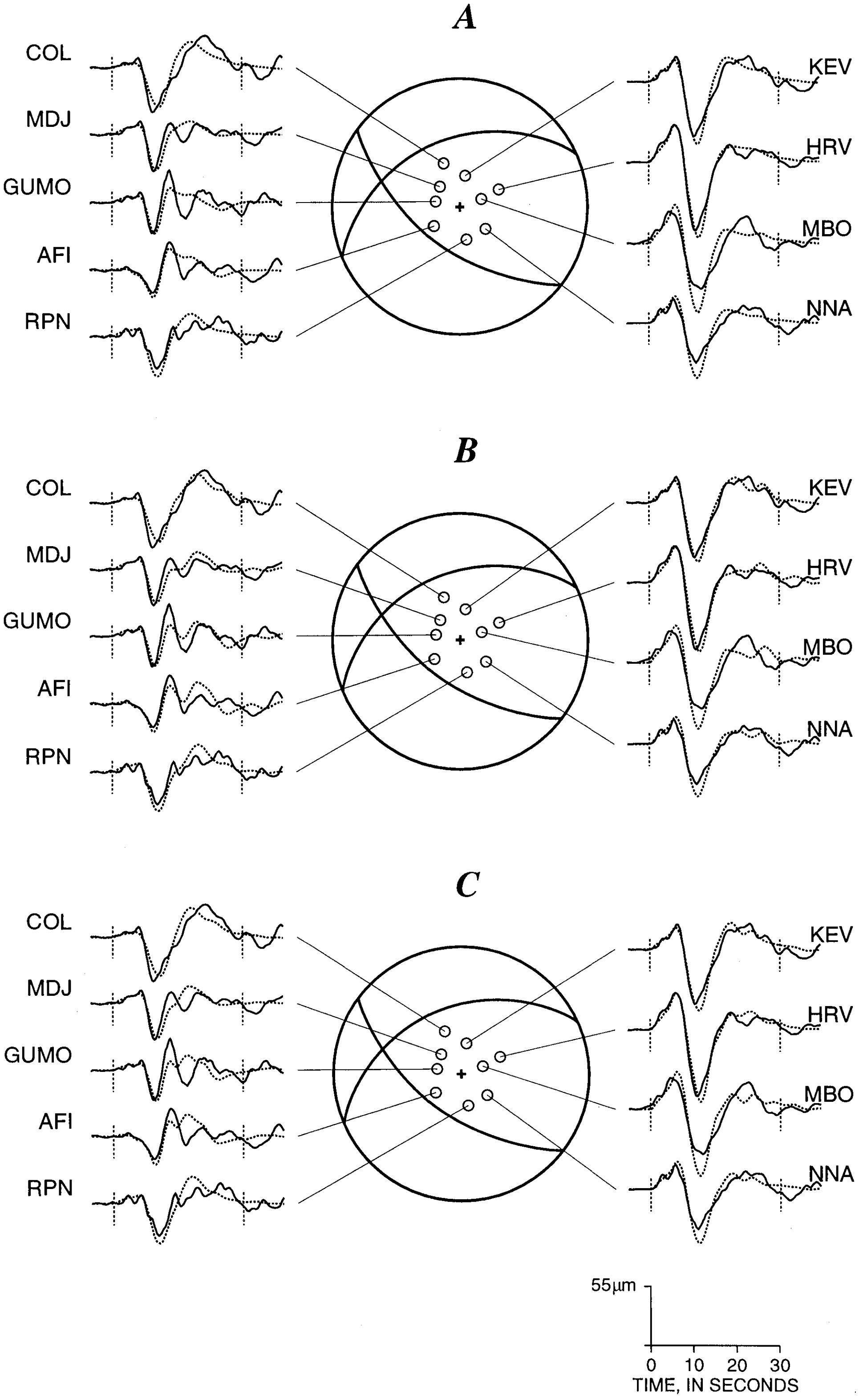

Figure 10.—Effect of various crustal models on *P* waveforms. *A*, Model listed in table 1, used in all inversions. *B*, Same model as in figure 10*A* but with a 5-km-thick low-velocity layer (v_p=5.37 km/s) at 20-km depth. *C*, Same model as in figure 10*A* but with a low-velocity layer at 15-km depth. Synthetic seismograms were computed for centroidal source parameters listed in table 2. Circles in focal-mechanism solution indicate nodal planes and takeoff directions of direct waves. To emphasize effect of crustal reflections, only first 10 s of moment-release-rate function shown in figure 1 was used.

the model listed in table 1. The same result was obtained for all crustal models with low-velocity, deep crustal layers. Structures with low-velocity zones could be admissible if the structure varied across the strike of the fault plane. Apparently, if low-velocity layers exist in the lower crust, they must be relatively deep to the west of the fault plane and relatively shallow or nonexistent to the east.

DISCUSSION

Our model results are summarized in table 2. Of these results, the most stable are those derived for the simplest source-model parametrizations. The average parameters represented by the point-source model agree closely with those derived from geodetic observations (Lisowski and others, 1990; Marshall and others, 1991; Snay and others, 1991), surface waves (Zhang and Lay, 1990; Romanowicz and Lyon-Caen, 1990; Wallace and others, 1991; see Velasco and others, this chapter), and aftershock distributions (Dietz and Ellsworth, 1990; Schwartz and Nelson, 1991), as well as with several other body-wave studies (for example, Hartzell and others, 1991; Wald and others, 1991). Extensive summaries of the estimates of centroidal parameters from various observations are given, for example, by Marshall and others (1991), Wald and others (1991), and Wallace and others (1991). Other studies dealing with the source parameters of the main shock include those by Barker and Salzberg, (1990), Choy and Boatwright (1990), Kanamori and Satake (1990), Langston and others (1990), and Ruff and Tichelaar (1990). The seismic-moment estimate presented here is slightly lower than that obtained by Nábělek (1990), owing to the inclusion of GEOSCOPE data in this study.

Most observations that bear on the depth extent of faulting appear to agree that essentially all moment release during the earthquake occurred within the depth range 5–8 km, with a large concentration near 10-km depth. A notable exception is the centroidal depth found from surface waves, at least 20 km, but there appear to be uncertainties in the Earth models used, which may be responsible for the bias in the source-depth estimate (see Velasco and others, this chapter). My investigation has shown that no significant moment release occurred below 20-km depth within 40 s after rupture initiation (figs. 5, 6). Because the seismic moment calculated here agrees well with that found from surface waves, it is difficult to appeal to additional slow moment release at depth, which would increase the centroidal depth derived from long-period surface waves. A strong argument against additional moment release on a long time scale comes from geodetic modeling (Lisowski and others, 1990; Marshall and others, 1991; Snay and others, 1991), whose results are consistent with the depth distribution of the moment release found here from body waves.

My results indicate that the rupture propagated bilaterally updip, although I am unable to resolve the details of the lateral propagation. The model parametrization used here puts very little inherent constraint on the behavior of the rupture, and so the characteristics of the vertical distribution of moment release found here do not depend strongly on such details. All lateral variations of the moment release at a given depth, however, are integrated into the characteristics of the corresponding gridpoint. The short duration (approx 4–5 s) of the moment-rate functions at most depths does not allow a large lateral distance for the rupture to propagate. Assuming bilateral spreading and a rupture velocity of 3 km/s, the 5-s duration indicates a fault length (alongstrike dimension) of no more than 30 km. As mentioned above, in our model the rupture appears to stop briefly at 7.5-km depth and then restart for a short time, possibly in response to interaction with the San Andreas fault. Possibly, the rupture did not really stop and restart at this depth, instead, the two pulses in the moment rate may represent two areas of intensified moment release separated by a large lateral distance in which the later pulse represents a more distant locus delayed by the time it took for the rupture front to reach it.

The least certain of the models presented here is the variable-mechanism model. Although this model appears to be well resolved, given the specific source parametrization, it does not have strong supporting evidence from other independent observations. The fault dip indicated by the model agrees well enough with the aftershock distribution (Dietz and Ellsworth, 1990; Schwartz and Nelson, 1991), and the mechanism found for the deep part of the fault where the rupture nucleated agrees with that found from first-motion polarities at regional distances (Oppenheimer, 1990). The model indicates a planar to slightly concave downward geometry. In the uppermost part of the fault, the model indicates a large increase in the thrust component. Kinematically, such a change in mechanism is difficult to understand. If indeed present, it may reflect a decrease in vertical stress at shallow depth. It may also be due to a complex interaction with the San Andreas fault (slip partitioning), whereby over many earthquake cycles, the San Andreas fault takes up most of the strike-slip component of motion at shallow depths, while the Loma Prieta fault takes up the dip-slip component. Oppenheimer reported a predominance of thrust mechanisms for aftershocks at shallow depths, which might be taken as supporting evidence for the variable-mechanism model; however, given the wide variety of mechanisms observed at all depths, this evidence is weak.

In comparison with other teleseismic body-wave studies that have investigated the change in source mechanism during the main-shock rupture, our solution is most similar to that of Hartzell and others (1991). They used a data set nearly identical to ours, except that they used ground-velocity records instead of displacement records for the broadband IRIS stations. Once the differences in the source parametrization are accounted for (they used a two-dimensional fault-surface model), the general features of their solution are remarkably similar to those of mine. They also performed an extensive analysis of the stability of their solutions. All of their models exhibit late-stage thrusting at shallow depths. Although their models show considerable instability in the lateral distribution of moment release, the vertical distribution appears to be stable and similar to that obtained here. In an earlier study, Romanowicz and Lyon-Caen (1990) also argued for the predominance of thrust faulting during the later stages of the rupture process. Although the teleseismic results reported by Wald and others (1991) are mostly consistent with mine, their model shows a remarkable uniformity in slip direction across the entire fault surface. In fact, their strong-motion model is nearly identical to mine in this respect.

Two strong-motion studies (Beroza, 1991; Steidl and others, 1991) reported strong slip partitioning between the northwestern and southeastern segments of the Loma Prieta fault, whereby the northwestern segment is characterized by thrust motion and the southeastern segment by strike-slip motion. An analysis of geodetic-elevation changes provides some support for such a model (Marshall and others, 1991). None of the teleseismic body-wave studies, however, provides independent support for such a form of slip distribution. As already mentioned, the effects of the finite extent and variation of the source in the horizontal direction are difficult to resolve with our data set. Both strong-motion and geodetic measurements, however, are, in principle, sensitive to lateral effects.

My results can be reconciled with the lateral-slip-partitioning model under the following scenario. The strong-motion modeling indicates that the rupture propagated nearly symmetrically during its early and main stages (possibly with somewhat more slip released in the south half). Two symmetrical loci of large moment release at about 10-km depth (one to the southeast and one to the northwest of the hypocenter) ruptured nearly simultaneously. Under these conditions, teleseismic ground-displacement data would integrate the contributions from the two segments, and the resulting effective slip direction would involve nearly equal amounts of strike slip and dip slip (possibly slightly more strike slip during the initial stages if the rupture to the south was slightly faster). If the rupture in the southeastern segment stopped earlier, while in the northwestern segment it continued to shallower depths, the teleseismic data would record an effective change in slip direction to thrusting at shallower depth, as exhibited in the variable-mechanism model.

CONCLUSIONS

The good azimuthal distribution and high quality of teleseismic digital recordings of body waves from the 1989 Loma Prieta earthquake provide an excellent data set from which an accurate, stable estimate of the centroidal source parameters can be determined. The teleseismic body-wave data also provide strong constraints on the depth distribution of moment release. A downdip change in slip direction is indicated but is less reliable, owing to a tradeoff between parameters and uncertainties in the Green's functions. The lateral extent of the source or possible lateral changes in slip direction, however, are unresolvable by the ground-displacement data used in this study.

ACKNOWLEDGMENTS

This research was supported by U.S. Geological Survey grant 14–08–0001–G1834. The manuscript was improved by comments from Anne Tréhu and Paul Spudich.

REFERENCES CITED

Barker, J.S., and Salzberg, D.H., 1990, Long-period and broad-band teleseismic body-wave modeling of the October 18, 1989 Loma Prieta earthquake: Geophysical Research Letters, v. 17, no. 9, p. 1409–1412.

Beroza, G.C., 1991, Near-source modeling of the Loma Prieta earthquake; evidence for heterogeneous slip and implications for earthquake hazards: Seismological Society of America Bulletin, v. 81, no. 5, p. 1603–1621.

Blümling, Peter, and Prodehl, Claus, 1983, Crustal structure beneath the eastern part of the Coast Ranges (Diablo Range) of central California from explosion seismic and near earthquake data: Physics of the Earth and Planetary Interiors, v. 31, no. 4, p. 313–326.

Blümling, Peter, Mooney, W.D., and Lee, W.H.K., 1985, Crustal structure of the southern Calaveras fault zone, central California, from seismic refraction investigations: Seismological Society of America Bulletin, v. 75, no. 1, p. 193–209.

Choy, G.L., and Boatwright, John, 1990, Source characteristics of the Loma Prieta, California, earthquake of October 18, 1989 from global digital seismic data: Geophysical Research Letters, v. 17, no. 8, p. 1183–1186.

Dietz, L.D., and Ellsworth, W.L., 1990, The October 17, 1989, Loma Prieta, California, earthquake and its aftershocks; geometry of the sequence from high-resolution locations: Geophysical Research Letters, v. 17, no. 9, p. 1417–1420.

Hartzell, S.H., Stewart, G.S., and Mendoza, Carlos, 1991, Comparison of L_1 and L_2 norms in a teleseismic waveform inversion for the slip history of the Loma Prieta, California, earthquake: Seismological Society of America Bulletin, v. 81, no. 5, p. 1518–1539.

Kanamori, Hiroo, and Satake, Keiiti, 1990, Broadband study of the 1989 Loma Prieta earthquake: Geophysical Research Letters, v. 17, no. 8, p. 1179–1182.

Langston, C.A., Furlong, K.P., Vogfjord, K.S., Clouser, R.H., and Ammon, C.J., 1990, Analysis of teleseismic body waves radiated from the Loma Prieta earthquake: Geophysical Research Letters, v.

17, no. 9, p. 1405–1408.

Lisowski, Michael, Prescott, W.H., Savage, J.C., and Johnston, M.J.S., 1990, Geodetic estimate of coseismic slip during the 1989 Loma Prieta, California, earthquake: Geophysical Research Letters, v. 17, no. 9, p. 1437–1440.

Marshall, G.A., Stein, R.S., and Thatcher, Wayne, 1991, Faulting geometry and slip from co-seismic elevation changes; the 18 October 1989, Loma Prieta, California, earthquake: Seismological Society of America Bulletin, v. 81, no. 5, p. 1660–1693.

Nábělek, J.L., 1984, Determination of earthquake source parameters from inversion of body waves: Cambridge, Massachusetts Institute of Technology, Ph.D. thesis, 360 p.

———1985, Geometry and mechanism of faulting of the 1980 El Asnam, Algeria, earthquake from inversion of teleseismic body waves and comparison with field observations: Journal of Geophysical Research, v. 90, no. B14, p. 12713–12728.

———1990, Rupture process of the October 18, 1989 Loma Prieta earthquake from broadband teleseismic body waves [abs.]: Seismological Research Letters, v. 61, no. 1, p. 46.

Oppenheimer, D.H., 1990, Aftershock slip behavior of the 1989 Loma Prieta, California earthquake: Geophysical Research Letters, v. 17, no. 8, p. 1199–1202.

Romanowicz, B.A., and Lyon-Caen, Hélène, 1990, The Loma Prieta earthquake of October 18, 1989; results of teleseismic mantle and body-wave inversion: Geophysical Research Letters, v. 17, no. 8, p. 1191–1194.

Ruff, L.J., and Tichelaar, B.W., 1990, Moment tensor rate functions for the 1989 Loma Prieta earthquake: Geophysical Research Letters, v. 17, no. 8, p. 1187–1190.

Schwartz, S.Y., and Nelson, G.D., 1991, Loma Prieta aftershock relocations with S–P travel times; effects of 3–D structure and true error estimates: Seismological Society of America Bulletin, v. 81, no. 5, p. 1705–1725.

Snay, R.A., Neugebauer, H.C., and Prescott, W.H., 1991, Horizontal deformation associated with the Loma Prieta earthquake: Seismological Society of America Bulletin, v. 81, no. 5, p. 1647–1659.

Steidl, J.H., Archuleta, R.J., and Hartzell, S.H., 1991, Rupture history of the 1989 Loma Prieta, California, earthquake: Seismological Society of America Bulletin, v. 81, no. 5, p. 1573–1602.

Wald, D.J., Helmberger, D.V., and Heaton, T.H., 1991, Rupture model of the 1989 Loma Prieta earthquake from the inversion of strong-motion and broadband teleseismic data: Seismological Society of America Bulletin, v. 81, no. 5, p. 1540–1572.

Wallace, T.C., Velasco, Aaron, Zhang, Jiajun, and Lay, Thorne, 1991, A broadband seismological investigation of the 1989 Loma Prieta, California, earthquake; evidence for deep slow slip?: Seismological Society of America Bulletin, v. 81, no. 5, p. 1622–1646.

Zhang, Jiajun, and Lay, Thorne, 1990, Source parameters of the 1989 Loma Prieta earthquake determined from long-period Rayleigh waves: Geophysical Research Letters, v. 17, no. 8, p. 1195–1198.

MECHANICAL MODELING OF A FAULT-FOLD SYSTEM, WITH APPLICATION TO THE EARTHQUAKE

By Ze'ev Reches,
Hebrew University, Jerusalem;
and
Mark D. Zoback,
Stanford University

CONTENTS

ABSTRACT

Some features of the deformation accompanying the 1989 Loma Prieta earthquake resemble that associated with earthquakes along deep-seated reverse faults. These features include ground breakage, surface deformation, aftershock distribution, and a component of reverse slip deduced from geodetic and strong-ground-motion data. To explore these deformational features of the earthquake, we derive an analytical model for the deformation of a layered sequence due to slip along a deep-seated fault. Our model includes horizontal elastic layers, using configurations with as many as nine layers of different shear moduli. We applied this layered model to the Loma Prieta region and found that the better solutions are for five-layer sequences in which the shear moduli of the layers increase downward. The model predicts the distribution of aftershocks in the upper 5 km better than a model with uniform rheology. The model also accurately predicts the location of the zone of horizontal extension in the Summit Road area and the zone of horizontal compression in the northeastern foothills of the Santa Cruz Mountains.

INTRODUCTION

Since the early 1980's, deep-seated faults concealed by folded structures have been recognized as a significant source for seismic hazard (for example, Stein and King, 1984). This recognition reflects observations of the 1980 El-Asnam, Algiers, the 1983 Coalinga, Calif., and the 1987 Whittier Narrows, Calif., earthquakes. In these and other earthquakes, the deep faults form a fault-fold system in which slip along a fault zone at depth appears as a fold or a flexure within the overlying sedimentary layers.

Fault-fold systems have been modeled by using several different methods. One common approach is kinematic analysis, for which the balanced cross section is the best known representative. This technique was developed to analyze large-scale deformation by assuming that rock volume (area in two-dimensional profiles) is conserved during deformation (Dahlstrom, 1969). Using this approach, the initial configuration and even the deformation path can sometimes be reconstructed from the geometry of the final deformed structure. The kinematic approach, however, has some severe limitations: Rock rheology is omitted, rock layers are merely lines drawn on profiles without mechanical properties, and the mechanical differences between layers are ignored. Therefore, although the kinematic analysis maintains geometric compatibility, it could violate known dynamic principles.

Another approach is the modeling of upper-crustal deformation by dislocations within a linear, elastic half-space. This modeling has been extensively used in the inversion of long-term geodetic data, as well as for seismic and postseismic displacements. Although half-space models can provide impressive fits to geodetic data (Lisowski and others, 1990), they do not incorporate the layering of crustal rocks and are limited to small deformation. For example, King and others (1988) extended such models by considering a thick, linear elastic layer over a viscous half-space; they modeled the development of crustal flexures by many repeating earthquakes, incorporating seismic slip, viscous-isostatic relaxation, erosion, and sedimentation. One surprising result of their analysis is that the calculated elastic thickness of the crust is only 2 to 4 km.

A different approach assumes that slip along deep-seated faults is accommodated within the overlying rocks by flexing, faulting, and tilting, which form such fault-fold systems as monoclines or asymmetric folds (Reches, 1978). Reches and Johnson (1978) derived a general model for the development of a fault-fold system and analyzed the mechanics of draping, buckling, and kinking within the sedimentary sequence. Because crustal rocks commonly display mechanical layering rather then uniform rheology, we believe that relevant models must incorporate this property.

The 1989 Loma Prieta earthquake resulted in several features that resemble the deformational features of earthquakes associated with deep-seated reverse faults: the types of surface deformation and ground breakage, the aftershock distribution, and the large amount of subsurface reverse slip deduced from inversion of geodetic (Lisowski and others, 1990) and strong-ground-motion data (Beroza, 1991). To explore the deformational style in the Loma Prieta region, we have derived a model for a layered rock sequence above a deep-seated fault. The analysis is for horizontal, incompressible, elastic layers subjected to fault-related displacement along the base of the sequence. Our model attempts to reproduce the location and style of surface deformation and aftershock distribution of the earthquake. We compare the results of this layered model with those from the uniform-rheology model.

ANALYSIS OF A FAULT-FOLD SYSTEM

APPROACH

We derive here an analytical solution for a fault-fold system that includes a sequence of layers overlying a basement (fig. 1). The basement is idealized as an elastic half-space that can deform by slip along planar faults; the layered sequence above the fault is idealized as horizontal layers with nonuniform moduli that are either bonded to each other or free to slip along their contacts. In theory, these layers can deform elastically or viscously; the analysis below is for linear, incompressible, elastic layers under plane-strain conditions. Details of the analytical procedure are presented below in the appendix (see Reches and Johnson, 1978).

The computations provide the displacement, stress, and strain fields within the layered sequence. By using a Fourier series of stepped waveforms, the solutions can handle the combination of continuous, periodic folding processes in the layers and discontinuous fault displacements in the basement.

DEFORMATION ABOVE A FAULTED RIGID BASEMENT

We first present the solutions for a simple fault-fold system that is common in regions of moderate tectonic deformation, such as the Colorado Plateaus, the Rocky Mountains, and the Middle East (Prucha and others, 1965; Reches, 1978; Stearns, 1978; Reches and others, 1981). This simple fault-fold system is a zone of flexed, bent, and tilted layers of sedimentary rocks above basement faults (fig. 2). In these structures, the layers are deformed

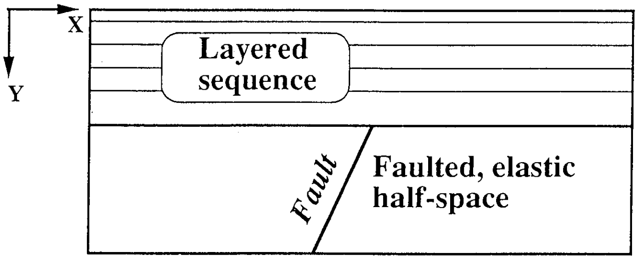

Figure 1.—Idealized geometry of a faulted basement overlain by a layered sequence.

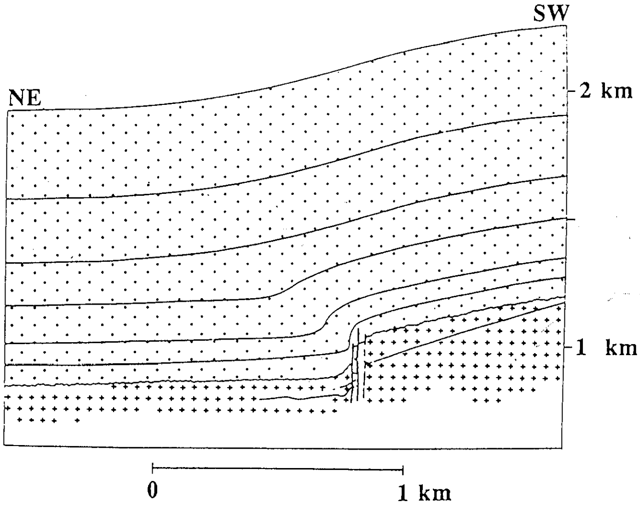

Figure 2.—Simple fault-fold system, showing a profile of the Palisades monocline, Grand Canyon, Ariz. Crosses, Precambrian units; dots, Paleozoic formations. Modified from Reches and Johnson (1978).

and tilted near the fault and almost undeformed and essentially flat away from the fault. The local deformation of the layers reflects the response of the layered sequence in part to the deep-seated faulting (Stearns, 1978) and in part to tectonic stresses within the layers (Reches and Johnson, 1978).

We restrict our analysis to fault-fold systems with small displacements of a few tens to a few hundreds of meters of fault slip. Following King and others (1988), we assume that such systems develop in cycles of seismic events alternating with long periods of interseismic elastic deformation. It is further assumed that in such systems, the interseismic elastic deformation in the basement is relaxed during seismic events, and so the basement may be regarded as rigid. A rigid basement implies that its top on both sides of the fault remains fairly planar and close to horizontal (fig. 2). In contrast, the overlying layers deform permanently by flexing and tilting. In systems with large displacements (>1 km), the basement may not be regarded as rigid because it deflects, owing to isostatic relaxation, erosion, sedimentation, or a combination of these processes (King and others, 1988).

REVERSE BASEMENT FAULT VERSUS NORMAL BASEMENT FAULT

We now present solutions for two idealized fault-fold systems, one with a reverse fault in the basement and the other with a normal fault in the basement (fig. 3). The two systems include six horizontal layers that are bonded to each other along their contacts. Each layer is 200 m thick, and the shear moduli alternate between 6 and 20 GPa (fig. 3*A*). In line with field observations (fig. 2) and the arguments in the preceding subsection, the top of the basement is maintained horizontal and planar during the deformation (which is linear in the two-dimensional approximation used).

The results for a normal fault that dips 60° to the right (fig. 3*B*) and for a reverse fault that dips 60° to the left (fig. 3*C*) are shown in figure 3; both systems have 1 m of vertical displacement of the basement. Each solution shows the displacement of the layers, the change in the local shear stress $\Delta\tau_E$ (see eq. 12), and the orientations of the maximum compressive stress induced by slip along the deep-seated fault.

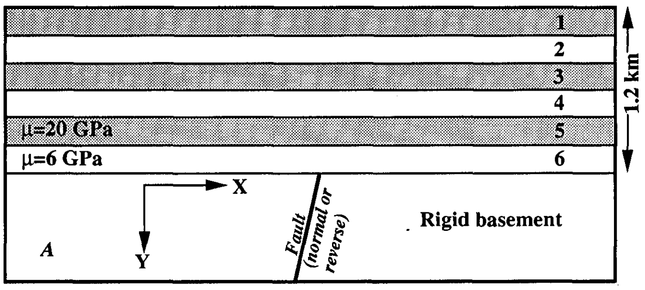

Figure 3.—Analytical solution for deformation of a sequence of six layers above a rigid basement. *A*, Model configuration: Layers are elastic, incompressible, with bonded contacts, 0.2 km thick; shear modulus alternates between 6 GPa in layers 1 (top), 3, and 5 and 20 GPa in layers 2, 4, and 6 (basal layer). *B*, Normal fault dipping 60° to right. *C*, Reverse fault dipping 60° to left. In figures 3*B* and 3*C*, fault tip is at 0-m distance (center); 180 wavelengths were used in Fourier series. Continuous curved lines, displacements of contacts between layers (short lines connect initial and final positions); short heavy bars, orientations of σ_1 axes. Gray tones (1–10 scale on right side) indicate intensity of change in normalized shear stress $\Delta\tau_E$ (see appendix, eq. 12).

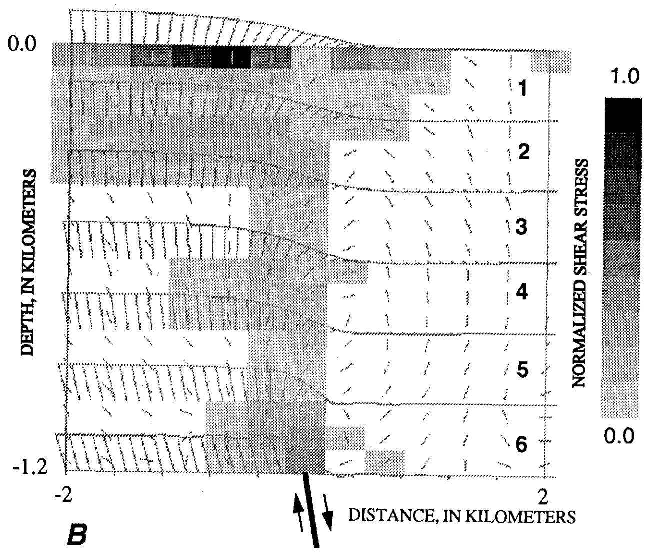

Figure 3.—Continued.

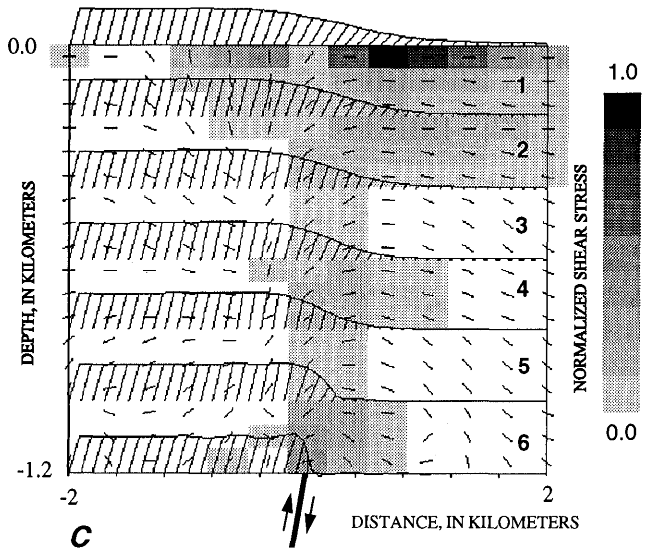

Figure 3.—Continued.

The most conspicuous feature in these solutions is the appearance of a zone of increasing shear stress $\Delta\tau_E$ above the fault (figs. 3*B*, 3*C*). The width of this zone varies significantly: It is a few hundred meters wide in the basal layer, about 1 km wide in the central part of the sequence, and a few kilometers wide close to the top (figs. 3*B*, 3*C*). Local increases in shear stress and the width of the zone occur within the layers of large shear modulus, layers 2, 4, and 6. This increase reflects the rule of thumb that the stiffer components in nonuniform materials—layered sequences or a medium with inclusions—concentrate the stresses. The stressed zone appears as a continuation of the basement fault: It dips generally to the right for the normal fault (fig. 3*B*), and to the left for the reverse fault (fig. 3*C*).

Another significant feature of the solutions shown in figure 3 are the orientations of the principal stresses within the stressed zone. To simplify the variations in the induced stress, we refer to three stress orientations: regions of layer-normal compression, in which the axes of maximum compression are inclined 60° or more to the subhorizontal layering; regions of layer-parallel compression, in which the axes of maximum compression are inclined 30° or less; and regions of layer-parallel shear, in which the axes of maximum compression are inclined 30°–60°. In the normal-fault system, most regions, particularly those with a relative increase in shear stress, are of the layer-normal compression type (fig. 3*B*). A region of layer-parallel compression appears to the right of the center, within the synclinal zone of the surface flexure. In the reverse-fault system, the situation is generally inverted, and most regions of shear stress increase with layer-parallel compression (fig. 3*C*).

These patterns of stress orientations could profoundly affect the structural development. The layer-parallel compression in the reverse-fault system could invoke two deformational modes: propagation of the basement reverse fault, or buckling and flexing of the layered sequence (Reches and Johnson, 1978). Buckling and flexing will prevail if the layers are thin, if considerable differences in elastic moduli exists between the layers, and if the friction along the bedding surfaces is relatively low. Under such conditions, the basement fault will be transformed into a monoclinal flexure in the layered sequence, and a fault-fold system would develop (Reches, 1978). This process of flexure above a fault may explain the absence of surface rupture above some active reverse faults.

The situation is different for the normal-fault system because layered sequences do not buckle under the effect of layer-normal compression. The stresses within the layers above a basement normal fault (fig. 3*B*) would enhance normal faulting and the propagation of the basement fault into the layered sequence. This process is further enhanced because rocks are significantly stronger under compression than under extension and the layers above the normal fault are more likely to yield by faulting rather than by folding.

THE 1989 LOMA PRIETA EARTHQUAKE

FEATURES OF THE EARTHQUAKE

The 1989 Loma Prieta earthquake occurred within the San Andreas fault system in the Santa Cruz Mountains, Calif. The hypocenter of the event was about 17 km deep, relatively deep for the San Andreas fault system. The focal-plane solution of the main shock (Oppenheimer, 1990) and the distribution of aftershocks (Dietz and Ellsworth, 1990) indicate that seismic slip occurred along a fault that dips about 70° SW., with mixed reverse and right-lateral slip. This sense was confirmed by inversion of the geodetic measurements, with a best fit of observations to 1.6±0.3 m of right-lateral strike slip and 1.2±0.4 m of vertical reverse displacement (Lisowski and others, 1990). The slip in this earthquake was apparently heterogeneous, as demonstrated by inversion of the strong-ground-motion data (Beroza, 1991). This analysis indicates that the slip can be divided into two separate segments, a northern segment with almost pure reverse slip and a southern segment with almost pure right-lateral slip; for both components, the peak local slip amplitude is 2.8 m (Beroza, 1991). Marshall and others (1991) analyzed the leveling data and considered solutions for two coplanar segments. Their best signal-to-noise ratio was obtained for a two-segment fault, dipping 62°, with a rake of 116° (almost pure reverse slip) in the northern segment and a rake of 163° (almost pure strike slip) in the southern segment.

Surface fractures of apparent tectonic origin were observed in three main zones. The first zone is an area of extensional features along Summit Road, west of Loma Prieta (vertical-lined area, fig. 4; Ponti and Wells, 1991). This zone is about 6 km long and 1 to 1.5 km wide; it is subparallel to the San Andreas fault and 1 to 2 km from its southwest side (the Pacific block). Most of the fractures display mixed displacement: extension normal to the fractures with either left- or right-lateral slip. The maximum measured displacement was 92 cm, with a left-lateral component of 42 cm (Ponti and Wells, 1991). Many of the observed fractures within this zone coincide in position and trend with those mapped by Sarna-Wojcicki and others (1975) and were also active during the 1906 San Francisco earthquake. Several investigators attributed this fracture zone to gravitational sliding, in part relating localization of the fractures to the topographic elevation (Ponti and Wells, 1991).

A second zone is situated along the northeastern foothills of the Santa Cruz Mountains, about 3 to 6 km northeast of the San Andreas fault (areas C, fig. 4). The dominant features here are fractures with reverse motion and small buckles mostly within manmade structures, such as roads or sidewalks (Plafker and Galloway, 1989).

The third zone includes surface fractures along the main trace of the San Andreas fault, southeast of Loma Prieta. Aydin and others (1992) mapped in detail the fractures here and found primarily fractures with right-lateral motion (max 30 cm) and reverse slip.

MODELING THE EARTHQUAKE AS A FAULT-FOLD SYSTEM

Some of the above-listed observations suggest that the 1989 Loma Prieta earthquake is similar to earthquakes along deep-seated reverse faults. The most relevant observations are the patterns of surface rupture, the occurrence of extensional features in the Pacific block and compressional features in the North American block, and the mixed reverse and right-lateral slip at great depth, with almost pure reverse slip along the northern part of the slipping fault segment. For these reasons, we analyze the deformation associated with slip along the northern part of the Loma Prieta rupture zone as a deep-seated reverse fault. The analyzed models were restricted to a vertical profile trending N. 40° E. (line AB, fig. 4), perpendicular to the slip surface determined by Dietz and Ellsworth (1990) and Oppenheimer (1990).

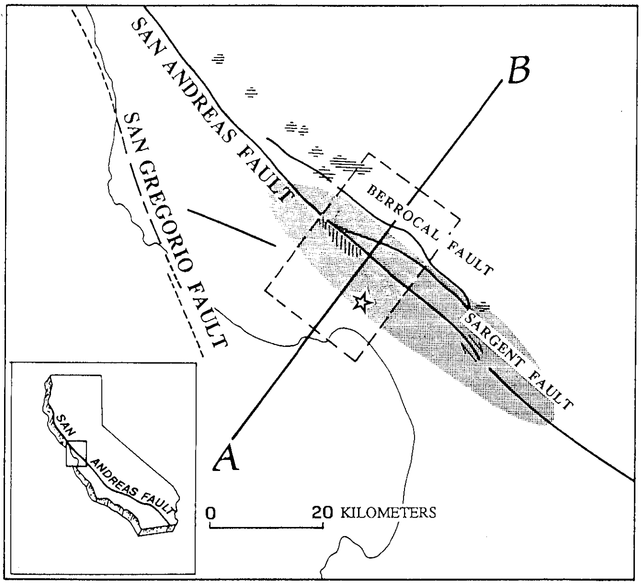

Figure 4.—Area of 1989 Loma Prieta earthquake (modified from Plafker and Galloway, 1989). Star, main-shock epicenter; shaded area, aftershock zone; vertical-lined area, zone of surface rupture with predominantly extensional fractures; horizontal-lined areas, zones of surface rupture with predominantly compressive features; line AB, profile in N. 40° E. direction for present model (see fig. 5); dashed rectangle, area of aftershocks used in present analysis (see fig. 5).

MECHANICAL LAYERING

The Loma Prieta region reveals a complex structure composed of major strike-slip faults, reverse faults, and large folds, which are generally subparallel to the San Andreas fault (McLaughlin and others, 1988; Clark and others, 1989). The exposed rocks along the Loma Prieta rupture zone are marine and nonmarine clastic units of Tertiary age that occupy at least the upper 1 km northeast of the San Andreas fault and 2 km or more on the southwest side. Basement rocks are exposed either southwest of the Zayante fault or northeast of the Berrocal fault (McLaughlin and others, 1988; Clark and others, 1989). The sedimentary rocks are intensely deformed by tight and isoclinal folds and faults (mostly reverse). The block between the San Andreas and Sargent faults seems to be more intensely faulted by reverse faults than the block southwest of the San Andreas fault. The layering in the Loma Prieta region has most likely facilitated the regional folding and flexing during the past few million years. However, because the available folding analyses are restricted to inclinations gentler than 10°–15° (Johnson, 1977), it is practically impossible to quantitatively analyze the deformation of the intensely deformed sequence of Loma Prieta in its present structure.

Another layered structure is reflected in seismic profiles of the region. Seismic-velocity models of the Loma Prieta region reveal a low-velocity (3.3–5.8 km/s) wedge between the Zayante and San Andreas faults that extends to depths of more then 8 km (fig. 5*B*; Eberhart-Phillips and others, 1990). This wedge was interpreted as marine sedimentary rocks of Tertiary age (Eberhart-Phillips and others, 1990). A high-velocity zone (6.4–6.7 km/s) that appears between the San Andreas and Sargent faults was interpreted as mafic intrusive rocks (fig. 5*B*).

The upper 3 to 5 km of the crust in the study area displays relatively simple, subhorizontal velocity layering (fig. 5*A*), with a gradual increase in *P*-wave velocity from 3.3 km/s at the surface to about 6 km/s at 5-km depth (fig. 5). This simple velocity layering is apparently unrelated to the complex folded structure of the sedimentary layers. The seismic velocity cannot be correlated with clear lithologic or stratigraphic units, and so the increase in velocity with depth is interpreted as reflecting the compaction and cementation of Tertiary clastic sedimentary rocks.

Following this interpretation of depth-controlled hardening, we consider the profile of seismic velocity (fig. 5) as reflecting mechanical layering in the upper 5 km of the crust. Accordingly, we used a ratio of 0.25 between the shear modulus of the top layer to the shear modulus of the basal layer, in general agreement with the ≈0.5 ratio of *P*-wave velocities in the top layer to those in the basal layer (fig. 5).

MODEL PARAMETERS

We calculated solutions with layered sequences consisting of one to nine layers and total thicknesses of 3, 5, and 7 km under plane-strain conditions. We examined layers that were either free to slip along their contacts or bonded to each other. The shear moduli of the layers were selected to show (1) a downward increase in modulus, from 4 GPa at the top to 16 GPa at the base; (2) a downward decrease in modulus, from 16 GPa at the top to 4 GPa at the base; or (3) a uniform modulus for the layers free to slip along their contacts. Depth variations of shear moduli were in equal steps according to the number of layers. As the basal displacements are specified (see appendix), the mechanical properties of the basement do not affect the solution. The basal displacement was calculated with the computer program DIS3D for a reverse slip of 1 m along a 70°-dipping reverse fault (see appendix).

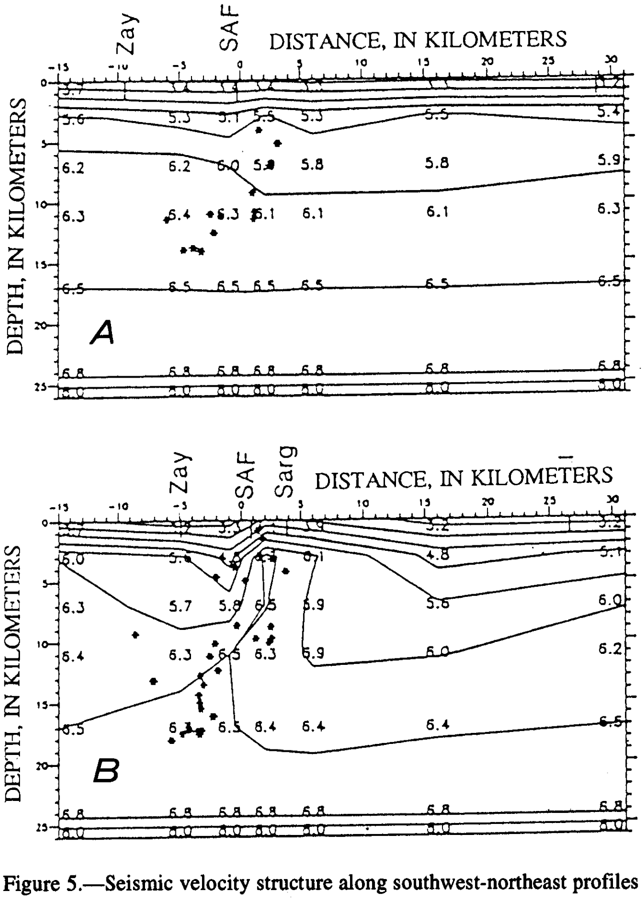

Figure 5.—Seismic velocity structure along southwest-northeast profiles 20 km northwest of main shock epicenter (*A*) and across main shock (*B*) (after Eberhart-Phillips and others, 1990).

A few groups of solutions were rejected in the early stages of the calculations for the following reasons. First, we correlated zones of increase in shear stress in the solution with zones of high density of aftershocks. Aftershocks of the earthquake were concentrated within a 2- to 3-km-wide zone that extends from 18- to about 1-km depth (Oppenheimer, 1990). The zones of shear-stress increase in an acceptable model should approximately coincide with the zone of high density of aftershocks, and so we rejected models that clearly do not conform to this correlation. In models with free-slip contacts, the upper layers are detached from the displacement at the basement, leading to shear-stress increase within a wide region of the basal layer, with no increase of the shear stresses in the upper layers. Second, models with shear moduli decreasing downward generated shear stress fields that contradicted the aftershock distribution. Furthermore, these models do not conform to the velocity profiles shown in figure 5. Similar contradictions appeared for single-layer solutions with a uniform shear modulus. Therefore, models with free slip between layers, with downward-decreasing moduli, and with uniform shear modulus (fig. 7) were all rejected in early stages of the calculations.

RESULTS

We found that models with five layers, downward-increasing shear moduli, and bonded contacts fit better the relevant field observations. The results of these models are displayed at different horizontal and vertical scales in figures 6*A* through 6*C*, which show the displacement of the layers, the change of the local shear stress $\Delta\tau_E$ (eq. 12), and the orientations of the maximum compressive stress.

SHEAR ZONES

One conspicuous feature of our models is the appearance of two distinct zones of intensive increase in shear stress. The first zone is a subvertical region above the basement fault and slightly to the northeast (fig. 6). This zone reflects the increase in shear stress within the stiffer lower layers, owing to the deformation localized above the fault. The zone is 4 to 5 km wide at the base and narrows to about 1 km wide at 1- to 2-km depth. The orientation of σ_1, the axis of maximum compression, varies spatially within the zone.

The second zone of shear-stress increase is a horizontal, 10- to 12-km-wide region in the upper layer (fig. 6*B*); the intense stresses here are restricted to the upper 200 to 300 m (fig. 6*C*). This second zone largely reflects the low lithostatic load at shallow depths because $\Delta\tau_E$ is the change in shear stress normalized by the lithostatic stress (see appendix, eq. 12). This zone is separable into two regions: a region of horizontal σ_1 on the northeast side and a region of vertical σ_1 on the southwest side; the positions of maximum shear-stress increase in these two regions are 6 to 7 km apart (fig. 6*B*). These regions correlate in position with the anticlinal and synclinal bends of the flexure of the top layer. The two regions of increased stresses within the subhorizontal zone (fig. 6*B*) correlate with the two regions of tectonic surface rupture mentioned above (fig. 4): the Summit Road zone with dominantly extensional fractures and the northeastern foothills of the Santa Cruz Mountains with compressional features. The projection of these two zones onto a N. 40° E. vertical section near California Highway 17 reveals a distance of 6 to 7 km along the profile, in good agreement with the model calculations (fig. 6). We calculated that the extension normal to the fault across a 4-km-wide zone, centered 2 km west of the San Andreas fault is about 7.5 cm.

Ponti and Wells (1991) noted that many of the major cracks in the Summit Road zone correlate with the local slope direction and are associated with landslides and bedding-plane slippage. They found that the cumulative, fault-normal extension across the fracture zone ranges from 65

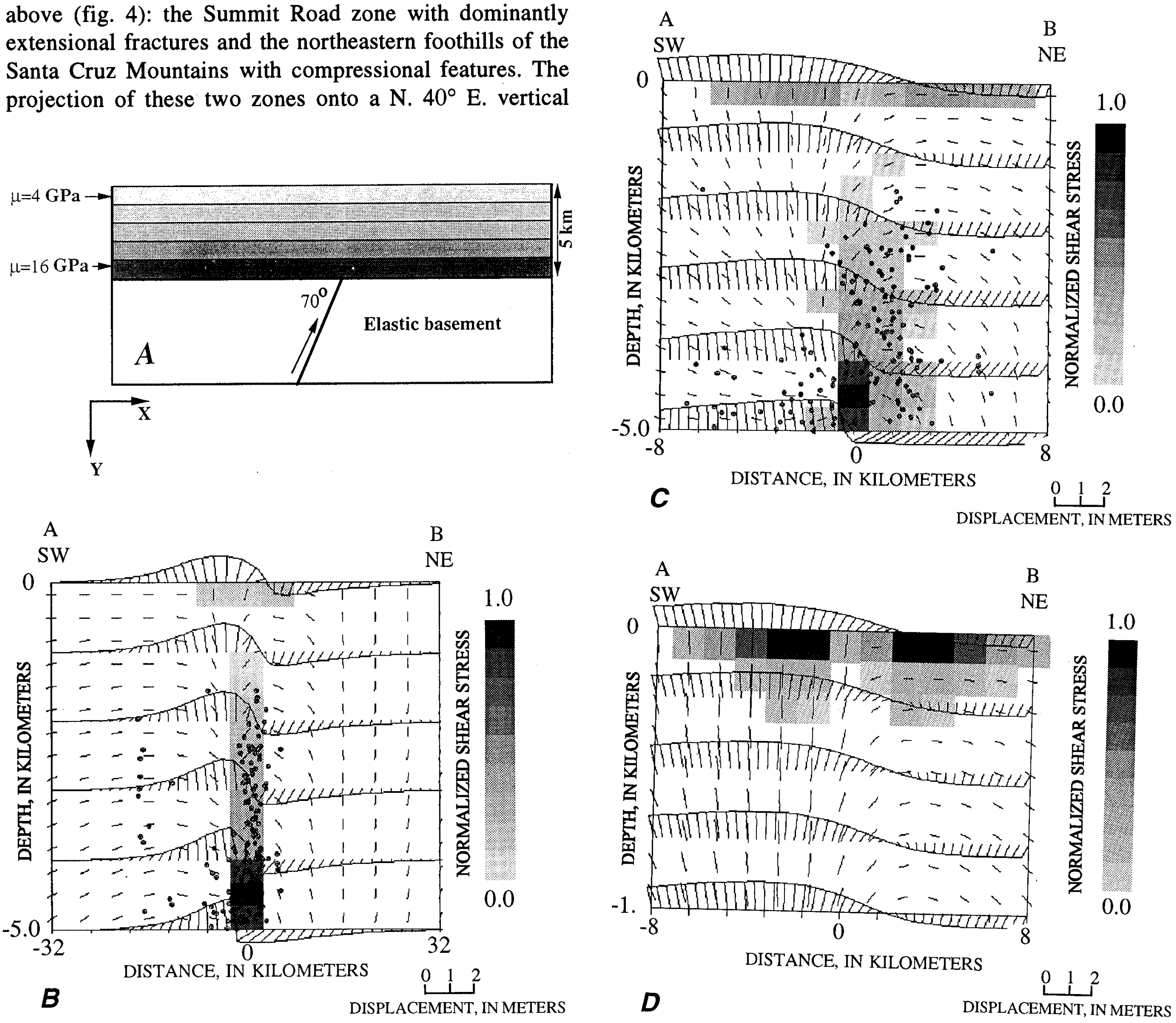

Figure 6.—Analytical solutions at different scales for deformation associated with an earthquake. *A*, Configuration of preferred model: a sequence of five elastic, incompressible layers, each 1 km thick and bonded to each other. Shear modulus (μ) of top layer is 4 GPa, increasing in equal steps to 16 GPa in basal layer. Basal displacements were calculated for 1 m of reverse slip along a 70°-dipping reverse fault within an elastic basement (see appendix for details). Displacement is transformed in a Fourier series with 160 wavelengths. *B*, Five-layer sequence. Fault is in center of base. *C*, Expanded view of figure 6*B*. *D*, Upper layer (layer 1). In figures 6*B* through 6*D*, fault tip is at 0-m distance (center). Dots, 215 aftershocks for period October 18–31, 1989 (after Dietz and Ellsworth, 1990), with hypocenters projected horizontally to section profile (see text). Continuous curved lines, displacements of contacts between layers (short lines connect initial and final positions); short heavy bars, orientations of σ_1 axes. Gray tones (1–10 scale on right side of fig. 6*B*) indicate intensity of change in normalized shear stress $\Delta\tau_E$ (see appendix, eq. 12).

to 104 cm (8 to 14 times the extension calculated in the present model). They proposed that the extension is due to ridgetop spreading rather than tectonic deformation.

Our interpretation is that the extension in the Summit Road zone is due to slip during the earthquake which was amplified by local topographic features. Horizontal extension is a common feature associated with the anticlinal bend above a deep-seated normal (fig. 3*A*) or reverse (fig. 3*C*) fault. Anticlinal extensional zones were recognized by Sanford (1959), and Reches and Johnson (1978), who applied these zones to analyze the mechanisms of monocline development. The compressional zone in the synclinal bend is the complement to the extensional zone in the anticlinal bend (figs. 3, 6).

We note, however, that the extension-compression pair reflects the *local* stress field associated with slip along the fault; the total stresses are the sum of these local stresses and the *remote* stresses (see appendix). If, for example, the remote stresses are compressional, they would enhance the compressional zone in the synclinal bend and diminish the extensional zone in the anticlinal bend (Reches and Johnson, 1978).

AFTERSHOCK DISTRIBUTION

Another result of our modeling is a prediction of the locations of shallow aftershocks. The locations of aftershocks for the period October 18–31, 1989, are plotted in figure 7. From the list of 1,173 best constrained hypocenters, we selected all 215 events with hypocenters that are no more than 5 km deep and with epicenters inside a frame 20 by 30 km on both sides of our modeling profile (fig. 4). These hypocenters are projected horizontally onto the N. 40° E.–S. 40° W. vertical surface and plotted on the derived solutions.

These aftershocks are well confined to the subvertical zone of shear-stress increase above the fault (figs. 6*A*, 6*B*). We examine whether this correlation between the aftershock pattern and the predicted zone of shear-stress increase depends on the layering in the model by calculating a solution for a single layer of uniform rheology (fig. 7); other parameters are the same as in figure 6. It is apparent that the single-layer solution in figure 7 displays a poor correlation between the intensity of the shear-stress increase and the aftershock distribution. The difference between the two solutions reflects the rheologic difference between the models: The lower layers of figure 6 have a high stiffness, and so they tend to be more highly stressed than the less stiff layers above them, whereas in the single-layer solution the shear-stress increase is concentrated at the surface, owing to the effect of the low normal stress (see appendix).

CONCLUSION: LAYERED VERSUS UNIFORM MEDIUM

The deformation associated with earthquakes is commonly calculated for one or more dislocations embedded within a uniform elastic half-space. The analytical solution presented here allows the shear modulus to vary between horizontal layers (fig. 1). By using these solutions, simple, but more realistic (nonuniform), rheologic models can be explored. The models presented here for the Loma Prieta region describe a sequence of layers in which the shear moduli vary by a ratio of 1:4 (fig. 6), in accordance

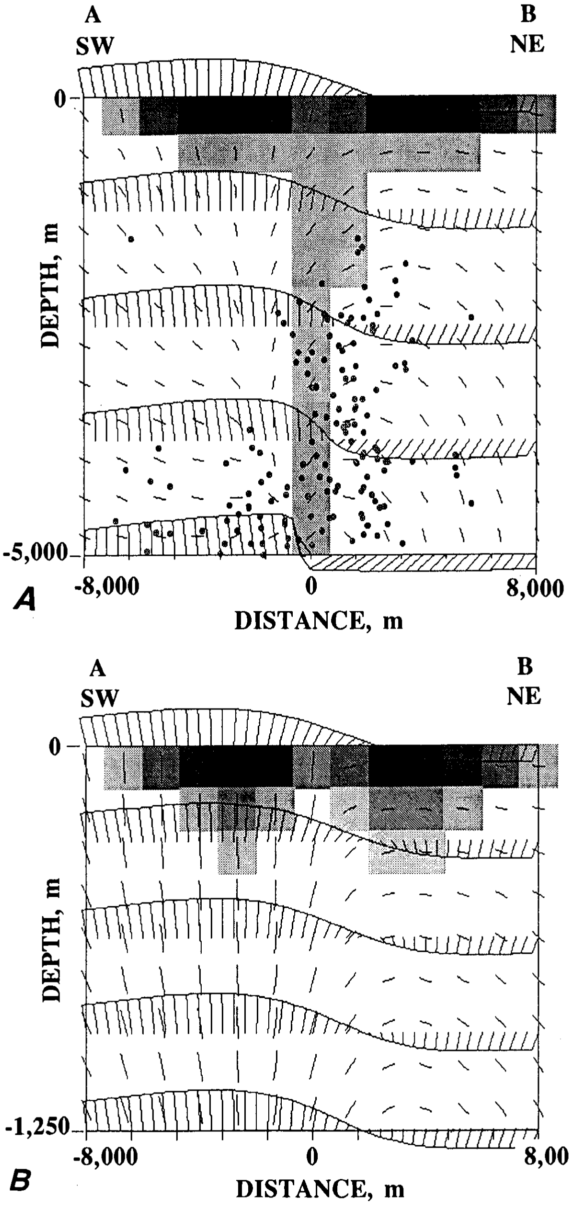

Figure 7.—Analytical solution for deformation of a single elastic layer, 5 km thick. Same basal displacement as in figure 6. *A*, Profile of entire layer. *B*, Details of upper 1.25 km. Same symbols as in figure 6.

with the *P*-wave-velocity ratio (≈1:2); (fig. 5). The present solutions seem to provide better predictions of the aftershock distribution than the uniform model (compare figs. 6, 7). Both models provide similar explanations for the two zones of surface deformation (extension in the Summit Road zone and compression in the foothill zone; figs. 4, 6*B*, 7). The present solution indicates that the aftershock zone should be centered between the regions of surface extensional deformation (Summit Road) and surface compressional deformation (foothills) (fig. 6).

We also compared the expected vertical displacement at the ground surface for the layered-medium model and for the uniform-layer model. Figure 8 shows that the vertical displacements in these two models deviate by only 2 to 5 percent from each other. This small difference suggests that leveling data are insensitive to rheologic variations with depth and the existence of layered media.

The present analysis provides a method to study the deformation in a layered medium above a faulted basement. Even the simple geometry of the basic model presented here (fig. 1) may generate a wide variety of stresses and displacements (figs. 3, 6) possibly related to the wide variety of focal-plane mechanisms of the aftershocks. We consider it an important result that the layering used in our preferred model for the 1989 Loma Prieta earthquake is consistent with the mechanical layering revealed by the seismic-velocity structure and that the calculated stresses and displacements agree well with the observed surface deformation and aftershock locations.

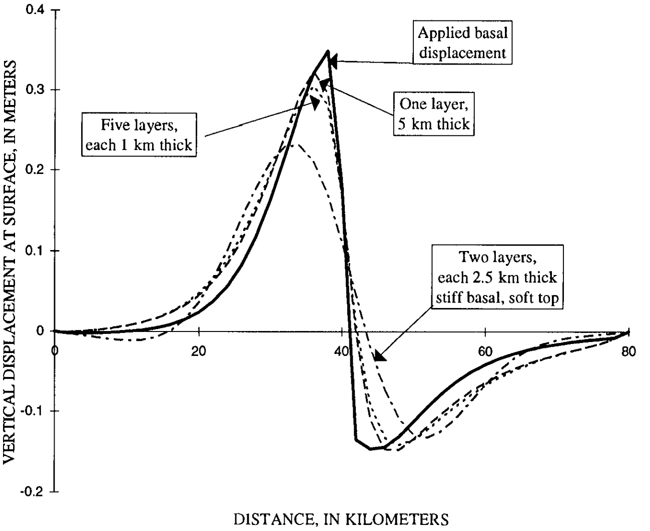

Figure 8.—Vertical displacements associated with a basement reverse fault, dipping 70° to left with 1 m of reverse slip (same conditions as in figs. 6, 7). Total thickness, 5 km; basal layer is 100 times stiffer than upper layer (dotted curve).

ACKNOWLEDGMENTS

This research was supported in part by U.S. Geological Survey grant 14080001–G–1853 to Stanford University. We thank Lynn Dietz of the U.S. Geological Survey for providing the aftershocks listing. Discussions with Paul Segall, Ross Stein, Bill Ellsworth, Dave Oppenheimer, Dan Ponti, Mike Lisowski, and Jim Dieterich are greatly appreciated. The reviews and comments by Ross Stein, Bob Simpson, Joe Andrews, and Paul Spudich contributed significantly to the manuscript.

REFERENCES CITED

Aydin, A., Johnson, A.M., and Fleming, R.W., 1992, Right-lateral/reverse surface rupturing along the San Andreas and Sargent fault zones during the October 17, 1989, Loma Prieta, California, earthquake: Geology, v. 20, p. 1063-1067.

Beroza, G.C., 1991, Near-source modeling of the Loma Prieta earthquake; evidence for heterogeneous slip and implications for earthquake hazard: Seismological Society of America Bulletin, v. 81, no. 5, p. 1603–1621.

Brace, W.F., and Kohlstedt, D.L., 1980, Limits on lithospheric stress imposed by laboratory experiments: Journal of Geophysical Research, v. 85, no. B11, p. 6248–6252.

Clark, J.C., Brabb, E.E., and McLaughlin, R.J., 1989, Geologic map and structure sections of the Laurel 7 ½′ Quadrangle, Santa Clara and Santa Cruz counties, California: U.S. Geological Survey Open-File Report 89–676, 31 p., scale 1:24,000, 2 sheets.

Dahlstrom, D.C.A., 1969, Balanced cross sections: Canadian Journal of Earth Sciences, v. 6, no. 4, pt. 1, p. 743–757.

Dietz, L.D., and Ellsworth, W.L., 1990, The October 17, 1989, Loma Prieta, California, earthquake and its aftershocks; geometry of the sequence from high-resolution locations: Geophysical Research Letters, v. 17, no. 9, p. 1417–1420.

Eberhart-Phillips, D.M., Labson, V.F., Stanley, W.D., Michael, A.J., and Rodriguez, B.D., 1990, Preliminary velocity and resistivity models of the Loma Prieta earthquake region: Geophysical Research Letters, v. 17, no. 8, p. 1235–1238.

Erickson, L., 1987, User's manual for DIS3D, a three-dimensional dislocation program with application to faulting in the earth: Stanford, Calif., Stanford University, Department of Applied Earth Sciences, 167 p.

Johnson, A.M., 1977, Styles of folding; mechanics and mechanisms of folding of natural elastic materials: New York, Elsevier, 406 p.

King, G.C.P., Stein, R.S., and Rundle, J.B., 1988, The growth of geological structures by repeated earthquakes, 1. Conceptual framework: Journal of Geophysical Research, v. 93, no. B11, p. 13307–13318.

Lisowski, Michael, Prescott, W.H., Savage, J.C., and Johnson, M.J.S., 1990, Geodetic estimate of coseismic slip during the 1989 Loma Prieta, California, earthquake: Geophysical Research Letters, v. 17, no. 9, p. 1437–1440.

Marshall, G.A., Stein, R.S., and Thatcher, Wayne, 1991, Faulting geometry and slip from co-seismic elevation changes: the 18 October 1989 Loma Prieta, California, earthquake: Seismological Society of America Bulletin, v. 81, no. 5, p. 1660–1693.

McLaughlin, R.J., Clark, J.C. and Brabb, E.E., 1988, Geologic map and structure sections of the Loma Prieta 7 ½′ quadrangle, Santa Clara and Santa Cruz counties, California: U.S. Geological Survey Open-

File Report 88–752, 32 p., scale 1:24,000, 2 sheets.

Oppenheimer, D.H., 1990, Aftershock slip behavior of the 1989 Loma Prieta, California earthquake: Geophysical Research Letters, v. 17, no. 8, p. 1199–1202.

Oppenheimer, D.H., Reasenberg, P.A., and Simpson, R.W., 1988, Fault plane solutions for the 1984 Morgan Hill, California, earthquake sequence; evidence for the state of stress on the Calaveras Fault: Journal of Geophysical Research, v. 93, no. B8, p. 9007– 9026.

Plafker, George, and Galloway, J.P., eds., 1989, Lessons learned from the Loma Prieta, California, earthquake of October 17, 1989: U.S. Geological Survey Circular 1045, 48 p.

Ponti, D.J., and Wells, R.E., 1991, Off-fault ground ruptures in the Santa Cruz Mountains, California; ridge-top spreading versus tectonic extension during the 1989 Loma Prieta earthquake: Seismological Society of America Bulletin, v. 81, no. 5, p. 1480–1510.

Prucha, J.J., Graham, J.A., and Nickelsen, R.P., 1965, Basement-controlled deformation in Wyoming province of Rocky Mountains foreland: American Association of Petroleum Geologists Bulletin, v. 49, no. 7, p. 966–992.

Reches, Ze'ev, 1978, Development of monoclines; part I. Structure of the Palisades Creek branch of the East Kaibab monocline, Grand Canyon, Arizona, *in* Matthews, Vincent, III, ed., Laramide folding associated with basement block faulting in the western United States: Geological Society of America Memoir 151, p. 235–271.

Reches, Ze'ev, and Johnson, A.M., 1978, Development of monoclines; part II. Theoretical analysis of monoclines, *in* Matthews, Vincent, III, ed., Laramide folding associated with basement block faulting in the western United States: Geological Society of America Memoir 151, p. 273-311.

Reches, Ze'ev, Hoexter, D.F. and Hirsch, Francis, 1981, The structure of a monocline in the Syrian Arc system, Middle East; surface and subsurface analysis: Journal of Petroleum Geology, v. 3, no. 3, p. 413-425.

Sanford, A.R., 1959, Analytical and experimental study of simple geologic structures: Geological Society of America Bulletin, v. 70, no. 1, p. 19–52.

Sarna-Wojcicki, A.M., Pampeyan, E.H., and Hall, N.T., 1975, Map showing recent active breaks along the San Andreas fault between central Santa Cruz Mountains and the northern Gabilan Range, California: U.S. Geological Survey Miscellaneous Field Studies Map MF–650, scale 1:24,000, 2 sheets.

Stearns, D.W., 1978, Faulting and forced folding in the Rocky Mountains foreland, in Matthews, Vincent, III, ed., Laramide folding associated with basement block faulting in the western United States: Geological Society of America Memoir 151, p. 1–37.

Stein, R.S., and King, G.C.P., 1984, Seismic potential revealed by surface folding; 1983 Coalinga, California, earthquake: Science, v. 224, no. 4651, p. 869–872.

APPENDIX: ANALYTICAL PROCEDURE

The mechanical deformation within a fault-fold system is derived here for the deformation of incompressible elastic or viscous layers overlying a faulted basement; the deformation is plane strain, restricted to the x–y plane (fig. 1). According to Reches and Johnson (1978, app. 1, eq. 10), the stress-strain relations, equilibrium equations, and compatibility equations are satisfied if the stress function Ψ satisfies the biharmonic equation

$$\frac{\partial^4\Psi}{\partial x^4} + 2\frac{\partial^4\Psi}{\partial x^2 y^2} + \frac{\partial^4\Psi}{\partial y^4} = 0. \tag{1}$$

The general solution for Ψ is

$$\Psi = \frac{1}{\lambda}\left\{\left[a + b(\lambda y - 1)\right]\exp(\lambda y) - \left[c + \mathrm{d}(\lambda y + 1)\right]\exp(-\lambda y)\right\} \cos(\lambda x), \tag{2a}$$

where
$$\lambda = 2\pi n/L, \tag{2b}$$

L is the longest wavelength, n is an integer indicating higher harmonic (n=1...N), and a, b, c, and d are constants to be determined from the boundary conditions. The formulas for the stresses, displacements and strains in the layers are derived from equations 2 (Reches and Johnson, 1978, app. 1). To generate the step geometry of the basement faulting we superposed as many as 180 wavelengths, as described below (also see Reches and Johnson (1978, app. 2).

The normal and shear stresses written for the *ith* layer and the nth wavelength are given by

$$\sigma_{xx} = 2\mu\lambda\left\{\left[a_i + b_i(\lambda y - 1)\right]\exp(\lambda y) + \left[c_i + d_i(\lambda y + 1)\right]\exp(-\lambda y)\right\} \sin(\lambda x) - \rho y \tag{3a}$$

$$\sigma_{yy} = -2\mu\lambda\left\{\left[a_i + b_i(\lambda y + 1)\right]\exp(\lambda y) + \left[c_i + d_i(\lambda y - 1)\right]\exp(-\lambda y)\right\} \sin(\lambda x) - \rho y \tag{3b}$$

$$\sigma_{xy} = 2\mu\lambda\left[(a_i + b_i\lambda y)\exp(\lambda y) - (c_i + d_i\lambda y)\exp(-\lambda y)\right] \cos(\lambda x); \tag{3c}$$

the horizontal displacement u and vertical displacement v by

$$u = \left[(a_i + b_i\lambda y)\exp(\lambda y) + (c_i + d_i\lambda y)\exp(-\lambda y)\right]\cos(\lambda x) \tag{4a}$$

$$v = \left\{\left[(a_i + b_i(\lambda y - 1))\right]\exp(\lambda y) - \left[c_i + d_i(\lambda y + 1)\right]\exp(-\lambda y)\right\} \sin(\lambda x) \tag{4b}$$

and the normal and shear strains by

$$\varepsilon_{xx} = -\lambda\left[(a_i + b_i\lambda y)\exp(\lambda y) + (c_i + d_i\lambda y)\exp(-\lambda y)\right] \sin(\lambda x) \tag{5a}$$

$$\varepsilon_{yy} = -\varepsilon_{xx} \tag{5b}$$

$$\varepsilon_{xy} = -\lambda\left[(a_i + b_i\lambda y)\exp(\lambda y) + (c_i + d_i\lambda y)\exp(-\lambda y)\right] \cos(\lambda x) \tag{5c}$$

where μ is the shear modulus, n is an integer indicating the wavelength (n=1...N), L is the longest wavelength considered, and a_i, b_i, c_i, and d_i are constants of the *ith* layer that depend on the geometry, properties, and boundary conditions of the problem.

The above equations indicate that the stresses, displacements, and strains in the *ith* layer are completely specified by four constants a_i, b_i, c_i, and d_i. Thus, four boundary conditions are needed for each layer to solve for the deformation. The boundary conditions are specified at the contacts between layers and are based on the continuity of stresses and displacements. For bonded contacts, the conditions at the contacts are

$$\{\sigma_{yy}\}_i = \{\sigma_{yy}\}_{i-1}, \tag{6a}$$

$$\{\sigma_{xy}\}_i = \{\sigma_{xy}\}_{i-1}, \tag{6b}$$

$$u_i = u_{i-1} \tag{6c}$$

$$v_i = v_{i-1}, \tag{6d}$$

and for free-to-slip contacts, the conditions at the contacts are

$$\{\sigma_{yy}\}_i = \{\sigma_{yy}\}_{i-1} \tag{7a}$$

$$\{\sigma_{xy}\}_i = 0 \tag{7b}$$

$$\{\sigma_{xy}\}_{i-1} = 0 \tag{7b}$$

$$v_i = v_{i-1}. \tag{7d}$$

The boundary conditions at the top of the model that is a stress-free surface are

$$\{\sigma_{yy}\}_{\text{top}} = 0, \tag{8b}$$

$$\{\sigma_{xy}\}_{\text{top}} = 0. \tag{8b}$$

The boundary conditions at the base of the layered sequence are presented in the next section (eqs. 9).

It can be shown that these boundary conditions generate $4K$ linear equations where K is the number of layers. This system is solved simultaneously to obtain the constants a_i, b_i, c_i, and d_i for all layers. These constants are then substituted into the stress and displacement equations to calculate the required deformation parameter, as follows.

CALCULATION AND PRESENTATION PROCEDURES

A set of dedicated computer programs based on the above analytical solutions were written in QuickBasic for the IBM PC. The programs are interactive, and their results are graphically presented on the screen. The programs includes five main steps as follows.

In the first step, the sequence of layers is selected. The number of layers ranges from 1 to 10, the thickness of the layers is unrestricted, and the contacts between them may be either bonded or free to slip.

In the second step, the basal displacement, which is the displacement of the base of the layered sequence, is calculated. This displacement reflects the slip along the fault (reverse or normal and inclination) and the deformation of the basement. We solve here for two classes of basal displacements. In the first class, the basement is approximated by perfectly rigid blocks with no internal deformation, separated by a weak fault. This approximation is based on field observations that indicate the planar geometry of basement blocks (Reches and Johnson, 1978; see section above entitled "Analysis of a Fold-Fault System"). The vertical displacement V_x and the horizontal displacement U_x at the base of the layered sequence are determined by the following Fourier series for a step:

$$V_{x(base)} = V_0 \sum_{n} \frac{4}{n\pi} \sin^2\left(\frac{n\pi}{4}\right) \sin\left(\frac{\pi n}{\lambda}\right) \tag{9a}$$

and

$$U_{x(base)} = U_0 \sum_{n} \frac{2}{n\pi} (-1)^n \sin^2\left(\frac{n\pi}{2}\right) \cos\left(\frac{\pi x}{\lambda}\right), \tag{9b}$$

where $\lambda = 2\pi n \,/\, \mathrm{L}, \quad (n = 1, 2, ...N)$

L is the longest wavelength considered (typically, 160 km in the present modeling), N is the maximum number of Fourier components considered (N=100–200), and V_0 and U_0 are the maximum vertical and horizontal displacements, respectively. $U_0=0$ indicates slip along a vertical fault, $U_0=V_0$ indicates slip along a 45°-dipping reverse fault, and $U_0=-V_0$ indicates slip along a 45°-dipping normal fault.

The second class of basal displacement, for a single earthquake, combines fault slip and the elastic deformation of the basement. To calculate this combined deformation, we used the computer program DIS3D (Erickson, 1987), which calculates the displacements, strains, and stresses in an elastic half-space due to slip along one or more dislocations. The selected fault slip and fault inclination were substituted into the program, and the displacements were calculated for plane-strain conditions. The basal displacements along a horizontal surface that is at the depth of the base of the layered sequence (generally, 5-km depth) are then transformed into a Fourier series in which the vertical component is the sine series and the horizontal component is the cosine series. We used 100 to 200 waves to obtain a good approximation of the displacement. The results of this transformation are substituted into the analytical solution of the layered sequence as the basal-displacement boundary condition. In so doing, we assume that the displacements at the top of the basement (that is, the base of the layers) due to slip along a fault embedded within it are only slightly affected by the layering above the basement.

The third step is the main computation stage. The stress and displacement equations (eqs. 3, 4) are substituted into the boundary conditions between the layers (eq. 6 or 7), at the top (eq. 8), and at the base (eq. 9). The $4K$ linear equations for each wavelength are solved simultaneously to determine the set of unknown constants a_i, b_i, c_i, and d_i. These process is repeated for all N wavelengths. Now, the stresses and displacement (eqs. 3, 4) can be calculated for every point within the layered sequence by summation of the N waves' contributions. The results are presented in cross sections that include the displacements and the orientation of the maximum-compressive-stress axes and the intensity of the shear stress (figs. 3, 6, 7).

The distribution and mode of aftershocks could serve as indicators for the slip during the earthquake and preearthquake stresses (Oppenheimer and others, 1988). The aftershocks of the Loma Prieta earthquake display a rather-confusing distribution of focal-plane solutions, with focal solutions of reverse faulting side by side with normal faulting or strike-slip events (Michael, 1991). Because this disorganized pattern persists also in the upper 5 km, we disregard here the focal solutions of the aftershocks and use their spatial distribution . This distribution is correlated with the intensity of the calculated shear stresses (see subsection above entitled "Aftershock Distribution").

The intensity of the shear stress is evaluated by the procedure of Brace and Kohlstedt (1980), who assumed that upper-crustal rocks yield by frictional slip according to Coulomb criteria, with the coefficients of Byerlee's law. Their equation 3 indicates that at a depth of a few kilometers, yielding occurs when

$$\tau = \frac{\sigma_1 - \sigma_3}{2} \approx 2\sigma_3, \qquad (10)$$

where σ_1 and σ_3 are the magnitudes of the maximum and minimum compressive stresses (assuming that $\mu=0.85$). Because the lithostatic load strongly affects frictional sliding τ is divided by the lithostatic pressure to obtained the normalized shear stress,

$$\tau_E = -\frac{\sigma_1 - \sigma_3}{2\rho g Y}, \qquad (11)$$

where ρ is the mean rock density, g is the acceleration due to gravity, and Y is the local depth. t_E can be related to field conditions if the principal stresses are assumed to be horizontal and (or) vertical, in which case it can be shown that

$\sigma_1 = \sigma_H > \sigma_h > \sigma_v = \sigma_3$ for thrusting,

$\sigma_1 = \sigma_H > \sigma_v > \sigma_h = \sigma_3$ for strike-slip conditions,

and $\sigma_1 = \sigma_v > \sigma_H > \sigma_h = \sigma_3$ for normal faulting,

where σ_H and σ_h are the maximum and minimum horizontal stresses and $\sigma_V=\rho g Y$ is the vertical stress. Substituting equation 10 and the conditions of the last three equations into equation 11 reveals that $\tau_E \geq 2$ for thrusting, $\tau_E \geq 1$ for strike-slip conditions, and $\tau_E \geq 0.4$ for normal faulting.

The above equations are for the total stresses, which include the unknown preearthquake stress; this stress is modified because of the slip during the earthquake. Oppenheimer and others (1988) selected various preearthquake stresses to calculate their failure parameter F (which is equivalent to the present parameter τ_E). Because the preearthquake stresses for the Loma Prieta region are unknown, we consider here only changes in the shear stresses. We anticipates that an increase in the shear stress would increase the tendency for local aftershocks. From equation 11, the change in the shear stress during the earthquake is defined as

$$\Delta\tau_E = -\frac{\Delta(\sigma_1 - \sigma_3)}{2\rho g Y}, \qquad (12)$$

which is equivalent to the parameter ΔF of Oppenheimer and others (1988).

In the calculations presented here, we consider shear-stress changes to be significant if $\Delta\tau_E \geq 0.05\tau_E$ (see Oppenheimer and others, 1988, p. 9020–9021). Rock density is assumed to be uniformly equal to 2,650 kg/m^3.

ARE RUPTURE MODELS CONSISTENT WITH GEODETIC MEASUREMENTS?[1]

By Jamison H. Steidl and Ralph J. Archuleta,
University of California, Santa Barbara

CONTENTS

ABSTRACT

We have inverted strong-motion waveform data from the 1989 Loma Prieta earthquake to determine the spatial and temporal distribution of slip during the rupture process. The best-fitting solution determined by matching numerically computed waveforms with the observed data is bimodal, with large slip amplitudes north and south of the hypocenter. South of the hypocenter, the slip is predominantly strike slip; north of the hypocenter, the slip is predominantly dip slip. This slip occurs between 7- and 19-km depth. These two regions both have at least 1.0 m of slip, and some interior localized areas have 3.0 to 4.0 m of slip. This heterogeneous distribution of slip produces a static-strain field that can be compared with the coseismic geodetic observations. The strain field determined from the strong-motion inversion (independent of the geodetic data) predicts many, but not all, of the geodetic measurements. We present forward calculations of the static-strain field and examine the source of misfit to the observations by comparing observed with calculated line-length changes. We compare the use of homogeneous velocity models with that of vertically heterogeneous velocity models in calculating the strain field. The geodetic monument on Loma Prieta peak is located in a nodal position with respect to the inferred fault surface. This location makes the observations at Loma Prieta difficult to match by using a fault surface located along the aftershock distribution. When the Loma Prieta monument is removed from the data set, faulting models offset from the aftershock distribution fit the rest of the data no significantly better than do faulting models located along the aftershock distribution.

INTRODUCTION

The 1989 Loma Prieta earthquake provided one of the most complete sets of near-source strong-motion data ever recorded. In addition, it occurred within a region where surface displacements have been monitored frequently, using electronic distance measurement (EDM), the Global Positioning System (GPS), and very long baseline interferometry (VLBI). This paper compares the static-strain field calculated by using the slip model determined from the acceleration records (Steidl and others, 1991) with these geodetic measurements.

Complex spatial distributions of slip have been demonstrated for many earthquakes (for example, Aki, 1968; Trifunac, 1974; Heaton and Helmberger, 1979; Archuleta and Day, 1980; Bouchon, 1982; Olson and Apsel, 1982; Hartzell and Heaton, 1983, 1986; Archuleta, 1984; Fukuyama and Irikura, 1986; Beroza and Spudich, 1988; Hartzell, 1989; Mendoza and Hartzell, 1989; Hartzell and Iida, 1990; Beroza, 1991; Hartzell and Mendoza, 1991; Hartzell and others, 1991; Steidl and others, 1991; Wald and others, 1991). Determination of the static-slip distribution is important because this distribution sets the stage for future events. Under the seismic-gap hypothesis, regions of high slip would have a lower probability of producing another event in the near future. The Loma Prieta rupture failed to reach the surface, leaving no direct measurements of the slip. The determination of slip is therefore left to be examined by an analysis of seismologic and geodetic data sets.

Our understanding of the rupture process and energy release during dynamic rupture cannot be examined by using geodetic measurements. Most geodetic modeling

---

[1] Contribution No. 0095–13EQ, Institute for Crustal Studies, University of California, Santa Barbara, CA 93106.

provides an estimate of only the average slip that occurs on a finite fault; information about the dynamic rupture process is left to seismologic modeling. In this paper, we discuss one of many dynamic-slip models determined from the seismologic data set and examine how well such a model can predict the geodetic measurements. We also examine the difference between using a homogeneous elastic half-space and a vertically layered elastic medium in calculating the surface displacements at geodetic stations.

In general, for large earthquakes, the distribution of aftershocks outlines the fault surface on which slip occurred during the main shock (Mendoza and Hartzell, 1988). The well-located aftershocks of the 1989 Loma Prieta earthquake are concentrated on a planar feature about 3 km wide. Although the dip of the aftershocks varies somewhat from south to north, they outline a consistent surface that dips approximately 70°. Modeling of the static horizontal deformation and the elevation changes due to the earthquake has provided best-fitting planar faults that are offset from the distribution of aftershocks by about 4 km (Lisowski and others, 1990; Marshall and others, 1991). In another study, Snay and others (1991) modeled horizontal deformation and determined a best-fitting model defined by a kinked fault surface, more consistent with the aftershock distribution.

We hypothesize that the use of observations at Loma Prieta (sta. LP), located along the updip projection of the aftershocks, caused this offset in fault location. Because station LP is nearly nodal for a fault surface consistent with the aftershock distribution, data from this station are pivotal in any analysis that allows the fault surface to move so as to reduce the misfit between predictions and observations. We examine the horizontal deformation by computing the displacements numerically for both nonuniform and uniform slip, as well as for both homogeneous and layered half-spaces, to try to resolve the source of this discrepancy. We compute line-length changes between station pairs from the model displacements and compare them with the observed line-length changes to determine how well each model fits the data.

DATA

The strong-motion data set used in this study is the same as that used by Steidl and others (1991). It consists of horizontal and vertical accelerograms recorded at stations operated by the California Division of Mines and Geology (CDMG) and the U.S. Geological Survey (USGS) (table 1). The distribution of stations is shown in figure 1.

Because of the difficulty in modeling high frequencies, the uncorrected acceleration records were integrated to particle velocity. The data were then bandpass filtered with corner frequencies at 0.05 Hz (that is, static displacements removed) and 1.0 Hz to allow for a direct comparison between data and synthetic seismograms in the same bandwidth.

The surface-displacement data used in this study consist of the relative changes in the positions of geodetic monuments, measured primarily by Geodolite and supplemented by a few GPS and VLBI observations. This data set is the same as that used by Lisowski and others (1990) to determine a model fault for the 1989 Loma Prieta earthquake. Errors in the measurements and information on preprocessing of the data to remove the secular motion and offsets due to previous earthquakes were discussed by Lisowski and others (1990). The coseismic line-length changes between monuments are the data that we attempt to match in our numeric calculations.

METHODS

STRONG-MOTION MODELING

The determination of the spatial and temporal rupture characteristics for the rupture model used in this study was described in detail by Steidl and others (1991). We summarize the method here. A fault surface striking 126° and dipping 70° is divided into equal-area subfaults (fig. 2). The fault surface is 38 km long and has a downdip width of 17 km, extending from 3- to 19-km depth. The allowable rupture zone comprises 152 subfaults, each 2 km by 2.125 km. The hypocenter is located midway along strike at 18-km depth (Langston and others, 1990; U.S. Geological Survey staff, 1990).

Complete synthetic ground motions, including body waves, surface waves, and leaky modes, are generated for every subfault in the frequency range 0.0–1.5 Hz, using discrete-wavenumber/finite-element (DWFE) Green's functions (Olson and others, 1984). The subfault synthetic time histories are then filtered and interpolated in exactly the same way as the data. For each station, subfault synthetic seismograms are summed to produce a total synthetic seismogram, using the method of Hartzell and Heaton (1983). Each subfault has a time delay that takes into account the rupture time, the time at which slip initiates on the subfault. The station synthetic seismograms are aligned with the data by matching the arrival time of the direct *S* wave off the hypocenter subfault with the arrival time of the direct *S* wave. The velocity model used in calculating the Green's functions is listed in table 2 (Dietz and Ellsworth, 1990).

The waveform-inversion technique used in generating the rupture model is a linearized iterative least-squares inversion that determines both the spatial and temporal dynamic characteristics of the rupture process (Hartzell, 1989). The initial conditions for the rupture model used in

Table 1.—*Strong-motion stations*

[APEEL, Andreas Peninsula Earthquake Engineering Laboratory; SAGO, San Andreas Geophysical Observatory; SLAC, Stanford Linear Accelerator Center; UC, University of California; VA, Veterans' Administration. Station owners: C, California Division of Mines and Geology; U, U.S. Geological Survey]

Station		Latitude °N.	Longitude °W.	Epicentral distance (km)	Owner and station No.	Components
Code	Name					
COR	Corralitos[1,2]	37.046	121.083	5	C–57007	90°, 0°
WAT	Watsonville[2]	36.909	121.756	20	C–47459	90°, 0°
CAP	Capitola[1]	36.974	121.952	10	C–47125	90°, 0°
UCS	UC Santa Cruz[1]	37.001	122.060	15	C–58135	90°, 0°
GOF	Gilroy, Historical Building[2]	37.009	121.569	30	C–57476	180°, 90°
GGC	Gilroy, Gavilan College[1]	36.973	121.568	30	C–47006	67°, 337°
GI1	Gilroy array station 1[1,2]	36.973	121.572	30	C–47379	90°, 0°
GI2	Gilroy array station 2[2]	36.982	121.556	30	C–47380	90°, 0°
GI3	Gilroy array station 3[2]	36.987	121.536	30	C–47381	90°, 0°
GI4	Gilroy array station 4[2]	37.005	121.522	30	C–57382	90°, 0°
GI6	Gilroy array station 6[1,2]	37.026	121.484	35	C–57383	90°, 0°
GI7	Gilroy array station 7[1]	37.033	121.434	40	C–57425	90°, 0°
SAR	Saratoga[1]	37.255	122.031	30	C–58065	90°, 0°
HOL	Hollister (South and Pine Sts.)[2]	36.848	121.397	50	C–47524	90°, 0°
ASH	Agnews State Hospital[2]	37.397	121.952	45	C–57066	90°, 0°
FRS	Foster City, Redwood Shores[2]	37.550	122.230	70	C–58375	90°, 0°
ADL	Anderson Dam, abutment[1]	37.166	121.628	30	U–1652	340°, 250°
ADD	Anderson Dam, downstream[1,2]	37.166	121.628	30	U–1652	340°, 250°
SUN	Sunnyvale[2]	37.402	122.024	45	U–1695	0°, 270°
HOA	Hollister Airport[2]	36.888	121.413	45	U–1656	255°, 165°
PAH	Palo Alto VA Hospital	37.400	122.140	50	U–1227	302°, 212°
SLA	Stanford, SLAC[2]	37.419	122.205	50	U–1601	0°, 270°
HCH	Hollister City Hall[2]	36.851	121.402	50	U–1575	0°, 270°
SPG	Stanford parking garage	37.431	122.171	50	U–(NA)	0°, 270°
MPH	Menlo Park VA Hospital	37.468	122.157	55	U–1230	110°, 20°
FRE	Fremont, Emerson Court[1]	37.535	121.929	55	U–1686	180°, 90°
RED	Redwood City, APEEL station 2	37.520	122.250	65	U–1002	133°, 43°
LEX	Lexington Dam, abutment[2]	37.202	121.949	20	C–57180	90°, 0°
CLD	Coyote Lake Dam, downstream[1,2]	37.118	121.550	30	C–57504	195°, 105°
CLA	Coyote Lake Dam, abutment[2]	37.124	121.551	30	C–57217	195°, 105°
HVL	Halls Valley, Grant Park[1,2]	37.338	121.714	35	C–57191	90°, 0°
SAG	SAGO South, Hollister[1,2]	36.753	121.396	50	C–47189	261°, 171°
SAL	Salinas[1,2]	36.671	121.642	45	C–47179	160°, 70°
MCH	Monterey City Hall[1,2]	36.597	121.897	50	C–47377	90°, 0°
WFS	Woodside Fire Station[1]	37.429	122.258	55	C–58127	90°, 0°
CSS	Crystal Springs Reservoir, Skyline[1]	37.465	122.323	65	C–58373	90°, 0°
CSP	Crystal Springs Reservoir, Pulgas[1,2]	37.490	122.310	65	C–58378	90°, 0°
FMS	Fremont, Mission San Jose[1,2]	37.530	121.919	55	C–57064	90°, 0°

[1] Station used in model 14 of Steidl and others (1991).

[2] Station with absolute time.

this study are low uniform slip and a constant rupture velocity of 3.0 km/s. The slip-rate function used is an isosceles triangle with a pulse width of 1.0 s (model 14 of Steidl and others, 1991, table 3). Subfault synthetic seismograms for strike-slip (180° rake) and dip-slip (90° rake) mechanisms are generated from each of the 152 subfaults, for all components, at every station. These subfault synthetic seismograms are summed to produce a total station synthetic seismogram. Slip-amplitude and rupture-velocity perturbations are determined simultaneously for each subfault at each iteration by solving an overdetermined system of linear equations that relates the synthetic to the observed time histories. The model is updated, and new synthetic seismograms are calculated, using the new perturbed model. This procedure is done iteratively until further iterations fail to provide a significant reduction in the rms residual error (Euclidean norm between observed and synthetic seismograms). The strike-slip component is constrained to be right lateral, and the dip-slip component is separately constrained to be reverse slip or thrusting. Both components have minimization and smoothing constraints, as used by Hartzell and Iida (1990).

GEODETIC MODELING

The method described above calculates the ground velocity at a particular location due to traction on the fault. This response includes zero frequency. Thus, we can use this technique to do a forward calculation of the static displacement at a particular location due to a specified rupture model. This method allows us to model the static displacements at geodetic stations, using a layered elastic half-space. We first use a three-dimensional-dislocation computer program, DIS3D (Erickson, 1986), to calculate the displacements for all models that use a homogeneous half-space. The elastic field equations in the program DIS3D are similar in form to those of Mansinha and oth-

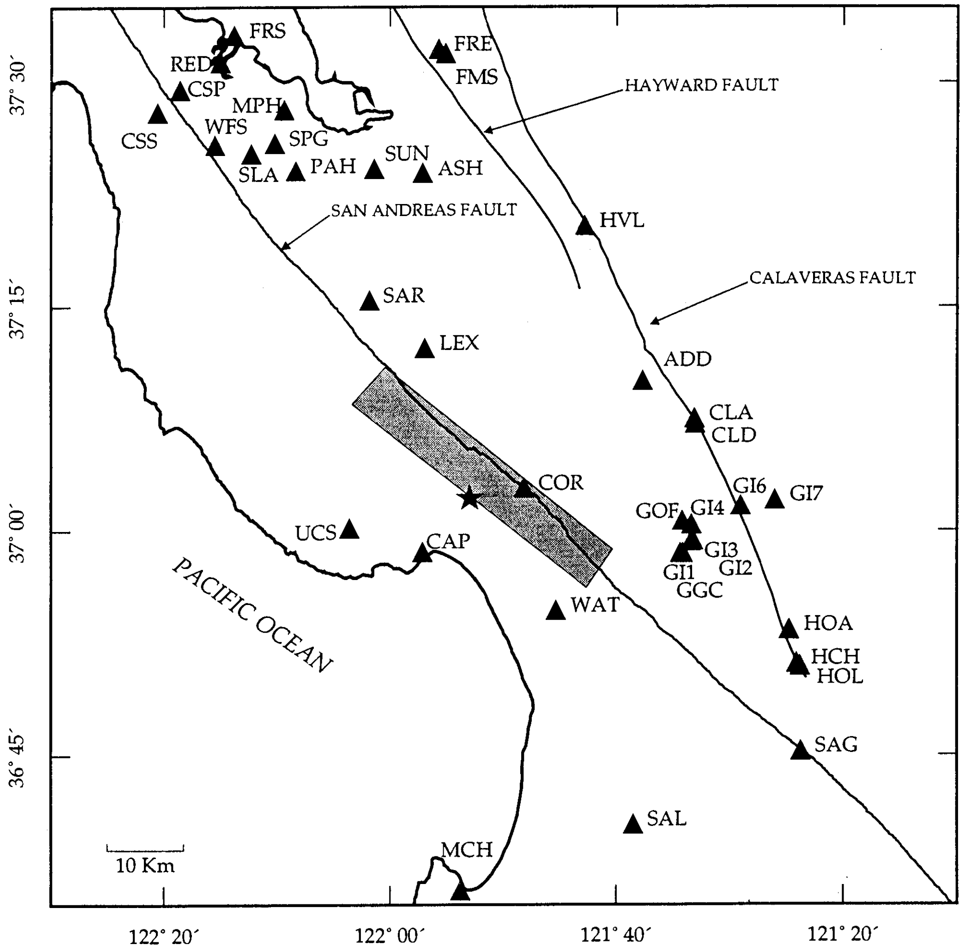

Figure 1.—Loma Prieta region, Calif., showing locations of strong-motion stations used in this study (triangles) and surface projection of inferred rupture zone (shaded area). Star, epicenter of 1989 earthquake. See table 1 for station names and codes.

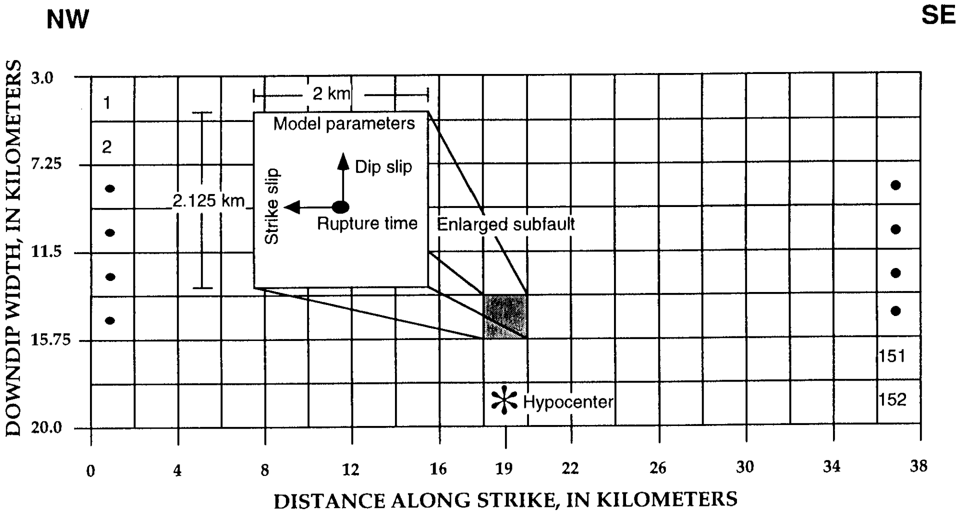

Figure 2.—Cross section of model fault used in this study, comprising a total of 152 subfaults with equal dimensions (2 by 2.125 km). Enlarged subfault shows inversion parameters.

Table 2.—*One-dimensional velocity structure*

Depth interval (km)	V_P (km/s)	V_S (km/s)	Density (g/cm^3)	Thickness (km)
0.0–0.5	3.34	1.67	2.5	0.5
.5–1.0	4.23	2.2	2.6	.5
1.0–3.0	5.01	2.89	2.65	2.0
3.0–5.0	5.63	3.25	2.72	2.0
5.0–7.0	5.89	3.4	2.76	2.0
7.0–9.0	6.24	3.6	2.79	2.0
9.0–13.0	6.26	3.61	2.8	4.0
13.0–18.0	6.3	3.64	2.82	5.0
18.0–25.0	6.69	3.86	2.9	7.0
>25.0	8.0	4.62	3.2	--

ers (1971). We then apply our method to the case of the layered elastic half-space listed in table 2 (Dietz and Ellsworth, 1990).

The parameters we vary in the geodetic forward calculation are the strike, the slip distribution, the fault location/geometry, and the medium properties. We examined strikes of 126° and 136°. We looked at the difference between using a single fault with uniform slip and using a nonuniform slip distribution with the fault parametrization shown in figure 2. We used two locations for the fault: (1) along the aftershock distribution, as mentioned in the fault parametrization of the strong-motion inversion; and (2) in the same place as Lisowski and others (1990), offset from the aftershock distribution. The various fault geometries used in this study are listed in table 3. We use either a homogeneous, isotropic elastic half-space or a vertically layered elastic half-space for the medium properties.

Our objective is to see how consistent the rupture models determined from the strong-motion data (independent from the geodetic data) are with the observed ground displacements. We are also interested in the difference between modeling the geodetic measurements with a uniform half-space (as most geodetic modeling has been done in the past) with a layered half-space. We did not, however, try to search the parameter space for a best fit to the geodetic data, but only examined end-member models.

We determine the error for all our models from the equation

$$W_{\mathrm{rms}} = \left[\frac{\sum_{l=1}^{N} \left(\frac{R_l}{\sigma_l} \right)^2}{N_{\mathrm{P}}} \right]^{1/2}, \qquad (1)$$

where the rms residuals, R_l, are the absolute value of the observed minus calculated line-length changes. Each rms residual is weighted by the standard deviation of the measured line-length change (σ_l); the total error, W_{rms}, for each model is the square root of the sum of the squares of these weighted rms residuals divided by the number of station pairs (N_P). The results of our geodetic forward modeling are summarized in table 4.

RESULTS

STRONG-MOTION MODELING

The slip distribution presented here is the best-fitting solution using horizontal and vertical records for 20 stations (fig. 1; table 1), as described by Steidl and others (1991). Other nonuniform-slip models have been proposed by Beroza and others (1991), Hartzell and others (1991), and Wald and others (1991). Contours of the slip distribution, projected onto the fault plane, are shown in figure 3. The bimodal distribution of slip, characteristic of all nonuniform-slip models for this event, is clearly visible in figure 3. Strike slip is dominant south of the hypocenter (fig. 3*A*; table 5), whereas dip slip is dominant north of the hypocenter (fig. 3*B*; table 6). The rake vector for the south and north halves of the fault clearly shows rotation in all the models presented by Steidl and others (1991). In figure 3, the average rake on the south half of the fault is 156°, whereas the average rake of the north half of the fault is 115°. We use the convention of Aki and Richards (1980) here in defining the rake angle. The average rake over the whole fault is 137°, comparable to the 135°±10° found in teleseismic and longer period studies (Choy and Boatwright, 1990; Kanamori and Satake, 1990; Romanowicz and Lyon-Caen, 1990; Zhang and Lay, 1990; Wallace and others, 1991). Far-field studies seem to show an average rake for the bimodal slip distribution in figure 3.

The slip in this model occurs between 7- and 19-km depth. Both the northern and southern fault patches have at least 1.0 m of slip, and some interior localized areas have 3.0 to 4.0 m of slip. The rupture front propagates outward from the hypocenter bilaterally at an average velocity of 3.0 km/s, and the main moment release, 3.35×10^{26} dyne-cm, is complete within 7.0 s. The unusually small amount of slip at the hypocenter agrees with the idea that the main shock began as a smaller event which then triggered the larger rupture. Ellsworth (1991, 1992) and Wald and others (1991) discussed evidence for this foreshock.

GEODETIC MODELING

The results of forward modeling of the geodetic data are summarized in table 4, where the column labeled "E_1" contains the W_{rms} error using all line-length changes.

Table 3.—*Fault geometry*

Geometry	Depth interval (km)	Length (km)	Location of upper northwest corner		Depth to upper northwest corner (km)	Strike	Dip
			Lat N.	Long W.			
A	5.0–17.5	37.0	37.195°	122.034°	5.0	136°	70°
B	5.0–17.5	37.0	37.187°	121.989°	5.0	136°	70°
C	3.0–19.0	38.0	37.184°	122.007°	3.0	126°	70°
D	3.0–19.0	38.0	37.194°	121.987°	3.0	136°	70°

Table 4.—*Geodetic forward-modeling results*

Model	Dislocation type	Slip	Geometry	E_1	Percentage of E_1 from station LP	E_2
1	1 dislocation surface----	Lisowski and others (1990)	A	3.01	29	2.76
2	1 dislocation surface----	do.	B	4.16	53	3.10
3	1 dislocation surface----	NL 14 (average)	C	3.87	30	3.49
[1]4	152 dislocations---------	NL 14	C	5.56	75	3.08
[1]5	152 dislocations---------	NL 14	D	5.04	75	2.76

[1] One-dimensional layered half-space (see table 2).

Model 1, which has the lowest W_{rms} error (E_1) and could be considered the best-fitting model for the complete data set, is the model of Lisowski and others (1990), with 1.19 m of dip slip and 1.66 m of strike slip. The fault geometry and location used in model 1 (fig. 4; geometry A, table 3) are identical to those of Lisowski and others. Model 1 is the control model for this study. We compare the error from models 2 through 5 with that from model 1 (table 4) for comparison with the preferred geodetic model of Lisowski and others. This difference does not become statistically significant (*F* test, 95-percent-confidence level) until the ratio of the W_{rms} error (model *N*/model 1, where N=2–5) exceeds 1.47. Therefore, the difference between models 1, 2, and 3 is not statistically significant (table 4). Models 4 and 5, however, which use a nonuniform slip distribution (fig. 3) and the one-dimensional layered half-space (table 2), fit the data significantly worse (table 4).

Station LP is located in a nodal position with respect to a fault surface defined by the distribution of aftershocks. This location makes the observed large displacements at station LP anomalous. Approximately 20 percent of the line-length measurements are tied to station LP. We now investigate the anomalously large displacements observed at station LP as a possible source for the misfit in the models. The contribution to the W_{rms} error from only the line-length changes tied to station LP ("percentage of E_1 from station LP") and the error from all line-length measurements except station LP ("E_2") are listed in table 4.

We compare the fit to the line-length changes of models 1 and 2 to examine why the geodetic measurements prefer the fault-plane offset from the aftershock distribution. Model 2 uses a fault with the same dimensions, orientation, and slip as model 1 but with a location moved onto the aftershock distribution (fig. 5; geometry B, table 3). Model 2 has 53 percent of the error due to station LP, whereas model 1 has 29 percent of the error due to station LP. The geodetic modeling of Lisowski and others (1990) prefers a fault plane offset from the aftershock distribution to better fit the line-length changes at station LP and reduce the overall error. The overall error (E_1) and the error excluding the data tied to station LP (E_2) are slightly larger, but not significantly different, for model 2 than for model 1 (table 4).

Next, we examine how well the average slip determined in the strong-motion model of Steidl and others (1991) can predict the geodetic measurements. Model 3 uses geometry C (table 3) and the average slip amplitudes from the nonuniform slip distribution shown in figures 3*A* and 3*B* (1.02 m of dip slip and 1.13 m of strike slip), adjusted for use in a homogeneous half-space. The fault geometry and location in model 3 are identical to that used in the strong-motion model. We find that the error due to station LP in model 3 is 30 percent, close to that in model 1. The overall error (E_1) and the error excluding the data tied to station LP (E_2) are slightly larger, but not significantly different, for model 3 than for model 1 (table 4).

Models 4 and 5 test the use of a vertically heterogeneous medium (table 2) and a nonuniform slip distribution (fig. 3) when calculating the displacements. Using a more complex (realistic) velocity structure and slip distribution, intuition suggests that we should be better able to predict the geodetic measurements. Contrary to intuition, however, table 4 shows that the overall error (E_1) is significantly larger after making these changes to more realistic models. Initial interpretation of these results suggests that the geodetic measurements are inconsistent with the rupture model determined from the strong-motion data. Closer examination of the source of error in these models allows for reinterpretation of these results.

The geometry of models 4 and 5 is listed in table 3 (geometries C and D, respectively). The only difference between models 4 and 5 is the strike of the fault. The overall error is less for a fault that strikes 136°, suggesting that the geodetic measurements prefer this strike, although the error does not differ significantly from that for a fault which strikes 126°. Models 4 and 5 have 75 percent of their error from station LP. When we remove station LP from the data set ("E_2", table 4), the errors decrease

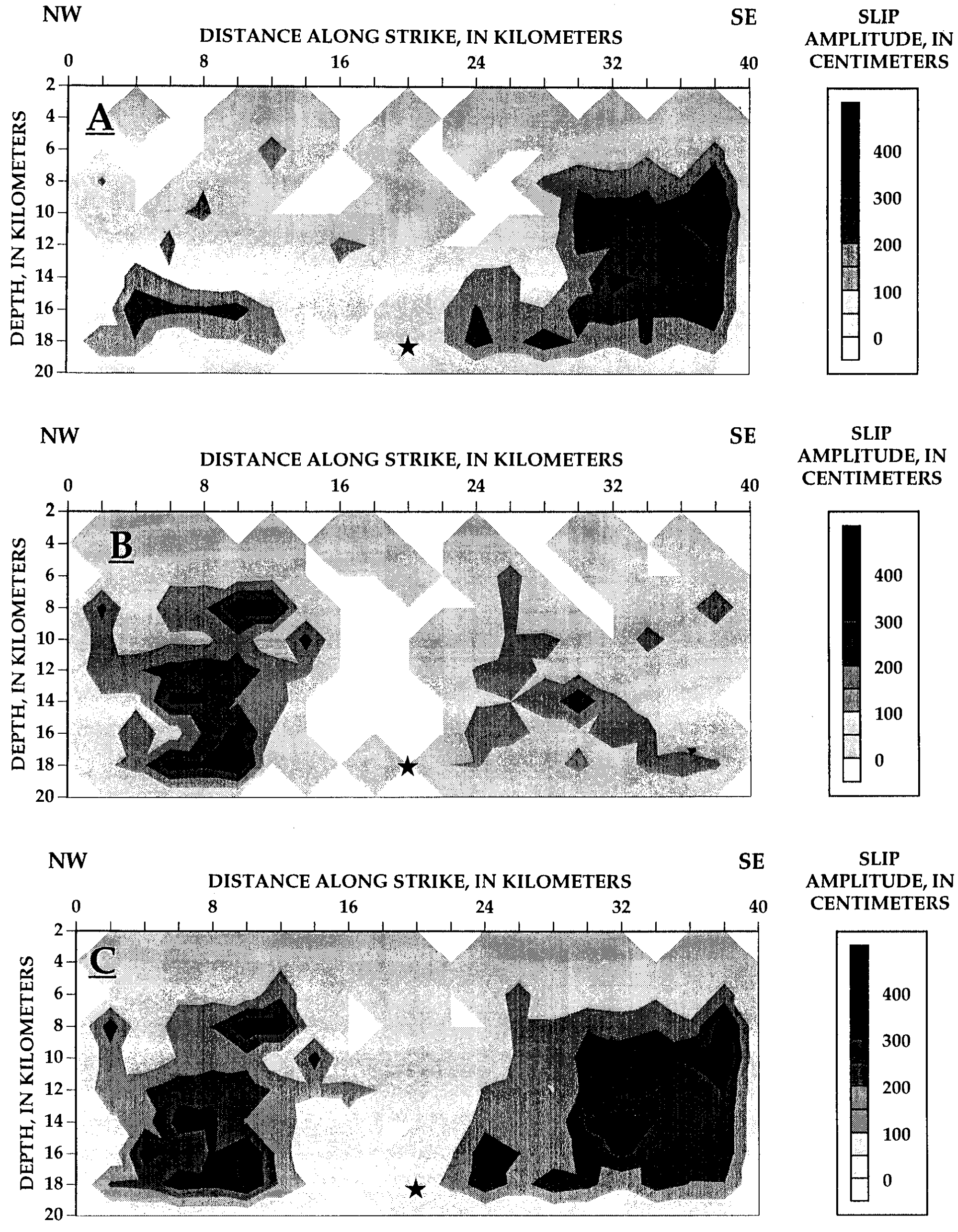

Figure 3.—Fault slip determined by inverting 40 horizontal and 20 vertical time histories (20.0 s) of ground velocity (model 14 of Steidl and others, 1991). Cross section of fault surface with depth is oriented perpendicular to fault from southwest; that is, variables are plotted on footwall. *A*, Strike-slip motion. *B*, Dip-slip motion. *C*, Total slip.

Table 5.—*Strike-slip displacements in strong-motion inversion for model 14 of Steidl and others (1991)*

[All values in centimeters at center of each subfault; positive values correspond to a rake of 180°. Distance along strike is from northwest end to center of each subfault]

	Depth to center of subfault (km)							
Distance along strike (km)	4	6	8	10	12	14	16	18
1	0	0	115	24	0	0	0	200
3	17	0	0	0	44	146	294	196
5	0	0	0	75	122	89	234	0
7	0	0	89	130	8	23	221	86
9	26	4	13	9	39	0	256	94
11	8	167	64	0	27	12	109	176
13	11	17	0	0	5	0	0	0
15	0	0	0	0	136	74	10	0
17	0	47	0	22	93	0	0	0
19	31	0	87	0	52	0	1	45
21	0	0	0	60	0	2	90	88
23	16	8	0	0	0	142	213	251
25	7	0	0	0	32	149	143	156
27	4	0	129	0	41	0	111	269
29	0	37	192	232	220	141	242	194
31	28	1	169	239	204	326	270	119
33	0	84	191	236	257	291	225	219
35	7	0	123	321	201	251	225	105
37	16	142	306	422	317	280	273	160

Table 6. —*Dip-slip displacements in strong-motion inversion for model 14 of Steidl and others (1991)*

[All values in centimeters at the center of each subfault; positive values correspond to a rake of 90°. Distance along strike is from northwest end to center of each subfault]

	Depth to center of subfault (km)							
Distance along strike (km)	4	6	8	10	12	14	16	18
1	49	0	233	147	183	76	20	81
3	84	20	0	14	193	69	187	129
5	61	72	167	79	243	323	38	362
7	22	69	184	74	281	318	216	324
9	0	43	397	166	252	191	350	416
11	75	60	393	13	174	192	92	0
13	0	0	17	244	125	0	0	75
15	31	0	0	0	0	0	0	0
17	59	0	0	0	0	0	0	63
19	0	24	0	0	0	0	0	0
21	0	0	0	4	19	0	0	97
23	14	18	0	17	112	91	158	111
25	0	154	132	119	145	99	143	35
27	0	0	5	126	87	137	68	61
29	18	0	0	72	69	281	74	130
31	22	21	0	0	39	121	167	31
33	0	0	25	153	27	64	130	135
35	13	0	29	52	0	10	10	167
37	0	15	209	1	7	0	12	118

to a level that is statistically indistinguishable from that in the other models, suggesting that the geodetic measurements are consistent with the strong-motion model except at one station, LP.

The calculated displacements (dashed vectors with tail located at station) for models 3 and 5 are plotted on top of the observed displacements (solid vectors) in figures 4 and 5, respectively. The observed displacements were calculated by using the "model coordinate" solution of Segall and Matthews (1988). The vertical surface projections of the four fault geometries used in this study are also shown in figures 4 and 5.

DISCUSSION

The results presented in the preceding section show that in modeling the geodetic measurements, the results can be strongly influenced by a single station. Station LP is used for many of the geodetic measurements; its location, almost directly updip from the buried fault surface, is nearly nodal in our theoretical fault geometry. With so many of the geodetic measurements tied to only one station, LP, modeling the horizontal deformation is strongly controlled by the fit to this station. The GPS and trilateration measurements at station LP show relatively large displacements, a result inconsistent with its nodal location. This seems to be the reason why geodetic modeling of the horizontal deformation has to force the location of the nodal plane to the southwest, either by moving the entire fault surface southwestward (Lisowski and others, 1990) or by placing a kink in the fault and projecting the upper half of the fault vertically upward to the surface (Snay and others, 1991). Unless evidence exists as to why the aftershocks and main-shock hypocenter would occur

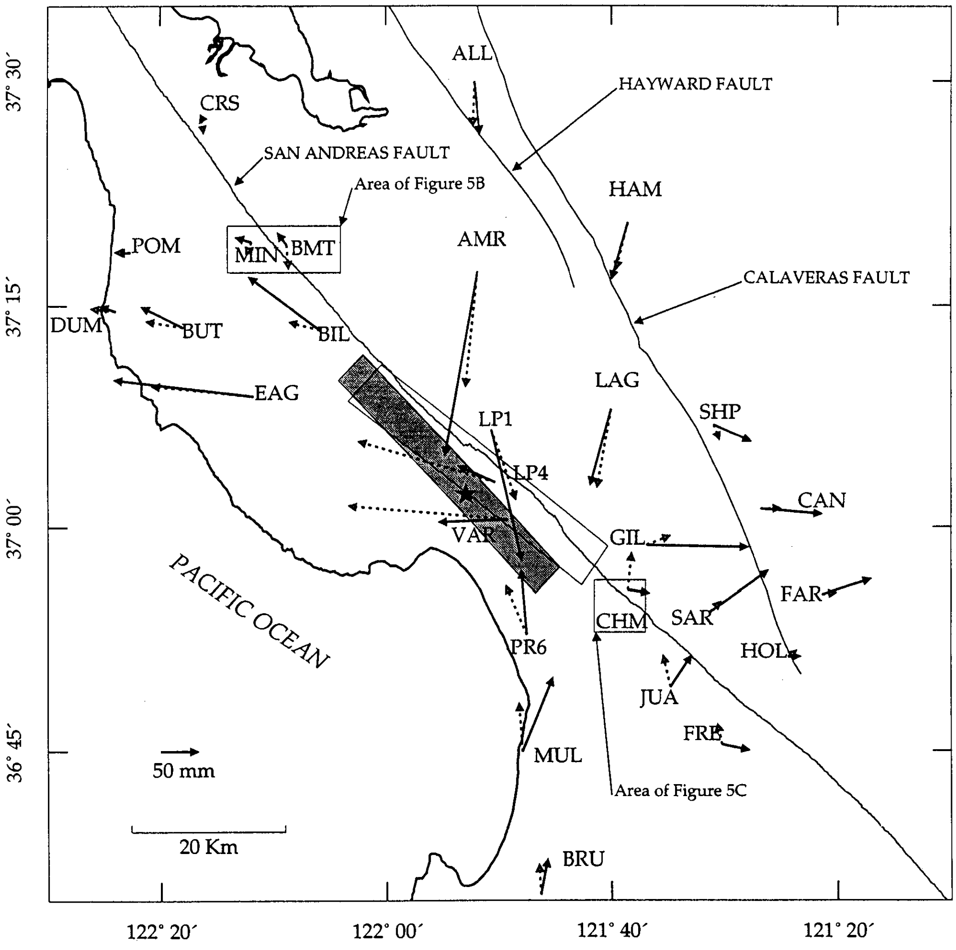

Figure 4.—Loma Prieta region, Calif., showing observed geodetic-station displacements (solid vectors) and displacements calculated by using slip distribution of model 3 (dashed vectors) (see table 4). Large clear rectangle, surface projection of fault geometry used in this model, with epicenter (star) located at bottom edge, midway along strike (geometry C, table 3); shaded rectangle, surface projection of fault geometry used in model 1 (geometry A, table 3). Small clear rectangles show areas of smaller networks in figures 5*B* and 5*C*.

systematically offset from the fault surface, we argue that better fits to the geodetic measurements must come from more realistic models of the local velocity structure and of the slip distribution, not from repositioning the fault.

Three-dimensional velocity models of the Loma Prieta region show large variations in the velocity structure from the simple one-dimensional model used in this study (Eberhart-Phillips and others, 1990a, b; Lees, 1990; Michael and Eberhart-Phillips, 1991; Eberhart-Phillips and Stuart, 1992; Lees and Shalev, in press). These variations affect the calculated surface deformations. The large velocity gradient from the hanging wall to the footwall (low to high velocity) in the vicinity of station LP has the effect of shifting the nodal plane of the surface displacements and increasing their amplitudes (Eberhart-Phillips and Stuart, 1992). This effect would account for the underprediction of the displacement at station LP when using simple homogeneous or vertically heterogeneous velocity models and a fault surface located along the aftershock distribution (figs. 4, 5).

The average seismic moment calculated from the strong-motion inversions, 3.5×10^{26} dyne-cm (Steidl and others, 1991), is comparable to the seismic moment determined from the geodetic data, 3.0×10^{26} dyne-cm (Lisowski and others, 1990). Increasing the slip amplitude to match the underprediction of the displacement at station LP would produce a seismic moment inconsistent with the accepted range of values for the earthquake, as well as destroy the fit to the amplitude of particle velocities in the strong-motion data. Owing to the band limitation of the strong-motion data, a long-duration, low-amplitude tail in the slip-rate function is unresolvable. We could add this tail to our slip-rate function without destroying the fit to the strong-motion data, and simultaneously increase the static

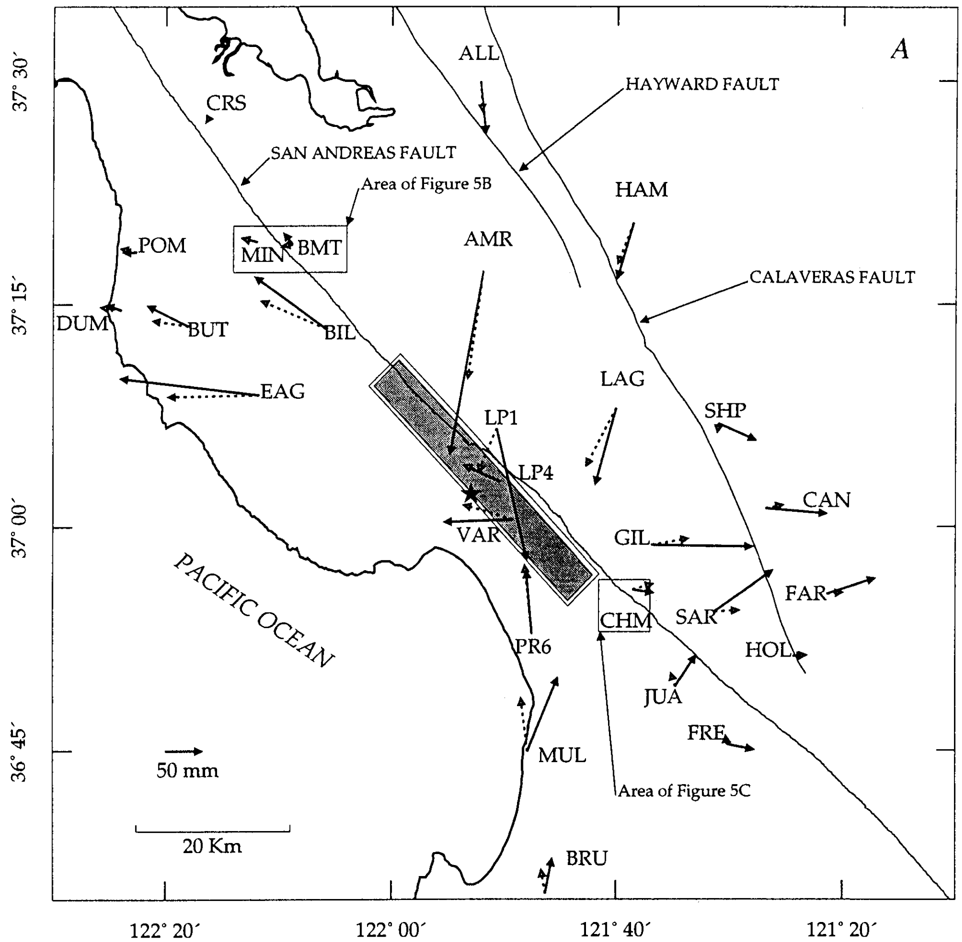

Figure 5.—Loma Prieta region, Calif. (*A*), showing observed geodetic-station displacements (solid vectors) and displacements calculated by using slip distribution of model 5 (dashed vectors) (table 4). Large open rectangle, surface projection of fault geometry used in this model, with epicenter (star) located at bottom edge, midway along strike (geometry D, table 3); shaded rectangle, surface projection of fault geometry used in model 2 (geometry B, table 3). *B*, Black Mountain network. *C*, Southern network.

displacements measured at the geodetic monuments, but not without increasing the seismic moment to values inconsistent with geodetic and far-field studies.

The fact that the strong-motion modeling produces the same seismic moment as do the longer period studies suggests that the slip is completely recovered by the strong-motion inversion. If local movements on faults in the vicinity of station LP had occurred aseismically immediately after the coseismic faulting, these movements could explain the anomalous displacement at this station. We choose to account for the underprediction of the displacement at station LP by invoking some local site condition (for example, lateral heterogeneities or aseismic movement on faults in the vicinity), not an absence of seismic moment in our model.

Apparently, we have run into the same limitations when modeling the geodetic measurements as when fitting the strong-motion data. We fail to take into account the inhomogeneities from the source to each specific receiver and therefore are unable to reproduce the response at each site exactly. In modeling the geodetic measurements from the earthquake, we chose not to relocate the fault surface offset from the aftershock distribution but to accept the misfit to the data as inherent to the simplification in our

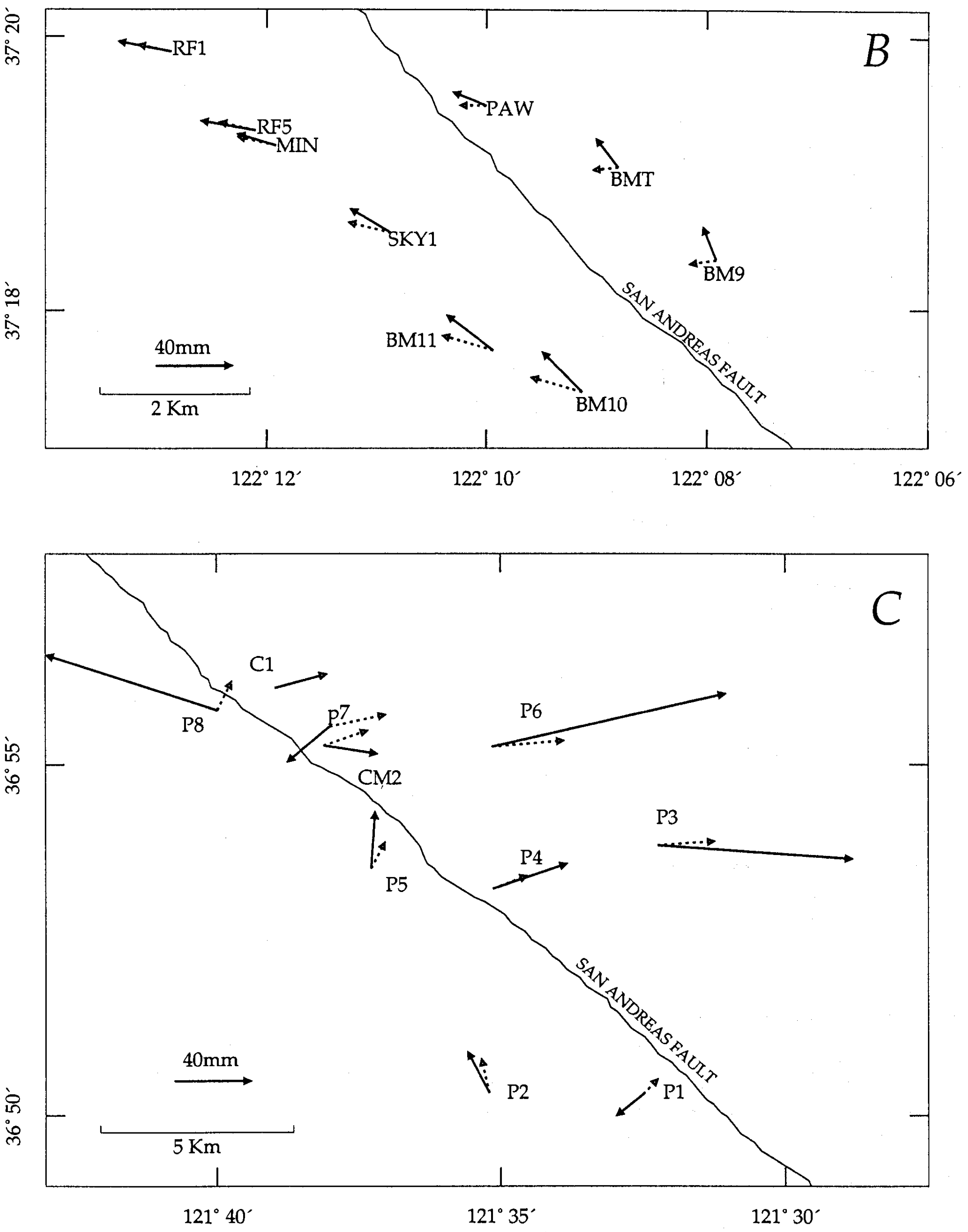

Figure 5.—Continued

model. This study clearly shows that we need to focus our research efforts in the direction of gaining a better understanding of path and site effects. Two- and three-dimensional finite element modeling of wave propagation through a heterogeneous medium should further this aim.

CONCLUSIONS

With our better understanding of how the observations at a single geodetic monument, station LP, can affect the results, we conclude that the rupture models are indeed consistent with geodetic measurements. The overall error for models that have a fault surface located along the aftershock distribution is strongly controlled by this one station. The nodal position of station LP relative to the faulting geometry defined by the aftershocks makes the large displacement observed at station LP anomalous. We suggest that the underprediction of the displacement at station LP is due either to inaccurate representation of the local elastic properties of the Earth or to local aseismic movements in the vicinity of this station. When station LP is removed from the data set, faulting models offset from the aftershock distribution fit the rest of the data no significantly better than do faulting models located along the aftershock distribution. Although moving the fault plane to account for more complex elastic properties of the Earth can improve the fit to the complete data set, we chose not to take this approach. Once agreement is achieved as to the location of the fault surface, improvement in fit to the complete data set must come from either a more complex velocity structure or a more complex model fault (for example, nonplanar).

ACKNOWLEDGMENTS

This research was supported in part by U.S. Geological Survey grant 14-08-0001-G1842. We thank Bob Simpson for providing the computer program DIS3D and for many helpful discussions. Mike Lisowski provided the "model coordinate" solution for the displacement vectors, as well as many helpful discussions. We thank Jim Savage and Paul Spudich for their careful reviews of the manuscript.

REFERENCES CITED

Aki, Keiiti, 1968, Seismic displacements near a fault: Journal of Geophysical Research, v. 73, no. 16, p. 5359–5376.

Aki, Keiiti, and Richards, P.G., 1980, Quantitative seismology; theory and methods: San Francisco, W.H. Freeman, 2 v.

Archuleta, R.J., 1984, A faulting model for the 1979 Imperial Valley earthquake: Journal of Geophysical Research, v. 89, no. B6, p. 4559–4585.

Archuleta, R.J., and Day, S.M., 1980, Dynamic rupture in a layered medium, the 1966 Parkfield earthquake: Seismological Society of America Bulletin, v. 70, no. 3, p. 671–689.

Beroza, G.C., 1991, Near-source modeling of the Loma Prieta earthquake; evidence for heterogeneous slip and implications for earthquake hazard: Seismological Society of America Bulletin, v. 81, no. 5, p. 1603–1621.

Beroza, G.C., and Spudich, Paul, 1988, Linearized inversion for fault rupture behavior; application to the 1984 Morgan Hill, California, earthquake: Journal of Geophysical Research, v. 93, no. B6, p. 6275–6296.

Bouchon, Michel, 1982, The rupture mechanism of the Coyote Lake earthquake of 6 August 1979 inferred from near-field data: Seismological Society of America Bulletin, v. 72, no. 3, p. 745–759.

Choy, G.L., and Boatwright, John, 1990, Source characteristics of the Loma Prieta, California, earthquake of October 17, 1989 from global digital seismic data: Geophysical Research Letters, v. 17, no. 8, p. 1183–1186.

Dietz, L.D., and Ellsworth, W.L., 1990, The October 17, 1989, Loma Prieta, California, earthquake and its aftershocks; geometry of the sequence from high-resolution locations: Geophysical Research Letters, v. 17, no. 9, p. 1417–1420.

Eberhart-Phillips, D.M., Labson, V.F., Stanley, W.D., Michael, A.J., and Rodriguez, B.D., 1990a, Preliminary velocity and resistivity models of the Loma Prieta earthquake region: Geophysical Research Letters, v. 17, no. 8, p. 1235–1238.

Eberhart-Phillips, D.M., Michael, A.J., Fuis, G.S., and Luzitano, R.D., 1990b, Three-dimensional crustal velocity structure in the region of the Loma Prieta, California, earthquake sequence from inversion of local earthquake and shot arrival times [abs.]: Seismological Research Letters, v. 61, no. 1, p. 48.

Eberhart-Phillips, D.M., and Stuart, W.D., 1992, Material heterogeneity simplifies the picture; Loma Prieta: Seismological Society of America Bulletin, v. 82, no. 4, p. 1964–1968.

Ellsworth, W.L., 1991, Nucleation and growth of the Loma Prieta earthquake [abs.]: Eos (American Geophysical Union Transactions), v. 72, no. 72, p. 293.

———1992, Imaging fault rupture without inversion [abs.]: Seismological Research Letters, v. 63, no. 1, p. 73.

Erickson, L.L., 1986, A three dimensional dislocation program with applications to faulting in the earth: Stanford, Calif., Stanford University, M.S. thesis.

Fukuyama, Eiichi, and Irikura, Kojiro, 1986, Rupture process of the 1983 Japan Sea (Akita-Oki) earthquake using a waveform inversion method: Seismological Society of America Bulletin, v. 76, no. 6, p. 1623–1640.

Hartzell, S.H., 1989, Comparison of seismic waveform inversion results for the rupture history of a finite fault; application to the 1986 North Palm Springs, California, earthquake: Journal of Geophysical Research, v. 94, no. B6, p. 7515–7534.

Hartzell, S.H., and Heaton, T.H., 1983, Inversion of strong ground motion and teleseismic waveform data for the fault rupture history of the 1979 Imperial Valley, California, earthquake: Seismological Society of America Bulletin, v. 73, no. 6, p. 1553–1583.

———1986, Rupture history of the 1984 Morgan Hill, California, earthquake from the inversion of strong motion records: Seismological Society of America Bulletin, v. 76, no. 3, p. 649–674.

Hartzell, S.H., and Iida, Mashiro, 1990, Source complexity of the 1987 Whittier Narrows, California, earthquake from the inversion of strong motion records: Journal of Geophysical Research, v. 95, no. B6, p. 12475–12486.

Hartzell, S.H., and Mendoza, Carlos, 1991, Application of an iterative least-squares waveform inversion of strong motion and teleseismic records to the 1978 Tabas, Iran, earthquake: Seismological Society of America Bulletin, v. 81, no. 2, p. 305–331.

Hartzell, S.H., Stewart, G.S., and Mendoza, Carlos, 1991, Comparison of L_1 and L_2 norms in a teleseismic waveform inversion for the slip history of the Loma Prieta, California, earthquake: Seismological Society of America Bulletin, v. 81, no. 5, p. 1518–1539.

Heaton, T.H., and Helmberger, D.V., 1979, Generalized ray models of the San Fernando earthquake: Seismological Society of America Bulletin, v. 69, no. 5., p. 1311–1341.

Kanamori, Hiroo, and Satake, Kenji, 1990, Broadband study of the 1989 Loma Prieta earthquake: Geophysical Research Letters, v. 17, no. 8, p. 1179–1182.

Langston, C.A., Furlong, K.P., Vogfjord, K.S., Clouser, R.H., and Ammon, C.J., 1990, Analysis of teleseismic body waves radiated from the Loma Prieta earthquake: Geophysical Research Letters, v. 17, no. 9, p. 1405–1408.

Lees, J.M., 1990, Tomographic P-wave velocity images of the Loma Prieta earthquake asperity: Geophysical Research Letters, v. 17, no. 9, p. 1433–1436.

Lees, J.M., and Shalev, Eylon, 1992, On the stability of P-wave tomography at Loma Prieta; a comparison of parameterizations, linear and non-linear inversions: Seismological Society of America Bulletin, v. 82, no. 4, p. 1821–1839.

Lisowski, Michael, Prescott, W.H., Savage, J.C., and Johnston, M.J.S., 1990, Geodetic estimate of coseismic slip during the 1989 Loma Prieta, California, earthquake: Geophysical Research Letters, v. 17, no. 9, p. 1437–1440.

Mansinha, Lalatendu, Smylie, D.E., and Orphal, D.L., 1971, The displacement fields of inclined faults: Seismological Society of America Bulletin, v. 61, no. 5, p. 1433–1440.

Marshall, G.A., Stein, R.S., and Thatcher, Wayne, 1991, Faulting geometry and slip from co-seismic elevation changes; the 18 October 1989, Loma Prieta, California, earthquake: Seismological Society of America Bulletin, v. 81, no. 5, p. 1660–1693.

Mendoza, Carlos, and Hartzell, S.H., 1988, Aftershock patterns and main shock faulting: Seismological Society of America Bulletin, v. 78, no. 4, p. 1438–1449.

———1989, Slip distribution of the 19 September 1985 Michoacan, Mexico, earthquake; near-source and teleseismic constraints: Seismological Society of America Bulletin, v. 79, no. 4, p. 655–699.

Michael, A.J., and Eberhart-Phillips, D.M., 1991, Relations among fault behavior, subsurface geology, and three-dimensional velocity models: Science, v. 253, no. 5020, p. 651–654.

Olson, A.H., and Apsel, R.J., 1982, Finite faults and inverse theory with applications to the 1979 Imperial Valley earthquake: Seismological Society of America Bulletin, v. 72, no. 6, pt. A, p. 1969–2001.

Olson, A.H., Orcutt, J.A., and Frazier, G.A., 1984, The discrete wave number/finite element method for synthetic seismograms: Royal Astronomical Society Geophysical Journal, v. 77, no. 2, p. 421–460.

Romanowicz, Barbara, and Lyon-Caen, Hélène, 1990, The Loma Prieta earthquake of October 18, 1989; results of teleseismic mantle and body wave inversion: Geophysical Research Letters, v. 17, no. 8, p. 1191–1194.

Segall, Paul, and Matthews, M.V., 1988, Displacement calculations from geodetic data and the testing of geophysical deformation models: Journal of Geophysical Research, v. 93, no. B12, p. 14954–14966.

Snay, R.A., Neugebauer, H.C., and Prescott, W.H., 1991, Horizontal deformation associated with the Loma Prieta earthquake: Seismological Society of America Bulletin, v. 81, no. 5, p. 1647–1659.

Steidl, J.H., Archuleta, R.J., and Hartzell, S.H., 1991, Rupture history of the 1989 Loma Prieta, California, earthquake: Seismological Society of America Bulletin, v. 81, no. 5, p. 1573–1602.

Trifunac, M.D., 1974, A three-dimensional dislocation model for the San Fernando, California, earthquake of February 9, 1971: Seismological Society of America Bulletin, v. 64, no. 1, p. 149–172.

U.S. Geological Survey staff, 1990, The Loma Prieta, California, earthquake; an anticipated event: Science, v. 247, no. 4940, p. 286–293.

Wald, D.J., Helmberger, D.V., and Heaton, T.H., 1991, Rupture model of the 1989 Loma Prieta earthquake from the inversion of strong motion and broadband teleseismic data: Seismological Society of America Bulletin, v. 81, no. 5, p. 1540–1572.

Wallace, T.C., Velasco, A.A., Zhang, Jiajun, and Lay, Thorne, 1991, A broadband seismological investigation of the 1989 Loma Prieta, California, earthquake; evidence for deep slow slip?: Seismological Society of America Bulletin, v. 81, no. 5, p. 1622–1646.

Zhang, Jiajun, and Lay, Thorne, 1990, Source parameters of the 1989 Loma Prieta earthquake determined from long-period Rayleigh waves: Geophysical Research Letters, v. 17, no. 8, p. 1195–1198.

THE LOMA PRIETA, CALIFORNIA, EARTHQUAKE OF OCTOBER 17, 1989:
EARTHQUAKE OCCURRENCE

MAIN-SHOCK CHARACTERISTICS

LONG-PERIOD SURFACE-WAVE OBSERVATIONS OF THE EARTHQUAKE[1]

By Aaron A. Velasco,[2] Thorne Lay, and Jiajun Zhang,
University of California, Santa Cruz

CONTENTS

ABSTRACT

The 1989 Loma Prieta earthquake produced a high-quality data set of global digital, long-period seismic recordings. Given the social and scientific importance of this earthquake, we display here many of the three-component long-period recordings from stations in the Global Seismic Network (GSN), International Deployment of Accelerometers (IDA), and GEOSCOPE (Institut National des Sciences de l'Univers, France). In combination, these stations provide azimuthally dense coverage that has enabled unprecedented high-resolution analysis of the long-period source process in several studies. Although the data presented here have been the most widely distributed and extensively analyzed, our compilation is not comprehensive, and additional high-quality records are available from international stations and arrays. Many direct Rayleigh- and Love-wave arrivals propagating along the short arc from the source to the station were recorded onscale and are particularly useful for studying the source process. The standardization of data-exchange format, with the major networks all adopting the Standard for the Exchange of Earthquake Data (SEED) format, has greatly simplified data retrieval and analysis procedures.

INTRODUCTION

Determination of the complexity involved in an earthquake rupture requires extensive ground-motion recordings. The 1989 Loma Prieta earthquake produced high-quality ground-motion data, ranging from near-field accelerations to teleseismic body waves, surface waves, and free oscillations. Both the location and timing of the earthquake were propitious in this regard because the Santa Cruz Mountains is a densely instrumented area, with many accelerometers, regional seismic array stations, and geodetic bench marks, and because 1989 was preceded by 15 years of development and deployment of global digital seismologic instrumentation and development of advanced data-analysis procedures. The completeness of the various data sets has allowed many detailed analyses of the earthquake rupture process, as described by other papers in this chapter. The long-period and broadband seismograms from global seismic networks in particular provide an excellent demonstration of the progress made during the 1980's in broadband, large-dynamic-range instrumentation, digital-recording capacity, and calibration technology. In this paper, we display many of the high-quality long-period observations for the 1989 earthquake.

GLOBAL LONG-PERIOD SEISMIC DATA

Although many seismic networks were operational at the time of the earthquake, we focus here on a subset of long-period global data that was readily available after the event. The data considered here are from long-period (LH) channels of three-component recordings from the Global Seismic Network (GSN; Incorporated Research Institution for Seismology, 1989), the very long period LaCoste-Romberg accelerometer recordings from the International Deployment of Accelerometers (IDA; Agnew and others, 1976) network, and very long period (VLP) channels of the three-component recordings from the broadband GEOSCOPE network (Institut National des Sciences de l'Univers, France; Romanowicz and others,

---

[1] Contribution No. 161, Charles F. Richter Seismological Laboratory and Institute of Tectonics, University of California, Santa Cruz, CA 95064.

[2] Current affiliation: Science Applications International Corporation, San Diego, CA 92121.

1984, 1991). The collective long-period data for the earthquake from these three networks have extensive surface coverage (fig. 1*A*). Additional digital stations that recorded the event were in the former Soviet Union (IDA/IRIS), Japan, Germany, Canada, Great Britain, and China. These data, which are also of high quality, in the future will be

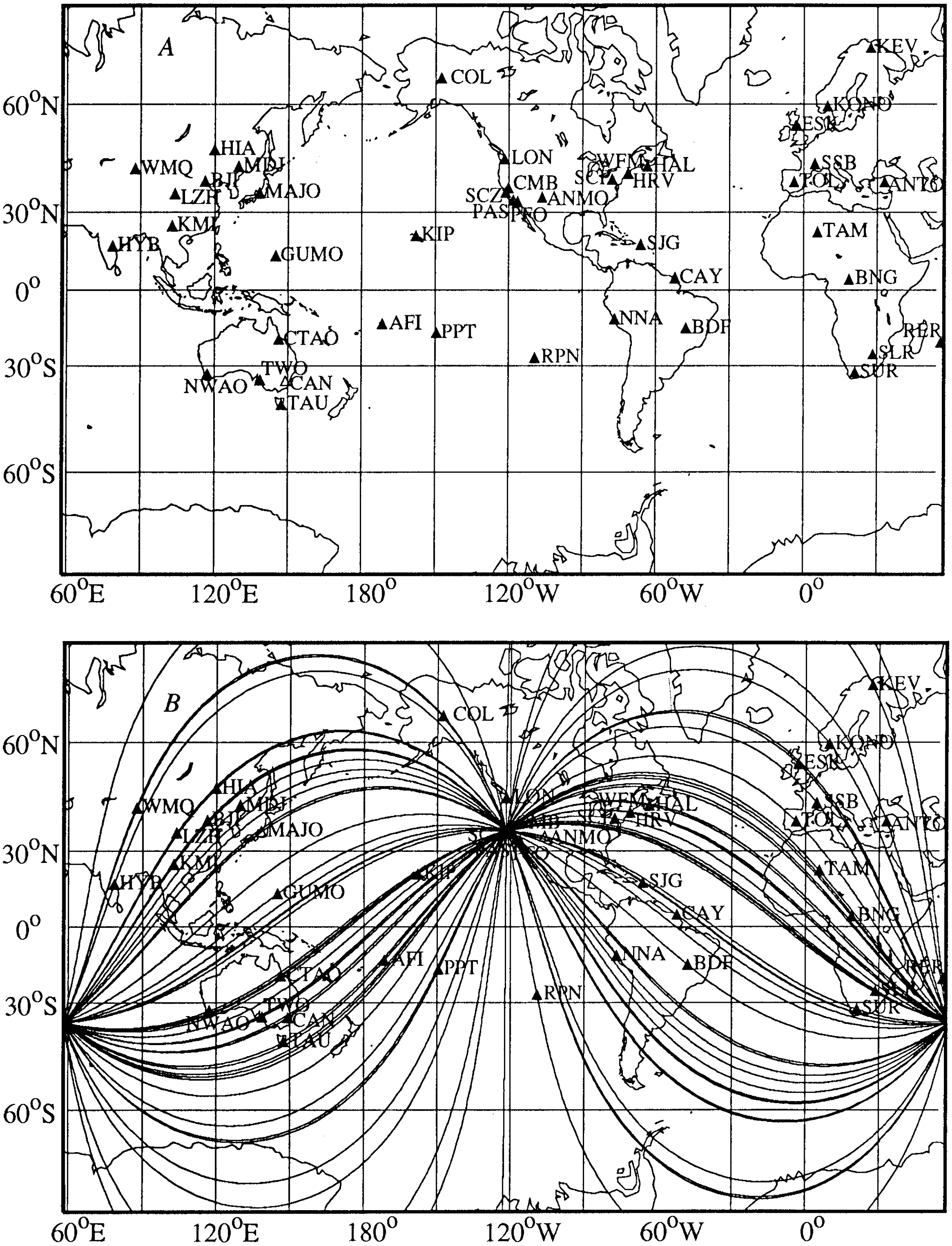

Figure 1.—The world. *A*, Distribution of long-period stations (triangles) in Global Seismic Network (GSN), GEOSCOPE (Institut National des Sciences de l'Univers, France), and International Deployment of Accelerometers/Incorporated Research Institution for Seismology (IDA/IRIS) seismic networks. *B*, Great-circle paths of minor- and major-arc surface-wave arrivals at these stations. Note excellent azimuthal coverage attainable for 1989 Loma Prieta earthquake.

Table 1.—*Long-period surface-wave data quality for the earthquake*

[Channels: LH, long period; VLP, very long period. Data quality of arrivals: c, clipped; g, glitches; m, missing; o, clear; x, noisy; - -, no horizontal components]

Station (fig. 1)	Channel	Azimuth (°)	Distance (°)	R_1	R_2	G_1	G_2
Global Seismic Network (GSN)							
AFI	LH	232.77	069.14	o	o	o	x
ANMO	LH	094.91	012.66	o	x	o	o
ANTO	LH	019.46	099.83	m	m	m	m
BCAO	LH	050.31	124.60	o	o	o	o
BJI	LH	319.37	086.47	o	o	c	o
CMB	LH	049.68	001.55	c	x	c	x
COL	LH	339.34	031.81	o	x	g	o
CTAO	LH	255.05	103.31	x	o	o	o
GUMO	LH	282.93	084.47	o	o	o	o
HIA	LH	324.02	078.09	o	o	o	o
HON	LH	253.58	034.96	c	x	c	x
HRV	LH	065.77	038.55	o	o	o	o
KEV	LH	010.94	070.97	o	x	o	x
KMI	LH	318.86	105.13	o	o	o	o
KONO	LH	023.08	075.53	o	x	o	o
LON	LH	000.34	009.71	c	x	c	x
LZH	LH	324.47	095.64	o	o	o	o
MAJO	LH	305.21	075.74	o	x	o	o
MDJ	LH	315.88	076.11	o	o	o	o
NWAO	LH	256.87	132.11	o	o	o	o
PAS	LH	132.62	004.19	o	o	o	o
SCP	LH	069.84	034.15	c	o	c	x
SLR	LH	073.88	152.26	x	x	x	x
TAU	LH	234.09	114.62	x	x	o	o
TOL	LH	043.01	084.40	o	o	o	x
WMQ	LH	339.05	094.99	o	o	o	o
GEOSCOPE (Institut National des Sciences de l'Univers, France)							
BNG	VLP	050.30	124.60	o	o	- -	- -
CAN	VLP	240.45	109.68	o	o	o	x
CAY	VLP	098.41	070.76	o	o	o	o
HYB	VLP	336.85	122.38	o	o	- -	- -
KIP	VLP	253.72	034.90	o	o	o	o
PPT	VLP	210.74	060.39	o	o	o	o
RER	VLP	007.93	164.01	o	o	o	o
SSB	VLP	034.69	084.73	o	o	o	o
TAM	VLP	048.52	102.45	o	o	o	o
WFM	VLP	065.60	038.59	o	x	o	x
International Deployment of Accelerometers (IDA)							
BDF	- -	111.82	087.09	o	o	- -	- -
BJT	- -	320.73	085.01	c	x	- -	- -
CMO	- -	339.24	031.79	c	o	- -	- -
GUA	- -	282.86	084.46	o	x	- -	- -
HAL	- -	061.04	043.87	c	o	- -	- -
KMY	- -	318.87	105.12	o	o	- -	- -
NNA	- -	129.84	064.66	c	o	- -	- -
PFO	- -	126.06	005.61	c	o	- -	- -
SJG	- -	095.29	052.12	c	o	- -	- -
SUR	- -	091.86	149.14	g	x	- -	- -
TWO	- -	245.39	116.92	o	o	- -	- -

readily available from various data centers. We do not discuss here these additional recordings or the historical development and instrumentation of any of the various international seismic arrays; for comprehensive information on instrumentation, the reader should contact the data centers for each network directly. Our purpose here is to demonstrate only the general characteristics of the long-period waves excited by the earthquake.

The GSN and IDA networks were in a transitional state at the time of the earthquake; various instrumentation associated with earlier networks was being upgraded to very broad band three-component recording, and new stations were being deployed (Incorporated Research Institution for Seismology, 1989). The GEOSCOPE network was relatively uniform in 1989. The data centers that distribute these data—the IRIS Data Management Center (IRIS/DMC; Ahern, 1989), IDA (Agnew and others, 1976), Project GEOSCOPE (Romanowicz and others, 1991), and the ORPHEUS data-management center—all provide complete digital recordings and instrument-response information for the recorded signals. In this paper, we utilize the long-period or very long period channels from each station.

The azimuthal coverage of minor- and major-arc surface waves recorded by the combined GSN, GEOSCOPE, and IDA networks is excellent (fig. 1*B*) and superior to the coverage by any one network alone. Owing to variations in the dynamic range of the recording systems, not all stations recorded useful long-period Rayleigh- and Love-wave arrivals. Those stations with long-period or very long period channels from the three seismic networks that we collected, and the quality of the primary Rayleigh-wave (R1, R2) and Love-wave (G1, G2) great-circle arrivals, are listed in table 1. All the GEOSCOPE recordings provided onscale R1 and G1 arrivals. Upgraded GSN and IDA stations recorded onscale minor-arc arrivals; some of the older GSN and IDA stations with lower-dynamic-range recorders clipped on the vertical and (or) horizontal components of the minor-arc arrivals (R1, G1), or had low signal-to-noise ratios for various reasons, as indicated in table 1. Despite these data dropouts, the overall data quality is quite high, and many useful long-period recordings can be retrieved.

To provide a visual appraisal of the long-period signal quality, we constructed seismogram profiles of edited subsets of the higher quality observations. The profiles of three-component seismograms, bandpass filtered between 125 and 500 s, are shown in figure 2. Multiple Rayleigh-wave (R1, R2, R3) arrivals can be identified on the vertical-component seismograms (fig. 2*A*). The signal-to-noise ratio varies between traces, owing to both site conditions and the azimuthal radiation pattern of the Rayleigh waves. These seismograms show high signal-to-noise ratios for R1 and R2 arrivals, but R3 arrivals tend to be noisier. The low signal-to-noise ratio for R3 arrivals is due to the relatively small seismic moment of the earthquake, which places a great value on the high-dynamic-range systems that record R1 arrivals onscale, because the R1 arrivals are more reliable for source analysis.

The horizontal ground motions transverse to the great-circle paths connecting the source and receivers are shown in figure 2*B*. The strong Love-wave (G1, G2, G3) arrivals have high signal-to-noise ratios except at stations near radiation nodes (for example, sta. SLR, fig. 1*A*). These traces show a few isolated glitches that produce spurious pulses in the filtered records which must be eliminated manually before any full waveform or spectral analysis. These glitches tend to be a larger problem on the less stable horizontal components than on the vertical components.

The horizontal longitudinal components of motion along great-circle paths are shown in figure 2*C*. The fundamental-mode Rayleigh-wave (R1, R2, R3) arrivals have lower signal-to-noise ratios than on the vertical components, as expected, but the Rayleigh-wave overtones (X1, X2, X3, X4) have higher amplitudes than on the verticals, particularly for shorter period passbands from 50 to 100 s. Note that several signals appear to have substantial Love-wave contamination on the longitudinal components (for example, stas. NWAO, TAU, ANMO, fig. 1). Although these signals tend to be from stations that recorded large-amplitude Love waves and small-amplitude Rayleigh waves, most of this contamination appears to stem from path deflections from a great circle, rather than from errors in relative gains of the horizontal-component recordings. Ultraprecise analysis of surface-wave polarization and phase, however, probably requires critical examination of the instrument responses of the horizontal components, rather than simple utilization of the nominal instrument-response curves given for each trace.

The 1989 Loma Prieta earthquake was sufficiently large that stable long-period signals were recorded globally, and so this data set has received much attention from many investigators in analyzing the long-period characteristics of the source process (see Velasco and others, this chapter). Accessing these data was more straightforward than ever for several reasons. First, there was the ongoing development of seismologic data centers that distribute the data in response to user requests, including the IRIS/DMC and the ORPHEUS data center, which distributes data collected in Europe. These centers assist in resolving instrument-response issues as well, and numerous questions

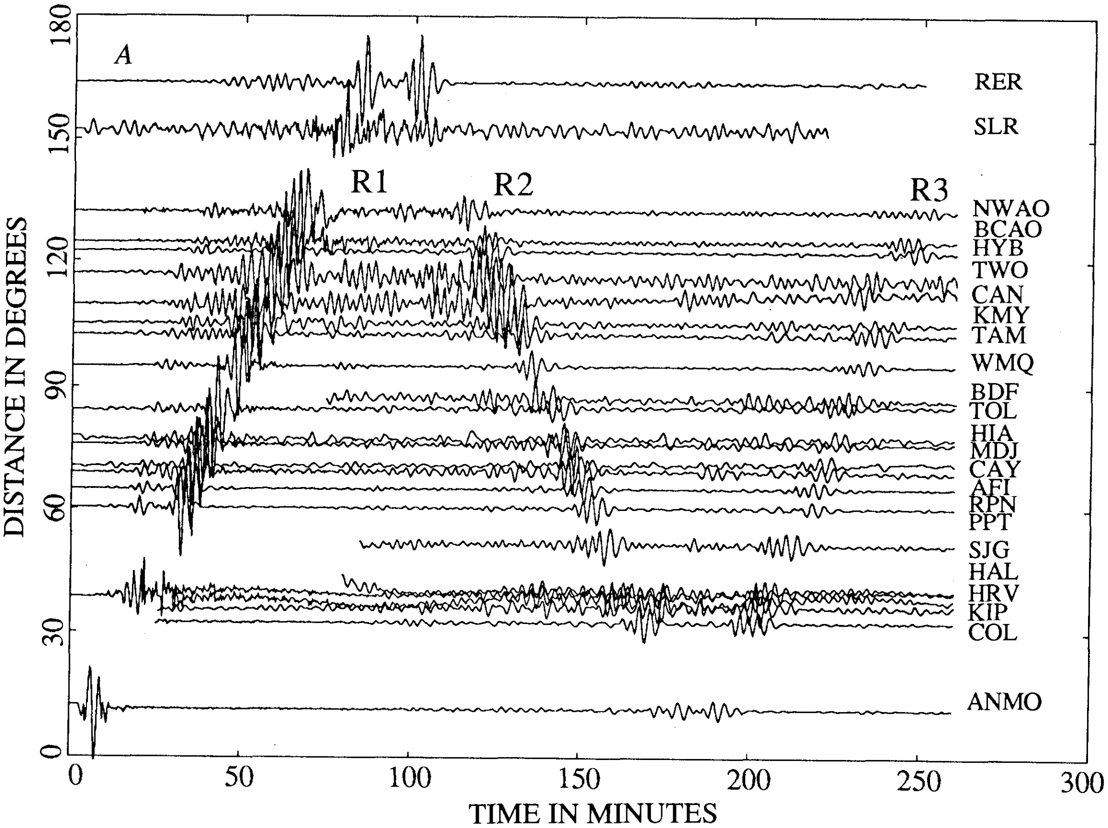

Figure 2.—Seismic profiles of bandpass-filtered (125–500 s) seismograms for long-period channels from three global seismic networks (Global Seismic Network, GEOSCOPE, International Deployment of Accelerometers). *A*, Vertical-component seismograms showing minor-arc (R1, R3) and major-arc (R2) great-circle Rayleigh waves. Data have fairly high signal-to-noise ratios except for some R3 arrivals. Amplitude of each trace is normalized, and so some varying noise levels reflect radiation-pattern variations of Rayleigh waves. Most traces with onscale R1 phases are from stations operating with high-dynamic-range systems, whereas nonlinear signals at other stations have been cut out. *B*, Transversely polarized horizontal-component seismograms for stations with clear great-circle Love-wave arrivals (G1, G2, G3). Rotation is with respect to great-circle paths. A few stations have minor glitches that produce spurious pulses. *C*, Longitudinally polarized horizontal-component seismograms showing great-circle Rayleigh-wave arrivals (R1, R2, R3), as well as multiple Rayleigh-wave overtone arrivals (X1, X2, X3, X4). R1 and R2 arrivals have high signal-to-noise ratios, whereas R3 arrivals are noisy. Multiple-overtone arrivals also are noisy over this period range.

arose about the new broadband responses of some systems soon after the earthquake. Second, a major development in the analysis of long-period data is the adoption by the major seismic networks of the Standard for the Exchange of Earthquake Data (SEED) format (Federation of Digital Seismographic Networks, 1990), which greatly facilitates computation of instrument responses and data-retrieval processes. With future efforts by the seismologic networks to fully conform to the SEED format for station information and data format, analysis of the data should become even easier.

CONCLUSION

The 1989 Loma Prieta earthquake occurred during a time when the global digital seismic network was extensive. The long-period data have excellent onscale Rayleigh- and Love-wave arrivals, with high signal-to-noise ratios, extensive azimuthal coverage, and reliable instrument calibration. Enough stations were available to record large-amplitude minor-arc arrivals, which are critical to a detailed analysis of the long-period source process.

ACKNOWLEDGMENTS

This research was partly supported by U.S. Geological Survey grant 14–08–0001–G1843 and U.S. National Science Foundation grant EAR–9017767, with facilities support from the W.M. Keck Foundation. We thank the many individuals involved in the various international efforts to collect global broadband digital seismic data for the earthquake, in particular, the Project IDA, GEOSCOPE, and GSN/IRIS personnel who assisted us in accessing these data and resolving instrumentation issues.

REFERENCES CITED

Agnew, D.J., Berger, Jon, Buland, R.P., Farrell, W.E., and Gilbert, J.F., 1976, International deployment of accelerometers; a network for very long-period seismology: Eos (American Geophysical Union Transactions), v. 57, no. 4, p. 180–187.

Ahern, T.K., 1989, Activities at the IRIS Data Management Center: Incorporated Research Institution for Seismology Newsletter, no. 8, p. 3–11.

Federation of Digital Seismographic Networks, 1990, Standard for the Exchange of Earthquake Data; reference manual: 149 p.

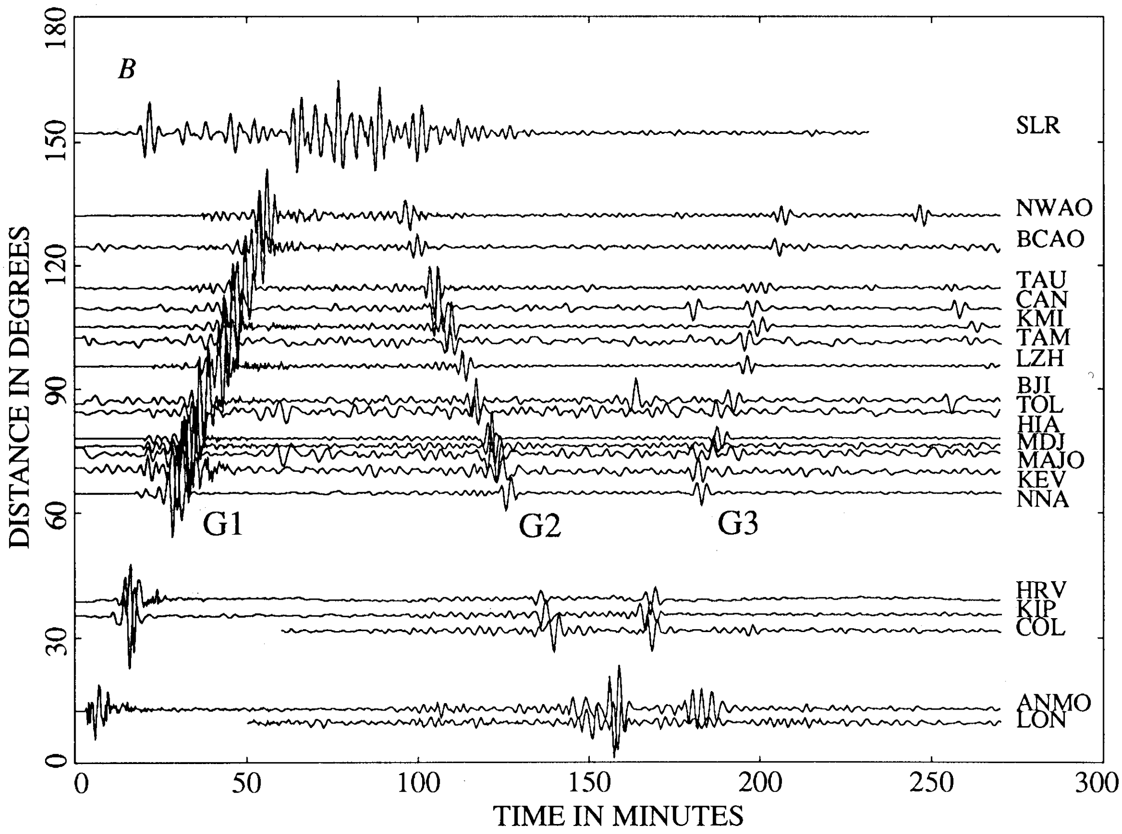

Figure 2.—Continued

Incorporated Research Institution for Seismology, 1989, IRIS Global Seismographic Network: Newsletter, no. 8, p. 19–24.

Romanowicz, Barbara, Cara, Michel, Fels, J.F., and Rouland, Daniel, 1984, GEOSCOPE; a French initiative in long-period three-component global seismic networks: Eos (American Geophysical Union Transactions), v. 65, no. 42, p. 753–754.

Romanowicz, Barbara, Karczewski, J.F., Cara, Michel, Bernard, Pascal, Borsenberger, Jean, Cantin, J.-M., Dole, Bernard, Fouassier, Danielle, Koenig, J.-C., Morand, Michel, Pillet, Robert, Pyrolley, Annick, and Rouland, Daniel, 1991, The GEOSCOPE program; present status and perspectives: Seismological Society of America Bulletin, v. 81, no. 1, p. 243–264.

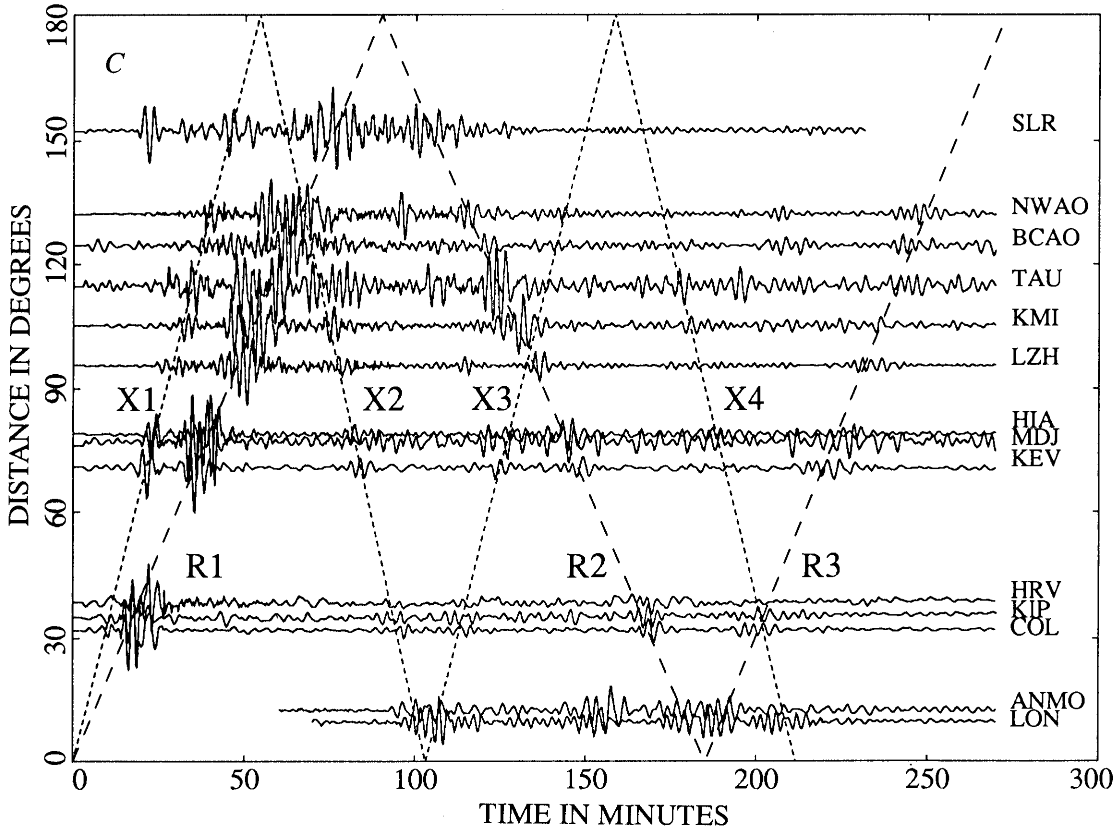

Figure 2.—Continued

MAIN-SHOCK CHARACTERISTICS

SOURCE PARAMETERS OF THE EARTHQUAKE, DETERMINED BY USING LONG-PERIOD SEISMIC WAVES[1]

By Aaron A. Velasco[2], Thorne Lay, and Jiajun Zhang,
University of California, Santa Cruz

CONTENTS

ABSTRACT

We have performed simultaneous seismic-moment tensor inversions of long-period (157–288 s) fundamental-mode Rayleigh and Love waves from the 1989 Loma Prieta earthquake to determine the long-period source process of the earthquake. Utilizing a two-step spectral-inversion technique, we explore the model dependence and centroid-location sensitivity of the surface-wave analysis to assess the confidence bounds of the inversion results. We find that estimates of the source duration and depth depend heavily on the choice of propagation, attenuation, and source-velocity-structure models. Including centroid-location parameters in the inversion stabilizes the moment-tensor estimates but yields a biased location away from the epicenter, owing to model inaccuracies. Our source-duration estimate is 11±5 s, using a recent velocity model, with the centroid time of 6 s significantly less than in earlier surface-wave studies (10–22 s) and thus more compatible with estimates of both body-wave and strong-motion durations. An unconstrained moment-tensor inversion at the optimum centroid location yields a stable major-double-couple solution (strike, 124°±6°; dip, 67°±6°; rake, 126°±7°) and a seismic-moment estimate ($(3.0\pm0.2)\times10^{19}$ N-m; $M_w=6.9$) similar to those of earlier long-period studies and to body-wave and geodetic results. The surface-wave centroid-depth estimate is 22±11 km, which overlaps the body-wave estimates (13±5 km). Thus, surface-wave source parameters for the earthquake, allowing for plausible model dependence, are fully compatible with body-wave determinations, and there is no evidence for any anomalous coseismic long-period source process.

INTRODUCTION

The 1989 Loma Prieta earthquake may be the best instrumentally recorded earthquake to date, with high-quality ground-motion data ranging from short-period strong ground motions (10-Hz signals) to static offsets (ground deformation). This unusually complete data set allows a detailed analysis of the earthquake rupture process by using the various signals, each of which has a different sensitivity to the source process. These data, in turn, provide an excellent opportunity to explore the compatibility and resolution of the different data sets and the associated seismic-inversion techniques. Ideally, earthquake source models should be independent of data type, frequency, or inversion technique; thus, strong-ground-motion results should be consistent with geodetic models. For many large earthquakes, however, results obtained by using short-period waves differ from those obtained by using long-period waves or geodetic measurements, and similar discrepancies have been reported for the 1989 Loma Prieta earthquake (Wallace and others, 1991).

The focal mechanisms from first motions and teleseismic body- and surface-wave studies, as summarized in figure 1, are virtually identical, suggesting negligible frequency dependence or faulting complexity. Furthermore, estimates of seismic moment, centroid depth, and rupture duration

---

[1] Contribution No. 156, Charles F. Richter Seismological Laboratory and Institute of Tectonics, University of California, Santa Cruz, CA 95064.

[2] Current affiliation: Science Applications International Corp., San Diego, CA 92121.

obtained from local, regional, and teleseismic body-wave studies are generally consistent with each other (Wallace and others, 1991). Long-period-surface-wave results, however, generally give larger seismic moments, deeper centroid depths, and longer rupture durations than do body-wave studies. These systematic discrepancies suggest a complex source phenomenon, such as deep, slow rupture propagating into the mantle (Wallace and others, 1991). Before accepting the possibility of such a complex source process, the reliability of the long-period results must be tested, and this study will demonstrate that no anomalous long-period source process occurred during the earthquake.

The various investigations of long-period seismic waves for the earthquake have yielded consistent focal mechanisms and seismic-moment estimates, as listed in table 1. Owing to the limited resolution of long-period waves, however, several studies have necessarily constrained some parameters of the inversions or used only limited surface-wave data sets. Romanowicz and Lyon-Caen (1990) and Zhang and Lay (1990b) used only Rayleigh-wave (R_1, R_2) arrivals from 15 and 25 stations, respectively, in spectral inversions for the source parameters (duration, depth, moment tensor). The only significant difference in the results of these two studies is the source-duration estimate, modeled in terms of a boxcar or trapezoidal time function (table 1), for which Romanowicz and Lyon-Caen calculated a total duration of 36 to 44 s, whereas Zhang and Lay (1990b) estimated a duration of 20 to 22 s. The difference is mainly due to the choice of phase-velocity model used to correct for propagation-phase delay; Romanowicz and Lyon-Caen (1990) preferred the PREM model (Dziewonski and Anderson, 1981), whereas Zhang and Lay (1990b) preferred the aspheric M84C model (Woodhouse and Dziewonski, 1984). This difference indicates the model dependence of the long-period-source-parameter determinations and raises questions about the true uncertainties of the estimates.

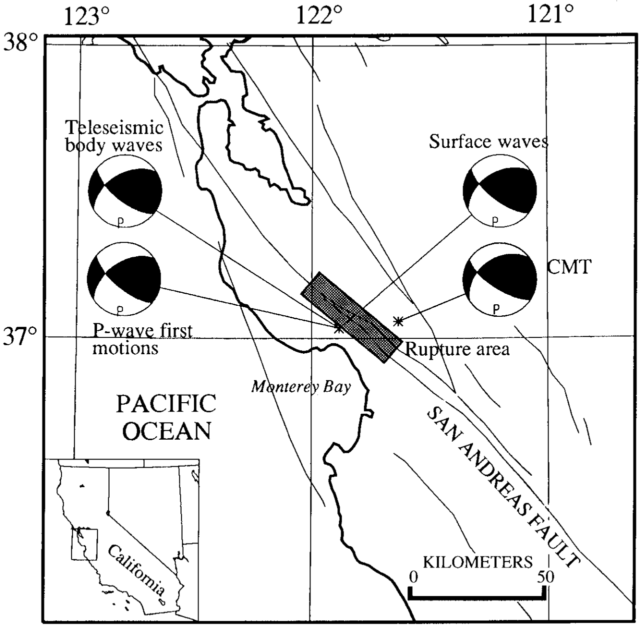

Figure 1.—Loma Prieta region, Calif., showing epicentral location (dot) from National Earthquake Information Center, locations of major faults (irregular thin lines), and approximate location of rupture area (for example, Wald and others, 1991) of 1989 earthquake. Major double-couple focal mechanisms from *P*-wave first motions (Oppenheimer, 1990), average teleseismic body-wave solutions (Barker and Salzberg, 1990; Choy and Boatwright, 1990; Kanamori and Satake, 1990; Langston and others, 1990; Nábělek, 1990; Romanowicz and Lyon-Caen, 1990; Ruff and Tichelaar, 1990; Wallace and Lay, 1990; Wallace and others, 1991), average surface-wave solutions (Dziewonski and others, 1990; Kanamori and Satake, 1990; Romanowicz and Lyon-Caen, 1990; Zhang and Lay, 1990b; Wallace and others, 1991), and centroid-moment-tensor (CMT) solution show nearly identical strike, dip, and rake. "P" on focal mechanisms denotes compressional axis. CMT solution has a centroid location east of epicenter (asterisk).

Kanamori and Satake (1990) applied both centroid-moment-tensor (CMT) and spectral-inversion methods to a small set of Rayleigh-wave (R_1) and Love-wave (G_1) arrivals from 10 stations. They constrained the source depth and rupture duration in their inversions, as well as the fault dip in the spectral inversion, which used only data at a period of 256 s. Their results (table 1) are similar to those from other long-period investigations, although they calculated the largest (most strike slip) rake (137°–144°) and among the smallest seismic-moment estimates ((2.5–2.8)$\times10^{19}$ N-m) of the published values. Dziewonski and others (1990) performed a CMT inversion of long-period body waves and surface waves with a more extensive data set, including the effects of the aspheric M84C model, and calculated a lower rake (128°) than Kanamori and Satake but a comparable moment (2.7$\times10^{19}$ N-m) (table 1).

Wallace and others (1991) inverted a very large data set of fundamental-mode Rayleigh-wave (R_1, R_2) and Love-wave (G_1, G_2) arrivals for the moment tensor, using a spectral technique for periods from 150 to 300 s. Their surface-wave data were from 31 globally distributed stations in the Global Seismic Network (GSN, long period three component) and networks of the International Deployment of Accelerometers (IDA, very long period vertical component) and GEOSCOPE (Institut de Physique du Globe de Paris, France, very long period three component). In the moment-tensor inversion, however, Wallace and others did not use the Love-wave estimate of the $\mathbf{M}_{yz}$ term of the moment tensor, owing to instability of the inversion relative to the Rayleigh-wave $\mathbf{M}_{yz}$ determination. They also did not use Love waves in solving for centroid depth, because the excitation functions calculated for various source structures varied little with depth and the uncertainties in the source-velocity structure cause problems in simultaneous modeling of Rayleigh- and Love-wave excitation.

Table 1.—*Major double-couple source parameters for the earthquake from surface waves and free oscillations*

[References: D, Dziewonski and others (1990); J, Jordan (1991); K, Kanamori and Satake (1990); R, Romanowicz and Lyon-Caen (1990); T, this study; W, Wallace and others (1991); Z, Zhang and Lay (1990b). Comments: CMT, centroid moment tensor; FO, free oscillations; G, Love waves; R, Rayleigh waves]

Strike (°)	Dip (°)	Rake (°)	Depth (km)	M_0 (10^{19} N-m)	Duration (s)	Reference	Comment
124±6	67±6	126±7	22±11	3.0±0.2	11±5	T	R, G
129±2	69±3	134±4	15–23	3.3±0.5	18±5	W	R, G
123	71	128	[1]19	2.7	40.0	D	CMT
128	70	137	15	2.5	- - -	K	CMT
129	[1]70	144	15	2.8	- - -	K	R, G
127±5	66±5	132±5	20±5	3.3±0.5	36.0–44.0	R	R
130±5	70±5	135±5	19±3	3.4±0.5	20.0–22.0	Z	R
- - -	- - -	- - -	- - -	3.2±0.4	16–54	J	FO

[1] Constrained in inversion.

Jordan (1991) analyzed free oscillations with periods from 67 to 400 s from nine vertical-component IDA accelerograms to determine a centroid time of 12.6±2.8 s, and a characteristic duration τ_c of 20±11 s. For a boxcar source-time function, this τ_c value corresponds to a source duration of about 35 s, whereas the centroid time would suggest 25 s. Jordan did not report results for the source depth or focal mechanism but estimated a seismic moment of $(3.2\pm0.4)\times10^{19}$ N-m. In his analysis, Jordan found no evidence for any statistically significant precursory long-period radiation from the source.

The small differences in the results of long-period analyses of the earthquake are largely attributable to different model assumptions. Wallace and others (1991) explicitly explored the model dependence of surface-wave spectral inversions to assess the resolution of the source parameters and to determine whether they could resolve any anomalous long-period source process. They found that the choice of propagation model, global-attenuation model, and source-velocity structure directly affects the determinations of depth, moment, and duration. By comparing their body- and surface-wave results, Wallace and others suggested that deep, slow slip may have occurred during the earthquake. The long-period-surface-wave inversions, however, were shown to have sufficient model dependence that this hypothesis could not be confirmed, and Wallace and others speculated that improved model corrections may eliminate any evidence for anomalous radiation.

In this paper, we further explore the model dependence of the long-period inversions by using various attenuation, phase-velocity, and source-velocity models. The introduction of new surface-wave-propagation models that have better resolution of Earth structure is a continuing process, and we apply one of the latest models that was not considered by Wallace and others (1991). We also investigate the sensitivity of long-period spectral inversions to the source-centroid location, which has not been done previously for very long period analyses. This investigation is motivated by the work of Zhang and Lay (1990a), who demonstrated the effects of incorrect source location on such inversions, and by the parametrization of the CMT inversion, which allows for a pseudosource location in the form of an optimal centroid location. Finally, we compare the result of our long-period source models to those of previous investigations, to assess the existence of any anomalous long-period radiation from the earthquake.

DATA

The long-period data for the 1989 Loma Prieta earthquake are of high quality, allowing a complete investigation of long-period source-parameter determinations. Some of these data, with well-defined Rayleigh-wave (R_1, R_2, R_3) arrivals observed at stations in three global seismic networks (GSN, IDA, GEOSCOPE), are plotted in figure 2. The R_1 and R_2 arrivals have a high signal-to-noise ratio. With the ongoing global deployment of very broad band stations during the late 1980's, numerous onscale R_1 arrivals were recorded that were unavailable for many previous events in such quantity. These onscale R_1 arrivals are desirable because the effect of inaccuracies in propagation models increases with the distance traveled by the waves. The 1989 Loma Prieta earthquake was a bit too small to generate high-quality recordings of long-period waves traveling more than one orbit on the surface; thus, the signal-to-noise ratio decreases significantly for R_3 arrivals. Zhang and Lay (1990b) found that existing propagation models have too much uncertainty to reliably estimate the short source duration of the earthquake from

R_3 arrivals, and so R_3 and G_3 arrivals are not used in our analysis.

Our data set, which is moderately increased over that used by Wallace and others (1991), comprises a total of 38 stations with 88 separate arrivals; the phases used are listed in table 2. Given the high signal-to-noise ratio and the good azimuthal coverage, these signals compose an excellent long-period data set for constraining the source parameters.

METHOD

We analyze long-period (157–288 s) Rayleigh and Love waves, utilizing the moment-tensor spectral-inversion method of Kanamori and Given (1981), modified to a two-step procedure that separates source-finiteness effects from determination of the centroid depth and moment tensor (Romanowicz and Guillemant, 1984). The simultaneous Rayleigh- and Love-wave inversion procedure was further described by Zhang and Kanamori (1988a). The complex source spectrum of surface waves excited by a point source is a linear function of the frequency-independent moment tensor ($\mathbf{M}_{xx}$, $\mathbf{M}_{yy}$, $\mathbf{M}_{zz}$, $\mathbf{M}_{xy}$, $\mathbf{M}_{yz}$, $\mathbf{M}_{xz}$). Our linear-inversion method uses the complex spectra of multiple surface-wave arrivals at several discrete periods. We use a group-velocity window for each fundamental-mode Rayleigh-wave (R_1, R_2) and Love-wave (G_1, G_2) arrival, and calculate the amplitude and phase spectra, from which we choose seven different periods (157, 175, 200, 225, 256, 275, 288 s) for our analysis. The observed surface-wave spectra must be corrected for instrument response, propagation effects, and source-finiteness effects, and these corrections affect the estimates of duration, depth, and moment tensor.

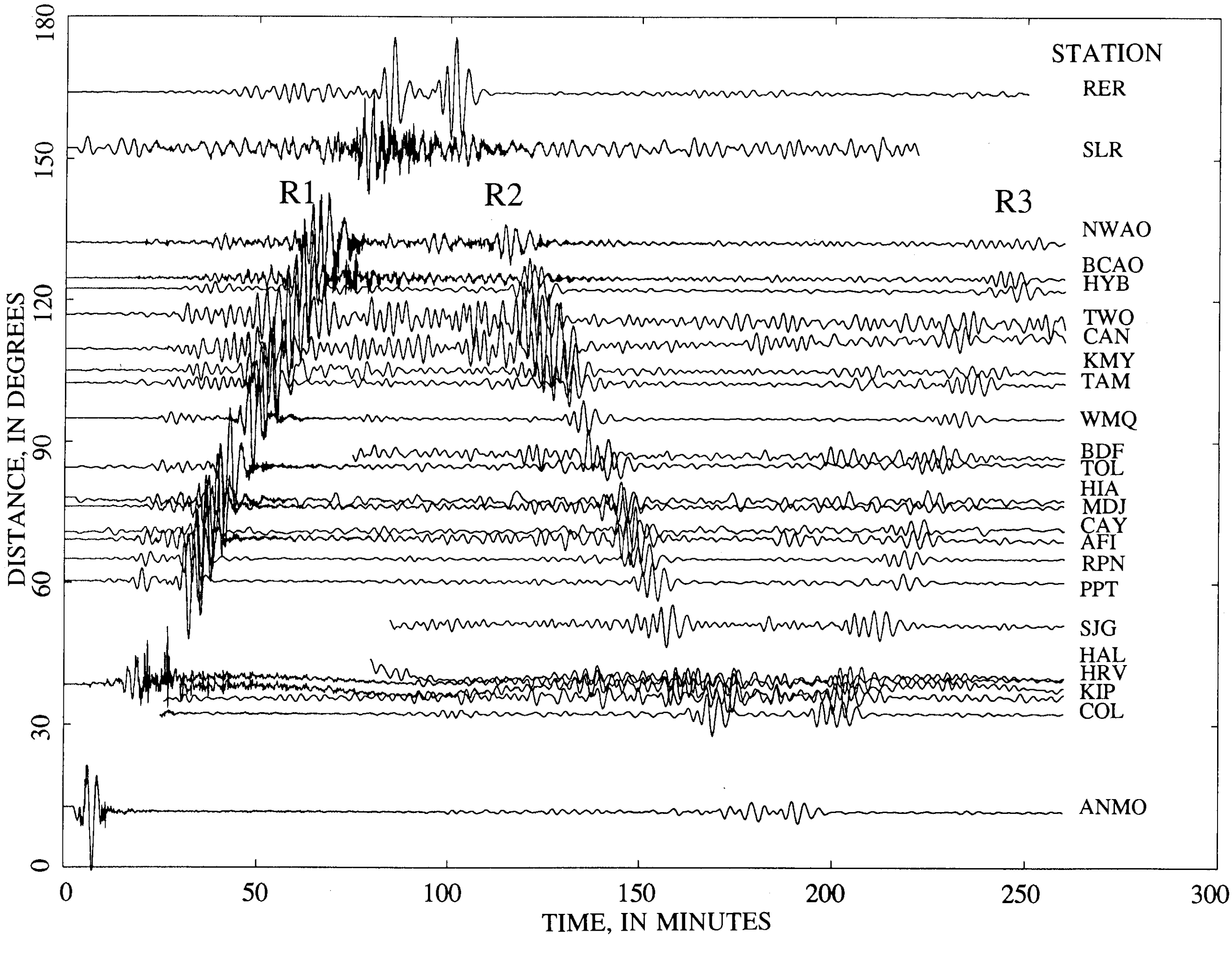

Figure 2.—Filtered (125–500 s) vertical-component velocity seismograms for long-period channels at stations in three seismic networks (GSN, IDA, GEOSCOPE). Amplitudes for all traces are scaled equally. Multiple great-circle Rayleigh waves (R1, R2) show high signal-to-noise ratios. Many broadband instruments recorded onscale R1 phases from earthquake; however, owing to moderate magnitude of main shock, R3 arrivals are noisy and so were not used in our analysis.

Table 2.—*Stations and phases used in this study*

[Networks: GEO, GEOSCOPE (Institut de Physique du Globe de Paris, France); GSN, Global Seismic Network (U.S. Geological Survey/Incorporated Research Institution for Seismology); IDA, International Deployment of Accelerometers (IDA/Incorporated Research Institution for Seismology)]

Station	Network	Azimuth (°)	Distance (°)	Phase
AFI	GSN	232.59	69.91	R_1, R_2
BCAO	GSN	050.08	124.86	R_1, R_2
BJI	GSN	319.23	86.44	R_1, R_2, G_2
COL	GSN	339.54	31.81	R_1, G_2
CTAO	GSN	074.88	77.06	R_2, G_1, G_2
GUMO	GSN	282.78	84.32	R_1, R_2, G_1, G_2
HIA	GSN	323.90	78.08	R_1, R_2, G_1, G_2
HRV	GSN	245.63	141.32	R_2
KEV	GSN	010.84	71.11	R_1, G_1, G_2
KMI	GSN	318.64	105.09	R_1, R_2, G_1
KONO	GSN	202.95	104.15	G_2
LZH	GSN	324.28	95.62	R_1, R_2
MAJO	GSN	305.10	75.67	R_1, G_1
MDJ	GSN	315.78	76.06	R_1, R_2, G_1, G_2
NWAO	GSN	076.67	48.25	R_2, G_1, G_2
SCP	GSN	249.67	145.74	R_2
TAU	GSN	233.95	114.38	G_1, G_2
TOL	GSN	042.86	84.65	R_1, R_2
WMQ	GSN	158.87	84.83	R_1, R_2, G_1, G_2
BNG	GEO	050.07	124.87	R_1, R_2
CAN	GEO	240.29	109.44	R_1, R_2, G_1
CAY	GEO	098.20	70.99	R_1, R_2, G_1, G_2
HYB	GEO	336.55	122.38	R_1, R_2
KIP	GEO	253.60	34.70	R_1, R_2, G_1, G_2
PPT	GEO	210.51	60.14	R_1, R_2, G_1, G_2
RER	GEO	007.04	164.05	R_1, R_2, G_1, G_2
SSB	GEO	034.53	84.97	R_1, R_2, G_1, G_2
TAM	GEO	228.33	77.30	R_2
WFM	GEO	065.45	38.85	R_1, G_1
BDF	IDA	111.67	87.27	R_1, R_2
CMO	IDA	159.46	148.06	R_2
HAL	IDA	240.92	135.97	R_2
KMY	IDA	318.65	105.07	R_1, R_2
NNA	IDA	309.60	115.30	R_2
RPN	IDA	347.36	114.90	R_2
SJG	IDA	275.05	127.83	R_2
TWO	IDA	065.22	63.43	R_2

Before the source-duration determination, we must correct the phase for propagation delay, assuming a phase-velocity model. We assume great-circle paths in calculating the phase-propagation corrections and neglect focusing and defocusing because these factors have been shown to have only second-order effects on waves for our period range for existing smooth-Earth models (Schwartz and Lay, 1988).

In the first-step inversion, we calculate the source-finiteness correction (eq. 9 of Zhang and Kanamori, 1988b) for a range of trapezoidal source durations. The source is assumed to be a point source because none of the previous analyses has resolved any source directivity affecting the long-period signals. A trapezoidal source model is used for convenience because the long-wavelength signals studied cannot resolve any fine structure in the short source-time function. Because the rise time appears to be approximately 10 percent of the observed rupture time for many earthquakes (Kanamori and Anderson, 1975), we assume a trapezoidal rise time equal to 10 percent of the source duration. We measure the misfit between the observed and theoretical source phase by using a weighted rms error, σ (Zhang and Lay, 1989); the duration that yields a minimum σ value is our estimate. The weighted rms error is a function of the source-process time and the propagation corrections, making the duration dependent on the propagation model used for correcting the phase back to the source.

In the second-step inversion, we determine the point-source depth and moment tensor, where the moment-tensor solution depends on the surface-wave-excitation functions used in the inversion. To proceed, we must account for attenuation of the surface-wave arrivals when correcting the observed spectral amplitudes back to the source. Thus, we must assume a global attenuation, or Q, model. The excitation functions, as given by Kanamori and Stewart (1976), depend on the elastic properties of the source region and the source depth, making the moment-tensor solution dependent on the assumed source structure. The global Q and source-velocity structure thus affect the moment-tensor and depth estimates. For a range of trial depths, using the optimal source-finiteness corrections obtained from the first step, we measure the misfit between the observed and synthetic spectra by using a weighted rms error, ρ, for this second step (Zhang and Lay, 1989). The depth at which we obtain a minimum ρ value gives the best depth and moment-tensor estimates.

The decision to use the spectral method is largely based on the ease with which various models can be used in correcting for propagation effects, in contrast to normal-mode-based spectral or time-domain procedures, such as the CMT inversion. However, we lose the advantage of including information from overtones or long-period body waves, which become a source of noise in this fundamental-mode analysis. Another advantage of the spectral-inversion technique is that it allows a separation of source-time-function determination from depth and moment-tensor estimation, making it an ideal method for studying the effects of various models on the inversions.

In performing a simultaneous inversion of Rayleigh and Love waves, we can either jointly estimate the moment-tensor terms from both data types, typically with some variance-based weighting functions, or separately estimate the combined moment-tensor terms for each data type and then merge the estimates. One advantage of determining the Rayleigh- and Love-wave moment-tensor elements separately is that inconsistencies can be easily identified. For example, an inconsistency between the $\mathbf{M}_{yz}$ estimates for Rayleigh and Love waves for the Loma Prieta earthquake prompted Wallace and others (1991) to not use the $\mathbf{M}_{yz}$ estimate from Love waves (this procedure was more stable than any simple averaging strategy implicit in the joint-estimation approach). Wallace and others attributed the instability of the Love-wave $\mathbf{M}_{yz}$ estimate to the shallow depth of the earthquake, in combination with the noise in the data, which generally is somewhat greater for Love waves than for Rayleigh waves. In general, the uncertainties in the $\mathbf{M}_{yz}$ and $\mathbf{M}_{xz}$ moment-tensor terms for both Rayleigh and Love waves are greatest for fundamental-mode surface waves from shallow events, making it necessary to identify such inconsistencies to assess the reliability of the solutions. Furthermore, the characteristic signal quality between Rayleigh and Love waves differs from event to event. Thus, we prefer to estimate moment-tensor terms separately for each data type and then combine the estimates.

The assumed source location also affects the moment-tensor inversion of long-period surface waves, as demonstrated by Zhang and Lay (1990a); this effect may be an alternative explanation for the $\mathbf{M}_{yz}$ inconsistency reported by Wallace and others (1991). Wallace and others assumed the source location given by the National Earthquake Information Center (NEIC) determination, forcing any residual phase anomalies into the moment-tensor inversion. Inaccuracies in the propagation models, particularly when anomalous relative results between Rayleigh and Love waves exist, may be reduced by determining an optimal centroid location, following the strategy of the CMT inversion. Zhang and Lay (1990a) found that an optimal centroid location determined by using Rayleigh waves alone may not give a good source model because of direct tradeoffs between location and source mechanism. Because Rayleigh and Love waves have different radiation patterns, a search for centroid location is more stable when simultaneously inverting both Rayleigh and Love waves, and most effective when including body-wave trains and overtones, as in the CMT inversion. We explore whether centroid-location optimization affects the source depth, duration, and moment-tensor solutions for the earthquake in the following analysis.

SOURCE-DURATION ESTIMATION

For the 1989 Loma Prieta earthquake, Wallace and others (1991) used a spectral-inversion method similar to ours and explored the model dependence of the duration estimate associated with phase velocities for two models, PREM (Dziewonski and Anderson, 1981) and M84C (Woodhouse and Dziewonski, 1984). We include a new model, MPA (Wong, 1989), which was derived by using far more data than were used in the development of the M84C model. The spatial patterns of phase velocities for Rayleigh and Love waves for the M84C and MPA models for periods near 220 s are compared in figure 3. The MPA model gives a somewhat more detailed picture of the Earth than does the M84C model, reflecting the truncation of the spherical-harmonic expansions of the heterogeneity at degrees 12 and 8, respectively. The MPA model appears to better match the expectations of global tectonics, with better definition of slow regions near active oceanic ridges, as well as in the tectonically active source region of the Western United States, and with fast regions beneath continents more closely related to shields. Although these models are still of limited resolution, the MPA model represents progress since 1984 toward developing more accurate models for very long period surface waves, and we now assess whether that progress affects our source models for the earthquake.

For a point source with the NEIC epicentral location and origin time, duration estimates for the PREM, M84C, and MPA propagation models demonstrate a substantial model dependence (fig. 4). To estimate duration, we plot the normalized, spectral-amplitude-weighted rms error, σ (Zhang and Lay, 1989), as a function of assumed trapezoidal source duration for Rayleigh and Love waves of a given period (157, 175, 200, 225, 256, 275, 288 s). The minimum of each curve is the best duration estimate from the corresponding period. The trapezoidal duration estimate (τ) is parametrized to be period independent. Thus, some of the scatter between periods could reflect more complex phenomena, such as slow slip, for which longer periods should give longer durations. Although a frequency-dependent trend is weakly indicated for the MPA model (τ_{150}=12 s; τ_{175}=7 s; τ_{200}=9 s; τ_{225}=9 s; τ_{256}=17 s; τ_{275}=19 s; τ_{288}=18 s), the scatter suggests uncertainties in the phase-velocity model rather than a source phenomenon. The period range is rather small for confidently establishing any complex source model, but the greater range considered by Jordan (1991) in a free-oscillation analysis also reveals no strong frequency dependence of the centroid time in the phase spectra.

For each propagation model, we estimate the source duration (τ) at the minimum σ value calculated for the seven different periods. The PREM model has the highest σ value and gives τ=30 s (fig. 4). The M84C model significantly reduces the overall variances for all periods and gives a shorter average duration (τ=20 s). This uniform improvement of the fit strongly indicates the need for aspheric-propagation corrections for the earthquake, as noted by Romanowicz and Lyon-Caen (1990) and Zhang and Lay (1990b). The MPA model further reduces the τ estimate to approximately 11 s, but the overall variance reduction is comparable to that for the M84C model. With both models, the σ value is similar to that obtained using Rayleigh waves alone (Zhang and Lay, 1990b; Wallace and others, 1991), indicating that the Rayleigh and Love waves are generally compatible in terms of a systematic source-phase shift and that both wave types have comparable residual phase scatter after propagation correction. This result is not general, at least with the current generation of aspheric models. In detail, we find that the shorter durations found for the MPA model relative to the M84C model reflect small shifts of the average phase velocities at each period in the models, rather than systematic improvement in path-specific corrections. The scatter between duration estimates at different periods is not reduced and is most likely due to the inadequacies of the models. Although both the M84C and MPA models reduce the normalized error relative to the PREM model and thus

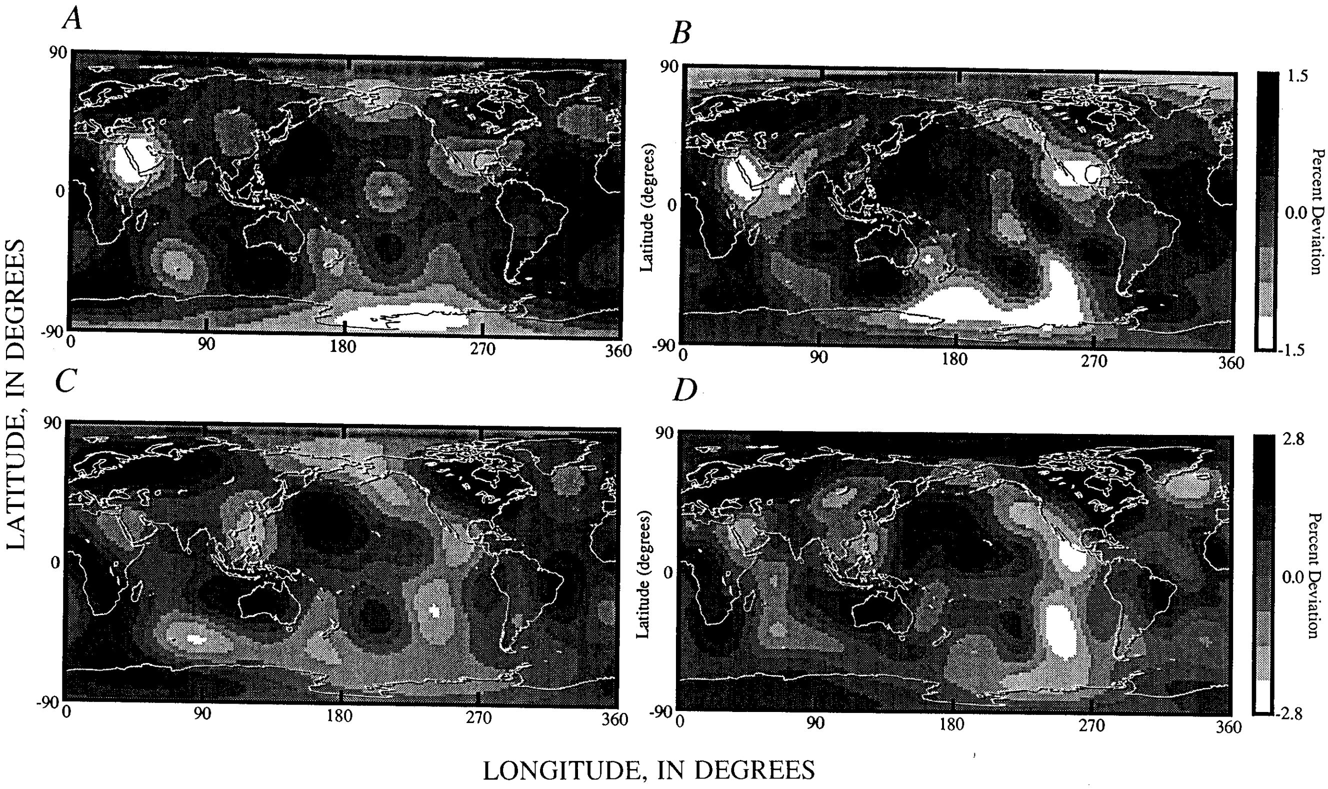

Figure 3.—Aspheric phase-velocity models used for phase-propagation corrections. *A*, M84C Rayleigh-wave model (degree 8) at 225 s (Woodhouse and Dziewonski, 1984). *B*, MPA Rayleigh-wave model (degree 12) at 220 s (Wong, 1989). *C*, M84C Love-wave model at 225 s. *D*, MPA Love-wave model at 220 s. Path anomalies calculated by integrating along great circle from source to receivers.

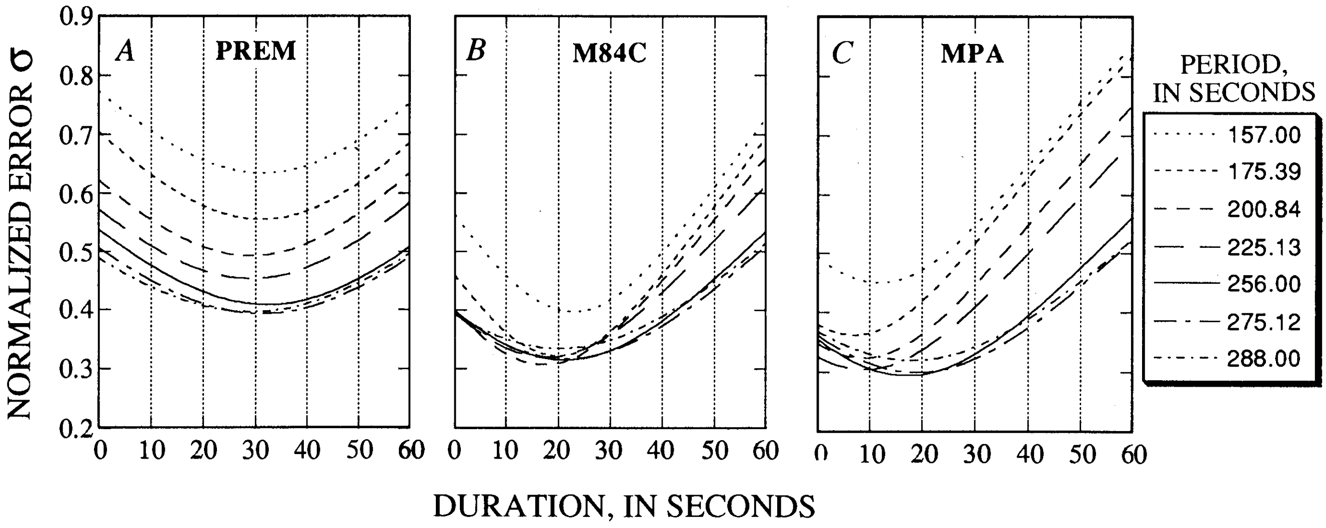

Figure 4.—Normalized error versus assumed trapezoidal source duration obtained in the first-step inversion, using PREM (*A*), M84C (*B*), and MPA (*C*) Earth models to make propagation corrections in combined inversion of Rayleigh and Love waves. Minimum of each curve is duration estimate from inversion of waves of that particular period. Estimates at each period are combined to determine optimal mean duration over period range. Mean duration estimates are 30, 20, and 11 s for PREM, M84C, and MPA models, respectively.

appear to give better estimates of the source duration, choosing between the two is difficult. The MPA model gives a source duration that is virtually identical to durations estimated from shorter period studies, and additional evidence favoring this solution is described below.

To test the propagation models further, we explored the effects of assuming different source locations in the first-step inversion. If systematic errors in the models can be mapped into a source relocation, this procedure can reduce those errors and potentially may reduce any bias in the duration estimate. This process can be visualized as locating the effective source position with a "best" point-source trapezoidal source-time function. Surface waves alone are not generally used for source-location determinations, owing to the limited resolution of the long-wavelength signals, which lack sensitivity to small location perturbations. Because our data set is of unusually high quality, we proceed to search for the source location that minimizes the first-step error, using a 112- by 112-km grid centered at the NEIC location. The gridpoints have 8-km spacing, and the spectra were corrected to each location by assuming that the NEIC origin time is unperturbed. We then invert for duration, using the first-step inversion at each gridpoint. By contouring the normalized rms error, σ, given by the average residual error for a given source duration for the seven different periods, we identify the optimal source location consistent with the corresponding propagation model and a trapezoidal representation of the source-time function.

The contours of σ over the grid obtained by using the PREM, M84C, and MPA models are shown in figures 5*A*, 5*B* and 5*C*, respectively. The contoured surfaces have well-defined minimums with a value σ_{min}, which are reasonably concentrated spatially. For the PREM model (fig. 5*A*), σ_{min}=0.483, larger than for the other models, and the minimum is located approximately 35 km northeast of the epicenter. This result should not be confused with a centroid location because we are not finding a best moment tensor in this search. Instead, we are determining how compatible the propagation models are with the observed traveltimes from the actual source location to the set of stations. The overall error reduction is only 15 percent over the grid for the PREM model. For the M84C model (fig. 5*B*), σ_{min}=0.325, the smallest value of the three models, and the apparent source location is just north of the epicenter. The area with σ values within 4 percent of σ_{min} encompasses the epicentral region. The variance reduction for the M84C model as a function of position over the grid is 30 percent, twice as large as for the PREM model. The results for the MPA model (fig. 5*C*) give σ_{min}=0.340, and the spatial-variance reduction in the grid is also 30 percent. The MPA model, however, locates the optimal source position directly on the actual epicenter, a remarkable demonstration of the consistency of the propagation corrections with the independently known source location. This result leads us to place additional confidence in the duration estimate using the MPA model, complementing the consistency with the body-wave analyses. For all three models, the actual duration estimate varies by only a few seconds over the grid (from 10 to 13 s

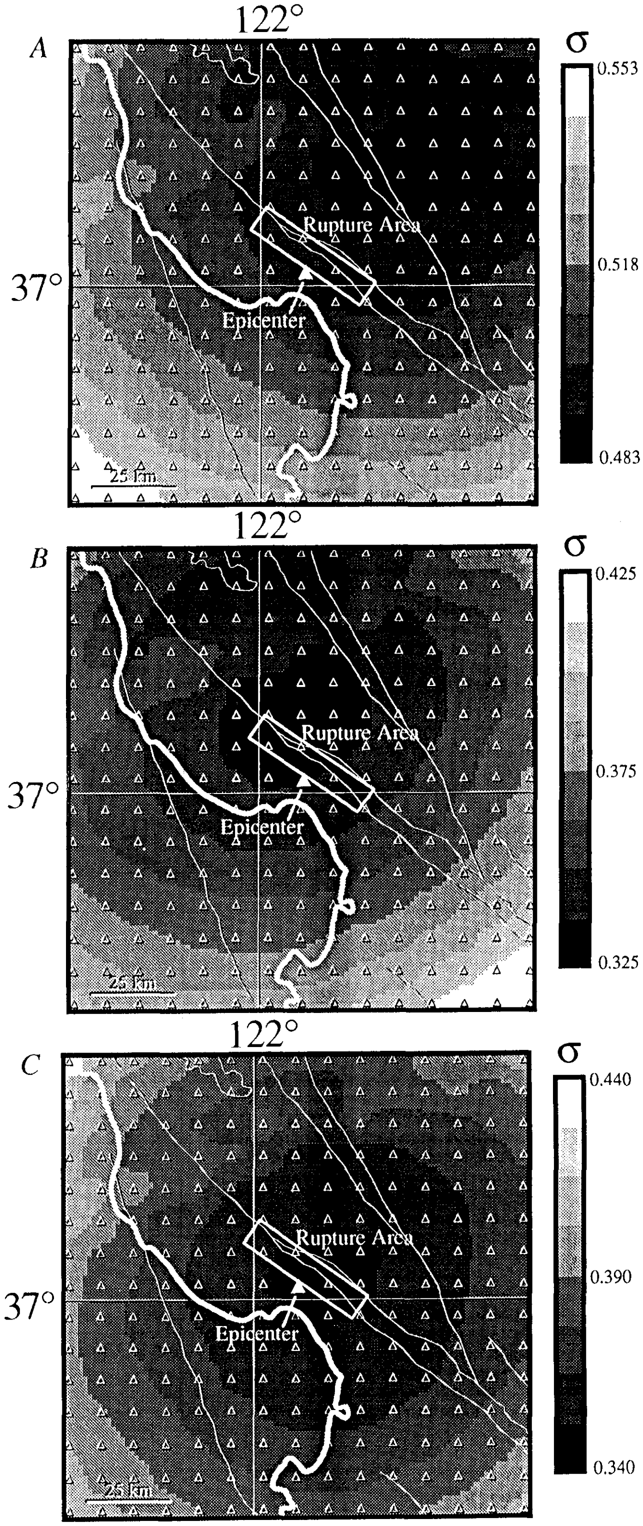

for the MPA model), and the variations are less than 1 s within the region of the lowest contour that includes the minimum. This result is important for the second-step inversion, in which we specify the source duration and then invert for the depth and moment tensor. It is thus reasonable to use a single value for the duration associated with a given propagation model when searching over the same grid for an optimal centroid location that yields the best moment-tensor fit to the data.

MOMENT TENSOR, CENTROID LOCATION, AND DEPTH ESTIMATION

The second-step inversion depends on the choice of *Q* model and source-velocity structure. Zhang and Lay (1990b) and Wallace and others (1991) explored the effect of a global *Q* model on source-depth determination, using the three models shown in figure 6, which are those of Masters and Gilbert (1983), Dziewonski and Steim (1982), Dziewonski and Anderson (1981) (subsequently referred to as the MG, DS, and PREM models, respectively). Depth determinations varied by 10 km for the 1989 Loma Prieta earthquake, depending on which model was assumed. We use the same global *Q* models in the present analysis because they represent a reasonable range of one-dimensional models. Although a new generation of aspheric *Q* models is presently emerging, correct utilization of these models requires simultaneously accounting for complex focusing and defocusing effects, owing to the velocity inhomogeneity. Such analysis is being undertaken but is not discussed further here.

The source-velocity structure used for calculating the excitation functions may be the least constrained set of model parameters required for the second-step inversion, given the complex tectonic history of the source region. Wallace and others (1991) used the four source-velocity models shown in figure 7, including the average- and young-ocean models of Regan and Anderson (1984), the average PREM model structure, and a case-specific model called LOMA, composed of the crustal P-wave-velocity model of Walter and Mooney (1982), the mantle *P*-wave-velocity model for the Western United States (GCA) of Walck (1985), and the mantle *S*-wave-velocity model for tectonic North America (TNA) of Grand and Helmberger (1985) (subsequently referred to as the RA, RA–yo, PREM, and LOMA models, respectively). Although these models span a reasonable range of upper-mantle structures expected for the tectonically active source region, a localized lithospheric model specific to the area is unavailable. Thus, an intrinsic uncertainty exists in all the source inversions. Because we have no new information regarding the appropriate structure, we utilize the same four models. Wallace and others found that the centroid depth varied by about 10 km, depending on the choice of source-excitation structure, but that other parameters are only weakly affected.

◄ Figure 5.—Loma Prieta region, Calif., showing contours of residual rms error in first-step inversion using PREM (*A*), M84C (*B*), and MPA (*C*) propagation models for different assumed source locations. 112- by 112-km grid of assumed epicentral locations, consisting of 225 points (triangles), was constructed around epicenter. Spectra were corrected back to each source location, with origin time held fixed at National Earthquake Information Center origin time. Minimum error gives optimal epicentral location for a point source. For PREM model, minimum error is located northeast of actual epicenter; for M84C model, minimum error is located slightly north of epicenter; and for MPA model, minimum error is located directly on epicenter. Duration estimates vary by only a few seconds over grid for each model.

MOMENT TENSOR AND CENTROID LOCATION

The source location affects the moment tensor through both its effects on the phase and minor amplitude effects due to propagation and attenuation, as demonstrated by Zhang and Lay (1990a). We proceed to use both Rayleigh- and Love-wave spectra to find the centroid location, depth, and moment tensor by searching over the same 112- by 112-km grid as used in the duration determination. Setting the source duration at the optimum for each propagation model, we performed numerous inversions to determine the moment tensor and depth at each gridpoint for the suite of global *Q* models (MG, DS, PREM), source-velocity models (RA, RA–yo, PREM, LOMA), and propagation models (PREM, M84C, MPA). The ρ values for each gridpoint were then contoured over the grid; the minimum ρ value gave an optimal centroid location because ρ is a measure of how well the data are fitted by the associated moment tensor for that source position. We found

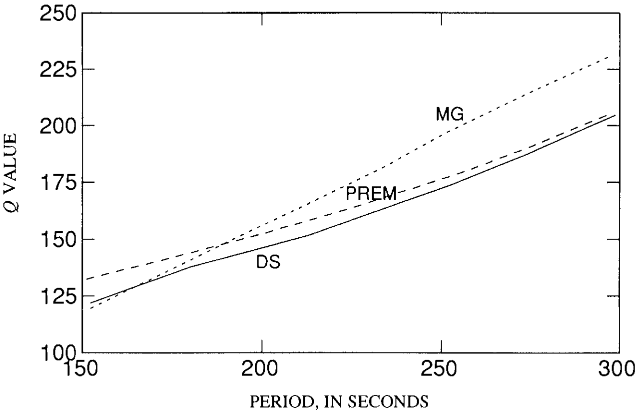

Figure 6.—Rayleigh-wave global *Q* models MG (short-dashed curve; Masters and Gilbert, 1983), PREM (long-dashed curve; Dziewonski and Anderson, 1981), and DS (solid curve, Dziewonski and Steim, 1982). Frequency-dependent variations trade off with excitation functions for a given source-velocity model, resulting in uncertainty in source depth.

that for each gridpoint the depth-resolution curves are relatively flat; however, the ρ values vary substantially over the grid, providing a fair estimate of the centroid location.

We first explore the effect of the propagation models on the second-step inversion by specifying the excitation structure to be the RA–yo model and the global Q model to be the MG model, and then inverting for depth and moment tensor at every gridpoint for the PREM, M84C, and MPA models. The resulting contours of ρ are shown in figure 8, where the duration is fixed at 30 s for the

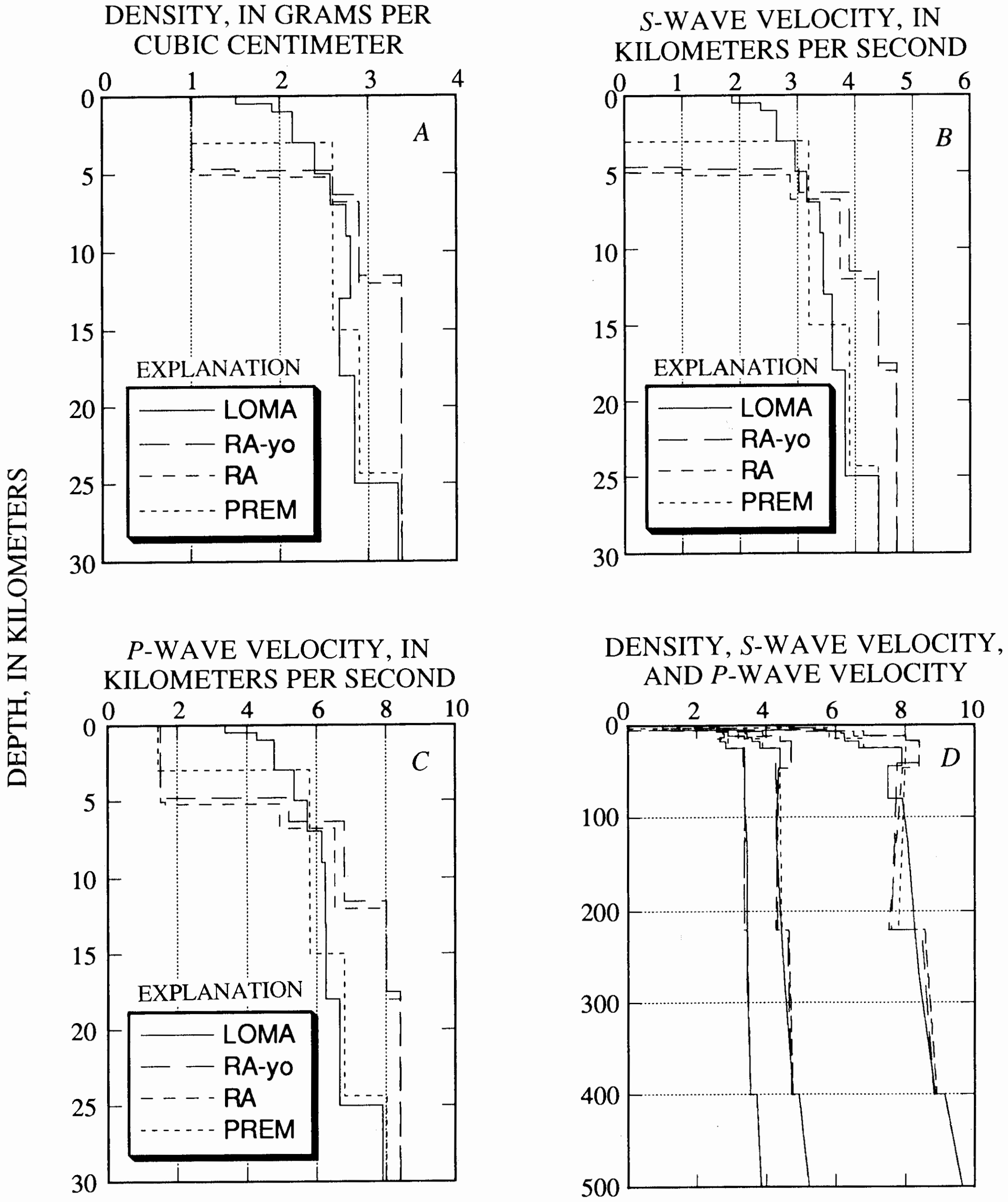

Figure 7.—Source-region velocity structures used in computation of excitation functions for surface-wave analysis. *A*, Density. *B*, *P*-wave velocity. *C*, *S*-wave velocity, *D*, Combined density, *P*-wave velocity, and *S*-wave velocity. LOMA model has *P*-wave-velocity crustal structure of Walter and Mooney (1982), with mantle-velocity structures from Walck (1985) and Grand and Helmberger (1985). RA and RA–yo models of Regan and Anderson (1984) are for average and young oceans, respectively. PREM model is from Dziewonski and Anderson (1981). Although significant uncertainty exists in correct structure to use for depths of 100 to 200 km, this suite of models spans plausible range of upper-mantle models for tectonically active source region of earthquake.

PREM model, 20 s for the M84C model, and 11 s for the MPA model. In the moment-tensor inversion, the spectra at each period are inversely weighted by the corresponding residual rms errors for the first-step inversion to accommodate the scatter in phase indicated in figure 4. Because significant differences in ρ_{min} exist between the phase-velocity models, the contour plots have been separately normalized to their ρ_{min} value, with the scale showing a range in ρ values from 1.0 to 1.5. For the PREM model (fig. 8*A*), the error reduction over the grid is only about 30 percent, and the minimum encompasses a broad region centered just north of the epicenter. The smallest ρ value (ρ_{min}=0.100) is about 30 percent higher than that for the M84C (ρ_{min}=0.0773, fig. 8*B*) and the MPA (ρ_{min}=0.0724, fig. 8*C*) models. For the M84C model (fig. 8*B*), the variation in ρ over the grid is approximately 50 percent, and the contours show a steep-sided well with a flat bottom encompassing the epicenter. The results for the MPA model (fig. 8*C*) are comparable to those for the M84C model, although ρ_{min} is slightly lower for the MPA model.

For the different propagation models, the location of ρ_{min} varies little. For the PREM, M84C, and MPA models, the centroid location is shifted just offshore about 24 km west of the epicenter. However, using the PREM propagation and excitation models shifts ρ_{min} 24 km northeast of the epicenter (fig. 8*A*). These shifts are comparable to those found for the CMT solution (fig. 1), which is heavily influenced by long-period body-wave trains in the records rather than fundamental-mode arrivals. Thus, the choice of propagation model affects not only the residual variance in the second-step inversion but also the centroid location.

The next model sensitivity that we test is the influence of the excitation structure, using the RA–yo, PREM, and LOMA models, where we specify the propagation model (MPA) and the global *Q* model (MG). The resulting contours of ρ as a function of point-source location in the source grid are shown in figure 9. The contours are scaled over a 40-percent variation in ρ to accentuate any possible differences. The LOMA model has a broad minimum (fig. 9*A*), with ρ_{min}=0.0985, whereas the PREM model (fig. 9*B*) has a lower ρ_{min}=0.0872. The result for the RA–yo model shown in figure 9*C* involves the same combination of models as in figure 8*C* but is plotted on a slightly different scale for comparison. This model has ρ_{min}=0.0724, the smallest value for the three excitation structures considered. Although a baseline shift occurs in the ρ_{min} estimates, depending on the excitation structure used, the ρ_{min} value on each surface does not vary and is located 24 km west of the epicenter. This result is obtained for various propagation models in combination with the different excitation structures. Thus, the centroid location is not affected significantly by the choice of source-velocity structure.

Our final sensitivity test is with respect to the global *Q* model used in the inversion. We specify the propagation model (MPA) and the excitation model (RA–yo), and then invert for the centroid depth and moment tensor, using the three global *Q* models (PREM, DS, MG). The centroid location results for the PREM, DS, and MG *Q* models are shown in figures 10*A*, 10*B*, and 10*C*, respectively. The choice of global *Q* model does not affect our centroid location or the shape of the minimum, and the ρ_{min} values are all virtually identical. Thus, the choice of global *Q* model strongly influences the centroid-depth and moment-

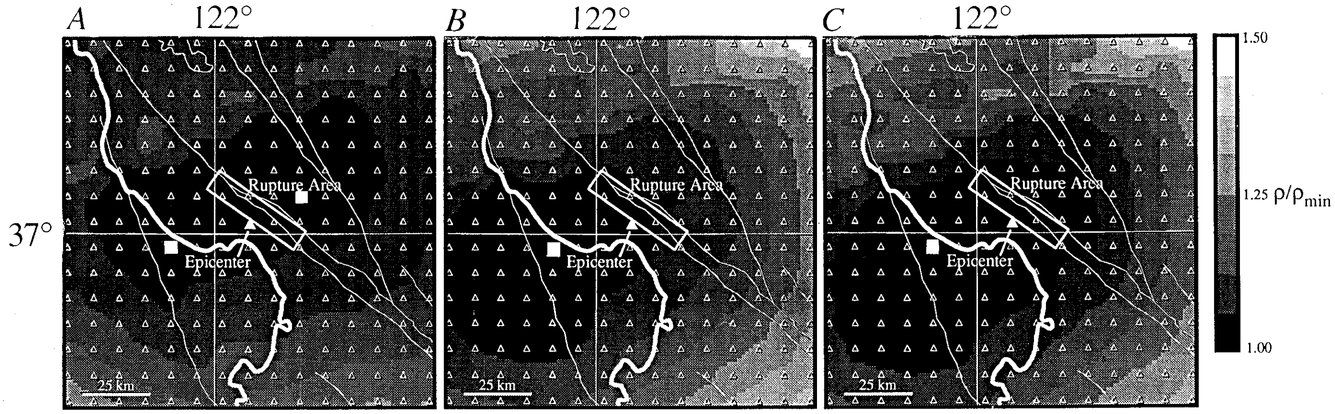

Figure 8.—Loma Prieta region, Calif., showing contours of residual rms error in second-step inversion for full moment tensor as a function of point-source location (triangles) for PREM (*A*), M84C (*B*), and MPA (*C*) propagation models. Second-step inversion is affected by choice of propagation models for a given excitation model (in this case, RA–yo young-ocean model of Regan and Anderson, 1984) and of global *Q* model (in this case, MG model of Masters and Gilbert, 1983). For PREM, M84C, and MPA models, centroid location (square) is shifted just offshore about 24 km west of epicenter (triangle). Minimum second-step error (ρ_{min}), which gives optimal centroid location for a particular combination of models, is 0.100, 0.0773, and 0.0724 for PREM, M84C, and MPA models, respectively. Using PREM propagation and excitation models results in a 20-km shift of centroid northeast of epicenter (fig. 8*A*). In each figure, minimums are broad and flat, and epicenter is encompassed by lowest contour level.

tensor estimates but not the centroid location. This result may change, however, with the advent of new aspheric global *Q* models that are currently under development.

The estimated optimal centroid locations are shifted from the epicenter, as in the CMT solution, but this location brings the Rayleigh- and Love-wave estimates of the $\mathbf{M}_{yz}$ moment-tensor element into better agreement for the MPA and M84C propagation models, yielding unconstrained moment-tensor inversions that are consistent with body-wave studies. The location bias is most likely due to errors in the models because the source does not have a significant spatial finiteness. Although the ρ value at the epicenter is within a few percent of that at the optimal centroid location for any of the model combinations, we found that the results generally are significantly more stable if we use the centroid location. Even a difference of a few percent in variance reduction can destabilize the inversion for such poorly constrained terms as $\mathbf{M}_{xz}$ and $\mathbf{M}_{yz}$. Inversions at the epicenter generally give strikes and rakes that are 10° lower than the centroid results, which are less consistent with the body waves. Thus, centroid optimization gives improved results over those of Wallace and others (1991), who considered only sources at the epicenter.

The stability of the moment-tensor inversions around the centroid location is illustrated in figure 11 for the particular combination of the MPA, RA–yo, and MG models, where the best double-couple solutions for each moment-tensor inversion are shown at nine source positions around the optimum centroid, as well as at the epicenter. Because the nine source locations are within the region where ρ is minimized (for example, fig. 10*C*), the mechanisms vary only slightly (4° in strike, 4° in dip, 6° in rake). At the epicenter, which is slightly farther from the minimum, the rake and strike vary by as much as 10°, and

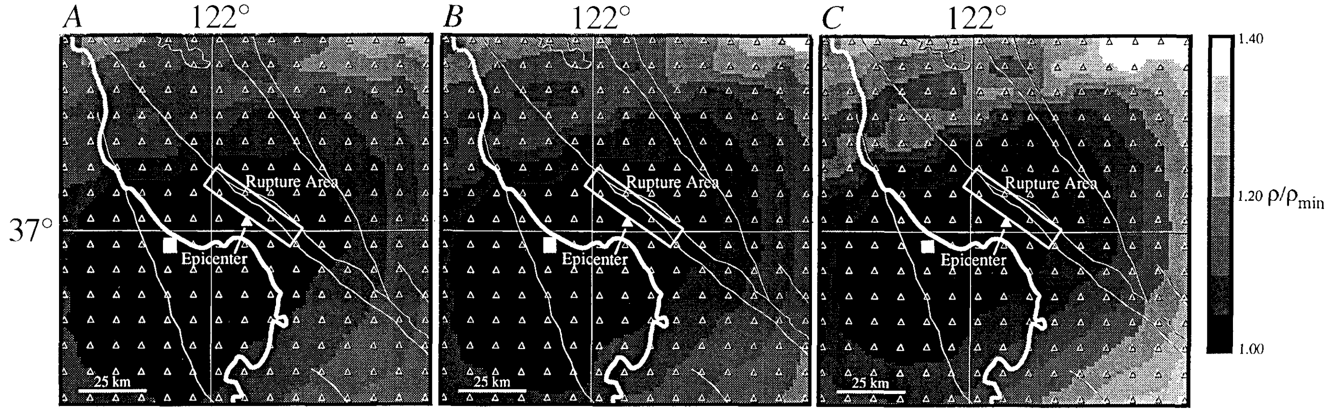

Figure 9.—Loma Prieta region, Calif., showing contours of residual rms error in second-step inversion for full moment tensor as a function of point-source location (triangles) for LOMA (*A*), PREM (*B*), and RA–yo (*C*) excitation models. Propagation model is MPA, and global *Q* model is MG. Centroid location (square) does not depend on the choice of excitation model, although RA–yo model has lowest absolute error and most spatially concentrated minimum.

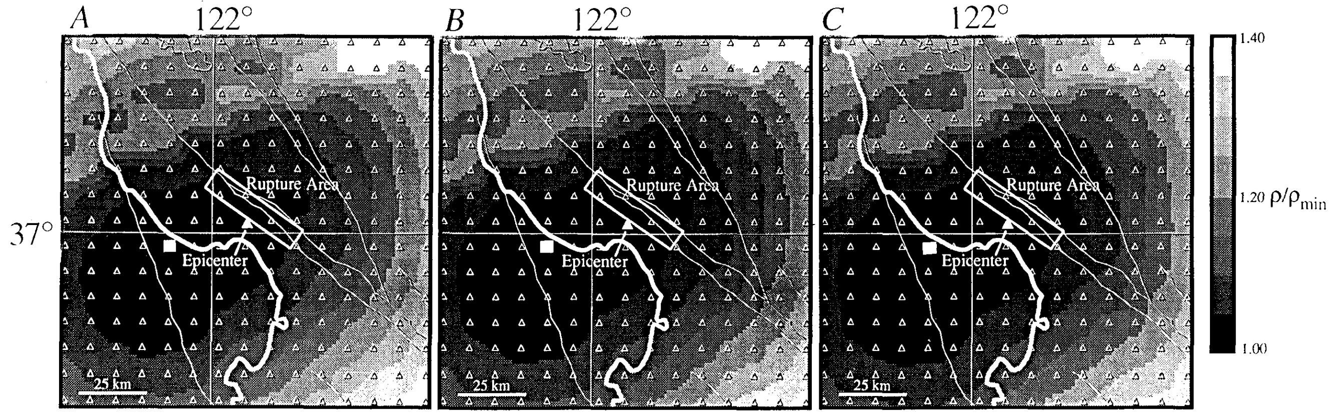

Figure 10.—Loma Prieta region, Calif., showing contours of residual rms error in second-step inversion for full moment tensor as a function of point-source location (open triangles) for PREM (*A*), DS (*B*), and MG (*C*) global *Q* models. Propagation model is MPA, and excitation model is RA–yo. Centroid location (square) does not depend on choice of global *Q* model.

the variations increase with distance from the optimum centroid. The results shown here are comparable to those obtained by using the RA–yo and MG models in combination with the M84C model, whereas using the PREM model with these models gives greater stability, with a difference of only a few degrees in mechanisms at the centroid and the epicenter. Using the PREM model alone, however, for propagation and excitation does not yield good results.

It is by no means obvious that using an effective source location which gives the best variance reduction for the moment tensor will necessarily give the best moment-tensor estimate. This consideration also holds for the CMT procedure. We find the encouraging result that no matter what the choice of phase velocity and attenuation model and for most reasonable source-excitation structures, the solutions for the simultaneous Rayleigh- and Love-wave inversion are essentially identical when performed at the optimal centroid location for the particular model combination. This stability suggests that the primary differences in the spectra corrected for the different models are small, slowly varying phase and amplitude patterns, as is apparent in the significant differences between moment-tensor inversions for different model combinations when the epicenter location (or any other common source location) is assumed. The centroid-location procedure projects most of these small, low-degree azimuthal patterns into the source relocation, finding in each case a comparable moment-tensor fit to the Rayleigh- and Love-wave spectra. This fit is stable only because of the significant differences in radiation pattern for these spectra, and the centroid optimization may not converge to the correct solution if only Rayleigh waves are used, as noted by Zhang and Lay (1990a). The CMT inversion is similarly stabilized by the differences in radiation pattern of the body- and surfaces-wave arrivals in the wave trains that are inverted. Because the centroid optimization somewhat reduces the dependence on the model parameters, we can establish realistic confidence bounds on our source-parameter estimates by comparing the suite of results for different model combinations.

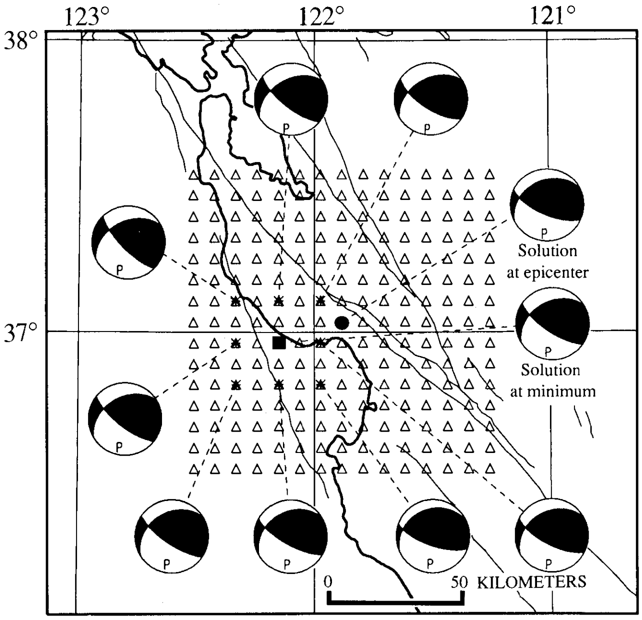

Figure 11.—Loma Prieta region, Calif., showing sensitivity to point-source location (triangles) for simultaneous Rayleigh- and Love-wave focal mechanism determinations for MPA phase-velocity, MG global *Q*, and RA–yo excitation models. Major double-couple solutions are plotted for centroid locations at trial source locations (asterisks). Dot, solution at actual epicenter; square, solution at optimum centroid location as defined by minimum error (ρ) of second-step inversion. Strike, dip, and rake vary little around minimum and are approximately 123°±4°, 71°±4°, and 124°±6°, respectively.

DEPTH

Associated with the moment-tensor inversions is a search over point-source depth at each source location. Depth-resolution curves generally have fairly well defined minimums for inversions that use only Rayleigh waves, whereas simultaneous only Rayleigh- and Love-wave inversions give flattened depth curves (fig. 12), as noted by Wallace and others (1991), owing largely to the absence of depth dependence of the Love-wave-excitation functions but also reflecting some source-model incompatibility with the joint Rayleigh- and Love-wave data. For example, results using different excitation structures, the MPA phase-velocity model, and the MG global *Q* model are plotted in figures 12*A* and 12*C* for the Rayleigh-wave and the simultaneous Rayleigh- and Love-wave inversions, respectively. In both figures, the RA–yo model significantly reduces the overall variance and gives shallower depth estimates relative to the other source structures. The simultaneous inversions show greater sensitivity to the excitation models, and the case-specific LOMA model apparently does not fit the Love-wave data particularly well relative to the other models, accounting for some of the unstable solutions found using this model.

The choice of global *Q* model also affects the depth estimate, as shown in figures 12*B* and 12*D*; shallower depths are obtained when using the MG model, which gives a slightly lower residual variance for the Rayleigh-wave inversion (fig. 12*B*) but no significant difference for the simultaneous inversions (fig. 12*D*). Clearly, a substantial uncertainty exists in the depth estimates, given both the flatness of these curves and our ignorance of which source-velocity structure is most appropriate. (The LOMA model is probably inadequate.) Thus, we assign large uncertainties to our depth estimate. Taking into account the variation in depth determinations for the different global *Q* models and source-velocity structures, our final depth estimate is 22±11 km. For the models with water layers (PREM, RA–yo) the depth into the solid crust is 5 km less, giving a centroid depth in the crust of about 17±11 km; however, changing the crustal structure from oceanic to continental has little effect on the depth estimate (Zhang and Lay, 1990b).

PREFERRED SOLUTION

In our final inversion, we use the MPA phase-velocity model, the RA–yo source-structure model, and the MG global *Q* model to demonstrate the fit to the data. In figure 13, the azimuthal patterns of observed amplitude (dots) and phase (squares) spectra are compared with the theoretical moment tensor (solid curves) found in the simultaneous inversion of Rayleigh and Love waves for six of the seven periods used in the inversion. (The 288-s data are not shown, but they closely resemble the 275-s data.) Each point is an observed spectral measurement of amplitude or phase for Rayleigh-wave (R_1, R_2) or Love-wave (G_1, G_2) arrivals. The high signal-to-noise ratio apparent in the time domain in figure 2 results in high-quality spectral measurements with very little scatter. Amplitude scat-

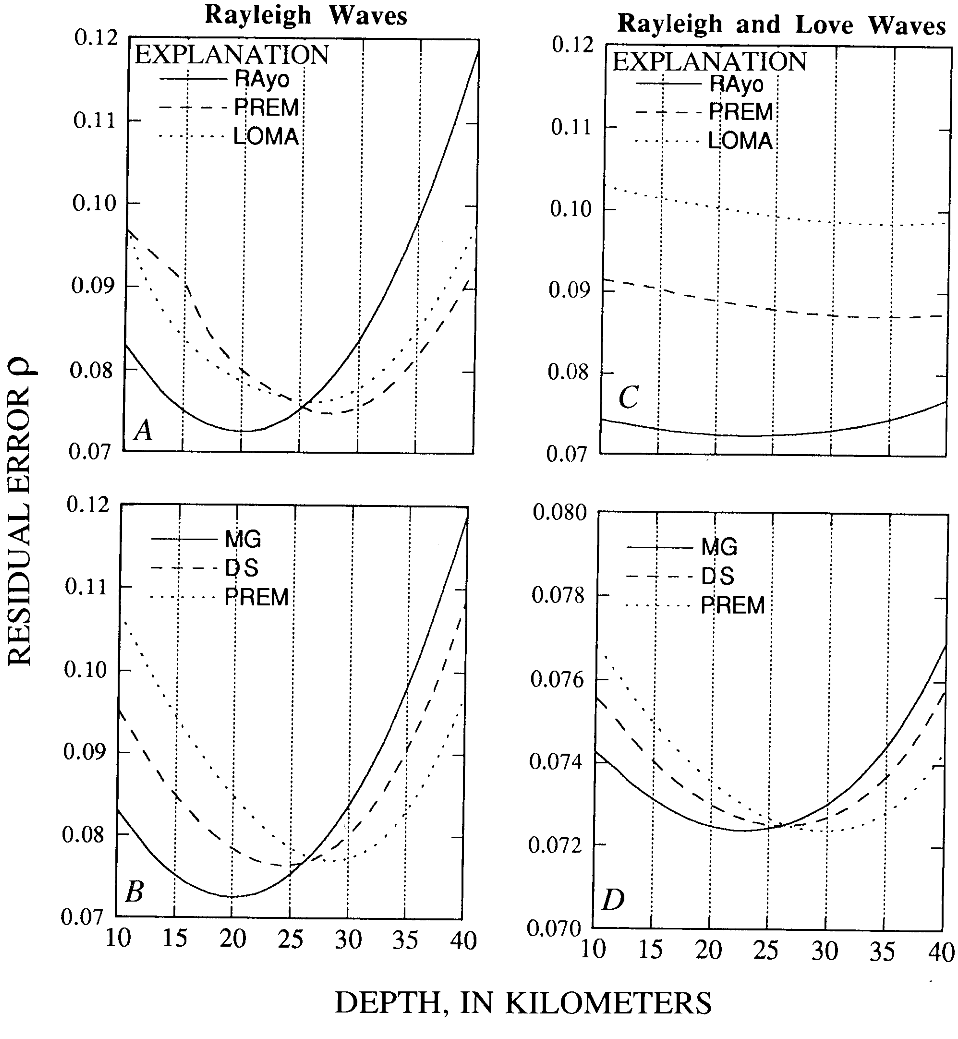

Figure 12.—Residual rms error versus depth for various combinations of excitation and global *Q* models at optimal centroid location, using MPA model for propagation corrections. *A*, Rayleigh-wave results using MG global *Q* model for RA–yo, PREM, and LOMA excitation models. *B*, Rayleigh-wave results using RA–yo excitation model for MG, DS, and PREM global *Q* models. *C*, Simultaneous-inversion Rayleigh- and Love-wave results using MG global *Q* model for RA–yo, PREM, and LOMA excitation models. *D*, Simultaneous-inversion Rayleigh- and Love-wave results using RA–yo excitation model for MG, DS, and PREM global *Q* models. Inclusion of Love waves in inversion flattens normalized error curve for second-step inversion, giving poor depth resolution. Overall depth estimate is 22±11 km for our preferred choices of source model (RA–yo) and global *Q* model (DS or MG).

ter increases for shorter periods, but the data generally are very well behaved and clearly exhibit coherent radiation patterns. The moment-tensor terms for this final solution are listed in table 3, along with those for the CMT solution of Dziewonski and others (1990); these results are generally quite compatible.

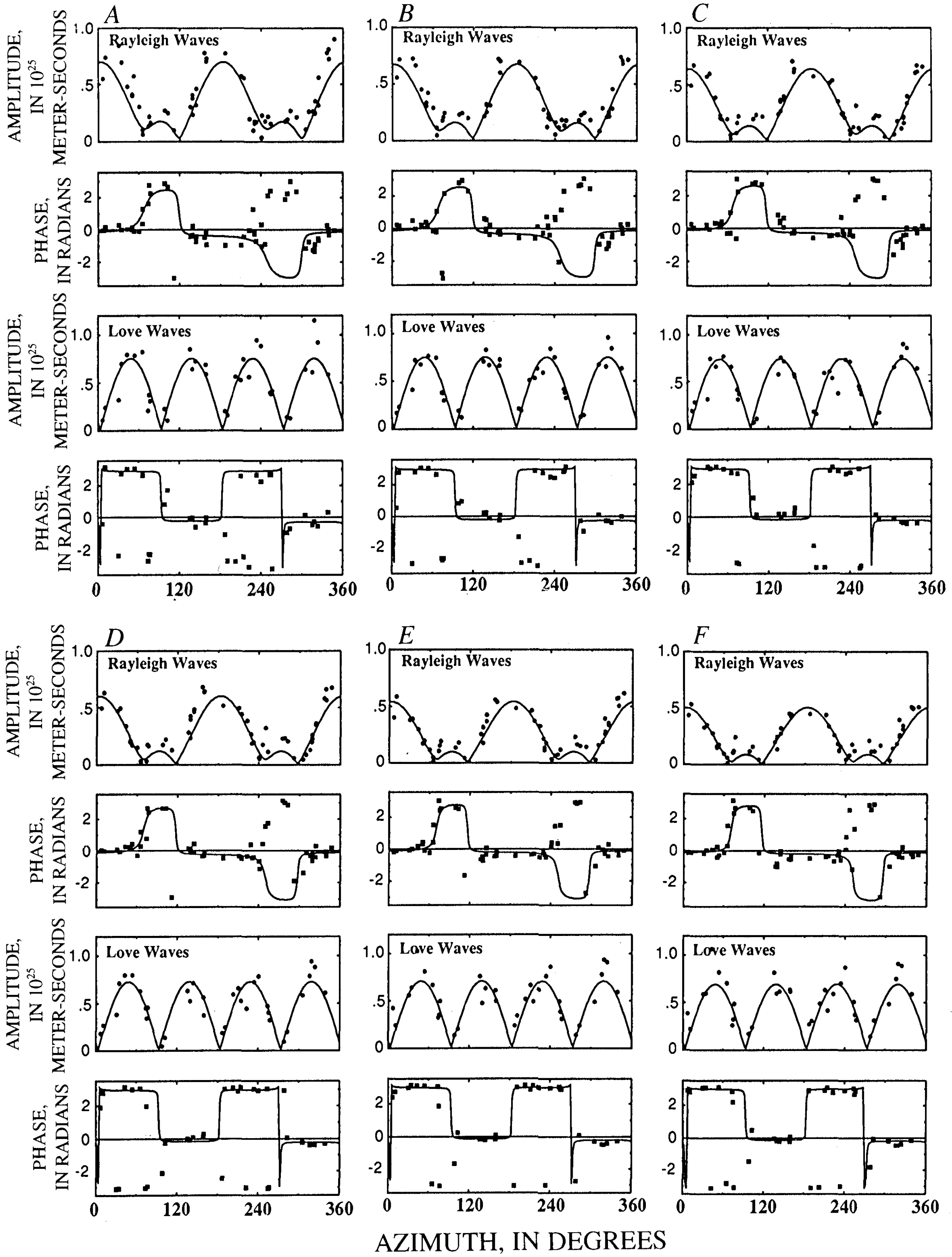

Figure 13.—Moment-tensor-inversion results from simultaneous inversions of Rayleigh and Love waves at periods of (*A*) 157, (*B*) 175, (*C*) 200, (*D*) 225, (*E*) 256, and (*F*) 275 s. Curves are theoretical fits determined from solution using RA–yo excitation, MG global *Q*, and MPA phase-velocity models. Dots, amplitude data; squares, phase data. Note excellent fit to observed spectra over period range investigated.

Table 3.—*Moment-tensor solutions for the earthquake*

[All values in 10^{19} N-m. CMT, centroid moment tensor]

This study		Resulting terms		CMT	
$\mathbf{M}_{yy} - \mathbf{M}_{xx}$	4.07±0.05	$\mathbf{M}_{zz}$	1.49	$\mathbf{M}_{rr} = \mathbf{M}_{zz}$	1.21±0.02
$\mathbf{M}_{yy} + \mathbf{M}_{xx}$	−1.49±0.10	$\mathbf{M}_{xx}$	−2.78	$\mathbf{M}_{\theta\theta} = \mathbf{M}_{xx}$	−2.37±0.02
		$\mathbf{M}_{yy}$	1.29	$\mathbf{M}_{\varphi\varphi} = \mathbf{M}_{yy}$	1.16±0.02
$\mathbf{M}_{xz}$	−1.61±0.77			$\mathbf{M}_{r\theta} = -\mathbf{M}_{xz}$	1.17±0.15
$\mathbf{M}_{yz}$	1.52±0.77			$\mathbf{M}_{r\varphi} = -\mathbf{M}_{yz}$	−.99±0.16
$\mathbf{M}_{xy}$	.24±0.05			$\mathbf{M}_{\theta\varphi} = \mathbf{M}_{xy}$	.10±0.02

It is encouraging to note that the new phase-velocity model, MPA, yields a stable solution consistent with those of previous studies, without employing any constraints on the inversions. The duration estimate of 11 s and the consistency of the phase with the epicentral location for the MPA model provides evidence that this model gives the most reliable results. We find, however, that for the simultaneous inversion of Rayleigh and Love waves, it is still important to determine an optimal centroid location to ensure a stable solution. On the basis of our preference for the MPA model, along with our consideration of the uncertainty in the source structure and global Q model, our final duration is τ=11±5 s, and our depth estimate is 22±11 km.

Taking into account the slight changes in mechanism due to uncertainties in choosing a preferred Earth-model combination, our preferred major double-couple representation for the earthquake has a mechanism with a strike of 124°±6°, a dip of 67°±6°, and a rake of 126°±7°, where the stated uncertainties include our assessment of the model dependence. Seismic-moment estimates vary little in the vicinity of the centroid, and for all model combinations that give reasonable solutions (some of the inversions with the LOMA model excitation functions do not), we obtain a moment M_0 of $(3.0\pm0.2)\times10^{19}$ N-m. The non-double-couple component varies by 5 to 30 percent, depending on the source location, global Q model, and source-velocity model; solutions near the centroid have about 10 percent minor double couples, which we deem to be noise effects. Comparison of these final parameters with the other long-period results listed in table 1 indicates a good consistency, particularly with the CMT solution of Dziewonski and others (1990).

DISCUSSION

We now compare our results with those of other investigations of the Loma Prieta source, with an emphasis on assessing any systematic frequency-dependent differences. Understanding any discrepancies between short- and long-period source models is essential for understanding the rupture processes of large earthquakes. One physical explanation for the frequency dependence of source properties may be a variation in energy release along a fault surface, with "patches" of large displacement that fail with rapid rupture, producing high-frequency body-wave radiation, while the surrounding regions slip slowly, with a predominantly long period signature. Both teleseismic and strong-motion investigations of the earthquake suggest some nonuniform slip on the fault, which would be unresolvable by our surface-wave analysis but could give rise to some frequency dependence of the source parameters. Another possible cause of a discrepancy could be slow coseismic slip in the lower crust or uppermost mantle at the base of the aftershock zone. High strain rates during the main-shock rupture may induce coseismic failure on the downdip extension of the fault, where grain size and thermal conditions may cause differences in rupture or particle velocities affecting the spectrum of seismic radiation (for example, Das, 1982).

All the available source-parameter determinations for the 1989 Loma Prieta earthquake are summarized in figure 14. Wallace and others (1991), in discussing the differences between their body- and surface-wave results, observed that the surface-wave rupture-duration and depth estimates were both larger than the body-wave estimates,

Figure 14.—Summary of (*A*) moment, (*B*) depth, and (*C*) duration estimates from this study and previous body-wave studies by (1) Wallace and others (1991), (2, 3) Kanamori and Satake (1990), (4) Choy and Boatwright (1990), (5) Ruff and Tichelaar (1990), (6) Romanowicz and Lyon-Caen (1990), (7, 8) Langston and others (1990), (9) Barker and Salzberg (1990), (10) Wallace and Lay (1990), (11) Nábělek (1990), (12) Ammon (1991), and (13) Wald and others (1991); long-period surface-wave studies of (14) this study, (15) Wallace and others (1991), (16) Dziewonski and others (1990), (17, 18) Kanamori and Satake (1990), (19) Romanowicz and Lyon-Caen (1990), (20) Zhang and Lay (1990b); and free-oscillation study of (21) Jordan (1991). Our moment and depth estimates overlap with those of other investigations. Duration results for our preferred propagation model (MPA) are consistent with those of body-wave studies.

whereas the seismic moment at long periods was marginally larger than at least some body-wave results, suggesting that deep, slow slip may have occurred during the earthquake. With our further surface-wave analysis, our seismic-moment estimate is slightly reduced to (3.0±0.2)×10^{19} N-m; other surface-wave and free-oscillation results give estimates of 2.5×10^{19} to 3.4×10^{19} N-m.

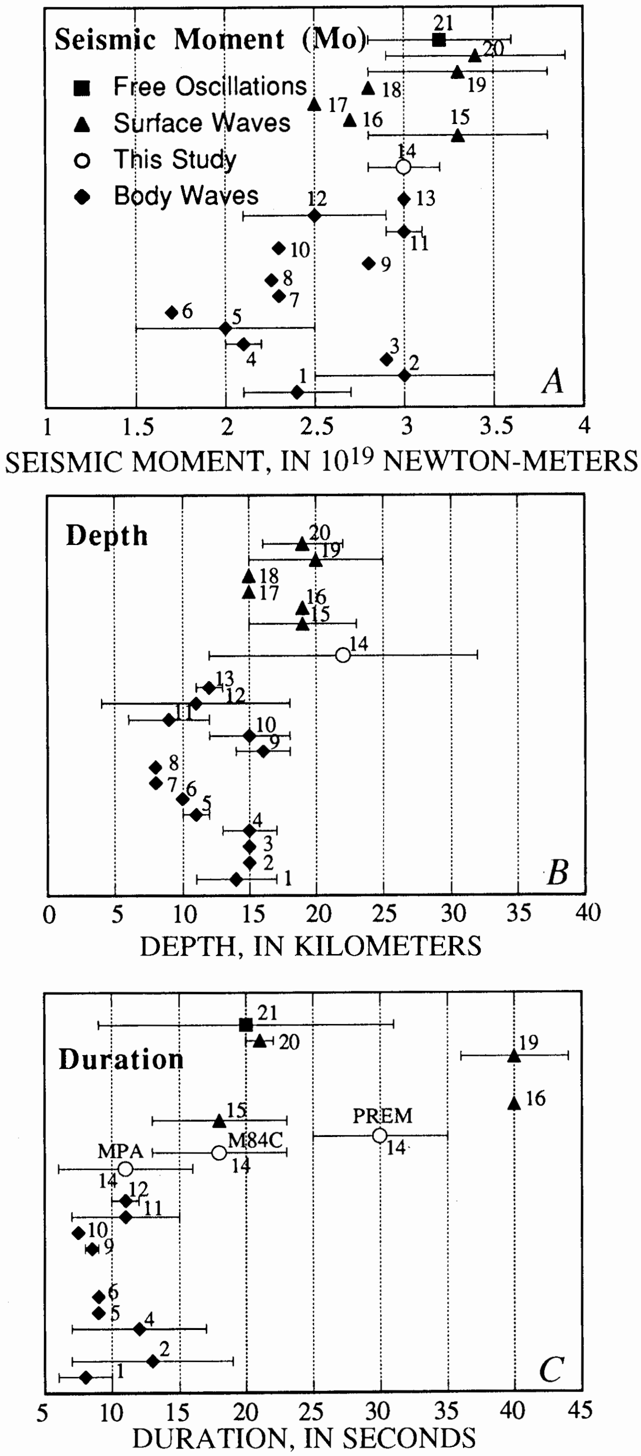

The body-wave results (fig. 14) for seismic moment range from 1.7×10^{19} to 3.0×10^{19} N-m, and the most complete body-wave studies (for example, Wald and others, 1991) yield the larger values. If these body-wave results are not biased by the renormalization procedure used in scaling up poorly matched strong-motion waveforms to fit peak amplitudes, then we can conclude that there is no discrepancy in the moment estimates, suggesting a fairly high corner frequency for the source. Comparing depth estimates (fig. 14), we note that our depth estimate has a larger uncertainty than other long-period estimates. This larger uncertainty in part reflects our inversion of both Rayleigh and Love waves, which increases the sensitivity of our estimate to poorly known source structure but includes our awareness of the strong model dependence. Thus, our error bars overlap with the results of previous body-wave studies, as well as of surface-wave and free-oscillation studies (fig. 14). Therefore, at present, no resolvable discrepancy appears to exist between long- and short-period depth estimates.

Finally, our results for source duration range from 11 s for the MPA model to 30 s for the PREM model. We prefer the results from the MPA model, for the reasons stated above. Thus, the centroid time of the moment release is 6.1 s after the onset of rupture. The surface waves we use are more sensitive to the centroid time than to the shape of the source function. To compare this result with the body-wave results, we must ensure a common origin time for reference. Wald and others (1991) discovered a 1.6-s precursor to the main rupture, which cannot be seen teleseismically but appears to correspond to the origin time of the local-array trigger, as reported by Dietz and Ellsworth (1990). Because we use this origin time (0004:15.21 G.m.t. Oct. 18, 1989) in our analysis, our time function must be shifted slightly from those obtained from teleseismic body-wave results (fig. 15). The source-time function from our study and that from teleseismic broadband body-wave deconvolutions (Wallace and others, 1991) have highly consistent centroid times. Given our preference for the results from the MPA model, we find no duration discrepancy. Thus, we see no evidence supporting the hypothesis of a significant frequency dependence of the source parameters, and thus no evidence for deep, slow slip or other anomalous long-period radiation.

Although our procedure provides an optimal centroid location for each model combination, we attach no significance to this location because it is probably a manifestation of model inadequacies. Comparing our centroid location from the second-step inversions to the CMT solution (fig. 1), we find that our centroid location is shifted to the west, whereas the CMT inversion shifts the centroid to the east, of the epicenter. This difference probably results from the different types of data used. If we use the CMT centroid location in the surface-wave inversion, we obtain unacceptable results, suggesting that the CMT inversion and centroid location primarily fit the body-wave part of the seismograms. We have demonstrated that global Q and source-velocity models have little effect on the centroid location. Furthermore, we note that the phase-velocity-propagation models affect the centroid location in the second-step inversion, despite our use of optimal source durations for the different models. This effect indicates that residual phase anomalies from the first-stage inversion can be suppressed in the second-stage inversion, which uses a complex-number representation of the spectra. We find that by minimizing the second-stage error, ρ, we can stabilize the estimation of source parameters, regardless of which propagation model is utilized, as long as the excitation and Q structures are compatible with the data.

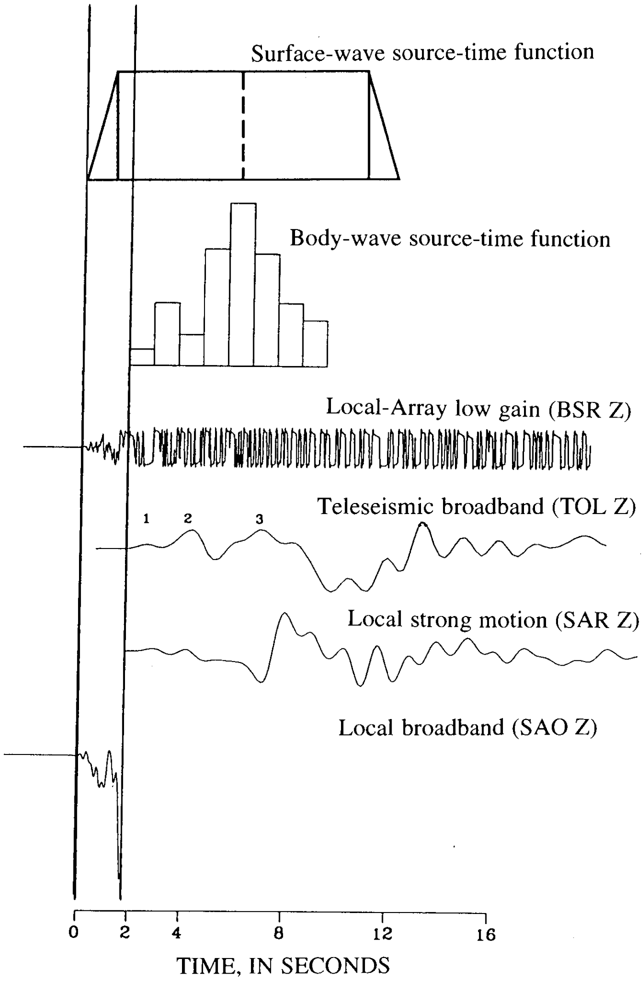

Figure 15.—Comparisons of our surface-wave source-time function, a deconvolved body-wave source-time function (Wallace and others, 1991), with local and teleseismic data (after Wald and others, 1991) for 1989 Loma Prieta earthquake. BSR Z, TOL Z, SAR Z, and SAO Z are vertical-component displacement seismograms recorded at local or teleseismic distances. Labels 1, 2, and 3 on TOL Z seismogram denote identified pulses of energy corresponding to subevents. A 1.6-s time shift of strong motions and teleseismic signals relative to local-array-triggering arrival, caused by a small precursory radiation, was identified by Wald and others (1991). Note consistency in centroid time of moment release between surface- and body-wave source-time functions.

CONCLUSIONS

In this study, we have extended the analysis of long-period fundamental-mode Rayleigh and Love waves for periods ranging from 157 to 288 s for the 1989 Loma Prieta earthquake, and further explored the stability of the estimates of focal mechanism, seismic moment, centroid depth, source duration, and centroid location. Source duration and centroid location are both influenced by the choice of propagation model. By including a recent spherical-harmonic degree 12 phase-velocity model, MPA, the long-period analysis gives a source duration and source location consistent with those from other studies. Attenuation and source-velocity-structure models mainly affect centroid-depth and moment-tensor estimates. We introduce a procedure for searching for an optimal centroid location that appears to significantly stabilize focal-mechanism determinations for simultaneous inversions of Rayleigh and Love waves. Although significant model uncertainty increases the confidence bounds on our source-parameter estimates, we find no significant discrepancies in the long-period parameters relative to the results for shorter period waves. Thus, we conclude that no evidence exists for anomalous long-period radiation from the main shock. Better resolution of frequency-dependent source phenomena will require improved propagation and attenuation models, many of which are currently being developed. Future application of these new models to the excellent Loma Prieta data is well justified, given the large confidence bounds in the present work and the value of this event for calibrating methodologies.

ACKNOWLEDGMENTS

This research was partly supported by U.S. Geological Survey grant 14–08–0001–G1843 and U.S. National Science Foundation grant EAR–9017767, with facilities support from the W.M. Keck Foundation. We thank the many individuals at IRIS and IDA, and Jean-Paul Montagner of GEOSCOPE, who supplied us with the long-period data. We also thank Barbara Romanowicz and Paul Spudich for their constructive reviews of the manuscript.

REFERENCES CITED

Ammon, C.J., 1991, A contribution to the inversion of seismic body waves for earth structure and seismic source parameters: University Park, Pennsylvania State University, Ph.D. thesis, 194 p.

Barker, J.S., and Salzberg, D.H., 1990, Long-period and broad-band teleseismic body waves modeling of the Loma Prieta earthquake: Geophysical Research Letters, v. 17, no. 9, p. 1409–1412.

Choy, G.L., and Boatwright, John, 1990, Source characteristics of the Loma Prieta, California, earthquake of October 18, 1989 from global digital seismic data: Geophysical Research Letters, v. 17, no. 8, p. 1183–1186.

Das, Shamita, 1982, Appropriate boundary conditions for modeling very long earthquakes and physical consequences: Seismological Society of America Bulletin, v. 72, no. 6, pt. A, p. 1911–1926.

Dietz, L.D., and Ellsworth, W.L., 1990, The October 17, 1989, Loma Prieta, California, earthquake and its aftershocks; geometry of the sequence from high-resolution locations: Geophysical Research Letters, v. 17, no. 9, p. 1417–1420.

Dziewonski, A.M., and Anderson, D.L., 1981, Preliminary reference Earth model: Physics of the Earth and Planetary Interiors, v. 25, no. 4, p. 297–356.

Dziewonski, A.M., Ekström, Goran, Woodhouse, J. H., and Zwart, Gretchen, 1990, Centroid-moment tensor solutions for October–December 1989: Physics of the Earth and Planetary Interiors, v. 62, no. 3–4, p. 194–207.

Dziewonski, A.M., and Steim, J.M., 1982, Dispersion and attenuation of mantle wave through waveform inversion: Royal Astronomical Society Geophysical Journal, v. 70, no. 2, p. 503–527.

Grand, S.P., and Helmberger, D.V., 1985, Upper mantle shear structure of North America: Royal Astronomical Society Geophysical Journal, v. 76, no. 2, p. 399–438.

Jordan, T.H., 1991, Far-field detection of slow precursors to fast seismic ruptures: Geophysical Research Letters, v. 18, no. 11, p. 2019–2022.

Kanamori, Hiroo, and Anderson, D.H., 1975, Theoretical basis of some empirical relations in seismology: Seismological Society of America Bulletin, v. 65, no. 5, p. 1073–1095.

Kanamori, Hiroo, and Given, J.W., 1981, Use of long-period surface waves for rapid determination of earthquake-source parameters: Physics of the Earth and Planetary Interiors, v. 27, no. 1, p. 8–31.

Kanamori, Hiroo, and Satake, Kenji, 1990, Broadband study of the 1989 Loma Prieta earthquake: Geophysical Research Letters, v. 17, no. 8, p. 1179–1182.

Kanamori, Hiroo, and Stewart, G.S., 1976, Mode of strain release along the Gibbs fracture zone, mid-Atlantic Ridge: Physics of the Earth and Planetary Interiors, v. 11, p. 312–332.

Langston, C.A., Furlong, K.P., Vogfjord, K.S., Clouser, R.H., and Ammon, C.J., 1990, Analysis of teleseismic body waves radiated from the Loma Prieta earthquake: Geophysical Research Letters, v. 17, no. 8, p. 1405–1408.

Masters, Guy, and Gilbert, Freeman, 1983, Attenuation in the earth at low frequency: Royal Society of London Philosophical Transactions, ser. A, v. 308, no. 1504, p. 479–522.

Nábělek, J.L., 1990, Rupture process of the October 18, 1989 Loma Prieta earthquake from broadband teleseismic body waves [abs.]: Seismological Research Letters, v. 61, no. 1, p. 46.

Oppenheimer, D.H., 1990, Aftershock slip behavior of the 1989 Loma Prieta, California, earthquake: Geophysical Research Letters, v. 17, no. 8, p. 1199-1202.

Regan, Janice, and Anderson, D.L., 1984, Anisotropic models of the upper mantle: Physics of the Earth and Planetary Interiors, v. 35, no. 4, p. 227–263.

Romanowicz, Barbara, and Guillemant, Philippe, 1984, An experiment in the retrieval of depth and source mechanism of large earthquakes using very long-period Rayleigh wave data: Seismological Society of America Bulletin, v. 74, no. 2, p. 417–437.

Romanowicz, Barbara, and Lyon-Caen, Hélène, 1990, The Loma Prieta earthquake of October 18, 1989: results of teleseismic mantle and body wave inversion: Geophysical Research Letters, v. 17, no. 8, p. 1191–1194.

Ruff, L.J., and Tichelaar, B.W., 1990, Moment tensor rate functions for the 1989 Loma Prieta earthquake: Geophysical Research Letters, v. 17, no. 8, p. 1187–1190.

Schwartz, S.Y., and Lay, Thorne, 1988, Effects of off great-circle propagation on the phase of long-period surface waves: Royal Astronomical Society Geophysical Journal, v. 91, no. 1, p. 143–154.

Walck, M.C., 1985, The upper mantle beneath the north-east Pacific rim; a comparison with the Gulf of California: Royal Astronomical Society Geophysical Journal, v. 81, no. 1, p. 243–276.

Wald, D.J., Helmberger, D.V., and Heaton, T.H., 1991, Rupture model of the 1989 Loma Prieta earthquake from the inversion of strong motion and broadband teleseismic data: Seismological Society of America Bulletin, v. 81, no. 5, p. 1540–1572.

Wallace, T.C., and Lay, Thorne, 1990, Source model for the Loma Prieta earthquake from regional and teleseismic body waves [abs.]: Seismological Research Letters, v. 61, no. 1, p. 46.

Wallace, T.C., Velasco, A., Zhang, Jiajun, and Lay, Thorne, 1991, A broadband seismological investigation of the 1989 Loma Prieta, California, earthquake; evidence for deep, slow slip?: Seismological Society of America Bulletin, v. 81, no. 5, p. 1622–1646.

Walter, A.W., and Mooney, W.D., 1982, Crustal structure of the Diablo and Gabilan ranges, central California; a reinterpretation of existing data: Seismological Society of America Bulletin, v. 72, no. 5, p. 1567–1590.

Wong, Y.K., 1989, Upper mantle heterogeneity from phase and amplitude data of mantle waves: Cambridge, Mass., Harvard University, Ph.D. thesis, 209 p.

Woodhouse, J.H., and Dziewonski, A.M., 1984, Mapping the upper mantle; three-dimensional modeling of Earth structure by inversion of seismic waveforms: Journal of Geophysical Research, v. 89, no. B7, p. 5953–5986.

Zhang, Jiajun, and Kanamori, Hiroo, 1988a, Depths of large earthquakes determined from long-period Rayleigh waves: Journal of Geophysical Research, v. 93, no. B5, p. 4850–4868.

———1988b, Source finiteness of large earthquakes measured from long-period Rayleigh waves: Physics of the Earth and Planetary Interiors, v. 52, no. 1–2, p. 56–84.

Zhang, Jiajun, and Lay, Thorne, 1989, Duration and depth of faulting of the 22 June 1977 Tonga earthquake: Seismological Society of America Bulletin, 79, no. 1, p. 51–66.

———1990a, Effects of centroid location on determination of earthquake mechanisms using long-period surface waves: Seismological Society of America Bulletin, v. 80, no. 5, p. 1205–1231.

———1990b, Source parameters of the 1989 Loma Prieta earthquake determined from long-period Rayleigh waves: Geophysical Research Letters, v. 17, no. 8, p. 1195–1198.

THE LOMA PRIETA, CALIFORNIA, EARTHQUAKE OF OCTOBER 17, 1989: EARTHQUAKE OCCURRENCE

MAIN-SHOCK CHARACTERISTICS

STRONG-MOTION AND BROADBAND TELESEISMIC ANALYSIS OF THE EARTHQUAKE FOR RUPTURE PROCESS AND HAZARDS ASSESSMENT[1]

By David J. Wald and Thomas H. Heaton,
U.S. Geological Survey
and
Donald V. Helmberger,
California Institute of Technology

CONTENTS

ABSTRACT

We have used broadband records from 18 teleseismic stations and three-component records from 16 local strong-motion stations in a formal inversion to determine the temporal and spatial distribution of slip during the earthquake. Separate inversions of the teleseismic (periods, 3–30 s) and strong-motion (periods, 1–5 s) data sets result in similar source models. The data require bilateral rupture, with relatively little slip in the region directly updip from the hypocenter. Slip is concentrated in two patches: one centered 6 km northwest of the hypocenter at 12-km depth with an average slip amplitude of 250 cm, and the other centered about 5 km southeast of the hypocenter at 16-km depth with an average slip amplitude of 180 cm. This bilateral rupture results in large-amplitude ground motions at sites both to the northwest and southeast along the fault strike. The northwestern patch, however, has a larger seismic moment and overall stress drop and thus is the source of the highest ground-motion velocities, a result consistent with observations. The bilateral rupture also results in relatively moderate ground motion directly updip from the hypocenter, in agreement with the ground motions observed at Corralitos, Calif. Furthermore, there is clear evidence of a foreshock (M~4.5–5.0) or slow rupture nucleation about 2 s before the main rupture; the origin time implied by strong-motion trigger times is systematically nearly 2 s later than that predicted from the high-gain regional-network data. The seismic moment obtained from either or both data sets is about 3.0×10^{26} dyne-cm, and the seismic potency is 0.95 km^3. Our analysis indicates that the rupture model determined from the teleseismic data set alone, independent of the strong-motion data set, is adequate to predict many characteristics of the local-strong-motion recordings.

INTRODUCTION

In this study, we use a least-squares linear inversion of strong-motion and teleseismic data to solve for the spatial and temporal distribution of slip during the 1989 Loma Prieta earthquake (M_S=7.1). Although the geometry of the fault plane is fixed in the inversion, we chose it to be compatible with the teleseismic waveforms and the aftershock distribution. Our estimates of the spatial and tem-

---

[1] Contribution No. 4935, Division of Geological and Planetary Sciences, California Institute of Technology, Pasadena, CA 91125.

poral distribution of slip should enhance studies of fault segmentation and earthquake recurrence (Working Group on California Earthquake Probabilities, 1988; King and others, 1990), which depend on reliable estimates of the rupture dimensions and slip amplitude. Furthermore, the variation in rake angle as a function of position along strike and downdip on the fault plane is critical to analyses of the complex fault interactions within the Sargent-San Andreas fault system (Dietz and Ellsworth, 1990; Olson, 1990; Schwartz and others, 1990; Seeber and Armbruster, 1990).

We use the method of Hartzell and Heaton (1983), which has been shown to provide valuable insight into the rupture history of other California earthquakes (Hartzell and Heaton, 1986; Mendoza and Hartzell, 1988; Wald and others, 1990), as have other finite-fault approaches (Olson and Apsel, 1982; Archuleta, 1984; Beroza and Spudich, 1988). In addition to providing an estimate of the rupture history for individual earthquakes, these studies also give new insight into the general characteristics of the rupture process that are common to many events. After studying slip models for several earthquakes, Mendoza and Hartzell (1988) suggested that large gaps in aftershock patterns commonly coincide with regions of relatively high slip. From the distribution of slip, we can also constrain the location and depth extent of significant energy release and characterize the distribution of stress changes on the fault. These results provide a starting point for calculating ground motions in future events comparable in size to the 1989 Loma Prieta earthquake. Such ground-motion calculations are important for augmenting the sparse data base of near-source strong-motion recordings of $M \geq 7$ crustal earthquakes.

The 1989 Loma Prieta earthquake was well recorded at both local-strong-motion and teleseismic broadband stations. The strong-motion velocity recordings used here are dominated by energy in the range 1–5 s, whereas the broadband teleseismic recordings show energy in the range 3–30 s. This wealth of data provides an opportunity to compare rupture models that are derived independently from either strong-motion or teleseismic data sets with those derived from combined data sets and over a wide range of frequencies. Our results give insight into the limitations of previous studies that used less extensive data sets.

DATA

Ground motions from the 1989 Loma Prieta earthquake were recorded over a wide range of frequencies and distances, from high-frequency waveforms observed on local accelerometers and regional seismic networks to very low frequency waveforms observed in teleseismic surface waves and geodetic line-length changes. Deterministic waveform inversion of high-frequency (>3 Hz) motion, however, requires an accurate and detailed knowledge of the wave propagation in the geologically complex structure of the Loma Prieta region. Furthermore, inversion of high-frequency waveforms requires a proliferation of free variables that significantly increases computation time and decreases the stability of the inversion process. Therefore, we chose to concentrate our study on the lower-frequency part of the rupture history. Near-source, low-pass-filtered strong-motion and teleseismic body waves seem to be the most suitable data sets to study the general characteristics of the slip history. Although geodetic data can also provide important constraints on an earthquake slip-distribution model, they can be overly sensitive to the geometry of the inferred fault plane and so are not always suitable for determining detailed variations in slip.

TELESEISMIC WAVEFORMS

The teleseismic stations chosen for this study are listed in table 1. The data are digital recordings obtained from Chinese Digital Seismograph Network (CDSN), Institut National des Sciences de l'Univers, France (GEOSCOPE), and Incorporated Research Institution for Seismology (IRIS) broadband components and Global Digital Seismograph Network (GDSN) intermediate-period components. These stations provide a uniform azimuthal coverage of the focal sphere and contain several near-nodal observations for both *P*- and *SH*-wave source radiation (fig. 1). In this analysis, instrument responses were deconvolved from the original recordings to obtain true ground velocities.

STRONG MOTION

The distribution of near-source ground velocities used in this study is mapped in figure 2; station abbreviations, station geometries with respect to the epicenter, and trigger times (where available) are listed in table 2. The velocity waveforms were obtained by integrating corrected acceleration recordings provided by the California Division of Mines and Geology (CDMG) (Shakal and others, 1989) and the U.S. Geological Survey (USGS) (Maley and others, 1989), and uncorrected recordings from the University of California, Santa Cruz (UCSC). The velocity waveforms were bandpass filtered between 0.1 and 1.0 Hz, using a zero-phase, third-order Butterworth filter. The horizontal components are rotated with respect to the epicenter to obtain "radial" and "tangential" components. Although this rotation is correct for energy originating near the epicenter, it is only approximate for source regions farther northwest and southeast along the fault.

Table 1.—*Teleseismic stations used in this study*

Station (fig. 1)	Distance (°)	Azimuth (°)	Backazimuth (°)	Phases used
AFI	69.2	232.6	040.8	*P*, *SH*
ARU	86.9	359.7	000.4	*P*, *SH*
CAY	70.8	098.6	307.6	*P*, *SH*
COL	31.8	339.4	138.5	*P*
HIA	77.9	324.0	045.9	*P*
HON	35.0	253.5	055.2	*P*
HRV	38.5	065.7	279.2	*P*
MDJ	76.0	305.2	051.3	*P*
NNA	64.8	130.1	321.5	*P*, *SH*
OBN	85.1	011.9	343.0	*P*, *SH*
PPT	60.5	210.6	025.2	*P*, *SH*
RPN	65.2	167.7	349.0	*P*, *SH*
SCP	34.1	067.8	278.3	*P*
SSB	84.6	034.7	319.8	*P*
TOL	84.3	043.0	314.8	*P*, *SH*
WFM	38.5	065.6	279.1	*P*

Two criteria were used to select stations for inclusion in the inversion: The observations should be both close to the aftershock zone and well distributed in azimuth. Within the epicentral region, peak ground motions are relatively independent of surface geology (Benuska, 1990). Care was also taken to avoid stations that seemed to have unusual site responses. For this reason, the CDMG station Agnew was not used, although it is at a similar distance and azimuth to station LEX (fig. 2). UCSC stations BRN, LGP, UCS, and WAH were included to provide important station coverage to the west and southwest of the epicenter. These stations, however, did not record absolute time and required additional processing to remove a few random spikes in the raw acceleration data. Although the despiking process that we used may be inadequate at high frequencies, it provides useful velocity recordings at the frequencies of interest in this analysis (0.1–1 Hz). The station LGP acceleration recording exhibited a permanent step on the vertical component that does not carry through in our bandpassed data; the horizontal components were apparently unaffected. Station BRN was set for 0.5 *g* maximum amplitude, and because amplitude reached close to that value, the accuracy of the response is unknown. We address the issue of estimating absolute time for these stations in the section below entitled "Inversion Method."

FAULT-RUPTURE MODEL

The fault parametrization and modeling procedure that we employ was described by Hartzell and Heaton (1983) in their study of the 1979 Imperial Valley, Calif., earthquake. Faulting is represented as slip on a planar surface that is discretized into numerous subfaults. The ground motion at a given station can be represented as a linear sum of subfault contributions, each appropriately delayed in time to simulate fault rupture. Formal inversion procedures are then used to deduce the slip distribution on these subfaults that minimizes the difference between the observed and synthetic waveforms.

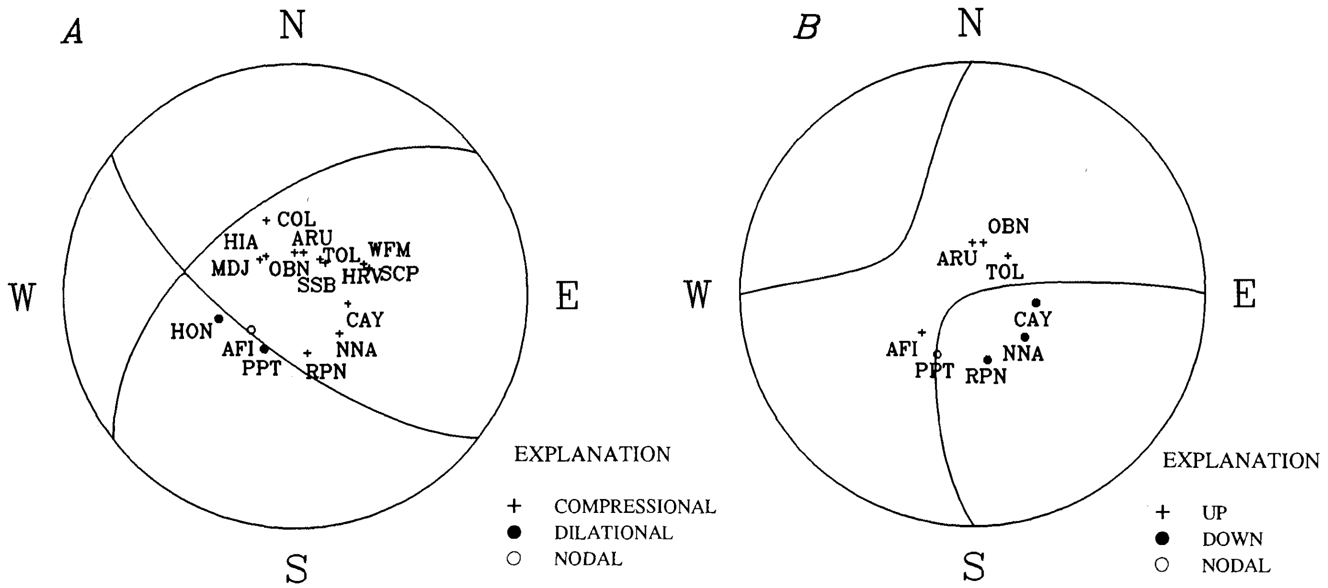

Figure 1.—Focal spheres with plot of takeoff angles of *P* (*A*) and *SH* (*B*) waves from 1989 Loma Prieta earthquake, showing global distribution of broadband teleseismic stations used in this study. Radiation patterns are for a source mechanism with a strike of 128°, a dip of 70°, and a rake of 138°. For *SH* waves, "up" refers to clockwise motion.

In this study, we represent the Loma Prieta rupture as a 40-km-long plane striking N. 128° E. and dipping 70° SW. As a point of reference, the northernmost corner of our assumed fault plane in at lat 37.193° N., long 122.020° W. The fault extends from 1.5- to 20.3-km depth and has a downdip width of 20 km (fig. 3).

We chose the overall dimensions of the fault to enclose the region of major aftershock activity (Dietz and Ellsworth, 1990); possible vertical strike-slip faulting on a second plane extending past the south end of our inferred rupture area is discussed below. The strike and dip of our fault plane (128° and 70°, respectively) were chosen from the broadband-inversion results of Kanamori and Satake (1990). This fault plane is also consistent with the aftershock lineation (Dietz and Ellsworth, 1990), the focal mechanism determined from first-motion data (Oppenheimer, 1990) and the *P*- and *SH*-wave teleseismic waveforms plotted in figure 4. Slight discrepancies in strike and dip would have little effect on our model results and conclusions.

The fault-plane geometry chosen for this study differs somewhat from that used by Lisowski and others (1990) to model the geodetic data. Although they also used a dip of 70°, they found that a strike of N. 136° E. (8° more northerly than ours) was needed to explain their data. Furthermore, their fault plane was shifted about 2 km to the west of our assumed plane, which was chosen to coincide with the aftershock distribution. In general, the geodetic data are more sensitive to fault geometry than are the waveform data, but they are not as powerful in resolving details of the slip distribution. Differences in the fault geometry inferred from static offsets, in comparison with waveform studies, may reflect complexities in the rupture process, such as a nonplanar fault surface or multiple-fault rupture. These complexities are not considered further in this study.

Our fault plane is discretized into 12 subfaults along strike and 8 subfaults downdip, each 2.5 km long and 3.33 km wide vertically (fig. 3). This subfault area is a compromise chosen to give sufficient freedom so as to allow the rupture variations needed to successfully model the ground motions and yet minimize computation time. The computation time for the inversion is proportional to the cube of the number of unknown parameters, in this

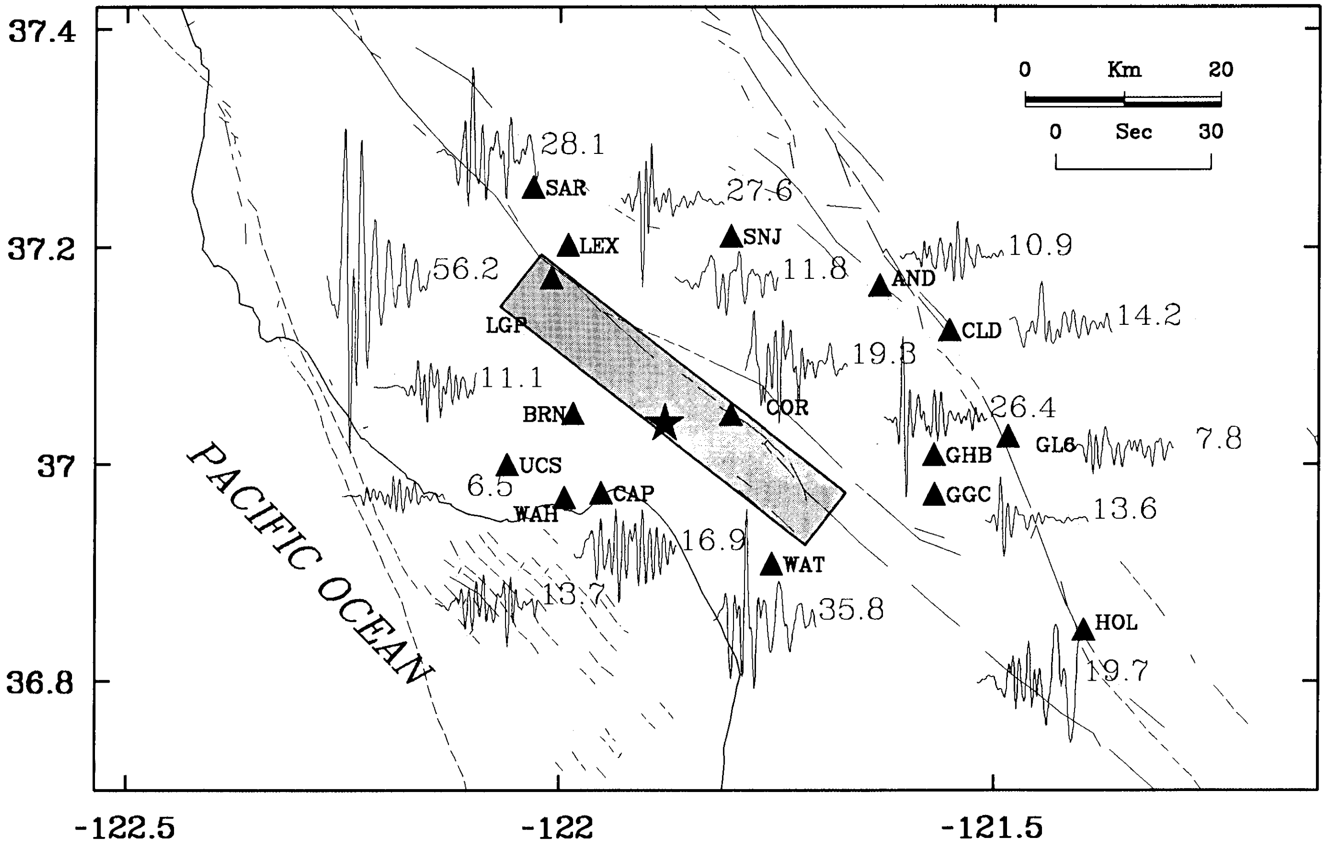

Figure 2.—Loma Prieta region, Calif., showing locations of strong-motion stations (triangles), epicenter of 1989 earthquake (star), and surface projection of model fault plane used in this study (shaded rectangle). Curves represent seismograms of radial (*A*) and tangential (*B*) components of velocity recorded at each station; number to right of each curve is peak velocity (in centimeters per second). Irregular thin lines, faults (dashed where inferred), digitized from major Quaternary faults mapped by Jennings (1975). Crosses (fig. 2*B*), aftershocks. Dashed outline (fig. 2*C*), modified Mercalli intensity (MMI) contour separating regions of MMI VII and VIII (from Stover and others, 1990).

case, the number of subfault slip amplitudes to be determined.

SYNTHETIC GREEN'S FUNCTIONS

The synthetic ground-motion contribution for each subfault was computed by using the Green's function summation and interpolation method of Heaton (1982) briefly summarized here. The subfault motions were obtained by summing the responses of numerous point sources distributed over each subfault. A total of 25 equally spaced point sources (see fig. 3), appropriately lagged in time, were summed to include the traveltime difference due to the varying source positions and to simulate the propagation of the rupture front across each subfault. In all, 2,400 point sources were summed to construct the teleseismic and strong-motion synthetic seismograms at each station for both a pure strike-slip and a pure dip-slip mechanism. Thus, each subfault includes the effects of directivity.

The point-source responses, or Green's functions, for teleseismic *P*- or *SH* body-wave synthetic seismograms were computed by using the generalized ray method (Langston and Helmberger, 1975). We included the responses of all rays up to two internal reflections in a layered velocity model, including free-surface and internal-phase conversions. A *Q* operator (Futterman, 1962) was applied, with an attenuation-time constant t^* of 1 and 4 s for *P* and *SH* waves, respectively.

The point-source responses for the strong motions were computed for a layered velocity model, using the discrete-wavenumber/finite-element (DWFE) methodology of Olson and others (1984) for frequencies as high as 3.5 Hz. In practice, we calculated a master set of synthetic seismograms for increments in depth from 1.5 to 20.3 km and for ranges of 0 to 75 km, to allow for the closest and farthest possible subfault-station combinations. Then, for each subfault-station pair, the required subfault response was derived by the summation of 25 point-source responses obtained by linear interpolation of the closest Green's functions available in the master set. The linear interpolation of adjacent Green's functions was performed by aligning the waveforms according to their shear-wave traveltimes. Subfault contributions from both a pure dip-slip and pure right-lateral strike-slip mechanism were then computed, using the assumed fault geometry. The relative weights of these fundamental mechanisms, as well as the amount of slip on each subfault, were determined in the inversion process, as described below.

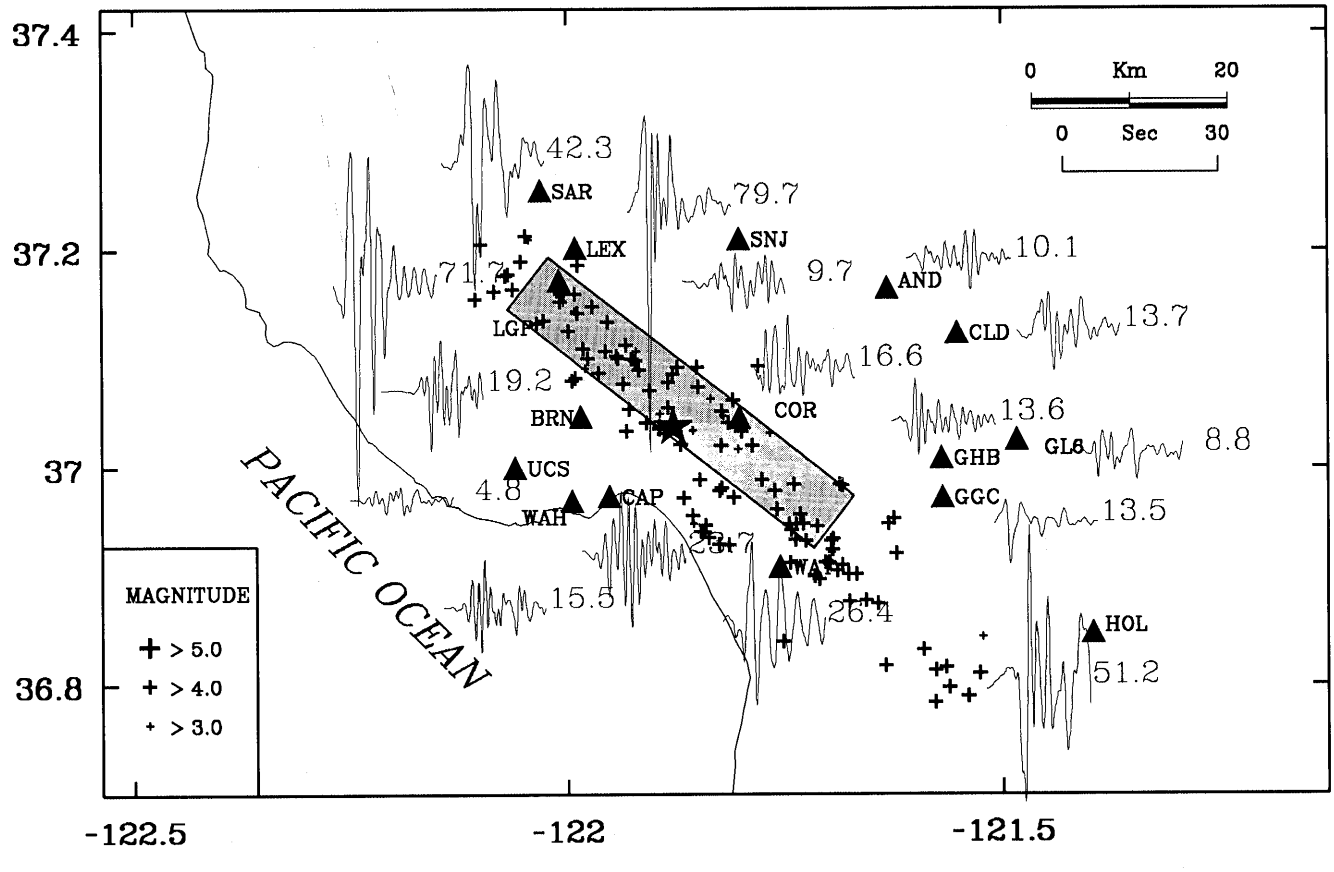

Figure 2.—Continued

Table 2.—*Strong-motion stations in the Loma Prieta region*

[Data sources: CDMG, California Division of Mines and Geology; UCSC, University of California, Santa Cruz; USGS, U.S. Geological Survey. Distance and azimuth measured from epicenter at lat 37°02.37′ N., long 121°52.81′ W. Station display adjusted to absolute time (see text). Trigger times measured from 0004:00.00 G.m.t. October 18, 1989; origin time measured from main shock at 0004:15.21 G.m.t. October 18, 1989]

Station (fig. 2)	Station name	Data source	Station No.	Distance (km)	Azimuth (°)	Delay (s)	Trigger time (s)	Origin time (s)
AND	Anderson Dam, downstream	USGS	1652	26.1	057.6	0.0	23.0	7.8
BRN	Branciforte Drive	UCSC	---	9.5	275.4	--	--	--
CAP	Capitola Fire Station	CDMG	47125	9.7	222.0	--	--	--
CLD	Coyote Lake Dam	CDMG	57504	30.7	072.1	.0	24.5	9.3
COR	Corralitos	CDMG	57007	6.8	083.5	.0	20.4	5.2
GGC	Gavilan College	CDMG	47006	28.6	104.8	–.4	[1]23.9	8.7
GHB	Gilroy Historical Building	CDMG	57476	27.8	096.9	–.2	23.4	8.2
GL6	Gilroy array station 6	CDMG	57383	35.2	092.4	.7	26.0	10.8
HOL	Hollister, Pine Street	CDMG	47391	47.9	116.3	1.9	27.5	12.3
LEX	Lexington Dam	CDMG	57180	19.1	331.0	–.3	21.1	5.9
LGP	Los Gatos Presentation Center	UCSC	---	18.8	321.7	--	--	--
SAR	Saratoga, Aloha Avenue	CDMG	58065	27.5	330.6	--	--	--
SNJ	San Jose, Santa Theresa	CDMG	57563	20.1	019.6	–.2	18.3	[2]3.1
UCS	University of California, Santa Cruz	UCSC	---	16.8	255.0	--	--	--
WAH	Walter's house	UCSC	---	12.9	233.4	--	--	--
WAT	Watsonville	CDMG	47459	18.1	142.8	.3	21.6	6.4

[1] Accurately estimated from time at Gilroy array station 1.

[2] Digital instrument with memory before trigger time (*P* wave at 1.7 s).

VELOCITY MODEL

The velocity model used to compute the DWFE Green's functions is listed in table 3. *P*-wave velocities were calculated by averaging the two velocity-depth profiles constructed by Dietz and Ellsworth (1990) for regions northeast and southwest of the San Andreas fault. We added a thin, lower-velocity layer to this model to better approximate elastic properties just beneath the strong-motion stations. *S*-wave velocities were calculated by assuming that the structure is a Poisson solid.

The velocity model used to compute the teleseismic Green's functions (table 4) is a four-layer approximation to the local-velocity structure used in the strong-motion

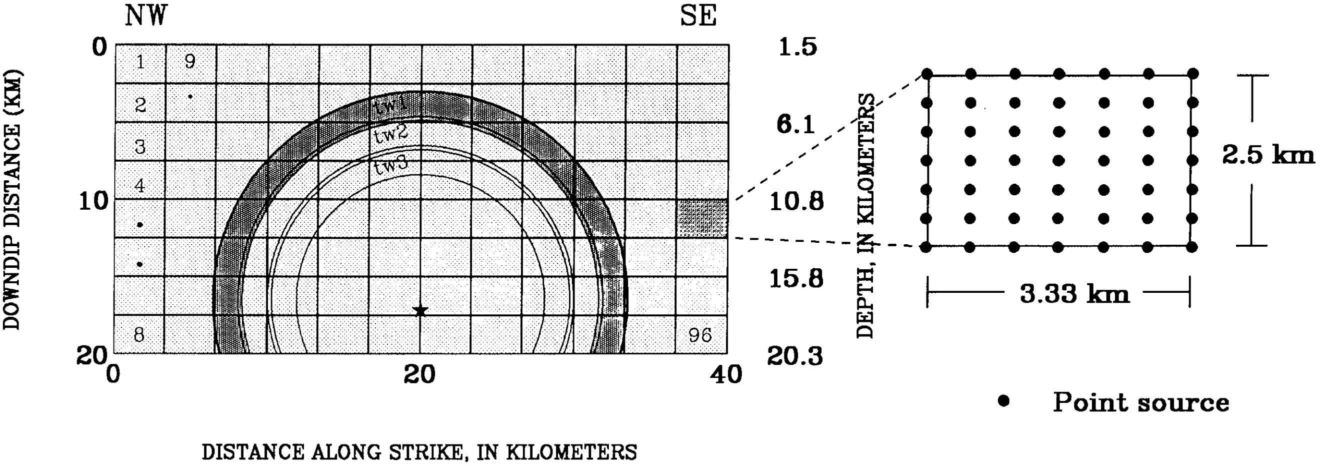

Figure 3.—Northwest-southeast cross section of fault-rupture model along fault plane, showing layout of subfaults (numbers 1–96) used in analysis. Enlargement shows distribution of point sources within each subfault. Largest circle radiating outward from hypocenter (star) represents position of rupture front after 5 s; smaller concentric circles delimit (slightly overlapping) fault regions slipping in time windows 1 (tw1, shaded), 2 (tw2), and 3 (tw3) (see fig. 18).

inversion (table 3). Heaton and Heaton (1989) discussed difficulties that arise when the seismic moments derived from different velocity models are compared. In this example, the seismic velocities are nearly constant for both the teleseismic and strong-motion velocity models in the depth range 7–18 km (the region of highest slip). This

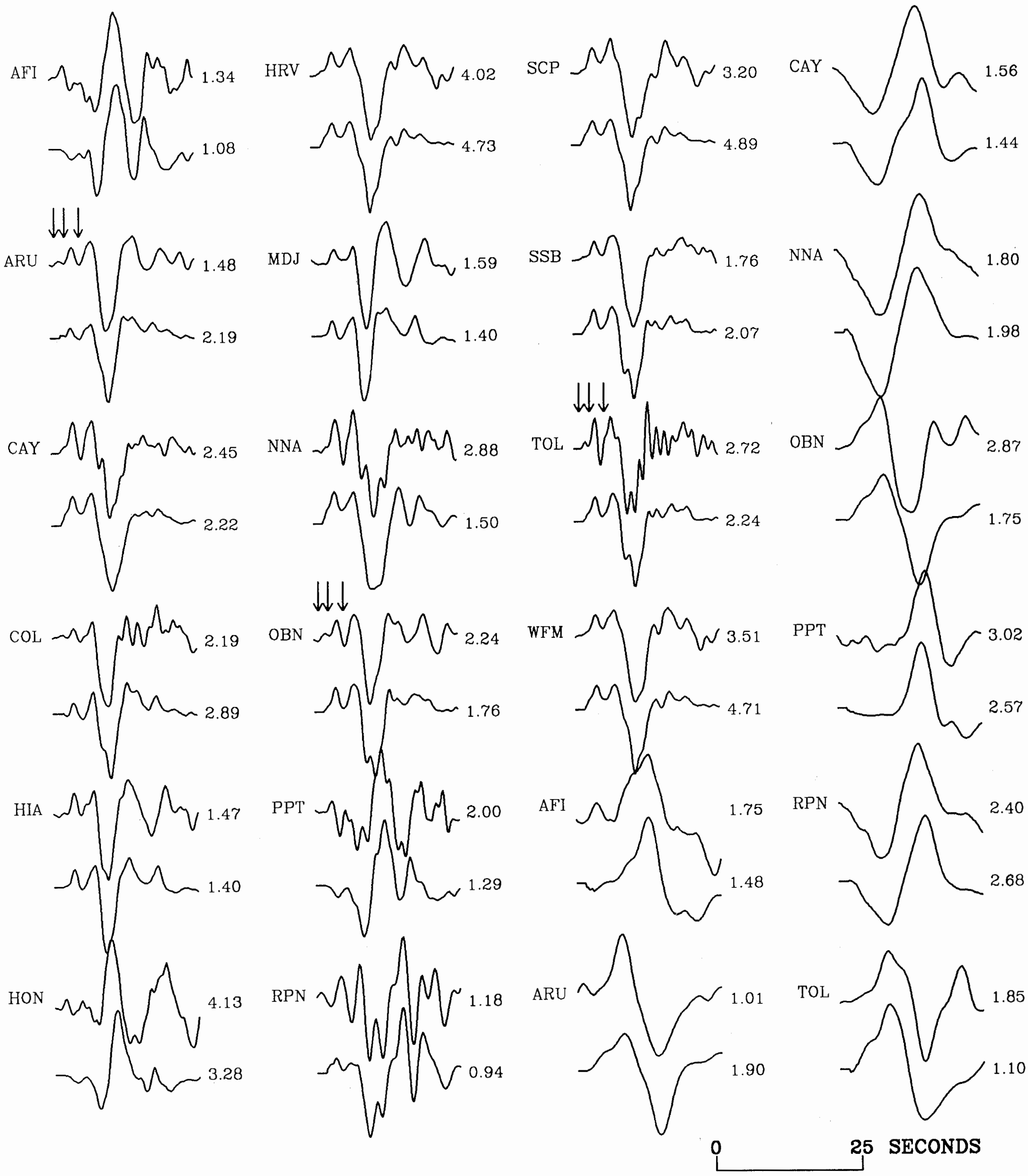

Figure 4.—Comparison of observed (upper curve) and synthetic (lower curve) seismograms recorded at broadband teleseismic stations (see fig. 1 for locations). First 16 stations are *P* waves, and last 8 stations are *SH* waves. Arrows denote arrivals detailed in figure 8.

Table 3.—*Loma Prieta velocity structure for strong-motion data modeling*

[V_p, *P*-wave velocity; V_s, *S*-wave velocity]

V_p (km/s)	V_s (km/s)	Density (g/cm^3)	Thickness (km)	Depth (km)
1.73	1.00	1.50	0.1	0.1
3.38	1.95	1.55	.4	.5
4.29	2.48	1.85	.5	1.0
4.80	2.77	2.05	2.0	3.0
5.37	3.10	2.26	2.0	5.0
5.74	3.31	2.45	2.0	7.0
6.15	3.55	2.58	2.0	9.0
6.25	3.61	2.62	4.0	13.0
6.27	3.62	2.63	5.0	18.0
6.67	3.85	2.77	7.0	25.0
8.00	4.62	3.28	50.0	---

Table 4.—*Loma Prieta velocity structure for teleseismic data modeling*

[V_p, *P*-wave velocity; V_s, *S*-wave velocity]

V_p (km/s)	V_s (km/s)	Density (g/cm^3)	Thickness (km)	Depth (km)
4.60	2.66	2.60	3.5	3.5
6.05	3.49	2.65	6.5	10.0
6.30	3.64	2.67	14.0	24.0
8.00	4.62	3.28	---	---

favorable coincidence means that a simple comparison of the seismic moments derived from teleseismic and strong-motion inversions is approximately valid.

SOURCE-TIME FUNCTION AND RUPTURE VELOCITY

The subfault synthetic seismograms are convolved with a dislocation-time history that we represent by the integral of an isosceles triangle with a duration of 0.7 s. This slip function was chosen on the basis of comparison of the synthetic velocity-pulse width for a single subfault with the shortest velocity-pulse width observed, as well as from previous experience with this inversion method (Heaton, 1990). As Hartzell and Mendoza (1991) pointed out, resolution of the slip function is difficult, although we are required by the strong-motion recordings to use a relatively short (<0.8 s) duration.

The rupture velocity is assumed to be a constant 2.7 km/s, or 75 percent of the shear-wave velocity in the main source region (table 3). Many observations, including the absence of tectonic surface slip (U.S. Geological Survey staff, 1990), indicate that little dislocation occurred above 4-km depth. The position of the rupture front 5 s after the nucleation time is mapped in figure 3.

Some flexibility in the rupture-velocity and slip-time history is achieved by introducing time windows (Hartzell and Heaton, 1983). In all inversions, each subfault is allowed to slip in any of three identical 0.7-s time windows after passage of the rupture front, thereby allowing for a possibly longer slip duration or a locally lower rupture velocity. Hartzell and Mendoza (1991) obtained nearly identical dislocation models for the 1978 Tabas, Iran, earthquake (M_S=7.4) using both a linear inversion parametrizing slip with three time windows (as is done here) and a nonlinear iterative inversion that allows a single rupture at each point on the fault but a varying rupture velocity.

In this study, each time window is separated by 0.6 s, allowing a small overlap in the 0.7-s-duration subfault source-time function. Thus, as mapped in figure 3, the region of the fault that is allowed to slip 5 s (for example) after rupture nucleation is within concentric bands occupied by the three time windows. We did not test for the possibility of a faster rupture velocity because initial indications from our modeling showed that regions toward the northwest required slightly lower rupture velocities than 2.7 km/s, which can be approximated given the flexibility allowed for by the three time windows.

INVERSION METHOD

A constrained, damped, linear least-squares inversion was used to determine the subfault dislocations that give the best fit to the strong-motion velocity waveforms. The inversion is stabilized by requiring that the slip be everywhere positive and that the difference in dislocation between adjacent subfaults (during each time window), as well as the total seismic moment, be minimized, as discussed by Hartzell and Heaton (1983).

Smoothing, or minimizing the difference is slip between adjacent subfaults, is required to avoid instabilities, as well as downplay the role in the inversion played by starting and stopping phases associated with each subfault. If large variations in slip are allowed, such phases dominate, although they represent artifacts of the subfault discretization. Because numerous subfaults are required to resolve the spatial variations in slip, smoothing constraints are needed. We expect the smoothing required for the teleseismic and strong-motion data to differ, in that the number of subfaults and their size remain fixed for each data set, although the dominant period of the energy varies.

The teleseismic data can generally be fitted with somewhat-isolated spikes of large slip, which would predict enormous (unphysical) localized slips and excessive high-frequency radiation. Thus, in practice, we increase the spatial-slip smoothing until the waveform fits begin to degrade. Because the strong-motion inversion is more sensitive to higher-frequency radiation, the inversion automatically limits extreme variations in rupture, which produce excessive short-period radiation. Therefore, the strong-motion inversion needs minor additional smoothing. And in fact, substantial smoothing would degrade the strong-motion waveform fits.

In essence then, the teleseismic rupture model may represent a lower bound on the actual fault roughness and thus represents a lower limit to high-frequency radiation. Similarly, we might expect the strong-motion model, derived from velocity waveforms, to underestimate much-higher-frequency accelerations, but it may be adequate for frequencies slightly higher than used in the inversion, possibly as high as 5 Hz.

Both the strong-motion observations and subfault synthetic seismograms were bandpass filtered from 0.1 to 1.0 Hz with a zero-phase Butterworth filter and resampled at a uniform rate of 10 samples per second. The teleseismic data were similarly filtered from 0.02 to 1.0 Hz with a time step of 10 samples per second. The upper-frequency limit is imposed by the characteristics of the strong-motion recordings. In general, more coherence is noticeable in the waveforms at periods above 1 s than at higher frequencies. Originally, the strong-motion data were low-pass filtered at 3 Hz, but we noticed significant complexity, apparently caused by local site responses. We modeled the first 25 s of the record for teleseismic data and between 14 to 22 s of the strong-motion records (depending on the individual record).

TIMING

The initial alignment over time of the observed and synthetic seismograms is a critical issue in modeling waveform data to determine the temporal and spatial distribution of slip on the fault plane. In this type of study, two approaches are possible. One approach (commonly used for teleseismic-waveform inversions) is to time-shift the synthetic waveform from a point-source hypocenter until the first significant motion aligns with that of the observed recording. Later source contributions (from the developing rupture process) can then be determined by modeling the remaining features of the record. This method is adequate when (1) the observed first arrival time is unambiguous and (2) the initial arrival is actually from the locally determined hypocenter (including the origin time). However, the first arrivals (observed on local seismic networks) for waves from the hypocenter may be too small to be seen teleseismically or on strong-motion recordings. These first arrivals are used to determine the hypocenter and origin time of the earthquake. Serious problems arise if the first arrival on a teleseismic-waveform or strong-motion record is erroneously assumed to be from the hypocenter determined from local-seismic-network data. Hartzell and Heaton (1983) showed how serious this problem is when interpreting the 1979 Imperial Valley, Calif., earthquake.

In the second approach, all correlations are done in absolute time, with appropriate time delays to accommodate errors introduced by inadequacies of the assumed velocity model. At teleseismic distances, these delays can be substantial, and so master-event techniques must be used (for example, Hartzell and Heaton, 1983). For local-strong-motion data, the use of absolute time is preferable if it is known for most of the recordings. We use this second approach in our strong-motion-modeling study.

When the trigger time on local strong-motion records is available (see table 2), both the observed and synthetic waveforms are aligned in absolute time. Slight adjustments are also made to allow for variations in traveltime not predicted by the assumed one-dimensional velocity structure (station delays, table 2). Although this procedure provides an approximate, static station delay, it does not eliminate timing errors introduced by lateral variations due to subfault-to-station travelpaths that vary significantly along the fault. This issue can be addressed later with the analysis of aftershock recordings at strong-motion sites when these data are available.

For strong-motion stations without absolute time, both the observed and synthetic waveforms will be aligned is we assume that the initial *P* wave triggers the instrument. The stations with timing are weighted heavily in the inversion, and those without timing are downweighted, effectively removing them from the inversion. Using the preliminary inversion results, synthetic waveforms were calculated for those stations without timing, and new time estimates were obtained by comparing the observed with the synthetic waveforms. At some stations (UCS, WAH, fig. 2), the forward modeling was insufficient to estimate the timing, and so these stations were not given significant weighting in subsequent inversions. We did, however, continue to compute waveforms for these stations for comparison with the observed waveforms and for later analysis.

TELESEISMIC MODELING

PRELIMINARY ANALYSIS

Several broadband teleseismic studies of the 1989 Loma Prieta earthquake have been completed; their overall conclusions were summarized by Wallace and others (1991). As pointed out by Choy and Boatwright (1990), three distinct arrivals are recognizable on most of the broadband teleseismic velocity recordings (arrows, fig. 4). The first arrival is quite small but is visible on the *P*-wave records, about 1 s into the trace, at stations ARU, OBN, and TOL (fig. 1). The first subevent is at the threshold of resolution for waveform modeling of teleseismic data.

In general, previous teleseismic models describe the earthquake as a simple two-point-source combination representing two later, dominant subevents. The seismic moments determined in these broadband studies range from 2.0×10^{26} to 3.0×10^{26} dyne-cm and show a wide variation in the ratio of the seismic moments for the third subevent relative to the second subevent, depending on the assumptions of the individual researcher. In addition, the estimate of the best point-source depths vary widely for the second and third subevents, or for a single estimate of the centroid location. This variation suggests that the rupture, though over a finite area, was not extensive enough to be easily resolved teleseismically (that is, $\lesssim$35 km), a result consistent with the limited extent of the rupture inferred from the aftershock distribution alone (Dietz and Ellsworth, 1990).

When teleseismic velocity waveforms are integrated into the displacements, arrivals become difficult to distinguish from individual subevents. In particular, the arrival from the second subevent appears as a subtle inflection in the large pulse from the third subevent. Although nearly identical results were obtained by modeling the teleseismic displacement waveforms, we find it easier to compare observed and synthetic velocity waveforms.

INVERSION RESULTS

The spatial distribution of slip obtained from inversion of only the teleseismic-waveform data is plotted in figure 5. We use a large contour interval (50 cm) to emphasize the robust features of our model; the dislocations shown represent the combined slip for the three time windows previously mentioned.

Our teleseismic model has a seismic moment of 2.8×10^{26} dyne-cm. The observed teleseismic records (upper curves) are compared with the synthetic seismograms (lower curves) predicted by the teleseismic dislocation model in figure 4. The main features of this model are (1) a two-lobed bilateral rupture with a slightly higher slip to the northwest, (2) concentration of the highest slip at a depth of 11 km for the northwestern patch and slightly deeper for the southeastern patch, and (3) low slip in the region updip from the hypocenter.

Directivity controls the waveform and amplitude only when the rupture front propagates at a velocity comparable to that of the phase of interest. Thus, the teleseismic body waves, all with steep takeoff angles, are limited in their ability to resolve rupture directivity along strike but are quite sensitive to updip or downdip rupture propagation. The absence of vertical directivity is apparent in our solution. Because the teleseismic-waveform data do not allow significant slip updip or downdip from the hypocenter, most slip must occur along strike from the hypocenter. Bilateral rupture is indicated by the timing of the second and third arrivals and by the absence of significant azimuthal arrival-time differences between the two dominant arrivals. As discussed in the next section, this model explains many of the features observed in the local-strong-motion data.

STRONG-MOTION MODELING

PRELIMINARY ANALYSIS

PEAK MOTIONS

Inspection of the pattern of near-source peak ground velocities (fig. 2) reveals that the largest motions occurred at stations located near the northwest (LEX, LGP, SAR)

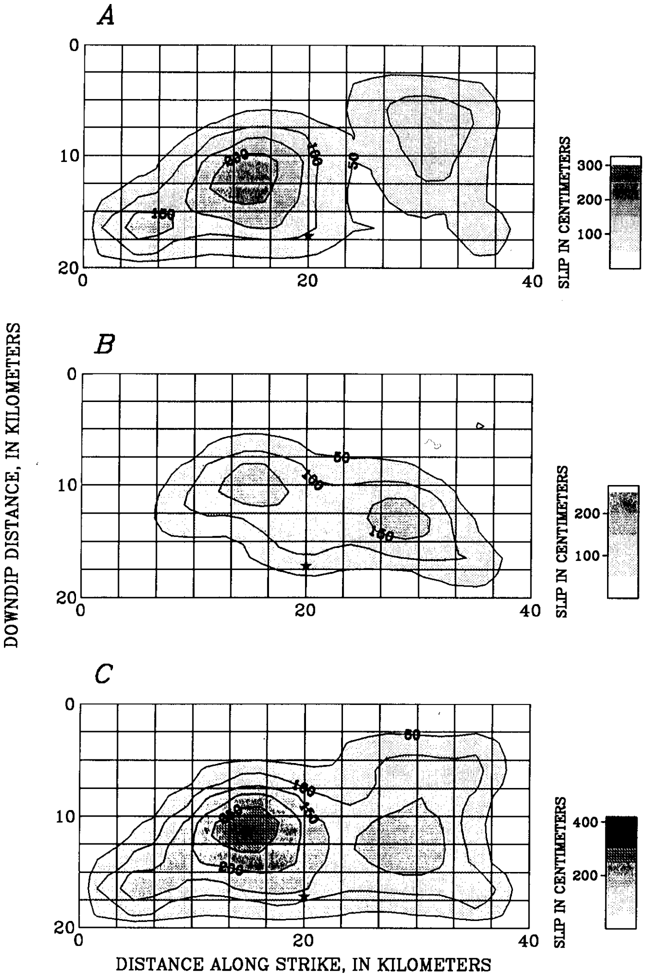

Figure 5.—Northwest-southeast cross section of model fault (fig. 3), showing contours of dislocation for strike slip (*A*), dip slip (*B*), and oblique slip (*C*) predicted from teleseismic inversion. Contour interval, 50 cm. Star, hypocenter of 1989 Loma Prieta earthquake.

and southeast (HOL, WAT, GHB) ends of the aftershock zone. A tendency for large motions at both ends of the aftershock zone, particularly to the northwest, is evident in the modified Mercalli intensity (MMI) VII isoseismal map (fig. 2*C*), in contrast to the relatively small amplitudes recorded at station COR, directly updip from the hypocenter, where we expected to see a strong directivity from a rupture propagating updip.

Additional evidence for bilateral rupture is the timing and similarity of the velocity recordings at stations GGC and SAR (fig. 6); these stations are symmetrically located about the fault plane and at nearly the same epicentral distance (fig. 2). Polarities for the radial and vertical components at station SAR are reversed to correct for the change in sign of the *P*- and *SV*-wave-radiation patterns and to enhance the comparison. Although absolute time unavailable for station SAR, the timing at this station was estimated by noting the similarity of the *S* waveform to that at station LEX (fig. 2) and then correcting for the additional shear-wave-propagation time from station LEX to station SAR. The timing and waveforms of the main arrivals at stations GGC and SAR are similar, although they are slightly earlier at station GGC than at station SAR; however, the peak amplitudes are considerably larger at station SAR (fig. 2). These observations demand a nearly symmetrical, bilateral rupture, with considerably more 1-Hz energy radiated northwestward. A single asperity centered at or above the hypocenter could also explain the symmetry in timing and waveform at these stations, although it is inconsistent with the small amplitudes observed at stations located near the center of the aftershock region (BRN, CAP, COR, UCS, WAH, fig. 2) that should otherwise be enhanced by a slip concentration in the center of the fault. Furthermore, a central asperity cannot easily account for the larger amplitudes observed to the northwest and the lower amplitudes observed to the south-

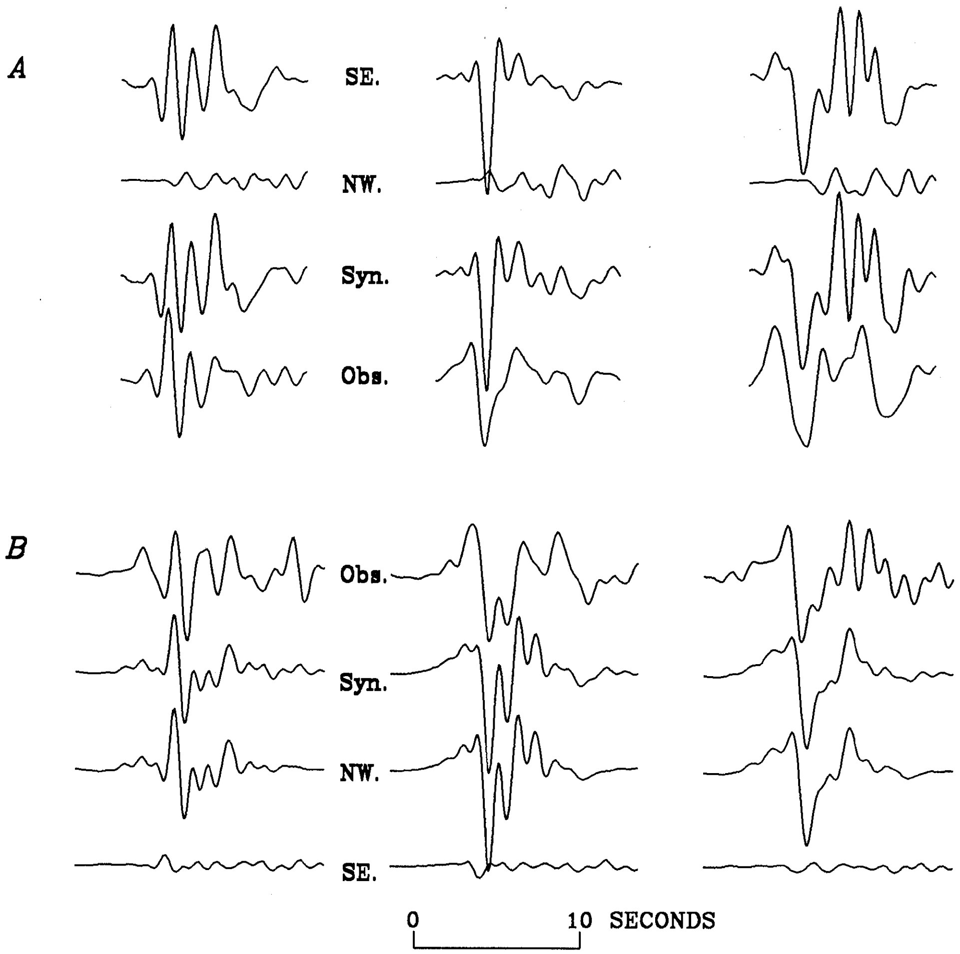

Figure 6.—Comparison of radial (left), tangential (middle), and vertical (right) components of velocity recorded at strong-motion stations GGC (*A*) and SAR (*B*) (see fig. 2 for locations), aligned vertically in absolute time, normalized to peak velocity, and shown at same scale. Polarities of components are reversed in figure 6*B* to enhance comparison. Obs., observed seismograms; syn., synthetic seismograms, with contributions from northwest (NW.) and southeast (SE.) halves of model fault.

east. These observations agree with the main features found from inversion of the teleseismic-waveform data.

TRIGGER TIMES AND RUPTURE INITIATION

We use the hypocentral parameters of Dietz and Ellsworth (1990), as listed in table 2. In figure 7, we compare the theoretical *P*-wave traveltimes at each station with the corresponding trigger times. Because strong-motion accelerometers are triggered only by vertical motions, they probably were triggered by *P*-wave arrivals. The accelerometers, however, were actually triggered nearly 2 s later than the *P*-wave arrival time predicted from the hypocentral parameters of Dietz and Ellsworth (1990). At station COR, nearly directly above the hypocenter (fig. 2), the observed trigger time is about 1.8 s after the *P*-wave-arrival time predicted by using the velocity model listed in table 3. Other stations show similar delays. We examine this delay in figure 8 by plotting the waveforms and timing of data from various instrument types: the low- and high-gain vertical components at USGS station BSR, teleseismic station TOL, strong-motion station SAR, and station SAO (San Andreas Geophysical Observatory), a University of California, Berkeley, broadband Streckeisen instrument. The waveforms for stations BSR and SAO are aligned on their first motions, and stations TOL and SAR are aligned according to our interpretation of the rupture initiation. That is, the simplest explanation for this 2-s delay is that a foreshock, too small ($M \leq 5$) to trigger the strong-motion instruments, occurred about 2 s before the main rupture; this foreshock was used to locate the hypocenter from the high-gain regional-network data. We suggest, however, that the initial 2 s represents the initial stage of rupture, possibly a smooth, slow growth episode (Wald and others, 1991). As plotted in figure 8, the initial stage of rupture clipped the nearby high-gain station BSR but shows a long-period characteristic in the low-gain component. This low-gain component clipped after about 1.6 s, after which (1) the first teleseismic energy becomes visible, (2) the strong-motion stations begin to trigger, and (3) the local broadband stations change from a long-period one-sided waveform and dramatically clip. These observations can be interpreted as a slow rupture nucleation that generated insufficient long-period energy to be seen teleseismically and insufficient high-frequency radiation to trigger the strong-motion instruments.

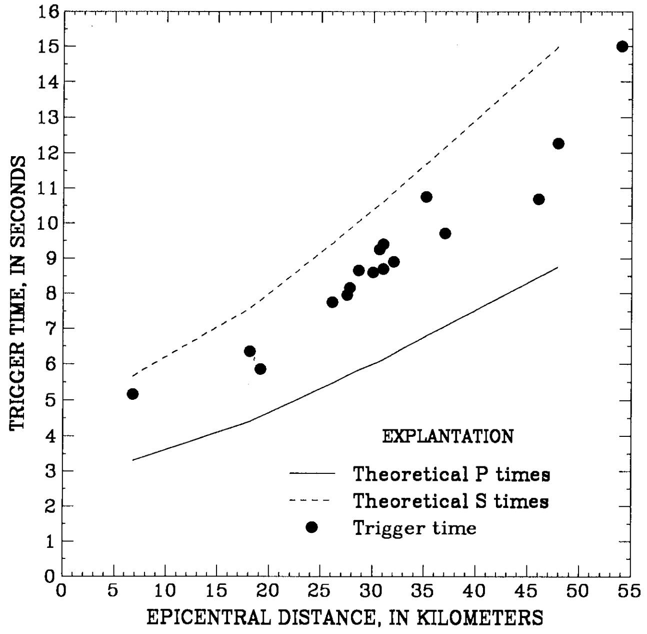

Figure 7.—Strong-motion trigger time versus epicentral distance for velocity model listed in table 3, based on origin time of main shock at 0004:15.21 G.m.t. October 18, 1989. Dot at 7 km distance is COR, Corralitos strong-motion station (fig. 2).

The observation that led to the discovery of this timing problem was the initial inversion of the strong-motion waveforms, using absolute time. The resulting slip-distribution model required a two-lobed pattern similar to that in the teleseismic-waveform data, but the centers of these lobes were forced toward the sides of the fault. This slip distribution was inconsistent with that derived from the teleseismic-waveform data and with the source region suggested by the aftershock pattern (Dietz and Ellsworth, 1990). Furthermore, it generated inferior fits to the strong-motion data.

Thus, the failure to account for this delay can seriously affect source models based on waveform inversion, using absolute timing. In particular, the modeled rupture front would already have progressed 5 km away from the hypocenter during this 2-s interval, when, in fact, probably very little rupture propagation occurred during this period. Owing to the initial weak 1.8 s of rupture, the strong-motion records appear to be delayed by 1.8 s with respect to Dietz and Ellsworth's (1990) origin time. We thus choose to ignore the foreshock or rupture initiation, and we begin modeling at the time of the first significant strong-ground motion. We assume that the main rupture began at or near Dietz and Ellsworth's (1990) hypocentral location 1.8 s after their origin time, and then allow the rupture to propagate outward from that location. This approach is consistent with our analysis of the teleseismic-waveform data, which also begins with the first significant rupture, because the initial rupture or foreshock was too small to be recorded teleseismically.

It is not uncommon for the hypocenter determined from high-gain regional-network data to represent a foreshock or an earlier stage of rupture not observed on other data sets. Wald and others (1990) discussed the rupture process of the 1987 Superstition Hills, Calif., earthquake and suggested that the network hypocenter represents an earlier foreshock and not the main rupture initiation. Therefore, on the basis of the strong-motion and teleseismic data, that event began rupturing in a different location from the hypocentral coordinates determined from the regional-network data.

INVERSION RESULTS

The distribution of slip calculated from the inversion of only the strong-motion velocities is plotted in figure 9, and the observed (upper curve) and synthetic (lower curve) strong-motion velocities are compared in figure 10. The strong-motion rupture model is similar to that derived from the teleseismic inversion (fig. 5). Again, slip is concentrated in two patches, one centered about 8 km northwest of the hypocenter at 12-km depth with a peak slip amplitude of 350 cm, and the other centered about 6 km southeast of the hypocenter at 16-km depth with a peak slip amplitude of 460 cm. These parameters are summarized in table 5. As for the teleseismic inversion, the largest localized slip concentrations are northwest of the hypocenter.

The overall pattern of the strong-motion slip duration and waveform complexity is explainable by the relative positions of individual stations with respect to the two lobes of concentrated slip. The observed (first curve) and synthetic (second curve) velocities at selected strong-motion stations are compared in figure 11, along with the surface projection of the fault plane and strong-motion slip distribution. To better understand our synthetic waveforms, the synthetic seismograms that result from rupture on only the northwest (third curve) and southeast (bottom curve) halves of the fault are also compared in figure 11. A similar breakdown of the synthetic ground motions for all components at stations GGC and SAR (fig. 2) is shown

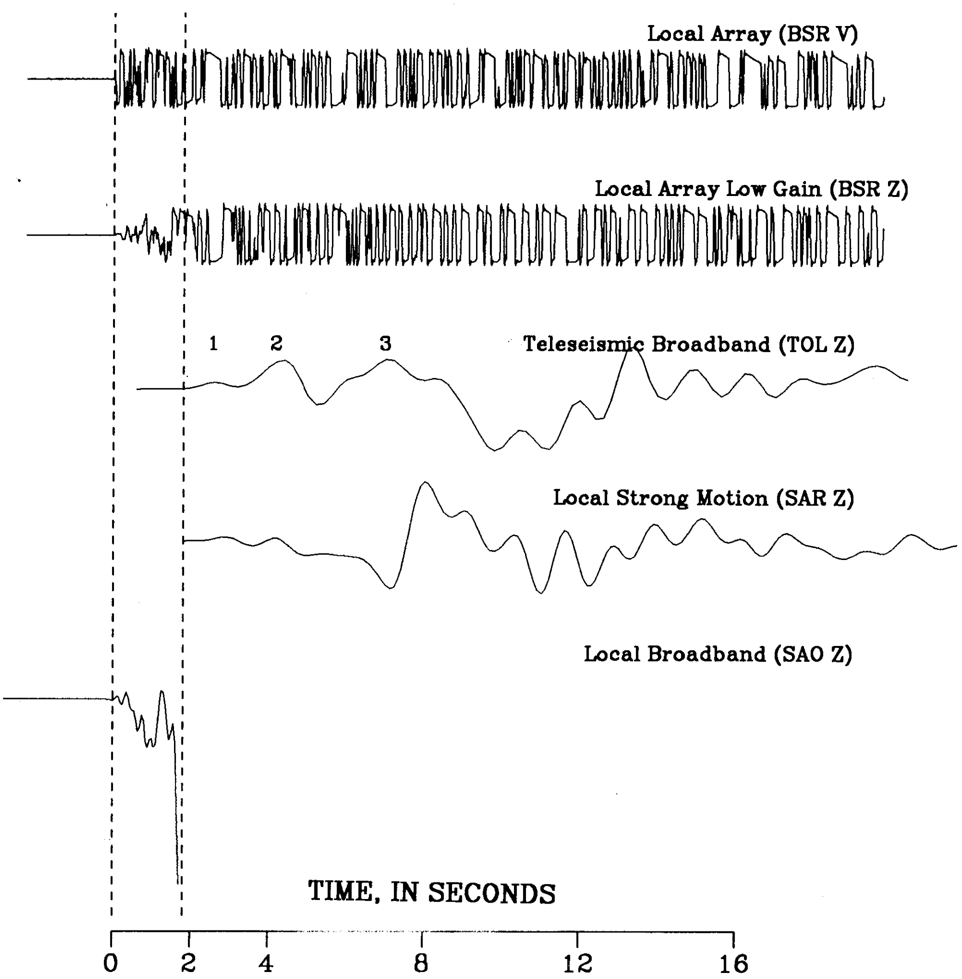

Figure 8.—Comparison of waveforms at broadband teleseismic stations (see fig. 1 for locations) indicating delay to main part of rupture, aligned in absolute time except for record at station TOL. Vertical dashed lines indicate times of 0.0 and 1.8 s. Z, vertical component of velocity. Numbers 1 through 3 on station TOL record refer to arrivals denoted by arrows in figure 4.

in figure 6. Velocities at stations located nearly along strike (LEX, SAR, GGC, GHB, fig. 2) are controlled by the nearby slip concentration and show little contribution from the farther lobe. This result is attributable to both the additional distance from the farther lobe of concentrated slip and the favorable source directivity at stations in the direction of rupture. Thus, the waveforms at alongstrike stations are simple, large in amplitude, and short in duration. Stations in the central section of the fault (CAP, COR, fig. 2) show smaller amplitudes and more waveform complexity, resulting from the absence of rupture directivity and the interference of contributions from the northwest and southeast regions of high slip. We expect these waveforms to be the most difficult to model, because the synthetic seismograms are controlled by interference of the wavefields from two propagating rupture fronts that are diverging from one another.

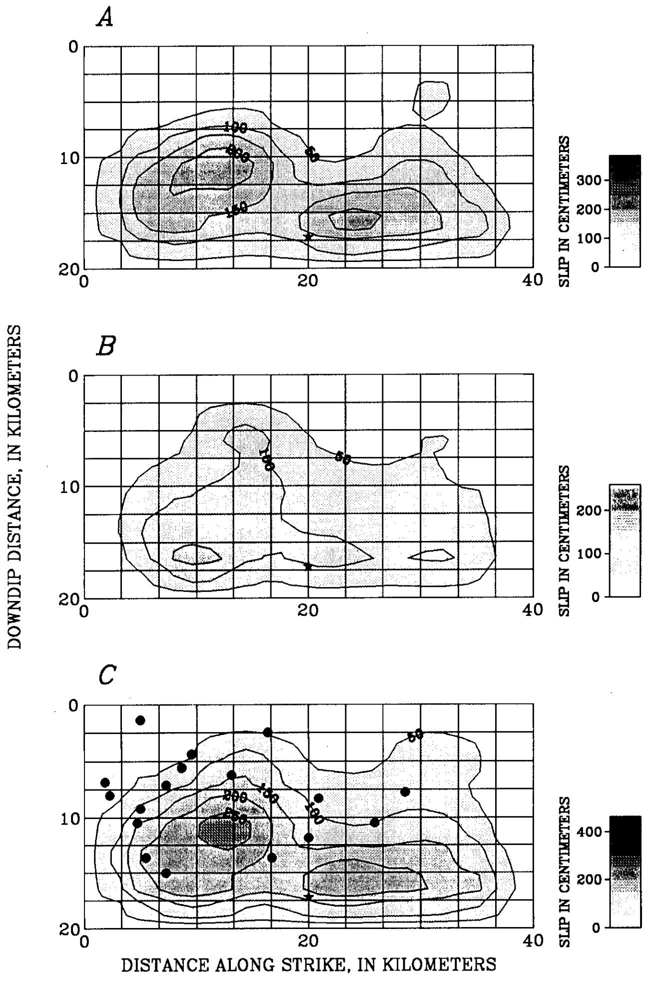

Figure 9.—Northwest-southeast cross section of model fault (fig. 3), showing contours of dislocation for strike slip (*A*), dip slip (*B*), and oblique slip (*C*) predicted from strong-motion inversion. Contour interval, 50 cm. Star, hypocenter of 1989 Loma Prieta earthquake; dots, aftershocks of $M \geq 4.0$ projected onto model fault plane.

SENSITIVITY TO STATION COVERAGE

Of concern when inverting waveform data for source rupture processes is the consideration of possible contamination from site effects and flawed data. John Vidale (oral commun., 1991) suggested that the strong-motion instrument at station LGP (fig. 2) moved during the main shock, resulting in data of questionable reliability. Although we believe that the data from this station are well behaved on the basis of its waveform data, frequency content, and amplitude similarities to the data from neighboring stations LEX and SAR (see figs. 2*B*, 2*C*), we performed a test inversion excluding the data from station LGP to be certain of the role of that station in the final solution. The result indicated that removal of the data from station LGP has almost no effect on the source model. This result might have been anticipated because any single station has only a limited role in the total solution and, in particular, the data from station LGP are nearly redundant, considering that the waveforms at adjacent stations SAR and LEX require a similar source contribution. In fact, forward modeling for station LGP with the solution determined without considering those data fits that record well, confirming our observation that the waveform is properly behaved and dominated by useful source information.

JOINT TELESEISMIC AND STRONG-MOTION INVERSION

Although the teleseismic and strong-motion models have several features in common, variations in the results are apparent. The teleseismic model shows considerably more strike slip in the shallow southeastern section of the fault. In addition, the overall depth of the slip concentration in the southeast half of the fault is deeper in the strong-motion model.

To test the compatibility of the teleseismic-waveform and strong-motion data, and to establish a model consistent with both, we performed a combined inversion of both data sets. In the combined inversion, we used the average of the smoothing weights used in the separate inversions. Also, because of the relatively small source dimensions, the near-source strong-motion data have more resolving power than the teleseismic-waveform data, which are dominated by a single velocity pulse that is not as sensitive to subtle changes in the details of the rupture process as are the higher-frequency strong-motion data. Accordingly, we chose to weight the strong-motion data by a factor of 2 over the teleseismic-waveform data in the combined inversion.

The slip distribution resulting from the combined inversion of the strong-motion and teleseismic-waveform data (fig. 12) is nearly identical to that resulting from the inversion of either data set. This result could have been anticipated because our previous models, which were derived from these independent data sets, are so similar. The combined model, which we prefer, represents a compromise between our two previous source models. To best satisfy both data sets, however, slip is more concentrated

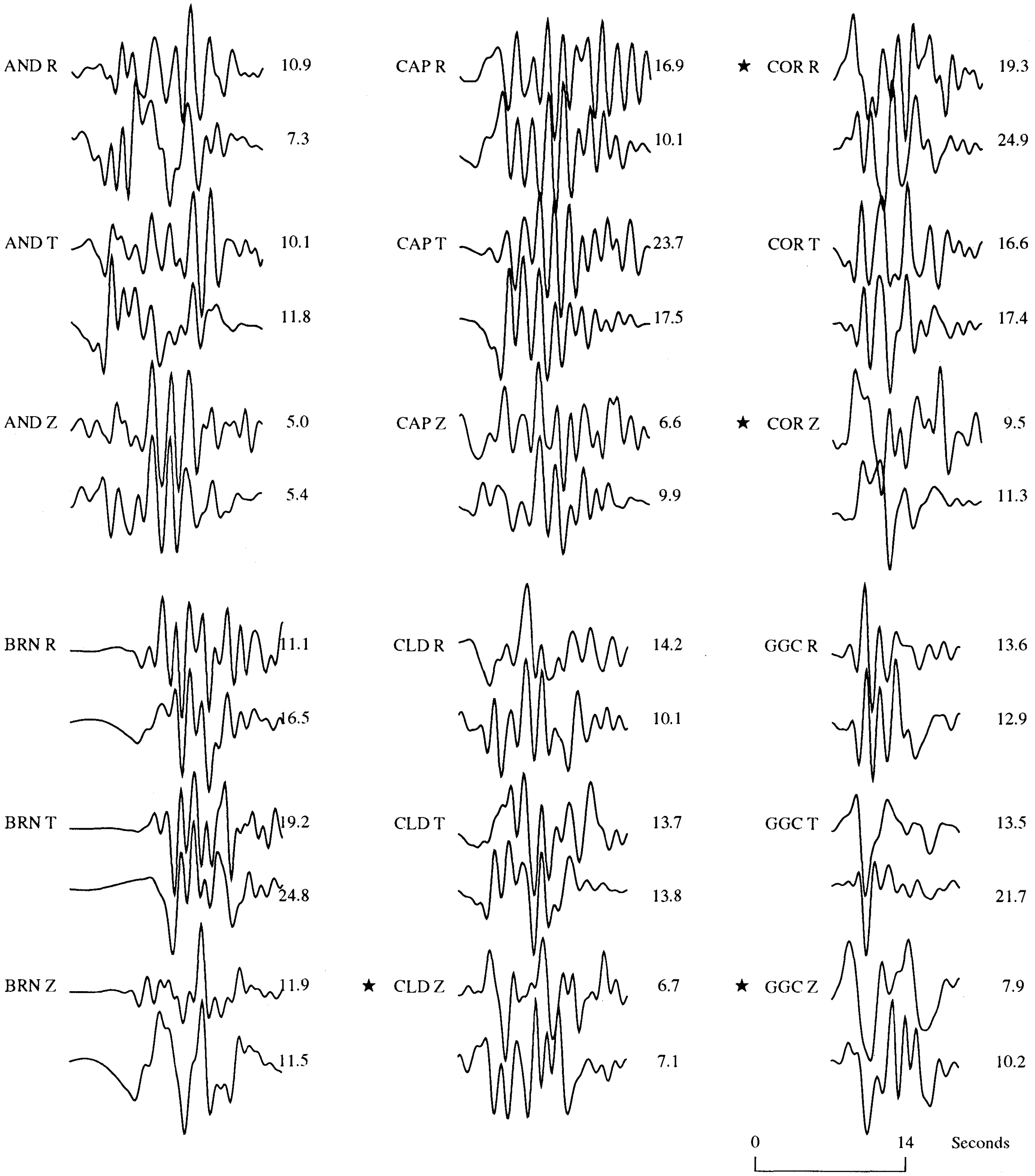

Figure 10.—Comparison of observed (upper curve) and synthetic (lower curve) seismograms of velocity at local-strong-motion stations (see fig. 2 for locations). Number to right of each curve is peak velocity (in centimeters per second). Stars, forward modeling only.

in the central part of the northwest lobe of dislocation, in comparison with the more diffuse slip in the previous models. The matchup of teleseismic waveforms is only slightly degraded, and the strong-motion synthetic seismograms are only slightly affected by the increased smoothing constraints.

FORWARD MODELING OF GROUND MOTION

In this section, we use our finite-fault-source inversion results to characterize ground motions more generally. First, we seek to determine whether the teleseismic-wave-

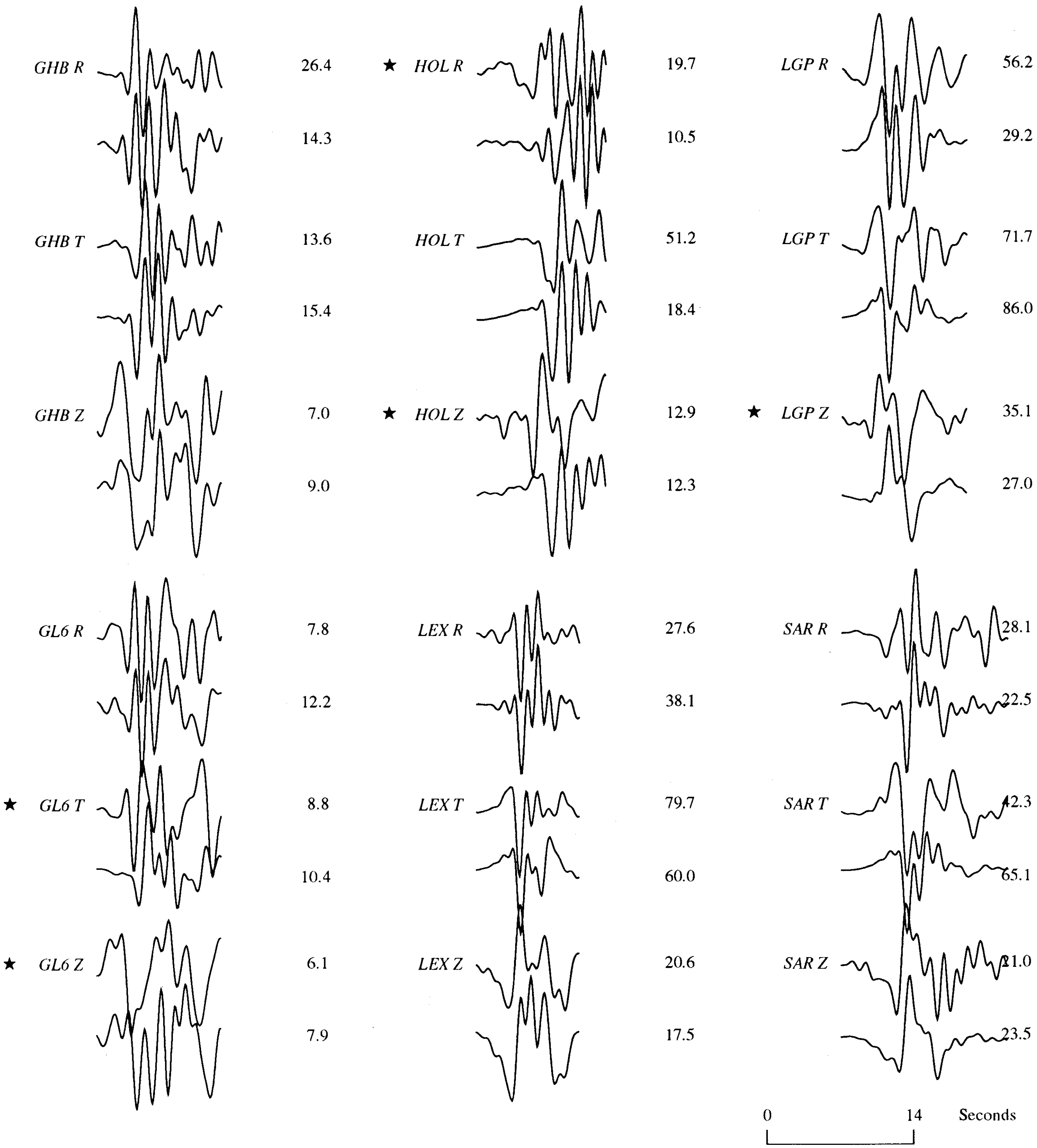

Figure 10.—Continued.

form data alone are sufficient to adequately resolve the source characteristics necessary to predict local strong ground motions. In forward modeling, this hypothesis was tested by predicting the strong motions, using the teleseismically derived source model. We then compared the strong motions predicted by the teleseismic source model with those predicted by the strong-motion source model.

Second, we show that the inversion of strong-motion data is useful for estimating the ground motions over the entire source region. The overall distribution of strong-

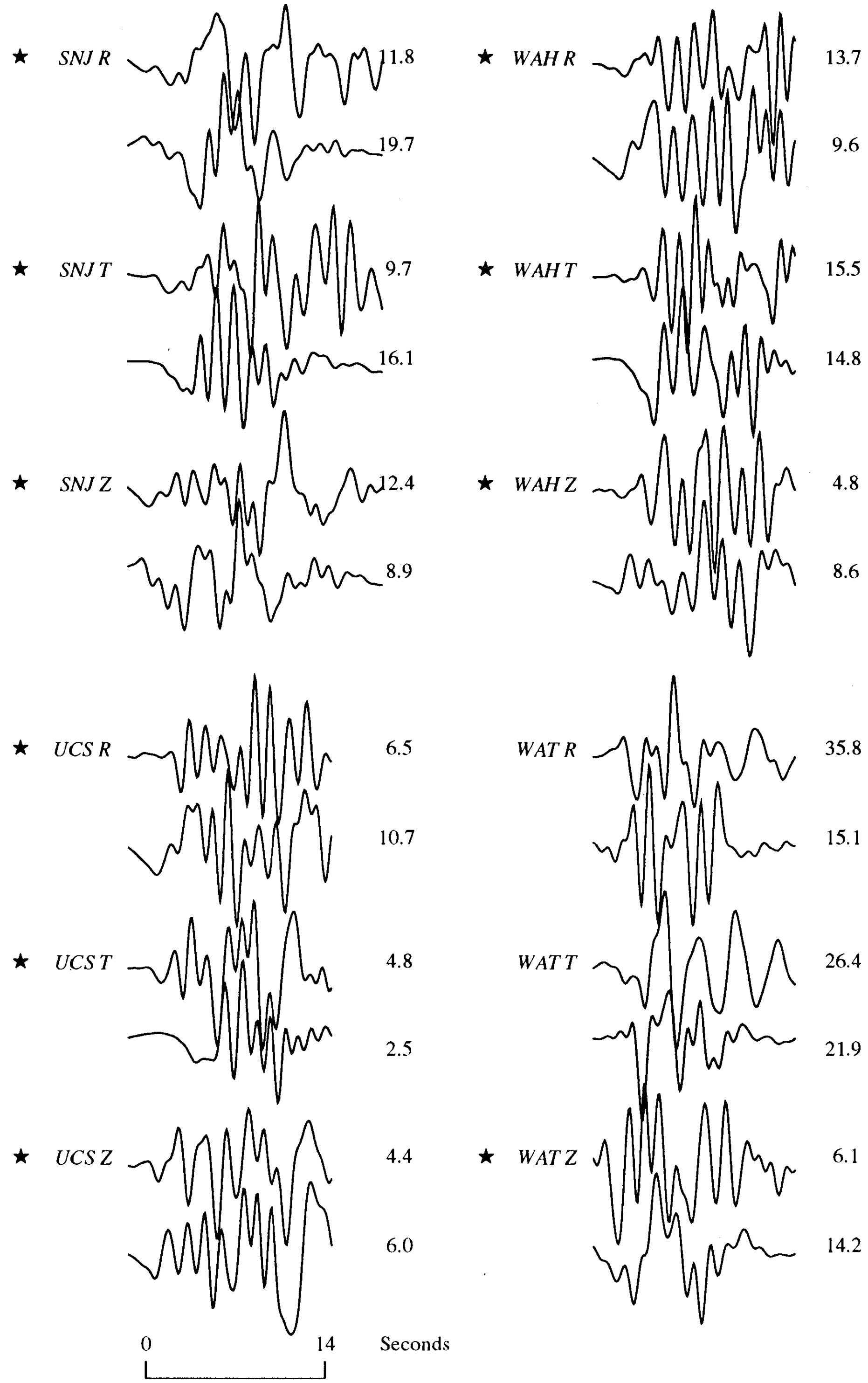

Figure 10.—Continued.

Table 5.—*Inversion model*

["Northwest" and "southeast" refer to halves of the fault. Radius is of asperity used in stress-drop calculations (figs. 12–14). Stress drop is of asperities in northwest and southeast halves of the fault (shading, fig. 12)]

Model	Seismic moment (10^{26} dyne-cm)	Peak slip amplitude (cm)	Radius (km)	Average slip (cm)	Stress drop (bars)
Strong motion:					
Northwest -------	1.9	350	7.2	209	138
Southeast --------	1.2	460	6.2	148	114
Total ---------	3.1	460	- - -	134	46
Teleseismic:					
Northwest -------	2.0	347	6.3	210	155
Southeast --------	.8	420	5.8	129	105
Total ---------	2.8	420	- - -	118	41
Strong motion and teleseismic:					
Northwest -------	2.2	491	5.3	248	218
Southeast --------	.8	371	6.2	181	136
Total ---------	3.0	491	- - -	141	- - -

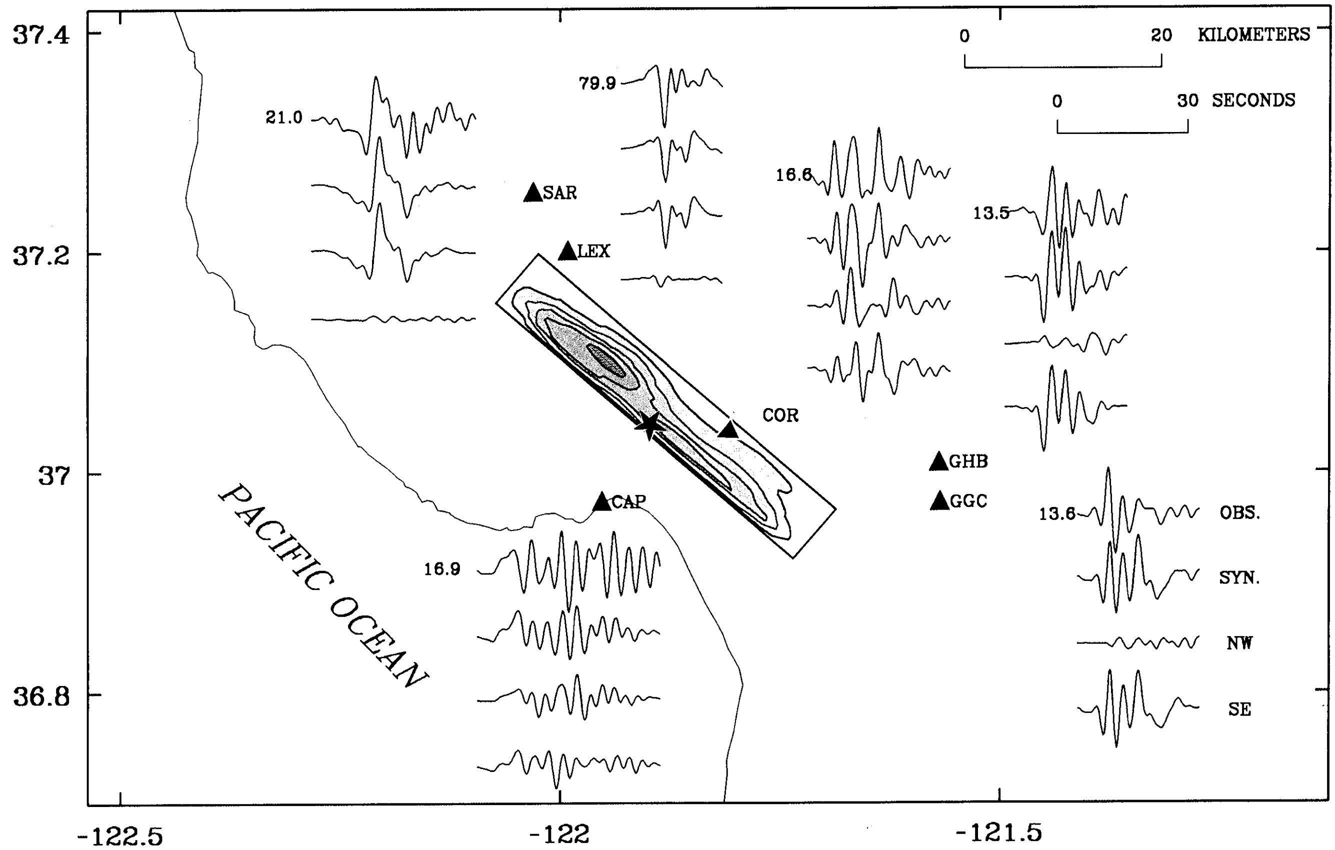

Figure 11.—Loma Prieta region, Calif., showing locations of strong-motion stations (triangles), epicenter of 1989 earthquake (star), and surface projection of model fault plane used in this study (shaded rectangle). Curves represent observed (uppermost) and synthetic (second) seismograms of ground motion, with synthetic contributions from northwest (third) and southeast (lowermost) halves of model fault. Number to left of uppermost curve is common peak velocity to which all curves for each station are scaled.

motion velocities was characterized by predicting ground motions at various sites not represented by strong-motion recordings. In addition, we modified the source-rupture model and analyzed the overall effect of fault geometry and rake on the resulting ground motions. Specifically, we preserved the slip distribution of the strong-motion model, constrained the slip to be strike slip on the adjacent vertical, shallow segment of the San Andreas fault, and then compared the resulting ground motions to those from the dipping, oblique-slip Loma Prieta rupture. This scenario of vertical strike-slip rupture is plausible for a future earthquake on this section of the San Andreas fault, and might be considered a lower bound on the ground motions sustained during the 1906 San Francisco earthquake.

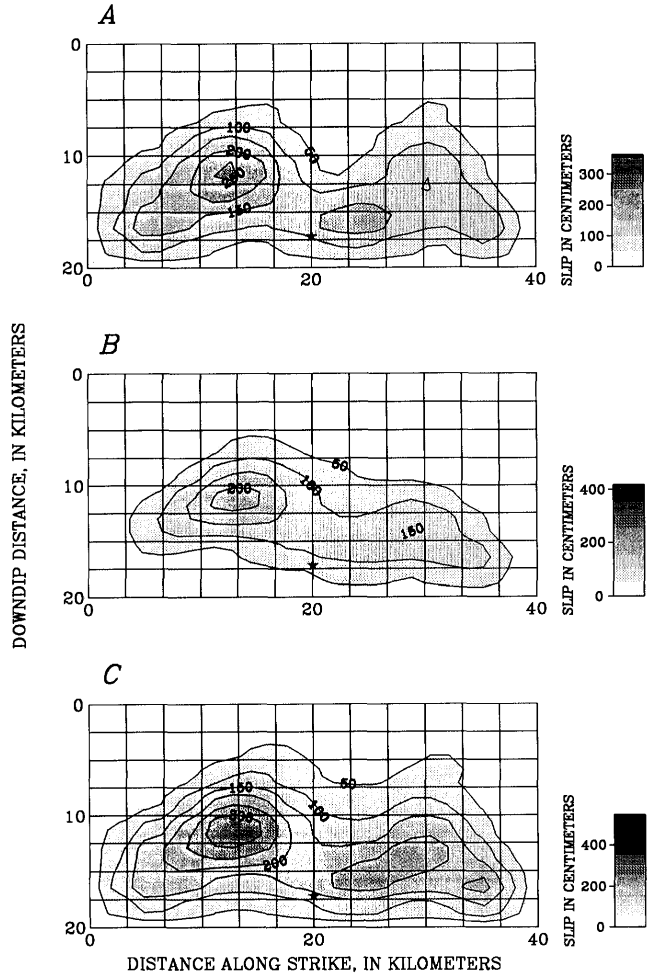

Figure 12.—Northwest-southeast cross section of model fault (fig. 3), showing contours of dislocation for strike slip (*A*), dip slip (*B*), and oblique slip (*C*) predicted from combined inversion of teleseismic-waveform and strong-motion data. Contour interval, 50 cm. Star, hypocenter of 1989 Loma Prieta earthquake.

GROUND-MOTION PREDICTION FROM TELESEISMIC MODEL

Given the rupture model determined from inversion of the teleseismic-waveform data exclusively (fig. 5), it is straightforward to compute the local ground motions at the 16 stations that recorded the strong motions (table 2): We simply replace the strong-motion slip model with the teleseismic slip model and forward-model the resulting ground velocities. Recall that the fault-model parametrization is identical for both the strong-motion and teleseismic-waveform data; only the spatial smoothing and final slip distribution, including the relative weights within each of the three time windows, vary.

We might expect that, given the similarities of the teleseismic model to the strong-motion model (figs. 5, 9), comparable strong motions would be predicted. The observed ground-motion velocities at selected stations are compared with the synthetic waveforms predicted by the strong-motion and teleseismic source models in figure 13. The various stations were chosen as representative of regions above the northwestern, central, and southern sections of the fault. This waveform comparison indicates that the teleseismic synthetic ground motions (lower curve) fit the overall amplitudes and durations of the observed ground motions (upper curve) quite well. We expected the amplitudes and phases of individual arrivals to differ from the strong-motion data, considering that this phase information was omitted from the teleseismic inversion. We note, however, a slightly longer period quality in the teleseismic synthetic ground motions (lower curve) than in the strong-motion synthetic (middle curve) and observed (upper curve) seismograms. This shift to longer periods is noticeable at station LEX (fig. 13).

For a more systematic comparison, we can quantify the misfit to observations for both the strong-motion and teleseismic source models by examining the difference in the response spectra of the observed and synthetic seismograms. We use the methodology of Abrahamson and others (1990) to evaluate the uncertainty in numeric strong-motion predictions as appropriate for engineering applications. We calculate the natural logarithm of the spectral acceleration at 5-percent damping on each horizontal component and then average the spectra for the two horizontal components. As shown by Abrahamson and others (1990), the estimated model bias is given by the mean error, ε, as a function of spectral frequency, *f*, by the relation:

$$\varepsilon(f)=\frac{1}{N}\sum_{i=1}^{N}(\ln \mathrm{SA}_i^o-\ln \mathrm{SA}_i^s),$$

where SA_i^o is the observed and SA_i^s is the synthetic spectral acceleration for the *i*th recording, and *N* is the total number of recordings. We compute the mean error only for spectral frequencies within the bandpass of the inversion (0.2–1.0 Hz).

The mean error averaged over both horizontal components of all stations, and the 90-percent-confidence interval of the bias for the strong-motion and teleseismic source models, are compared in figure 14. The model is considered unbiased if its bias does not differ significantly from zero at the 90-percent-confidence level (Abrahamson and others, 1990). Over this frequency range, the strong-motion synthetic seismograms show very little bias in comparison with the observed seismograms. This result is not surprising, considering that the solution was determined by using a least-squares fit between the synthetic and observed strong-motion seismograms.

In the teleseismic model, within the 90-percent-confidence interval, the bias differs only marginally from zero. The synthetic seismograms slightly overpredict the velocity at frequencies below 0.4 Hz and underpredict it at higher frequencies. This result indicates, however, that the teleseismic source models, determined independently from the strong-motion data, can be used to predict the near-fault ground motions for comparable earthquakes that might lack strong-motion recordings.

We note that the forward prediction of strong motions from the teleseismic-waveform data is sensitive to the spatial smoothing chosen for the teleseismic model. For this reason, the 1989 Loma Prieta earthquake, with abundant teleseismic-waveform as well as local data, presents a

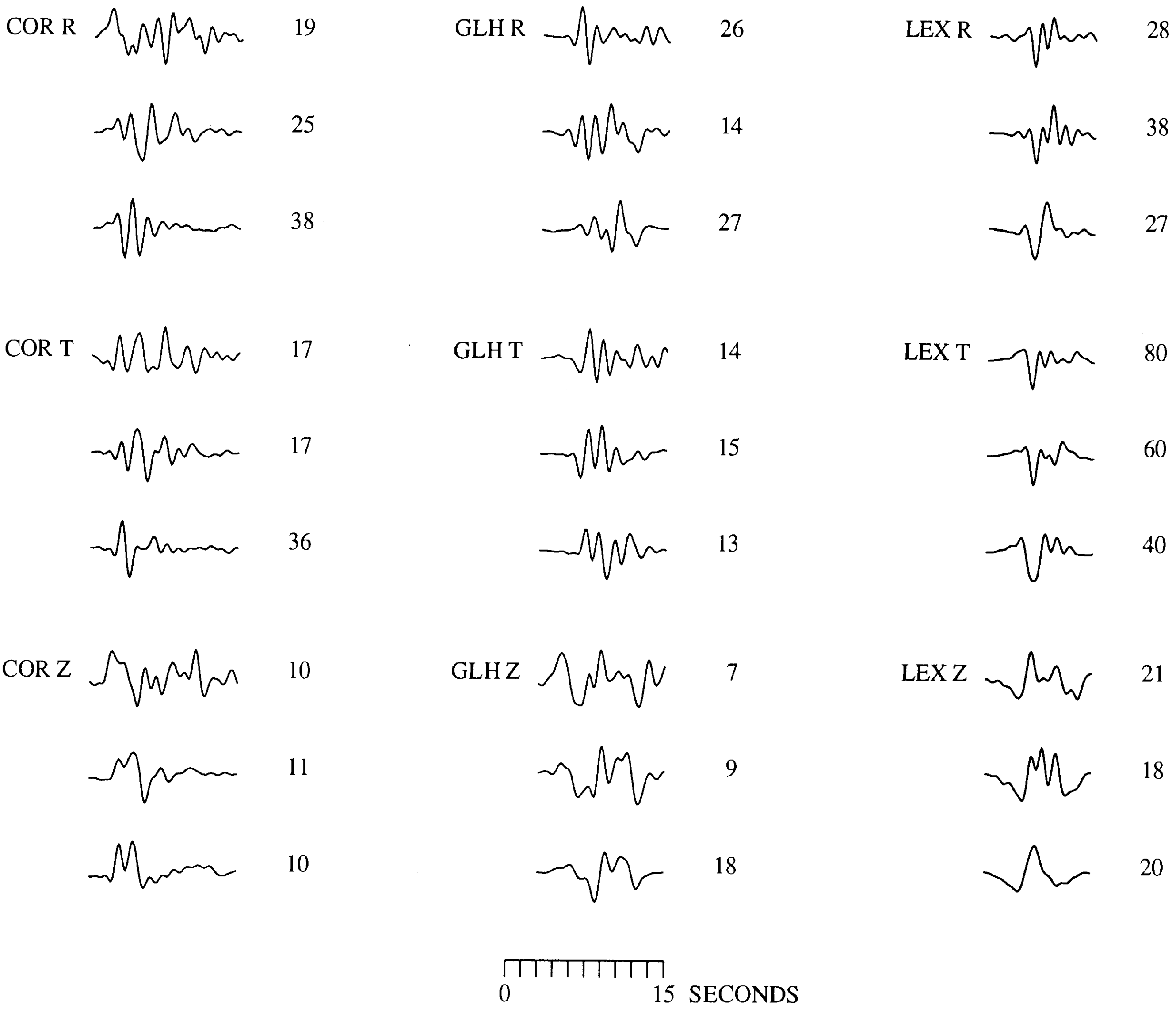

Figure 13.—Comparison of observed seismograms (top curve), synthetic seismograms produced with strong-motion dislocation model (middle curve), and synthetic seismograms produced with teleseismic dislocation model (bottom curve) for radial (R), tangential (T), and vertical (Z) components of velocity at local-strong-motion stations COR, GLH, and LEX (fig. 2). Number to right of curve is peak velocity (in centimeters per second).

unique chance to examine the relation between these parameters. Because inversions of teleseismic-waveform data alone generally tend to prefer solutions with numerous isolated, high-slip subfaults, significant smoothing was required to minimize the variation of slip between adjacent subfaults. Thus, as presented here, the teleseismic-waveform model represents a lower estimate of the fault slip heterogeneity. The net effect is a noticeable underprediction of the higher-frequency (>0.7 Hz) energy, as shown in figure 14, and a slight overprediction of longer-period (<0.4 Hz) energy.

Our estimation of the smoothing required for the teleseismic model appears to be reasonable, considering the sufficient fit to the strong-motion predictions (figs. 13, 14). In our future work, we will more fully examine the relation between the theoretical spatial smoothing used for teleseismic modeling and the effects on estimations of higher-frequency radiation.

ESTIMATED PEAK-GROUND-VELOCITY DISTRIBUTION

The dislocation model derived from inversion of the teleseismic and strong-motion data can also be used to characterize the ground motions at a site anywhere within the source region (fig. 1). For example, Hartzell and Iida (1990) used their rupture model of the 1987 Whittier Narrows, Calif., earthquake, derived from inversion of local strong-motion data, to forward-model the ground motions over the entire epicentral region. In using this approach, we are limited only by the farthest distance to which adequate Green's functions are available. For the Loma Prieta source area, we computed synthetic ground-motion velocities over a grid of stations (crosses, fig. 15), with east-west separations of 9 km and north-south separations of 5 km, at a total of 64 locations in addition to the 16 original station locations (table 2). The peak ground velocity was determined at each gridpoint station, and then these values were contoured over the source area.

Two lobes of high peak velocities are apparent in figure 15, one in the southeastern section of the fault and the other in the northwestern section. The largest-amplitude simulations, more than 70 cm/s, are concentrated above the northwestern section of the fault. These two lobes represent the combined effects of the two asperity depths and locations (fig. 9), together with the source radiation pattern. The oblique mechanism, with an average rake of 142°, favors radiation toward the northwest, even for a uniform slip distribution.

The overall pattern of peak velocities (fig. 15) agrees well with many of the observed indicators of strong ground shaking during the earthquake, confirming that areas above the northwestern section of the fault underwent the strongest shaking. The largest ground velocities were measured at stations (LEX, LGP, SAR, fig. 2) within the northwest lobe of large computed ground motions. Furthermore, the MMI map of Stover and others (1990) (fig. 2*C*) shows a localized concentration of MMI VIII observations within the northwest lobe of large computed ground motions. This area of the southern Santa Cruz Mountains was also where most ground ruptures and fissures formed during the earthquake, particularly along Summit Road and Skyline Ridge. Ponti and Wells (1991) attributed these

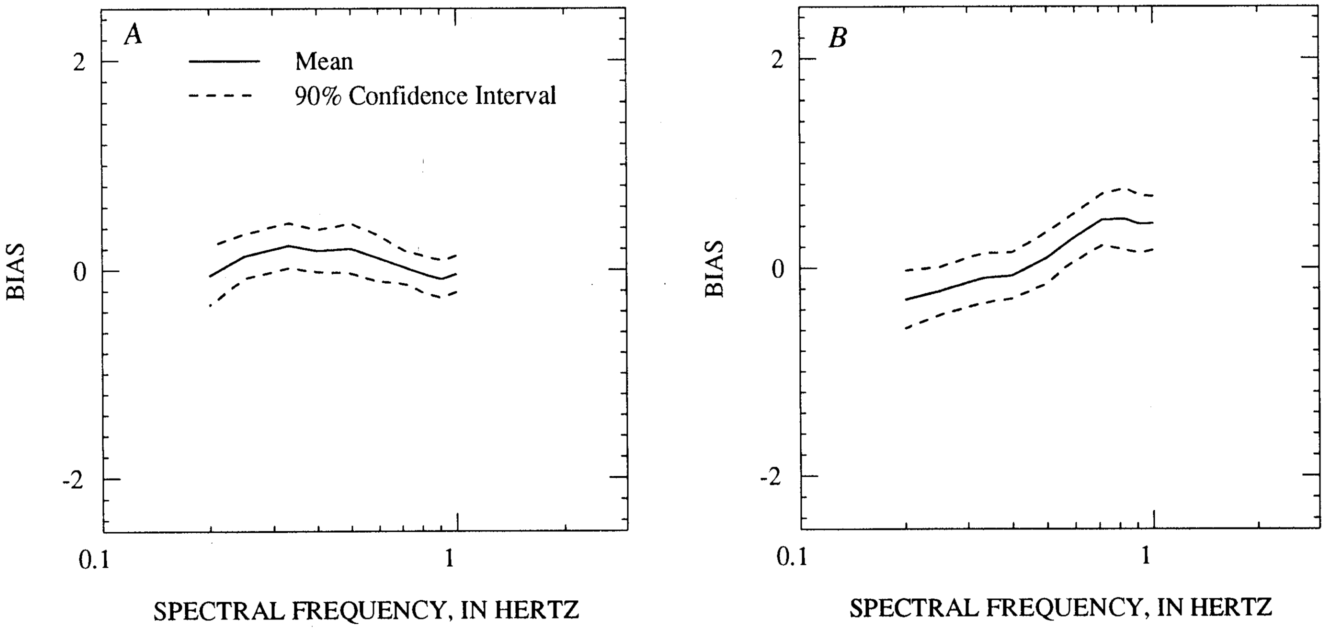

Figure 14.—Bias and 90-percent-confidence interval of bias versus spectral frequency for strong-motion inversion (*A*) and teleseismic inversion (*B*).

displacements to shaking-induced gravitational spreading of ridges and downslope movement, and noted that the greatest damage to competent structures and the highest concentration of topped trees, displaced boulders, and seismically activated landslides were in this area.

Finally, to further characterize the ground-motion hazards in this area, we modified the strong-motion rupture model to simulate a vertical strike-slip rupture along the San Andreas fault with a comparable slip distribution to the Loma Prieta strong-motion model. By rotating the model fault to a vertical plane and constraining the dislocation to be pure right-lateral strike slip, we approximate rupture along the San Andreas fault. For consistency with the average depth of significant slip from other strong-motion waveform inversions of California vertical strike-slip earthquakes (Hartzell and Heaton, 1983; Beroza and Spudich, 1988; Wald and others, 1990), we needed to decrease the asperity depth relative to the Loma Prieta model fault by bringing the top of the fault to within 0.5 km of the surface and translating the slip (see fig. 9) 5 km closer to the top of the fault (fig. 16). The strike was kept identical to that in the Loma Prieta model, causing a minor discrepancy in the strike of the model fault (straight line, fig. 17) relative to the strike of the San Andreas fault. The absolute amplitude of slip was preserved, resulting in a slightly smaller total seismic moment (owing to the reduced rigidity at the depths of the shallower slip). The slight difference in the contours (compare figs. 9 and 16) results from compressing the fault width over which slip occurs.

The overall pattern of the resulting peak ground velocities computed with the vertical strike-slip-fault model (fig. 16) is shown in figure 17. Note that the overall velocities are higher than in the Loma Prieta model. These higher velocities are attributable to the relatively shallow slip relative to the Loma Prieta model. Note that the asperity toward the northwestern section of the fault is shallower than that toward the southeastern section (fig. 16), suggesting that near-source ground motions during the earthquake were moderated by the relatively large average depth of significant slip.

DISCUSSION

We have presented our slip models by using contour maps that are spatially smoothed to deemphasize the abrupt subfault boundaries used in our inversion scheme. To com-

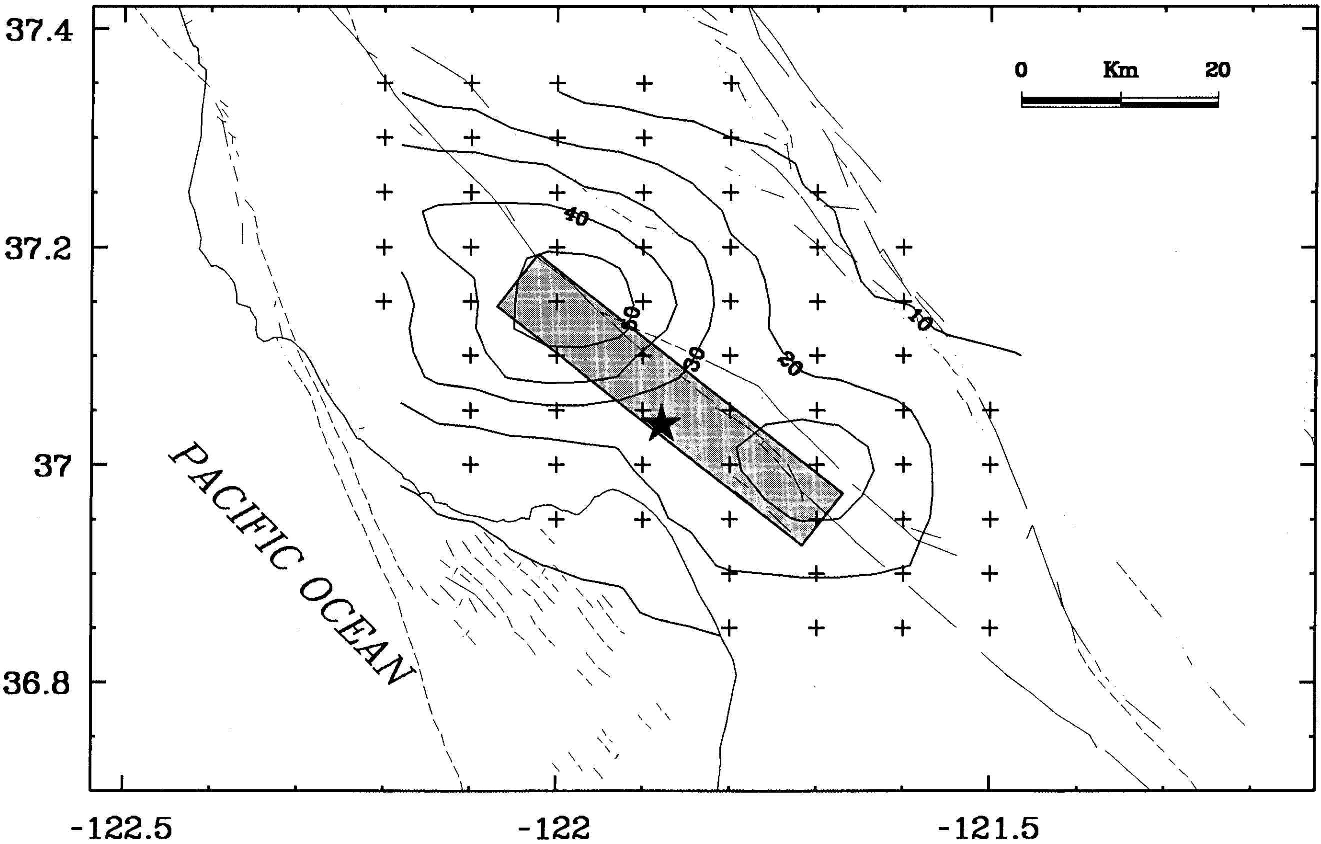

Figure 15.—Loma Prieta region, Calif., showing epicenter of 1989 earthquake (star), surface projection of model fault plane used in this study (shaded rectangle), and contours of peak ground velocity predicted from strong-motion source model. Contour interval, 10 km/s. Crosses, grid of stations used in forward modeling.

pare our inversion models in more detail, the slip vectors for individual subfaults are shown in figure 18, and the maximum absolute slip amplitudes are listed in table 5. The average rake angles, based on the relative components of strike slip and dip slip for the strong-motion, teleseismic, and combined inversions are 142°, 144°, and 145°, respectively, in agreement with the range of values reported in teleseismic point-source studies by other researchers and with the geodetic modeling results (Lisowski and others, 1990).

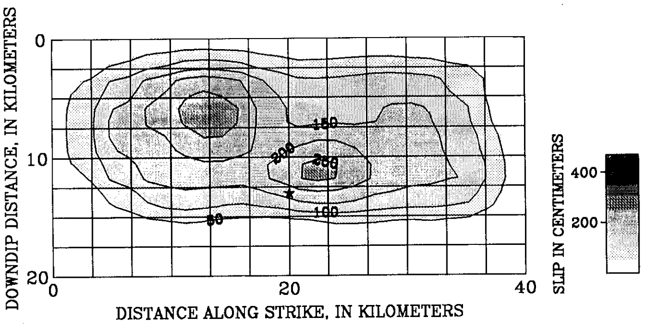

Figure 16.—Northwest-southeast cross section of model fault (fig. 3), showing contours of dislocation for vertical strike slip predicted from strong-motion model. Contour interval, 50 cm. Star, hypocenter of 1989 Loma Prieta earthquake.

Although inversion of only the teleseismic-waveform data does not result in systematic spatial variations of the rake angle (fig. 18*B*), inversion of the strong-motion data (figs. 18*A*, 18*C*) shows a clear tendency for more nearly vertical rake angles of slip to the northwest of the hypocenter and more nearly horizontal rake angles of slip to the southeast. Although our model assumes that all slip occurs on a single, 70°-dipping plane, this systematic change in rake angle coincides with an apparent change in dip of the aftershock zone from about 70° for the segment northwest of the hypocenter to nearly vertical near the southeast edge of the fault plane (Dietz and Ellsworth, 1990).

One shortcoming of our model is its failure to predict the large transverse motions observed at station HOL (fig. 10), although site-response studies indicate significant site amplifications at this station (Keiiti Aki, written commun., 1991). Station HOL, which is located along the southeastward projection of the fault, has an unusually large motion perpendicular to the fault strike (fig. 2*B*). This

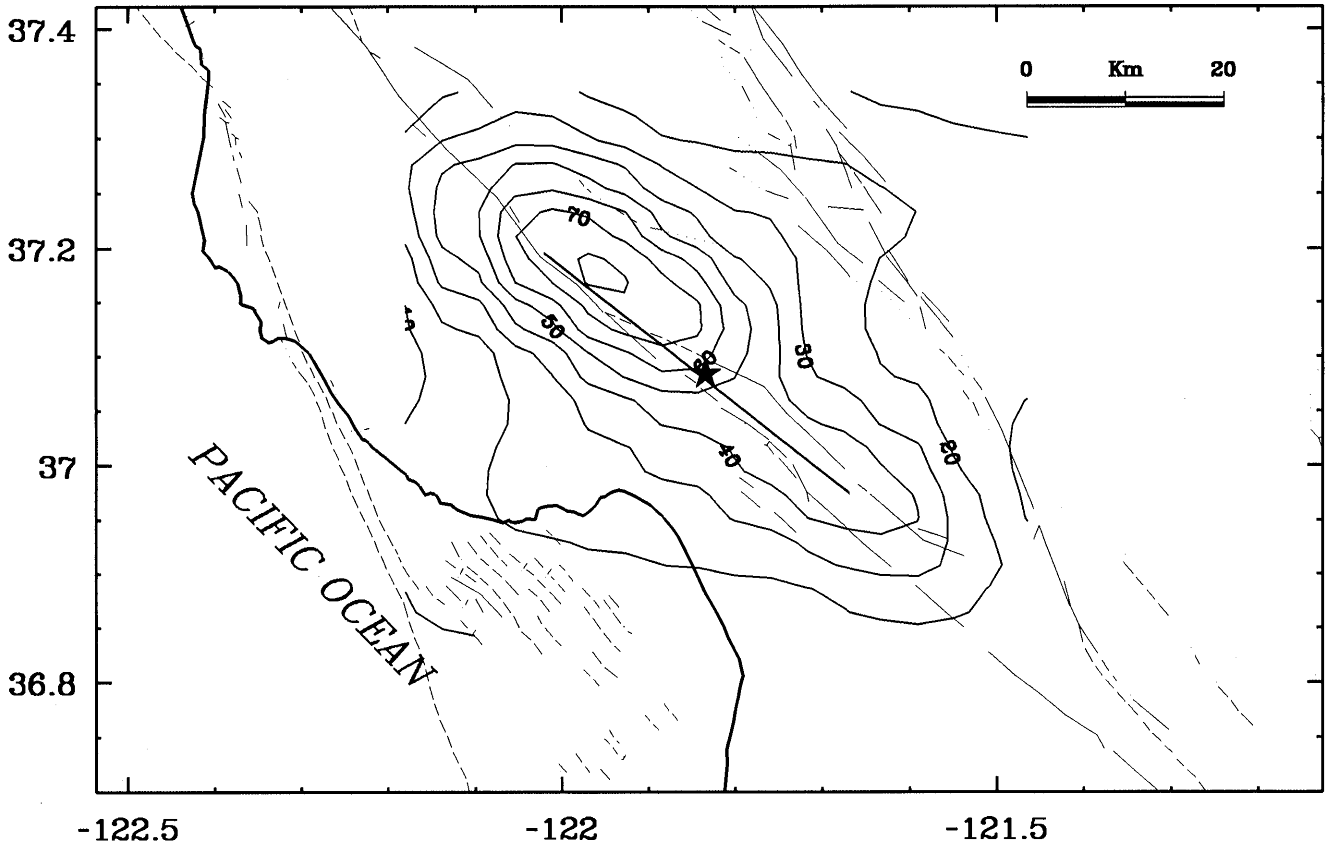

Figure 17.—Loma Prieta region, Calif., showing predicted contours of peak ground velocity from a vertical strike-slip rupture along the San Andreas fault, based on 1989 Loma Prieta slip distributions. Contour interval, 10 cm/s. Irregular thin lines, faults (dashed where inferred), digitized from major Quaternary faults mapped by Jennings (1975); straight line, model fault length; star, epicenter of 1989 Loma Prieta earthquake.

waveform suggests strike-slip faulting on a separate, vertically dipping, southeast-trending fault plane at the southeast end of the aftershock area (possibly the San Andreas fault). The radiation pattern from a vertical strike-slip mechanism would greatly enhance the tangential component and yet not contribute to the near-nodal radial and vertical components. Such a model is consistent with the near-vertical aftershock distribution and strike-slip mechanisms near the southeast edge of the inferred rupture zone (Dietz and Ellsworth, 1990). Although a minor amount of pure strike-slip motion occurs on the shallow southeastern section of our model fault inferred from the teleseismic-waveform data (2.5–7.5 km downdip, 23–36 km along strike; fig. 18), such motion is not seen in models inferred from the strong-motion data.

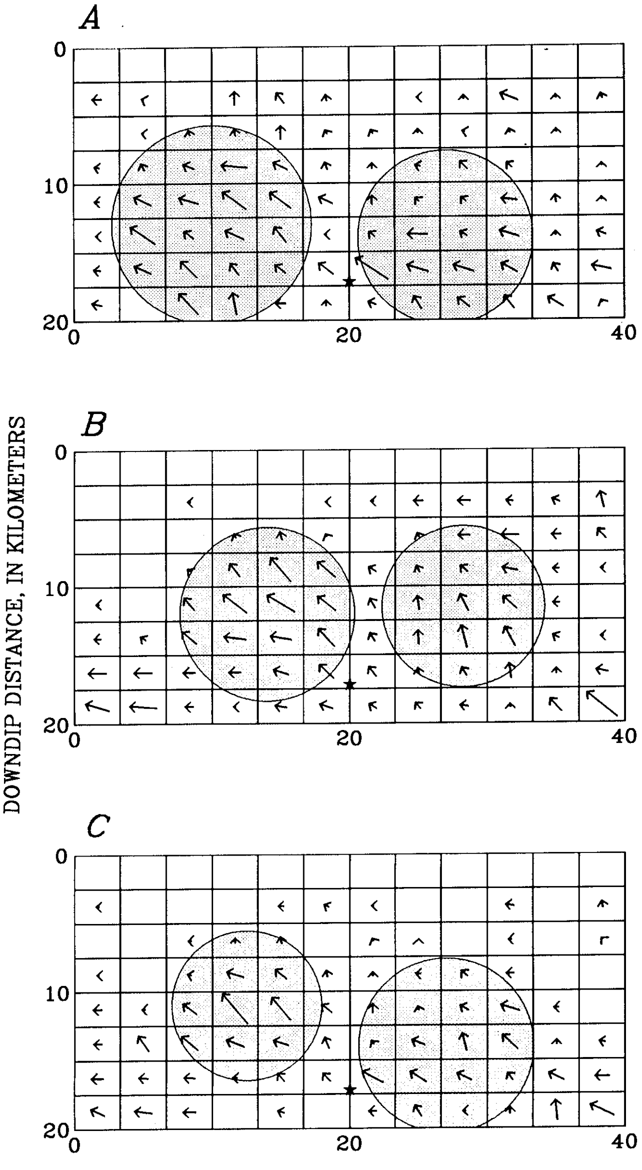

Figure 18.—Northwest-southeast cross section of model fault (fig. 3), showing rake angle (vector) for each subfault as determined from inversion of strong-motion (*A*) and teleseismic (*B*) data sets, and from combined inversion of both data sets (*C*). Length of each vector is normalized to peak slip on model fault plane. Shaded circles, patches where most slip is concentrated; star, hypocenter of 1989 Loma Prieta earthquake.

To estimate the stress drop for the regions of concentrated slip, we approximate their area with a circle and calculate the average slip amplitude within that circle (shaded circles, fig. 18). Using the stress-drop relation of Eshelby (1957) for a circular fault, $\Delta\sigma=7\pi\mu\bar{u}/16a$, where μ is the rigidity (3.4×10^{11} dyne/cm^2), $\bar{u}$ is the average dislocation, and a is the radius, we obtain the stress drops listed in table 5. For the entire fault rupture, the relation of Parsons and others (1988) is more appropriate for a long, buried strike-slip fault: $\Delta\sigma=C\mu\bar{u}/w$, where w is the downdip fault width and C is a constant dependent on the fault-plane dimensions. Using our fault dimensions, their results require that $C\simeq1.75$. Setting w=17 km, we obtain the stress drops for all three inversions listed in table 5.

In general, the rupture dimensions of significant slip agree well with the overall slip dimensions based on the active perimeter of the aftershock zone (Dietz and Ellsworth, 1990). This result is consistent with the observation of Mendoza and Hartzell (1988) that aftershocks commonly cluster along the margin of fault regions that underwent large coseismic slips. The regions of major slip in our model coincide with a region of relatively few aftershocks in the central part of the aftershock zone, although our model suggests less updip rupture than that inferred by Dietz and Ellsworth (1990) from the aftershock distribution alone. Thus, whereas the general features of the rupture can generally be inferred from aftershock activity, significant features of the rupture may be obscured in the aftershock patterns. The exact details of the aftershock pattern from the earthquake vary significantly, depending on the time period chosen for the analysis (for example, Dietz and Ellsworth, 1990, figs. 3a–3c). Therefore, we consider only larger (M>4.0) aftershocks, including those within the first 34 minutes after the main shock (Simila and others, 1990), and find that they tend to cluster around the major slip concentrations in our model (fig. 9*C*), particularly in the northwestern section of the fault.

The use of three time windows (each of 0.7 s) allows several general observations about the rupture-velocity and slip-time history. We expect regions requiring a locally lower rupture velocity to make use of the later time windows so as to compensate for the lower, fixed rupture velocity. Likewise, regions with a higher rupture velocity would take advantage of only the first rupture window. Overall, in both the strong-motion and teleseismic inversions, slip in time window 1 dominates, and only minor slip occurs in time windows 2 and 3 (fig. 19) over much of the fault. This result implies that the rupture timing in our model satisfies the data and that large variations in rupture velocity are unnecessary. In addition, a locally lower rupture velocity or somewhat longer slip duration may be evident along the outer northwestern margin of the northwestern asperity, in the same region where most $M>4.0$ aftershocks occurred.

The concentration of most slip in time window 1 indicates that short slip durations (<1 s) are preferred in our model at a given point on the fault, implying that only a small part of the entire rupture surface is slipping at any given time. For example, the section of the fault rupturing 5 s after the nucleation time in figure 3 is shown as the shaded area within time window 1. Short slip durations, which have also been inferred for other earthquakes, have an important implications for rupture mechanics (Heaton, 1990).

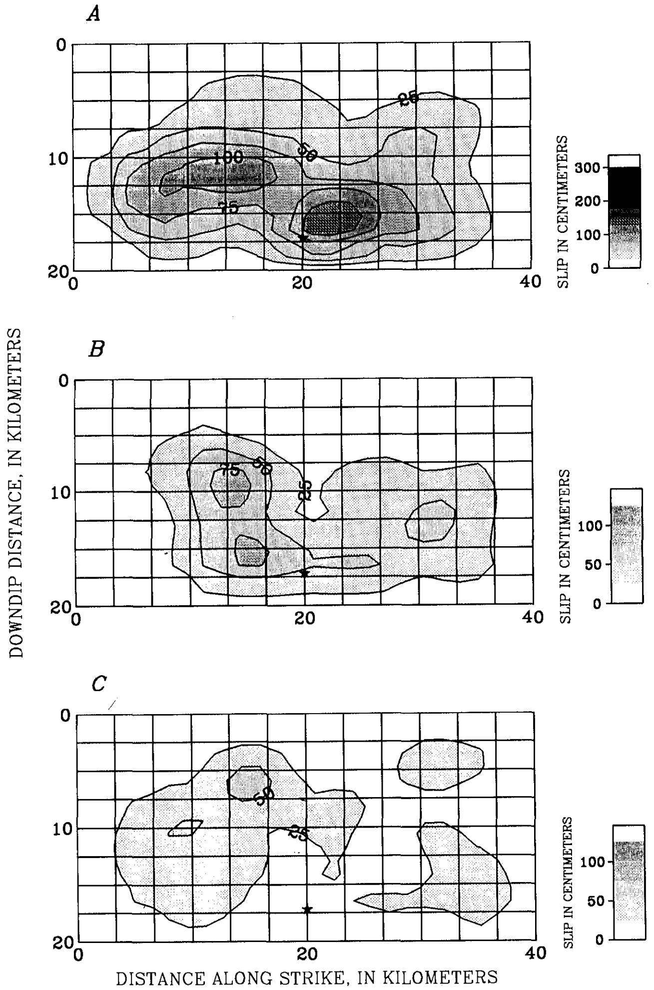

Figure 19.—Northwest-southeast cross section of model fault (fig. 3), showing contours of oblique slip predicted from strong-motion inversion for time windows 1 (*A*), 2 (*B*), and 3 (*C*). Contour interval, 50 cm. Star, hypocenter of 1989 Loma Prieta earthquake.

CONCLUSIONS

From our analysis of the three inversions, we find a bilateral dislocation pattern, with two main regions of oblique slip: the first centered about 6 to 8 km northwest of the hypocenter at 11- to 13-km depth and the other centered at 7 to 9 km southeast of the hypocenter at 15- to 16-km depth. The northwestern patch, which has a larger seismic moment, a larger average slip amplitude, and thus a higher overall stress drop (table 5), is the source of the largest observed strong-motion velocities, recorded about 20 km northwest of the epicenter (see figs. 2, 11). Dominant radiation toward the northwest is also confirmed by the overall damage patterns and landslides concentrated in areas northwest of the epicenter (Benuska, 1990). Likewise, an azimuthal dependence in the peak ground motions was observed by Boore and others (1989) (see fig. 6), who noted a tendency for high residuals relative to predicted peak velocities at rock sites toward the northwest relative to all other azimuths.

We now compare our slip model with the other finite-fault dislocation models for this earthquake (Beroza, 1991; Hartzell and others, 1991; Steidl and others, 1991). Although significant differences in the amplitude and direction of slip vectors exist between our model and the others, they all agree remarkably well on the overall characteristics of this rupture. All researchers conclude that a bilateral rupture with relatively low slip updip from the hypocenter best explains the waveforms, and researchers find that most slip occurred on two relatively small patches nearly equidistant from the hypocenter, one to the northwest and the other to the southeast. All studies indicate that a fairly uniform rupture velocity of approximately 80 percent of the local shear-wave velocity, together with a relatively short slip duration at any point (≲1.5 s) best explains the observed waveforms.

Although our model is similar in most respects to the others presented in this chapter, it differs substantially in two aspects. First, the local rake vectors vary significantly among the models discussed below. On average, the rake vectors of about 145° in the area southeast of the hypocenter agree between our model and that of Hartzell and others (1991). Both of these models have similar oblique rake components in the northwestern asperity. In contrast, the southeastern asperity in the models of Beroza (1991) and Steidl and others (1991) shows rake angles indicating nearly pure strike slip (rake, ~160°–170°, yet they have almost pure thrusting rake vectors (80°–90°) within the northwestern asperity. These two models require an approximately 80° change in rake vector from the south half to the north half of the fault and no corresponding change in dip. We emphasize that, although the slip distributions of Beroza (1991) and Hartzell and others (1991) look similar, the rake vector in the region of dominant slip for these models (the southeastern asperity) differs by about

40° and would likely produce substantially different near-field ground motions.

Second, in addition to variation in the local rake directions, the partitioning of total slip along strike in asperities northwest and southeast of the epicenter in our model requires more slip in the northwestern asperity (figs. 5, 9, 18; table 5); the other models require most of the slip in the southeastern asperity. Considering that rise times, rupture velocities, and source geometries are similar among the various models, disparities in the resulting slip distribution most likely reflect variations in the data sets employed. Other parameters being comparable, station coverage and weighting may be the most critical elements controlling the slip partitioning. A source of dominant radiation northwest of the epicenter is required by the strong-motion data used in our study (see fig. 2). In particular, the large coherent arrivals at stations SAR, LEX, and LGP require significant slip and directivity. A comparison of the waveform fits at station SAR by the various models is particularly revealing and reflects the differences in modeling strategy.

The strategy adopted by Steidl and others (1991) was to obtain the largest possible azimuthal coverage by including stations out to 60 km. Thus, they modeled several distant stations to the north quite well, while doing a relatively poor job in fitting both waveform and amplitude at station SAR (fig. 2). They did not use stations LEX and LGP, which recorded the largest ground velocities, and so the wavefield at these ray parameters is downweighted relative to distant samples. If their Green's functions are adequate for these distant stations and ours prove less than desirable at stations LEX, SAR, and LGP, then they have a more reasonable interpretation. A detailed study of aftershock recordings at the various stations is one way to resolve this particular issue, because local receiver structures can be recognized and the adequacy of the theoretical Green's functions may be examined.

It is not so clear why the slip distribution of Beroza (1991) differs from ours. Although he did not use the vertical components of ground motion, his station selection in the northwestern section of the fault is similar to that in our study. Waveforms fits at his northwestern stations, however, show significant differences from those of our model. The differences in slip distribution may partly be due to differences in the applied Green's functions, as he suggested; we used the complete layered-space solutions, whereas he used only geometric-ray approximations. Again, a comparison of near- and far-field Green's functions with simple aftershocks at stations SAR and other stations should help resolve this issue.

Slip in the southeastern asperity is evidently constrained by the southeastern stations, as described in figure 11. We used station WAT (fig. 2) and a few of the Gilroy array stations. We observed that the other Gilroy array stations have complex receiver functions, and so we omitted these stations from our analysis. The data sets used in the other studies excluded station WAT and included additional stations from the Gilroy array. The use of a dense set of stations over limited distance and azimuthal ranges provides redundant coverage and may favor slip in the southern section of the fault.

Clearly, the teleseismic-waveform data have less resolving power along strike than the strong-motion data, as shown by comparison of the *P* and *SH* waveforms from this study and those of Hartzell and others (1991). Although the slip models differ considerably and are nearly northwest-southeast reversed, they produce nearly identical teleseismic waveforms, suggesting an absence of resolution from this data set. The teleseismic-waveform data, however, resolve updip directivity and require a bilateral rupture with little updip slip. Again, the differences in the teleseismic source models probably result from variations in station coverage. Hartzell and others (1991) used similar teleseismic stations to ours but added several additional stations, particularly in the northwestern and northeastern azimuths. These additional stations, however, do not substantially augment azimuthal coverage and may actually bias the results. Removal of these stations from their inversion results in a model similar to ours, favoring northwestern slip (S.H. Hartzell, oral commun., 1990).

We note that even though the slip distribution and rake vectors vary, the net result of any of these models will be nearly the same at long periods. This similarity can be explained by the fact that the bilateral rupture radiates from both asperities simultaneously. Thus, as long as the net rake vector and total seismic moment are preserved, the resulting models should produce similar and adequate teleseismic-waveform matches, though not necessarily for the near-field data. That the waveform comparisons for all the strong-motion models are less than remarkable may reflect the need for a more complex rupture surface than the idealized flat-planar models used here.

In general, the rupture process of the 1989 Loma Prieta earthquake was fairly simple for an M=7.1 earthquake, rupturing only a relatively short (<35 km long) fault segment (Kanamori and Satake, 1990). The relatively short duration of strong motion is partly attributable to the bilateral rupture. Furthermore, the relatively great depth of slip concentrations moderated the amplitude of ground velocities in the near-source region.

Most of our current knowledge of fault-asperity characteristics has been derived from ground-motion frequencies lower (<1 Hz) than the frequency range of most interest in earthquake engineering. Wald and others (1987, 1988) found that large-scale asperity models derived from longer-period velocity data also explained many characteristics of the higher-frequency accelerograms. Our results here indicate that the asperities which control broadband teleseismic waveforms (3–30 s) also dominate higher-frequency strong motions (1–5 s).

In an effort to understand the radiation of the higher-frequency motions during the 1989 Loma Prieta earthquake, we performed an inversion with the observed and synthetic seismograms bandpass filtered from 0.1 to 3 Hz. We used a finer discretization of the fault plane into 200 subfaults, each with dimensions of 2.0 km along strike and 2.0 km downdip. We also reduced the duration of the source-time function to 0.5 s. Our results indicate that the same regions of large slip which control the longer-period teleseismic waveforms and the strong-motion velocities as high as 1 Hz are also responsible for higher-frequency (>1.0 Hz) radiation. We also note that the inversion using higher-frequency data appears to favor slightly more concentrated asperities. Understanding the relation between long-period source models of large earthquakes and the radiation of high frequencies is critical for a prediction of ground motions in the frequency range of engineering interest. Our future work will address the characteristics of the high-frequency radiation further. Such study will require more sophisticated timing corrections based on the aftershock data recorded at many of the strong-motion stations used here, as well as a more detailed treatment of the variations in propagation paths and site effects at individual stations.

ACKNOWLEDGMENTS

This work was supported by the U.S. Geological Survey under contracts 14-08-0001-21912 and 14-08-0001-G1832. Reviews by Hiroo Kanamori, Paul Somerville, Paul Spudich, and Lisa Wald improved the manuscript. We thank Steve Hartzell for useful discussions and advice on the use of his inversion software, and Norm Abrahamson and Nancy Smith for providing programs to compute the response-spectral bias.

REFERENCES CITED

Abrahamson, N.A., Somerville, P.G., and Cornell, C.A., 1990, Uncertainty in numerical strong motion predictions: U.S. National Conference on Earthquake Engineering, 4th, Palm Springs, Calif., 1990, Proceedings, v. 1, p. 407–416.

Archuleta, R.J., 1984, A faulting model for the 1979 Imperial Valley, California, earthquake: Journal of Geophysical Research, v. 89, no. B6, p. 4559–4585.

Benuska, Lee, ed., 1990, Loma Prieta earthquake reconnaissance report: Earthquake Spectra, v. 6, supp. 90–01, 448 p.

Beroza, G.C., 1991, Near-source modeling of the Loma Prieta earthquake; evidence for heterogeneous slip and implications for earthquake hazards: Seismological Society of America Bulletin, v. 81, no. 5, 81, p. 1603–1621.

Beroza, G.C., and Spudich, Paul, 1988, Linearized inversion for fault rupture behavior; application to the 1984 Morgan Hill, California, earthquake: Seismological Society of America Bulletin, v. 93, no. B6, p. 6275–6296.

Boore, D.M., Seekins, L.C., and Joyner, W.B., 1989, Peak accelerations from the 17 October 1989 Loma Prieta earthquake: Seismological Research Letters, v. 60, no. 4, p. 151–166.

Choy, G.L., and Boatwright, John, 1990, Source characteristics of the Loma Prieta, California, earthquake of October 18, 1989 from global digital seismic data: Geophysical Research Letters, v. 17, no. 8, p. 1183–1186.

Dietz, L.D., and Ellsworth, W.L., 1990, The October, 17, 1989, Loma Prieta, California, earthquake and its aftershocks; geometry of the sequence from high-resolution locations: Geophysical Research Letters, v. 17, no. 9, p. 1417–1420.

Eshelby, J.D., 1957, The determination of the elastic field of an ellipsoidal inclusion, and related problems: Royal Society of London Proceedings, ser. A, v. 241, no. 1226, p. 376–396.

Futterman, W.I., 1962, Dispersive body waves: Journal of Geophysical Research, v. 67, no. 13, p. 5279–5291.

Hartzell, S.H., and Heaton, T.H., 1983, Inversion of strong ground motion and teleseismic waveform data for the fault rupture history of the 1979 Imperial Valley, California, earthquake: Seismological Society of America Bulletin, v. 73, no. 6, pt. A, p. 1553–1583.

———1986, Rupture history of the 1984 Morgan Hill, California, earthquake from the inversion of strong motion records: Seismological Society of America Bulletin, v. 76, no. 3, p. 649–674.

Hartzell, S.H., and Iida, Mashiro, 1990, Source complexity of the 1987 Whittier Narrows, California, earthquake from inversion of strong motion records: Journal of Geophysical Research, v. 95, no. B8, p. 12475–12485.

Hartzell, S.H. and Mendoza, Carlos, 1991, Application of an iterative least-squares waveform inversion of strong motion and teleseismic records to the 1978 Tabas, Iran, earthquake: Seismological Society of America Bulletin, v. 81, no. 2, p. 305–331.

Hartzell, S.H., Stewart, G.S., and Mendoza, Carlos, 1991, Comparison of L_1 and L_2 norms in a teleseismic inversion for the slip history of the Loma Prieta, California, earthquake: Seismological Society of America Bulletin, v. 81, no 5, p. 1518–1539.

Heaton, T.H., 1982, The 1971 San Fernando earthquake; a double event?: Seismological Society of America Bulletin, v. 72, no. 6, p. 2037–2062.

———1990, Evidence for and implications of self-healing pulses of slip in earthquake rupture: Physics of the Earth and Planetary Interiors, v. 64, no. 1, p. 1–20.

Heaton, T.H., and Heaton, R.E., 1989, Static deformations from point forces and force couples located in welded elastic Poissonian half-spaces; implications for seismic moment tensors: Seismological Society of America Bulletin, 79, no. 3, p. 813–841.

Jennings, C.W., compiler, 1975, Fault map of California, with locations of volcanoes, thermal springs, and thermal wells: California Division of Mines and Geology Geologic Data Map 1, scale 1:750,000.

Kanamori, Hiroo, and Satake, Kenji, 1990, Broadband study of the 1989 Loma Prieta earthquake: Geophysical Research Letters, v. 17, no. 8, p. 1179–1182.

King, G.C.P., Lindh, A.G., and Oppenheimer, D.H., 1990, Seismic slip, segmentation, and the Loma Prieta earthquake: Geophysical Research Letters v. 17, no. 9, p. 1449–1452.

Langston, C.A., and Helmberger, D.V., 1975, A procedure for modelling shallow dislocation sources: Royal Astronomical Society Geophysical Journal, v. 42, no. 1, p. 117–130.

Lisowski, Michael, Prescott, W.H., Savage, J.C., and Johnston, M.J.S., 1990, Geodetic estimate of coseismic slip during the 1989 Loma Prieta, California, earthquake: Geophysical Research Letters, v. 17, no. 9, p. 1437–1440.

Maley, R.P., Acosta, A.V., Ellis, F., Etheredge, E.C., Foote, L.J., Johnston, D.A., Porcella, R.L., Salsman, M.J., and Switzer, J.C., 1989, U.S. Geological Survey strong-motion records from the northern California (Loma Prieta) earthquake of October 17, 1989: U.S. Geological Survey Open-File Report 89–568, 85 p.

Mendoza, Carlos, and Hartzell, S.H., 1988, Aftershock patterns and main shock faulting: Seismological Society of America Bulletin, v. 78, no. 4, p. 1438–1449.

Olson, A.H. and Apsel, R.J., 1982, Finite faults and inverse theory with application to the 1979 Imperial Valley earthquake: Seismological Society of America Bulletin, v. 72, no. 6, p. 1969–2001.

Olson, A.H., Orcutt, J.A., and Frazier, G.A., 1984, The discrete wave number/finite element method for synthetic seismograms: Royal Astronomical Society Geophysical Journal, v. 77, no. 2, p. 421–460.

Olson, J.A., 1990, Seismicity in the twenty years preceding the Loma Prieta, California earthquake: Geophysical Research Letters, v. 17, no. 9, p. 1429–1432.

Oppenheimer, D.H., 1990, Aftershock slip behavior of the 1989 Loma Prieta, California earthquake: Geophysical Research Letters, v. 17, no. 8, p. 1199–1202.

Parsons, I.D., Hall, J.F., and Lyzenga, G.A., 1988, Relationships between the average offset and the stress drop for two- and three-dimensional faults: Seismological Society of America Bulletin, v. 78, no. 2, p. 931–945.

Ponti, D.J., and Wells, R.E., 1991, Off-fault ground ruptures in the Santa Cruz Mountains, California; ridge-top spreading versus tectonic extension during the 1989 Loma Prieta earthquake: Seismological Society of America Bulletin, v. 81, no. 5, p. 1480–1510.

Schwartz, S.Y., Orange, D.L., and Anderson, R.S., 1990, Complex fault interactions in a restraining bend on the San Andreas Fault, southern Santa Cruz Mountains, California: Geophysical Research Letters, v. 17, no. 9, p. 1207–1210.

Seeber, Leonardo, and Armbruster, J.G., 1990, Fault kinematics in the 1989 Loma Prieta rupture area during 20 years before that event: Geophysical Research Letters, v. 17, no. 9, p. 1425–1428.

Shakal, A.F., Huang, M.J., Reichle, Michael, Ventura, C.E., Cao, T.Q., Sherburne, R.W., Savage, M., Darragh, R.B., and Petersen, C., 1989, CSMIP strong-motion records from the Santa Cruz Mountains (Loma Prieta), California earthquake of 17 October 1989: California Division of Mines and Geology, Office of Strong Motion Studies Report OSMS 89–06, 196 p.

Simila, G.W., McNally, K.C., Nava, E., Protti-Quesada, M., and Yellin, Joseph, 1990, Evidence of very early aftershock activity along the northwest portion of the 18 October 1989 earthquake rupture zone: Geophysical Research Letters, v. 17, no. 10, p. 1785–1788.

Steidl, J.H., Archuleta, R.J., and Hartzell, S.H., 1991, Rupture history of the 1989 Loma Prieta, California, earthquake: Seismological Society of America Bulletin, v. 81, no. 5, p. 1573–1602.

Stover, C.W., Reagor, B.G., Baldwin, F.W., and Brewer, L.R., 1990, Preliminary isoseismals map for the Santa Cruz (Loma Prieta), California, earthquake of October 18, 1989 UTC: U.S. Geological Survey Open-File Report 90–18, 24 p.

U.S. Geological Survey staff, 1990, The Loma Prieta, California, earthquake; an anticipated event: Science, v. 247, no. 4940, p. 286–293.

Wald, D.J., Burdick, L.J., and Somerville, P.G., 1988, Simulation of acceleration time histories close to large earthquakes, *in* Von Thun, J.L., ed., Proceedings; Earthquake Engineering and Soil Dynamics II; recent advances in ground-motion evaluation: American Society of Civil Engineers Geotechnical Special Publication 20, p. 430–444.

Wald, D.J., Helmberger, D.V., and Hartzell, S.H., 1990, Rupture process of the 1987 Superstitions Hills earthquake from the inversion of strong-motion data: Seismological Society of America Bulletin, v. 80, no. 5, p. 1079–1098.

Wald, D.J., Helmberger, D.V., and Heaton, T.H., 1991, The rupture initiation process of a large earthquake; Loma Prieta [abs.]: Seismological Research Letters, v. 62, no. 1, p. 29.

Wald, D.J., Somerville, P.G., and Helmberger, D.V., 1987, Compatibility of accelerograms of the 1979 Imperial Valley earthquake with slip-distribution asperity models [abs.]: Seismological Research Letters, v. 58, no. 1, p. 10.

Wallace, T.C., Velasco, A.A., Zhang, Jiajun, and Lay, Thorne, 1991, A broadband seismological investigation of the Loma Prieta, California, earthquake; evidence for deep slow slip?: Seismological Society of America Bulletin, v. 81, no. 5, p. 1622–1646.

Working Group on California Earthquake Probabilities, 1988, Probabilities of large earthquakes occurring in California on the San Andreas Fault: U.S. Geological Survey Open-File Report 88–398, 62 p.

THE LOMA PRIETA, CALIFORNIA, EARTHQUAKE OF OCTOBER 17, 1989: EARTHQUAKE OCCURRENCE

MAIN-SHOCK CHARACTERISTICS

COSEISMIC DISPLACEMENTS MEASURED WITH THE GLOBAL POSITIONING SYSTEM

By Chesley R. Williams and Paul Segall,
Stanford University

CONTENTS

ABSTRACT

Coseismic displacements during the 1989 Loma Prieta earthquake were measured with the Global Positioning System (GPS). During February and March 1989, the California Department of Transportation (Caltrans) conducted a GPS survey in the Santa Cruz, Calif., area and southward to Watsonville, using single-frequency Trimble 4000SL GPS receivers. In March 1990, we reoccupied eight of the Caltrans stations with dual-frequency Trimble 4000SDT GPS receivers. Relative displacements were determined by differencing the two sets of station coordinates obtained from the preearthquake and postearthquake GPS surveys. During both surveys, U.S. Geological Survey GPS receivers were collecting data on Loma Prieta at station LP1. Incorporation of these data allowed us to tie the relative displacements in the local network to the coseismic displacement of station LP1 determined by GPS measurements from the very long baseline interferometry site at Fort Ord, Calif. The peak horizontal displacement is 41.3±1.9 cm, and the peak vertical displacement is 34.1±2.7 cm. The uncertainty in the observed displacements is dominated by the Caltrans survey because the data are single frequency and the observation sessions were short in duration (15–90 minutes). Examination of repeated baseline measurements indicates that the precision of the preearthquake data is 1 cm in the horizontal components and 3.5 cm in the vertical components. Because our data were collected with dual-frequency receivers during 6-hour sessions, errors in the postearthquake survey are significantly smaller (0.5 cm in the horizontal components and 2–3 cm in the vertical components).

INTRODUCTION

The 1989 Loma Prieta earthquake was the largest to occur in northern California since the great 1906 San Francisco earthquake, which geologic and geodetic data indicated was a vertical right-lateral strike-slip event (Lawson, 1908). It was assumed that crustal deformation in the Santa Cruz Mountains resulted solely from strike-slip motion along a vertical San Andreas fault, but this assumption is clearly invalid. The 1989 earthquake exhibited large components of both right-lateral strike slip and reverse slip. The focal mechanism and aftershock distribution for this earthquake indicate that the rupture occurred on a 70° SW dipping plane (Dietz and Ellsworth, 1990), suggesting that the earthquake occurred on a different fault from that in 1906 and that crustal deformation in the Santa Cruz Mountains involves complex fault interactions (Olson, 1990; Segall and Lisowski, 1990).

To effectively assess the seismic hazards in the Santa Cruz Mountains, a more complete understanding of crustal deformation in the region is needed. The first step is to examine the deformation associated with the 1989 Loma Prieta earthquake by determining the surface displacements, which will provide important constraints on fault geometry and slip distribution. The earthquake occurred within a region where the U.S. Geological Survey (USGS) maintains a geodetic network that was reoccupied shortly after the earthquake; coseismic displacements were reported by Lisowski and others (1990). The USGS has occupied stations throughout the San Francisco Bay region for 25 years using electronic distance measurement (EDM) and during the past 10 years using the Global Positioning System (GPS). For 15 years, the U.S. National Aeronautics and Space Administration (NASA) and the U.S. National Geodetic Survey (NGS) have also occupied stations in the region, using very long baseline interferometry (VLBI) (Clark and others, 1990). These VLBI measurements provide changes in station coordinates (displacements) relative to sites on "stable" North America, far removed from effects of the earthquake. EDM provides information about the distance between stations, whereas GPS allows high-precision determinations of the three-dimensional vectors between stations. In addition, leveling bench marks were reoccupied after the earthquake. These data provide information about relative vertical coseismic displacements throughout the Santa Cruz Mountains, including the epicentral region (Marshall and others, 1991). Both VLBI and GPS data provide displacements relative to sites outside the deformation zone of the earthquake. We refer to the displacements determined relative to such sites as "absolute," and to the displacements determined relative to local sites as "relative."

This study was undertaken to determine coseismic displacements in the epicentral region west of the San Andreas fault, where the USGS network was sparse. Shortly after the earthquake, we learned that the California Department of Transportation (Caltrans) had performed a GPS survey in the epicentral region during February and March 1989. We reoccupied eight of their stations with GPS receivers in March 1990 (fig. 1). Relative displacements are determined by differencing the preearthquake and postearthquake station coordinates. We can obtain absolute displacements by incorporating data collected at Loma Prieta (sta. LP1, fig. 1) during both the preearthquake and postearthquake surveys. The displacement of station LP1 is determined relative to the VLBI site at Fort Ord, Calif. We have calculated the precision of our relative displacements through a statistical examination of repeated measurements and found it to be within 1 to 2 cm for the horizontal components and within 3 to 4 cm for the vertical components.

DATA COLLECTION

During February and March 1989, 7 months before the earthquake, Caltrans conducted an extensive GPS survey in the Santa Cruz-Watsonville area (fig. 1). The Caltrans survey consisted of 36 stations, which were occupied with single-frequency Trimble 4000SL GPS receivers during multiple sessions of 15 to 90 minutes. The Caltrans data used in this project are listed in table 1. Because this survey was made in the epicentral region on the hanging-wall block, the coseismic displacements were expected to be much larger than the noise level in this short-session, single-frequency data set. In March 1990, we reoccupied eight of these Caltrans stations to determine the postearthquake relative coordinates. The stations were chosen to provide the widest distribution across the region, with five stations in a line parallel and four stations in a line perpendicular to the fault (fig. 1). The Stanford GPS data were collected on dual-frequency Trimble 4000SDT receivers during the 6-hour sessions (table 2). Relative coseismic displacements were calculated by comparing the relative coordinates of the stations before and after the earthquake.

During both the preearthquake and postearthquake surveys, the USGS collected data on Loma Prieta at station LP1 (fig. 1) with a dual-frequency TI–4100 receiver (table 3). Station LP1 is part of an extensive USGS geodetic network that allows us to tie the Santa Cruz network to stations which were not disturbed by the earthquake. GPS measurements from stations LP1 to Brush2 (Fort Ord) before and after the earthquake enabled us to determine the motion of station LP1 relative to the absolute, VLBI-derived coseismic displacement of Fort Ord (Clark and others, 1990). Absolute displacements within the Santa Cruz network are determined by using this displacement for station LP1.

An important part of the data collection is centering the GPS antenna on the tripod directly over the bench mark and measuring the vertical distance between the antenna and the bench mark. We used a rotating optical plumb to center the tripod over the bench mark. The antenna was leveled by using a sensitive bubble in a rotating carrier that clamps into the tribrach. To center and level the antenna, both Caltrans and USGS used bayonets, with bull's-eye leveling bubbles, that extended from the top of the tripod directly down to the bench mark. We determined the antenna height by measuring the slant height from the station marker to the top of the antenna ground plane. As a check, we also measured the vertical height from the bench mark to the base of the antenna adapter. Adding the height between the antenna adapter and the top of the ground plane (0.355 m) yields an independent measure of the antenna height (fig. 2). Vertical height and slant height were measured in both inches and meters. Caltrans measured antenna height by using a Wild height hook, whereas the USGS measured the slant height in both inches and meters before and after the data collection.

GPS measurements determine the intersite vector between the electrical phase centers of the two antennas. These phase centers commonly are offset vertically from the physical top of the antenna and may also be offset horizontally from the antenna center. If identical antennas are used, the phase-center offsets cancel; however, if different antennas are used, the relative phase-center offset must be known. The preearthquake survey used Trimble 4000SL antennas except at station LP1 (fig. 1), which was occupied by a TI–4100 antenna. The postearthquake survey used Trimble 4000SDT antennas except at station LP1, which was again occupied by a TI–4100 antenna. Thus, the displacement of station LP1 relative to the Santa Cruz network stations will depend on the phase-center offsets. We have used the vertical offsets reported by Gurtner and others (1989), with the following exception:

We assume that the L1 and L2 phase centers of the TI–4100 antenna are 0.227 and 0.212 m, respectively, above the antenna base (Prescott and others, 1989). Because we recorded the antenna height to the top of the antenna ground plane for the Trimble antennas, we obtain an L1 vertical offset of -0.007 m and an L2 offset of +0.011 m for the dual-frequency Trimble 4000SDT antenna, and an L1 offset of -0.015 m for the single-frequency Trimble 4000SL antenna. We make no correction for horizontal phase-center offsets because these offsets are considerably smaller and less well determined. The tie between Loma Prieta (sta. LP1) and the Santa Cruz sites is sensitive to the relative offset between the TI–4100 and Trimble antennas, whereas the displacements between the Santa Cruz sites are independent of the antenna offsets.

DATA ANALYSIS

The preearthquake data were processed together in a network solution. The USGS data collected at station LP1 (fig. 1) on March 1, 1989, and all of the Caltrans data

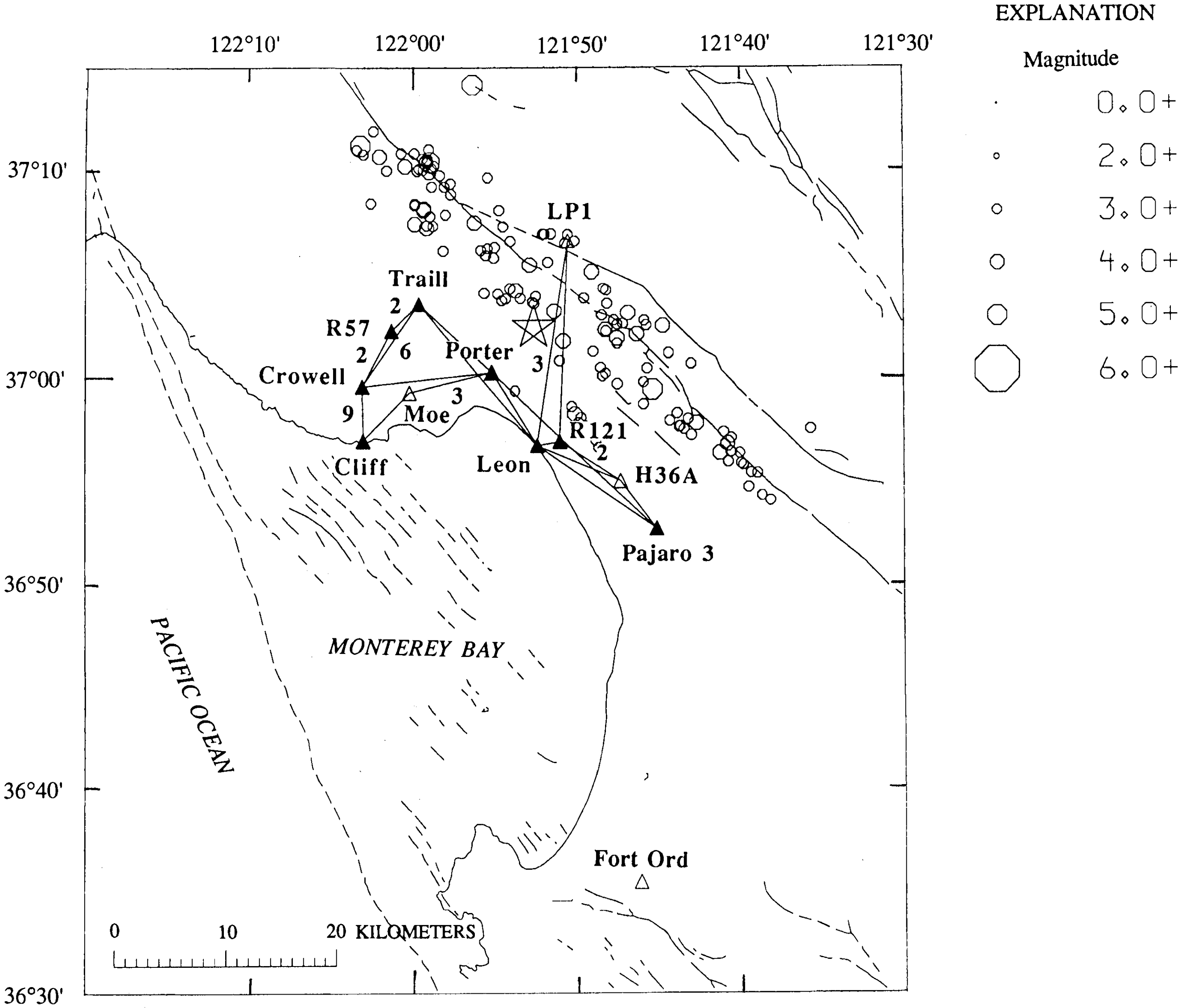

Figure 1.—Loma Prieta region, Calif., showing locations of major faults (thin irregular lines, dashed where inferred, queried where uncertain) and Global Positioning System stations (triangles) used to determine coseismic displacements near epicenter of 1989 earthquake (star). Solid triangles, stations occupied by California Department of Transportation (Caltrans) before earthquake and by us after earthquake. Stations Moe and H36A were occupied by Caltrans and used to strengthen preearthquake solution but were not reoccupied after earthquake; station LP1 was occupied by U.S. Geological Survey (USGS) during preearthquake and postearthquake surveys, and data from station LP1 were used to tie Santa Cruz network to USGS network. Numbers denote number of times baselines were measured during preearthquake survey; lines without numbers were measured only once.

Table 1.—*Preearthquake Global Positioning System data collected by the California Department of Transportation with single-frequency Trimble 4000SL receivers*

[Sampling interval, 15 s. Antenna height is vertical distance measured form bench mark to antenna's electrical phase center]

Date	Julian day	Session	Station (fig. 1)	Start time (G.m.t.)	Stop time (G.m.t.)	Antenna height (m)	Number of satellites
Feb. 27, 1989	58	1	Crowell	4:54	6:14	2.1230	5
	58	1	H36A	5:02	6:15	1.4600	5
	58	1	Pajaro3	5:08	6:14	2.9130	5
	58	1	Porter	5:07	6:16	1.4550	5
	58	2	H36A	6:29	7:59	1.5800	6
	58	2	Leon	6:59	8:00	1.5250	6
	58	2	Porter	6:59	7:59	1.5450	6
	58	2	Traill	7:02	8:00	1.4430	6
	58	3	Crowell	8:40	9:41	2.1320	5
	58	3	Leon	8:40	9:39	1.5100	5
	58	3	Pajaro3	8:55	9:39	1.6930	3
	58	3	Traill	8:40	9:39	1.2790	5
Feb. 28, 1989	59	4	H36A	8:31	9:15	1.6260	5
	59	4	R121	9:00	9:14	1.6020	4
Mar. 1, 1989	60	1	H36A	3:46	4:59	1.2880	4
	60	1	R121	3:46	5:02	1.7260	4
	60	2	Leon	5:31	6:30	1.2720	5
	60	2	R121	5:22	6:31	1.7540	5
	60	3	Leon	6:39	8:16	1.4310	6
	60	4	Leon	8:40	9:11	1.5110	4
Mar. 2, 1989	61	3	Porter	7:50	9:03	1.4820	4
	61	3	Moe	8:18	9:00	2.5080	4
Mar. 3, 1989	62	1	Porter	3:40	6:17	1.4050	5
	62	1	Moe	3:46	6:15	2.5540	5
	62	3	Porter	6:28	8:05	1.4690	6
	62	3	Moe	6:27	8:00	2.5460	6
Mar. 8, 1989	67	1	Crowell	3:48	5:02	2.2210	5
	67	1	Traill	3:54	5:02	1.4700	4
	67	2	Crowell	5:25	6:18	2.0680	5
	67	2	R57	5:25	6:15	1.7010	5
	67	2	Traill	5:25	6:21	1.4070	5
	67	3	Crowell	6:43	7:31	2.1670	6
	67	3	R57	6:43	7:29	1.6800	6
	67	3	Traill	6:45	7:32	1.3540	4
	67	4	Crowell	7:51	8:42	2.2230	5
	67	4	Traill	7:51	8:32	1.2960	5
Mar. 9, 1989	68	1	Cliff	4:23	5:00	1.6230	5
	68	1	Crowell	4:23	4:59	2.1080	5
	68	2	Cliff	5:04	6:14	1.6230	5
	68	2	Crowell	5:09	6:16	2.1780	5
	68	3	Cliff	6:20	7:31	1.6230	6
	68	3	Crowell	6:26	7:24	2.1280	6
	68	4	Cliff	7:33	8:25	1.6230	4
	68	4	Crowell	7:33	8:28	2.0820	5
Mar. 10, 1989	69	1	Cliff	4:27	5:00	1.5460	4
	69	1	Crowell	4:27	5:14	2.1230	5
	69	1	Porter	4:27	5:16	1.6130	5
	69	1	Traill	4:27	5:15	1.2810	5
	69	2	Cliff	5:03	6:45	1.5460	5
	69	2	Crowell	5:25	6:44	1.8600	5
	69	2	Moe	5:46	6:46	2.5060	5
	69	2	Traill	5:24	6:45	1.3160	5
	69	3	Cliff	6:57	8:15	1.5460	5
	69	3	Crowell	6:58	7:59	1.7310	5
	69	3	Traill	6:57	8:15	1.4130	5
Mar. 11, 1989	70	1	Cliff	4:24	5:00	1.4250	5
	70	1	Crowell	4:24	4:59	2.0460	5
	70	2	Cliff	5:03	6:30	1.4250	5
	70	2	Crowell	5:07	6:29	1.8870	5

Table 2.—Postearthquake Global Positioning System data collected by Stanford University with dual-frequency Trimble 4000SDT receivers

[Sampling interval, 15 s. Antenna height is vertical distance measured from bench mark to top of antenna ground plane]

Date	Julian day	Station (fig. 1)	Start time (G.m.t.)	Stop time (G.m.t.)	Antenna height (m)	Number of satellites
Mar. 28, 1990	86	Leon	2:31	8:00	1.2865	11
	86	Pajaro3	2:31	8:00	1.4545	11
	86	Porter	2:37	8:00	1.3090	11
	86	R121	2:31	8:00	1.5630	11
Mar. 29, 1990	87	Crowell	3:08	7:32	1.9920	10
	87	Porter	2:32	8:00	1.4440	10
	87	R57	2:32	7:39	1.3580	10
	87	Traill	2:32	7:59	1.1910	11
Mar. 30, 1990	88	Cliff	2:33	7:49	1.2440	10
	88	Crowell	2:22	7:36	1.7630	10
	88	Porter	2:22	7:50	1.1640	10
	88	Traill	2:26	7:49	1.3435	10

Table 3.—*Global Positioning System data collected by U.S. Geological Survey with dual-frequency TI–4100 receivers*

[Sampling interval, 30 s. Antenna height is vertical distance measured from benchmark to base of antenna preamplifier]

Date	Julian day	Station (fig. 1)	Start time (G.m.t.)	Stop time (G.m.t.)	Antenna height (m)	Number of satellites
Mar. 1, 1989	60	LP1	3:34	11:11	1.7579	7
Mar. 30, 1990	88	LP1	2:12	7:49	1.4926	8

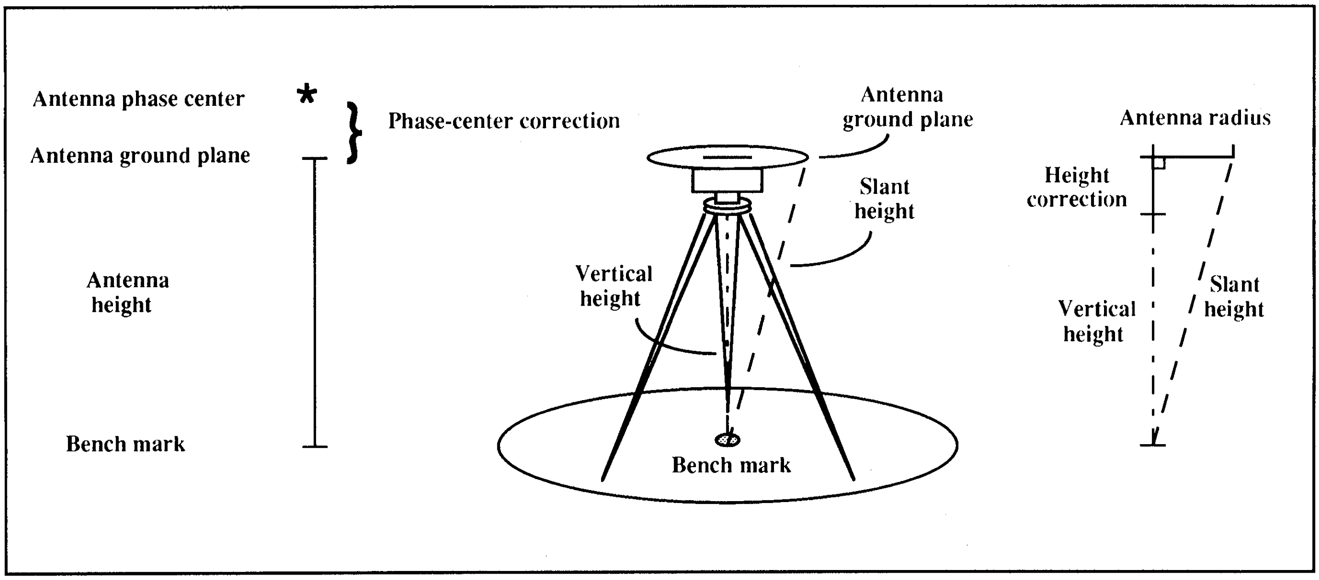

Figure 2.—Diagram showing how antenna height was determined in postearthquake survey. Both slant height and vertical height were measured, and height correction was added to field-measured height to give height to top of antenna ground plane. Vertical distance from bench mark to antenna ground plane was used as antenna height. Phase-center correction, which is included in processing, is defined as offset between center of antenna ground plane and antenna's electrical phase center.

were used, except those collected at station Pajaro3 during session 581, the results from which yield unreasonable height changes at station Pajaro3, and so we believe that the antenna height (2.913 m) may be in error. For the postearthquake solution, all of the Stanford data plus the USGS data collected at station LP1 on March 30, 1990, were combined in a single network solution. In both solutions, the coordinates of station LP1 were fixed, and the coordinates of the other stations were estimated relative to station LP1.

We processed the GPS data from the preearthquake and postearthquake surveys by using the Bernese GPS analysis software, version 3.2, with broadcast orbits. Because the scale of the Santa Cruz network is less than 35 km and broadcast orbits are believed to have a precision of ~5 parts in 10^7 or better (Hager and others, 1991), the error in the longest baselines due to orbital error should be $\lesssim$17.5 mm. We show below that the coseismic displacements in the epicentral region are approximately hundreds of millimeters, and so the error introduced by using broadcast orbits is comparatively small.

The satellite clock errors are approximated by polynomials in time by using the coefficients sent as part of the navigation message from the satellite. Receiver clock corrections were determined at each epoch by using C/A code pseudorange, and residual satellite and receiver clock errors were eliminated by double-differencing the carrier phase. In processing the postearthquake survey, receiver clock corrections and initial coordinates were determined simultaneously from the C/A code pseudorange data. Because the short sessions of the preearthquake Caltrans data did not provide enough information to estimate position and receiver clock errors simultaneously, we estimated the clock corrections while constraining the receiver coordinates to the postearthquake survey positions. The coseismic displacements are negligible relative to the error in the pseudorange-determined coordinates and may safely be neglected in determining receiver clock corrections.

Before further parameter estimation, single-difference phase files were created and cleaned of carrier-beat-phase cycle slips and outliers, using both automatic and manual programs. All the single-difference files were visually inspected to ensure that they were "clean." The station coordinates, tropospheric zenith delay, and integer-phase ambiguities were estimated by using double-differenced carrier-phase observations. During these estimations, a 20° elevation cutoff angle was used to minimize antenna multipath effects. The propagation delay due to the troposphere, which depends on temperature, humidity, and pressure, was estimated in the solution by using the atmospheric-zenith-delay model of Saastamoinen (1972). Zenith-delay parameters were estimated at each station for each day. Each integer-phase ambiguity was estimated as a real number and fixed to the closest integer if one and only one integer was within 3σ of the estimate, where σ is the larger of either the formal error of the estimated ambiguity or 0.05 cycle. Then, the remaining parameters (station coordinates and tropospheric parameters) were reestimated. Fixing ambiguities to their integer values can significantly strengthen the solution (for example, Davis and others, 1989).

The ionosphere affects the GPS results in two ways: as a differential delay when the GPS signals pass through ionosphere with a different free-electron density, and as a systematic shortening due to an overall lensing effect of the ionosphere. First-order ionospheric effects can be eliminated by forming a linear combination of the two carrier frequencies. Because the Caltrans data had been collected with single-frequency receivers, the ionospheric delay could not be removed in the preearthquake survey. Georgiadou and Kluesberg (1988) found the lensing effect of the ionosphere to be 0.6 ppm for baselines ranging in length from 10 to 30 km. Because the longest baselines in the Caltrans network are 30 km long, the error in the baselines due to the ionosphere might be ~18.0 mm. Although the 1989 Caltrans survey was close to a solar maximum, the data were collected during the night, when the ionosphere is more stable and the electron density is low. This circumstance suggests that variations in the ionosphere may have been small across the network and that the lensing effects may have been minimal. Indeed, the difference between single- and dual-frequency results from an 8-km-long permanent GPS baseline across the Hayward fault are very small when the observing sessions are at night (N. King, oral commun., 1991).

The short station occupations used by Caltrans (15–90 minutes) makes it difficult to resolve the integer-phase ambiguities. To strengthen the network solution for the preearthquake survey, data from two additional stations (Moe, H36A, fig. 1) were incorporated into the analysis, even though they were not occupied after the earthquake. Including stations Moe and H36A in the network solution allowed us to include more data and to form shorter single-difference baselines.

Repeated GPS measurements into Loma Prieta indicate that during the March 1, 1989, survey, the antenna was set up ~2.8 cm to the east of the bench-mark center (Mark Murray, oral commun., 1991). We have corrected for this offset in our analysis.

The postearthquake data were degraded by the implementation of selective availability (SA) by the U.S. Department of Defense. SA involves the addition of random noise and offset in the clocks of Block II satellites. In differential GPS, the SA effects are eliminated as long as the two receivers simultaneously sample the phase. All the stations, except LP1 (fig. 1), were occupied with Trimble 4000SDT receivers. Station LP1 was surveyed with a TI–4100 receiver, and so the tie to station LP1 was degraded by SA effects. In the processing, we eliminated the data from satellite PRN 19, the only Block II satellite observed at station LP1. We also did not use any data from satellite PRN 13 on March 29, 1990, because the satellite was repositioned on this day.

Despite the problems in both surveys, nearly all of the integer-phase ambiguities were resolved, and the rms residuals of single differences were less than 1 cm. From the preearthquake survey, 136 of the 137 ambiguities were fixed to integers, and for the postearthquake survey, 53 of the 54 could be fixed to integers. The rms residual of single differences for the preearthquake survey was 6.3 mm with 25,731 double-difference phase observations, and for the postearthquake survey, 4.0 mm with 32,216 phase observations.

GPS MEASUREMENT ERRORS

PREEARTHQUAKE SURVEY

Uncertainties in the Caltrans preearthquake survey dominate the errors in the estimated coseismic displacements because the data are single frequency and the observation sessions were short. Fortunately, Caltrans reoccupied some of their stations (fig. 1) many times. When more than two stations were occupied simultaneously, the shortest baselines were used to form the single differences. We note that the baselines in the northwestern part of the network were measured many more times than those in the southeastern part, and so the southeastern stations are not so well tied into the network.

Two baselines were measured many more times than the rest: Crowell to Cliff and Crowell to Traill (fig. 1). The baseline Crowell to Cliff was measured nine times, whereas the baseline Crowell to Traill was measured eight times. Each of these observations was reprocessed independently in special single-difference solutions. The scatter of the repeated measurements about the preearthquake network solution was utilized to determine the precision of the data. Each measurement was processed in two ways: once by estimating the integer-phase ambiguities, and a second time by fixing the ambiguities to those determined in the network solution. Because many of the observation sessions were so short, not all of the integer-phase ambiguities could be resolved for individual sessions. Therefore, when integer-phase ambiguities are estimated, the session solutions show a larger scatter about the network solution and have larger formal errors.

The network and session solutions for the repeated measurements of the baselines Crowell to Cliff and Crowell to Traill are plotted in figure 3. The scatter in the session-determined-ambiguity solutions is a pessimistic estimate of the precision of the final network solution because far fewer data were utilized in the parameter determinations. In figure 3*B*, the session-determined-ambiguity solution for session 583 has very large error bars because so few data were obtained during this session and few of the integer-phase ambiguities were resolved. Also in figure 3*B*, the session-determined-ambiguity solution for session 671 is an obvious outlier in all components except the vertical. Examining the scatter in the session-determined-ambiguity solutions gives a good estimate of the precision of the baselines that were repeatedly measured only a few times and for which few data are available, such as the baselines in the southeastern part of the network.

Most of the integer ambiguities were fixed in the network solution, and so it is much stronger. Fixing the ambiguities to those determined by the network solution should give a reasonable estimate of the precision of the network solution. In this case, the scatter about the network solution is smaller, and the formal errors are generally smaller, than with the other technique (fig. 3). However, because uncertainties in the coordinates are scaled by the fit to the data, the formal errors may actually increase if the session data are incompatible with the network-determined ambiguities. For example, a suspected setup error during session 701 on the baseline Crowell to Cliff might have cause those session data to be incompatible with the rest of the data and would account for the large uncertainties in the coordinates of the network-determined-ambiguity solution.

The formal errors computed by the GPS analysis software appear to have underestimated the true errors, probably owing to neglect of the effect of errors in the broadcast orbits and failure to model signal multipathing. To estimate by what factor these errors have been underestimated, a reduced χ_ν^2 value was calculated, according to the relation

$$\chi_\nu^2 = \frac{1}{N-1}\sum_{i=1}^{N}\left(\frac{r_i}{\sigma_i}\right)^2, \qquad (1)$$

(Bevington, 1969), where N is the number of measurements, r_i is the difference between the session solution and the network solution, and σ_i is the formal standard deviation of the session solution. Assuming that none of the stations moved during the 13-day period when Caltrans collected their data and that the formal uncertainties are correct, then χ_ν^2 should equal 1.0. The square root of the reduced χ_ν^2, value, $(\chi_\nu^2)^{1/2}$, provides an estimate of the factor by which we need to scale the formal errors. The $(\chi_\nu^2)^{1/2}$ values calculated for the baselines Crowell to Cliff and Crowell to Traill determined with both processing techniques are listed in table 4. From these calculations, we determined 11.0 to be a reasonable scaling factor for the formal errors in the horizontal components and 7.75 for the formal errors in the vertical components; the error bars in figure 3 have been scaled by these factors. When the formal errors in the network solution for the baselines

Crowell to Cliff and Crowell to Traill are scaled by these factors, they fall in the range 0.4–0.8 cm for the horizontal components and in the range 3.2–4.7 cm for the vertical components.

To estimate the precision of the preearthquake network solution, we used the weighted rms misfit of individual baseline solutions about the network solution given by the expression

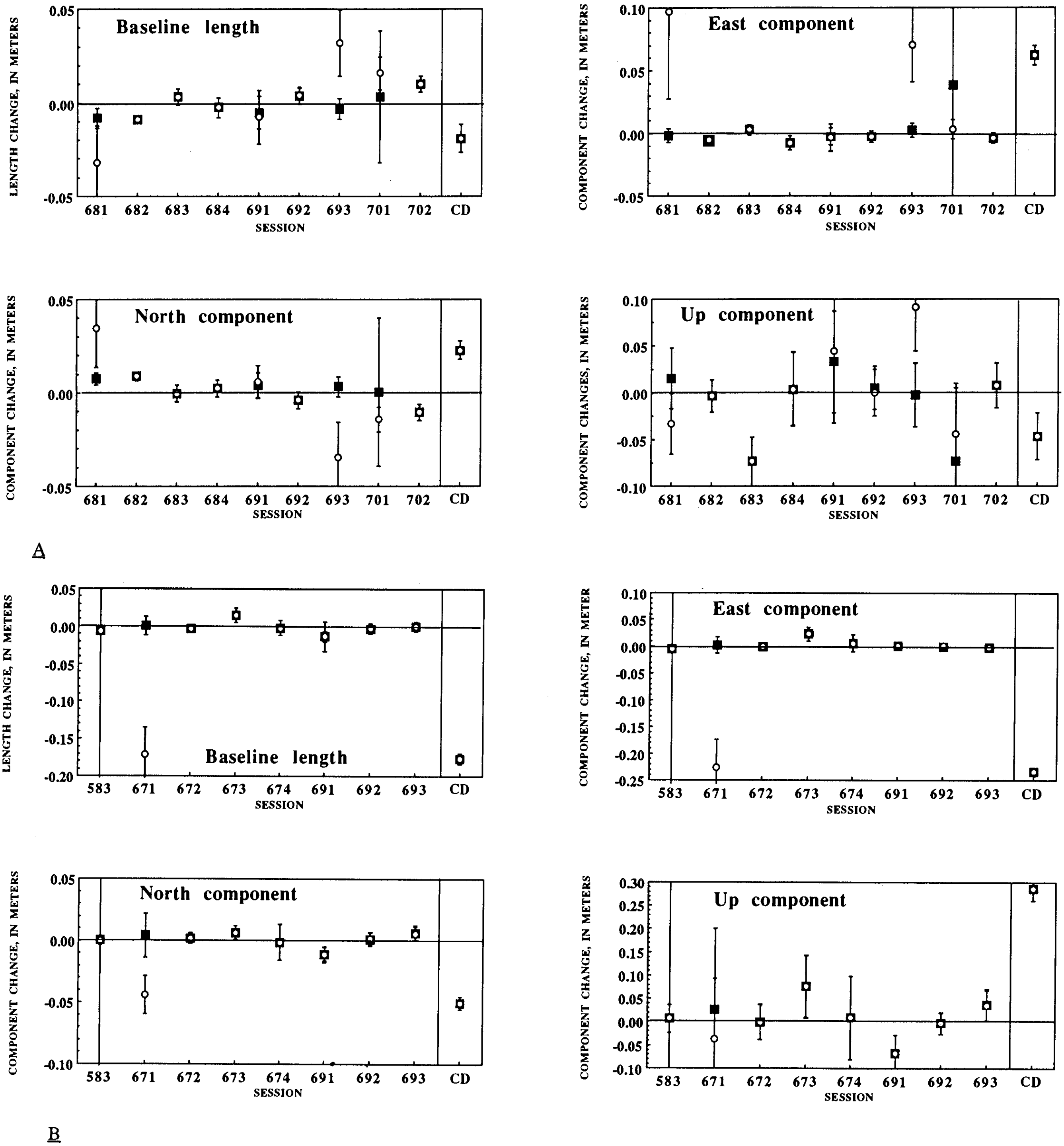

Figure 3.—Scatterplots of repeated measurements along baselines Crowell to Cliff (*A*) and Crowell to Traill (*B*) (see fig. 1 for locations). Circles, solutions obtained with estimation of integer-phase ambiguity for each session; solid squares, solutions obtained using preearthquake-network-determined ambiguities. Differences in individual session solutions with respect to preearthquake network solution are plotted for baseline length and north, east, and up components. CD, coseismic displacement for baseline, that is, difference between preearthquake and postearthquake network solutions. Error bars represent scaled 1σ formal errors from Bernese software; no error bar is shown where error is smaller than size of plotted symbol.

Table 4.—*Square root of the reduced χ^2 of repeated measurements of baselines Crowell to Cliff and Crowell to Traill*

[Reduced χ^2 calculated using equation 1 (see text). Values in parentheses were determined excluding data from session 671, an obvious outlier]

Baseline (fig. 1)	Source of ambiguity	North component	East component	Up component
Crowell to Cliff	Session	21.0	14.5	10.2
Crowell to Traill	Session	15.6 (11.1)	20.1 (9.0)	6.9 (7.4)
Crowell to Cliff	Network	18.5	5.5	8.5
Crowell to Traill	Network	9.9	9.3	6.8

$$\text{weighted rms misfit} = \left(\frac{1}{N-1} \sum_{i=1}^{N} r_i^2 \omega_i^2 \right)^{1/2}, \quad (2)$$

where ω_i^2 is the weighted-average variance (Bevington, 1969), given by

$$\omega_i^2 = \left(\frac{\bar{\sigma}}{\sigma_i} \right)^2, \quad (3)$$

where σ_i^2 is the variance of the *i*th measurement determined by the Bernese software and $\bar{\sigma}^2$ is the average variance, given by

$$\bar{\sigma}^2 = \frac{1}{\frac{1}{N} \sum_{i=1}^{N} \left(\frac{1}{\sigma_i} \right)^2} \quad (4)$$

(Bevington, 1969). The results of these calculations for the baselines Crowell to Cliff and Crowell to Traill are listed in table 5. The estimations for the baseline Crowell to Traill were calculated both including and excluding the outlier in session 671. When individual sessions were used to determine the ambiguities, the unweighted rms misfit for the baselines is 10 to 40 mm in the horizontal components and ~45 mm in the vertical components. Because the outliers tend to have large uncertainties, the weighted rms misfit is less than the unweighted values. The weighted rms misfit for the baselines is 5 to 9 mm in the horizontal components and ~40 mm in the vertical components. Using the network-determined ambiguities, the unweighted rms misfit is 6 to 14 mm in the horizontal components and ~40 mm in the vertical components, whereas the weighted rms misfit is 5 to 8 mm in the horizontal components and 30 to 35 mm in the vertical components. Conservatively, these calculations indicate that the horizontal measurements are reproducible to within 1 to 2 cm, whereas the vertical measurements are slightly less reproducible to within ~3.5 cm.

POSTEARTHQUAKE SURVEY

The postearthquake survey included very few repeated measurements. During the 3-day period of data collection, the baselines Crowell to Traill and Crowell to Porter were both measured twice. The baselines lengths were repeatable to within 0.6 to 5.9 mm, whereas the north, east, and up components were repeatable to within 0.5 to 1.1, 0.8 to 5.9, and 5.1 to 17.2 mm, respectively. Repeated measurements with the same receivers in a 60-km-wide network with 10-km-long baselines suggest that the horizontal measurements are repeatable to within 0.5 cm and the vertical measurements to within 2 to 3 cm (Bürgmann and Segall, 1991). For the error level in the postearthquake survey to be comparable to the repeatability, scaling factors of 11 in the horizontal components and 5 in the vertical components were used.

COSEISMIC DISPLACEMENTS

We calculated coseismic displacements by differencing the station coordinates estimated from the preearthquake and postearthquake network solutions. In both solutions, the station coordinates were estimated relative to station LP1 (fig. 1). The coseismic displacement of station LP1 was calculated from GPS measurements, made before and after the earthquake, at stations LP1 and Brush2 (Fort Ord) (Michael Lisowski, oral commun., 1992). The coseismic displacement of Fort Ord relative to "stable" North America was determined by VLBI (Clark and others, 1990). By combining these measurements, station LP1 was found to have moved 17.6±0.8 cm to the south, 3.7±1.0 cm to the east, and 10.4±5.0 cm down. The calculated horizontal coseismic displacements are mapped in figure 4*A*, with 95-percent-confidence error ellipses determined by using the formal errors of the network solutions scaled as described in the preceding section; the uncertainties in the displacement of station LP1 have been propagated into the confidence ellipses of the Santa Cruz

Table 5.—*Statistical analysis of scatter in repeated measurements of the baselines Crowell to Cliff and Crowell to Traill*

[Unweighted rms misfit calculated using equation 2 (see text) with $\omega_i^2=1$; weighted rms misfit calculated using equation 2. Values in parentheses were determined excluding data from session 671, an obvious outlier]

Baseline (fig. 1)	Source of ambiguity	Length (mm)	North component (mm)	East component (mm)	Up component (mm)
		Unweighted rms misfit			
Crowell to Cliff	Session	17.9	18.8	42.5	48.7
Crowell to Traill	Session	65.3 (8.8)	17.5 (5.9)	86.0 (10.0)	42.8 (43.8)
Crowell to Cliff	Network	6.4	6.0	14.2	39.3
Crowell to Traill	Network	8.1	5.7	9.3	42.1
		Weighted rms misfit			
Crowell to Cliff	Session	9.3	9.0	6.9	37.9
Crowell to Traill	Session	13.2 (5.5)	8.9 (6.3)	13.2 (5.9)	37.2 (39.9)
Crowell to Cliff	Network	7.8	7.2	4.8	30.7
Crowell to Traill	Network	7.0	4.7	5.3	33.6

stations. The calculated coseismic displacements are listed in table 6. These uncertainties are relative; that is, they do not include uncertainties associated with the displacement of station LP1 relative to sites external to the earthquake. Note that the inferred displacements are as large as 41 cm at station Traill (fig. 1).

The displacements were determined relative to station LP1 (fig. 1), which is not strongly tied to the Caltrans stations. Station LP1 is tied to the Caltrans network through three repeated measurements at station Leon (sessions 602–604) and through one session to station R121. Two of the measurements of the baseline LP1 to Leon (sessions 602, 603) agree to within 1.5 to 3.0 cm. Session 604 has large uncertainties because it involves only 30 minutes of data, using a maximum of four satellites. The postearthquake survey data for station LP1 are also weak because only five Block I satellites were observed. The large error ellipses observed for the horizontal coseismic displacements in figure 4*A* primarily result from the poor tie to station LP1. The error ellipses that result if the scaled formal errors are determined relative to station Porter instead of station LP1 are mapped in figure 4*B*, which shows that the relative displacements within the Caltrans network are much better determined than are the absolute motions. The greatest uncertainties are at stations LP1 and Pajaro3, both of which were occupied only a few times during the initial survey. The absolute displacements of the Santa Cruz stations, together with those of the other sites in the area determined by Segall and Lisowski (1990) from a combination of GPS, EDM, and VLBI data, are mapped in figure 5.

The vertical coseismic displacements were determined by differencing the two solutions relative to station Cliff (fig. 1), which is near a leveling bench mark that was uplifted 2.5±1.2 cm during the earthquake relative to more distant stations (Marshall and others, 1991). The coseismic uplift of the GPS stations, assuming that station Cliff moved up 2.5 cm, is mapped on figure 6; the largest uplift, 34.1±2.7 cm, was observed at station Traill. The vertical displacements determined by GPS are qualitatively consistent with the results from repeated leveling (Marshall and others, 1991). From the VLBI results at Ford Ord and the GPS measurements connecting stations LP1 and Brush2 (Fort Ord), station LP1 was determined to have subsided ~10.4±5.0 cm. Using the uplift at station Cliff estimated from leveling, we obtain 9.5±5.6 cm of subsidence at station LP1. The two results agree to within 1 cm, well within the uncertainties of the measurements.

By comparing the solutions from two GPS surveys that were made 1 year apart, we have been able to resolve horizontal and vertical coseismic displacements due to the earthquake that are relatively unbiased by interseismic deformation (table 6). In contrast, the leveling data (Marshall and others, 1991) and the geodetic data examined by Snay and others (1991) span several decades and so are potentially biased by interseismic deformation. Snay and others (1991) determined displacements by comparing preearthquake triangulation/trilateration data with postearthquake GPS data. In particular, they calculated displacements at three stations at or near stations for which we have estimated displacements: Traill, Crowell, and Pajaro3 (figs. 1, 7). The horizontal displacements calcu-

Table 6.—*Coseismic displacements at Global Positioning System stations, with scaled formal error*

[Formal errors calculated by multiplying 1σ Bernese formal errors by scaling factor (see text). Displacements of horizontal (north, east) components computed by using the displacement of station LP1 (fig. 1), as determined by Michael Lisowski (oral commun., 1992); uncertainty in the displacement of station LP1 is omitted in uncertainties at other stations. Displacement of vertical (up) components computed by using the vertical displacement of station Cliff (fig. 1), as measured by leveling survey (Marshall and others, 1991); uncertainty in the uplift of station Cliff is omitted in uncertainties at other stations]

Station	Latitude N.	Longitude W.	North component (m)	East component (m)	Up component (m)
Cliff	36°56′59.1120″	122°03′05.7407″	0.0277±0.0105	−0.1108±0.0107	0.0250±0.0000
Crowell	36°59′34.4289″	122°03′08.4529″	.0053±0.0102	−.1707±0.0105	.0615±0.0255
Leon	36°56′26.2136″	121°52′26.2136″	.0152±0.0100	−.1586±0.0098	.0729±0.0434
LP1	37°06′34.5450″	121°50′40.6843″	−.1760±0.0000	.0370±0.0000	−.0954±0.0559
Pajaro3	36°52′44.4895″	121°45′12.7001″	.1726±0.0148	.0042±0.0175	−.1430±0.5394
Porter	37°00′15.1505″	121°55′11.6902″	−.0463±0.0103	−.2776±0.0101	.2567±0.0315
R57	37°02′14.2179″	122°01′19.9046″	−.0297±0.0114	−.3101±0.0123	.1994±0.0417
R121	36°56′57.3827″	121°51′04.4980″	.0172±0.0100	−.1609±0.0101	.0905±0.0524
Traill	37°03′30.9678″	121°59′39.1251″	−.0491±0.0103	−.4100±0.0102	.3414±0.0271

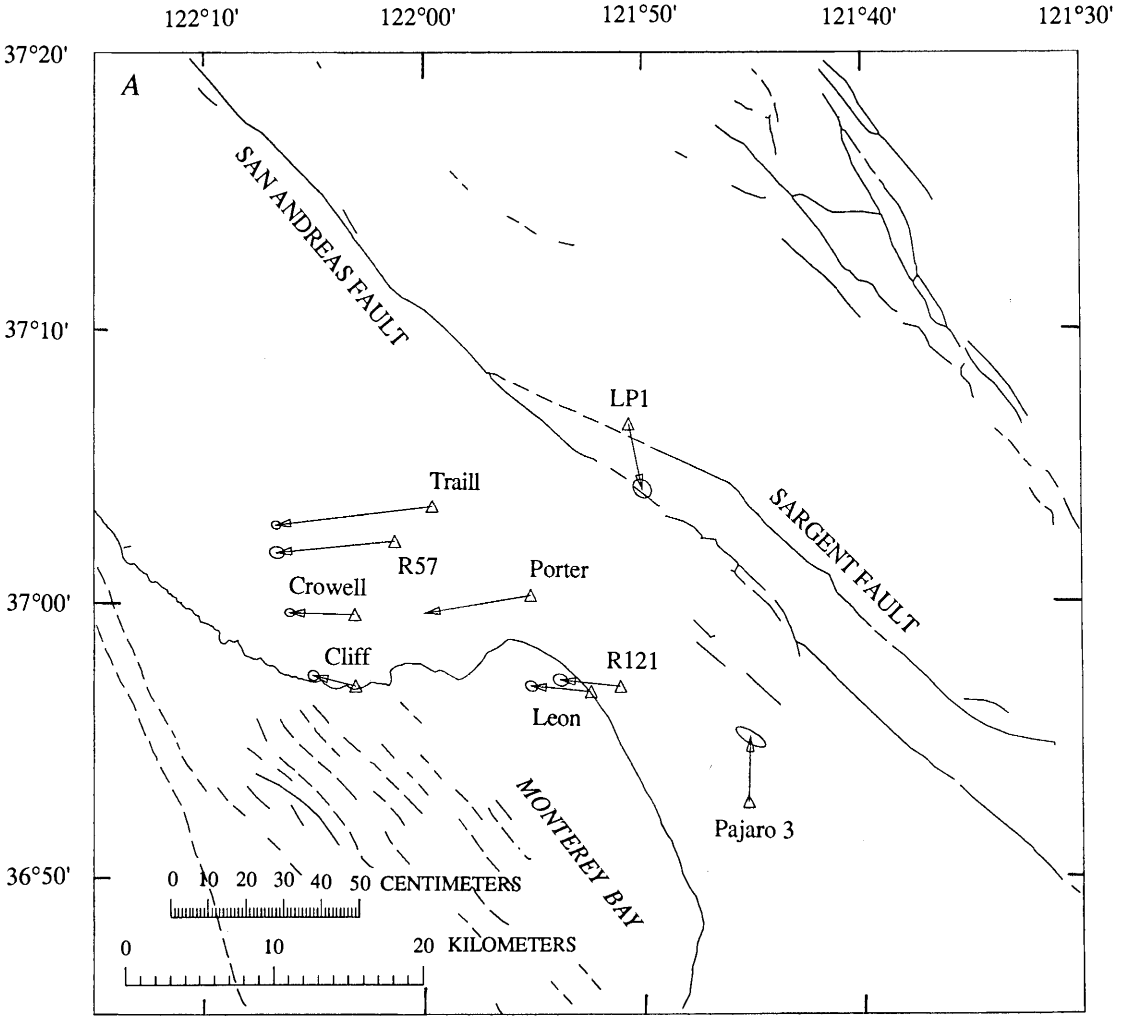

Figure 4.—Loma Prieta region, Calif., showing horizontal coseismic displacements at Global Positioning System stations relative to station LP1. Error ellipses are 95-percent-confidence interval computed relative to stations LP1 (*A*) and Porter (*B*). Irregular thin lines, faults (dashed where inferred, queried where uncertain). In figure 4*A*, uncertainties in station LP1 vector propagate into those of other stations.

lated by Snay and others (1991) agree reasonably well with those estimated here; their displacements are somewhat larger than ours, possibly owing to their incomplete correction for interseismic deformation.

CONCLUSIONS

We have measured the horizontal and vertical coseismic deformation resulting for the 1989 Loma Prieta earthquake, using GPS data. The horizontal displacements fill in a gap in the USGS geodetic network (Lisowski and others, 1990) in the epicentral region on the hanging-wall side of the fault. These data provide useful constraints in determining the characteristics of the seismic source. The calculated vertical displacements agree quite well with leveling observations in the Santa Cruz Mountains area.

ACKNOWLEDGMENTS

This research was supported by U.S. National Science Foundation grant EAR–9003575. We thank Richard Snay for bringing the Caltrans network to our attention, and John Fundus and Steven Bourn of the California Department of Transportation for providing the raw GPS data and field sheets. Thora Árnadóttir, Roland Bürgmann, Lanbo Liu, Mark Matthews, Cleavy McKnight, and Sarah Saltzer assisted in the fieldwork. The USGS GPS data collected at station LP1 were provided by Mike Lisowski and Jerry Svarc.

REFERENCES CITED

Bevington, P.R., 1969, Data reduction and error analysis for the physical sciences: San Francisco, McGraw-Hill, 336 p.

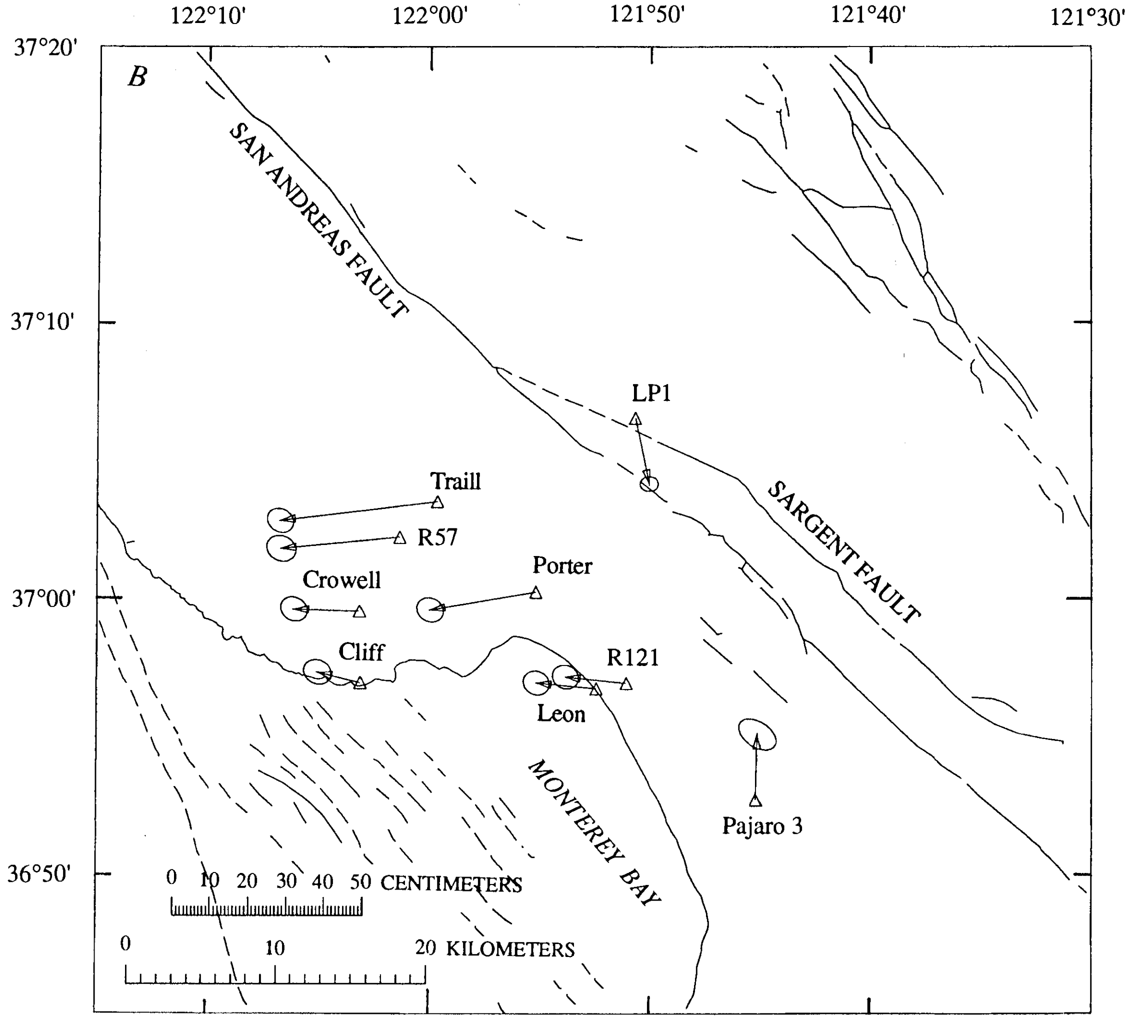

Figure 4.—Continued.

Bürgmann, Roland, and Segall, Paul, 1991, Postseismic GPS monitoring NW of the 1989 Loma Prieta rupture zone [abs.]: Eos (American Geophysical Union Transactions), v. 72, no. 44, p. 119.

Clark, T.A., Ma, Choppo, Sauber, J.M., Ryan, J.W., Gordon, David, Shaffer, D.B., Caprette, D.S., and Vandenberg, N.R., 1990, Geodetic measurement of deformation in the Loma Prieta, California, earthquake with very long baseline interferometry: Geophysical Research Letters, v. 17, no. 8, p. 1215–1218.

Davis, J.L., Prescott, W.H., Svarc, J.L., and Wendt, K.J., 1989, Assessment of Global Positioning System measurements for studies of crustal deformation: Journal of Geophysical Research, v. 94, no. B10, p. 13635–13650.

Dietz, L.D., and Ellsworth, W.L., 1990, The October 17, 1989, Loma Prieta, California, earthquake and its aftershocks; geometry of the sequence from high-resolution locations: Geophysical Research Letters, v. 17, no. 9, p. 1417–1420.

Georgiadou, Yola, and Kluesberg, Alfred, 1988, On the effect of ionospheric delay on geodetic relative GPS positioning: Manuscripta Geodaetica, v. 13, no. 1, p. 1–8.

Gurtner, Werner, Beutler, Gerhardt, and Rothacher, Markus, 1989, Combination of GPS measurements made with different receiver types: International Geodetic Symposium on Satellite Positioning, 5th, Las Cruces, N. Mex., 1989, Proceedings.

Hager, B.H., King, R.K., and Murray, M.H., 1991, Measurement of crustal deformation using the Global Positioning System: Annual Review of Earth and Planetary Sciences, v. 19, p. 351–382.

Lawson, A.C., chairman, 1908, The California earthquake of April 18, 1906; Report of the State Earthquake Investigation Commission: Carnegie Institution of Washington Publication 87, 2 v.

Lisowski, Michael, Prescott, W.H., Savage, J.C., and Johnson, M.J.S., 1990, Geodetic estimate of coseismic slip during the 1989 Loma Prieta, California, earthquake: Geophysical Research Letters, v. 17, no. 9, p. 1437–1440.

Marshall, G.A., Stein, R.S., and Thatcher, Wayne, 1991, Faulting geometry and slip from co-seismic elevation changes; the 18 October 1989, Loma Prieta, California, earthquake: Seismological Society

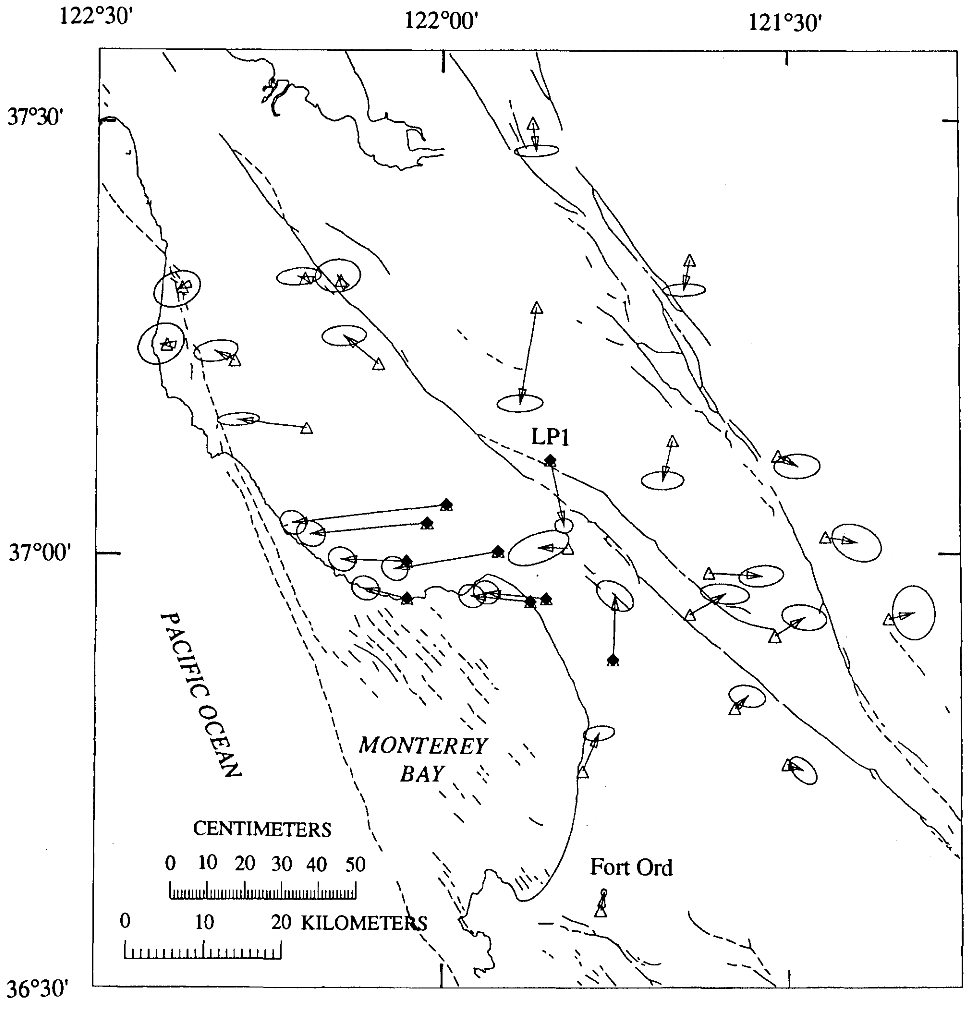

Figure 5.—Loma Prieta region, Calif., showing horizontal coseismic displacements at stations in Santa Cruz network (diamonds) and displacements estimated by Segall and Lisowski (1990) (triangles). Error ellipses are 95-percent-confidence intervals. Irregular thin lines, faults (dashed where inferred, queried where uncertain).

of America Bulletin, v. 81, no. 5, p. 1660–1693.

Olson, J.A., 1990, Seismicity in the twenty years preceding the Loma Prieta, California earthquake: Geophysical Research Letters, v. 17, no. 9, p. 1429–1432.

Prescott, W.H., Davis, J.L., and Svarc, J.L., 1989, Height of L2 phase centers for TI antennas: International Coordination of Space Technology for Geodesy and Geodynamics, Commission VIII Bulletin, v. 2, no. 2, p. 13.

Saastamoinen, J., 1972, Atmospheric correction for the troposphere and stratosphere in radio ranging of satellites, in Henriksen, S.W., Mancini, Armando, and Chovitz, B.H., eds., The use of artificial satellites for geodesy: American Geophysical Union Geophysical Monograph 15, p. 247–251.

Segall, Paul, and Lisowski, Michael, 1990, Surface displacements in the 1906 San Francisco and 1989 Loma Prieta earthquakes: Science, v. 250, no. 4985, p. 1241–1244.

Snay, R.A., Neugebauer, H.C., and Prescott, W.H., 1991, Horizontal deformation associated with the Loma Prieta earthquake, Seismological Society of America Bulletin, v. 81, no. 5, p. 1647–1659.

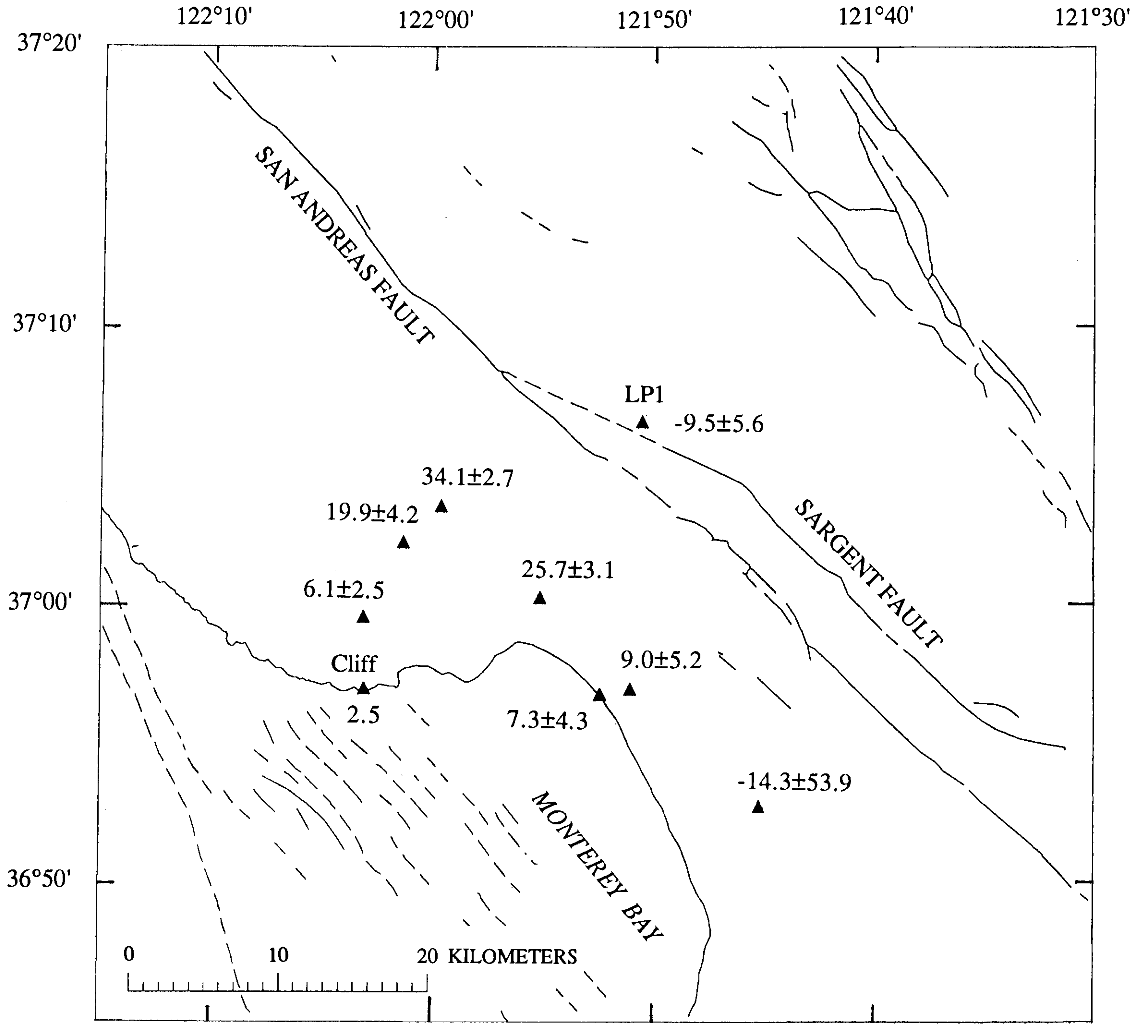

Figure 6.—Loma Prieta region, Calif., showing observed uplift (in centimeters) relative to station Cliff, determined by assuming that station Cliff was uplifted 2.5 cm in 1989 Loma Prieta earthquake. Irregular thin lines, faults (dashed where inferred, queried where uncertain).

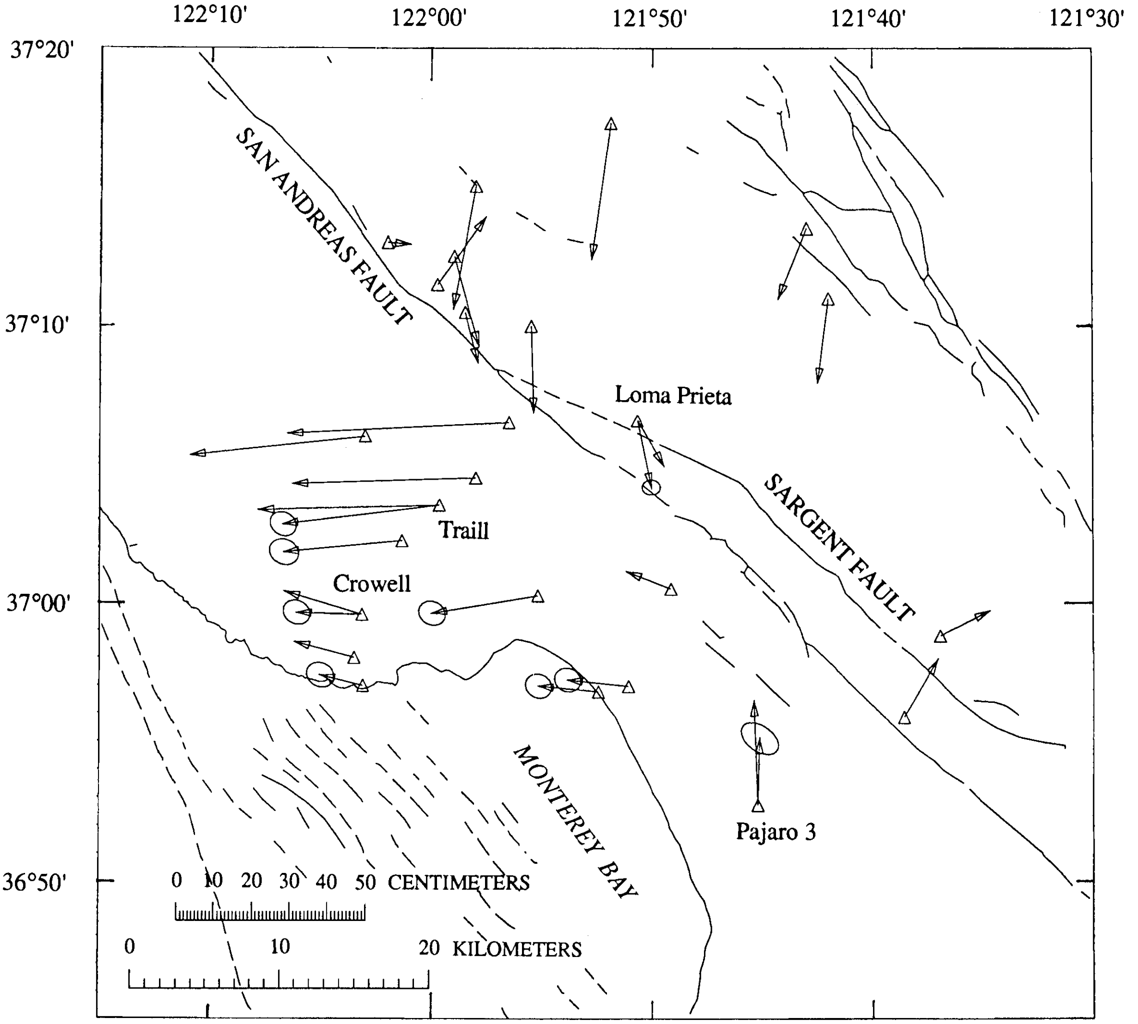

Figure 7.—Loma Prieta region, Calif., showing vectors of observed displacement at Global Positioning System stations (with error ellipses that are 95-percent-confidence interval) and displacements calculated by Snay and others (1991). Irregular thin lines, faults (dashed where inferred, queried where uncertain).

THE LOMA PRIETA, CALIFORNIA, EARTHQUAKE OF OCTOBER 17, 1989: EARTHQUAKE OCCURRENCE

MAIN-SHOCK CHARACTERISTICS

ESTIMATION OF THE RUPTURE VELOCITY OF THE MAIN SHOCK FROM THE LOVE-WAVE GROUP VELOCITY

By Francis T. Wu,
State University of New York, Binghamton

CONTENTS

ABSTRACT

The group velocity of a surface wave measured from a large earthquake is perturbed by the dynamic rupture propagation of the seismic source. Using a moving-source model, the deviation of this group velocity from the intrinsic group velocity can be shown to depend on the rupture velocity, the fault length, the direction of rupture propagation, and the distance from the source. If this deviation can be measured, then the rupture parameters can be determined. The group velocity of a surface wave from an earthquake whose source dimension is much smaller than the wavelengths of the surface wave being studied is essentially the same as the intrinsic group velocity. The differential group velocities determined for a large and a small earthquake (say, more than two magnitude units smaller) can then be readily used to determine the rupture parameters. I apply this method to calculate the rupture velocity of the 1989 Loma Prieta earthquake (M_S=7.1), using broadband, wide-dynamic-range seismograms recorded at a station in Pasadena, Calif. The intrinsic group velocities of Love waves were obtained from the records of an M_S=4.5 foreshock. The locations of this foreshock and the Loma Prieta main shock are assumed to be known, and the rupture length of the main shock is estimated from the aftershock distribution. For a rupture half-length of 25 km, the rupture velocity thus calculated ranges from 1.85 to 2.45 km/s. The upper limit is obtained by assuming that the rupture was initiated 1.8 s after a weak foreshock, and the lower limit by assuming that a slow rupture was initiated at the time of the foreshock.

INTRODUCTION

The direction of rupture propagation, the rupture velocity, and the fault length are important earthquake source parameters to be determined because they control the amplitude of ground motion as a function of azimuth (Ben-Menahem, 1961) and are probably related to the stress intensity (Wu and others, 1972). Ben-Menahem (1961) and Ben-Menahem and Toksöz (1962) used the spectral ratios of long-period surface waves to calculate the rupture velocities of several large earthquakes. Kanamori (1970), Kanamori and Given (1981), and Zhang and Kanamori (1988) used mantle surface waves to study the source mechanisms of many large events; the long-period waves used in these studies generally are insensitive to the source finiteness.

In teleseismic body-wave or near-field source studies for the Loma Prieta main shock (Beroza, 1991; Hartzell and others, 1991; Steidl and others, 1991; Wald and others, 1991) the rupture-propagation parameters mentioned above are either held fixed (Beroza, 1991; Wald and others, 1991) or treated as variables (Hartzell and others, 1991; Steidl and others, 1991). With variable parameters, the amplitude residuals are used as criteria for choosing a particular rupture velocity; the results of these studies are summarized in table 1. As Hartzell and others (1991, table 3) and Steidl and others (1991, table 3) showed in their source modeling, the results are nearly insensitive to rupture velocity. Although Steidl and others chose 3 km/s as their preferred rupture velocity, a value of 2.5 km/s and a different set of rise-time and slip functions actually give a smaller residual.

Table 1.—*Rupture velocity of the Loma Prieta main shock*

Author	Method	c_0 (km/s)	Range
Beroza (1991)----------	Inversion using data from 20 strong-motion stations.	2.7–3.1 (80 percent of v_s)	Fixed.
Hartzell and others (1991).	Inversion of teleseismic *P* and *SH* waves.	2.5	2.1–3.1
Wald and others (1991).	Joint inversion of teleseismic body waves and strong-motion data.	2.7	Fixed.
Steidl and others (1991).	Inversion using strong-motion data from 38 stations.	3.0	2.5, 2.8, 3.0

Press and others (1961, p. 3484) described earlier methods for determining fault length and rupture velocity, noting that the finiteness of a seismic source can affect the group velocities measured at a single station. They presented a formula relating the group velocity to rupture-propagation parameters and estimated that for a fault length of 1,000 km, the effect may be as large as 10 percent. Although they did not so state, if the "intrinsic group velocity" of the medium is measurable, then the group velocities measured from a large earthquake clearly can be used to determine the rupture-propagation parameters. In this paper, I apply this concept to a study of the rupture process of the Loma Prieta main shock. This study was made possible by the installation of a broadband, wide-dynamic-range station in Pasadena, Calif. (PAS, fig. 1), in 1988. Regional events of M_S=4.5 can be recorded with high signal-to-noise ratio, and events of M_S=7 can remain on scale. Because M_S=4.5 events have a fault length of about 1 km and an M_S=7 event may have a fault length of several tens of kilometers, the group velocity measured from smaller events, U_S, can be viewed as the intrinsic velocity, and the group velocity measured from larger events, U_L, can then be used for rupture-propagation studies. Because only one appropriate station was available for such studies of the Loma Prieta main shock, accurate epicentral locations and origin times are important because they are used directly in estimating group velocities. With the dense telemetered U.S. Geological Survey network in central California and the availability of reasonably detailed velocity models, the locations are probably as good as can be obtained. Whereas the rupture velocity is one of the model parameters in other Loma Prieta main-shock studies, it is determined more directly in this work and can therefore provide an independent assessment of this important quantity.

GROUP VELOCITY OF SURFACE WAVES FROM A MOVING SOURCE

THEORY

The group velocity is well defined when the source is a point in space and impulsive in time. For a large earthquake on a finite fault formed from rupture propagation, the group velocity measured is not the intrinsic velocity of the medium. Assuming a unilaterally propagating point source, Ben-Menahem (1961) showed that the surface waves radiated from the source can be written as

$$f(t,\Delta)=\int_{-\infty}^{\infty}F(\omega)\exp\left\{\omega t-k\Delta-\frac{kb}{2}\left[\frac{c(\omega)}{c_0}-\cos\theta_0\right]\right\}d\omega,$$

where ω is the frequency; t is the time; k is the wave number; Δ is the epicentral distance; c_0 is the velocity of source propagation; θ_0 is the azimuthal angle of the station, measured clockwise from the direction of source propagation; b is the fault length; and $c(\omega)$ is the phase velocity. For a stationary phase

$$\frac{d}{d\omega}\left\{\omega t-k\Delta-\frac{kb}{2}\left[\frac{c(\omega)}{c_0}-\cos\theta_0\right]\right\}=0.$$

After differentiation, we obtain

$$\Delta U(\omega)=U'(\omega)-U(\omega)=-\frac{b}{2t}\left[\frac{U(\omega)}{c_0}-\cos\theta_0\right], \qquad (1)$$

where $U=d\omega/dk$ is the intrinsic group velocity appropriate for the path and $U'=\Delta/t$ is the velocity that would be measured for a source propagating at the velocity c_0. This expression was first derived by Press and others (1961), who emphasized the necessity of correcting the group velocity when the effect of source finiteness is strong. Consider a few special cases:

(1) when $\theta=0$, $$\Delta U = -\frac{b}{2t}\left(\frac{U}{c_0}-1\right).$$

If $U>c_0$, $\Delta U < 0$;

if $U=c_0$, $\Delta U = 0$;

and if $U<c_0$, $\Delta U > 0$.

(2) When $\theta=\pi$, $$\Delta U = -\frac{b}{2t}\left(\frac{U}{c_o}+1\right).$$

In this case, $\Delta U<0$ is always true.

(3) When $\theta=\pm\pi/2$, $$\Delta U = -\frac{b}{2t}\left(\frac{U}{c_o}\right).$$

In this case, $\Delta U<0$, but its value will be smaller than in special case 2.

The limitation of this method comes from (1) the difficulty in obtaining the intrinsic group velocity along the path between the source and the receiver, and (2) the fact that ΔU depends on b/t; in other words, short fault length or large distance could make the difference ΔU too small to be used in this method. For the 1989 Loma Prieta earthquake, the circumstances were such that both obstacles can be overcome. For the intrinsic group velocity, we can use seismograms from a foreshock that is at least two magnitude units smaller. In comparison with the main shock, the dimensions of the fault associated with this

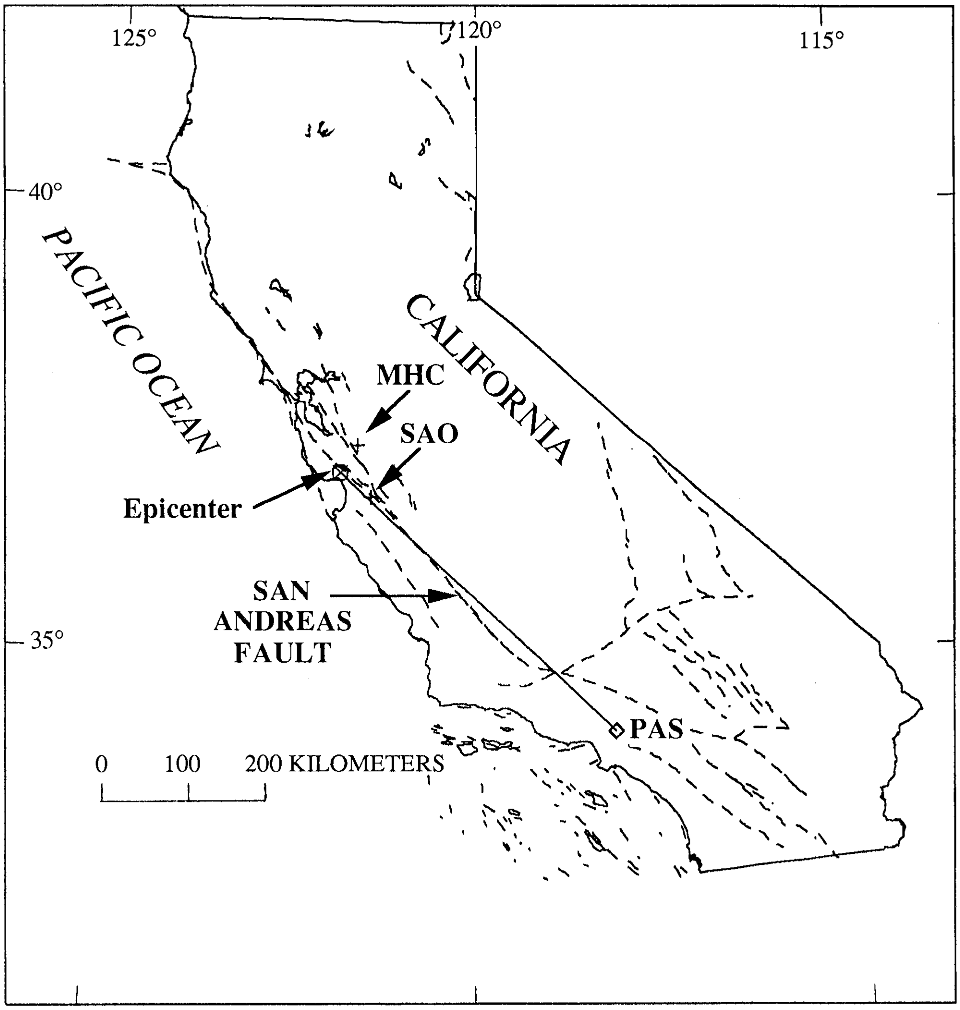

Figure 1.—California, showing locations of Loma Prieta main shock, station PAS, and major faults (irregular dashed lines). Notice that line from station to main shock lies nearly along strike of the San Andreas fault in the Loma Prieta region. Surface-wave propagation path almost coincides with trace of the San Andreas fault in northern California; surface-wave velocities along this path are very low.

foreshock are so small that it can be approximated as a point source. For example, using the relation of Slemmons and DePolo (1986, p. 55), for an event of M_S=4.5, the fault is about 1 km long; and for the main shock, the fault is 40 to 60 km long.

Note that, in contrast to other methods involving matching synthesized waveforms with observations, only phase information is used here, as shown in the derivation above. Nonetheless, this method assumes an unilateral fault propagating at an uniform velocity—clearly an approximation. This question is addressed in the section below entitled "Discussion."

EXPERIMENTAL DETERMINATION

The determination of the group velocity is well established; the main quantity to be determined is the group delay

$$\tau(\omega) = \frac{\Delta}{U(\omega)} + \psi_0'(\omega),$$

where $\psi'_0(\omega)$ is the initial phase and the prime indicates differentiation with respect to the frequency ω (for example, Keilis-Borok, 1989, p. 137). For waves with periods much longer than the source rise time, the far-field source-time function can be considered impulsive, and the rate of change of the initial phase can be neglected. Thus, for foreshocks with a source time of about 1 s, the group delay can be ignored. For the main shock, the finiteness of the source-time function is assumed to be the result of a moving source; in other words, the rise time at each source point is still very short. This assumption is consistent with the conclusion from near-source modeling (Steidl and others, 1991) that the rise-time function is very short at each source element.

To obtain the group velocity at one period, we can design a filter that isolates the energy within a narrow band centered on the period, and so the arrival time of the peak of the envelope represents the group delay. The filtering techniques used in this design were described in detail by Dziewonski and Hales (1972). Once ΔU is obtained, we can solve equation 1 for c_0:

$$c_0 = \frac{U}{\cos\theta_0 - \dfrac{2t\Delta U}{b}}. \tag{2}$$

Since U is a function of frequency, whereas c_0 is assumed to be constant, we can calculate c_0 from equation 2 by averaging over values at different frequencies or least-squares inversion when data at several azimuths are available.

OBSERVATIONS

It is fortuitous that not long before the 1989 Loma Prieta earthquake, the establishment of broadband stations began. One of the first such stations was located in southern California (sta. PAS, fig. 1). As shown in figure 1, the path from the epicenter to station PAS is nearly along the strike of the San Andreas fault near Loma Prieta. Two foreshocks and the main shock, which were recorded clearly at station PAS, were used in this study; the location parameters are listed in table 2. The foreshock locations are from the USGS' central California network (Calnet; Jean Olson, written commun., 1992). The main shock location, which is from the USGS' Preliminary Determination of Epicenters, is essentially the same as that of Dietz and Ellsworth (1990, p. 1418). By relocating the known shotpoints, Dietz and Ellsworth (1990, p. 1417) estimated a bias in the epicentral locations of about 1 km, due to the differences in velocity on both sides of the fault; the relative error of the epicentral locations is estimated to be much less, about 0.3 km. An rms error in arrival time of less than 0.1 s is indicated for the solutions (Jean Olson, written commun., 1992).

FORESHOCKS

The August 8, 1989, foreshock was one of two Lake Elsman earthquakes that were recognized as unusual (Olson, 1990) and most probably precursory to the Loma Prieta main shock (Seeber and Ambruster, 1990). The event is located 11 km to the north of the Loma Prieta epicenter, at nearly 14-km depth, and has M_L=5.1 (table 1), m_b=4.9, and M_S=4.5 (Preliminary Determination of Epicenters). Because of its location and source mechanism, this foreshock is generally thought to have occurred along a buried fault east of the fault associated with the Loma Prieta main shock. Unfiltered and filtered seismograms of the Love waves from the August 8, 1989, foreshock recorded at station PAS (fig. 1) are plotted in figure 2*B*.

Records of the June 13, 1988, foreshock north of the Lake Elsman area are used to estimate how well group velocities can be determined in this area. Unfiltered and filtered seismograms of Love wave from this event recorded at station PAS (fig. 1) are plotted in figure 2*B*. Notice the similarity of the first few cycles of the filtered seismograms in figures 2*A* and 2*B* (solid curves).

MAIN SHOCK

The Loma Prieta main shock is well located (table 1). The origin time of the main rupture, however, is an interesting question and most relevant to this study. Wald and

Table 2.—*Location parameters of the events used in this study*

[RMS, root-mean-square error in arrival time; ERH, standard error in horizontal location; ERZ, standard error in vertical location]

Date	Time	Latitude N.	Longitude W.	Depth (km)	RMS (s)	ERH (km)	ERZ (km)
880613	0145:36.52	37°23.58′	121°44.40′	9.84	0.07	0.1	0.4
890808	0813:27.36	37°08.67′	121°55.65′	13.89	.09	.2	.3
891018	0004:15.20	37°02.37′	121°52.81′	17.80	---	---	---

others (1991) deciphered a foreshock or slow rupture nucleation about 1.8 s before the main rupture. This difference will directly affect the rupture velocity determined here. As far as the rupture process is concerned, it is commonly agreed that the rupture associated with the Loma Prieta main shock was bilateral. The length of the rupture used by various investigators differs; for example, Hartzell and others (1991) used a fault half-length of 30 km, Wald and others (1991) a fault half-length of 20 km, Steidl and others (1991) a fault half-length of 19 km, and Beroza

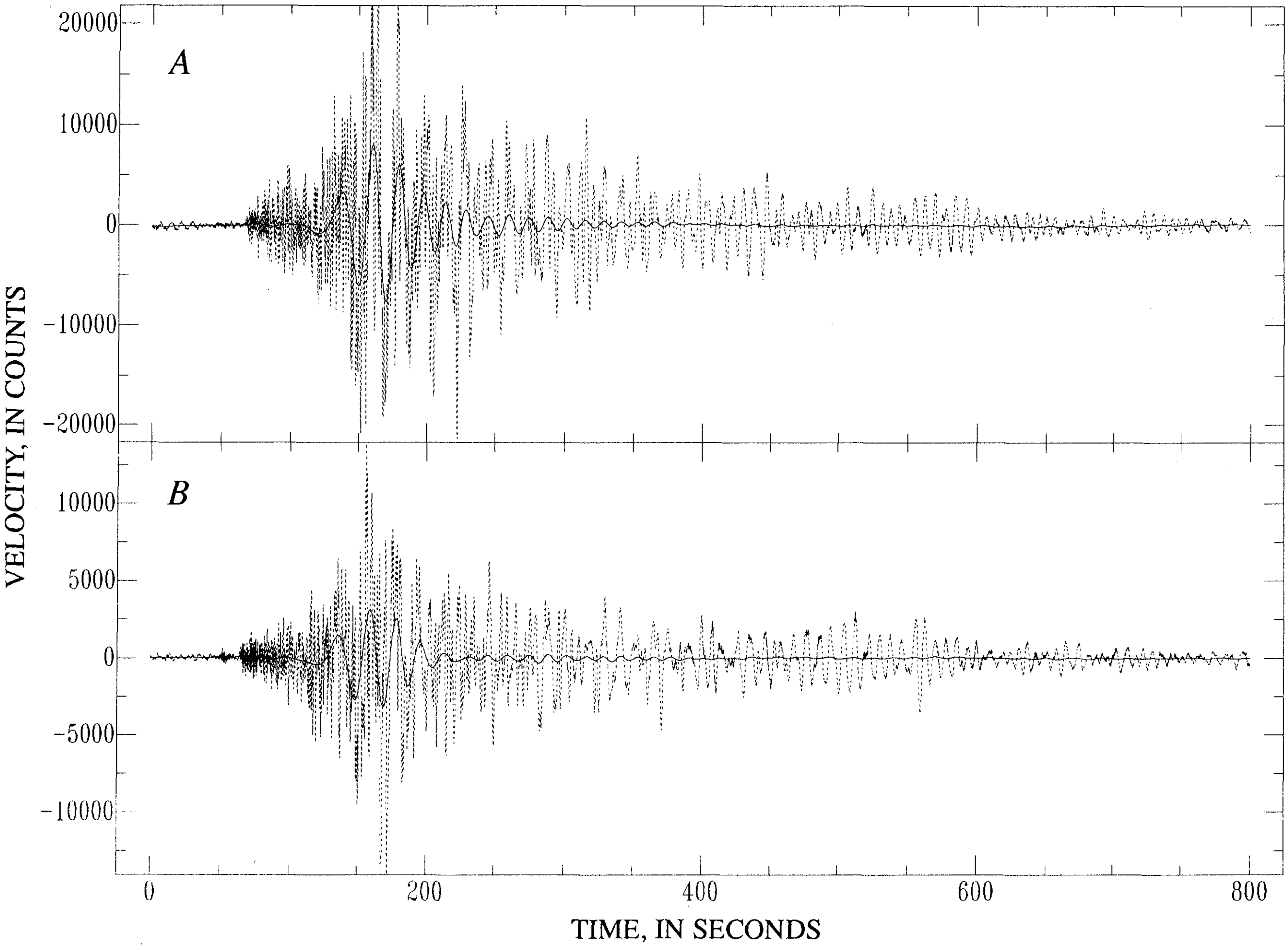

Figure 2.—Unfiltered (dashed curve) and filtered (solid curve) seismograms of Love wave from two Loma Prieta foreshocks: (*A*) June 13, 1988, Lake Elsman earthquake, which was located about 18 km north of main shock; and (*B*) August 8, 1989, Lake Elsman earthquake, which was located about 11 km north of main shock. Unfiltered seismogram was obtained by rotating two original horizontal (north-south and east-west) components of velocity into transverse direction (positive is counterclockwise from radial direction); filtered seismogram was obtained from two passes of a low-pass, four-pole Butterworth filter with a corner frequency at 0.06 Hz.

(1991) a fault half-length of 20 km in their waveform modeling based on strong motion and (or) teleseismic data. Judging from the distribution of aftershocks within the first 24 hours after the main shock (Dietz and Ellsworth, 1990) and assuming that they occurred within the region of main-shock rupture, the fault half-length could range from 20 to more than 30 km.

Unfiltered and filtered seismograms of the Love wave from the Loma Prieta main shock recorded at station PAS (fig. 1) are plotted in figure 3. The filtered seismogram is nearly identical to that of the August 8, 1989, foreshock (inset). The main shock evidently is richer in low-frequency signal content, as shown in figure 4.

GROUP VELOCITIES

The Love-wave group velocities of the two foreshocks of June 13, 1988, and August 8, 1989, are plotted in figure 5. At periods beyond 32 s and below 20 s, the group velocities of the two foreshocks begin to crisscross. The phase spectra of the main shock and the August 8, 1988, foreshock (fig. 4) are most stable within the period range 22–30 s. The dispersion curves for the two foreshocks (squares and triangles, fig. 5) have a discrepancy of less than 0.02 km/s, slightly larger than the 2s that could arise from the relative errors in epicentral location (0.3 km) and origin time (0.1 s). A systematic error in location or origin time cannot be ruled out.

The Love-wave group velocities of the Loma Prieta main shock are also plotted in figure 5, both assuming a 1.8-s delay in origin time (circles) and without such a delay (diamonds). As expected, the group velocities computed with the delay are higher than those without the delay; the average difference is 0.035 km/s.

The measured group velocities are quite low. The path between Loma Prieta and station PAS follows quite closely the San Andreas fault in central California, a region of

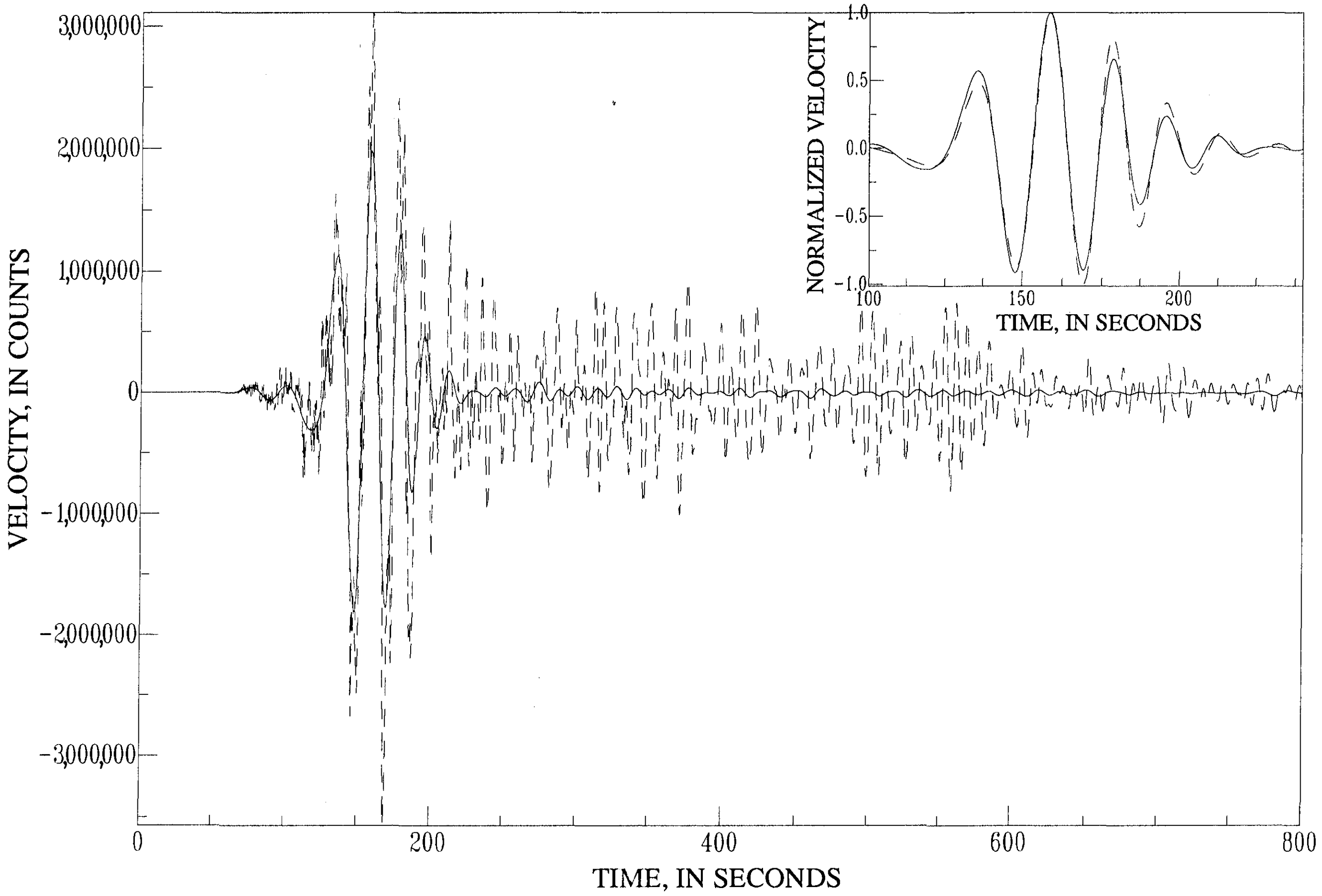

Figure 3.—Unfiltered (dashed curve) and filtered (solid curve) seismograms of Love wave from Loma Prieta main shock. Unfiltered seismogram clearly shows long-period (>10 s) signal, in contrast to unfiltered seismograms of foreshocks plotted in figure 2; this contrast evidently reflects differences in source spectra. Filtered seismogram, however, is nearly identical to that for August 8, 1989, foreshock (inset). Seismograms obtained as described in figure 2.

known low velocity (fig. 1). Tanimoto (1990), for example, observed that surface waves propagating between the epicenter of the 1987 Whittier Narrows, Calif., earthquake and station SAO or MHC in the San Francisco Bay region show a delay of 25 s relative to a station in eastern California at about the same distance. He found that group and phase velocities for surface waves traveling along the Coast Ranges are 20 percent lower than those traveling through eastern California. Thus, the low group velocities calculated here, though not heretofore reported, are not unexpected.

RUPTURE-VELOCITY DETERMINATION

Because the group velocities measured from the main shock are lower than those for the two foreshocks (fig. 5) calculated from equation 2, we can ascertain that $U>c_0$ (otherwise, $\Delta U \leq c_0$). On the basis of previous modeling, the main-shock rupture is assumed to propagate bilaterally from the epicenter. For the reasons presented in the next section, only the southeastward-propagating source is taken into account. Therefore, the half-length of the fault is used.

The rupture velocity of the main shock for several fault half-lengths, calculated from equation 2 with or without the delays discussed by Wald and others (1991), are plotted in figure 7. Only the results for the period range 22–30 s are used; at longer or shorter periods, the values fluctuate rapidly. Assuming a fault half-length of 25 km, as suggested by the aftershock distribution within the first 24 hours after the main shock, the rupture velocity would be 2.35 km/s, with the 1.8-s delay of rupture propagation after the origin time (table 2) incorporated. Without this delay—in other words, with a surface-wave-radiating, slow rupture propagation beginning at the origin time—the rupture velocity would be as low as 1.8 km/s. If the fault half-length is increased, the calculated rupture velocity will increase, as shown in equation 2; and the converse is also true. For example, assuming a fault half-length of 30 km (Hartzell and others, 1991, p. 1531), a rupture velocity of about 2.45 km/s is obtained.

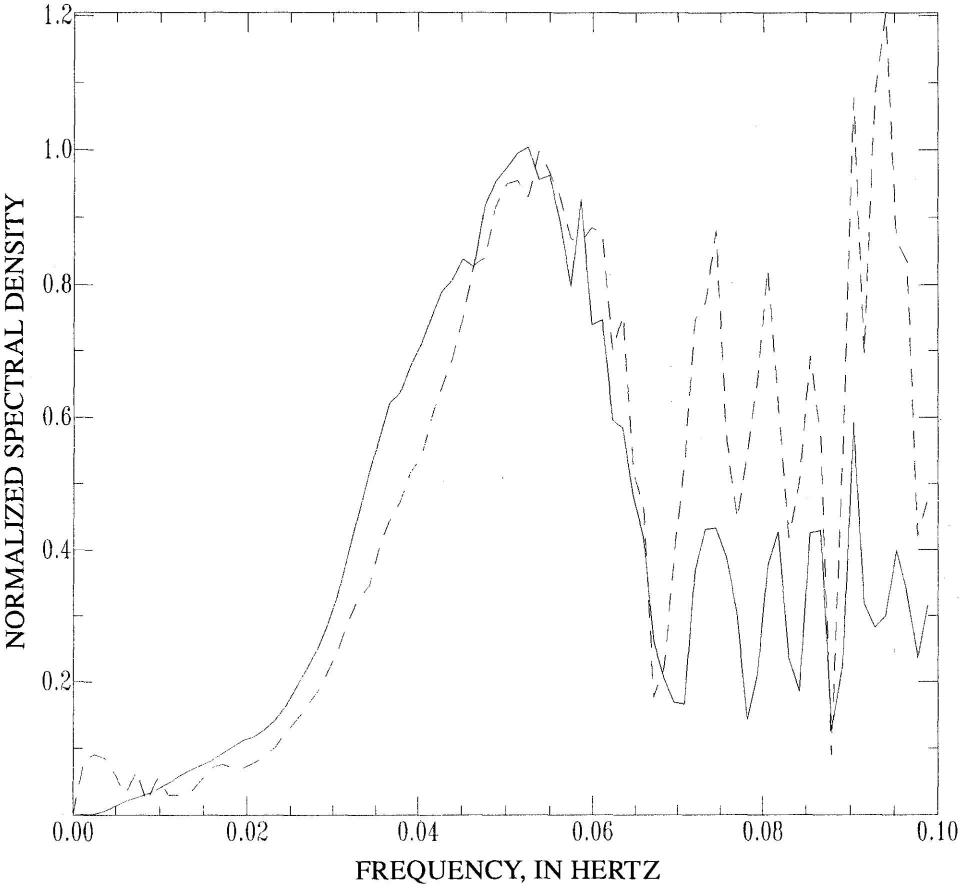

Figure 4.—Relative spectral densities of Loma Prieta main shock (solid curve) and August 8, 1989, foreshock (dashed curve). Notice relatively steep spectral slope above 0.055 Hz (or below a period of 18.2 s), above which phase spectra become rather unstable, especially for foreshock.

By incorporating a 1.8-s delay in main shock rupture propagation, the group-velocity method yields a rupture velocity of 2.35 to 2.45 km/s, at the low end of the values calculated by other investigators (table 1). The significance of these values is discussed below.

DISCUSSION

The rupture velocity calculated here is an average, obtained on the basis of a unilaterally propagating source. It may not be too surprising that the source appears to be unilateral at station PAS (fig. 1), with the source propagating toward it. This appearance is consonant with the fact that in this direction the radiated wavelets from successive sources interfere constructively; when the rupture velocity and the surface-wave velocity are equal, maximum constructive interference occurs. For a source propagating in the opposite direction, however, the waves from later sources will not catch up with the waves that had left the previous source points, and constructive interference will not occur. As shown in figure 3, the Loma Prieta main shock show no significant energy at the trailing end of the Love wave, in contrast to the August 8, 1989, foreshock—a phenomenon that should be seen if the northwestward-propagating rupture contributes significantly to the waveform. This dominance of the rupture propagating toward a station is also seen in strong-motion modeling (fig. 11 in Wald and others, 1991).

The determination of rupture-propagation parameters by this method would be much more robust if the seismograms at several stations around a source were available. The distance between station PAS and the source (fig. 1) was ideal for this application, and with the establishment of more broadband stations in northern and southern California, this method can be used to study the rupture characteristics of future M_S>6 events in this region. The reason why this method can be used at all in a study of the Loma Prieta main-shock rupture is that the epicenters of the two foreshocks and the main shock were well located by

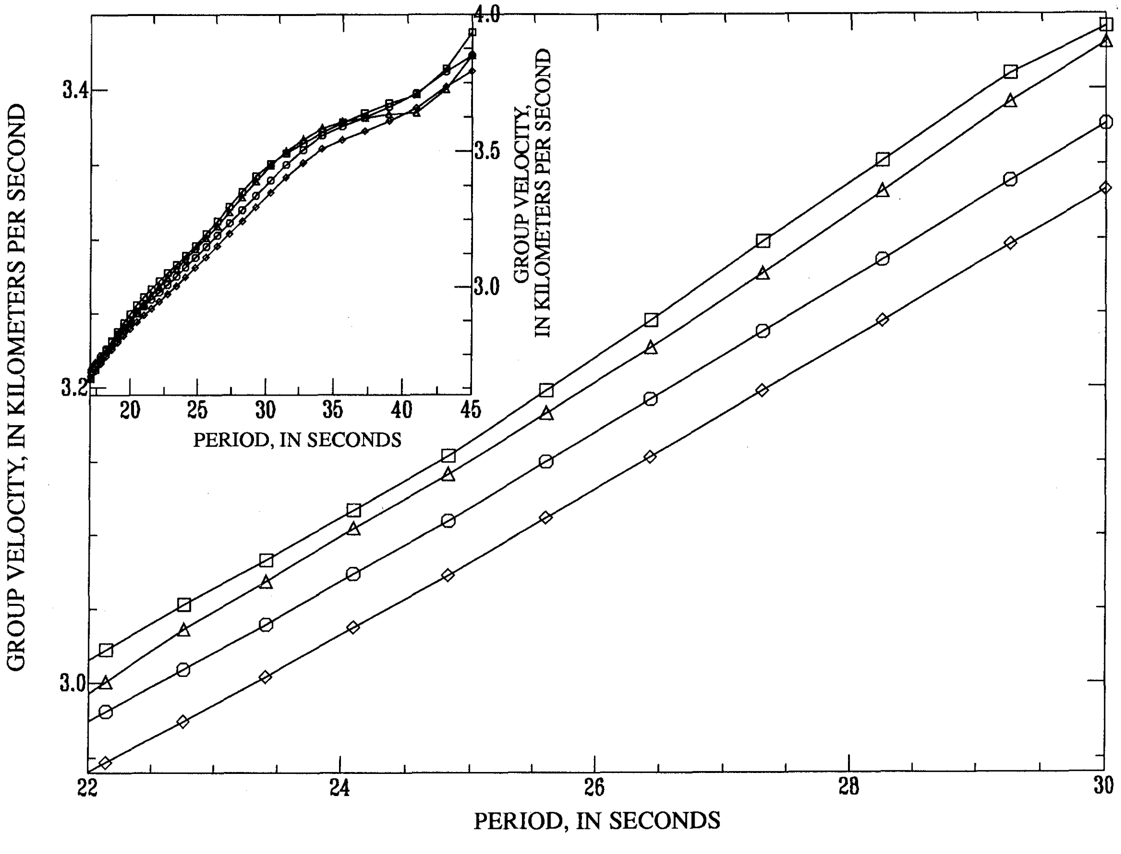

Figure 5.—Group velocities versus period for Love waves from Loma Prieta main shock (circles, triangles) and two foreshocks of June 13, 1988 (squares), and August 8, 1989 (triangles). Two curves for main shock assume 1.8-s (circles) and 0.0-s (diamonds) delay in origin time (see table 2). Inset shows data plotted over period range 17-45 s.

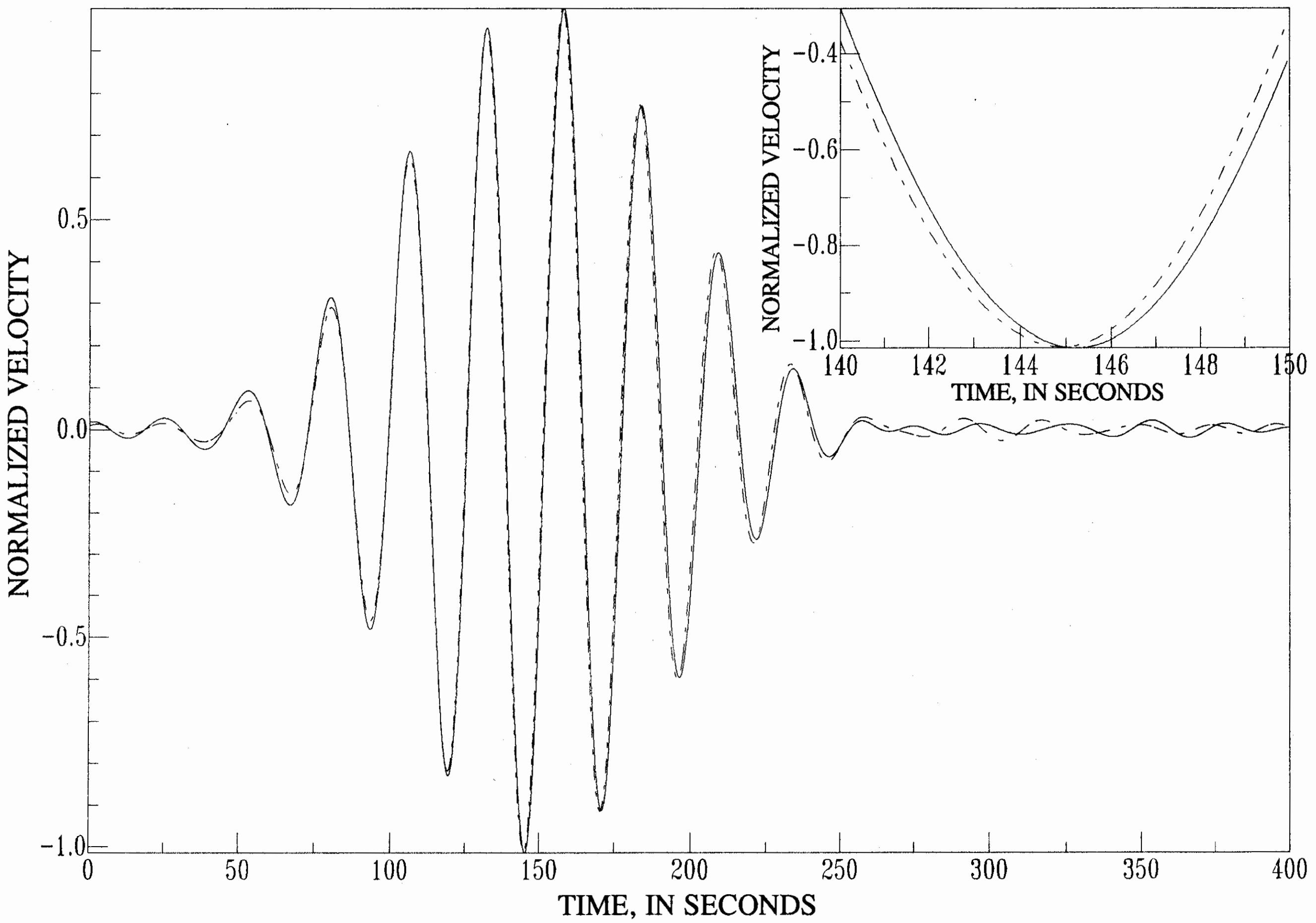

Figure 6.—Bandpass-filtered seismograms for Loma Prieta main shock (solid curve) and August 8, 1989, foreshock (dashed curve). Seismogram of foreshock precedes that of main shock by a fraction of a second (inset).

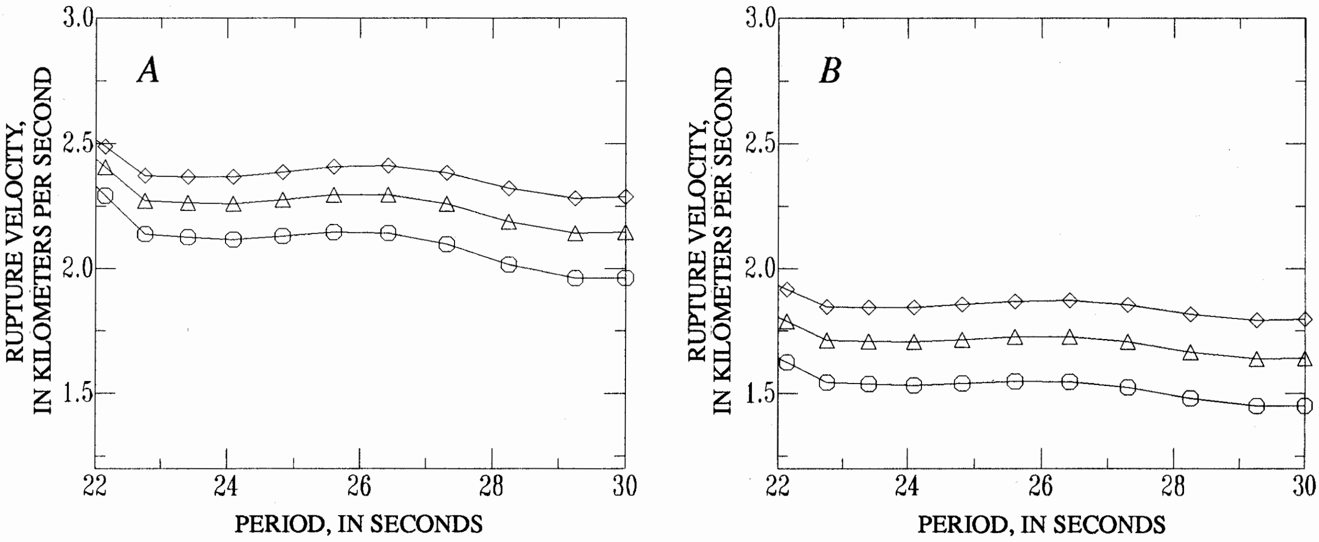

Figure 7.—Rupture velocities versus period for Loma Prieta main shock. Rupture velocity was calculated from group velocity, using fault lengths of 20 km (circles), 25 km (triangles), and 30 km (diamonds) and assuming delay times of 1.8 s (*A*) and 0.0 s (*B*) from origin time.

Calnet; many of the sources of errors in event location and timing have been removed. With more stations, we could ideally solve for the fault length, b, as well as the rupture velocity.

The source duration calculated from a rupture velocity of 2.45 km/s and a fault half-length of 30 km is 12.2 s, or 10.6 s with a rupture velocity of 2.35 km/s and a fault half-length of 25 km. Note that the time function obtained from teleseismic-waveform or near-source modeling of the earthquake has source durations of 7.5 to 15 s (Wallace and others, 1991, p. 1628). In this regard, the results presented here are consistent with those of other models.

CONCLUSION

This study is a first attempt at determining the rupture velocity of a large earthquake by using the difference between the group velocity measured from the earthquake and the intrinsic group velocity, which is defined here as the group velocity measured from an event more than two magnitude units smaller. As the number of broadband, wide-dynamic-range stations increases, such a determination can be routinely made for many events. When more than one station around an earthquake epicenter is used, both the fault length and the rupture velocity could also be determined.

The method used in this paper depends only on the phase information contained in the waveforms. Because this information does not involve the amplitude spectrum, the tradeoffs between slip amplitudes and rupture velocity used by Steidl and others (1991) may be avoided. As the method is presently formulated, however, only average rupture properties can be calculated.

ACKNOWLEDGMENTS

This research was supported by U.S. National Science Foundation grant EAR–9011449. Alan Jones' assistance in editing is appreciated. My study was made possible by the timely data-retrieval service provided by Marcie Palmer of Incorporated Research Institutions for Seismology's Data Management Center in Austin, Tex. I also thank Jean Olson of the USGS for providing updated hypocentral locations for the events studied.

REFERENCES CITED

Ben-Menahem, Ari, 1961, Radiation of seismic waves from finite moving sources: Seismological Society of America Bulletin, v. 51, no. 2, p. 401–435.

Ben-Menahem, Ari, and Toksöz, M.N., 1962, Source-mechanism from spectra of long-period seismic surface-waves. 1. The Mongolian earthquake of December 4, 1957: Journal of Geophysical Research, v. 67, no. 5, p. 1943–1955.

Beroza, G.C., 1991, Heterogeneous slip at Loma Prieta: Seismological Society of America Bulletin, v. 81, no. 5, p. 1603–1621.

Dietz, L.D., and Ellsworth, W.L., 1990, The October 17, 1989 Loma Prieta, California, earthquake and its aftershocks; geometry of the sequence from high-resolution locations: Geophysical Research Letters, v. 17, no. 9, p. 1417–1420.

Dziewonski, A.M., and Hales, A.L., 1972, Numerical analysis of dispersed seismic waves, *in* Bolt, B.A., ed., Computational physics: New York, Academic Press, v. 11, p. 39–85.

Hartzell, S.H., Stewart, G.S., and Mendoza, Carlos, 1991, Comparison of L_1 and L_2 norms in a teleseismic waveform inversion for the slip history of the Loma Prieta, California, earthquake: Seismological Society of America Bulletin, v. 81, no. 5, p. 1518–1539.

Kanamori, Hiroo, 1970, Synthesis of long-period surface waves and its application to earthquake source studies, Kurile islands earthquake of October 13, 1963: Journal of Geophysical Research, v. 75, no. 26, p. 5011–5027.

Kanamori, Hiroo, and Given, G.W., 1981, Use of long-period surface waves for rapid determination of earthquake-source parameters: Physics of the Earth and Planetary Interiors, v. 27, no. 1, p. 8–31.

Keilis-Borok, V.I., ed., 1989, Seismic surface waves in a laterally inhomogeneous earth: Boston, Kluwer Academic Publishers, 293 p.

Olson, J.A., 1990, Seismicity in the twenty years preceding the Loma Prieta, California earthquake: Geophysical Research Letters, v. 17, no. 9, p. 1429–1432.

Press, Frank, Ben-Menahem, Ari, and Toksöz, M.N., 1961, Experimental determination of earthquake fault length and rupture velocity: Journal of Geophysical Research, v. 66, no. 10, p. 3471–3485.

Romanowicz, B.A., and Lyon-Caen, Hélène, 1990, The Loma Prieta earthquake of October 18, 1989; results of teleseismic mantle and body-wave inversion: Geophysical Research Letters, v. 17, no. 9, p. 1191–1194.

Seeber, Leonardo, and Ambruster, J.G., 1990, Fault kinematics in the 1989 Loma Prieta rupture area during 20 years before that event: Geophysical Research Letters, v. 17, no. 9, p. 1425–1428.

Slemmons, D.B., and DePolo, C.M., 1986, Evaluation of active faulting and associated hazards, *in* Active tectonics: Washington, D.C., National Academy Press, p. 45–62.

Steidl, J.H., Archuleta, R.J., and Hartzell, S.H., 1991, Rupture history of the 1989 Loma Prieta, California, earthquake: Seismological Society of America Bulletin, v. 81, no. 5, p. 1573–1602.

Tanimoto, Toshiro, 1990, Modelling curved surface wave paths; membrane surface wave synthetics: Geophysical Journal International, v. 102, no. 1, p. 89–100.

Wald, D.J., Helmberger, D.V., and Heaton, T.H., 1991, Rupture model of the 1989 Loma Prieta earthquake from the inversion of strong-motion and broadband teleseismic data: Seismological Society of America Bulletin, v. 81, no. 5, p. 1540–1572.

Wallace, T.C., Velasco, A.A., Zhang, Jiajun, and Lay, Thorne, 1991, A broadband seismological investigation of 1989 Loma Prieta, California, earthquake; evidence for deep slow slip?: Seismological Society of America Bulletin, v. 81, no. 5, p. 1622–1646.

Wu, F.T., Thompson, K.C., and Kuenzler, H., 1972, Stick-slip propagation velocity and seismic source mechanism: Seismological Society of America Bulletin, v. 62, no. 6, p. 1621–1628.

Zhang, Jiajun, and Kanamori, Hiroo, 1988, Source finiteness of large earthquakes measured from long-period Rayleigh waves: Physics of the Earth and Planetary Interiors, v. 52, no. 1, p. 56–84.

MAIN-SHOCK CHARACTERISTICS

USE OF STRESS-DROP MODELS TO INTERPRET GEODOLITE/GLOBAL POSITIONING SYSTEM AND LEVELING MEASUREMENTS AT LOMA PRIETA

By Mingdong Wu and John W. Rudnicki,
Northwestern University

CONTENTS

ABSTRACT

We interpret the coseismic surface deformation associated with the 1989 Loma Prieta earthquake by approximating the rupture as a planar elliptical zone embedded within an elastic half-space. In contrast to dislocation models, in which the slip is prescribed, the stress change in our model is prescribed on the fault surface. The stress drop is assumed to be uniform, with a component $\Delta\tau_s$ along the strike direction and a component $\Delta\tau_d$ along the dip direction of the fault. The stress drop and rupture-zone geometry are adjusted until the calculated surface deformation agrees as closely as possible with that observed. As in simple dislocation models, stress-drop models of this type are found to fit the Geodolite/Global Positioning System (GPS) and leveling data separately much better than the combined data. The main differences between the models fitting the Geodolite/GPS and leveling data are the dip on the fault surface (73° versus 65°, respectively) and a fault center 2 km farther northeast, as inferred from the Geodolite/GPS data. The discrepancies between the two models suggest that both of these models are too simple to capture fully the actual rupture-zone geometry and stress-drop distribution. The alongstrike and alongdip stress-drop components, geodetic moment, and maximum energy-release rate, respectively, inferred from the Geodolite/GPS data are as follows: $\Delta\tau_s$=1.5 MPa, $\Delta\tau_d$=1.4 MPa, $M_0=2.5\times10^{19}$ N-m, and $G_{max}=5.5\times10^6$ J/m^2. The average slip amplitudes in the strike and (reverse) dip direction, respectively, are $[\bar{u}_s]$=1.3 m and $[\bar{u}_d]$=1.1 m. The rupture area inferred from the leveling data is slightly smaller than that inferred from the Geodolite/GPS data (408 versus 518 km^2), and so $\Delta\tau_s$, $\Delta\tau_d$, M_0, and G_{max} in the model fitting the leveling data are all slightly larger. The G_{max} value in both models is near the upper end of the range inferred for crustal faults, a result consistent with other evidence suggesting that Loma Prieta-type events are relatively infrequent.

INTRODUCTION

Surface displacements associated with the 1989 Loma Prieta earthquake (M_s=7.1) have been interpreted as due to slip on an oblique fault plane with subequal components of strike-slip and reverse faulting (Lisowski and others, 1990; Marshall and others, 1991). Lisowski and others inferred the coseismic slip on the fault surface by comparing the line lengths measured by a Geodolite and a few vector-component changes detected by Global Positioning System (GPS) observations at Loma Prieta with those calculated from a model of uniform slip over a rectangular region embedded in an elastic half-space (Mansinha and Smylie, 1971). Marshall and others used the same modeling approach but focused on the vertical deformation measured by leveling surveys of the Loma Prieta leveling network before and after the earthquake. Although the geometries of the model faults inferred from these two data sets differ moderately, both models predict similar values for the coseismic strike and reverse dip slip.

In this paper, we analyze the data of Lisowski and others (1990) and Marshall and others (1991) but use a stress-drop model (Wu and others, 1991); that is, the stress drop, rather than the slip, is specified on the fault surface and adjusted (along with the geometry) to fit the measured surface deformation. Although dislocation models are convenient and widely used for inferring the geometry of the rupture zone and the amplitude of slip, one limitation of this approach is that it is purely kinematic: It relates the surface deformation to slip at depth but only indirectly yields information about the stresses that produced the slip and the conditions for propagation and termination of the rupture. Typically, dislocation models approximate the slip as uniform over the entire fault surface or in elements, and so the slip amplitude drops to zero discontinuously near the edge of the rupture zone. Therefore, the average stress change and the strain-energy changes in volumes containing the rupture-zone edge are unbounded.

The stress-drop method of Wu and others (1991) provides an alternative approach. Though computationally demanding, this method constrains the stress drop directly by using it as a model parameter to fit the surface deformation. Because their method uses the exact asymptotic form for the slip distribution near the edge of the rupture zone, it is mechanically consistent: Although the stresses near the rupture-zone edge are singular, with the characteristic dependence on the inverse square root of distance from the edge, the strain-energy changes in volumes containing the edge are finite. Therefore, the distribution of the energy-release rate along the rupture front, which Wu and others used to estimate the critical energy-release rate at the termination of rupture, can be calculated. Furthermore, comparison of the fault geometries inferred by this method with those inferred from dislocation models provides information about the resolving power of the data among solutions.

In this study, we apply the stress-drop method of Wu and others (1991) to the coseismic-deformation data associated with the 1989 Loma Prieta earthquake. In particular, we assume an elliptical rupture zone, with uniform stress drops in the strike and dip directions. The dimension and orientation of the rupture zone and the magnitude of stress drops are determined by comparing predicted with observed surface displacements. Once the rupture-zone geometry and stress drops are determined, the slip distribution, geodetic moment, and critical energy-release rate at the termination of rupture can be calculated. Then, we compare our estimated rupture-zone geometry, slip amplitude, and geodetic moment with those calculated by Lisowski and others (1990) and Marshall and others (1991), and discuss the implications of our results.

DATA

Coseismic surface deformation associated with the 1989 Loma Prieta earthquake has been observed by geodetic measurements in the San Francisco Bay region. The deformation data used in this paper consist of electronic distance measurement (EDM), a few Global Positioning System (GPS) relative-position changes (fig. 1*A*), and elevation changes along seven leveling lines (fig. 1*B*). The characteristics of the EDM and GPS systems were described by Lisowski and others (1990), and the leveling data by Marshall and others (1991). We briefly review the data quality and uncertainty below.

The distances between the geodetic stations shown in figure 1*A* have been measured by the U.S. Geological Survey (USGS) since the early 1970's (Prescott and others, 1981). The precision of measurements made by a Geodolite, a laser distance-measuring instrument, is about 0.2 ppm (Savage and Prescott, 1973); some lines measured with a short-range distancemeter (model HP3808) have a precision of 2 ppm. GPS observations of the position vectors between Loma Prieta and stations Eagle Rk, Allison, Hamilton, and Brush 2 have been obtained since 1985; the data precision is about 0.2 ppm, depending on the orientation of the line and the data-processing techniques used (Prescott and others, 1989). Specifications of the observed coseismic offsets in the relative positions of the geodetic stations and the associated data uncertainties are discussed by Lisowski and others (this chapter) and listed in table 1.

Preearthquake surveys of the Loma Prieta leveling network (fig. 1*B*) were performed by both the U.S. National Geodetic Survey (NGS) and the USGS between 1947 and 1989. Postearthquake leveling surveys were conducted from February through June 1990 (Marshall and others, 1991). Because little postseismic slip was observed between October 1989 and June 1990 (Behr and others, 1990; Langbein, 1990), the elevation changes between the preearthquake and postearthquake surveys are treated as coseismic, following Marshall and others. Errors in leveling measurements accumulate with the square root of the distance; the observed errors in the leveling data can be expressed as $\sigma_0 = \sqrt{L_C \delta_i}$, where the δ_i are the relative uncertainties and L_c (=10 km) is the characteristic length scale for the leveling network (Marshall and others, 1991). Specific absolute elevation changes and relative uncertainties were reported by Marshall and others. A constant can be freely added to these elevation-change observations; Marshall and others determined a constant of +28 mm for their modeling. In this paper, we adopt the same constant, and so we add a datum shift of +28 mm to the absolute elevation changes listed by Marshall and others (1991, table 2A).

STRESS-DROP MODEL

The presence of two adjacent faults, the San Andreas and Sargent faults (fig. 1), in the Loma Prieta rupture zone and the aftershock sequence of the earthquake (Dietz and Ellsworth, 1990) suggest that the rupture may have involved complex fault interactions. Nevertheless, Lisowski and others (1990) and Marshall and others (1991) showed that most of the coseismic surface deformation can be modeled adequately with buried oblique slip on a single planar fault surface. We follow a similar approach and attempt to model the surface deformation as due to a single planar zone of prescribed stress drop. Although our procedure can accommodate arbitrary-shape rupture zones and spatially distributed stress drops, we assume that the rupture zone is elliptical and the stress drop is uniform. We make these simplifying assumptions because insufficient information is contained in the geodetic data to constrain the details of slip (Lisowski and others, 1990; Marshall and others, 1991). We also ignore the possibility of fault interaction suggested by the topographic model of Schwartz and others (1990) and the seismicity study of Olson (1990).

The uniform-stress-drop model of an elliptical rupture zone is illustrated in figure 2. The procedure for calculating the displacements and stresses due to a zone of prescribed stress drop embedded within an elastic half-space was described in detail by Wu and others (1991) and is briefly summarized here. Wu and others begin with an expression for the stress in the half-space due to a prescribed displacement discontinuity. When this expression is evaluated on the surface of discontinuity, it becomes an integral equation for the unknown distribution of displacement discontinuity arising from the prescribed stress drop. This integral equation is then solved by converting it to a set of linear algebraic equations. Once the appropriate distribution of displacement discontinuity is determined,

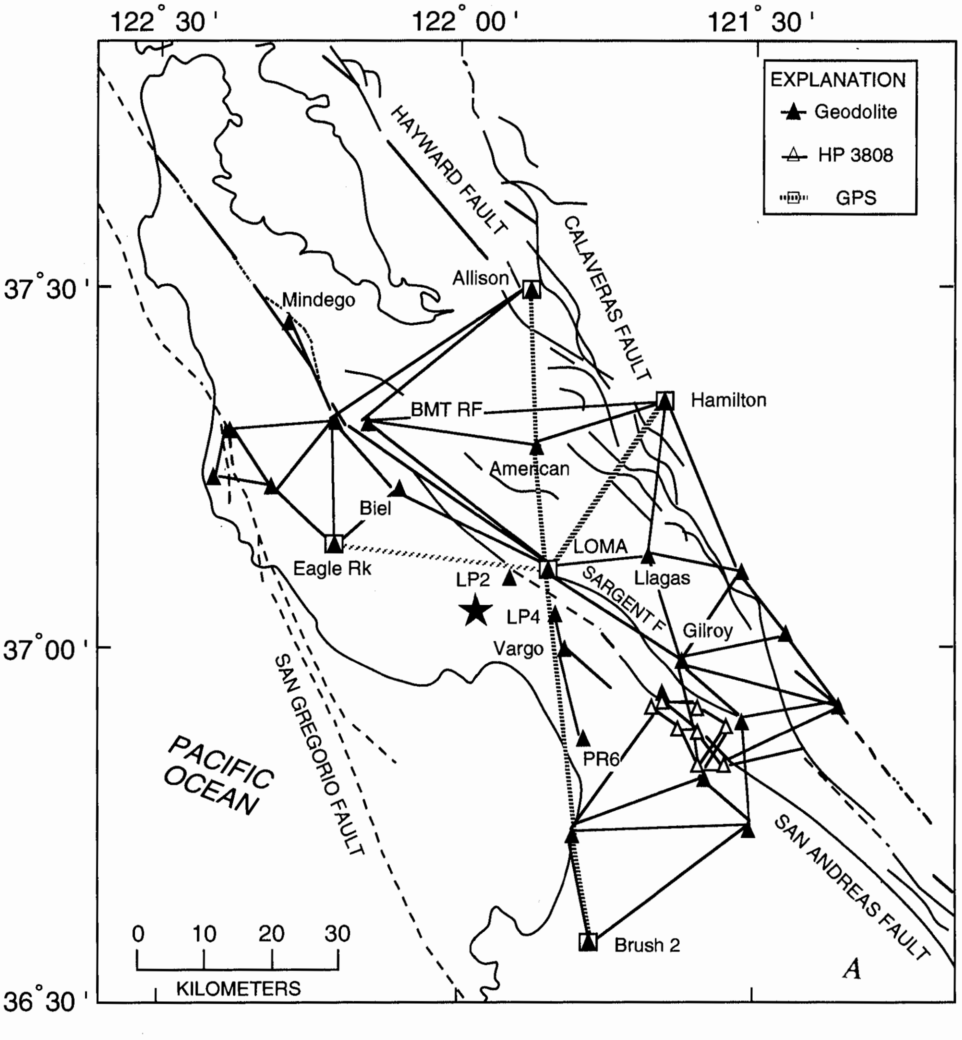

Figure 1.—Loma Prieta region, Calif., showing locations of major faults (dotted where buried, dashed where inferred) and of (*A*) Geodolite, electronic distance measurement, and Global Positioning System stations (station names are shown only selectively for simplicity; for more details, see Lisowski and others, 1990) and (*B*) leveling network of 211 bench marks (after Marshall and others, 1991). Star, epicenter of 1989 Loma Prieta earthquake. Inset in figure 1*B* shows locations of leveling lines 1 through 7; circled dots correspond to first stations of leveling lines in figure 3.

other quantities of interest, such as the surface displacements and the stresses near the edge of the rupture zone, can be calculated. An important feature of this solution is that the exact asymptotic form of the displacement field near the edge of a crack (rupture zone) in elastic solids is used to approximate the kernels of the integral equation. Therefore, the stress-intensity factors (coefficients of the $\sqrt{r}$ singularity at the edge of the rupture zone, where r is the distance from the edge; see Rice, 1968) can be calculated accurately. Then, the energy-release rate G—that is, the amount of energy released per unit area of advance of the rupture—can be calculated by using the following expression (Rice, 1968):

$$G = \frac{1-\nu}{2\mu}\left(K_{\mathrm{I}}^2 + K_{\mathrm{II}}^2 + \frac{K_{\mathrm{III}}^2}{1-\nu}\right), \tag{1}$$

where μ is the shear modulus, ν is Poisson's ratio, and K_{I}, K_{II}, and K_{III} are the stress-intensity factors for modes I, II, and III, respectively. A common and simple criterion for both quasi-static and dynamic modeling of rupture propagation is to assume that rupture propagation occurs when the local energy-release rate is equal to a critical value which reflects the material resistance to slip. Although this criterion is too simple to describe in detail the actual rupture process, it provides a good description when slip occurs in a region near the edge of the rupture zone on a length scale much smaller than other relevant lengths, for example, fault-rupture length, distance to the free surface, and so on (Rice, 1980, 1983; Rudnicki, 1980). If we assume that the rupture propagates according to the criterion that the energy-release rate is equal to a critical value, then the maximum G value, G_{max}, estimated here is a lower bound on the critical energy-release rate at the termination of rupture. If this critical energy-release rate varies strongly with position and (or) velocity, as is likely, then the G_{max} value estimated here may differ from those calculated with dynamic rupture models (for example, Beroza and Spudich, 1988).

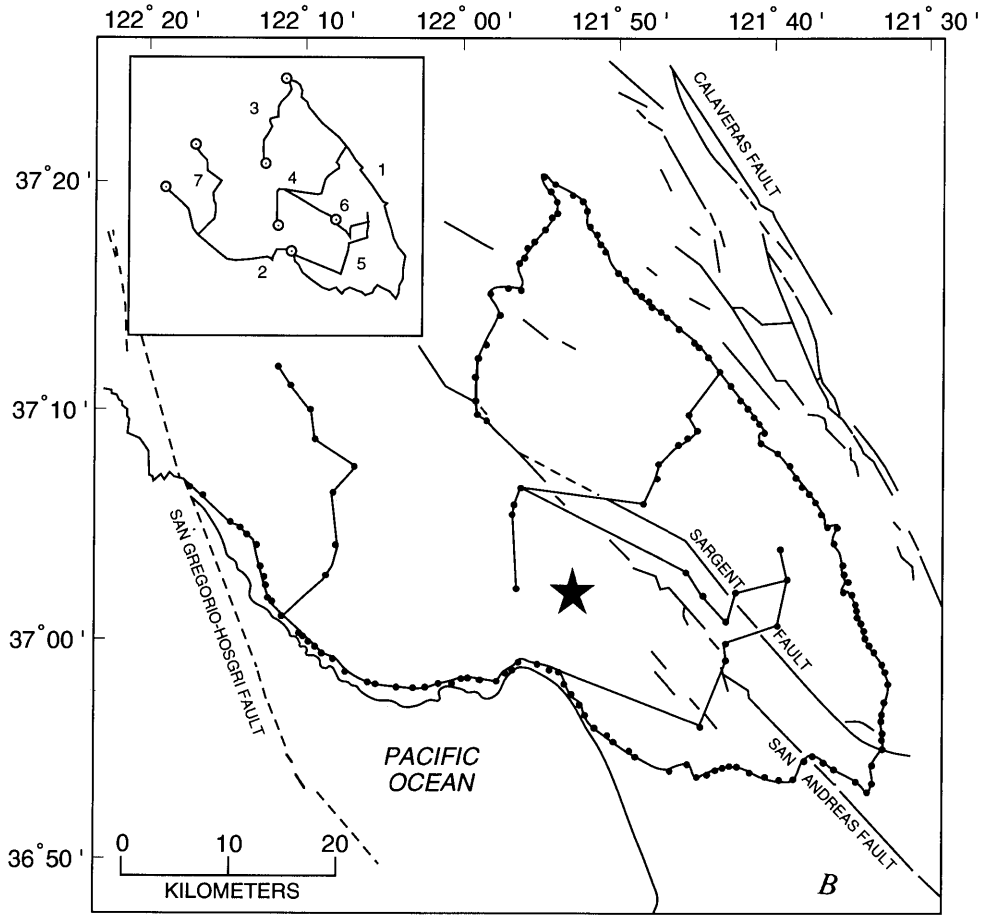

Figure 1.—Continued.

Table 1.—*Model fit of coseismic offset to Geodolite/Global Positioning System data*

[All values in millimeters. GPS, Global Positioning System]

Beginning station (fig. 1)	Ending station (fig. 1)	Coseismic offset		Residual
		Observed	Calculated	
		Geodolite line-length changes		
Allison	BMT RF	−39.2±11.8	−25.1	−14.1
Allison	Hamilton	−19.5±12.4	−13.1	−6.4
Allison	Mindego	−26.2±18.1	−19.1	−7.1
American	BMT RF	−27.6±25.4	.4	−28.0
American	Hamilton	75.0±9.4	58.7	16.3
American	LOMA USE	−66.5±7.8	−48.8	−17.7
Biel	Eagle Rk	101.5±7.2	80.3	21.2
Biel	LOMA USE	235.4±11.6	218.4	17.0
Biel	Mindego	−107.5±8.8	−98.1	−9.4
BMT RF	LOMA USE	176.2±18.1	116.9	59.3
BMT RF	Mindego	7.6±4.1	14.6	−7.0
Butano	Dump	−39.7±5.7	−32.3	−7.4
Butano	Eagle Rk	−95.2±5.5	−76.2	−19.0
Butano	Mindego	6.5±6.8	10.7	−4.2
Butano	Pom	−46.2±11.1	−32.9	−13.3
CROSSRM1	Mindego	−15.9±7.1	−22.8	6.9
Dump	Pom	−6.3±9.6	.2	−6.5
Eagle Rk	Mindego	−20.4±6.8	−9.5	−10.9
Gilroy	Llagas	−48.5±7.9	−50.8	2.3
Gilroy	LP1	−19.0±14.1	−40.8	21.8
Hamil Ec	Llagas	37.3±8.9	23.4	13.9
Hamil Ec	SHEEPRM2	−42.1±12.7	−24.9	−17.2
Llagas	LP1	−54.0±6.0	−15.0	−39.0
Llagas	SHEEPRM2	74.3±11.9	54.6	19.7
LOMA USE	Mindego	175.0±12.8	132.9	42.1
Mindego	Pom	−1.8±7.5	6.2	−8.0
BMT10	BMT9	6.9±4.0	−.8	7.7
BMT10	Pawt	−17.1±5.0	−22.3	5.2
BMT10RM1	BMT9	10.3±4.4	−.8	11.1
BMT11	BMT8	1.6±4.0	−5.9	7.5
BMT11	BMT9	12.2±5.0	11.0	1.2
BMT11	Pawt	−15.1±6.9	−17.9	2.8
BMT8	BMT9	1.1±3.9	−.4	1.5
BMT8	RF5Reset	23.0±4.6	18.9	4.1
BMT9	SKY1	12.2±4.6	16.0	−3.8
Pawt	RF1	9.6±4.0	8.9	.7
Pawt	SKY1	1.5±6.2	−2.5	4.0
Allison	Lomancer	109.0±8.0	92.1	16.9
Eagle Rk	Lomancer	259.7±5.8	232.5	27.2
Hamilton	Lomancer	51.1±6.0	52.6	−1.5
LOMADWR	PR6	−274.1±20.1	−256.9	−17.2
LP1	LP2	−40.9±5.2	40.0	−80.9
LP1	LP4	−212.0±7.9	−221.1	9.1
Brush 2	Fremont	−18.1±10.0	−9.7	−8.4
Brush 2	Mulligan	49.4±6.9	35.1	14.3
Chamber	Juan	−4.4±6.3	−10.5	6.1
Chamber	Mulligan	−9.4±8.9	−20.4	11.0
Chamber	Vargo	123.9±7.2	127.9	−4.0
Fairview	Juan	8.1±21.5	5.4	2.7
Fremont	Juan	42.5±6.0	26.3	16.2
Fremont	Mulligan	−5.0±10.5	2.0	−7.0
Gilroy	Juan	−63.4±11.4	−43.8	−19.6
Hollis	Juan	−22.6±40.3	−9.3	−13.3
Juan	Mulligan	−36.8±8.7	−13.2	−23.6
Juan	Sargent	33.9±12.2	8.1	25.8
LP1	Vargo	−204.0±15.3	−225.0	21.0
		Geodolite line-length changes—Continued		
Fremont	Sargent	54.2±12.9	25.6	28.6
Canada	Fairview	−39.3±12.2	−18.0	−21.3
Canada	Sargent	−86.3±25.0	−41.4	−44.9
Fairview	Gilroy	−68.2±13.7	−39.3	−28.9
Gilroy	Sargent	−89.9±12.6	−46.1	−43.8
Canada	SHEEPRM2	−32.7±23.5	−13.2	−19.5
Gilroy	SHEEPRM2	−69.8±11.1	−29.0	−40.8
Canada	Gilroy	−51.9±7.5	−18.7	−33.2
P1	P2	−3.5±13.4	5.2	−8.7
P1	P3	4.2±20.8	−8.6	12.8
P1	P4	−10.0±19.8	−3.4	−6.6
P1	P6	−6.8±29.9	−13.7	6.9
P2	P3	44.6±23.1	5.5	39.1
P2	P4	−10.4±17.3	−9.3	−1.1
P2	P5	−10.3±19.9	−3.3	−7.0
P2	P6	7.5±28.3	−12.9	20.4
P2	P7	−5.3±31.8	−10.5	5.2
P3	P4	66.6±14.0	15.2	51.4
P3	P5	66.6±23.1	21.3	45.3
P3	P6	3.5±15.5	−2.1	5.6
P4	P5	46.0±11.3	16.3	29.7
P4	P6	11.9±12.7	−.7	12.6
P4	P7	18.5±18.6	6.6	11.9
P5	P6	87.3±13.7	20.8	66.5
P5	P7	−43.3±13.5	−9.6	−33.7
P7	P8	73.7±10.6	38.0	35.7
P5	C1	−31.5±17.2	−9.5	−22.0
P5	Chamb 2	−41.8±12.0	−17.3	−24.5
		GPS east		
LP1	Allison	34.8±5.9	55.2	−20.4
LP1	Eagle Un	225.2±11.8	243.6	−18.4
LP1	Hamilton	65.6±7.0	66.0	−.4
LP1	Brush 2	41.3±15.6	78.4	−37.1
		GPS north		
LP1	Allison	−110.6±3.8	−103.7	−6.9
LP1	Eagle Un	−205.4±5.6	−185.3	−20.1
LP1	Hamilton	−106.6±2.6	−96.2	−10.4
LP1	Brush 2	−229.2±4.6	−205.1	−24.1
		GPS up		
LP1	Allison	−105.5±33.4	−129.1	23.6
LP1	Eagle Un	−211.8±24.7	−202.6	−9.2
LP1	Hamilton	−114.4±25.5	−131.4	17.0
LP1	Brush 2	−40.0±27.8	−93.4	53.4

RESULTS AND DISCUSSION

Marshall and others (1991) found that the fault model that best fits the leveling data is not fully consistent with the model used by Lisowski and others (1990) to fit the geodetic/GPS data. More specifically, Marshall and others found that using the parameters calculated by Lisowski and others to model the elevation changes produces a misfit twice as large as that for their best-fitting model. In our modeling, therefore, we search for the models that best fit separately the Geodolite/GPS data of Lisowski and others and the leveling data of Marshall and others. We then search for the model that best fits both the Geodolite/GPS and the leveling data. The best-fitting models are determined by trial and error. The starting fault surface is suggested by the main-shock and aftershock locations (Dietz and Ellsworth, 1990).

Reasonable agreement with the EDM (line-length changes) and GPS vector changes of Lisowski and others (1990) is obtained with a model for which the strike, dip, depth to center, length, width, and area of the rupture zone are about 132°, 73°, 11 km, 44 km, 15 km, and 518

Table 2.—*Modeling of the Geodolite/Global Positioning System and Leveling Data*

[GPS, Global Positioning System]

	Geodolite/GPS data		Leveling data	
	Dislocation model of Lisowski and others (1990)	This study	Dislocation model of Marshall and others (1991)	This study
Length ($2L$) (km)	37	44	34	40
Depth to top ($d\sin\alpha$) (km)	5	3.8	4	3.6
Width (D–d) (km)	13.3	15	11	13
Rupture area (km^2)	492	518	372	408
Dip (α) (°)	70	73	60	65
Slip amplitude along strike (m).	1.6	avg 1.3	2.4	avg 1.8
Slip amplitude along dip (m).	1.2	avg 1.1	1.7	avg 1.5
Geodetic moment (M_0) (10^{19} N-m).	2.8	2.5	3.0	2.8
Alongstrike stress-drop component ($\Delta\tau_s$) (MPa).	---	1.45	---	1.7
Alongdip stress-drop component ($\Delta\tau_d$) (MPa).	---	1.35	---	1.95
Maximum energy-release rate ($G_{\max}$) (10^6 J/m^2).	---	5.5	---	5.8
Misfit-to-noise ratio	2.3	2.4	1.6	1.9

km^2, respectively. The surface location of the rupture-zone center is lat 37.07° N., long 121.83° W. The stress-drop components are $\Delta\tau_s=1.45$ MPa (along strike) and $\Delta\tau_d=1.35$ MPa (along dip), and the calculated geodetic moment is 2.5×10^{19} N-m. The maximum energy-release rate, which occurs near the top of the model fault, is about 5.5×10^6 J/m^2; the minimum energy-release rate is about 2.0×10^6 J/m^2. In general, the location of the maximum energy-release rate depends on the aspect ratio of the rupture zone and the ratio of the stress-drop components (Wu and others, 1991). The distribution of slip over the fault surface would be elliptical for uniform stress drop on a planar elliptical zone embedded within an infinite space. Here, within the elastic half-space, the slip distribution is approximately elliptical but is skewed toward the free surface. More specifically, the peak slip amplitude does not occur at the geometric center but at a distance from the center equal to a fourth of the half-width closer to the free surface. The average slip amplitudes in the strike and (reverse) dip direction, respectively, are $[\bar{u}_s]=1.3$ m and $[\bar{u}_d]=1.1$ m. The fit of the best model to the Geodolite/GPS data is listed in table 1, and the model parameters are compared with those of Lisowski and others (1990) in table 2. The misfit-to-noise ratio is 2.4, and the largest misfit occurs on line LP1–LP2 (table 1). As pointed out by Lisowski and others, this line probably was affected by local movements accompanying the widespread surface cracking and secondary faulting observed in the epicentral area (U.S. Geological Survey staff, 1990). The geodetic moment, dip, rupture area, and strike-slip and dip-slip amplitudes are close to those (2.8×10^{19} N-m, 70°, 492 km^2, 1.6 m, 1.2 m) obtained by Lisowski and others. Because our method is more computationally demanding than the conventional dislocation method, we tested the sensitivity of the model fit only approximately. Nevertheless, we found that the model fit can be degraded significantly for rupture zones with lengths ($2L$) less than 40 km, although greater lengths are permitted by the Geodolite/GPS data. In addition, the dip of the model fault can be varied between 70° and 75° without increasing the model misfit significantly.

The best-fitting model for the leveling data of Marshall and others (1991) corresponds to a moderately different fault geometry. Specifically, the strike, dip, depth to center, length, width, and area of the rupture zone are about 133°, 65°, 9.5 km, 40 km, 13 km, and 408 km^2, respectively. In addition, the surface location of the rupture-zone center (lat 37.06° N., long 121.88° W.) is about 2 km southwest of that in the Geodolite/GPS model. The rupture-zone area inferred here is slightly smaller than that inferred from the Geodolite/GPS data, but the alongstrike and alongdip stress-drop components, geodetic moment, and maximum energy-release rate are all slightly larger: $\Delta\tau_s$=1.7 MPa, $\Delta\tau_d$=1.95 MPa, M_0=2.8×10^{19} N-m, and G_{max}=5.8×10^6 J/m^2, respectively. The rupture-zone area is close to that (372 km^2) obtained by Marshall and others (1991). The average slip amplitudes in the strike and (reverse) dip directions, respectively, are $[\bar{u}_s]$=1.8 m and $[\bar{u}_d]$=1.5 m, and the misfit-to-noise ratio is 1.9. The fit of the best model to the leveling data is profiled in figure 3, and the model parameters are compared with those of Marshall and others in table 2. As shown in figure 3, the calculated elevation changes agree reasonably well with the observed data along the leveling lines (fig. 1*B*), but, similar to the result of Marshall and others, notable misfits occur in several places along some leveling lines. Approximate sensitivity tests suggest that the leveling data are more sensitive to the length of the rupture zone than are the Geodolite/GPS data. Specifically, the model fit to the leveling data can be degraded significantly for rupture-zone lengths greater than 44 and less than 34 km. The dip of the model fault here is about 5° greater than that obtained by Marshall and others, but decreasing the dip to 63° gives only a slightly larger misfit.

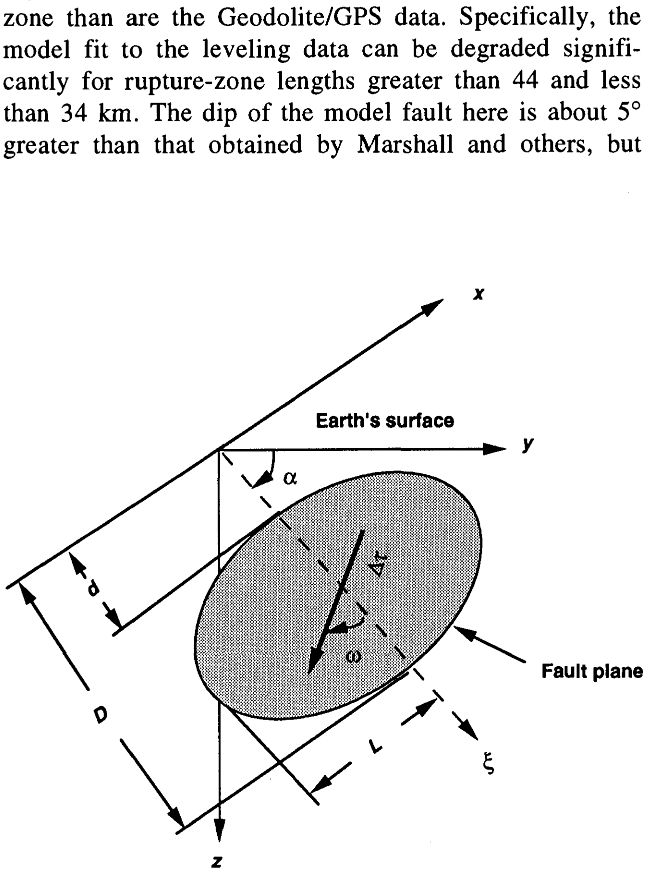

Figure 2.—Schematic sketch of rupture-zone model, showing a planar elliptical zone (shaded oval) embedded within an elastic half-space. *x*-*y* plane coincides with half-space surface, *x*-axis is parallel to strike of rupture zone and to semimajor axis of ellipse, and *z*-axis points downward into half-space. *x*-, *y*-, and *z*-axes are all orthogonal. ξ-axis, which is intersection of vertical *y*-*z* plane and slip plane, is parallel to minor axis of ellipse. α, angle between ξ- and *y*-axes; *d*, depth to top of rupture zone (along x direction); *D*, depth to bottom of rupture zone (along ξ direction); *L*, half-length of rupture zone. Orientation of stress drop Δτ is defined by angle ω measured from ξ direction; thus, vertical depth to top of rupture zone is *d*sin α, and width of rupture zone is *D*-*d*. Two stress-drop components along strike and dip directions are $\Delta\tau_s=\Delta\tau\sin\omega$ and $\Delta\tau_d=\Delta\tau\cos\omega$, respectively.

As found by Marshall and others (1991), if we use the parameters of the best-fitting Geodolite/GPS model to interpret the leveling data, the misfit-to-noise ratio increases to 3.4. Similarly, using the parameters of the best-fitting leveling model produces a misfit-to-noise ratio of 3.2 to the Geodolite/GPS data. If we combine these two data sets, the best-fitting model suggests a fault geometry somewhat between those for the two best-fitting models obtained from the Geodolite/GPS and leveling data. Specifically, the strike, dip, depth (to center), length, and width of the rupture zone are about 132°, 70°, 10.5 km, 42 km, and 13.5 km, respectively. However, then the misfit-to-noise ratio is 3.0, about 50 percent larger than the best-fitting Geodolite/GPS and leveling models.

The discrepancy between the two model fits indicates that our model does not capture fully the actual faulting behavior. Indeed, the aftershock locations of Dietz and Ellsworth (1990) suggest a kinked fault with a joint at about 6-km depth, rather than the simple planar surface we have assumed here. Future analysis of the mechanical behavior of a kinked rupture zone (of prescribed stress change) may lead to a better understanding of the ground-surface response to such a complex rupture. In addition, other modifications on the surface displacements may be introduced, owing to variations in stress drop and a nonelliptical shape of the rupture zone. Our model fits probably could be improved by allowing a nonuniform stress drop and shapes other than elliptical. However, because of the tradeoff between the stress-drop distribution and the configuration of the rupture zone, there is little point in doing so before additional constraints on the rupture-zone geometry are determined.

Although the long-term rates of horizontal and vertical displacement in the Loma Prieta region differ substantially, the inferred stress-drop components (and average slip components) along strike and dip are approximately equal. Because the long-term horizontal-displacement rates exceed the vertical rates by more than a factor of 10 in the San Francisco Bay region (Bradley and Griggs, 1976; Prescott and others, 1981; Hanks and others, 1984), stress drops along the strike directions might be expected to be much larger than those along the dip directions for rupture zones in this region. As pointed out by many investigators (for example, Anderson, 1990; Segall and Lisowski, 1990; Valensise and Ward, 1991), this result suggests that Loma Prieta-type events with subequal components of stress drop along strike and dip must be relatively infrequent.

The maximum energy-release rate for the 1989 Loma Prieta earthquake is toward the upper end of the range of the critical energy-release rate inferred for crustal faulting (Rudnicki, 1980; Li, 1987): from 10^0 to 10^8 J/m^2, with most values ranging from 10^5 to 10^8 J/m^2. This result is consistent with the inferred infrequency of a Loma Prieta-type event: High maximum energy-release rates suggest that the rupture propagated through relatively intact or largely rehealed rock. The recent study by Wu and others (1991) estimated critical values of 1.5×10^6 J/m^2 for the 1966 Parkfield, Calif. (M_s=5.6), 1.2×10^6 J/m^2 for the 1983 Borah Peak, Idaho (M_s=6.9), and 2×10^8 J/m^2 for the 1987 Whittier Narrows, Calif. (M_s=6.0), earthquakes. Among them, the critical value of 1.5×10^6 J/m^2 for the 1966 Parkfield earthquake is consistent with the 2.0×10^6 J/m^2 estimated by Beroza and Spudich (1988), using a dynamic rupture model, and with the 0.8×10^6 J/m^2 estimated by Aki (1978), using a barrier model for the same event. These values and the estimate for the 1989 Loma Prieta earthquake are about 100 times larger than those (of approx 10^4) inferred from slip experiments on sawcut laboratory specimens, as collected by Wong (1982, 1986), and those (ranging from 5×10^2 to 2×10^4 J/m^2) inferred from field observations of slip along small faults in granite rock, as reported by Martel and Pollard (1989). Currently available estimates of the critical energy-release rate for crustal faulting exhibit considerable variation, and further efforts in estimating their values and variation throughout the crust are needed to better understand the mechanism of earthquake faulting.

ACKNOWLEDGMENTS

This research was supported by U.S. Geological Survey grant 14–08–0001–G1847 and U.S. National Science Foundation grants EAR–8707392 and EAR–9105467. Thoughtful comments by Paul Spudich and the reviewers improved the manuscript. We thank Grant Marshall for checking our use of the data and pointing out a datum-shift error.

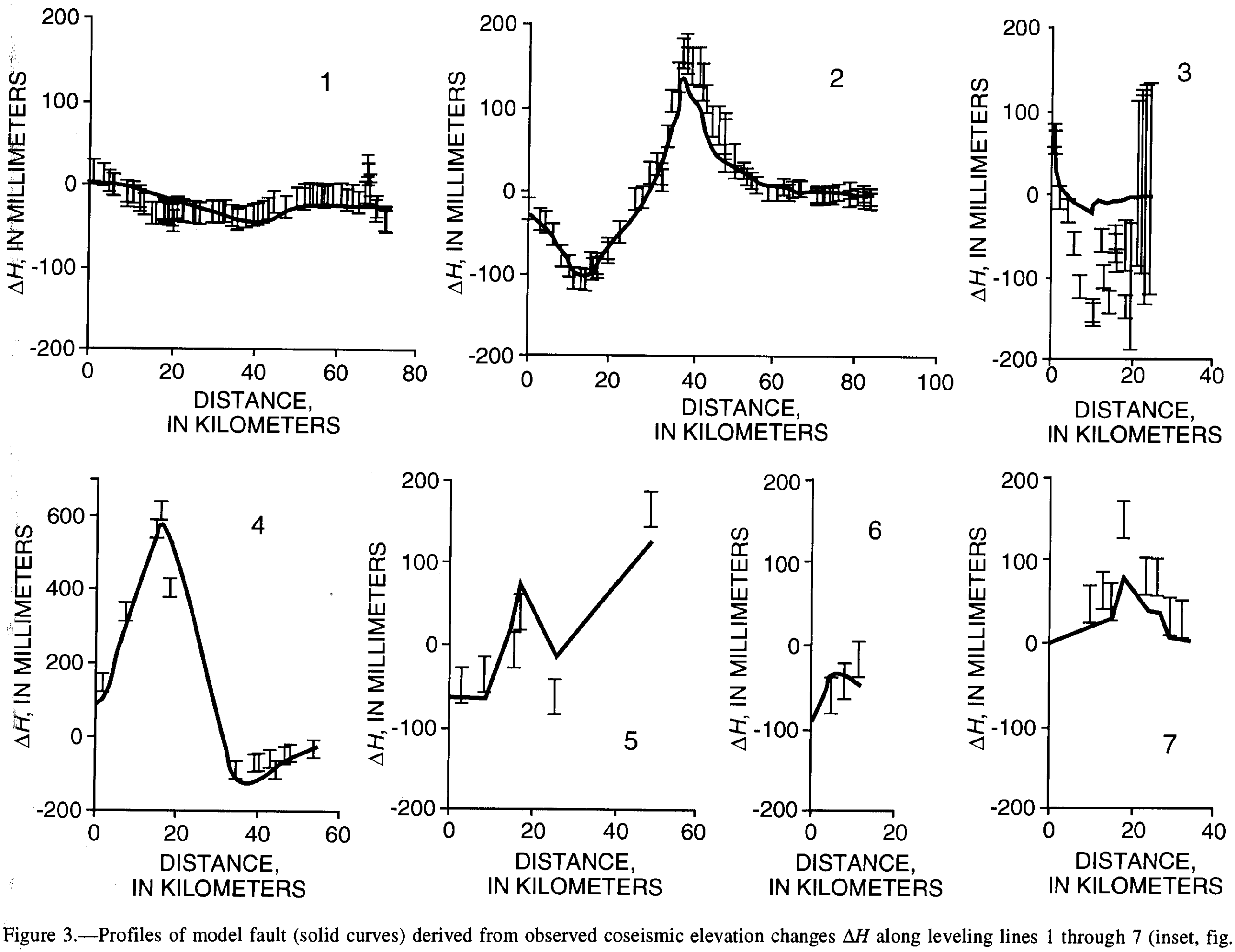

Figure 3.—Profiles of model fault (solid curves) derived from observed coseismic elevation changes ΔH along leveling lines 1 through 7 (inset, fig. 1*B*). Error bars indicate relative uncertainty in leveling data. Note that vertical scale for leveling line 4 is about twice as larger as that for other leveling lines.

REFERENCES CITED

Aki, Keiti, 1978, Origin of the seismic gap; what initiates and stops a rupture propagation along a plate boundary?, *in* Proceedings of Conference VI; Methodology for Identifying Seismic Gaps and Soon-to-Break Gaps: U.S. Geological Survey Open-File Report 78-943, p. 3–46.

Anderson, R.S., 1990, Evolution of the northern Santa Cruz Mountains by advection of crust past a San Andreas Fault bend: Science, v. 249, no. 4967, p. 397–401.

Behr, Jeffrey, Bilham, Roger, Bodin, Paul, Burford, R.O., and Bürgmann, Roland, Aseismic slip on the San Andreas fault south of Loma Prieta: Geophysical Research Letters, v. 17, no. 9, p. 1445–1448.

Beroza, G.C., and Spudich, Paul, 1988, Linearized inversion for fault rupture behavior; application to the 1984 Morgan Hill, California, earthquake: Journal of Geophysical Research, v. 93, no. B6, p. 6275–6296.

Bradley, W.C., and Griggs, G.B., 1976, Form, genesis, and deformation of central California wave-cut platforms: Geological Society of America Bulletin, v. 87, no. 3, p. 433–449.

Dietz, L.D., and Ellsworth, W.L., 1990, The October 17, 1989, Loma Prieta, California, earthquake and its aftershocks; geometry of the sequence from high-resolution locations: Geophysical Research Letters, v. 17, no. 9, p. 1417–1420.

Hanks, T.C., Bucknam, R.C., Lajoie, R.K., and Wallace, R.E., 1984, Modification of wave-cut and faulting-controlled landforms: Journal of Geophysical Research, v. 89, no. B7, p. 5771–5790.

Langbein, J.O., 1990, Post-seismic slip on the San Andreas Fault at the northwestern end of the 1989 Loma Prieta earthquake rupture zone: Geophysical Research Letters, v. 17, no. 8, p. 1223–1226.

Li, V.C., 1987, Mechanics of shear rupture applied to earthquake zones, *in* Atkinson, B.K., ed., Fracture mechanics of rock: London, Academic Press, p. 351–428.

Lisowski, Michael, Prescott, W.H., Savage, J.C., and Johnston, M.J.S., 1990, Geodetic estimate of coseismic slip during the 1989 Loma Prieta, California, earthquake: Geophysical Research Letters, v. 17, no. 9, p. 1437–1440.

Mansinha, Lalatendu, and Smylie, D.E., 1971, The displacement fields of inclined faults: Seismological Society of America Bulletin, v. 61, no. 5, p. 1433–1440.

Martel, S.J., and Pollard, D.D., 1989, Mechanics of slip and fracture along small faults and simple strike-slip fault zones in granitic rock: Journal of Geophysical Research, v. 94, no. B7, p. 9417–9428.

Marshall, G.A., Stein, R.S., and Thatcher, Wayne, 1991, Faulting geometry and slip from coseismic elevation changes; the 18 October 1989, Loma Prieta, California, earthquake: Seismological Society of America Bulletin, v. 81, no. 5, p. 1660–1693.

Olson, J.A., 1990, Seismicity in the twenty years preceding the Loma Prieta, California earthquake: Geophysical Research Letters, v. 17, no. 9, p. 1429–1432.

Prescott, W.H., Davis, J.L., and Svarc, J.L, 1989, Global Positioning System measurements for crustal deformation; precision and accuracy: Science, v. 244, no. 4910, p. 1337–1340.

Prescott, W.H., Lisowski, Michael, and Savage, J.C., 1981, Geodetic measurement of crustal deformation on the San Andreas, Hayward and Calaveras faults near San Francisco, California: Journal of Geophysical Research, v. 86, no. 11, p. 10853–10869.

Rice, J.R., 1968, Mathematical analysis in the mechanics of fracture, *in* Liebowitz, Harold, ed., Fracture; an advanced treatise: New York, Academic Press, p. 191–311.

———1980, The mechanics of earthquake rupture, *in* Dziewonski, A.M., and Boschi, Enzo, eds., Physics of the Earth's interior: Amsterdam, North Holland, p. 555–649.

———1983, Constitutive relations for fault slip and earthquake instabilities: Pure and Applied Geophysics, v. 121, no. 3, p. 444–475.

Rudnicki, J.W., 1980, Fracture mechanics applied to the Earth's crust: Annual Review of Earth and Planetary Science, v. 8, p. 489–525.

Savage, J.C., and Prescott, W.H., 1973, Precision of Geodolite distance measurements for determining fault movements: Journal of Geophysical Research, v. 78, no. 26, p. 6001–6007.

Segall, Paul, and Lisowski, Michael, 1990, Surface displacements in the 1906 San Francisco and 1989 Loma Prieta earthquakes: Science, v. 250, no. 4983, p. 1241–1244.

Schwartz, S.Y., Orange, D.L., and Anderson, R.S., 1990, Complex fault interactions in a restraining bend on the San Andreas fault, southern Santa Cruz Mountains, California: Geophysical Research Letters, v. 17, no. 8, p. 1207–1210.

U.S. Geological Survey staff, 1990, The Loma Prieta, California, earthquake; an anticipated event: Science, v. 247, no. 4940, p. 286–293.

Valensise, Gianluca, and Ward, S.N., 1991, Long-term uplift of the Santa Cruz coastline in response to repeated earthquakes along the San Andreas Fault: Seismological Society of America Bulletin, v. 81, no. 5, p. 1694–1704.

Wong, Teng-fong, 1982, Shear fracture energy of Westerly Granite from post-failure behavior: Journal of Geophysical Research, v. 87, no. B2, p. 990–1000.

———1986, On the normal stress dependence of the shear fracture energy, *in* Das, Shamita, Boatwright, John, and Scholz, C.H., eds., Earthquake source mechanics: American Geophysical Union Geophysical Monograph 37, p. 1–11.

Wu, Mingdong, Rudnicki, J.W., Kuo, C.H., and Keer, L.M., 1991, Surface deformation and energy release rates for constant stress drop slip zones in an elastic half-space: Journal of Geophysical Research, v. 96, no. 10, p. 16509–16524.

☆ U.S. GOVERNMENT PRINTING OFFICE: 1997 - 573-046 / 20064 REGION NO. 8